



NASA CR-159,869



NASA CR-159869

R80AEG369

NASA-CR-159869
19810009323

AERODYNAMIC/ACOUSTIC PERFORMANCE OF YJ101/DOUBLE BYPASS VCE WITH COANNULAR PLUG NOZZLE

Final Report

January 1981

VCE COMPONENT TEST PROGRAM EXHIBIT B

For

NATIONAL AERONAUTICS AND SPACE ADMINISTRATION
LEWIS RESEARCH CENTER
21000 BROOKPARK ROAD
CLEVELAND, OHIO 44135

LIBRARY COPY

MAR 5 1981

LEWIS RESEARCH CENTER
LIBRARY, NASA
HAMPTON, VIRGINIA

Contract NAS3-20582

GENERAL  ELECTRIC

Aircraft Engine Business Group
Technology Programs and
Performance Technology Department
Cincinnati, Ohio 45215



1. Report No. NASA CR-159869	2. Government Accession No.	3. Recipient's Catalog No.	
4. Title and Subtitle Aerodynamic/Acoustic Performance of YJ101/Double Bypass VCE With Coannular Plug Nozzle		5. Report Date January 1981	6. Performing Organization Code
		8. Performing Organization Report No. R80AEG369	
7. Author(s) John W. Vdoviak, Paul R. Knott, Jon J. Ebacker		10. Work Unit No.	
9. Performing Organization Name and Address General Electric Company Aircraft Engine Business Group Cincinnati, Ohio 45215		11. Contract or Grant No. NAS3-20582 Exhibit B	
		13. Type of Report and Period Covered Final Report	
12. Sponsoring Agency Name and Address National Aeronautics and Space Administration Washington, D.C. 20546		14. Sponsoring Agency Code	
		15. Supplementary Notes Project Manager, A.G. Powers, NASA-Lewis Research Center, 21000 Brookpark Road, Cleveland, Ohio 44135	
16. Abstract This report incorporates the results of a forward Variable Area Bypass Injector (VABI) test and a Coannular Nozzle test performed on a YJ101 Double Bypass Variable Cycle Engine. These components are intended for use on a Variable Cycle Engine being studied under the Supersonic Cruise Research Program. Both tests accomplished all objectives. The forward Variable Area Bypass Injector test demonstrated the mode shifting capability between single and double bypass operation with less than predicted aerodynamic losses in the bypass duct. The acoustic nozzle test demonstrated that coannular noise suppression was between 4 and 6 PNdB in the aft quadrant. The YJ101 VCE equipped with the forward VABI and the coannular exhaust nozzle performed as predicted with exhaust system aerodynamic losses lower than predicted both in single and double bypass modes. Extensive acoustic data were collected including far field, near field, sound separation/internal probe measurements and Laser Velocimeter traverses.			
17. Key Words (Suggested by Author(s)) Acoustic Test YJ101 VCE VCE Inverted Profile VABI Coannular Nozzle		18. Distribution Statement Unclassified - Unlimited	
19. Security Classif. (of this report) Unclassified	20. Security Classif. (of this page) Unclassified	21. No. of Pages 292	22. Price*

* For sale by the National Technical Information Service, Springfield, Virginia 22151



ACKNOWLEDGEMENTS

The authors wish to acknowledge the valuable contributions made by several General Electric personnel:

Mr. John F. Brausch for key contributions to the acoustic test and facility planning, testing activities, and with the analysis of many of the acoustic test results.

Dr. P.K. Bhutiani for preparing and analyzing the engine data/component noise prediction comparisons, and the projections of static full scale engine data to flight.

Dr. R.K. Majjigi for his analysis of the engine coannular plug nozzle laser velocimeter test measurements and the comparison of model scale and engine velocity field information.

Mr. V.L. Doyle who was responsible for the analysis of the core noise and sideline traverse acoustic measurements.

Mr. Walt Minzner who was responsible for the planning and carrying out the acoustic data acquisition, data merging and reduction of the acoustic test results.

Messrs. R. Whittaker and C. Wagenknecht for direct contribution to the design and evaluation of the nozzle aerodynamic performance.

Messrs. R. Piredda, and R. Wilford who were the engine operator, and engine vibration specialists respectively. And to the many General Electric Edwards Flight Test Center personnel, headed by J. Kirkpatrick, without whose unique engine test expertise and enthusiasm, the reported tests would not have been accomplished.

Additionally, the authors wish to express their appreciation to Messrs. A. Powers, J. Stone, O. Gutierrez, H. Wesoky and J. Whitlow of the NASA-Lewis Research Center for their high interest and encouragement in the work accomplished, and to the Boeing Company for their collaboration regarding the high/low microphone arrangement and the spectral merging for this two-microphone system.

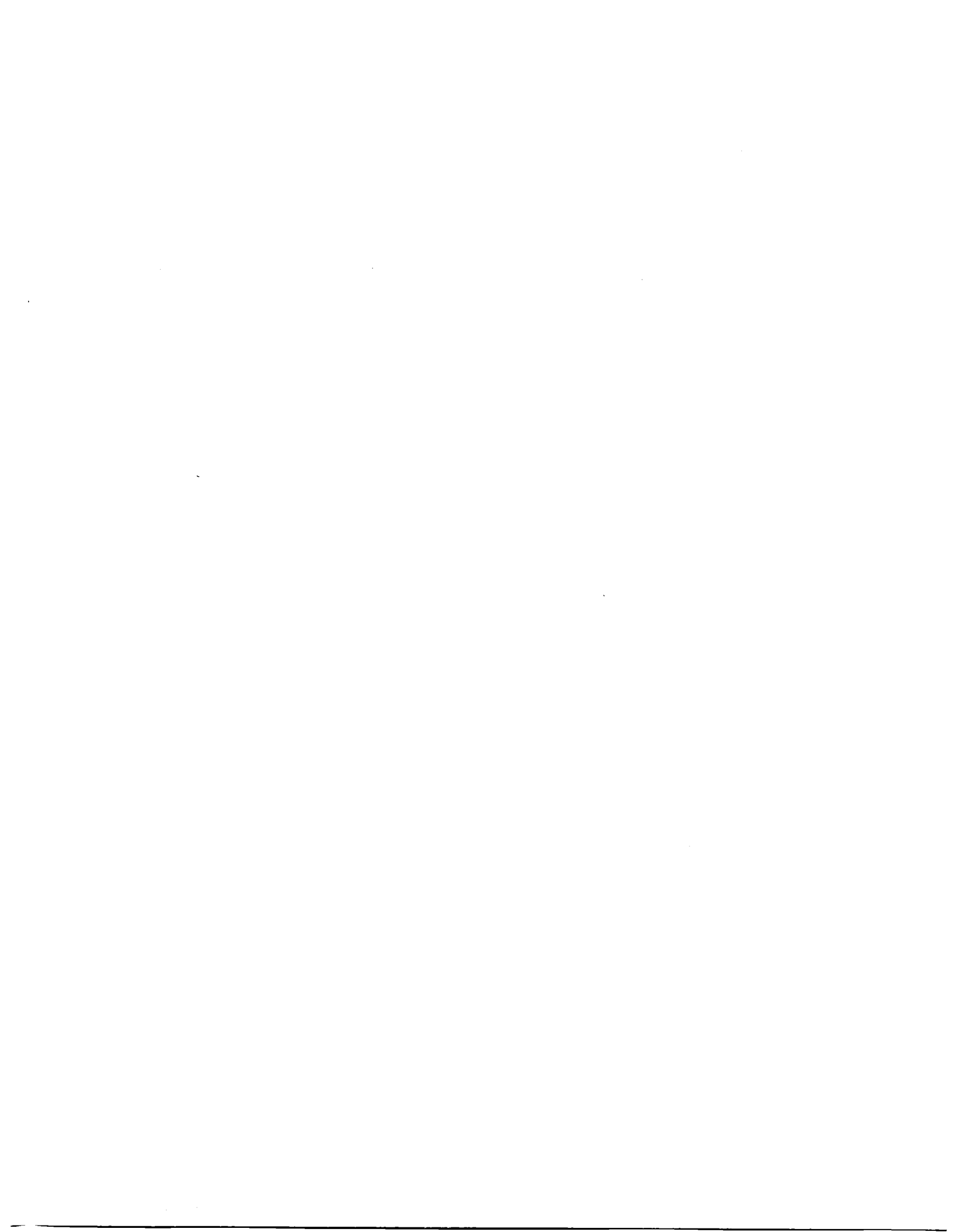


TABLE OF CONTENTS

<u>Section</u>	<u>Page</u>
1.0 SUMMARY	1
2.0 INTRODUCTION	3
3.0 DESIGN	6
3.1 Variable Cycle Engine (VCE) Description	6
3.2 Split Fan Description	11
3.3 Forward Variable Area Bypass Injector (VABI)	12
3.4 Variable Area Low Pressure Turbine Nozzle (VATN)	14
3.5 Rear Variable Area Bypass Injector for Forward VABI Test	14
3.6 Coannular Nozzle and Associated Rear VABI	17
3.7 Control System	20
3.7.1 Forward VABI Test Control System	20
3.7.2 Acoustic Nozzle Test Control System	23
4.0 FORWARD VABI TEST	27
4.1 Test Objectives	27
4.2 Test Description	27
4.3 Test Results	30
4.3.1 Summary of Results	30
4.3.2 Engine Performance	32
4.3.2.1 Overall Performance	32
4.3.2.2 Transitioning	32
4.3.2.3 Distortion	41
4.3.3 Forward VABI Aero Performance	41
5.0 ACOUSTIC TEST OF THE COANNULAR PLUG NOZZLE	46
5.1 Acoustic Nozzle Test Objectives	46
5.2 Test Results	47
5.2.1 Test Summary	47
5.2.2 Summary of Results	53
5.3 Test Facility Description and Data Reduction Procedures	56
5.3.1 Edwards Air Force Base Test Facility	56
5.3.1.1 Test Site	56
5.3.1.2 Sound Field	57
5.3.1.3 Microphone Arrangement	57
5.3.1.4 Special Measurement Systems	60
5.3.1.5 Description of Engine Performance and Nozzle Aerodynamic Instrumentation Setups	64

TABLE OF CONTENTS (Continued)

<u>Section</u>	<u>Page</u>
5.3.2 Acoustic Data Acquisition and Reduction Procedures	64
5.3.2.1 Acoustic Data Acquisition and Reduction Systems	68
5.3.2.2 Spectral Merging for the Two Microphone System	69
5.3.2.3 Acoustic Data Confidence	70
5.3.3 Engine and Nozzle Aerodynamic Performance Data Acquisition and Reduction	72
5.4 Acoustic Test Configurations and Test Scope	74
5.4.1 Test Configurations	74
5.4.2 Test Scope	84
5.5 Acoustic Test Results	86
5.5.1 Verification of Coannular Plug Nozzle Jet Exhaust Noise Reduction	87
5.5.1.1 General Results	87
5.5.1.2 Influence of Radius Ratio on Coannular Plug Nozzle Jet Noise Reduction	96
5.5.1.3 Influence of Area Ratio on Coannular Plug Nozzle Jet Noise Reduction	96
5.5.1.4 Influence of Outer Stream Nozzle Exit Termination	102
5.5.1.5 Influence of Aft VABI Sideplate on the Coannular Plug Nozzle Jet Noise	113
5.5.1.6 Influences of Engine Cycle Parameters on Coannular Plug Nozzle Exhaust Noise Reduction	117
5.5.2 Acoustic Scaling	125
5.5.2.1 Conic Nozzle Results	125
5.5.2.2 Coannular Plug Nozzle Scaling	130
5.5.2.3 Summary of Observations	130
5.5.3 Fan Inlet Noise and Treated Inlet Effectiveness	130
5.5.3.1 Fan Inlet Noise	134
5.5.3.2 Treated Inlet Effectiveness	138
5.5.3.3 Summary of Observations	150
5.5.4 Core Noise and Sideline Traverse Measurements	151
5.5.4.1 Core Noise Results	151
5.5.4.2 Sideline Traverse Results	158
5.5.5 Laser Velocimeter Measurements	168

TABLE OF CONTENTS (Concluded)

<u>Section</u>	<u>Page</u>
5.5.5.1 Conic Nozzle Test Results	168
5.5.5.1.1 Near Sonic Conic Jet	168
5.5.5.1.2 Supersonic Conic Jet	168
5.5.5.1.3 Comparison of Engine and Model scale Test Results	174
5.5.5.2 Coannular Plug Nozzle Test Results	174
5.5.5.2.1 Coannular Nozzle with $A_T^i = 0.2$, $R_r = 0.853$	174
5.5.5.2.2 Comparison of Engine and Model Scale Test Results	181
5.5.5.3 Summary of Observations	181
5.5.6 Engine Data Noise/Prediction Comparisons	186
5.5.6.1 Methodology of Predictions	186
5.5.6.2 Illustration of Engine Component Noise Breakdown and Comparison with Predictions	188
5.5.7 Projection of Static Full-Scale Engine Data to Flight	220
5.5.7.1 Methodology Used for Product Engine Jet Noise Flight Projections	220
5.5.7.2 Discussion of Results	222
5.6 Engine and Acoustic Nozzle Performance	232
5.6.1 Engine and Nozzle Performance Summary	232
5.6.2 Engine and Nozzle Performance Results	232
5.6.2.1 Engine Performance	232
5.6.2.2 Nozzle Delivery Conditions and Overall Performance Effects	254
5.6.3 Rear VABI Aero Performance	254
5.6.4 Nozzle Aerodynamic Performance	266
6.0 SUMMARY OF RESULTS, CONCLUSIONS AND RECOMMENDATIONS	276
6.1 Summary of Results	276
6.2 Conclusions and Recommendations	277
SYMBOLS AND ABBREVIATIONS	279
REFERENCES	287



LIST OF ILLUSTRATIONS

<u>Figure</u>	<u>Page</u>
1. YJ101 VCE Concept Demonstrators.	4
2(a). NASA Forward Variable Area Bypass Injector VCE/YJ101 Test Configuration.	7
2(b). Schematic Cross-Section of NASA Front VABI Test Configuration.	8
3(a). NASA Coannular Acoustic Nozzle Test Configuration.	9
3(b). Schematic Cross-Section of NASA Coannular Acoustic Nozzle Test Configuration.	10
4. Modulation Valve (Inner Bypass) and Inner Fairing.	13
5. Forward Variable Area Bypass Injector.	15
6. YJ101/VCE Rear VABI Configuration Used in Forward VABI Test.	16
7. Rear VABI Assembly.	18
8. Schematic of Rear VABI/Acoustic Nozzle Used in Edwards Aeroacoustic Test.	19
9. Acoustic Nozzle Assembly.	21
10. Schematic of Baseline Fixed Conic Nozzle.	22
11. Forward VABI Fan Speed and Variable Geometry Control.	24
12. Fan Speed and Variable-Geometry Control for Acoustic Nozzle.	25
13. Forward VABI Engine Installed in Test Cell (Forward Looking Aft).	28
14. Forward VABI Engine Installed in Test Cell (Aft Looking Forward).	29
15. YJ101/VCE Schematic and Instrumentation Plane Definition.	33
16. 2x1 Forward VABI Performance.	34
17. SFC Versus Airflow at 50% Gross Thrust.	35

LIST OF ILLUSTRATIONS (Continued)

<u>Figure</u>		<u>Page</u>
18.	Transition Mapping - 95% Fan Speed.	36
19.	Transition Mapping - 90% Fan Speed.	37
20.	Transition Mapping - 80% Fan Speed.	38
21.	95% NL Transition.	39
22.	95% NL Integrated Transition with Raised Rear Block Operating Line.	40
23.	Distortion Screens for Forward VABI Testing.	42
24.	Bypass Stream Losses Resulting from NASA Forward VABI Engine Test.	44
25.	NASA Forward VABI Engine Test Results at Several Key SCAR Mission Throttle Conditions.	45
26.	GE/Edwards Air Force Base North Test Site.	48
27.	Edwards Acoustic Test Site Showing Microphone Setup.	49
28.	Engine Mounting Arrangement with Baseline Conic Mixed Flow Nozzle and Standard Untreated YJ101 Bellmouth Inlet with Protective Screen.	50
29.	Coannular Plug Nozzle, $A_r^i = 0$, $R_r^o = 0.853$.	51
30.	Early Acoustic Test Vehicle with Treated J79 Bellmouth Inlet and Coannular Exhaust Nozzle; Traversing Microphone System Installed.	52
31.	Early Acoustic Test Vehicle with Laser Velocimeter.	54
32.	Illustration of Sound Field Layout.	58
33.	Illustration of Microphone Setup.	59
34.	Laser Velocimeter System Application to the YJ101 Test Program.	61
35.	Sideline Traversing Microphone System Application to the YJ101 Test Program.	63

LIST OF ILLUSTRATIONS (Continued)

<u>Figure</u>		<u>Page</u>
36.	Kulite Instrumentation on YJ101/VCE Coannular and Conic Nozzle Configurations.	65
37.	Illustration of Spectral Merging.	71
38.	Data Acquisition System.	73
39.	Schematic of YJ101 and J79 Inlets/Conical Exhaust Nozzle for YJ101 Test Program.	75
40.	J79 Treated Inlet/YJ101 Engine/Conical Nozzle at GE-Edwards AFB North Test Site.	76
41.	Schematic of Acoustically Treated Inlet.	78
42.	Conical Nozzle.	79
43.	$R_r^o = 0.853$ Convergent-Divergent and $R_r^o = 0.853$ Convergent Outer Annular Nozzle Systems.	80
44.	$R_r^o = 0.816$ Convergent-Divergent Outer Annular Nozzle System.	81
45.	$R_r^o = 0.875$ Convergent-Divergent Outer Annular Nozzle System.	82
46.	$R_r^o = 0.853$ Convergent-Divergent Outer Annular Nozzle System with $A^i/A^o = 0.2$ Setting of the Inner Annular Nozzle.	83
47.	Verification of Coannular Plug Nozzle Engine Jet Noise Reduction for a Typical FAR 36 (1969) Sideline Acoustic Range at Peak Aft Angle.	88
48.	Verification of Coannular Plug Nozzle Engine Shock Noise Reduction.	89
49.	Verification of Coannular Plug Nozzle Engine Jet Noise Reduction for a Typical FAR 36 (1978) Sideline Acoustic Range.	92
50.	Verification of Coannular Plug Nozzle Engine Shock Noise Reduction for a Typical FAR 36 (1978) Sideline Acoustic Range.	93

LIST OF ILLUSTRATIONS (Continued)

<u>Figure</u>		<u>Page</u>
51.	Typical Engine PNL Directivity Characteristics - Conical and Coannular Plug Nozzle.	94
52.	Typical Engine Spectra Characteristics - Conical and Coannular Plug Nozzle.	95
53.	Influence of Radius Ratio on Jet Noise.	97
54.	Influence of Outer Nozzle Radius Ratio on Coannular Nozzle Noise Spectra Characteristics.	98
55.	Influence of Outer Nozzle Radius Ratio on Coannular Plug Nozzle PNL Directivity.	99
56.	Influence of Area Ratio on Peak Noise for Coannular Plug Nozzles.	101
57.	Area Ratio Effects on Coannular Plug Nozzle Jet Noise Reduction - $\theta_i = 90^\circ$.	103
58.	Influence of Area Ratio Variation on Coannular Plug Nozzle Spectra - $V_j \sim 701$ m/sec (2300 ft/sec)	104
59.	Influence of Area Ratio Variation on Coannular Plug Nozzle Spectra - $V_j \sim 646$ m/sec (2120 ft/sec)	105
60.	Influence of Area Ratio Variation on Coannular Plug Nozzle Spectra - $V_j \sim 441$ m/sec (1447 ft/sec)	106
61.	Influence of Outer Nozzle Termination on Coannular Plug Nozzle, Jet Peak Perceived Noise.	107
62.	Influence of Outer Stream Nozzle Termination on Coannular Plug Nozzle, Jet Perceived Noise at $\theta_i = 90^\circ$.	108
63.	Influence of Outer Stream Nozzle Termination on Coannular Plug Nozzle Shock Noise at $\theta_i = 50^\circ$.	109
64.	Influence of Outer Stream Nozzle Termination on Coannular Plug Nozzle Spectral Characteristics Near Design Point P_r^o .	111
65.	Influence of Outer Stream Nozzle Termination on Coannular Plug Nozzle Spectral Characteristics at Subsonic Conditions in Both Streams.	112

LIST OF ILLUSTRATIONS (Continued)

<u>Figure</u>		<u>Page</u>
66.	Influence of Aft VABI Sideplates on Coannular Plug Nozzle Jet Noise a) Normalized Peak Noise PNL b) Normalized PNL at $\theta_i = 90^\circ$.	114
67.	Influence of Aft VABI Sideplates on Coannular Plug Nozzle Spectral Characteristics at $V_j^{\text{mix}} = 443$ m/sec (1452 ft/sec).	115
68.	Influence of Aft VABI Sideplates on Coannular Plug Nozzle Spectral Characteristics at $V_j^{\text{mix}} = 333$ m/sec (1095 ft/sec).	116
69.	Inner to Outer Stream Velocity Variation with Specific Thrust for the Coannular Plug Nozzles Tested.	118
70.	Comparisons of Normalized PNL for Single Bypass and Double Bypass Engine Operation a) Normalized Peak PNL b) Normalized PNL at $\theta_i = 90^\circ$.	119
71.	PNL Directivity Comparison Between Single and Double Bypass Engine Operation at the Same Specific Thrust.	121
72.	Spectra Comparisons Between Single and Double Bypass Engine Operation at the Same Specific Thrust.	122
73.	Effect of Velocity Ratio Variation on the Normalized Peak PNL.	123
74.	Comparison of the Measured and Predicted Variation of Normalized Peak PNL Versus $10 \log_{10} (v_j^{\text{mix}}/a_0)$.	124
75.	Conic Nozzle Peak PNL Acoustic Scaling Comparisons.	126
76.	Conic Nozzle YJ101 Engine/Model Scale PNL Directivity Comparison.	127
77.	Conic Nozzle YJ101 Engine/Model Scale Spectral Comparisons; $V_j = 663.55$ m/sec (2177 ft/sec).	128
78.	Conic Nozzle YJ101 Engine/Model Scale Spectral Comparisons; $V_j = 732.59$ m/sec (2403 ft/sec).	129
79.	Coannular Plug Nozzle Peak PNL Acoustic Scaling Comparison.	131
80.	Coannular Plug Nozzle Directivity Acoustic Scaling Comparison.	132

LIST OF ILLUSTRATIONS (Continued)

<u>Figure</u>		<u>Page</u>
81.	Coannular Plug Nozzle Scaling.	133
82.	Fan Inlet Turbomachinery Noise, YJ101 Data Relative to Previous Sources (a) Standardized Fan Inlet Turbomachinery Noise Prediction Curve (b) YJ101 Data Comparison to Standardized Prediction Curve.	136
83.	Spectra at $\theta_i = 50^\circ$ for Fan Inlet Turbomachinery Noise Identification.]37
84.	YJ101 Narrow Band Spectrum for Rdg 67 at $\theta_i = 30^\circ$.	139
85.	YJ101 Narrow Band Spectrum for Rdg 67 at $\theta_i = 50^\circ$.	139
86.	YJ101 Narrow Band Spectrum for Rdg 67 at $\theta_i = 90^\circ$.	140
87.	YJ101 Narrow Band Spectrum for Rdg 67 at $\theta_i = 140^\circ$.	140
88.	Effectiveness of Treated Inlet on Perceived Noise Level Reduction.	142
89.	Comparison of Treated to Untreated Inlet, OASPL Directivity, 65-90 Percent Corrected Fan Speed.	143
90.	Comparison of Treated to Untreated Inlet, PNL Directivity, 65-90 Percent Corrected Fan Speed.	144
91.	Spectral Comparison of Treated Versus Untreated Inlet at $\theta_i = 30^\circ$.	146
92.	Spectral Comparison of Treated Versus Untreated Inlet at $\theta_i = 50^\circ$.	147
93.	Spectral Comparison of Treated Versus Untreated Inlet at $\theta_i = 90^\circ$.	148
94.	Spectral Comparison of Treated Versus Untreated Inlet at $\theta_i = 140^\circ$.	149
95.	VCE Core Probe for Conic Nozzle Immersion 3; Fan Speed of 65 Percent.	152
96.	Internal-to-Far Field Cross-Correlation Results for the Conic Nozzle at 65 Percent Fan Speed.	153

LIST OF ILLUSTRATIONS (Continued)

<u>Figure</u>		<u>Page</u>
97.	Internal to Far Field Coherent Spectra Results for Un-suppressed Conic Nozzle at 65 Percent Fan Speed.	154
98.	Internal to Far Field Noise Survey at 65 Percent Speed from Core Exhaust to 120° Microphone.	156
99.	Internal to Far Field Noise Survey at 65 Percent Speed from Fan Exhaust to 120° Microphone.	157
100.	Narrow Band Spectrum from YJ101/VCE Internal Acoustic Sensor.	159
101.	Narrow Band Spectrum from YJ101 AST/VCE Acoustic Far Field Microphone.	159
102.	Magnitude of Correlation Coefficient Versus Acoustic Angle for Coannular Nozzle.	160
103.	Peak Angle Distributions for Far Field and Traverse Microphones.	162
104.	Source Location Effect on Noise Radiation Angles.	163
105.	Source Location for YJ101/VCE Unsuppressed Conic Nozzle.	164
106.	Source Location for YJ101/VCE $0.853 R_T^O$ Coannular Nozzle.	165
107.	Strouhal Distribution of Peak Noise Source Locations and Far Field Radiation Angles for J79 and YJ101/VCE Conic Nozzles, $V_j = 518$ m/sec (1700 fps).	166
108.	Strouhal Number Distribution as a Function of Peak Noise Source Locations at $V_j^{mix} = 518$ m/sec (1700 ft/sec) for Conic and Coannular Plug Nozzles.	167
109.	Laser Velocimeter Measured Mean and Turbulent Velocities at Two Radial Locations for a Near Sonic YJ101 Engine Conic Nozzle.	169
110.	Conic Nozzle Exit Plane Mean and Turbulence Velocity Profiles.	170
111.	Chordwise Traverse at $X/D = 0.6$.	171

LIST OF ILLUSTRATIONS (Continued)

<u>Figure</u>		<u>Page</u>
112.	Influence of Rear VABI Chutes on Mean and Turbulent Velocity Profiles with Conic Nozzle, as Determined by LV Measurements.	172
113.	Laser Velocimeter Measured Mean and Turbulent Velocities at Two Radial Locations for a Supersonic Conic Nozzle.	173
114.	Comparison of Measured Mean and Turbulent Velocities for YJ101 Engine and Scale Model Conic Nozzles.	175
115.	Comparison of Measured Mean and Turbulent Velocities for YJ101 and Scale Model Conic Nozzles.	176
116.	Comparison of Measured Mean and Turbulent Velocities for YJ101 Engine and Model Scale Conic Nozzles.	177
117.	Normalized Mean Velocity Variation at Four Radial Locations.	178
118.	N-S Traverse of the Jet at $X/D_{eq} = 1.1$.	179
119.	Laser Velocimeter Measured Radial Velocity Profiles at $X/D_{eq} = 5$ in Two Mutually Perpendicular Directions (VABI Open).	180
120.	Laser Velocimeter Measured Radial Velocity Profiles at $X/D_{eq} = 5$ in Two Mutually Perpendicular Directions (VABI Closed).	182
121.	Influence of Flow Struts on Mean and Turbulent Velocity Profiles.	183
122.	Influence of Chutes on Mean Velocity and Turbulent Velocity Profiles.	184
123.	Comparison of Measured Mean Velocity of Two Radial Locations for YJ101 Engine and Model Coannular Plug Nozzles.	185
124.	Comparison of the Measured YJ101 Coannular Plug Nozzle Engine OASPL Directivity with that Predicted for Jet Mixing and Shock Noise.	189
125.	Comparison of the Predicted Jet Mixing and Shock Sound Pressure Spectra with the Measured Coannular Plug Nozzle Engine Data at $V_j^{mix} = 713.8$ m/sec (2342 ft/sec), a Typical Takeoff Condition.	191

LIST OF ILLUSTRATIONS (Continued)

<u>Figure</u>		<u>Page</u>
126.	Comparison of the Predicted Jet Mixing and Shock Sound Pressure Spectra with the Measured Coannular Plug Nozzle Engine Data at $V_j^{mix} = 507.8$ m/sec (1666 ft/sec), a Typical Takeoff Cutback Condition.	192
127.	Comparison of the Predicted Jet Mixing Sound Pressure Spectra with the Measured Coannular Plug Nozzle Engine Data at $V_j^{mix} = 368.2$ m/sec (1208 ft/sec), a Typical Approach Condition.	193
128.	Comparison of the Measured and Predicted Variation of Normalized PNL at $A_r^i = 0.1$.	194
129.	Comparison of the Measured and Predicted Variation of Normalized PNL at $A_r^i = 0.2$.	195
130.	Comparison of the Measured and Predicted Variation of Normalized PNL at $A_r^i = 0.475$.	196
131.	Comparison of the Measured and Predicted Variation of Normalized PNL at $R_r^o = 0.816$.	197
132.	Comparison of the Measured and Predicted Variation of Normalized PNL at $R_r^o = 0.853$.	198
133.	Comparison of the Measured and Predicted Variation of Normalized PNL at $R_r^o = 0.875$.	199
134.	Comparison of the Measured Engine OASPL Directivity with the Predicted Fan Inlet and Exhaust Noise.	201
135.	Comparison of the Measured Engine Spectra with the Predicted Fan Noise Spectra at $V_j^{mix} = 713.8$ m/sec (2342 ft/sec).	202
136.	Comparison of the Measured Engine Spectra with the Predicted Fan Noise Spectra at $V_j^{mix} = 507.8$ m/sec (1666 ft/sec).	203
137.	Comparison of the Measured Engine Spectra with the Predicted Fan Noise Spectra at $V_j^{mix} = 368.2$ m/sec (1208 ft/sec).	204
138.	Narrow Band Analysis of the Measured YJ101 Coannular Plug Engine Data Showing Humps in the 5 kHz - 20 kHz 1/3 Octave Bands.	205

LIST OF ILLUSTRATIONS (Continued)

<u>Figure</u>		<u>Page</u>
139.	Narrow Band Analysis of the Measured YJ101 Coannular Plug Engine Data Showing Humps in the 5 kHz - 20 kHz 1/3 Octave Bands.	206
140.	Comparison of the Measured Engine OASPL Directivity with the Predicted Turbine Noise.	208
141.	Comparison of the Measured Engine SPL Spectra with the Predicted Turbine Noise Spectra at Test Point 330.	209
142.	Comparison of the Measured Engine SPL Spectra with the Predicted Turbine Noise Spectra at Test Point 324.	210
143.	Comparison of the Measured Engine SPL Spectra with the Predicted Turbine Noise Spectra at Test Point 288.	211
144.	Comparison of the Measured Coannular Plug Nozzle Engine OASPL Directivity with the Predicted Core Noise.	212
145.	Comparison of the Measured Coannular Nozzle Engine Spectra with the Predicted Core Noise Spectra at Test Point 330.	213
146.	Comparison of the Measured Coannular Nozzle Engine Spectra with the Predicted Core Noise Spectra for Test Point 324.	214
147.	Comparison of the Measured Coannular Nozzle Engine Spectra with the Predicted Core Noise Spectra for Test Point 288.	215
148.	Comparison of the Measured Coannular Nozzle Engine OASPL Directivity with that Predicted for Strut Noise.	216
149.	Comparison of the Measured Coannular Nozzle Engine Spectra with Predicted Strut Noise Spectra at Test Point 330.	217
150.	Comparison of the Measured Coannular Nozzle Engine OASPL Directivity with That Predicted for Strut Noise at Test Point 324.	218
151.	Comparison of the Measured Coannular Nozzle Engine Spectra with Predicted Strut Noise Spectra at Test Point 288.	219
152.	Variation of the Flight Effects Index, $m(\theta_i)$, for Several Proposed Flight Simulation Models.	223

LIST OF ILLUSTRATIONS (Continued)

<u>Figure</u>		<u>Page</u>
153.	Variation of Projected Flight PNL for Several Flight Effects Methods for a Typical Sideline Noise Condition at $V_j^{\text{mix}} = 692$ m/sec (2272) ft/sec).	225
154.	Variation of Projected Flight PNL for Several Flight Effects Methods for a Typical Sideline Noise Condition at $V_j^{\text{mix}} = 639.5$ m/sec (2098 ft/sec).	226
155.	Variation of Projected Flight PNL for Several Flight Effects Methods for a Typical Cutback Noise Condition.	228
156.	Variation in Projected Flight PNL for Several Flight Effects Methods for a Typical Approach Noise Condition.	229
157.	Total Inlet Corrected Airflow Versus Front Block Corrected Speed.	233
158.	Front Block Pressure Ratio Versus Total Inlet Corrected Airflow.	235
159.	Rear Block Corrected Airflow Versus Rear Block Corrected Speed.	237
160.	Rear Block Pressure Ratio Versus Rear Block Corrected Airflow.	239
161.	HP Compressor Corrected Airflow Versus HP Compressor Corrected Speed.	241
162.	HP Compressor Pressure Ratio Versus HP Compressor Corrected Airflow.	243
163.	Engine Pressure Ratio Versus Overall Fuel to Air Ratio.	245
164.	Overall Bypass Ratio Versus Total Inlet Corrected Airflow.	246
165.	Overall Bypass Ratio Versus Corrected Ideal Thrust.	248
166.	Corrected Ideal sfc Versus Corrected Ideal Thrust.	250
167.	Exhaust System Pressure Loss Versus Tailpipe Mach Number.	252

LIST OF ILLUSTRATIONS (Continued)

<u>Figure</u>		<u>Page</u>
168.	Mixed Nozzle Pressure Ratio Versus Total Inlet Corrected Airflow.	255
169.	Mixed Nozzle Corrected Ideal Velocity Versus Total Inlet Corrected Airflow.	257
170.	Mixed Nozzle Corrected Ideal Velocity Versus Corrected Ideal Thrust.	259
171.	Overall Bypass Ratio Versus Total Inlet Corrected Airflow.	261
172.	Corrected Ideal sfc Versus Corrected Ideal Thrust.	263
173.	NASA Acoustic Nozzle Performance Results, Conic Nozzle Configuration.	265
174.	NASA Acoustic Nozzle Performance Results, Coannular Nozzle Configuration.	267
175.	NASA Acoustic Nozzle Performance Comparisons.	268
176.	Thrust Coefficients for Configuration 2 [$R_T^O = 0.902$, $R_T^I = 0.8$, Conical Inner Plug] with High Inner Flow Rates.	269
177.	Thrust Coefficients for Configuration 3 [$R_T^O = 0.902$, $R_T^I = 0.902$, Conical Inner Plug] with High Inner Flow Rates.	270
178.	Thrust Coefficients for Configuration 5 [$R_T^O = 0.853$, $R_T^I = 0.8$, Conical Inner Plug] with High Inner Flow Rates.	271
179.	Nozzle Thrust Coefficient.	272
180.	Conic Nozzle Performance.	274
181.	Coannular Nozzle Performance.	275

LIST OF TABLES

<u>Table</u>		<u>Page</u>
I.	Emergency Shutdown Variable Geometry Logic - Forward VABI Test.	23
II.	Emergency Shutdown Variable Geometry Logic - Acoustic Nozzle Test.	26
III.	Major Test Milestones.	30
IV.	Acoustic Nozzle Test Instrumentation Engine/Gas Generator Requirements.	66
V.	Acoustic Nozzle Instrumentation.	67
VI.	Ground Plane and Engine Centerline Microphone Weighting Factor.	70
VII.	Combination of Inlet and Exhaust Configurations.	74
VIII.	Summary of Far Field Acoustics and Special Instrumentation Tests.	85
IX.	Fan Inlet Noise Data Points.	135
X.	PNL Field Shape Variations.	224
XI.	Conic Nozzle EPNL Projections Using Several Jet Noise Flight Projection Methods for Typical Sideline, Cutback, and Approach Conditions.	230
XII.	Projected Difference in EPNL Between the Conic Nozzle and Coannular Plug Nozzle at Typical Sideline, Cutback and Approach Conditions.	231



1.0 SUMMARY

Two sequential YJ101/VCE tests were conducted as part of a multiphase, multiyear GE/NASA test-bed engine program to investigate key technology features applicable to an AST powerplant. The engineering work for both tests was initiated in late 1977, and the tests were accomplished in 1978. The key features were the Forward Variable Area Bypass Injector (VABI) and the Coannular Acoustic Exhaust Nozzle. The Forward VABI test was conducted in Lynn in June 1978, and the test highlights are summarized as follows:

- Transitioning between single bypass and double bypass operating modes was accomplished with no problems.
- Engine aerodynamic performance met or surpassed predictions. (Better part power sfc than predicted).
- Forward VABI and associated ducting aerodynamic performance surpassed predictions (i.e., lower losses than expected).

The acoustic nozzle engine test was conducted to evaluate the coannular nozzle concept in engine scale hardware, in conjunction with the previously tested forward VABI configuration. This testing was accomplished in October 1978 at an outdoor test facility (Edwards AFB, California) to allow extensive acoustic measurements. These test highlights are summarized as follows:

- Engine aerodynamic performance met predictions.
- The exhaust system aerodynamic losses for the Rear Variable Area Bypass Injector and the flow inverting struts and ducting were lower than predicted in both single and double bypass modes.
- The key acoustic test conditions (to allow comparison with counterpart scale model tests) were attained, including: 2.9 nozzle pressure ratio in single bypass mode, 762 meters/sec (2500 ft/sec) exhaust velocity in conic baseline tests and 610 meters/sec (2000 ft/sec) exhaust velocity in double bypass mode with the coannular nozzle.
- Extensive acoustic data were collected, including; far field, near field, sound separation probe/internal probe measurements, and laser velocimeter wake traverses.
- Testing was accomplished with three geometric variations of coannular nozzle radius ratio. Acoustic results confirm that the predicted coannular nozzle noise suppression benefits were obtained (i.e., 4-6 PNdB reduction in aft quadrant).

- Coannular nozzle acoustic scaling was verified. Good agreement was obtained with prior scale model results relative to overall suppression and key acoustic parameters. Verification of key geometric and flow parameters such as radius ratio, area ratio and velocity ratio was obtained.
- Both engine and nozzle mechanical performance were excellent. No mechanical problems or limitations were encountered. Over 136 hours of testing was satisfactorily accomplished in both phases.

These test results substantially advance two of the most critical technologies of the General Electric Company double bypass cycle concept engine; namely the forward VABI system and the Coannular Acoustic Nozzle. The conceptual soundness and feasibility of the forward VABI system operating in conjunction with the coannular nozzle was verified in a double bypass engine environment. Bypass system aerodynamic losses were lower than expected, and noise reduction due to coannular flow was in agreement with predictions.

2.0 INTRODUCTION

As part of the overall NASA Supersonic Cruise Research (SCR) Program, the General Electric Company has been conducting advanced supersonic propulsion studies with the objective of identifying the most promising advanced engine concepts and related technology programs necessary to provide a sound basis for design and possible future development of an advanced supersonic propulsion system. Previous studies (Reference 1) included the design and analysis of several conventional supersonic engines and several supersonic engines having variable cycle features. Follow-on studies in which specific variable cycle features or arrangements were incorporated in a mixed-flow turbofan cycle identified a double-bypass variable cycle engine having a high-flow fan and an annular nozzle as the most attractive of those arrangements, considering range, performance, and noise, (Reference 2).

Further studies in conjunction with Boeing, Douglas, and Lockheed have indicated aircraft range improvements using the installed performance advantages associated with a double-bypass VCE. This engine concept provides high airflow at takeoff to meet FAR part 36 noise requirements and at the same time provides the performance advantage of a smaller cruise-size engine which is well matched to supersonic airplane characteristics. This concept also provides the added capability of excellent subsonic installed performance which makes a mixture of subsonic and supersonic operation a practical consideration.

The NASA VCE Component Test Program in conjunction with U.S. Air Force and Navy test programs have allowed General Electric to run all of the variable cycle engine features on a test-bed engine. General Electric initiated preliminary design studies of VCE Concepts for mixed mission applicability in the mid 70's and subsequently conducted this series of YJ101 engine tests to verify the VCE technologies. Concurrently a NASA sponsored design study identified the advantage/applicability of the coannular exhaust nozzle, (Reference 3).

This report describes the work accomplished under NASA/Lewis contract auspices to test the Forward Variable Area Bypass Injector (Forward VABI) and Coannular Acoustic Exhaust Nozzle which were previously identified as two of the most critical technologies for further verifying the General Electric double bypass VCE engine concept for supersonic cruise application. To date, General Electric has accomplished five sequential YJ101/VCE test programs under combined USAF/Navy and NASA auspices, starting in 1976. These sequential test programs, along with the individual and cumulative features are shown in Figure 1. In summary, more than 300 hours of VCE testing has been successfully accomplished in this integrated program.

The principle advantage of the forward VABI concept is that it allows a VCE engine to operate in either single or double bypass operating modes with a single bypass duct, and (in conjunction with a rear VABI) to be integratable

VCE Features

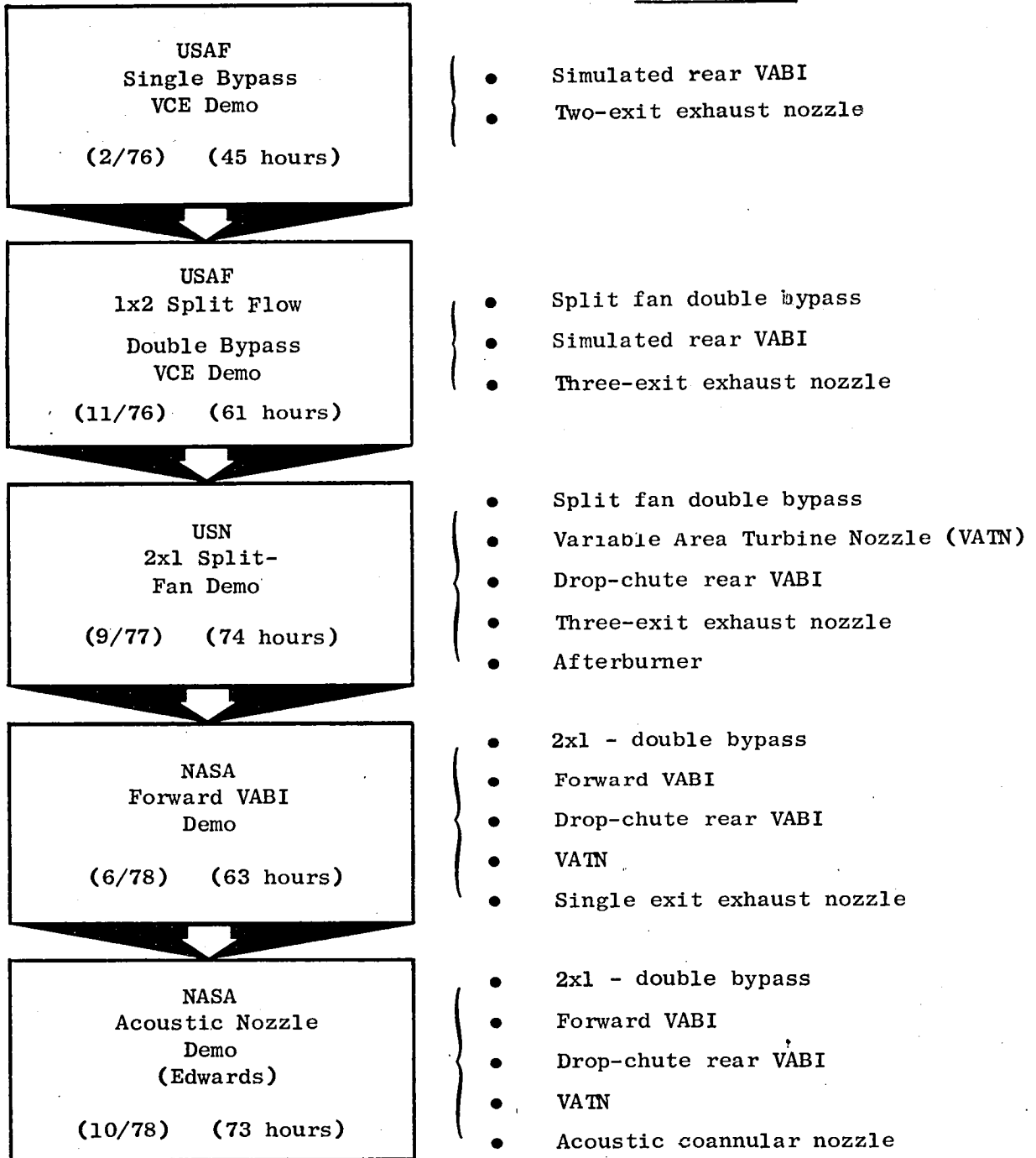


Figure 1. YJ101 VCE Concept Demonstrators.

with the coannular acoustic exhaust nozzle. The test objectives were to demonstrate that stable and effective aerodynamic and mechanical operation in conjunction with a split fan could be attained and that transitioning between bypass operating modes could be accomplished over a range of engine speeds. In addition to the specific SCR objectives, this work relates to the general problem of integrating compression systems of varying pressure ratio into a common discharge. The coannular nozzle provides a method for reducing the exhaust noise at low performance penalties by utilizing the inverted exit temperature profile principle. The test objectives of the nozzle testing were to verify this suppression benefit in engine scale hardware by comparison to typical conic nozzle test results; and also to provide confirmation of acoustic scaling criteria by comparison with previously completed counterpart scale model test results, also accomplished under NASA auspices.

The NASA Forward VABI Test was completed in Lynn in June 1978 and utilized the Navy 2x1 split fan VCE test-bed engine configuration as a departure point. This test, using a modified Navy 2x1 exhaust system, was followed in October 1978 by the first VCE test accomplished at a remote outdoor test site for evaluation of the aerodynamic and acoustic characteristics of the coannular acoustic nozzle. Several geometric variations of the coannular nozzle were aerodynamically and acoustically tested and compared with a reference, conic baseline nozzle. Extensive acoustic information including far field, near field, internal sound separation probe and laser velocimeter exhaust plume surveys was obtained to allow detailed comparison with counterpart scale model test results and predicted scaling criteria.

All technical objectives for the forward VABI and acoustic nozzle engine tests were successfully accomplished and are reported herein. These results have provided the basis for a continuing NASA YJ101 component test-bed program and continued coannular scale model acoustic development.

The purpose of the NASA Forward VABI and Acoustic Test Program was to:

- Evaluate engine aerodynamic and mechanical performance in single and double bypass operating modes including forward VABI transitioning, rear block for IGV redesign for sfc improvement at part power double bypass operation, part power front block fan airflow extension capability, and coannular exhaust nozzle performance.
- Measure and evaluate acoustic characteristics of the coannular plug exhaust nozzle, deep chute rear VABI and a sound absorbing bellmouth inlet system versus a single stream mixed-flow conic baseline nozzle configuration, with a goal to achieve 5 PNdB of noise suppression in the aft quadrant.
- Correlate full-scale engine and scale model acoustic test results and verify analytical prediction methodology. Additional data taken during the conduct of these tests can be found in Reference 4.

3.0 DESIGN

3.1 VARIABLE CYCLE ENGINE (VCE) DESCRIPTION

The NASA VCE testbed [Figures 2(a) and (b)] is a variable-bypass-ratio (0.22-0.66) turbofan engine utilizing a GE-YJ101 engine core.

The advantage of a VCE over a conventional turbofan engine is that the VCE separates the fan into two blocks with a double bypass: an outer bypass duct between the fan blocks, plus the normal bypass duct after the second fan block. Because of the additional bypass duct the airflow size of the front block can be larger than for the rear block. In a conventional turbofan all fan stages are sized for the same airflow.

A major advantage of the split-fan configuration in an SST application is that for the high takeoff airflow sizing which may be dictated by jet acoustic considerations, only the front block fan and low-pressure turbine are affected. Thus, a large weight savings is realized over that of a conventional turbofan or turbojet engine sized for the same takeoff airflow and noise level. Other advantages accrue from the fact that airflow-holding capability is improved at part-throttle subsonic cruise or community cutback flyover conditions. The higher airflow can reduce throttle-dependent installation drag at cruise and reduce the required jet velocity at flyover for lower noise.

The five variable-cycle features that make the double-bypass VCE [Figures 3(a) and (b)] more flexible than mixed-flow turbofans are:

- Split fan (outer bypass duct between the rear block with its variable inlet guide vanes and higher-flow front block)
- Fan variable-area bypass injector (Forward VABI)
- Exhaust variable-area bypass injector (Rear VABI)
- Variable-area low-pressure turbine nozzle (VATN)
- Coannular exhaust nozzle system, for reduced noise levels.

The first four VCE features allow the independent control of the high- and low-pressure rotor speeds to provide, at subsonic part-throttle conditions and at transonic/supersonic high thrust conditions, airflow levels that are higher than would be possible with conventional fixed-geometry mixed-flow turbofans, thus resulting in a variable-bypass-ratio engine. The last item, the variable-area coannular exhaust, accommodates the passage of the additional takeoff fan flow at reduced specific thrust with an inverted jet velocity profile for low noise.

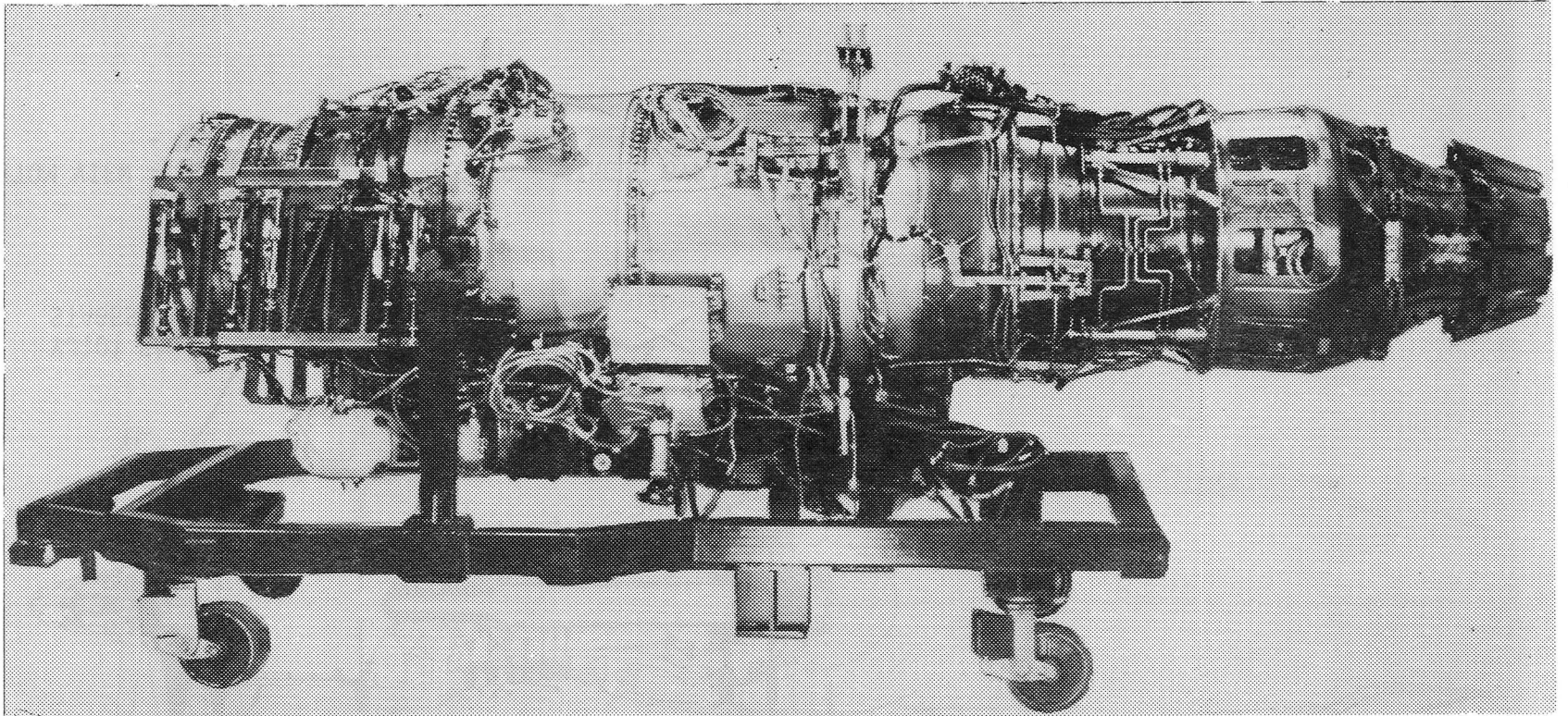
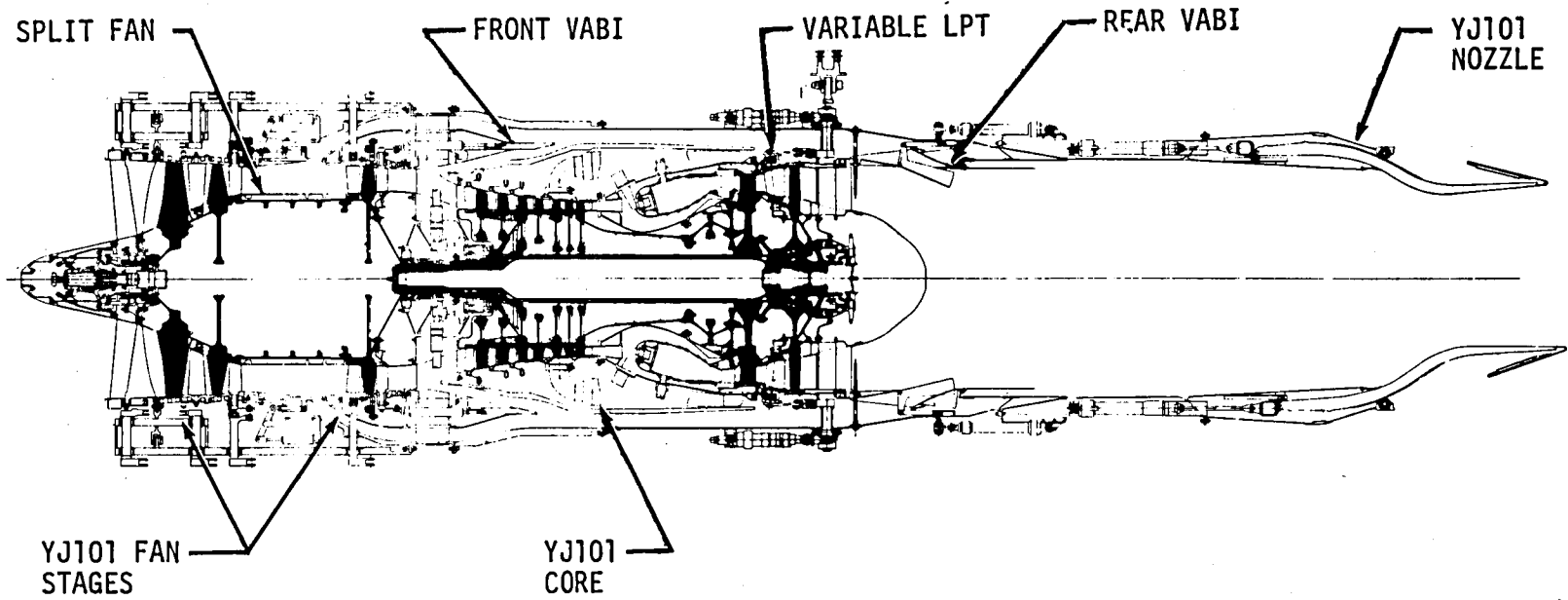


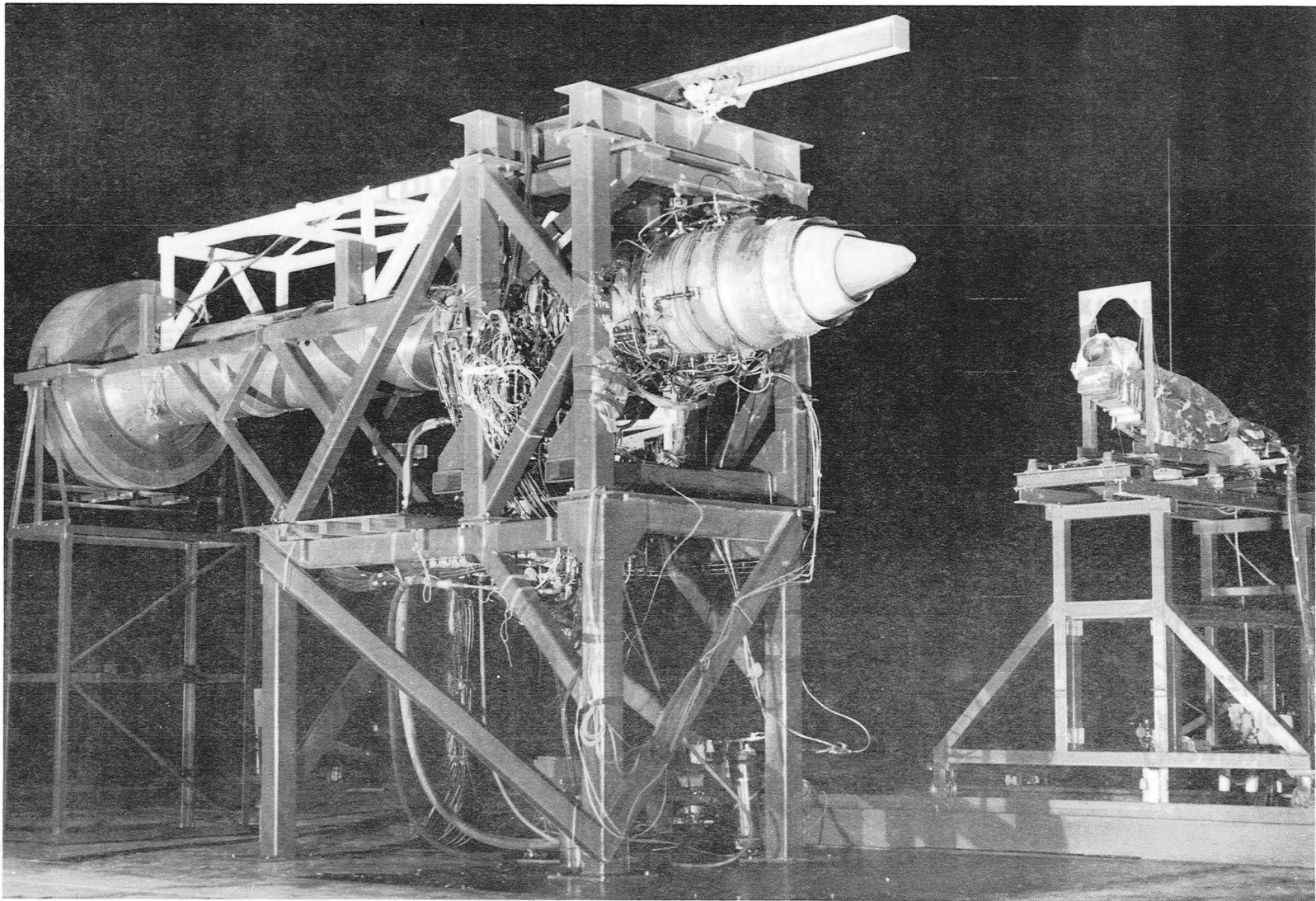
Figure 2 (a). NASA Forward Variable Area Bypass Injector VCE/YJ101 Test Configuration.

TOP VIEW - OUTER DUCT VALVE OPEN - DOUBLE BYPASS OPERATION
- LOW NOISE MODE / PART POWER MODE



BOTTOM VIEW - OUTER DUCT VALVE CLOSED - SINGLE BYPASS OPERATION
- MAX THRUST

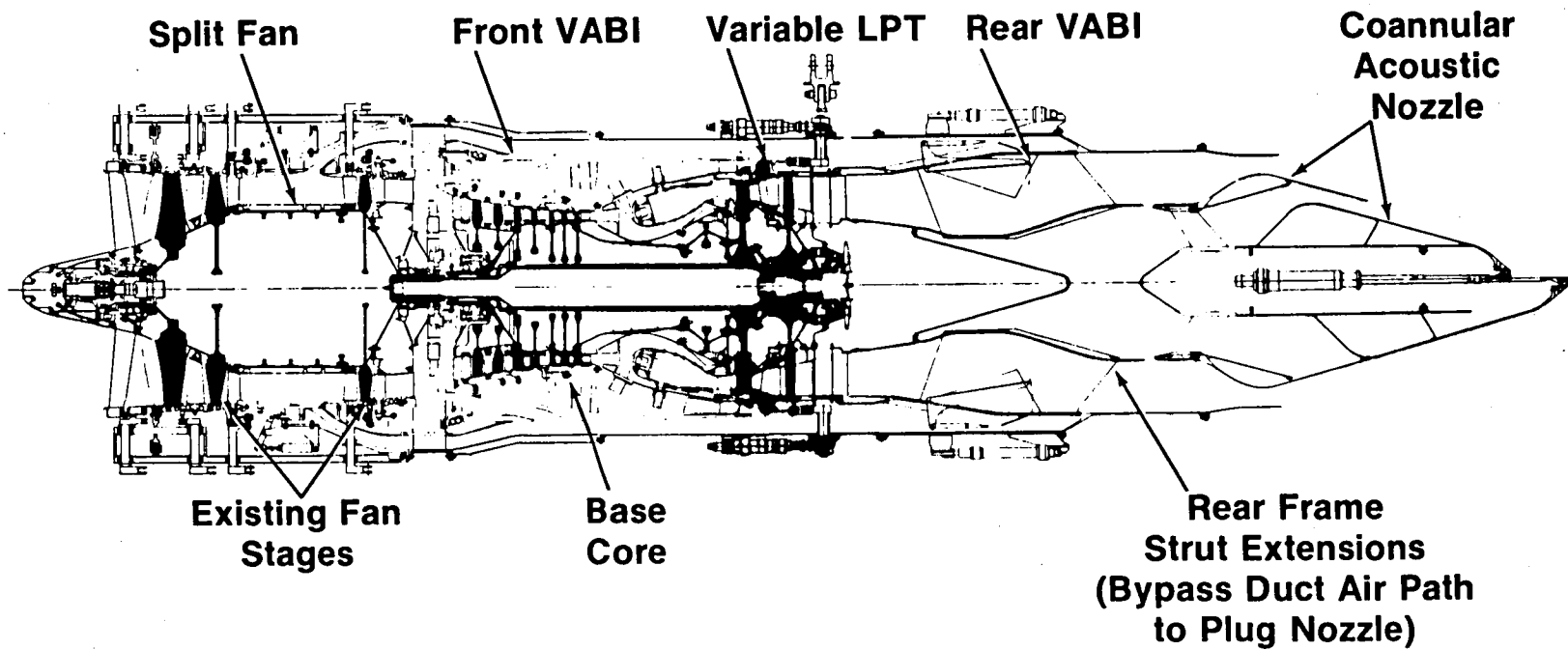
Figure 2 (b). Schematic Cross Section of NASA Front VABI Test Configuration.



μικροφωνική εγκατάσταση ACE κεντρικού και περιφερειακού

Initial Double Bypass VCE Noise Test Configuration

Top View - Low Noise Test Mode (Double Bypass)



Bottom View - High Thrust Mode (Single Bypass)

Figure 3 (b). Schematic Cross Section of NASA Coannular Acoustic Nozzle Test Configuration.

The engine for this test was built from the Navy 2x1 demonstrator engine with the following special configuration requirements:

- Split Fan - from Navy 2x1 configuration with rear block fan IGV redesign.
- Forward Outer Casing - New Part - This incorporates the outer flow-path of the outer bypass air stream and the selector valve. (This part encountered a crack problem in the initial manufacture and the alternative design action was to fabricate it in two sections.)
- Modified Main Frame - Modified Navy 2x1 frame.
- Outer Aft Casing (New Part) - This forms the outer flowpath of the outer bypass stream and the mixed bypass stream.
- Modulating Valve and Fairings (New Parts).
- Split Inner Casing and Fairing (New Parts) - This forms the inner flowpath of the inner bypass stream and provides support for the modulating valve.
- Aft Outer Duct (New Part) - This serves as the outer flowpath of the mixed bypass stream and ducts the flow to the LPT turbine axial station.
- LPT VATN - From Navy 2x1 configuration with new bellcrank linkages.
- Aft Mounting Ring (New Part) - This is a mounting ring of increased diameter similar in concept to that used on the prior Navy 2x1 demonstrator.
- Rear VABI - Navy drop-chute rear VABI - modified for larger-diameter ducting and increased flow requirements for forward VABI test. New design with stationary detachable side plates and provision for bypass cross-over struts in acoustic tests.
- Exhaust Duct and Nozzle - Modified Navy 2x1 parts for the forward VABI test. New conannular inverted flow plug nozzle for the Early Acoustic Test.

3.2 SPLIT FAN DESCRIPTION

The split fan is a three stage low-pressure turbine driven system with a two stage front block and a single stage rear block (2x1). The front block is the same as the YJ101 first two stages. The rear block is the third stage of the YJ101 with a variable IGV to modulate flow when in the double bypass mode of operation. This is the same configuration as the Navy 2x1 fan with the exception of the rear block IGV which was redesigned for improved performance in closed position. When the engine is operated at high bypass ratios, the

rear block IGV is closed and the excess front block airflow passes through the outer bypass duct. This 2x1 split fan is similar to that for the GE21 AST Concept Study engine. However, the Concept Study split fan would have an enlarged front block that would be utilized in the following manner. For the low-noise takeoff mode, the front block fan is set for high flow. The rear fan block is operated in such a way as to tailor the velocity and flow of the jet exhaust to the desired thrust/noise relationship for takeoff. The VCE exploits the concept of coannular suppression by allowing adjustment of the velocities and flows of the inner and outer exhaust streams to meet takeoff thrust and noise requirements.

During subsonic cruise operation, the front fan block is set to provide the best match between inlet spillage and internal performance. In this mode, the second fan block is set to provide the proper cruise thrust. A high inlet airflow can be maintained for typically reduced subsonic cruise thrust, reducing the afterbody drag and practically eliminating inlet spillage drag.

In the climb/acceleration and supersonic cruise modes, the front block fan is set to satisfy the aircraft inlet flow supply, the rear block fan is set to pass all of the front block fan flow, and the engine operates in the single bypass, high specific thrust mode similar to a conventional low-bypass-ratio turbofan engine.

The high-flow front fan block provides the high-takeoff and subsonic-transonic airflow capability of the VCE without having the weight penalty incurred by oversizing the complete engine. The maximum dry-power airflow can be maintained down to the subsonic cruise thrust requirement, eliminating the spillage drag that is present when a conventional mixed-flow turbofan is throttled back. As the VCE subsonic cruise thrust is obtained at constant inlet airflow, the variable inlet guide vanes on the rear fan block are modulated to reduce the flow going into the HP compressor, bypassing the excess air. Cycle performance is improved by the VCE's higher bypass ratio, and, therefore, higher propulsive efficiency. This improvement, together with the reduction in installation losses made possible by eliminating inlet spillage drag and reducing the afterbody drag, lowers installed subsonic sfc by about 15% over a conventional mixed-flow turbofan.

With the operational flexibility provided by the split fan with an enlarged front block and an inlet sized for supersonic cruise, the off-design inlet flow supply characteristic can be matched by the engine, resulting in only minimal spillage drag and also an increased acceleration thrust from the higher engine airflow compared to a conventional fan engine.

3.3 FORWARD VARIABLE AREA BYPASS INJECTOR (VABI)

The forward (or front) VABI, shown in Figure 4, is comprised of a dual valve system which permits operation of a split fan in either mode - single bypass (high specific thrust) mode or double bypass (high airflow handling/reduced exhaust velocity) - with a single bypass exit flowpath. These two operating modes with their corresponding valve operations are illustrated in

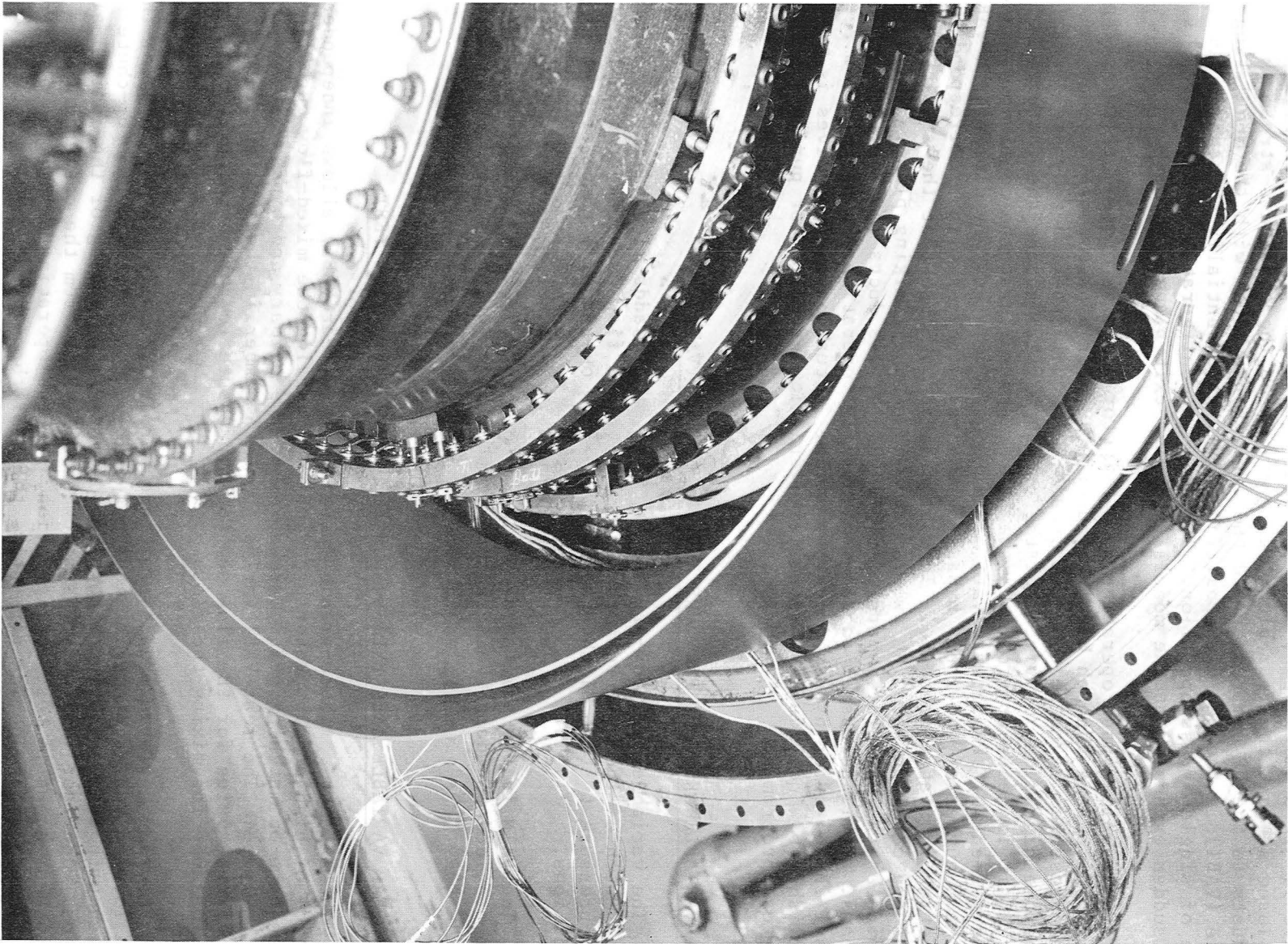


Figure 4. Modulation Valve (Inner Bypass) and Inner Fairing.

Figure 5. In single bypass mode operation (lower sketch) the selector valve is closed so that the rear block fan operates on the total air stream which exhausts to the HP compressor and the inner bypass duct with the modulating valve (VABI) in the max/open position. This is essentially the conventional mode of single bypass operation. The salient configurational difference is the sudden expansion at the modulating valve exit plane.

For double bypass operation, the selector valve is opened, allowing fan flow to discharge through both the outer and inner bypass ducts. Since the total pressures of these two streams are not equal (the inner bypass stream's being the higher one by virtue of the pressure ratio across the fan aft block), it is necessary to match the static pressures at the confluency plane by adjustment of the forward VABI modulating valve area. By closing the VABI, the Mach number of the inner bypass stream is increased with a corresponding reduction in static pressure. This area is adjusted so that the static pressures are equal between the two fan streams at their mixing plane. This eliminates the need for separate full-length bypass ducts for the two bypass streams. It is necessary to program the valve operations so that a flow reversal in the outer bypass duct is avoided. Actuation of the valves is accomplished by individually controlled hydraulic actuators for purposes of the test program.

3.4 VARIABLE AREA LOW PRESSURE TURBINE NOZZLE (VATN)

The variable-area low-pressure turbine stator adds flexibility by allowing a match of the low-pressure turbine entrance flow requirement with the high-pressure turbine discharge corrected flow over a wide range of operating conditions.

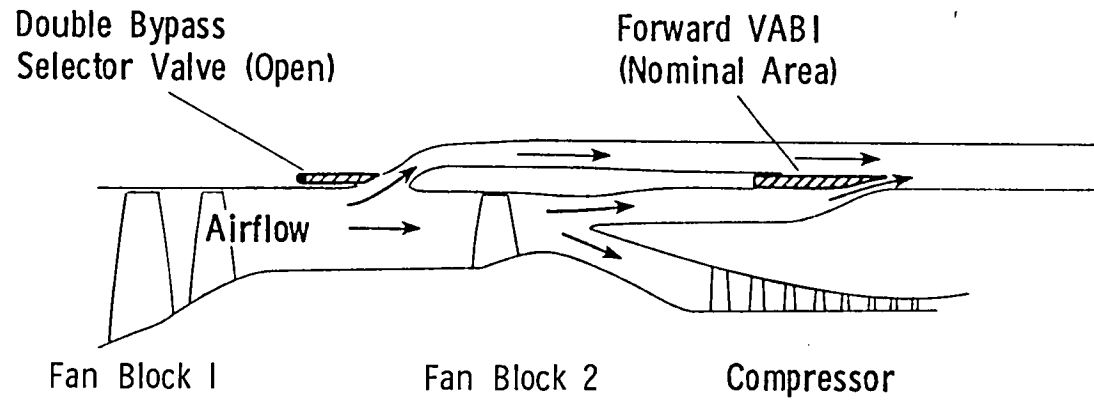
The VATN is the same nozzle utilized on the Navy 2x1 VCE. New bellcranks were provided to adapt the actuators to the larger outer bypass duct casing of the NASA VCE.

3.5 REAR VARIABLE AREA BYPASS INJECTOR FOR FORWARD VABI TEST

The exhaust variable-area bypass injector (rear VABI) allows independent control of high and low rotor speeds by eliminating the mixed-flow turbofan's dependence on matching static pressures of the primary and bypass streams in the tailpipe. The rear VABI varies the Mach number in the bypass stream to the correct value for the flow and total pressure to obtain the static pressure balance for mixing the flows.

The rear variable area bypass injector (VABI) configuration used for the NASA forward VABI test engine is shown in Figure 6. It is a 24-drop-chute design with area variation accomplished by radial pivoting of the individual chutes. The rear VABI shown is somewhat different from the one used in the subsequent acoustic test configuration, but the operating principles are generally the same. The fan air enters the VABI through the annular duct which communicates with the forward VABI. The fan air flows in two routes: through

Double Bypass Mode



Single Bypass Mode

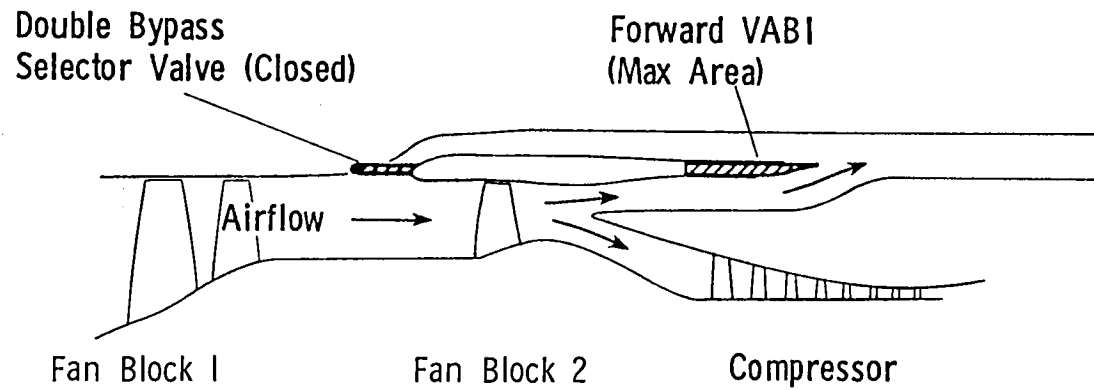


Figure 5. Forward Variable Area Bypass Injector.

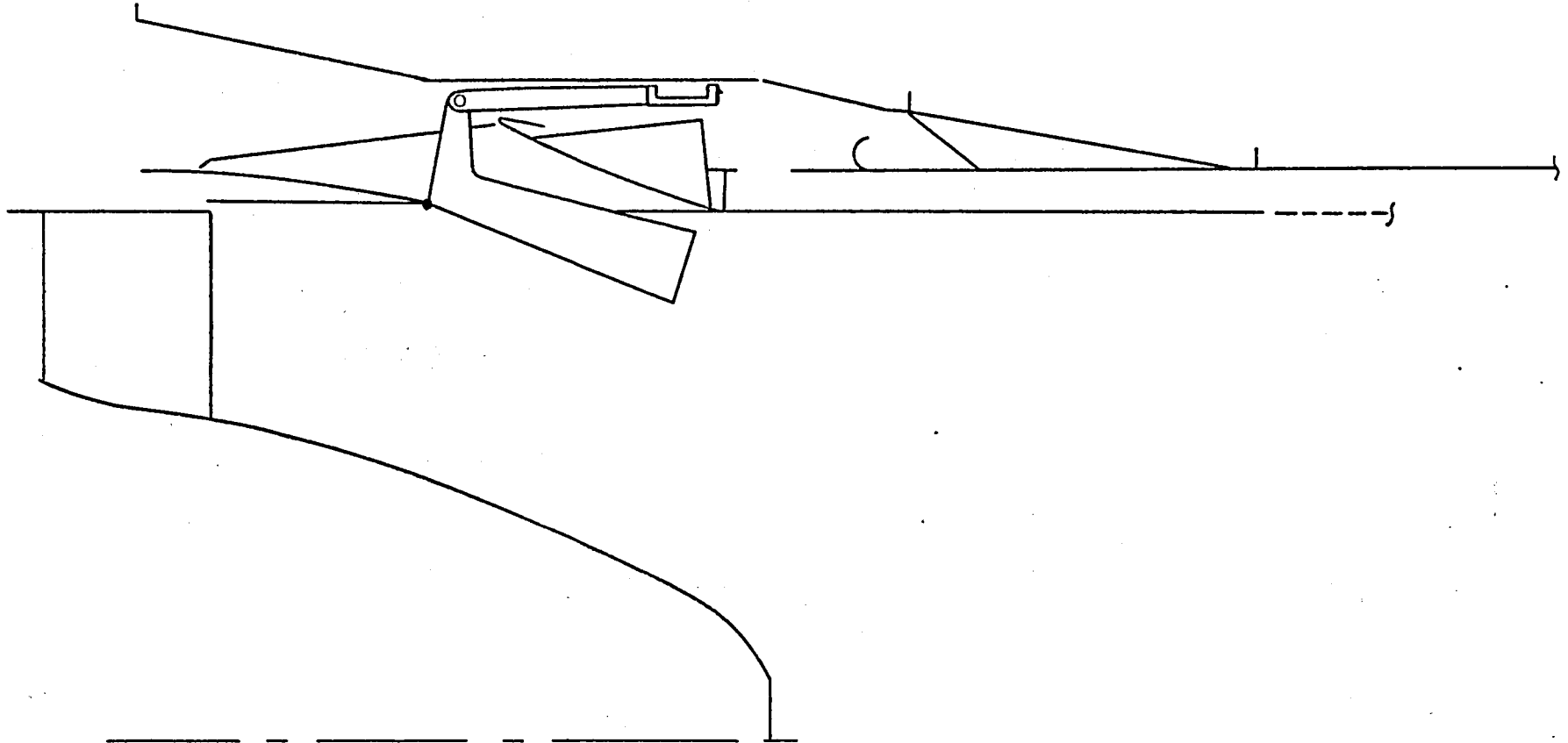


Figure 6. YJ101/VCE Rear VABI Configuration Used in Forward VABI Test.

the variable-position hinged chutes into the exhaust duct and through the liner flow control valve into the augmentor liner. The airflow split between the chutes and liner can be adjusted by varying either the chute position or the liner flow control valve. Figure 7 is a photo of the rear VABI assembly.

The chute discharge area is fully adjustable through a wide range. The chutes are opened or closed by four synchronized actuators. The actuators act through a double crank mechanism that drives the unison ring linked to the chutes. The chute position or bypass area is monitored by two linear variable differential transformer transducers that are externally mounted and connected to the actuator rod.

The liner flow control valve is a manually operated, four-position valve. The valve consists of eight segments, or cover plates, that are held by spring-loaded guides. Each cover plate can be axially moved to uncover air slots to regulate the amount of air entering the liner.

3.6 COANNULAR NOZZLE AND ASSOCIATED REAR VABI

The rear VABI/Acoustic Nozzle, shown schematically in Figure 8 consists of the following major components:

- Rear Variable Area Bypass Injector (VABI)
- Centerbody Support Assembly
- Translating Plug
- Outer Nozzle Crown and Shroud

The rear Variable Area Bypass Injector (VABI) is a variable-geometry chuted mixer of a hinged drop-chute design constructed so that the chute discharge area can be varied by radial movement of the chutes. Twenty-four chutes, evenly spaced between eight struts are provided to achieve a temperature mixing effectiveness of 80% during dry operation. In this design, the VABI sideplates are stationary and detachable. Aeroacoustic tests were later conducted both with and without these sideplates to determine their impact on both performance and noise.

The chute area is adjusted by four synchronized hydraulic actuators which drive the actuation ring through four double crank mechanisms that penetrate the duct casing wall. The actuation ring is linked to the chutes so that axial movement of the actuation ring uniformly opens or closes the chutes to vary A_{16} , the area of the cold bypass stream at the mixing plane with the hot core stream, as required by the cycle. When the chutes are open, their trailing edges protrude into the main stream to provide effective mixing of the fan air before it enters the nozzle for peak propulsion efficiency (that is, for uniform nozzle temperature profile). The position of the chute is determined from the signal from two externally mounted linear variable differential transformers (LVDT) mounted on the VABI actuators.

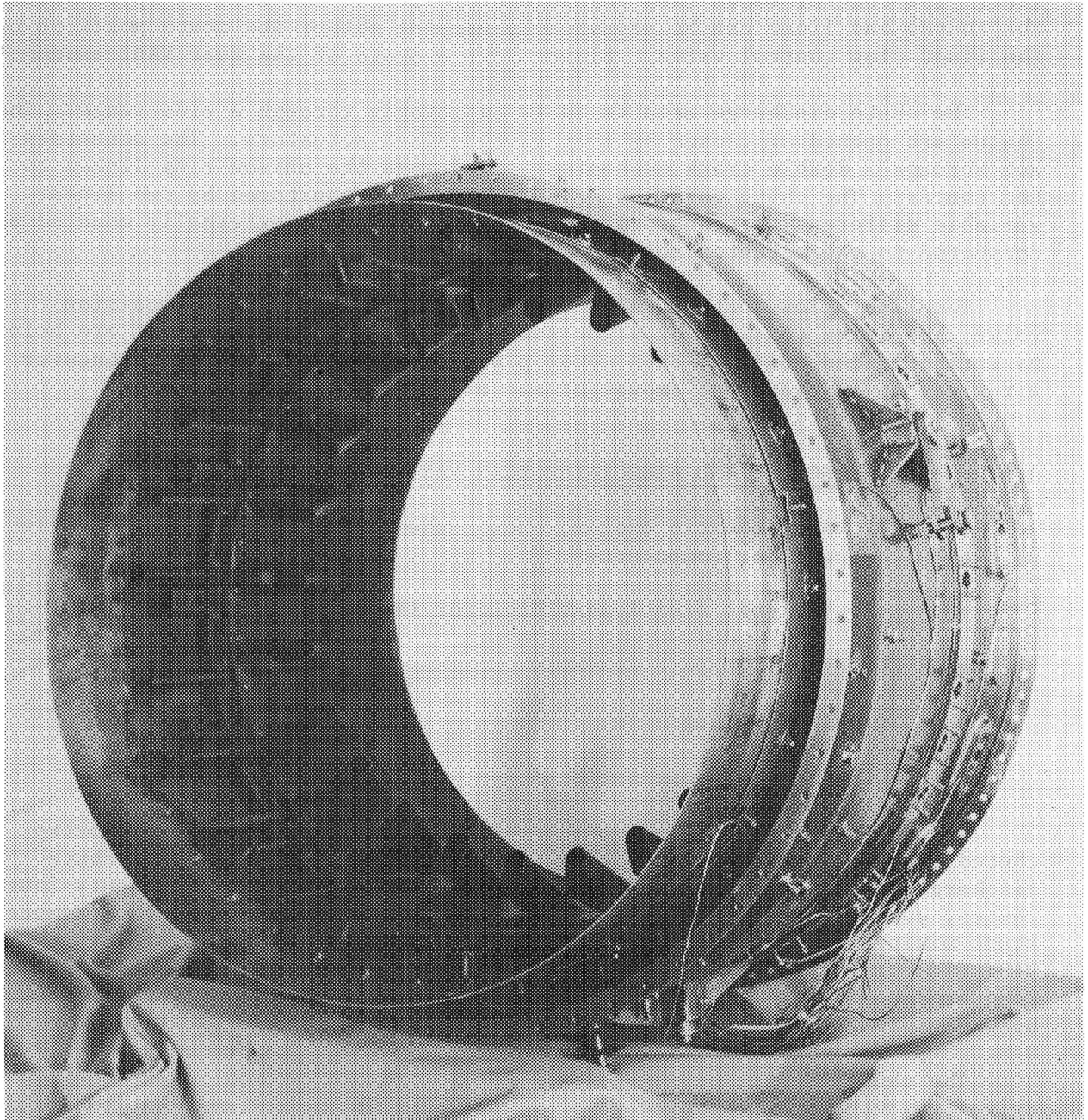


Figure 7. Rear VABI Assembly.

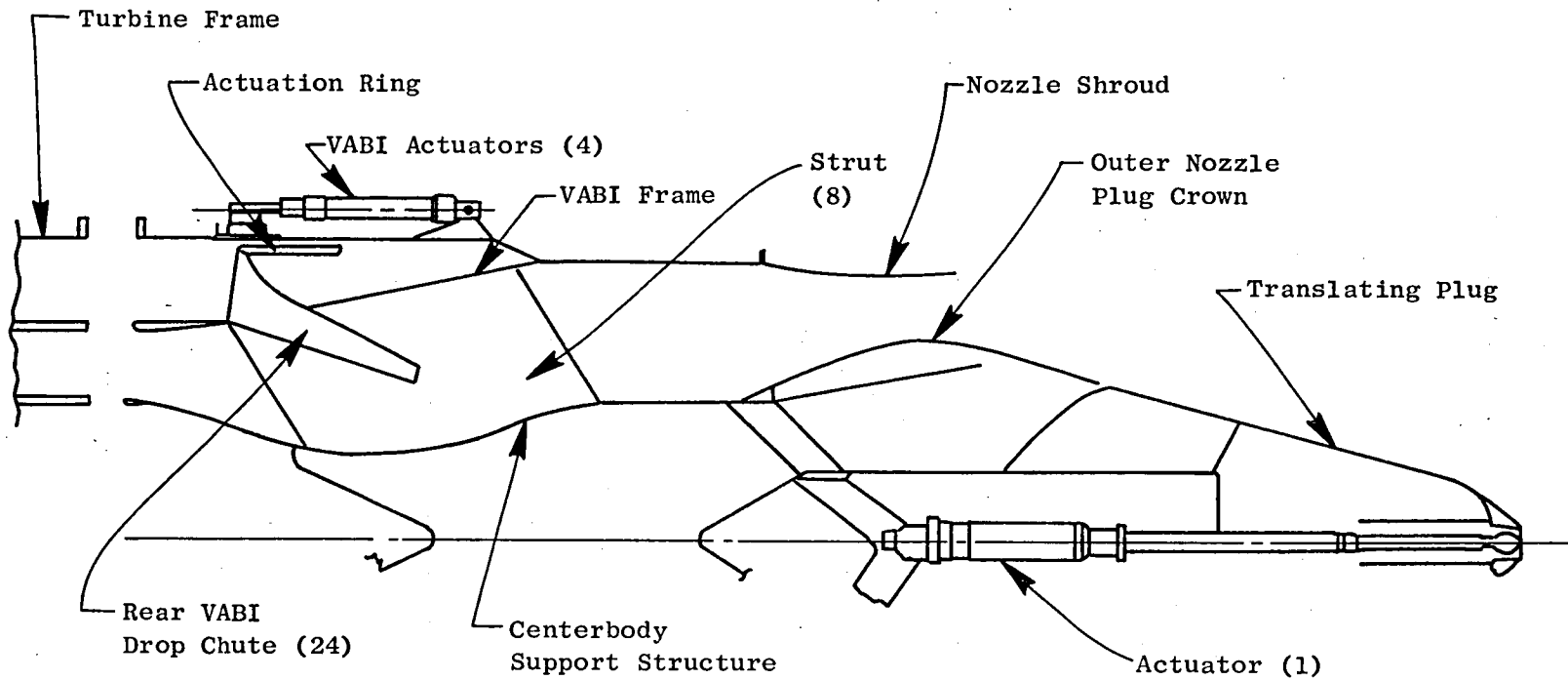


Figure 8. Schematic of Rear VABI/Acoustic Nozzle Used in Edwards Aeroacoustic Test.

The eight fan air struts (Figure 8) serve two purposes:

1. To support the plug nozzle
2. To duct the fan air through the hot core stream to the inner annular nozzle.

The throat area of the inner annular nozzle can be varied over the full area range from fully open to fully closed by axially translating the center plug which is actuated by a single actuator. An integral LVDT transducer provides an electrical feedback signal to establish the position of the center plug and the throat area of the nozzle.

The outer annular nozzle consists of a fixed crown and shroud. Three different sets of crowns and shrouds were tested, providing radius ratios of 0.816, 0.853, and 0.875, to determine the effect of radius ratio on acoustic performance. The radius ratio is defined as the inner diameter of the annulus divided by the outer diameter of the annulus. A photograph of the acoustic nozzle is shown in Figure 9.

The conic nozzle configuration shown in Figure 10 was used as the reference or baseline nozzle against which the acoustic characteristics of the coannular acoustic nozzle were compared. The configuration consisted of the rear VABI and a fixed 7° conic nozzle attached to the VABI support casing flange. A spool section was added to the centerbody and attached to the turbine frame to match the annular flow area to simulate the pressure distribution and Mach number at the chute exit to achieve a comparable acoustic signature for the reference nozzle.

3.7 CONTROL SYSTEM

3.7.1 Forward VABI Test Control System

The control system for the forward VABI test engine was basically the same as was used on the Navy 2x1 VCE test program, except for the following modifications:

1. An open loop for positioning the forward VABI mode selector valve (A94)
2. An open loop for positioning the forward VABI (A148)
3. The emergency response system which returns the variable geometry to an optimum position for engine shutdown was modified to perform the logic as shown in Table I.

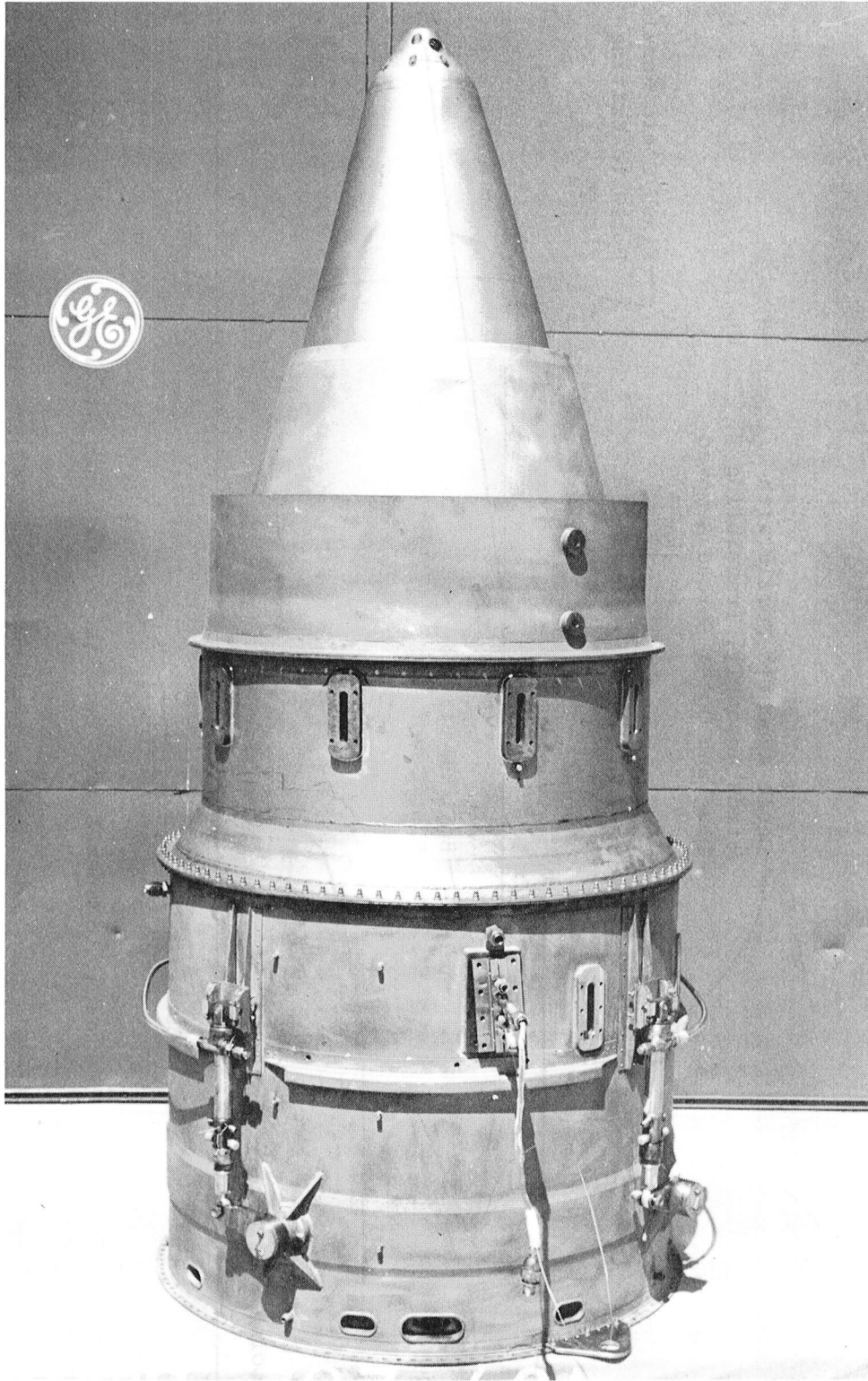


Figure 9. Acoustic Nozzle Assembly.

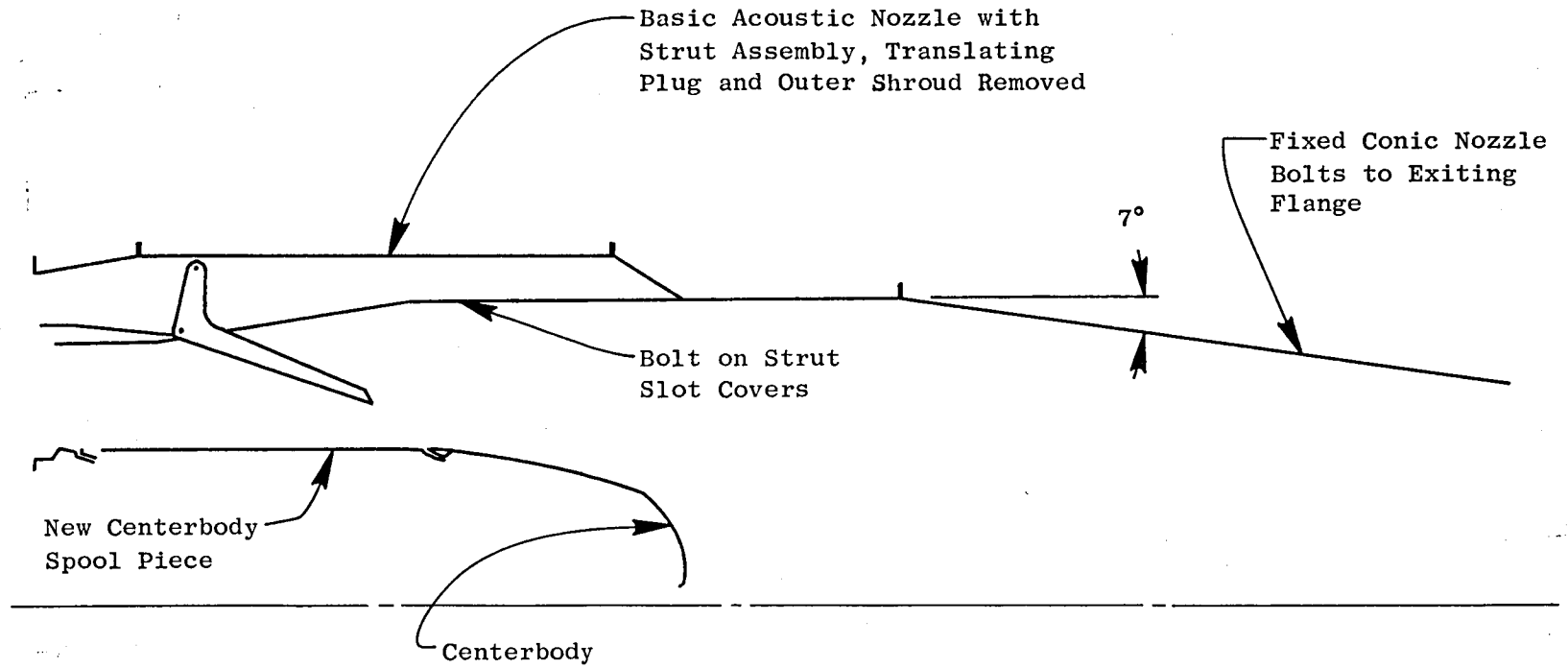


Figure 10. Schematic of Baseline Fixed Conic Nozzle.

Table I. Emergency Shutdown Variable Geometry Logic Forward VABI Test.

Geometry	Engine Operating Mode	
	Single Bypass	Double Bypass
Mode Selector Valve (A ₉₄)	Closed	Full Open
IGV-3 Rear Block Fan	Maintain Position	Close 5°
IGV-1 Front Block Fan	Maintain Position	Close 5°
A _{14.8} Forward VABI	Maintain Position	Open to 80 in. ²
A ₁₆ Rear VABI	Maintain Position	Open to 65 in. ²
A ₈ Nozzle Throat	Maintain Position	Open to Nominal
A ₄₇ VATN	Maintain Position	Open 50% of Demand

See Figure 11 for Control System Schematic.

3.7.2 Acoustic Nozzle Test Control System

The control system for the Acoustic Nozzle VCE demonstrator engine was basically the same control system as that used on the forward VABI test except for special features for the acoustic nozzle and protective features derived from forward VABI testing.

As shown in Figure 12, the A₈ loop was replaced by an open loop control of the acoustic nozzle. Interlocks were provided on IGV-3 to:

1. Limit closure as a function of selector valve position to protect front block stall margin.
2. Limit opening as a function of forward VABI setting to protect rear block stall margin.
3. Limit closure as a function of rear VABI setting to protect both front and rear block stall margin.

The engine control system retains the emergency shutdown system designed for the forward VABI test engine. Activation of the emergency switch, following throttle retard, unloads the engine in a prescribed, safe manner by setting the variable features as shown in Table II.

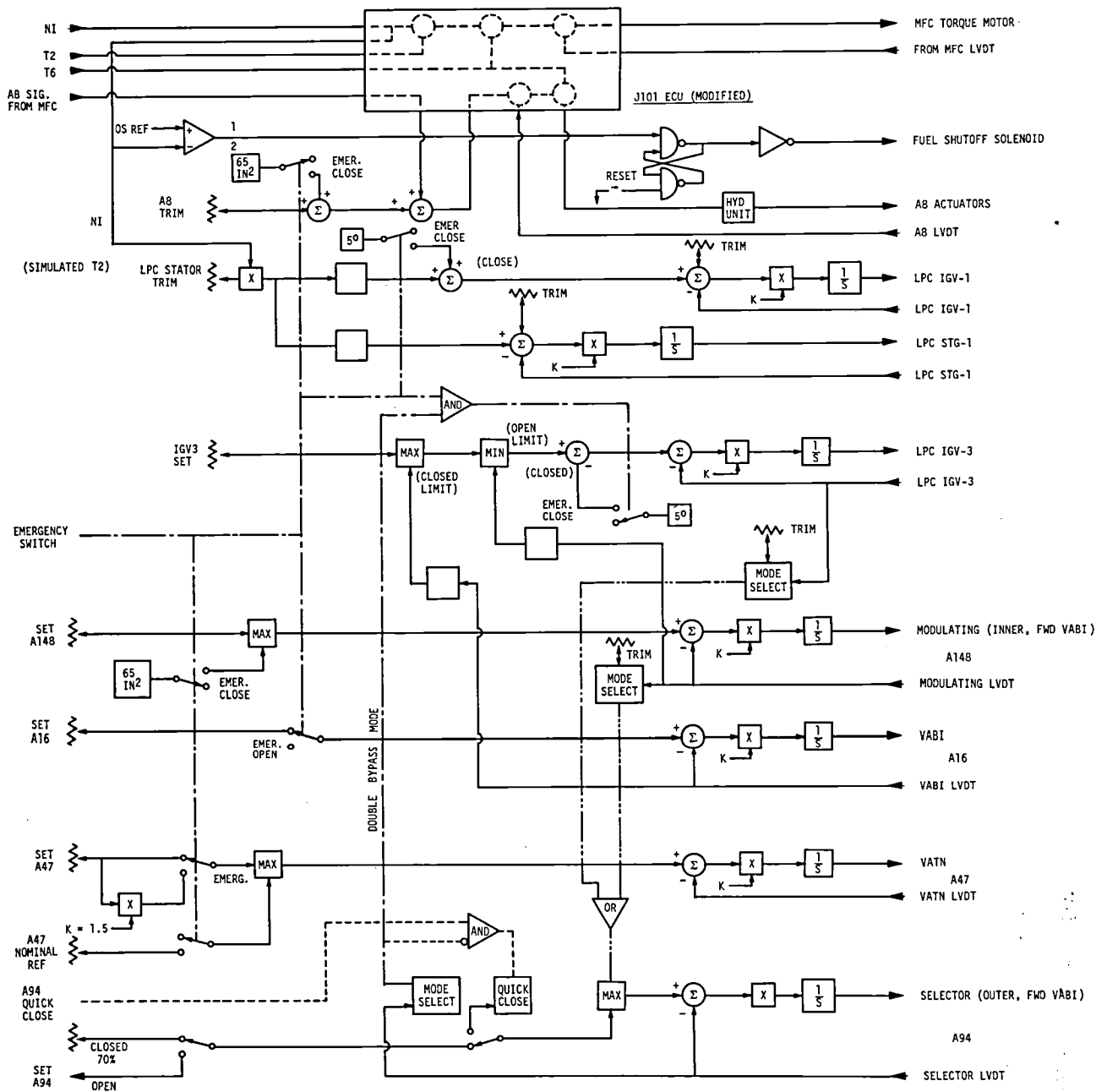


Figure 11. Forward VABI Fan Speed and Variable Geometry Control.

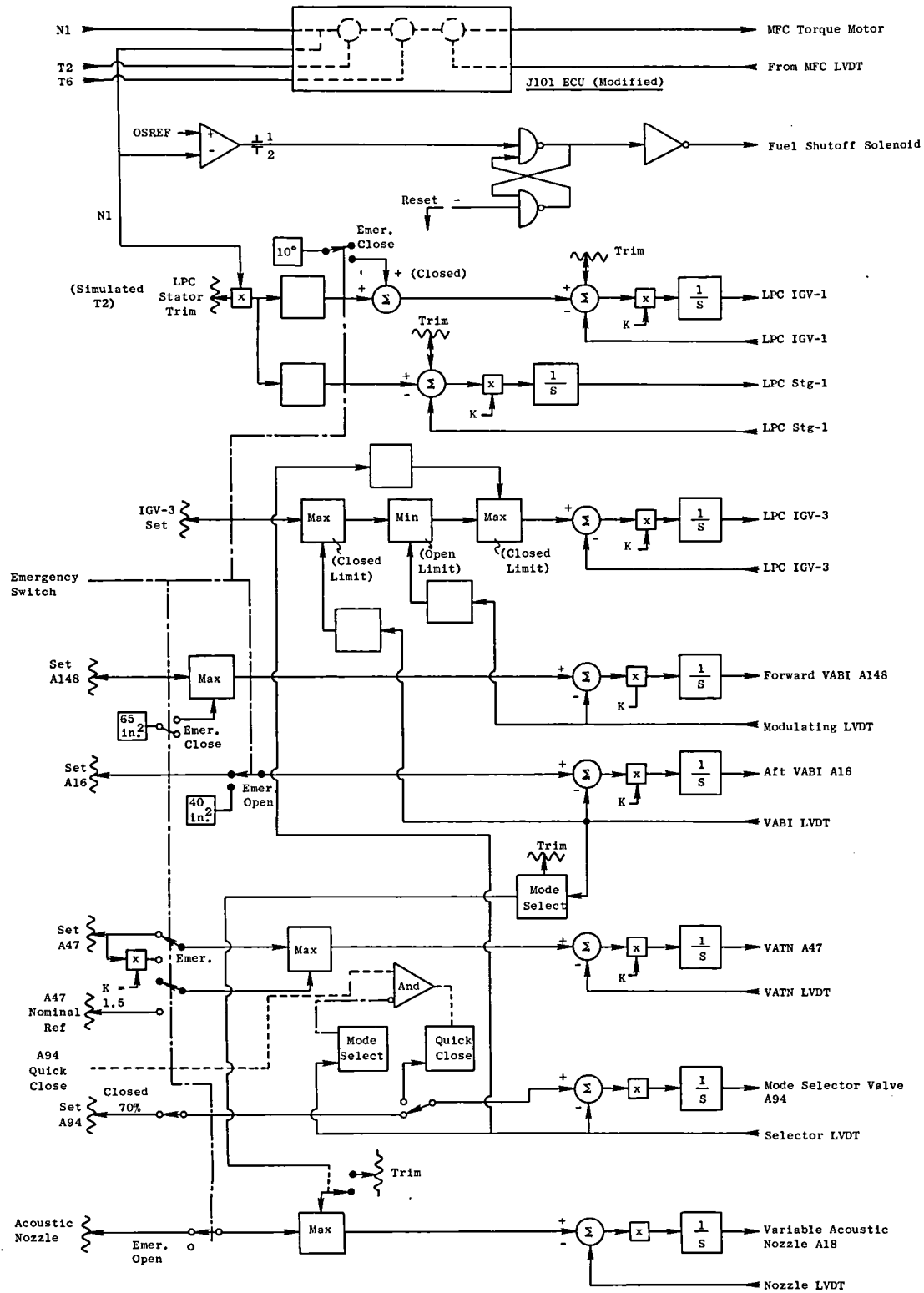


Figure 12. Fan Speed and Variable-Geometry Control for Acoustic Nozzle.

Table II. Emergency Shutdown Variable Geometry Logic
Acoustic Nozzle Test.

Geometry	Engine Operating Mode	
	Single Bypass	Double Bypass
Mode Selector Valve (A ₉₄)	Stay Closed	Stay Full Open
IGV-1	Close 10°	Close 10°
A _{14.8}	Control 65 in. ²	Control 65 in. ²
A ₁₆	Open to 40 in. ²	Open to 40 in. ²
A ₁₈	Open	Open
A ₄₇	1.5 x Demand or 92.5 in. ² (Which- ever is Greater)	1.5 x Demand or 92.5 in. ² (Which- ever is Greater)

4.0 FORWARD VABI TEST

4.1 TEST OBJECTIVES

The objectives of the NASA forward VABI test program were to:

1. Evaluate aerodynamic and mechanical performance of the forward VABI.
2. Demonstrate transitioning from single to double bypass with a forward VABI.
3. Evaluate VCE engine performance in single and double bypass operating modes (with emphasis on (a) sfc improvement at part power and (b) airflow extension capability).
4. Test VCE engine operating conditions for the ensuing acoustic nozzle test.
5. Evaluate VCE engine/component performance with inlet pressure distortion.
6. Test a 2x1 split fan with the rear block inlet guide vane redesigned for improved aerodynamic performance relative to the previous Navy 2x1 test.

4.2 TEST DESCRIPTION

Assembly and instrumentation of the forward VABI test engine were completed on May 5, 1978. The test setup was completed May 23, 1978 and the test itself was completed on June 19, 1978. Test hours totalled 63.02, of which 5.08 were carried out with distorted inlet conditions. Three hundred-twenty-one test points were accumulated. Table III shows the major test milestones and chronology.

Testing was conducted in Cell 108 at the General Electric Aircraft Engine Business Group Plant in Lynn, Massachusetts. Until several years ago, this test cell was configured to test only F404 engines, but when the VCE Demonstrator Program was initiated, the test cell was modified to also accept the YJ101/VCE demonstrator engines. Figures 13 and 14 show the engine installed in the test cell.

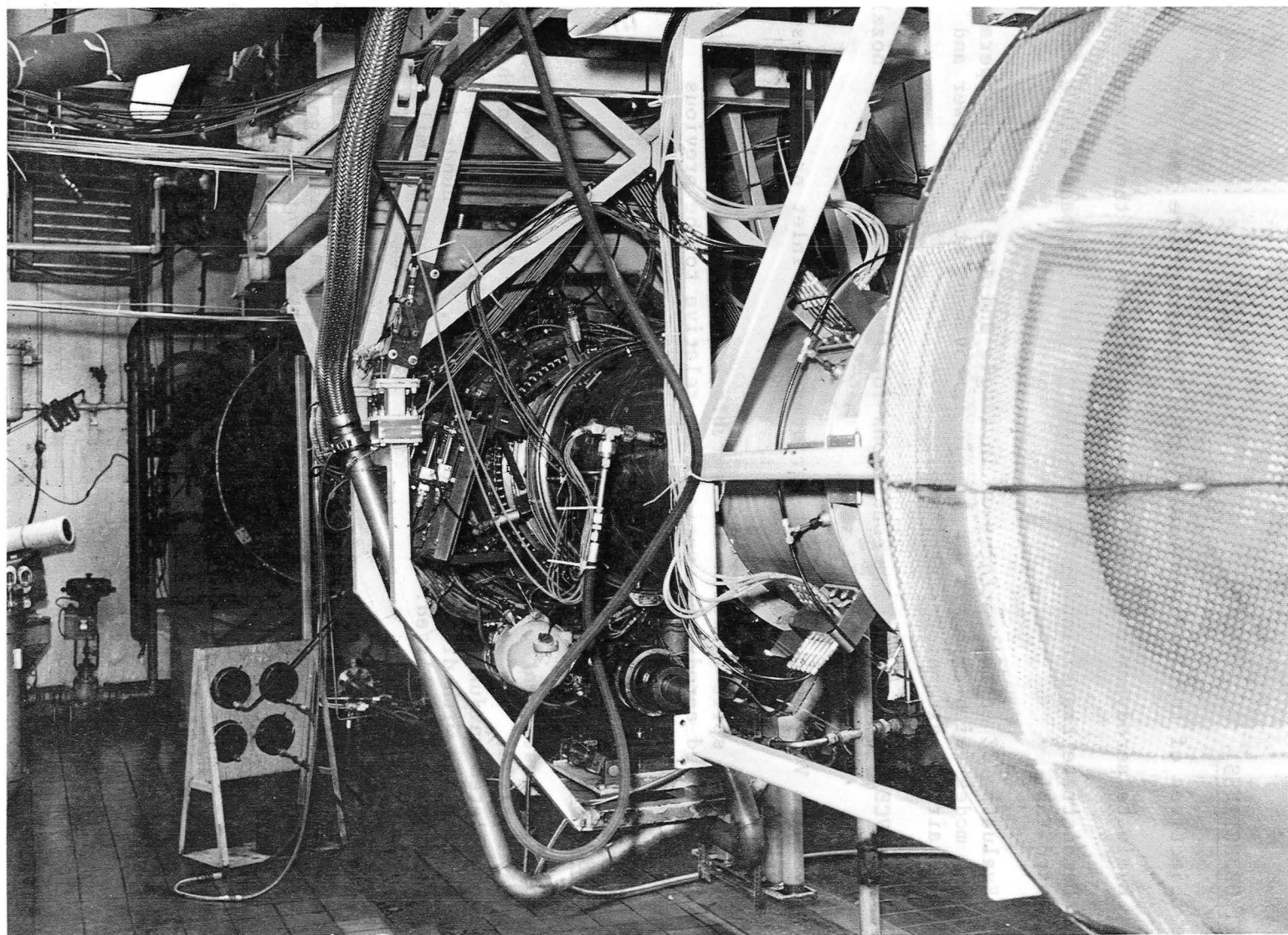


Figure 13. Forward VABI Engine Installed in Test Cell - Forward Looking Aft.

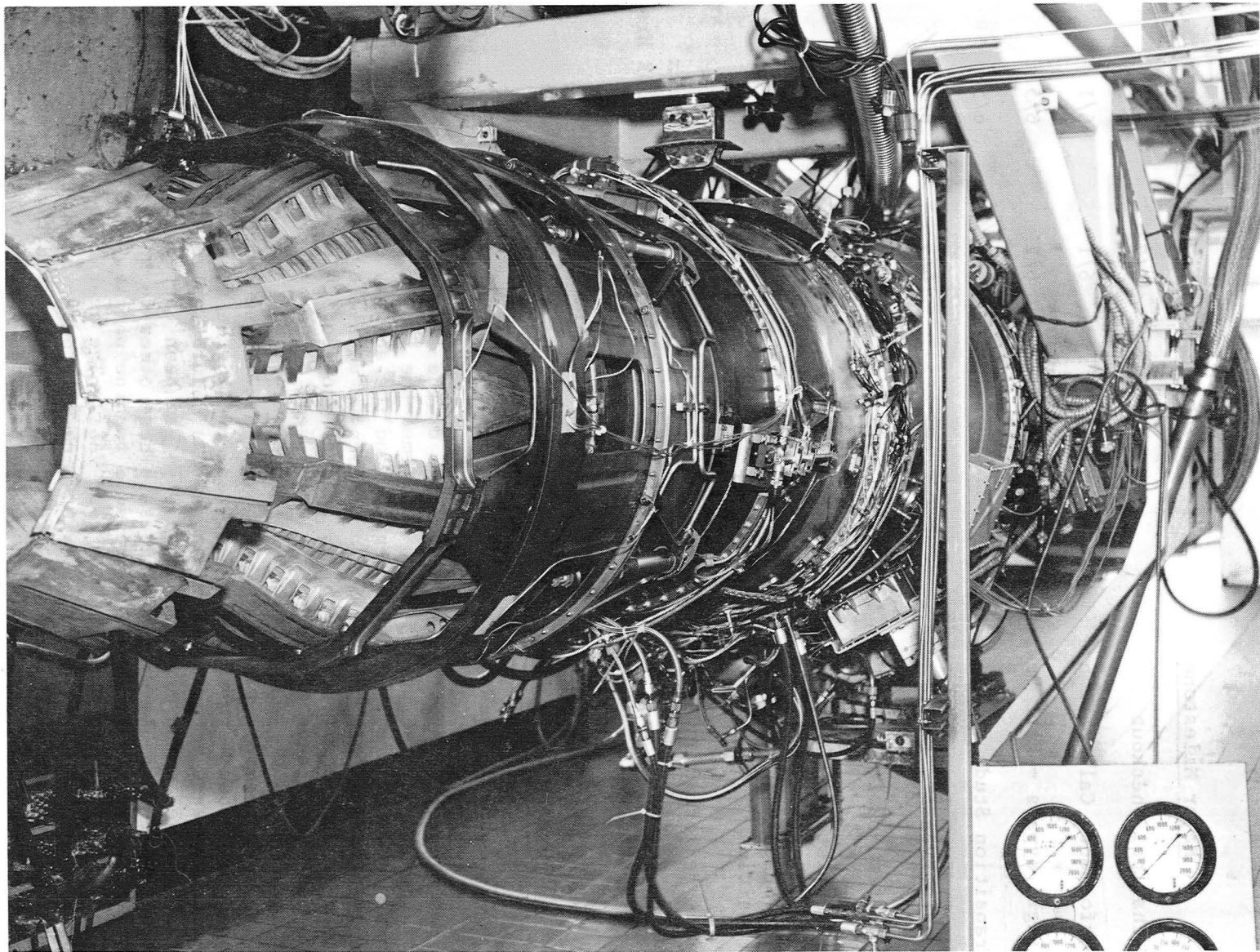


Figure 14. Forward VABI Engine Installed in Test Cell - Aft Looking Forward.

Table III. Major Test Milestones.

<u>Major Milestone</u>	<u>No. of Test Points</u>	<u>Initiated</u>	<u>Completed</u>
Mechanical Checkout	24	5/23	6/1
Performance Calibration	10	6/1	6/1
Single Bypass - Part Power	40	6/2	6/5
Transition Study	35	6/5	6/5
Double Bypass - Part Power	82	6/5	6/9
Acoustic Nozzle Simulation Points	29	6/9	6/10
Inlet Distortion (2 Screens)	23	6/16	6/18
High Speed/High Operation Line Transition	38	6/19	6/19
Final Performance Calibration	<u>30</u> (Daily Recall Points)		
	321 Test Points		63.02 Hrs

4.3 TEST RESULTS

4.3.1 Summary of Results

The overall feasibility and advantage of the forward VABI concept were satisfactorily demonstrated. Tests confirmed the forward VABI aerodynamic performance, mechanical design integrity and the ability of the engine to transition from single bypass (SB) operation to double bypass (DB) and back. Eighteen transitions (from SB to DB mode and back to SB) were accomplished over a fan speed range of from 80 to 90% speed.

The aerodynamic performance of the unique VABI subcomponents met or exceeded predicted levels. This test represented the first time that these VABI subcomponents - the selector valve, the modulating valve and associated ducting and the common/mixed bypass duct - had been tested in conjunction with the other variable cycle features. These other features included a 2x1 split fan, variable area low pressure turbine nozzle (VATN) and a rear VABI modified from the earlier Navy rear VABI. The overall aerodynamic performance of the YJ101 VCE engine in which all these variable features were integrated was excellent. At typical part-power conditions, performance levels in both single and double bypass modes exceeded predictions.

The specific fuel consumption (sfc) in single bypass mode at 50% rated thrust was 1.9% lower than predicted. The best double bypass sfc (that is, the lowest sfc attainable through manipulation of the VCE geometry settings) was 5.2% better than the single bypass sfc at the same thrust level.

This compares with a 3.8% double/single differential obtained in the earlier Navy 2x1 VCE test. Variable cycle engine benefits are expected in two areas:

1. Internal sfc improvement, as described above and
2. Airflow increases at constant thrust are easier to accommodate, avoiding inlet spillage drag and high afterbody boattail angles. Also, during low-altitude noise abatement fly-over procedures, high airflow operation can reduce the jet noise level.

The test results showed that by operating the engine in double bypass mode, an airflow extension capability of 13% at the best sfc and 29% at the same sfc as single bypass could be achieved. These values compare with 12% and 28% for the prior Navy 2x1 test. The improvement in engine performance beyond predicted results was attributed to better-than-predicted split-fan-aerodynamic performance and lower than predicted exhaust duct losses.

Aerodynamic performance levels of the forward VABI and associated ducting (on a component basis) were in excellent agreement with expected levels, including measured aerodynamic characteristics and pressure losses for the outer and forward bypass duct (front fan block duct), the inner and rear bypass duct (aft fan block duct), and the mixed-stream ducting from the confluency plane to the rear VABI inlet. The only significant pressure loss deviation from predicted levels occurred in the inner bypass duct with high airflow extensions in the single bypass operating mode. This greater-than-expected loss was caused by locally high Mach numbers and choking at the plane of the main frame structural strut and bypass splitter lip interface. This problem can be solved in future designs by flowpath refinement in this local area.

Transitioning from one operating mode to the other was smooth and uneventful at all test conditions. No fan blading aerodynamic instabilities or excitations were observed from strain gage indications. No significant aerodynamic instabilities or separations were observed or measured in the forward VABI valving and ducting. The transition "windows" (operating regimes of transition capability) were in good agreement with predicted results. In addition to the initial transitions, which varied the selector valve and aft fan block inlet guide vanes sequentially, two "integrated" transitions adjusted the selector valve and aft fan block inlet guide vane simultaneously as a product-type, integrated control system.

Throughout the clean inlet testing, the strain gages on the fan blade and vanes registered less than 35% of the fan and compressor aeromechanical limits. With distorted-inlet testing, the stress levels were below those

measured on the counterpart YJ101 (unsplit) fan using the same inlet pressure distortion test patterns. One inadvertent stall was encountered. It was caused by an incorrect setting of the selector valve, but was cleared almost instantaneously.

In addition to the component and engine performance testing described, special test points pertinent to clearing the engine for the ensuing Acoustic Nozzle Test were accomplished.

Improved split fan aerodynamic performance was attained as expected. For this test, a redesign of the inlet guide vane for the aft fan blade was accomplished and implemented to improve double bypass performance. This work was accomplished under auspices other than this NASA contract, but was included in this test per NASA agreement.

4.3.2 Engine Performance

4.3.2.1 Overall Performance

An engine schematic and instrumentation plane definition for the VCE is shown in Figure 15.

Figure 16 compares the forward VABI performance prediction to the test results. Test results show better sfc than was predicted, 1.9% at the minimum sfc point for single bypass operation and 4.3% better than predicted in double bypass. The general sfc thrust trend was as predicted.

Although the single bypass engine's air-swallowing capability was as predicted, the trend for the double bypass engine showed a divergence from predicted results at the higher thrust levels (3.6% higher at 50% thrust).

Figure 17 displays the sfc versus flow trends at 50% thrust. By going from single bypass to double, minimum sfc was improved 5.2% and airflow increased 13%. In double bypass, at the minimum sfc obtained in single bypass, the engine airflow can be extended by 29%.

4.3.2.2 Transitioning

Before the actual transitioning from single to double bypass, mapping of the fan stall margins was done, and the level of positive driving pressure was measured at 95%, 90% and 80% fan speed. The data in Figures 18 through 20 show that transitioning was possible at 95% speed with a somewhat better selector valve pressure ratio than was predicted for large forward VABI areas. In the actual transitioning, no instabilities were observed circumferentially at the inlet or inside the duct. Figure 21 describes the variation in front block pressure ratio for the 95% transition. Transitioning with a raised rear block operating line causes rear block stall margin to drop by approximately 10 points (Figure 22).

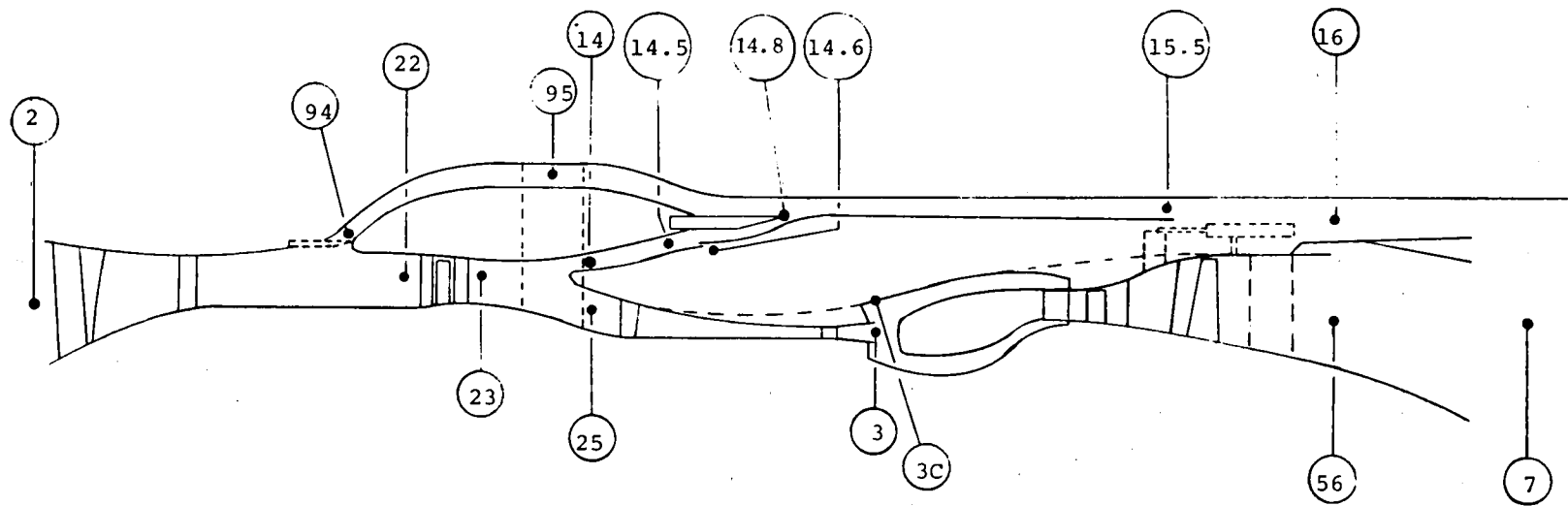


Figure 15. YJ101/VCE Schematic and Instrumentation Plane Definition.

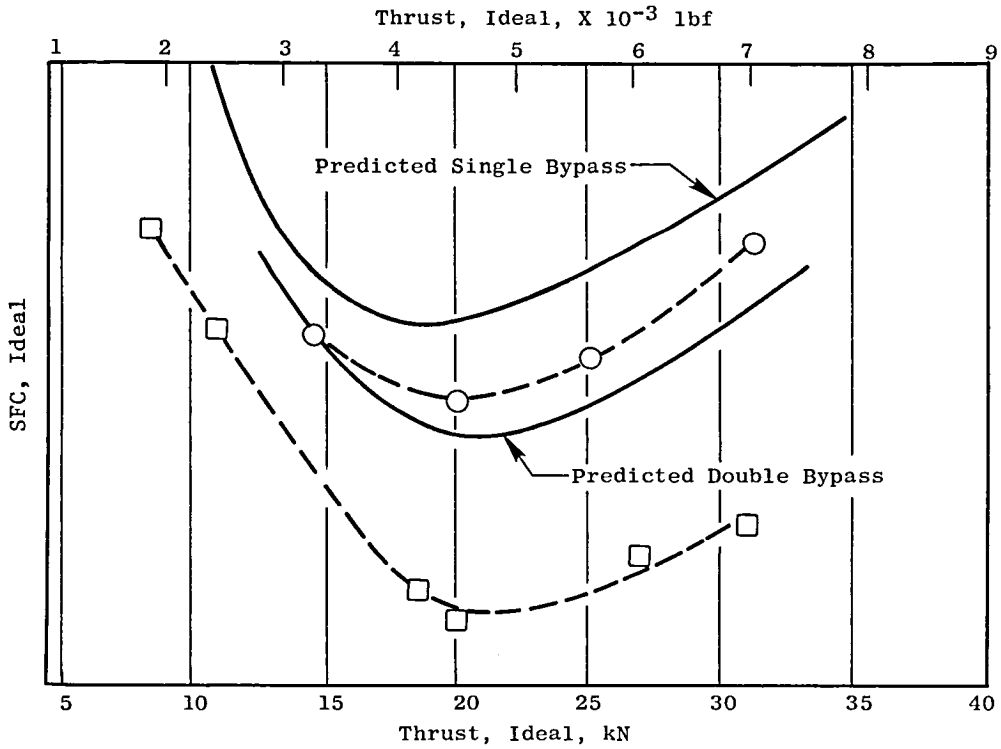
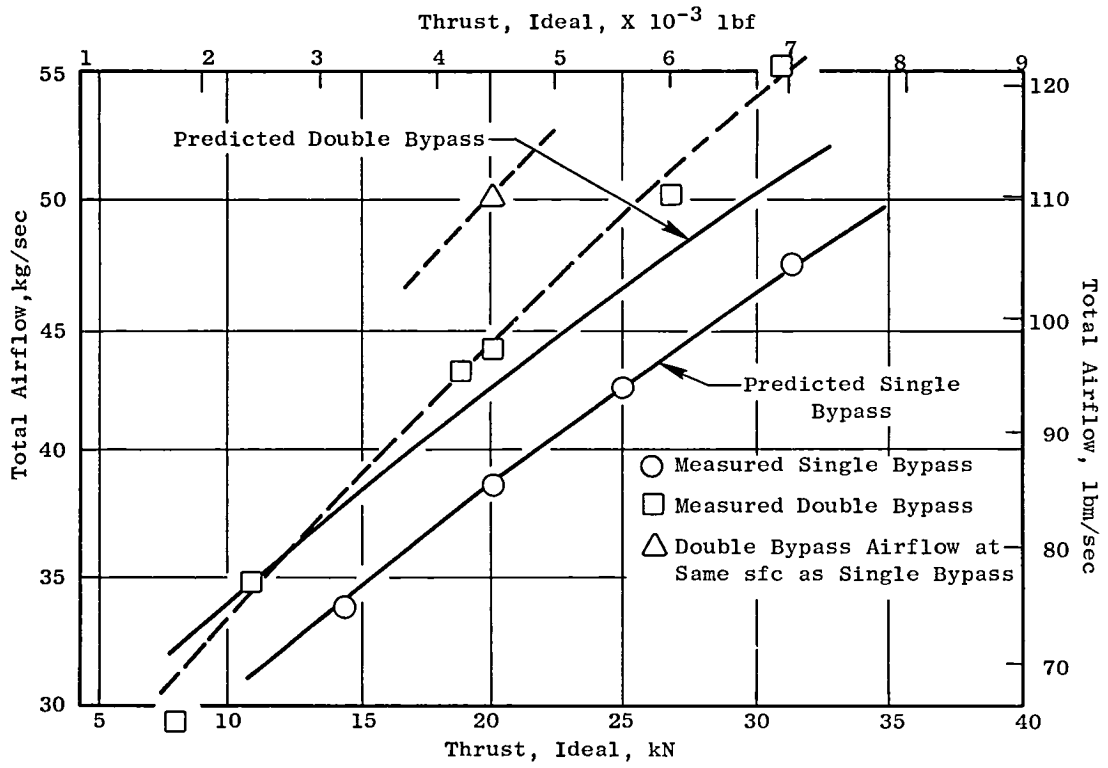


Figure 16. 2x1 Forward VABI Performance.

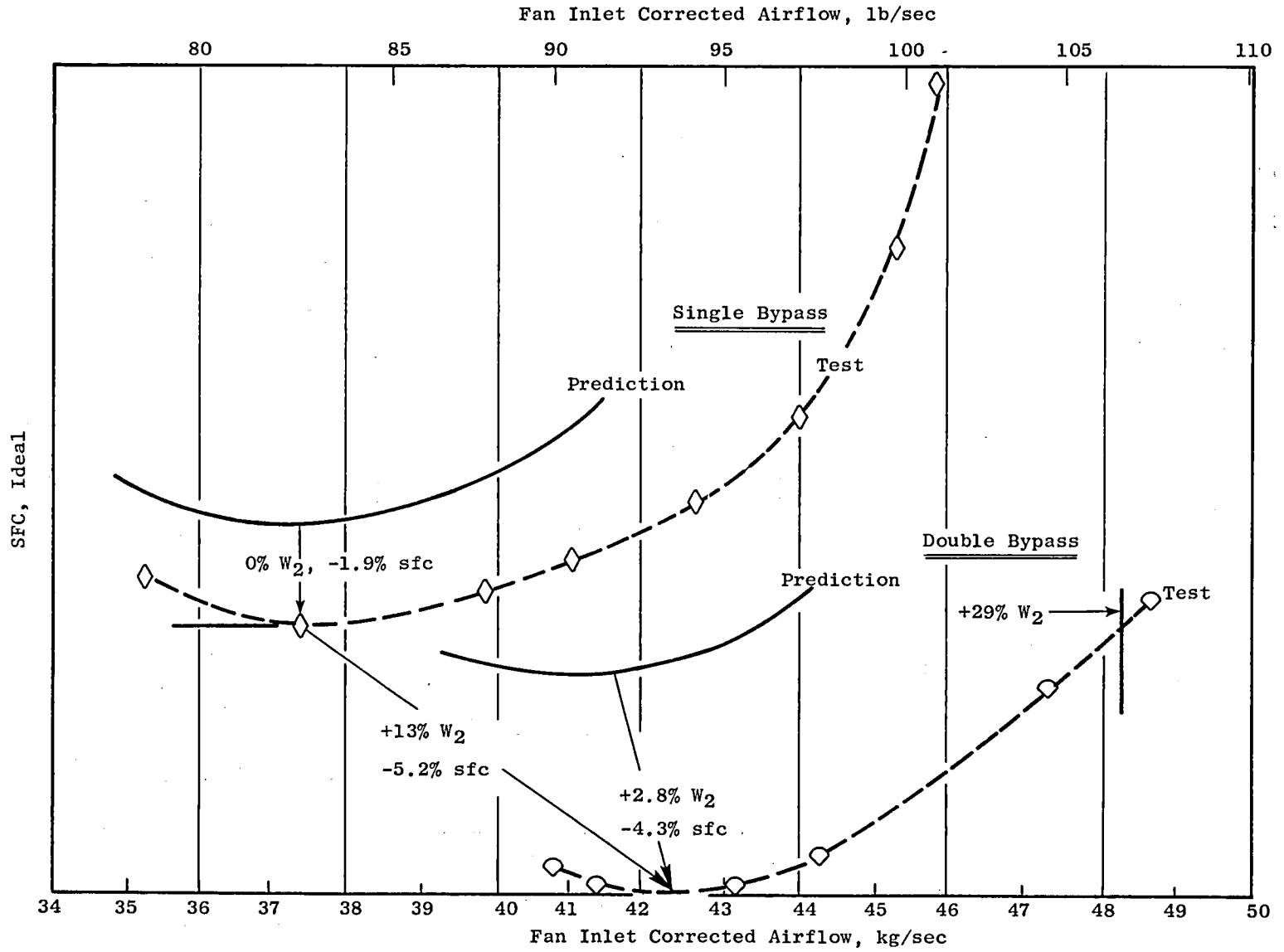


Figure 17. SFC Versus Airflow at 50% Gross Thrust.

- 95% Fan Speed
- $A_{16} = 110 \text{ cm}^2$ (17 in.²)
- $A_{\text{Liner}} = 484 \text{ cm}^2$ (75 in.²)
- $VATN = 597 \text{ cm}^2$ (92.5 in.²)

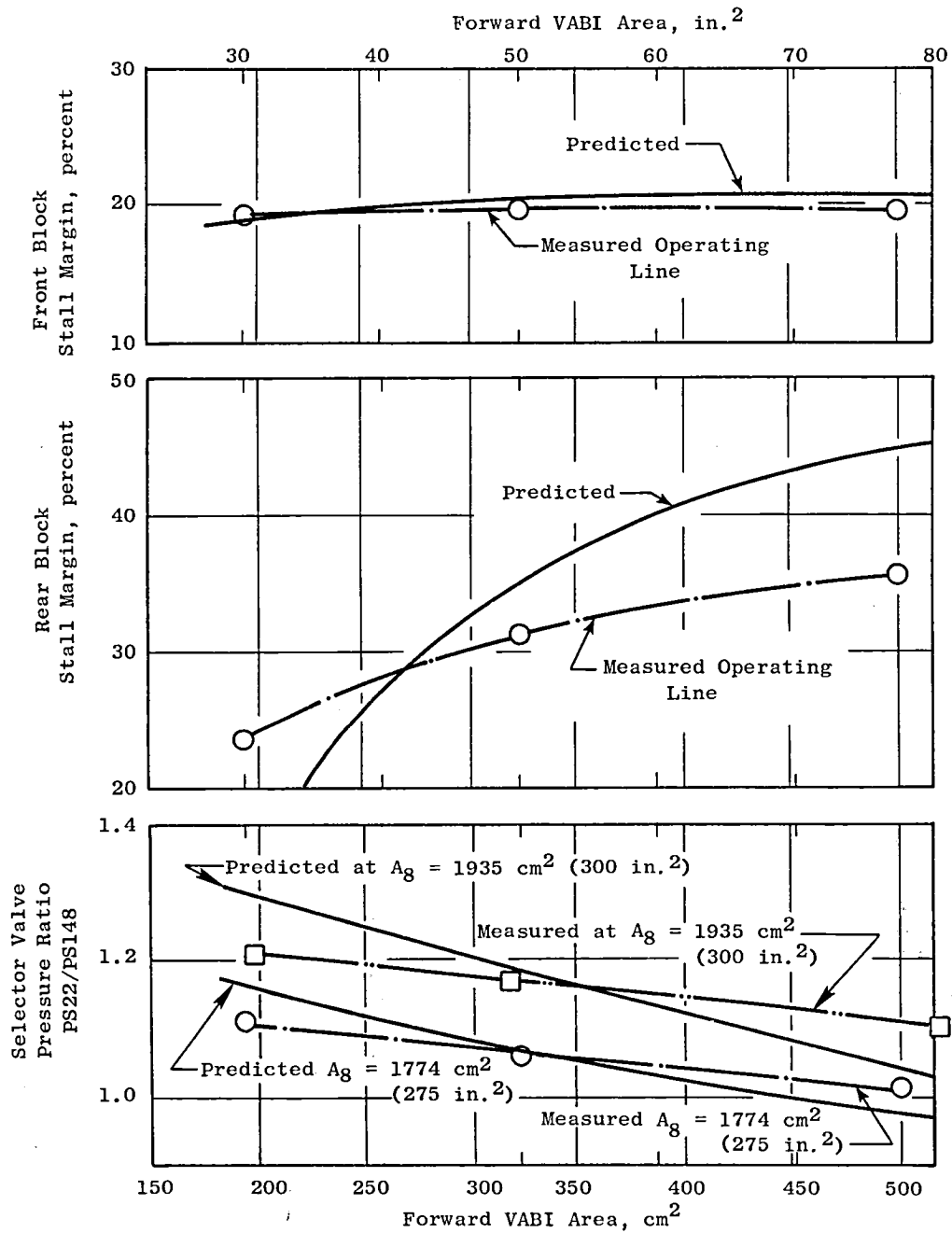


Figure 18. Transition Mapping - 95% Fan Speed.

- 90% Fan Speed
- A16 = 300 cm² (46.5 in.²)
- A Liner = 322 cm² (50 in.²)
- VATN = 597 cm² (92.5 in.²)

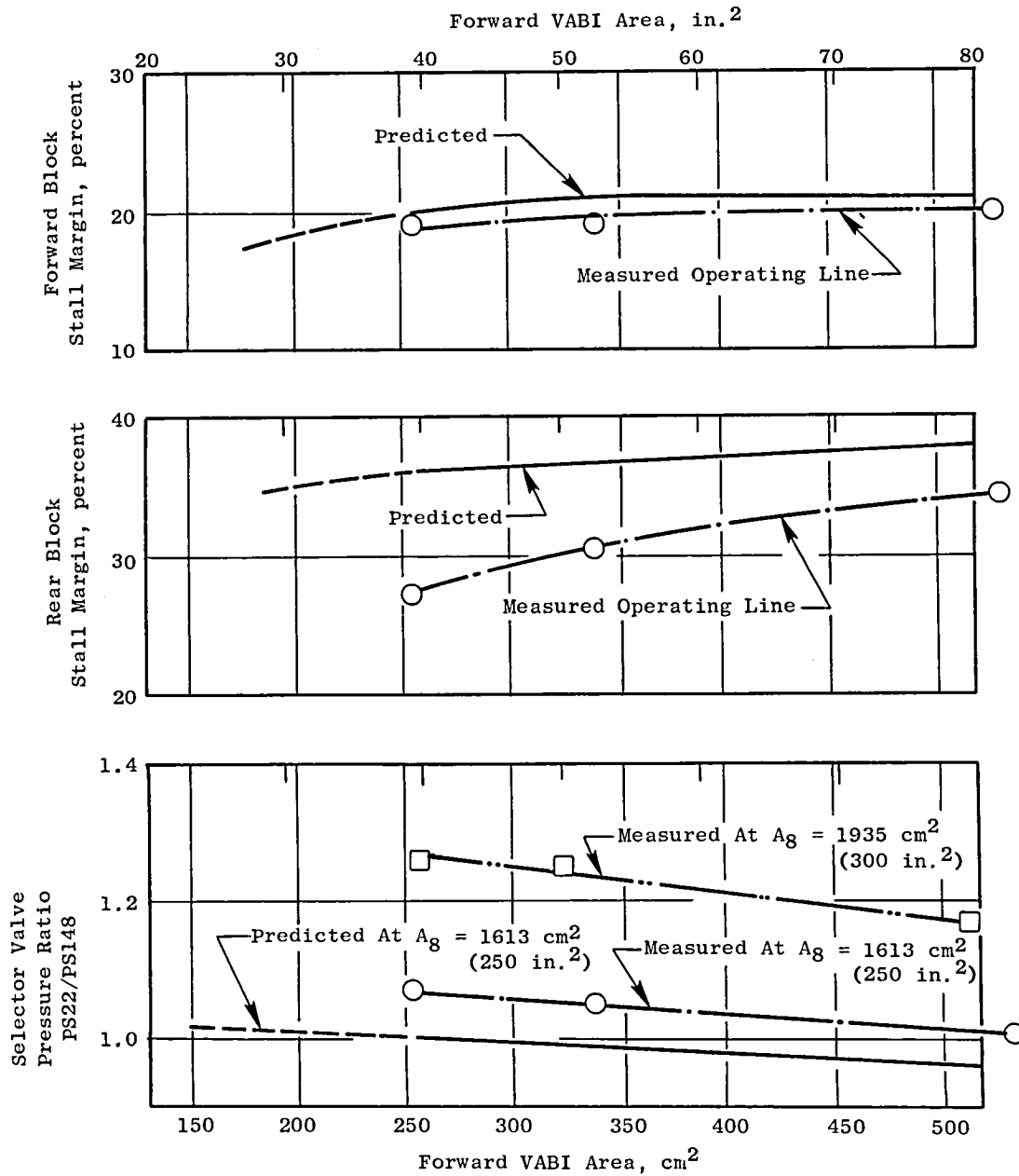


Figure 19. Transition Mapping - 90% Fan Speed.

- 80% Fan Speed
- A16 = 300 cm² (46.5 in.²)
- A Liner = 322 cm² (50 in.²)
- VATN = 597 cm² (92.5 in.²)
- A₈ = 1935 cm² (300 in.²)

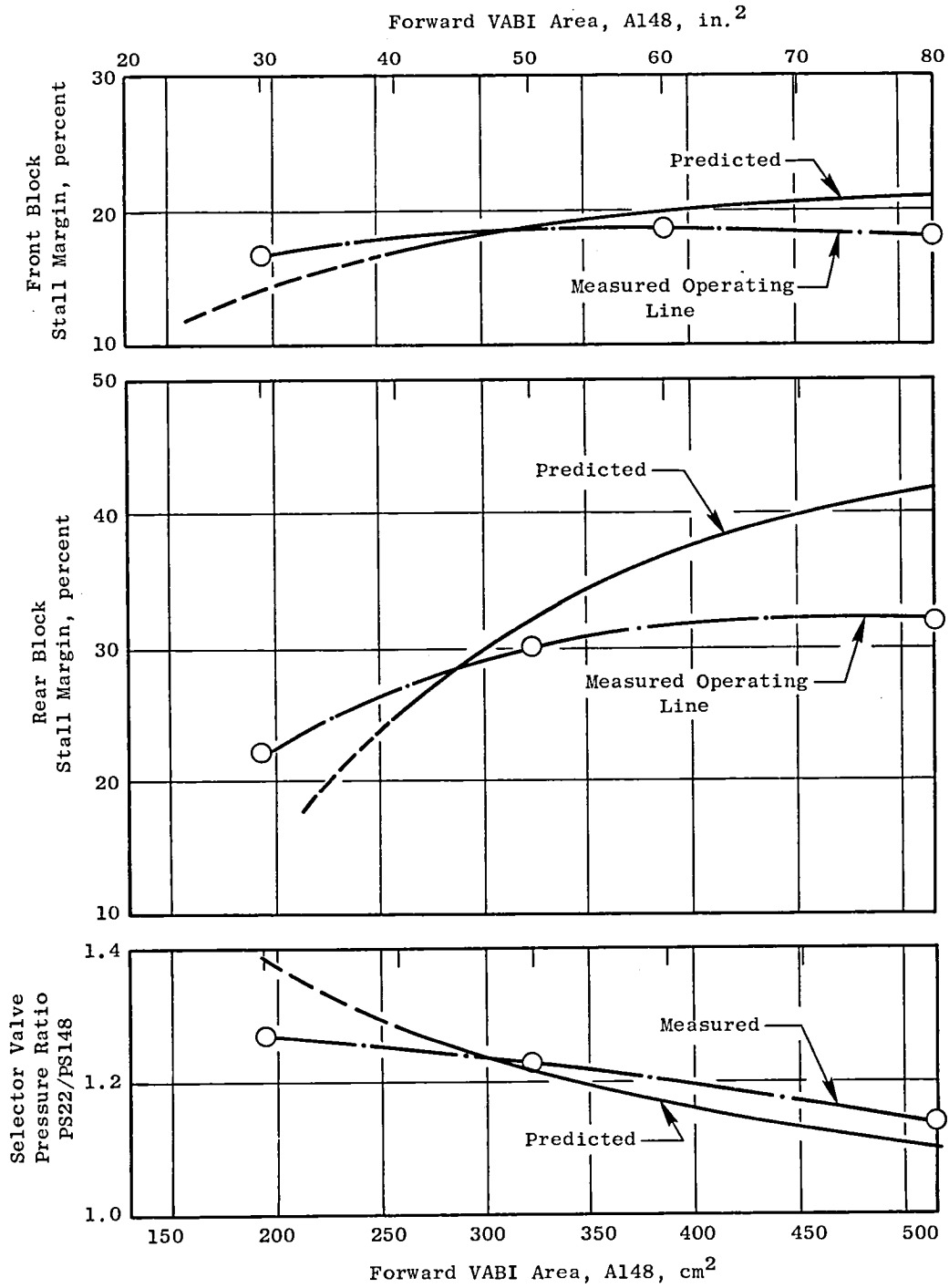


Figure 20. Transition Mapping - 80% Fan Speed.

95% NL TRANSITION

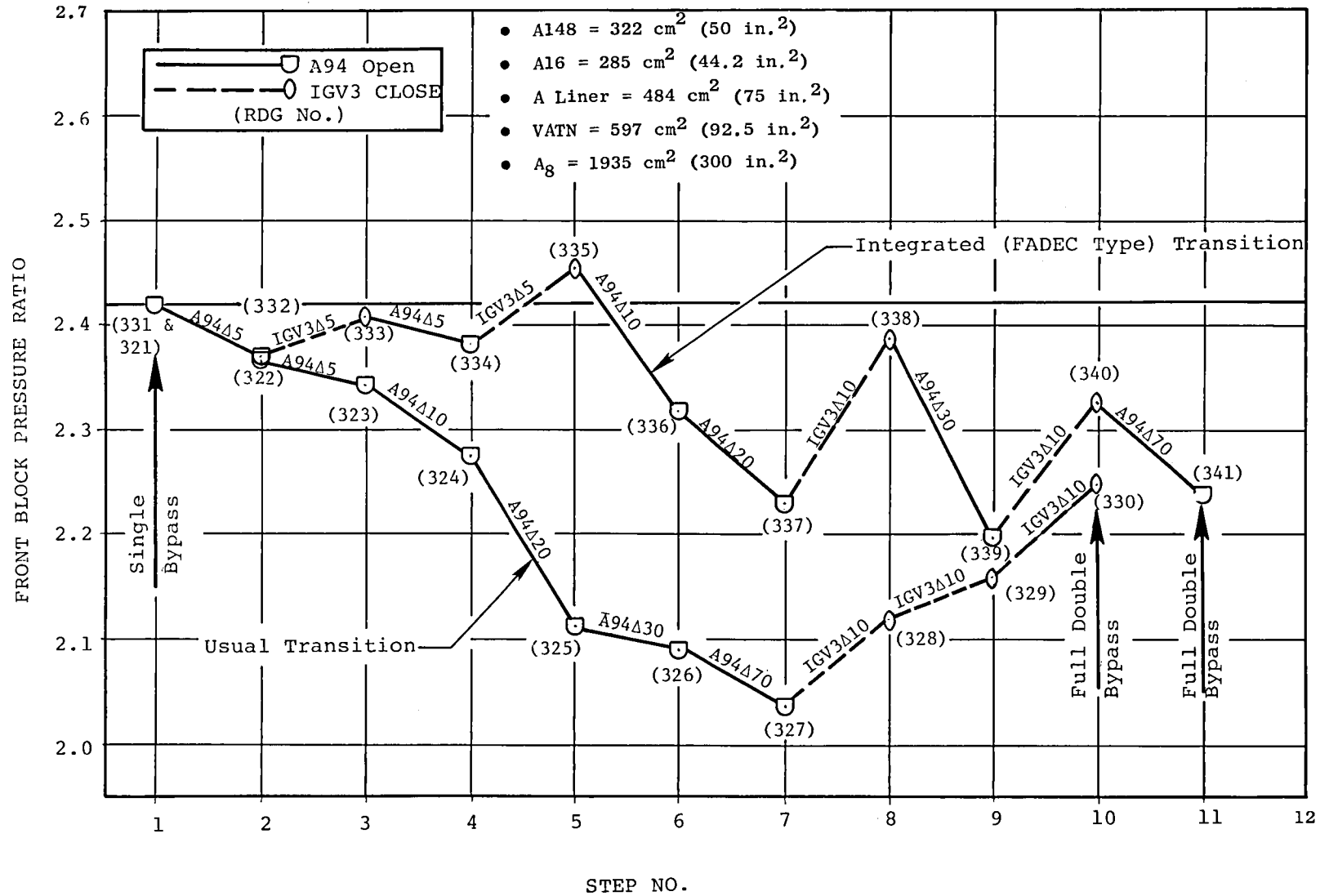
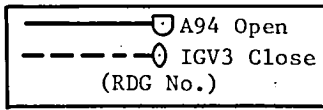


Figure 21. 95% NL Transition.

95% NL INTEGRATED TRANSITION
 WITH RAISED REAR BLOCK OPERATING LINE



- A148 = 194 cm² (30 in.²)
- A16 = 285 cm² (44.2 in.²)
- A Liner = 322 cm² (50 in.²)
- VATN = 597 cm² (92.5 in.²)
- A8 = 1677 cm² (260 in.²)

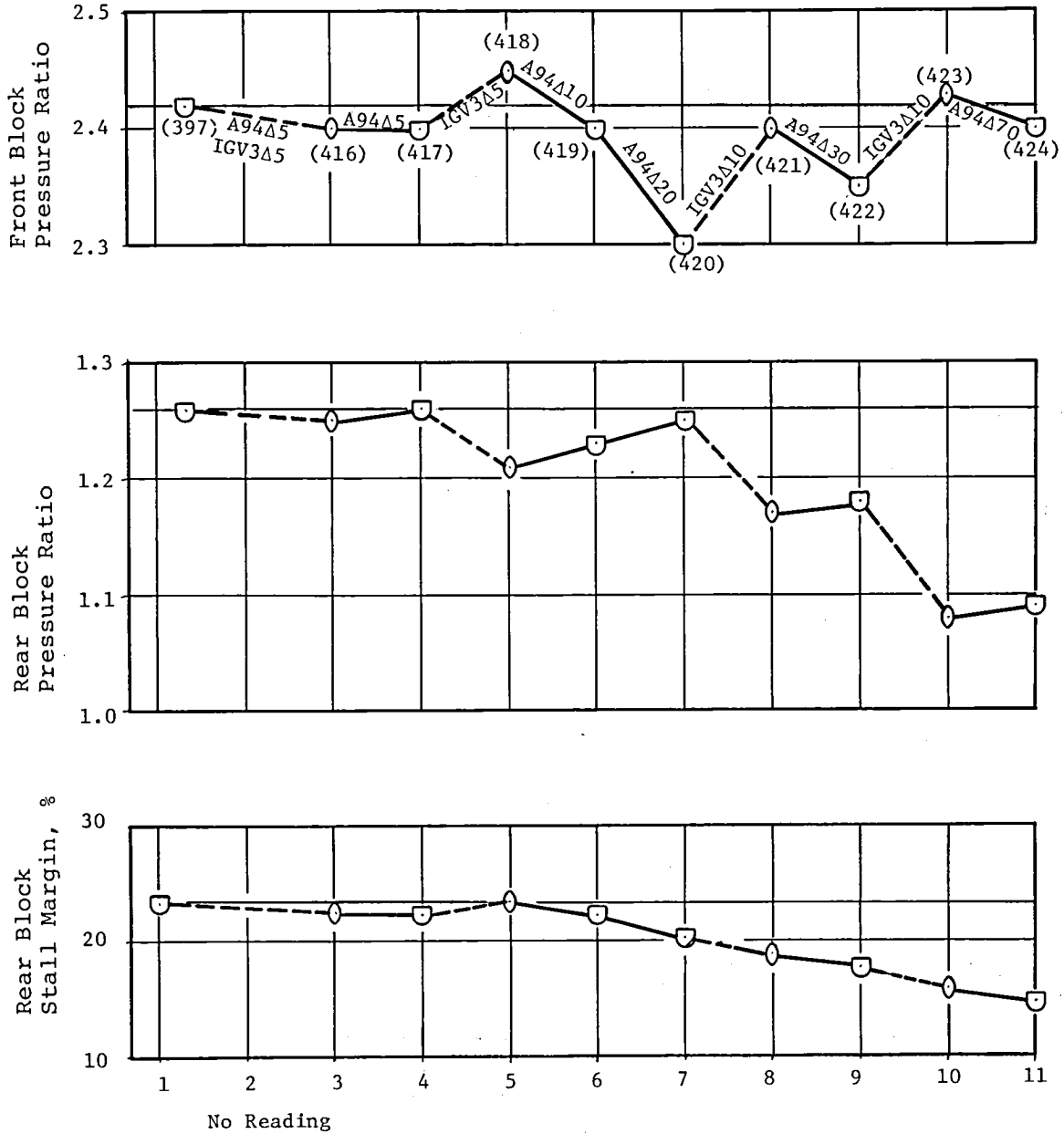


Figure 22. 95% NL Integrated Transition with Raised Rear Block Operating Line.

Two basically different types of transition were demonstrated during the forward VABI testing. The first was a simple approach and was used for the bulk of the transitions going from single bypass to double and back to single. After choosing a set of VCE geometries compatible with both single and double bypass, transition would be achieved solely by a change in the position of the selector valve (A_{g4}). Such a transition is shown by Readings 321 to 327 in Figure 21. The result is a significant lowering of the front block operating line. Readings 327 to 330 show the impact of adjusting IGV-3 from its single bypass position to a typical double bypass setting. This almost restores the front block to its original operating line. Simulation of a more product-like transition involves integrating IGV-3 closure with A_{g4} opening so that its fan front block is held near its operating line throughout the transition, as shown by Reading 331 to 340 in Figure 21. Both of the transitions shown in Figure 21 have low fan rear block operating lines because A_g was open to 0.19 m^2 (300 in.^2) to provide increased forward VABI reverse flow margin.

Figure 22 shows the results of the second type of transition used, an "integrated" transition with the rear block operating line raised to more product-type levels by closing A_g to 0.17 m^2 (260 in.^2). This transition more closely resembles in all respects the way a product engine would respond during a transition from single bypass to double.

4.3.2.3 Distortion

The 2x1 VCE with forward VABI was tested with two inlet distortion screens:

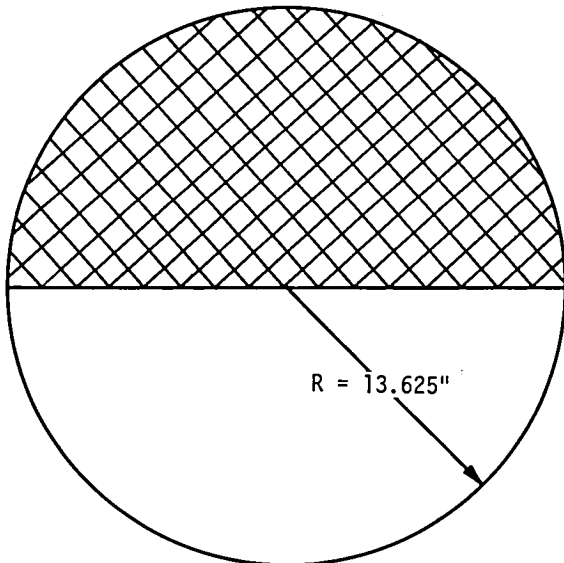
1. 180 degree - 1/rev-type, pattern L100
2. YJ101 flight-type, pattern L401.

The screen patterns and resulting distortion levels are shown in Figure 23. Steady-state readings were taken along the operating line that gave the best sfc in single and double bypass. No significant stress levels or instabilities were observed during the distortion testing.

4.3.3 Forward VABI Aero Performance

To verify the forward VABI component feasibility prior to the coannular acoustic nozzle test program, aerodynamic performance data were obtained from the forward VABI engine demonstration. Component performance data for the forward VABI consisted of total pressure and total temperature data taken at the entrance to the forward VABI and at the exit of the bypass duct just aft of the turbine frame. To verify the individual performance elements of the forward VABI system, total temperature, and static pressure measurements were made at several intermediate locations.

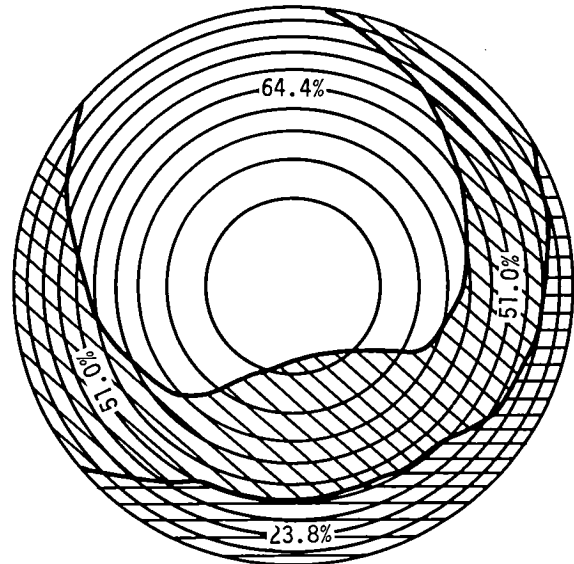
One-Per-Rev
(180° Extent)



• Screen L100

(Subsonic Pattern)

- Altitude = 10,972 m (36,000 ft)
- Mach = 0.8



• Screen L401

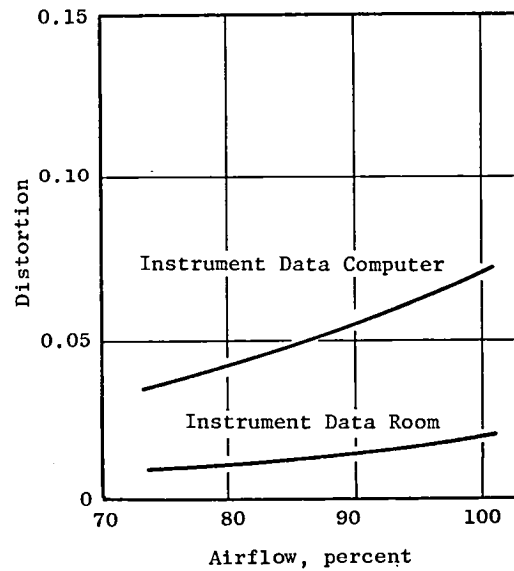
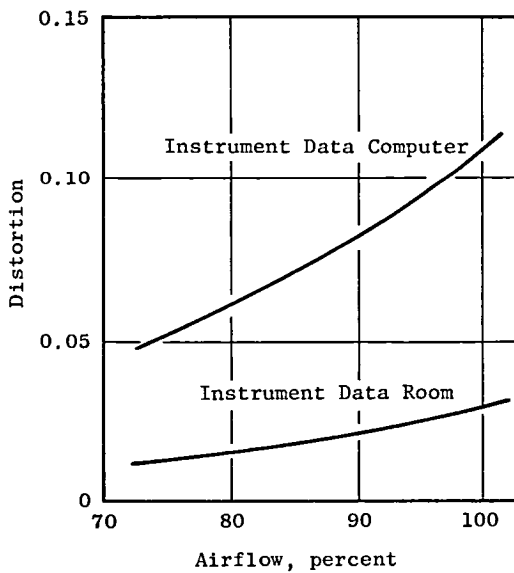


Figure 23. Distortion Screens for Forward VABI Testing.

The overall pressure loss characteristics for the forward VABI and associated ducting are presented in Figure 24. In the figure, typical data are presented for both the single bypass mode and the double bypass mode. During the single bypass mode, the most significant VABI loss agency is sudden expansion from the VABI into the bypass duct. The parameters that most significantly affect this mechanism are Mach number prior to expansion and the area ratio of the expansion. The VABI operating conditions are such that, during single bypass, the forward VABI area is open to reduce overall duct losses. In order to transition from single to double bypass, however, the VABI area is reduced in order to lower the static pressure in the outer bypass duct to values less than the fan air stream at the selector valve (i.e. PS_{22}/PS_{148} must be > 1.0). This area reduction results in an increased overall bypass duct loss, as illustrated by the parametric data in Figure 24. During the double bypass mode, the sudden-expansion loss mechanism is reduced by the introduction of outer bypass duct fan air. This is illustrated in the figure by data taken during increasing amounts of outer duct flow. In the range of interest - full double bypass - the expansions have been minimized and the flow characteristics of the two VABI airstreams are such that the stream mixing losses are minimal. This characteristic was demonstrated both with and without inlet distortion screens.

Figure 25 shows how the aerodynamic performance data apply to potential SCAR mission legs. The figure presents the loss data as a pressure loss relative to the mass-weighted VABI inlet total pressure for typical operating modes. This method of presentation allows an approximate comparison between single and double bypass duct loss levels, and also allows an assessment of the total impact of sudden expansion, duct friction/diffusion, and mixing losses. The data in Figure 25 point to two observations: (1) at key fuel burn legs, the losses are comparable to current-technology engine ducting, and (2) excessive losses occur only during brief mission legs or at favorable performance trade points.

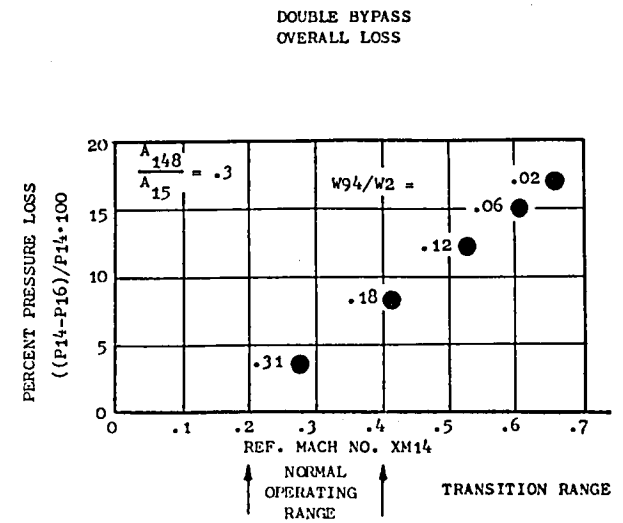
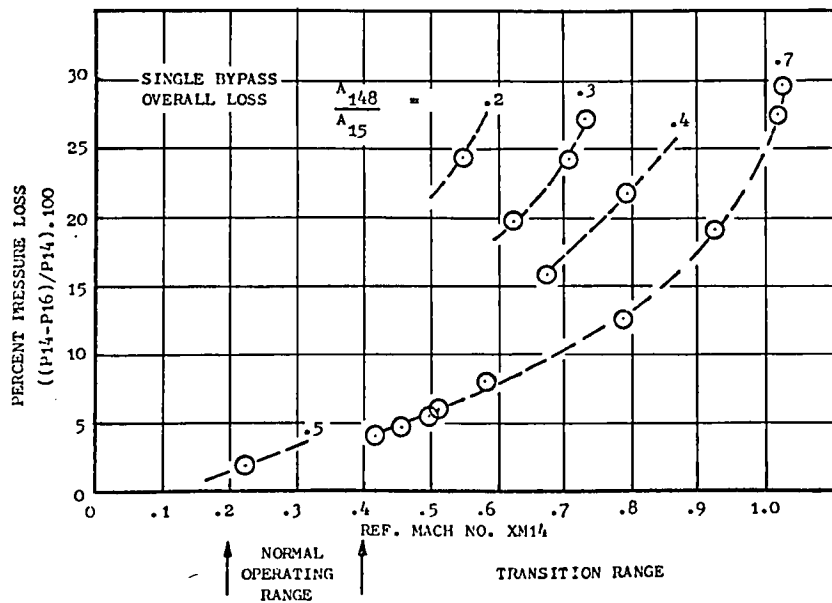
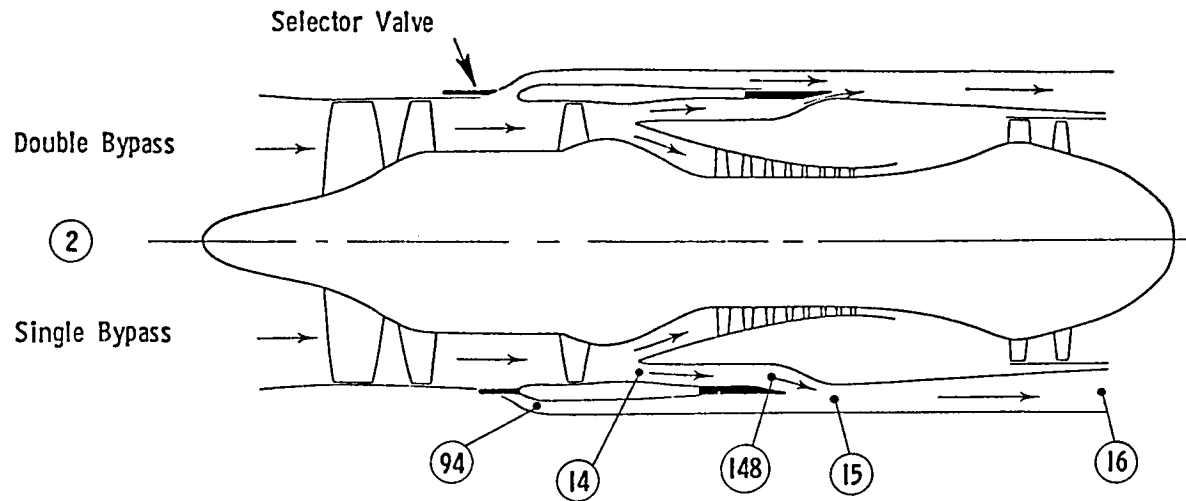


Figure 24. Bypass Stream Losses Resulting from NASA Forward VABI Engine Test.

NASA FORWARD VABI DEMO TEST RESULTS

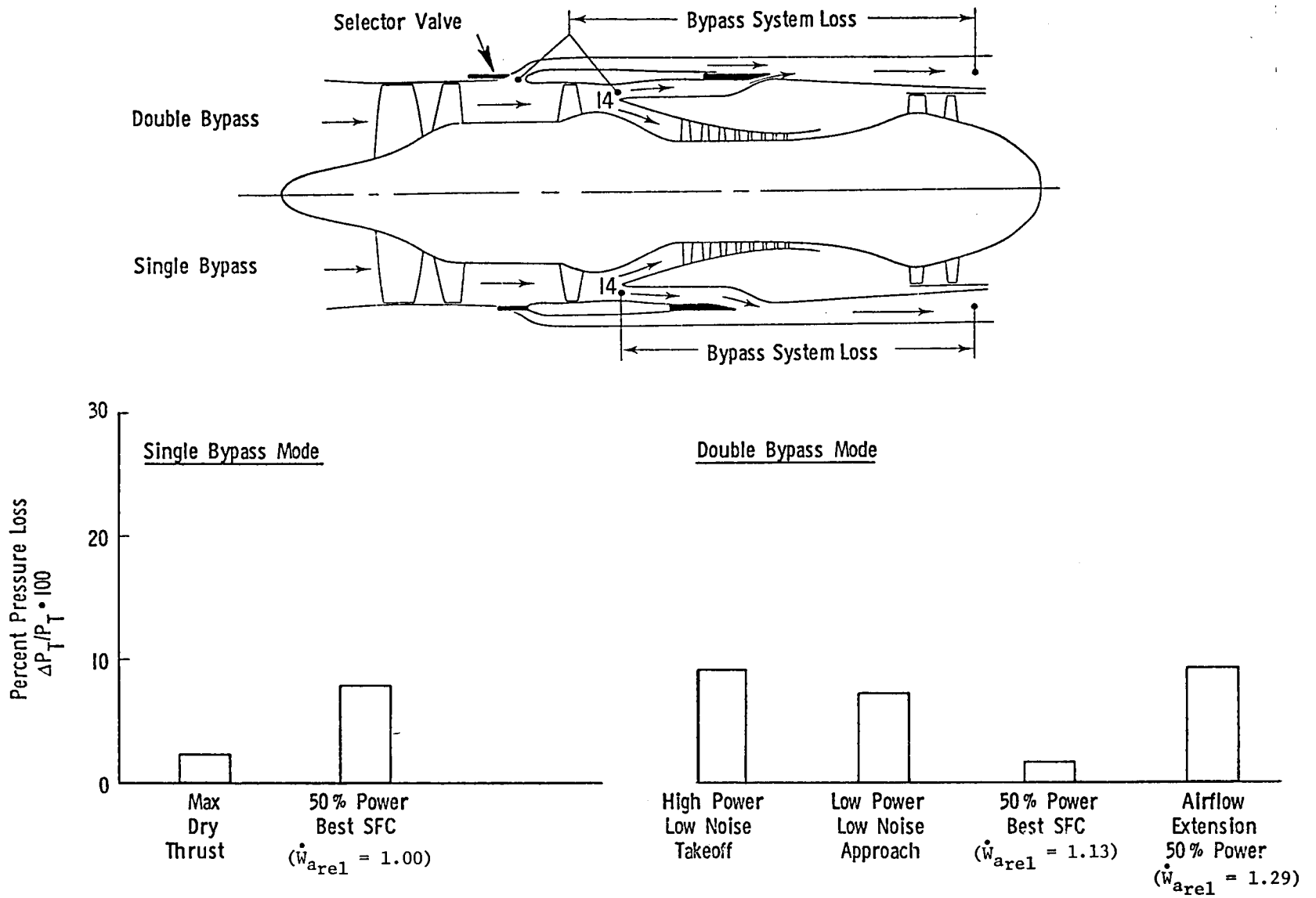


Figure 25. NASA Forward VABI Engine Test Results at Several Key SCAR Mission Throttle Conditions.

5.0 ACOUSTIC TEST OF THE COANNULAR PLUG NOZZLE

5.1 ACOUSTIC NOZZLE TEST OBJECTIVES

The overall objective of the acoustic portion of this engine demonstration was to verify, in YJ101 engine size, the jet acoustic benefit of General Electric's unsuppressed high-radius-ratio coannular plug nozzle. Other significant test objectives for the test program were:

1. To demonstrate acoustic correlation between results from full-scale engine test and those from counterpart scale-model tests in the significant acoustic characteristics.
2. To show agreement between full-scale engine test results and analytical prediction methods, and/or to provide basis for analytical prediction methodology refinement.
3. To accomplish special acoustic testing, including laser velocimeter jet wake traversing, sound separation probe traverses, and ten-foot-sideline noise surveys, in addition to the typical far field surveys, for additional acoustic/aerodynamic information.
4. To test a typical VCE engine with both standard and sound-absorbing bellmouth inlet systems to allow fan radiated noise components to be separated from jet noise.
5. To evaluate three geometric variations of coannular nozzle diameter ratio for acoustic characteristics and to accomplish baseline conic nozzle acoustic and aerodynamic tests to provide a comparison level with the coannular nozzles.
6. To evaluate aerodynamic and performance characteristics of the deep chute rear VABI and a geometric variation of a rear VABI (i.e., side plate removal effects).
7. To demonstrate aerodynamic performance characteristics of the flow-inverting strut system, exhaust duct, and coannular nozzle.
8. To demonstrate overall VCE engine aerodynamic performance characteristics with addition of the coannular nozzle exhaust system.
9. To demonstrate the mechanical feasibility of the coannular exhaust nozzle, including absence of aeromechanical instability and actuation system.

5.2 TEST RESULTS

5.2.1 Test Summary

The NASA VCE Acoustic Nozzle Test followed the forward VABI test and utilized the basic engine/gas generator from that prior test. The acoustic test by its nature required evaluation in an outdoor acoustic facility. The four prior tests had been accomplished in the Lynn sea-level-static (SLS) test facility, Cell 108. The acoustic test was performed at the North Site at Edwards Air Force Base.

An aerial photograph of the overall Edwards facility is shown in Figure 26 showing the test pad, control room and pertinent performance and acoustic data recording facilities with the YJ101/VCE installed. This photo together with Figure 27 also shows the microphone array used for the far field acoustic measurements.

Initial testing was accomplished with baseline conic nozzle with two different inlet configurations. A standard untreated YJ101 bellmouth inlet was tested to verify engine aerodynamic performance and consistency with the prior Lynn results. Figure 28 shows the engine with this inlet configuration and the conic nozzle installed. Following engine performance calibrations in which engine flow-speed and other major performance parameters were measured/verified, a special sound-absorbing (treated) inlet was installed. This was a larger (J79 size) bellmouth with a long treated duct with treated splitters. The treated inlet provided substantial attenuation of the fan forward radiated noise. Acoustic measurements for jet noise were accomplished over a range of engine power settings with three different acoustic instrumentation setups:

- (a) Far field microphone array
- (b) Ten-foot sideline traversing microphone from NASA-Ames
- (c) Internal kulites and sound separation probe traverses to determine engine internal noise sources

In addition, laser velocimeter (LV) wake surveys were made to determine the velocity profile at the nozzle discharge plane and several downstream stations. Approximately 24 hours of testing were accomplished with the conic baseline nozzle.

This was followed by installation of the coannular plug nozzle of 0.853 radius ratio (i.e., inner-to-outer radius ratio for the outer annulus) shown in Figure 29. Outer radius ratio was one of the nozzle design parameters evaluated.) Figure 30 shows the engine with the previously described treated inlet section and the coannular nozzle installed. This photo also illustrates the NASA-Ames ten foot sideline microphone setup.

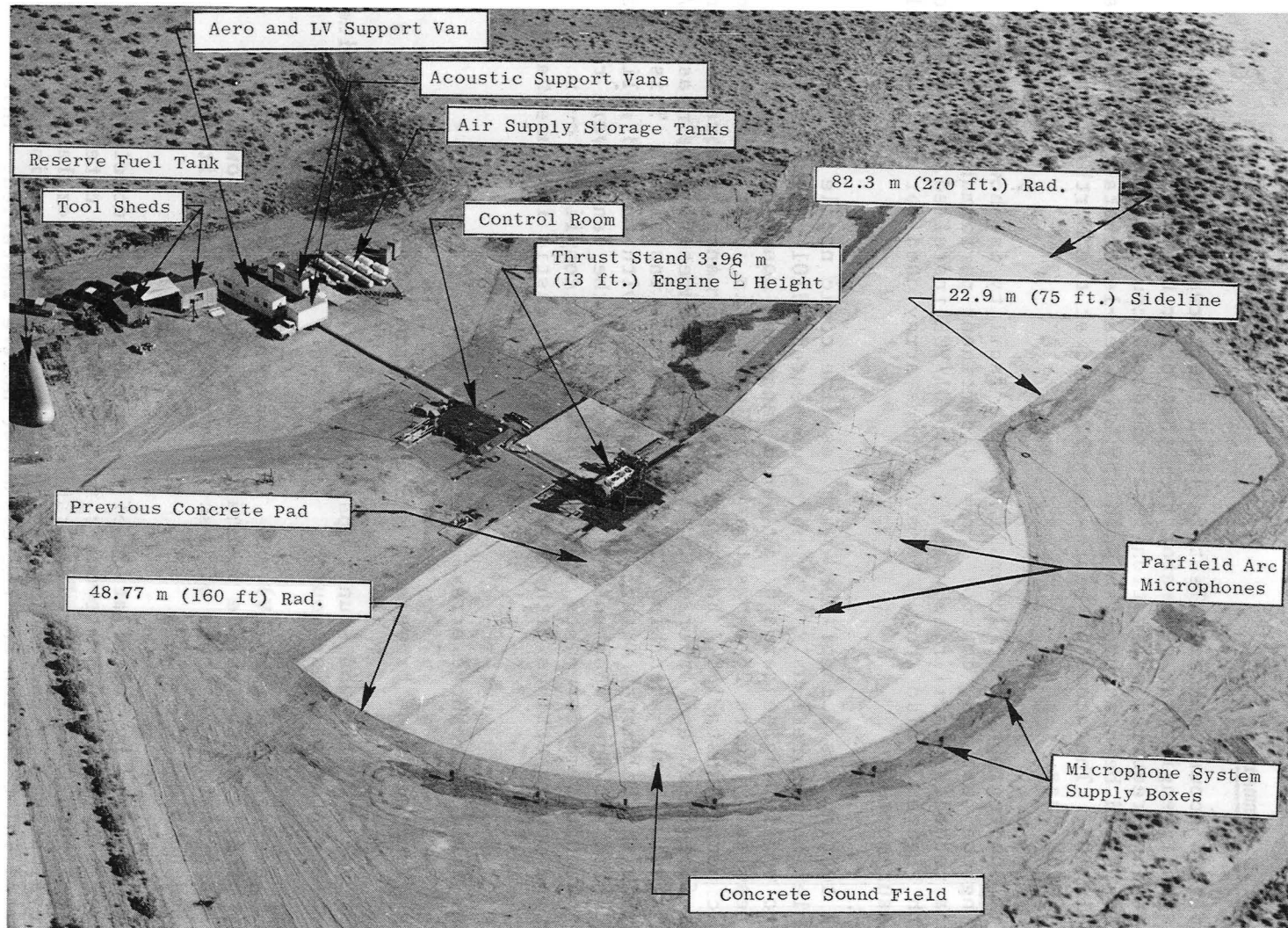


Figure 26. Edwards Air Force Base North Test Site.



Figure 27. Edwards Acoustic Test Site Showing Microphone Setup.

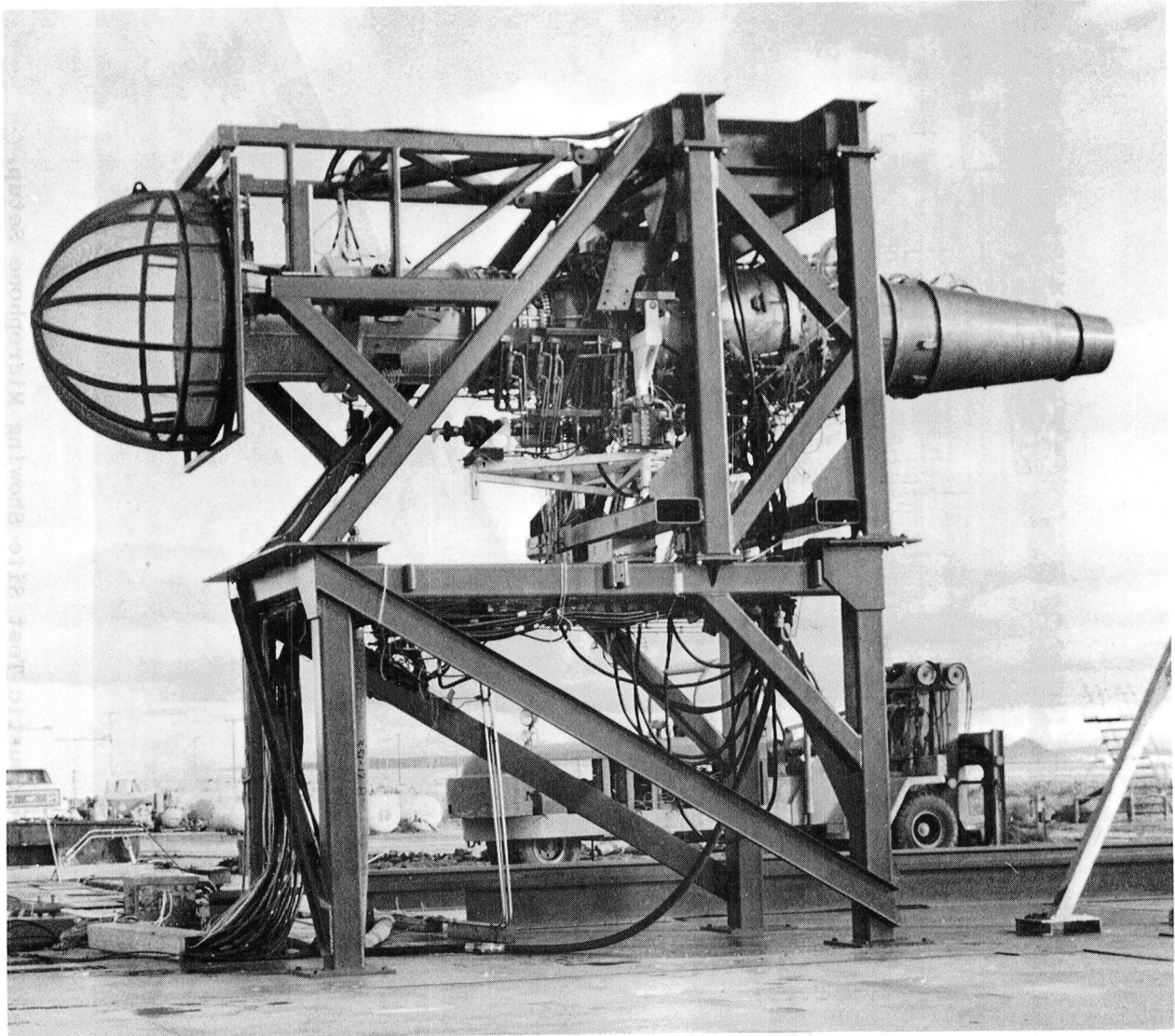


Figure 28. Engine Mounting Arrangement with Baseline Conic Mixed Flow Nozzle and Standard Untreated YJ101 Bellmouth Inlet with Protective Screen.

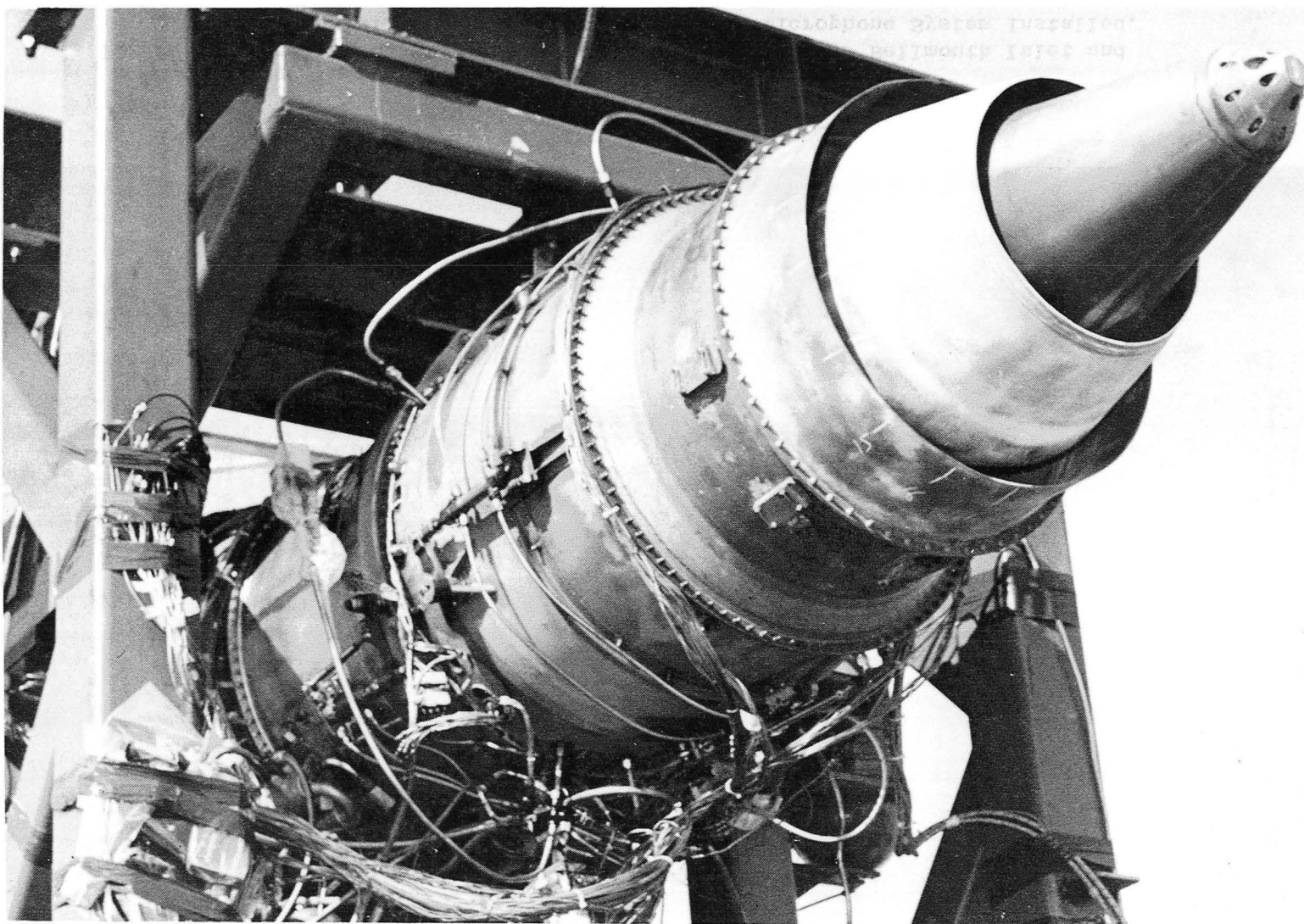


Figure 29. Coannular Plug Nozzle, $A_r^i = 0.475$, $R_i^o = 0.853$.



Figure 30. Early Acoustic Test Vehicle with Treated J79 Bellmouth Inlet and Coannular Exhaust Nozzle; Traversing Microphone System Installed.

Performance and acoustic testing over a broad range of engine power settings was accomplished in both single bypass and double bypass operating modes. Additionally, variations in nozzle area ratio (i.e., inner-to-outer coannular area ratio) were evaluated in the single bypass mode. Variations in the rear VABI geometry were also evaluated, with removal of the rear VABI side plates. The three different acoustic measuring methods described in relation to the conic test were also accomplished for the coannular nozzle. Figure 31 shows the laser velocimeter apparatus in position for coannular nozzle velocity surveys. Far field and aerodynamic performance tests were accomplished on two other geometric variations of the coannular nozzle (0.816 and 0.875 radius ratio).

In total, approximately 73 hours of testing were accomplished, of which approximately 49 hours were with the coannular nozzle installed.

5.2.2 Summary of Results

The results of the YJ101 engine, and select model scale acoustic tests performed under a separate contract (NAS3-20619), have shown that a significant amount of acoustic technology advancement has been achieved for Advanced Supersonic Cruise type aircraft. From the static YJ101 VCE test program the following summary of acoustic results is listed:

- For the first time anywhere, rather comprehensive advanced acoustic (far field, near field, probe, and coherence) measurements were successfully and systematically performed on a high performance VCE engine test vehicle with a high-radius-ratio coannular plug nozzle.
- Significant static jet noise reduction (4-6 PNdB peak aft angle) and shock noise reduction (approximately 7 PNdB) was verified in YJ101 engine size for General Electric's high-radius-ratio coannular plug nozzle.
- Scale model and engine jet noise scaling criteria for coannular plug nozzles were verified.
- A unique spectral prediction method of jet and shock noise for coannular plug nozzles was successfully developed and illustrated.
- Probe and coherence measurements showed no significant core noise contribution relative to the jet noise.
- Typical supersonic three (3) stage closely coupled fan noise was measured - inlet radiated noise was approximately 5 PNdB higher than high bypass fans under static conditions.

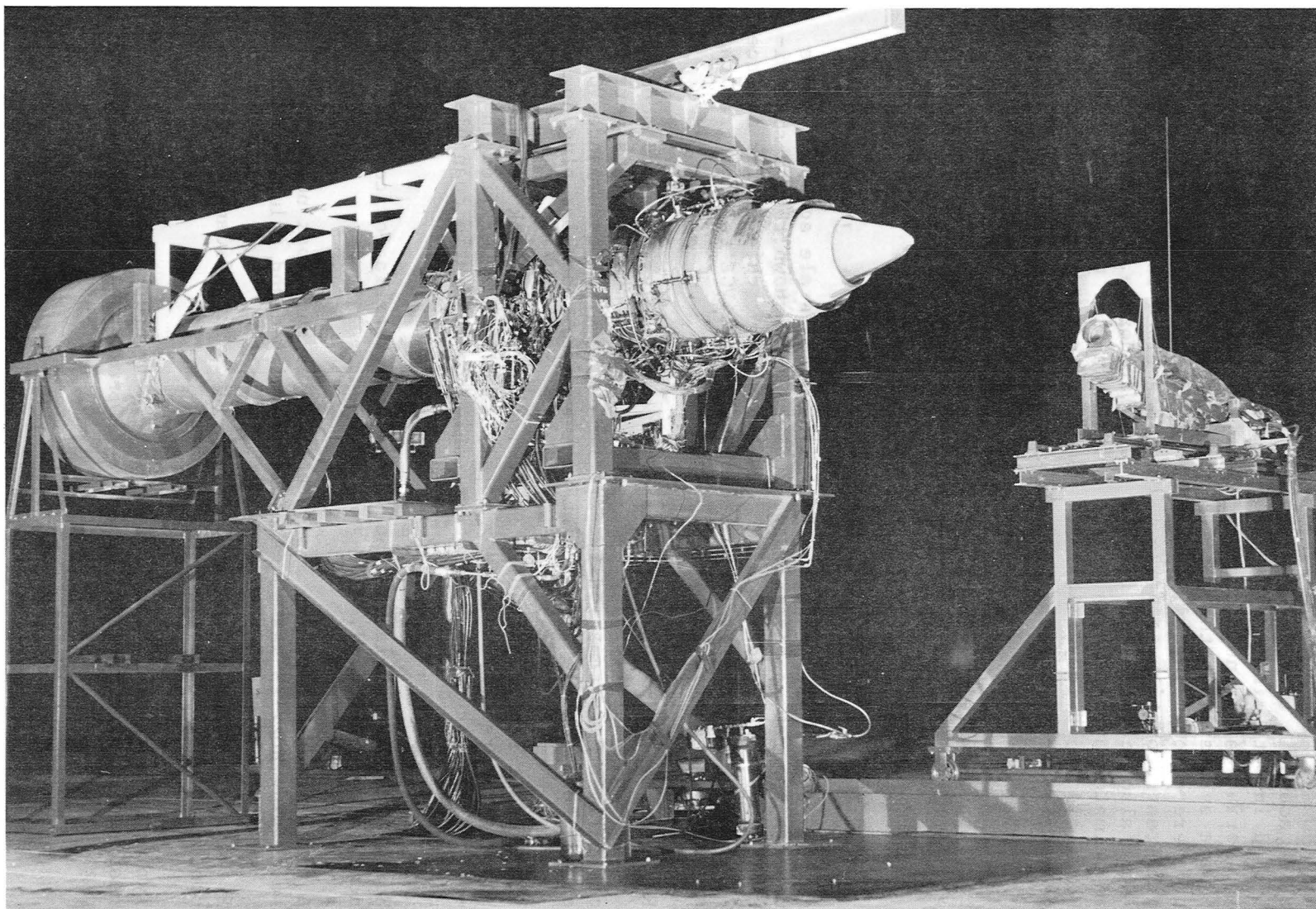


Figure 31. Early Acoustic Test Vehicle with Laser Velocimeter.

- Extensive laser velocimeter mean velocity and turbulence velocity measurements were acquired. The YJ101 engine exhaust plane turbulence levels were measured to be relatively low (approximately 4%). Comparison of engine measurements with model scale measurements was found to be very good.

Additional significant accomplishments of the Edwards test program were the following:

- The engine aerodynamic performance met or exceeded predicted levels, due in large part to lower than expected pressure losses in both the flow inverting strut system and the core engine diffuser/exhaust. Open variable IGV schedules were employed to assure attainment of test flow conditions in both the front block fan and high pressure compressor at the lower shaft speeds necessitated by excessive No. 4 bearing vibrations. There was no observable change in engine aerodynamics and mechanical characteristics over the course of the test. Acoustic tests were conducted at pressure ratios up to 2.9 in the single bypass mode, yielding a 760 m/s (2500 fps) exhaust velocity for the conic baseline tests. For the coannular nozzle, mass averaged velocities up to 610 m/s (2000 fps) were obtained.
- Most of the Edwards testing was accomplished at night to realize low background noise and low winds. No test delays/interruptions were encountered that were due to environmental effects.
- The mechanical operation of the coannular nozzle and associated new rear VABI was excellent. No vibration/instability was observed under any of the operating conditions. Smooth and responsive positioning of the axially translating inner plug (to vary area ratio and select mode) was observed. Nozzle metal temperatures were within prescribed limits and no metal distress was noted on the hardware at the conclusion of the test.
- An additional accomplishment was the successful remote computer hookup which allowed transmission of engine measured data over a special telephone hookup to computer facilities in Lynn and Evendale and transmission of calculated test results to the Edwards test site so that on-line test results were available to guide/monitor the test. This was particularly important in that this was the first YJ101 VCE test configuration to be run outside of Lynn. All of the prior VCE tests had been accomplished in Cell 108/Lynn. Very limited data-system-incurred delays were experienced throughout the test, using this data system.

Beyond the excellent mechanical operation of the coannular nozzle and VABI, which were the unique, new components in the test, the other VCE features of this YJ101/VCE configuration operated satisfactorily with no observed problems. A large amount of testing was accomplished quickly because

of this and the efficiency of hardware changeovers, which allowed multiple configurations to be tested in extended test runs.

5.3 TEST FACILITY DESCRIPTION AND DATA REDUCTION PROCEDURES

A primary objective of this contract effort was to verify in a YJ101 engine size the jet acoustic benefit derived from an inverted velocity profile in a coannular plug nozzle, demonstrated previously in small-scale model nozzle tests. To achieve this objective a number of selected far field acoustic, near field acoustic, internal acoustic, and exhaust plume velocity measurements were performed on a conic nozzle and on coannular plug nozzle configurations.

Described below are the new acoustic arrangements of the Edwards Air Force Base Test site; far field acoustic and engine aerodynamic performance instrumentation; plus special instrumentation in the form of a laser velocimeter (LV), sideline traverse microphone system, Kulites, and a sound separation probe (SSP).

5.3.1 Edwards Air Force Base Test Facility

5.3.1.1 Test Site

To perform the acoustic measurements for this program, the Edwards Air Force Base North Test Site was resurfaced as shown in Figure 26. The sound field used for this program was paved with concrete to provide a smooth "broom" finished hard-surface for more accurate, closer-toleranced noise measurements. It has a 48.77 m (160 ft) forward quadrant radius and a 82.3 m (270 ft) aft quadrant radius with a 22.86 m (75 ft) lateral sideline connecting the two arcs. The forward quadrant arc is centered for fan noise measurements and the aft quadrant arc is centered on the exhaust.

Microphone power and signal wiring are located in conduits around the perimeter of the pad, terminating in waterproof boxes at 16 locations, each providing the requirements for two microphone systems. Additionally, an aft quadrant fixed box provides service and signal wiring for 16 microphone systems. Cables are laid from these boxes to the microphones. Movable microphone stands are available for variation of the sound field layout, each stand allowing for both ground plane and centerline microphone placement.

The desert terrain makes the facility completely clear of any natural acoustic reflecting surfaces. The control room is semi-buried, the 0.76 m (2.5 ft) of exposed block wall being covered with angled plywood to prevent any possible reflective path to the sound field. Acoustic and aerodynamic/LV data acquisition equipment carriers, fuel tank, compressed air tanks, tool sheds, vehicular traffic pattern, etc., were positioned remote to the engine. This allowed that any possible reflected sound had been attenuated sufficiently so that it would not contaminate the measured engine noise. Air supply

and hydraulic systems were electrically powered and either of inherent low noise level or muffled sufficiently to prevent interference with engine noise measurements.

5.3.1.2 Sound Field

A typical sound field layout (see Figure 32) consisted of:

- a. A 30.48 m (100 ft) radius microphone array, centered on the exhaust nozzle center point (engine station 333.8 for the conical nozzle and engine station 296.8, nominal core exhaust plane, for the coannular nozzles). Both engine centerline height and ground plane microphones were used at 10° increments from $\theta_i = 10^\circ$ through 160°.
- b. An array of 9 ground plane microphones on a 21.34 m (70 ft) lateral sideline, paralleling the engine centerline and located at $\theta_i = 35^\circ, 115^\circ, 125^\circ, 135^\circ, 145^\circ, 150^\circ, 155^\circ, 160^\circ$ and 165°; referenced to the exhaust nozzle center point as in (a) above. The sideline microphones in the aft quadrant were 1.524 meter (5 ft) in from the edge of the concrete pad.

A special sound field layout for fan noise measurements, while using the YJ101 (untreated) inlet, substituted a 30.48 m (100 ft) arc of 9 microphones centered on the inlet in-lieu-of the 21.34 m (70 ft) sideline array in (b) above. These microphones were at the 3.96 m (13 ft) engine centerline height and at 10° increments from $\theta_i = 10^\circ$ through 90°.

For the conical nozzle and a selected coannular nozzle, a traversing microphone system, borrowed from NASA-Ames, was utilized on a 3.048 m (10 ft) sideline. The system was capable of approximately 24.4 m (80 ft) of traverse and positioned for near equal travel forward and aft of the nozzle exhaust planes. The traversing microphones were positioned at engine centerline height. Further details of this system are in Section 5.3.1.4.

Sound field layouts were varied consistent with fulfilling test goals for each configuration. More specific details for each layout can be found in the companion Comprehensive Data Report (Reference 4).

5.3.1.3 Microphone Arrangement

In concert with the basic purpose of acquiring acoustic data whose reflective characteristics are uniform and can be adjusted for in order to ultimately produce pseudo free-field measurements, dual microphone systems were used at each of the basic arc locations shown in Figure 32. A schematic of the movable stand and microphone mount arrangement is shown in Figure 33. The standard setup consisted of:

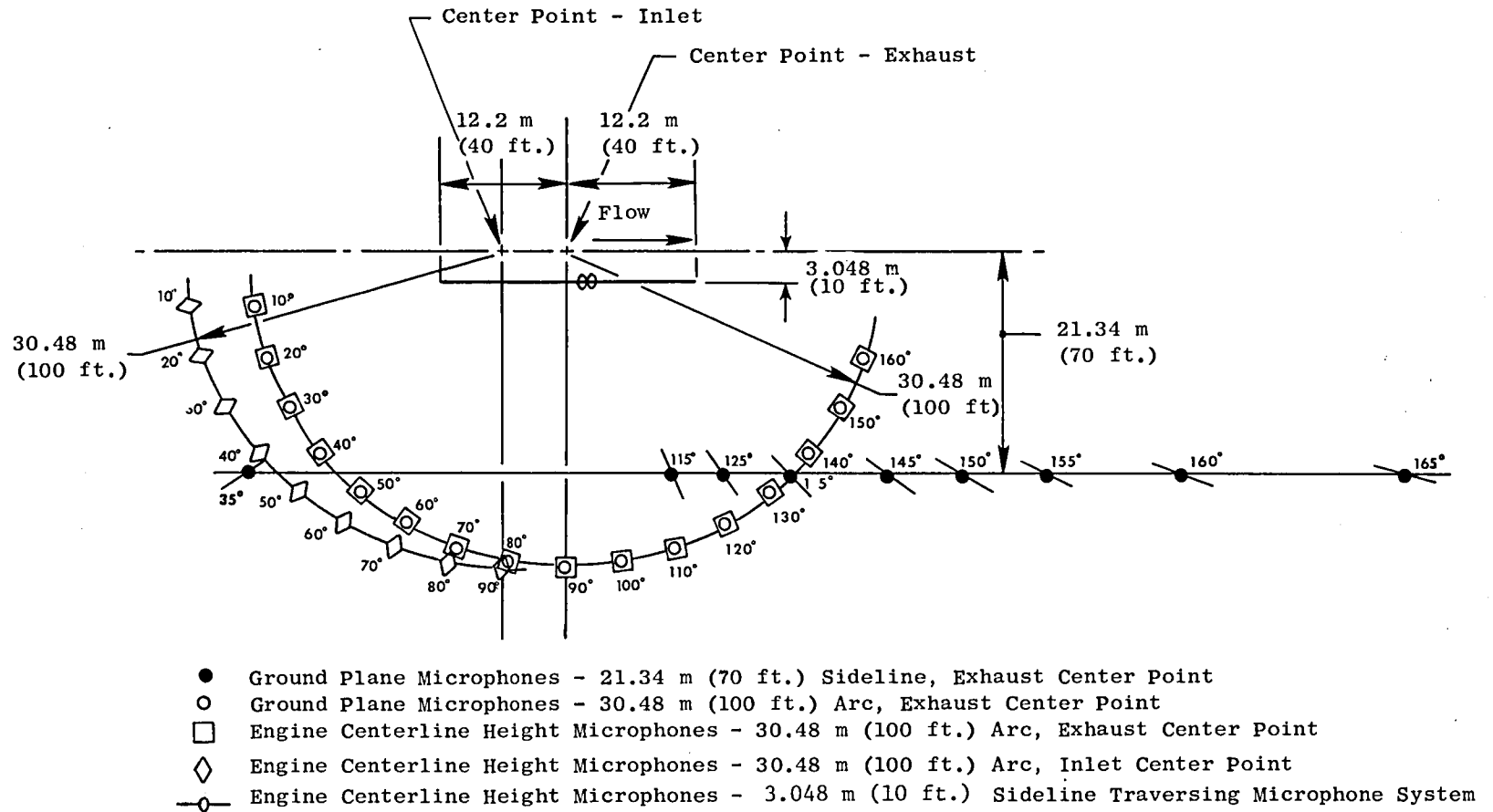


Figure 32. Illustration of Sound Field Layout.

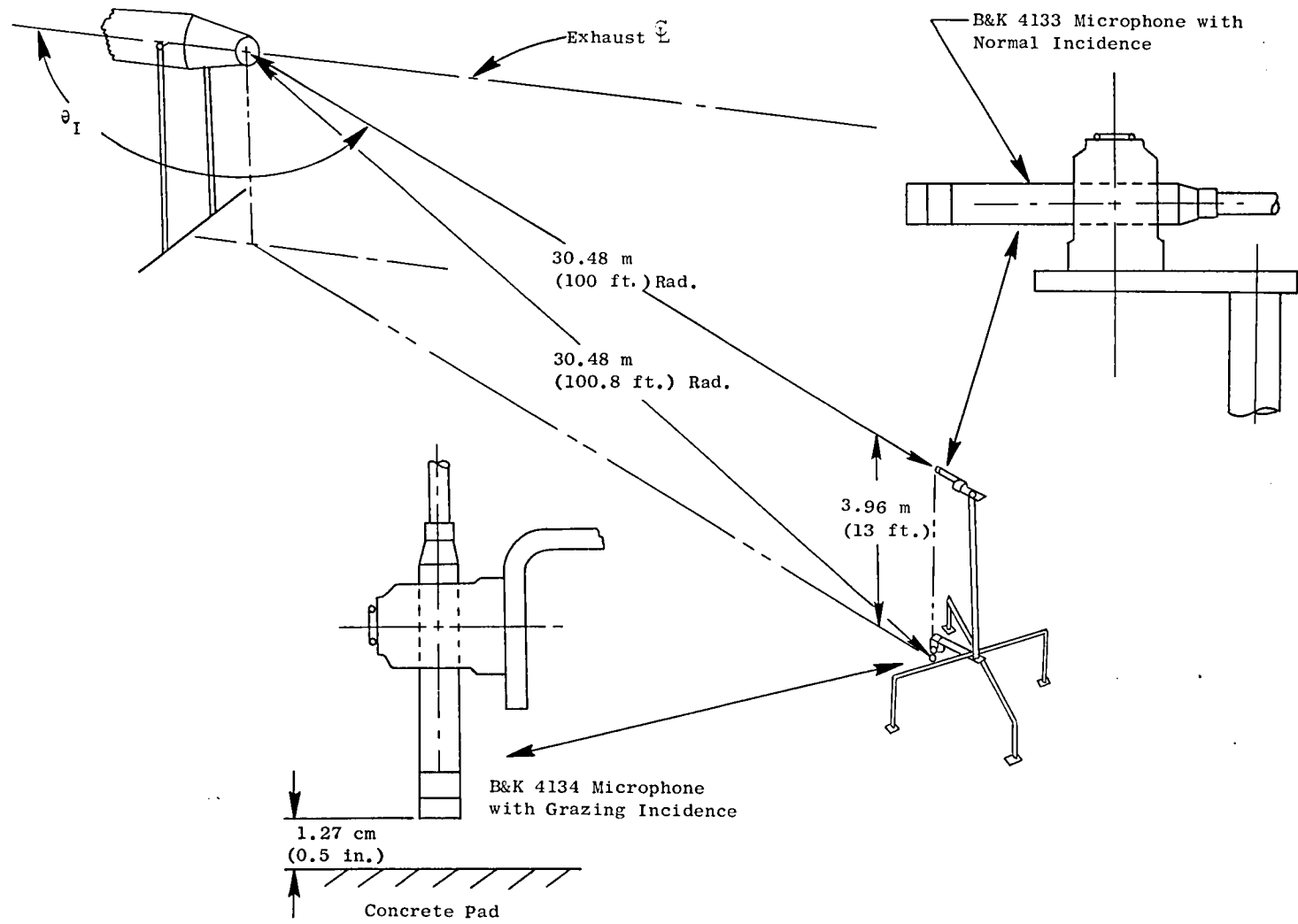


Figure 33. Illustration of Microphone Setup.

- a. B&K 4133 microphones at 3.96 m (13 ft) engine centerline height oriented toward the nozzle exhaust for normal incidence and positioned at 10° increments of θ_i in the plane of the engine centerline.
- b. B&K 4134 microphones accurately positioned 1.27 cm (0.5 in.) above the concrete pad for grazing incidence and located directly under the centerline height microphone; thus, positioned on a true 30.724 m (100.8 ft) arc relative to the exhaust nozzle centerpoint. Deviation from the true angular location relative to the θ_i notation established by the centerline microphones varied from zero for $\theta_i = 90^\circ$ to only 1.3° and 2.4° for the $\theta_i = 160^\circ$ and 10° microphones, respectively. The 1.83 m (6 ft) span of the support legs assured against potential interference and noise reflection problems. Care was taken to assure that the support legs were not in a blocking pattern of noise transmission to the ground plane microphones. As acoustic test periods were scheduled at night when winds were extremely low, wind screens were not required for the ground plane microphones.

5.3.1.4 Special Measurement Systems

In addition to the basic far field acoustic array, special measurement systems were used, including a laser velocimeter, traversing microphones, kulites located in the outer nozzle, and a sound separation probe used for internal measurements in the inner stream of the coannular nozzle as well as in the mixed conic nozzle.

Laser Velocimeter (LV)

The General Electric Laser Velocimeter was developed under a USAF/DOT sponsored program; detailed descriptions of its historical development, principles of operation, signal processing equipment, seeding arrangements, data acquisition and reduction technique, etc. are found in Reference 5. Its use within this program was dedicated to measurements on the conical nozzle to (a) establish mean and turbulent velocity profiles in comparison to conventional conical baseline systems, and (b) to ascertain influence of aft VABI chutes on plume characteristics, and, on the $R_r = 0.853$ coannular nozzle to (1) define possible flow asymmetry associated with any possible nozzle mechanical asymmetry, (2) define mean and turbulent velocity decay characteristics of the annular jet plume relative to the conical nozzle, and (3) ascertain influence of struts and rear VABI chutes on plume characteristics.

An existing LV traversing system used on FAA/DOT Contract DOT-OS-30034 was adapted for this program. The system was placed on the north side of the thrust pad, per Figure 34, opposite side to that of the sound field, such that it could be retracted behind the engine when not in use to eliminate

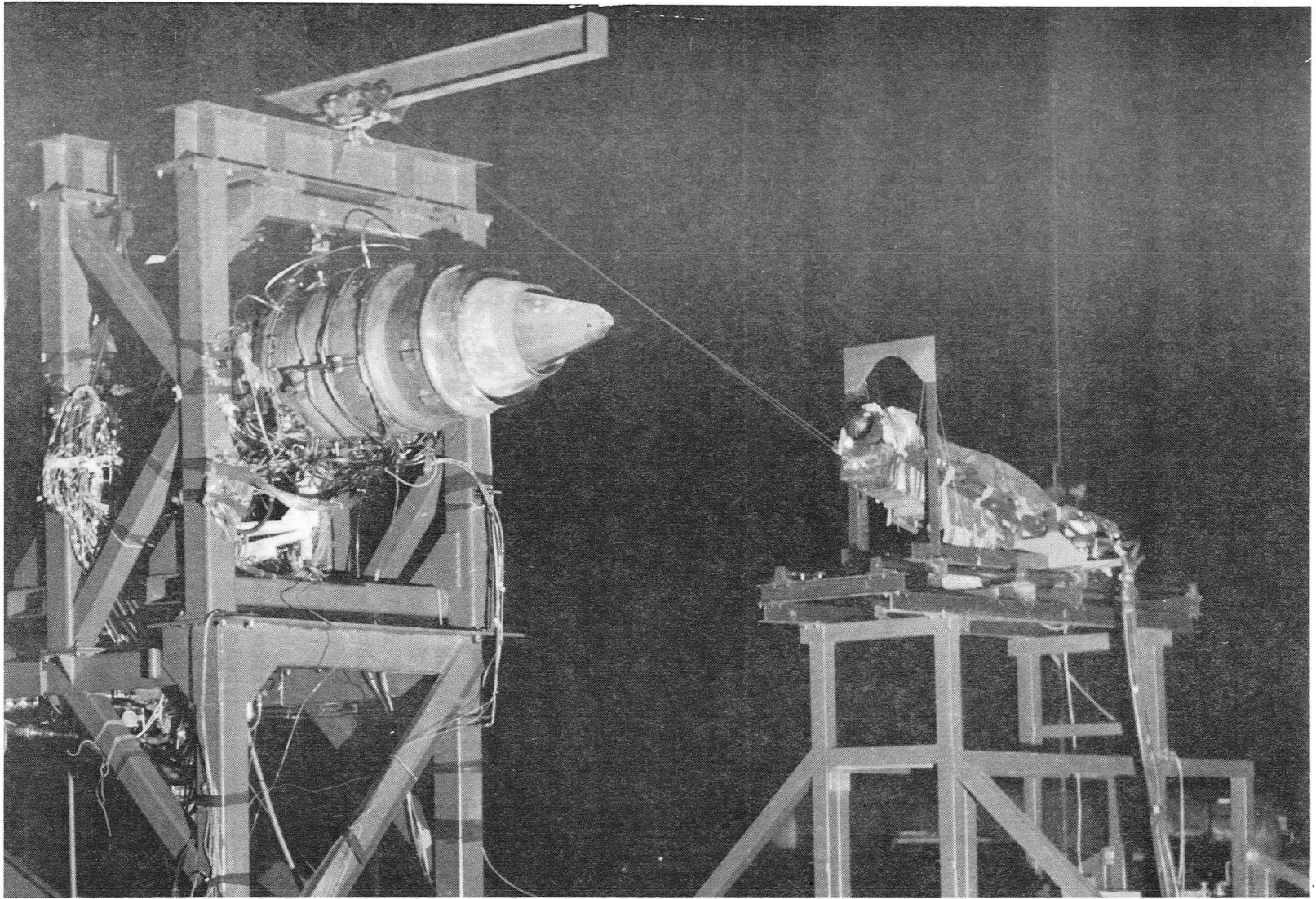


Figure 34. Laser Velocimeter System Application to the YJ101 Test Program.

potential noise reflection. Physical placement of the LV's three-dimensional actuation system was done to maximize utilization of its traverse capabilities in fulfilling the required plume measurements. The 1.65 m (65 in.) horizontal traversing capability was split to allow 0.64 m (25 in.) of travel past the flow centerline and 1.02 m (40 in.) of withdrawal. The cart system was modified to provide similar vertical plume coverage. In the axial direction, approximately 8.23 meter (27 ft) of traverse was available for plume definition through $X/D_{eq.} = 20$.

Seeding rings and probes for injection of aluminum oxide powder were applied prior to LV testing as follows:

- An annular seeding ring at engine station 253 to provide core flow seeding upstream of the VABI chutes and support struts.
- Seeding probes at engine station 248 to provide seeding within the bypass duct prior to the rear VABI chutes.
- An annular seeding ring just aft of engine station 290 within the inner nozzle, to supply seeding to the bypass flow ducted through the support struts.
- An external seeding ring placed the exit plane to seed entrained ambient flow.

Sideline Traversing Microphone System

A traversing microphone system consisting of two B&K 4136 microphones with wind screens was used in conjunction with the fixed sound field arrays to identify source locations for the conical and $R_T^o = 0.853$ coannular nozzles. The traverse system, illustrated in Figure 35, (on loan from NASA-Ames) was located on a 3.048 m (10 ft) lateral sideline to the engine axis and was capable of 24.38 m (80 ft) of traverse, encompassing acoustic angles of $\theta_i = 40^\circ$ through 165° . The rail was mounted on a 3.048 m (10 ft) high ground support stands. The microphones were mounted on a boom support affixed to the traversing rail cart giving a total microphone height equal to the engine centerline height of 3.962 m (13 ft). Traverse of the cart/microphone system along the rail was accomplished by a chain drive mechanism, powered by a variable speed motor. The system was capable of delivering a constant linear rate of travel; approximately 2.93 m/minute (9.6 ft/minute) being set for this test. Monitoring the output of a 40-turn potentiometer, connected to the drive system, allowed for rail calibration in output voltage versus traverse distance. This signal was also parallel recorded with the microphone signal. The microphones at engine centerline height consisted of a primary and secondary (spare) system which were recorded simultaneously during each data traverse along the rail. The primary microphone signal was split and recorded at both normal and 10-dB down gain to accommodate full signal dynamic range requirements.

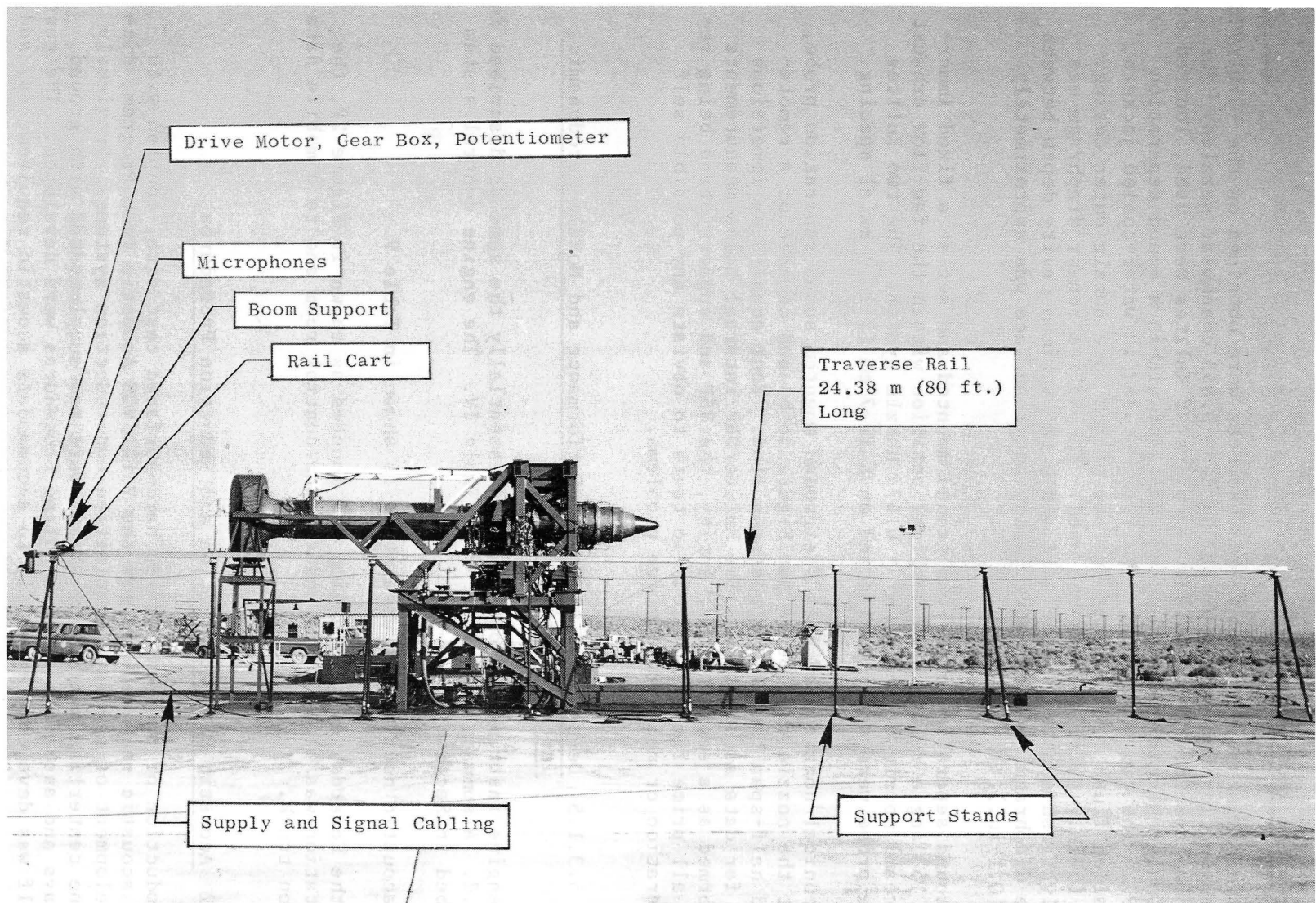


Figure 35. Sideline Traversing Microphone System Application to the YJ101 Test Program.

Kulite Instrumentation

Internal fluctuating pressure measurements were obtained on the YJ101/VCE test-bed engine for both the conical and $R_T^o = 0.853$ coannular nozzles. For the coannular nozzle, Figure 36(a), two pairs of Kulites were used, located on the core (outer stream) exhaust nozzle wall and within a sound separation probe (SSP). The two wall mounted Kulites, housed in water-cooled jackets, were installed flush to the inner surface of the core nozzle outer casing. A 12.7 cm (5 in.) axial spacing was used. The Kulite sensor diaphragm was essentially flush mounted to the wall since the maximum cavity depth between the Kulite diaphragm and the water jacket outer surface was approximately 0.254 cm (0.1 in.).

The sound separation probe was ground mounted and set at a fixed immersion on a 15° angle relative to vertical position within the fan-flow exhaust (inner stream) nozzle of the $A^i/A^o = 0.475$ nozzle system. The two Kulites within the probe were water cooled and on a 12.7 cm (5 in.) axial spacing.

The conical nozzle used only the ground mounted sound separation probe, located at the nozzle exit plane per Figure 36(b) and capable of a remote-controlled half-span traverse across the flow. Four equal-area immersions were used for data acquisition. The Kulite/SSP internal noise measurements were performed as a separate test entity, the SSP and support stand being removed for all prime far field acoustic tests to obviate any possible self noise generation or noise reflection problems.

5.3.1.5 Description of Engine Performance and Nozzle Aerodynamic Instrumentation Setups

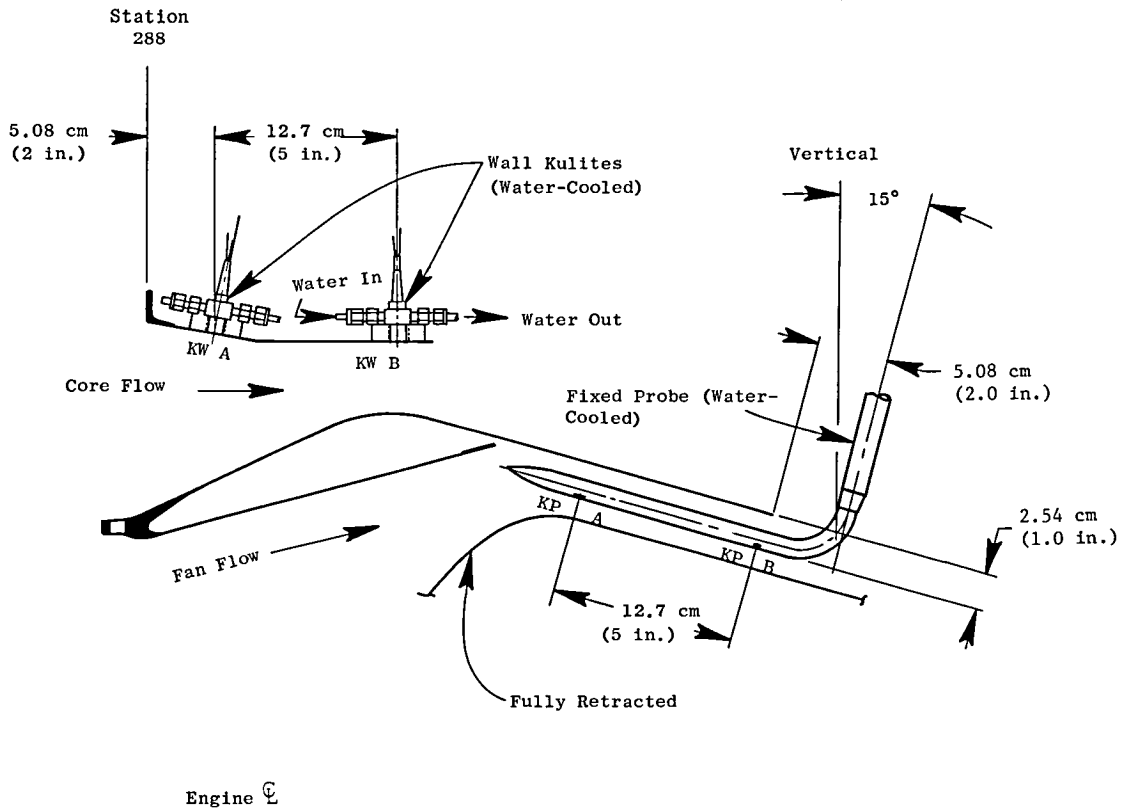
The engine instrumentation setup was essentially the same as described in Section 4.2. A summary is presented in Table IV. The engine control system is described in Section 3.7.

The acoustic nozzle instrumentation is shown in Table V.

For the Edwards test the engine was mounted as shown in Figure 28, the instrumentation was piped to an underground control room and to a mobile data acquisition truck.

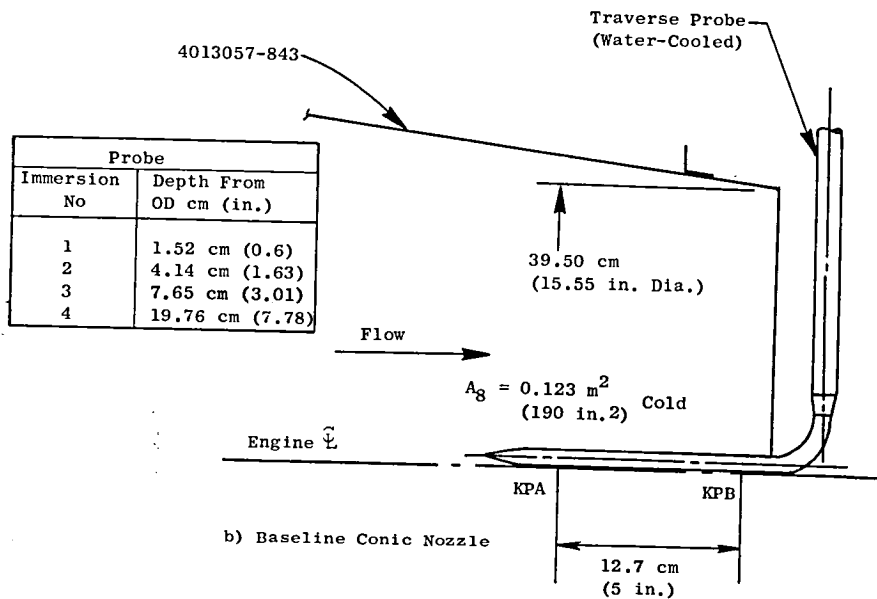
5.3.2 Acoustic Data Acquisition and Reduction Procedures

Introduction of the new Edwards hard-surfaced test site, coupled with stringent acoustic requirements for the YJ101/VCE Acoustic Test Program, dictated development of new data acquisition and reduction systems. Previously used engine centerline microphone arrays were now supplemented with ground plane arrays and associated data handling procedures were developed. The test site itself was developed primarily to accommodate acoustic requirements, and, with its acoustically-favorable environment, yielded data of high confidence.



Engine \bar{L}

a) Coannular Nozzle, 0.85 Radius Ratio



b) Baseline Conic Nozzle

Figure 36. Kulite Instrumentation on YJ101/VCE Coannular and Conic Nozzle Configurations.

Table IV. Acoustic Nozzle Test Instrumentation
Engine/Gas Generator Requirements.

<u>Station</u>	<u>No. of Rakes or Taps</u>	<u>No. of Elements Available</u>	<u>Type</u>	<u>Quantity Utilized</u>	
				<u>P</u>	<u>T</u>
2	4	6	P/PS (Pitot Statics)	48	-
2	8	3	T	-	12
22	4	5	P/T	20	10
25	4	5	P/T	20	10
3	4	4	T	-	16
3C	2	1	PS (Wall)	1	-
56	4	5	P/T	20	20
94	4	3	P/T	12	6
14	4	3	P/T	12	6
14.5	4	5	P	20	-
14.8	4	1	PS (Base)	4	-
16	4	3	P/T	8	12
16	4	1	P	4	-
22	4	1	PS (Wall) OD	4	-
14.5	4	2	PS (Wall) OD (1) ID (1)	8	-
94	4	2	PS (Wall) OD ID	4	-

Table V. Acoustic Nozzle Instrumentation.

<u>Engine Station Location</u>	<u>No. of Rakes</u>	<u>No. of Elements</u>	<u>Type</u>
259.0	1	1	PT
260.0	1	3	PT
264.5	1	3	PT
265.5	2	8	PT
269.0	1	3	PT
274.0	1	3	PT
276.0	1	1	PT
283.0	8	8	PT and Temp.
289.5	3	5	PT and Temp.
290.0	1	1	Kulite
295.0	1	1	Kulite
308.0	1	1	Sound Separation
313.5	1	1	Accelerometer
Various	42	1	P-Static
269/301	2	1	T/C Skin

- For the conic nozzle a 30 element PT and Temp. probe was provided.

5.3.2.1 Acoustic Data Acquisition and Reduction Systems

Primary far field acoustic data were acquired on a 30.48 m (100 ft) arc far field array, selected for the following reasons:

- Model conical and conular jet noise measurements from NASA Contract NAS3-20619 were scaled to YJ101 engine size and had shown that the anticipated noise signature at a 30.48 (100 ft) distance could be accommodated within the dynamic range of the planned recording equipment.
- Measurements to 20 kHz, considered necessary for accurate scaling to full scale VCE [linear scale factor of ≈ 2.5 from YJ101 size to a 0.9032 m^2 (1400 in.^2) AST size would set data through 8 kHz], would be possible without jeopardizing the high frequency, low noise level, portion of the noise signature.

The spectra to be reported are obtained by combining data from centerline and ground microphones.

Engine Centerline 3.96 m (13 ft) Microphone Systems

As these systems supplied the high frequency portion of the merged spectra, the requirement for data accuracy to 20 kHz was imposed. B&K systems were used with Type 4133 microphones mounted in normal incidence for flat frequency response to 20 kHz. A Honeywell 28-channel recorder was used, operated at 152.4 cm/sec (60 in./sec) in Wideband Group I, double extended with carrier frequency = 108 kHz. Pretest checks indicated an approximate 50 dB response from optimal peak to the 20 kHz 1/3 octave band for this recorder. As further assurance to provide extended dynamic range for $\theta_i = 110^\circ$ to 160° , hi-pass filters were used with $f_{hi-pass} = 8 \text{ kHz}$, such that the signals of the six aft quadrant microphones could be double recorded. This was done to provide a greater dynamic range, required to accommodate the fast drop-off characteristics of both conical and coannular spectra at the aft quadrant angles.

Ground Plane 1.27 cm (0.5 in.) Microphone Systems

As these systems supplied the lower frequency portion of the merged spectra, the requirement for data accuracy to 10 kHz was imposed. B&K systems were used with Type 4134 microphones mounted in grazing incidence for flat response to 10 kHz. A Genesco 28-channel recorder, operated at 152.4 cm/sec, (60 in./sec) in extended-intermediate mode with carrier frequency of 54 kHz, provided a pretest calibrated range of about 50 dB response from optimal peak to the 10 kHz 1/3 octave band.

Sideline (Ground Plane) Microphone Systems

The 21.34 m (70 ft) sideline microphone systems were similar to the 30.48 m (100 ft) arc ground plane microphone systems.

On-line data monitoring was provided through a bank of seven scopes for each recorder as well as through a General Radio 1/3 Octave Band Spectral Analyzer coupled to an X-Y plotter. Pre- and posttest pistonphone calibrations were done as applicable for each test period. Pink noise system calibrations were performed for establishing data acquisition and data reduction systems' response prior to the major test elements and at intervals as elements of the microphone systems were replaced.

Wet and dry bulb temperatures plus barometric pressure, to be used in normalizing acoustic data to a standard day, as well as wind speed and direction were measured in the vicinity of the control room. Acoustic testing was conducted at night as desert winds were very low, normally from 0.9 to 2.7 mps (2 to 6 mph). Relative humidity was normally within a band from 30 to 50% and contributed to reliable operation of the microphone systems.

Off-line data reduction of the analog data tapes was performed at GE-Evendale using an automated 1/3 octave band reduction system. This system included a GEC3700B 28 channel tape system coupled with a General Radio 1/3 octave band analyzer and controlled by a GEPAC-30 computer with operator-provided information. A 32 second integration time was used to provide adequate sampling of the low frequency portion of the data signal. Interface with the GEPAC-30 computer corrected the data for frequency response of the acquisition and reductions systems (as determined from the pink noise calibration) and for the microphone head response, then merged the standard and hi-pass filtered data for the $\theta_i = 110^\circ$ through 160° microphone systems. Processing through the FTFSR-21 acoustic data reduction computer program corrected the data for atmospheric attenuation from the ambient measuring day to a 288 K (59° F)/70% relative humidity standard day using Shields & Bass absorption model (Reference 6). Processing the engine centerline and ground plane microphone data through the DATPROC-21 Program merged the spectra sets (see Section 5.3.2.2), displayed the data in YJ101 size on the 30.48 m (100 ft) measuring arc, scaled the data to an AST 0.9032 m² (1400 in.²) size, displayed it on a 731.5 m (2400 ft) sideline, and calculated all pertinent OASPL, PNL and PWL values. These data sets can be found in the companion Comprehensive Data Report (Reference 4).

5.3.2.2 Spectral Merging for the Two-Microphone System

Prior to scaling and extrapolation to AST size and sideline, the measured static 30.48 m (100 ft) arc far field data from the two-microphone system at each angle were corrected to approximate free field conditions and merged as follows:

$$F_i = R_i (G_i - 6) + S_i (P_i - 3)$$

where:

i = the index of the one-third octave band, ranging from $i = 17$ to 43 for the 50 Hz through 20 kHz bands

F_i = Free field SPL

G_i = SPL measured by the ground plane microphone

P_i = SPL measured by the engine centerline height microphone

Note: G_i and P_i have been corrected for system response and to a 288° K (59° F), 70% relative humidity standard day prior to this merge procedure.

R_i = Weighting factor for the ground plane microphone according to Table VI.

S_i = Weighting factor for the engine centerline microphone according to Table VI.

Table VI. Ground Plane and Engine Centerline Microphone Weighting Factors.

Band No. (i)		17 to 30	31	32	33	34	35	36 to 43
1/3 O.B. Cent. Freq., Hz.		50 to 1K	1.25K	1.6K	2.0K	2.5K	3.15K	4K to 20K
Weighting Factors	R_i	1.0	0.83	0.67	0.50	0.33	0.17	0.0
	S_i	0.0	0.17	0.33	0.50	0.67	0.83	1.0

Figure 37 shows typical conical and coannular nozzle 100 ft arc ground plane and engine centerline height microphone measurements and the resultant merged free-field spectra using the above technique.

5.3.2.3 Acoustic Data Confidence

Generally favorable meteorological conditions at the Edwards test site, such as consistently low winds and moderate humidity, led to a high degree of confidence in the acquired acoustic data. Thus equipment problems and lost test days due to adverse weather were minimal and the total test was accomplished over a short time period in a near-consistent ambient environment. These factors led to a repeatable and consistent data base.

Conical Nozzle

- Rdg 103, 90% Corr. Fan Spd.
- $\theta_i = 130^\circ$
- 30.48 m (100 ft) Arc
- 288 K (59° F), 70% R.H. Std Day

Coannular Nozzle, $R_r^o = 0.853$,
 $A_i^o / A^o = 0.2$

- Rdg 331, 90% Corr. Fan Spd.
- $\theta_i = 150^\circ$
- 30.48 m (100 ft) Arc
- 288 K (59° F), 70% R.H. Std Day

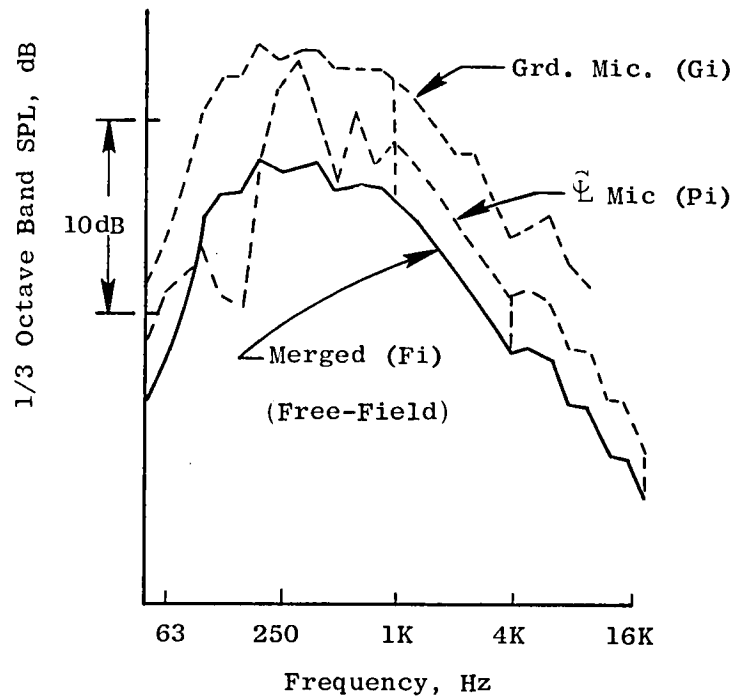
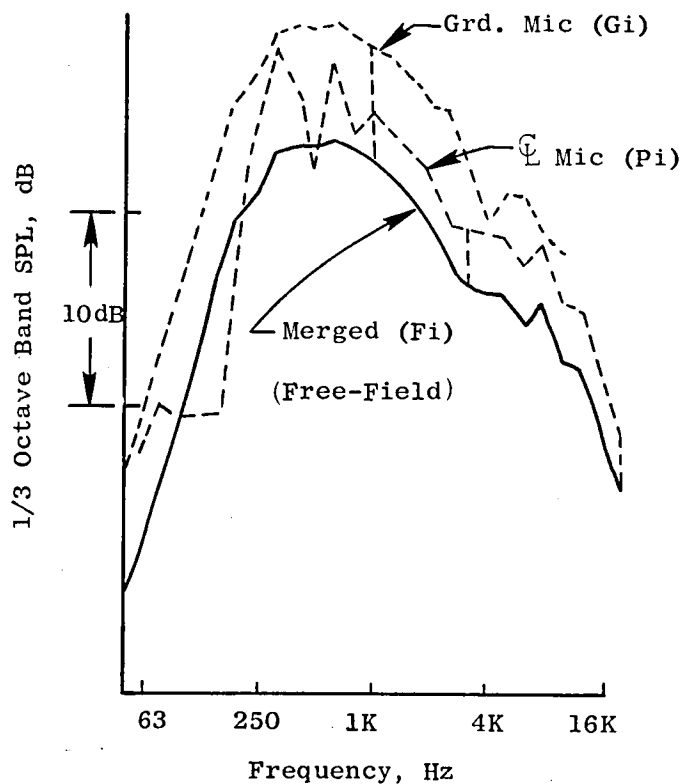


Figure 37. Illustration of Spectral Merging.

The overall acoustic test matrix was also executed, as follows, to also help ensure a high data confidence level:

- Major test configurations were subjected to a 13 point operating line to provide smooth data trends over a wide speed range.
- Repeat data points were acquired at prime speed points along the engine operating line.
- Safeguard acoustic data were acquired during aero/mechanical engine checkout tests and broadened the available acoustic data base.
- Most configurations were tested both with and without exhaust nozzle condition monitoring rakes as the influence of possible rake shedding noise on the far field data was yet uncertain. Acoustic data were also acquired during most of these "rakes-in" tests and provided an extended data base for consistency checks.

A statistical analysis of the reduced data was performed for eleven sample repeat points, each repeat point being within 0.5% corrected fan speed. The following resulted:

- On a peak PNL basis, the average error of measurement, \bar{S} (see Reference 7 for definition of average error of measurement), was 0.27 PNdB and the 95% confidence interval for \bar{S} was ± 0.02 PNdB.
- On the basis of 1/3 OBSPL at the peak frequency and peak noise angle, the average error of measurement, \bar{S}' , was 0.46 dB and the 95% confidence interval for \bar{S}' was ± 0.17 dB.

In general, sufficient independent data samples were acquired and near ideal test conditions prevailed. Confidence in the acoustic data is, therefore, considered quite high.

5.3.3 Engine and Nozzle Aerodynamic Performance Data Acquisition and Reduction

The engine and nozzle aerodynamic performance data reduction system used for the NASA VCE Acoustic Nozzle Test at Edwards is described in the schematic of Figure 38.

Raw data (millivolts) from the data acquisition trailer (aero and LV support van shown in Figure 26) was transmitted through a dial-up line via a 1200 band terminal through a Vadic modem to the Lynn H6000. (Data transmission through the newly installed dedicated line into the Lynn H6000 was not functional for this test.) Conversion of raw data to engineering units, editing and averaging, and performance calculations were accomplished on the Lynn H6000. The raw, converted, edited and averaged data and results of performance calculations were transmitted back to Edwards via the dedicated line, and printed on a high speed Versatec printer. Output was also transmitted

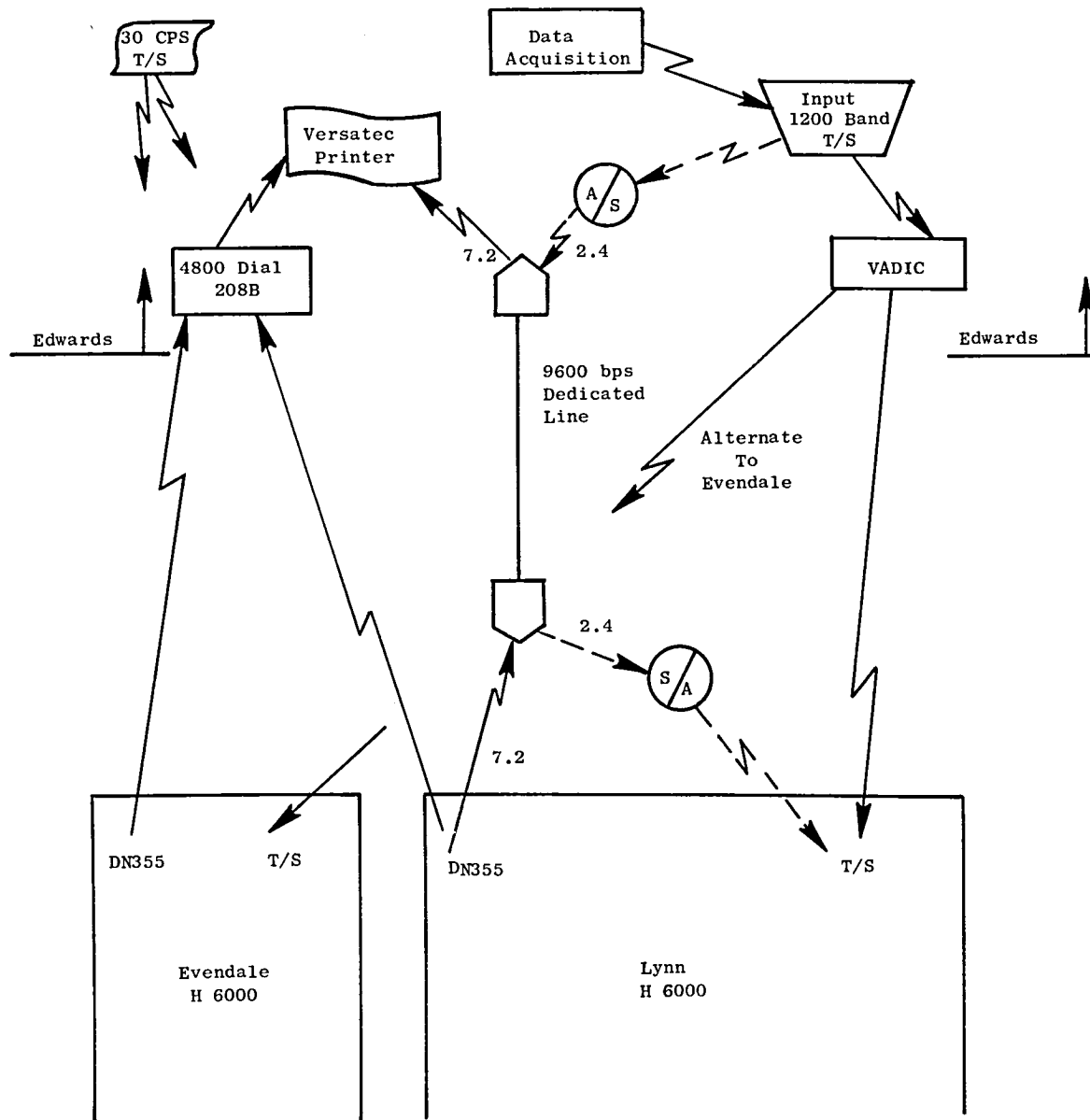


Figure 38. Data Acquisition System.

on a back-up basis from Lynn to Edwards through a 4800 band dial-up line to the Versatec printer.

As shown on the schematic, the Evendale H6000 served as a back-up for use during Lynn H6000 outages. Raw data was transmitted through a dial-up line via a 1200 band terminal through a Vadic modem to the Evendale H6000, and output returned to Edwards via a dial-up 4800 band line to the Versatec printer.

Access to both the Lynn and Evendale computers was provided through a 30 CPS portable T/S terminal with acoustic coupler to on-line monitor the test as backup to the Versatec printer, and to maintain quick access files required for data reduction.

5.4 ACOUSTIC TEST CONFIGURATIONS AND TEST SCOPE

5.4.1 Test Configurations

YJ101 engine acoustic test configurations for the concept demonstrator program consisted of combinations of YJ101 (untreated) and J79 treated inlets with conical, $R_r^\circ = 0.816$, 0.853 and 0.875 convergent-divergent, and $R_r^\circ = 0.853$ convergent coannular exhaust nozzles, as shown in Table VII below.

Table VII. Combinations of Inlet and Exhaust Configurations.

Inlet	Exhaust Nozzle
YJ101 (Untreated)	Conical Single Stream
J79 (Treated)	Conical Single Stream
J79 (Treated)	$R_r^\circ = 0.853$ Convergent-Divergent Coannular Plug Nozzle
J79 (Treated)	$R_r^\circ = 0.853$ Convergent Coannular Plug Nozzle
J79 (Treated)	$R_r^\circ = 0.816$ Convergent-Divergent Coannular Plug Nozzle
J79 (Treated)	$R_r^\circ = 0.875$ Convergent-Divergent Coannular Plug Nozzle

Schematics of the YJ101 and J79 inlets, basic engine and conical exhaust nozzle are shown in Figure 39. The YJ101 bellmouth, as employed in the GE-Lynn Forward VABI Test, was used for initial tests with the conical nozzle. The acoustically treated inlet (photograph in Figure 40) was available from a previous J79 engine acoustic evaluation program and consisted of a J79 bellmouth, a J79/CJ805 acoustic duct and a new conic adapter which mates the

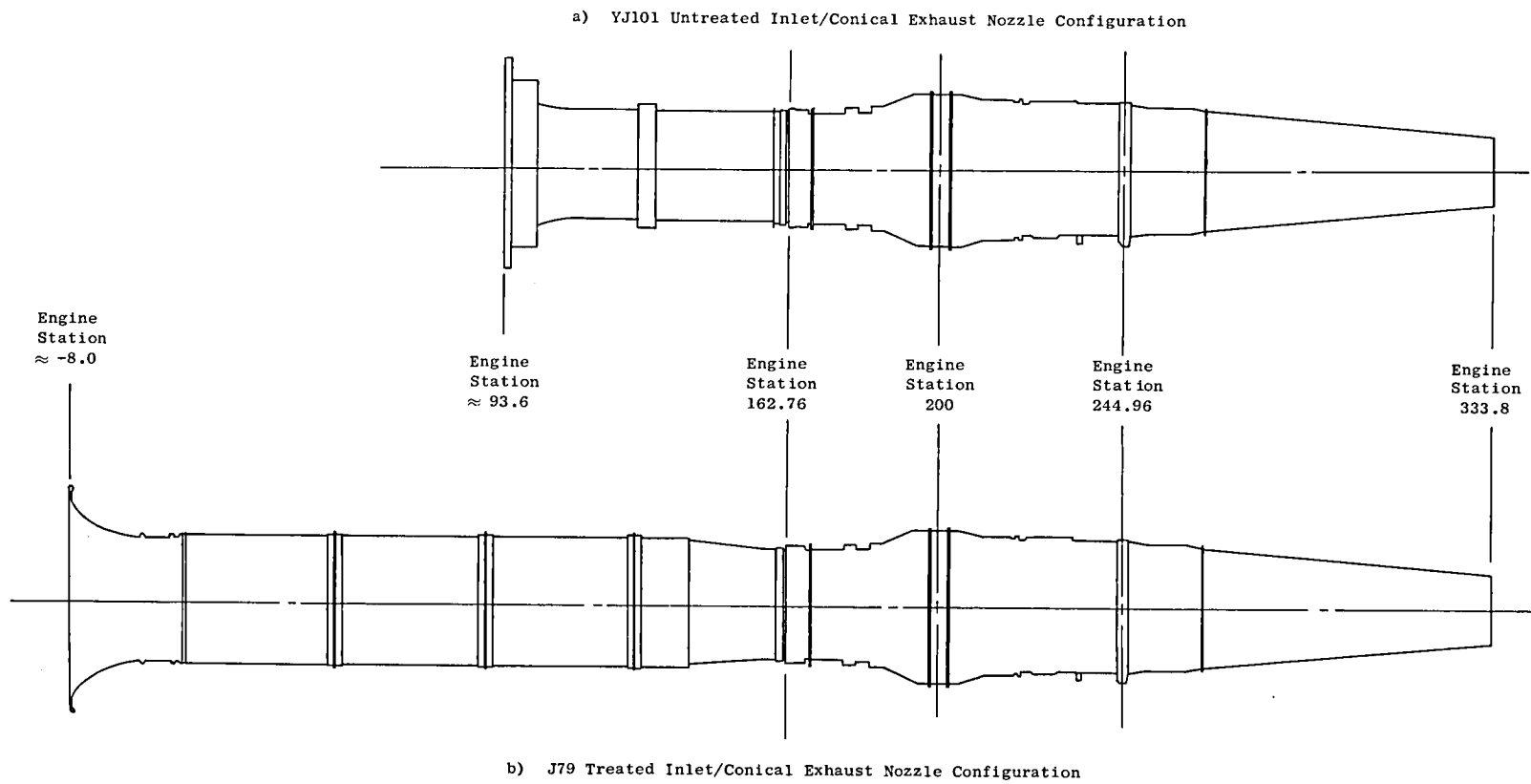


Figure 39. Schematic of YJ101 and J79 Inlets/Conical Exhaust Nozzle For YJ101 Test Program.

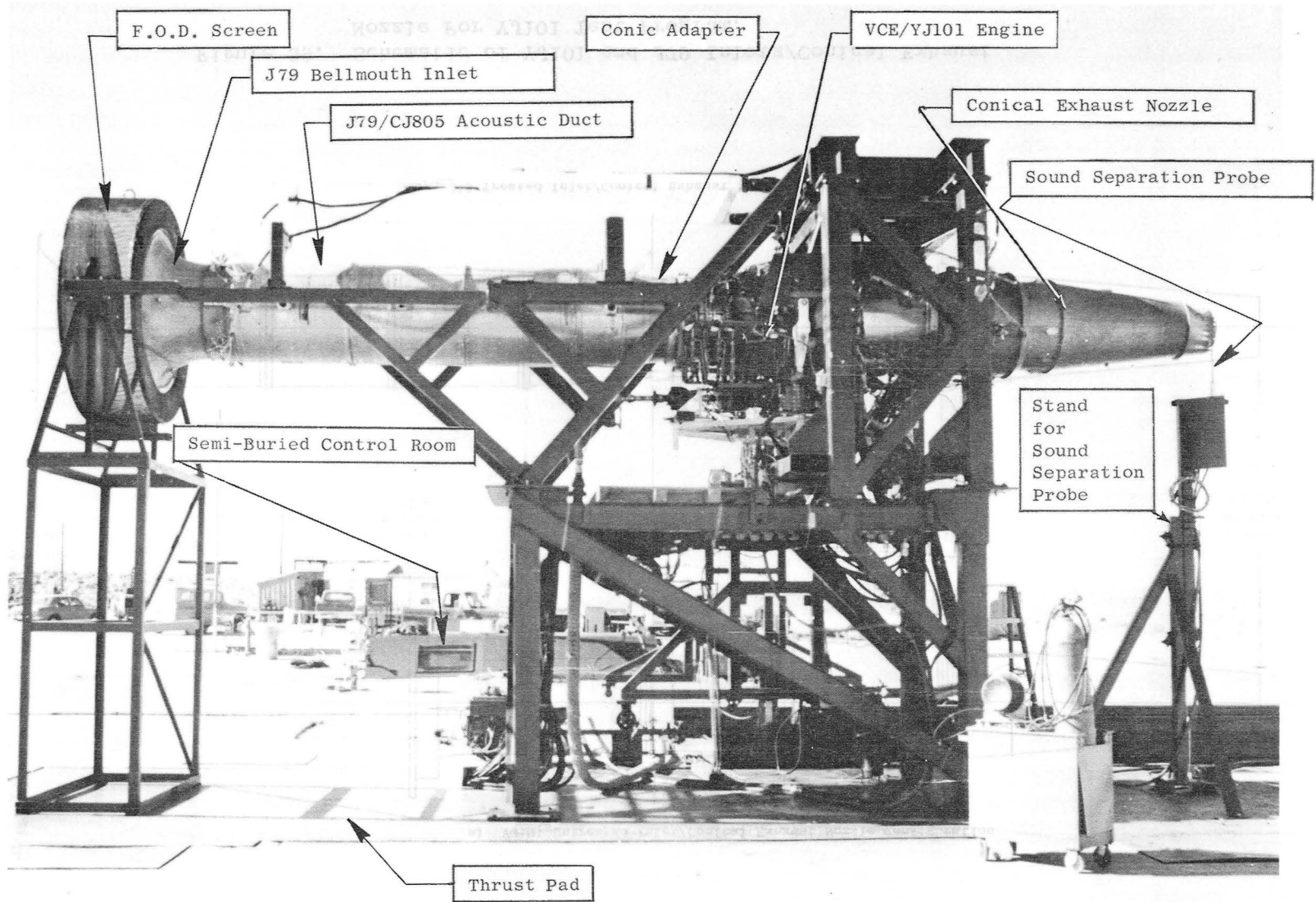


Figure 40. J79 Treated Inlet/YJ101 Engine/Conical Nozzle at Edwards AFB North Test Site.

larger 77.14 cm (30.37 in.) diameter duct with the 67.97 cm (26.76 in.) diameter VCE/YJ101 fan front frame. The acoustically treated inlet was used for the majority of testing. The overall length of the treated inlet system is ≈ 4.24 m (13.9 ft). Further details of the acoustic duct are seen in the schematic of Figure 41 and in Reference 8. The duct is a 3.175 m (10 ft, 5 in.) long acoustically lined cylinder with a treated splitter. The treatment design was Cerafelt with a porous faceplate. The inlet splitter was supported by airfoil-shaped struts at 0° , 90° , 180° and 270° in reference to vertical.

To provide a reference acoustic baseline to which the characteristics of the coannular nozzles could be compared, the conical nozzle, (sketch in Figure 42 and photograph in Figure 40) was employed. The configuration consisted of the rear VABI and a fixed 7° half-angle cone attached to the VABI support casing flange. A 0.472 m (18.59 in.) long spool section was added to the centerbody and attached to the turbine frame to match the annular flow area in order to simulate the pressure distribution and Mach number at the chute exit to achieve a comparable acoustic signature for the reference nozzle. The nozzle exit was trimmed to provide a throat area of 0.123 m^2 (190 in.²). A 30 element P_T/T_T rake was used for gas stream condition monitoring within the nozzle but was removed for prime acoustic and LV tests.

Schematics of the three basic coannular nozzles are included as Figures 43, 44 and 45 for the $R_r^\circ = 0.853$, 0.816 and 0.875 convergent-divergent outer annular nozzle systems, respectively, where R_r° is outer stream radius ratio and is defined as the annulus inner radius divided by the outer radius. The outer annular nozzles consisted of fixed crown and shroud pieces, three different sets being manufactured to provide the three radius ratios. Hardware manufactured dimensions and throat areas are included on the sketches. In each of the three configurations the outer shroud length was trimmed to the length indicated, to effect a convergent-divergent flowpath designed for isentropic expansion at a nozzle pressure ratio of 2.9.

The basic inner annular nozzle was common to each coannular configuration, and consisted of (a) fixed outer shroud forming both the inner nozzle outer flowpath and the outer nozzle plug flowpath and (b) a translatable center plug. The throat area of the inner annular nozzle was varied from fully closed (minimum of approximately 32.25 cm^2 (5 in.²)) through an annulus of average 0.15 cm (0.006 in.) gap height, to approximately 535.5 cm^2 (83 in.²); nominal test values of inner to outer area ratio, A^i/A^o , being set at ≈ 0 , 0.1, 0.2 and 0.475. A photograph of the $R_r^\circ = 0.853$ system, with convergent-divergent outer annular nozzle at an $A^i/A^o = 0.2$ setting of the inner annular nozzle, is shown in Figure 46.

An additional test configuration of the $R_r^\circ = 0.853$ convergent outer annular nozzle flowpath was obtained by trimming the outer shroud to a 0.190 m (7.476 in.) length, as indicated in Figure 43, maintaining all other hardware as in the convergent-divergent configuration. It was acoustically tested in the $A^i/A^o = 0.2$ system configuration.

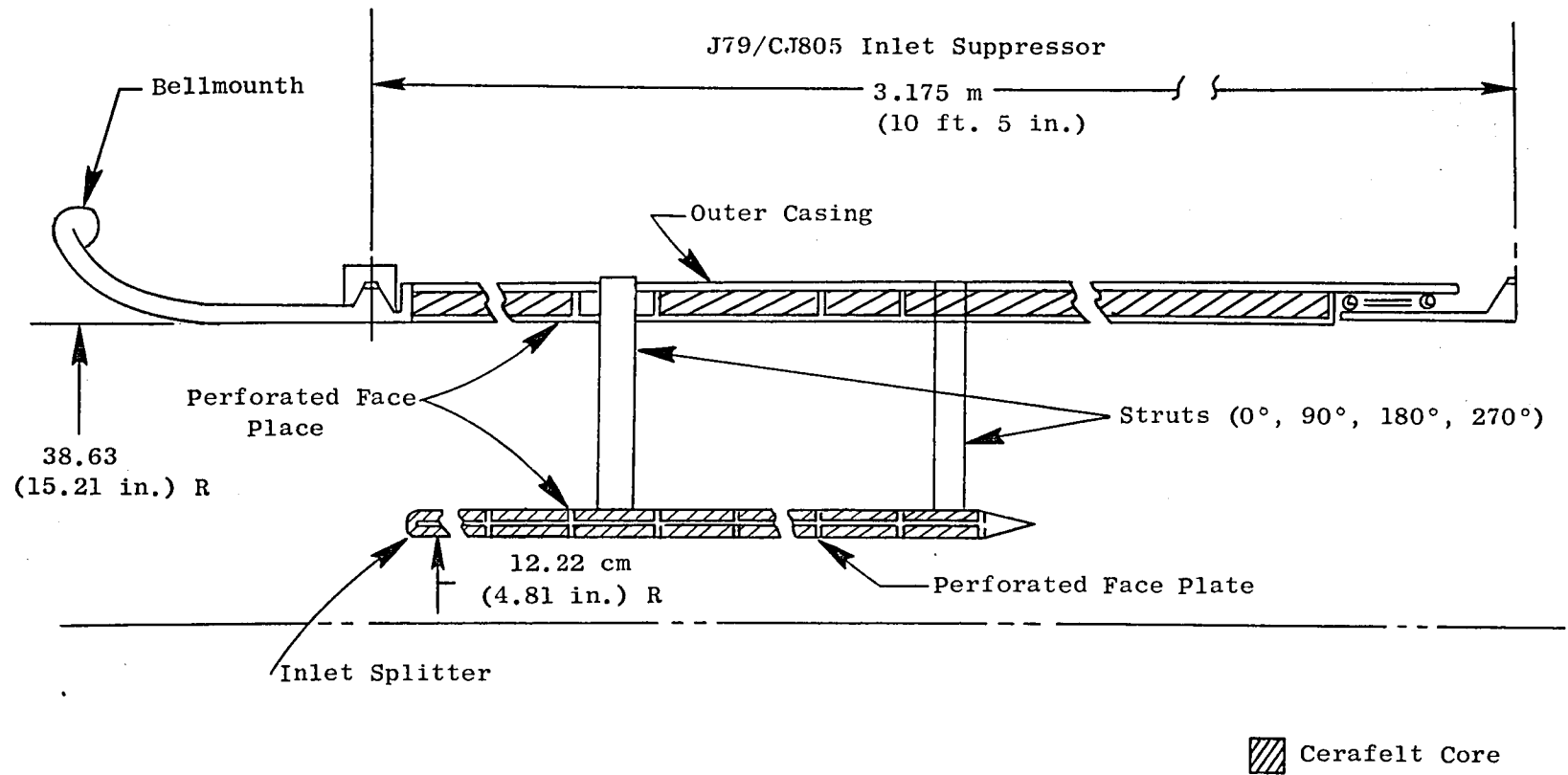


Figure 41. Schematic of Acoustically Treated Inlet.

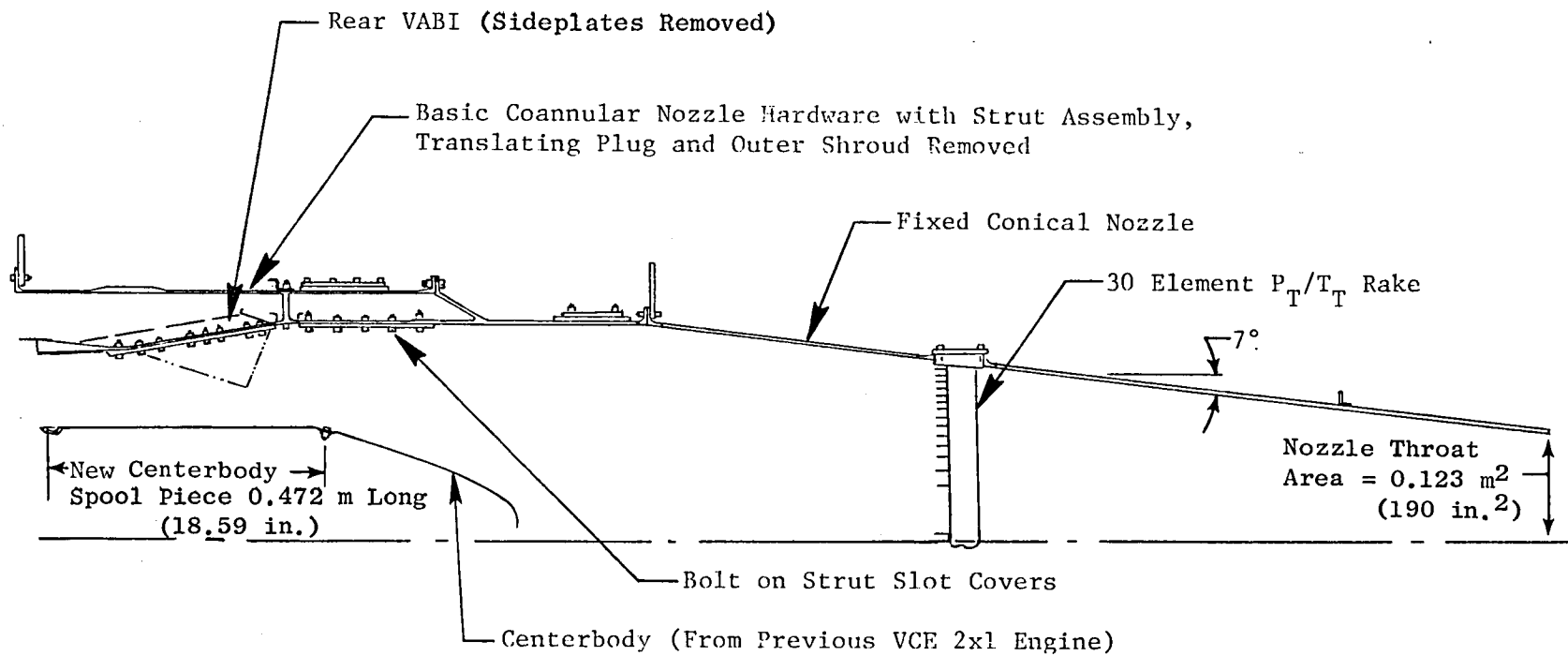


Figure 42. Conical Nozzle.

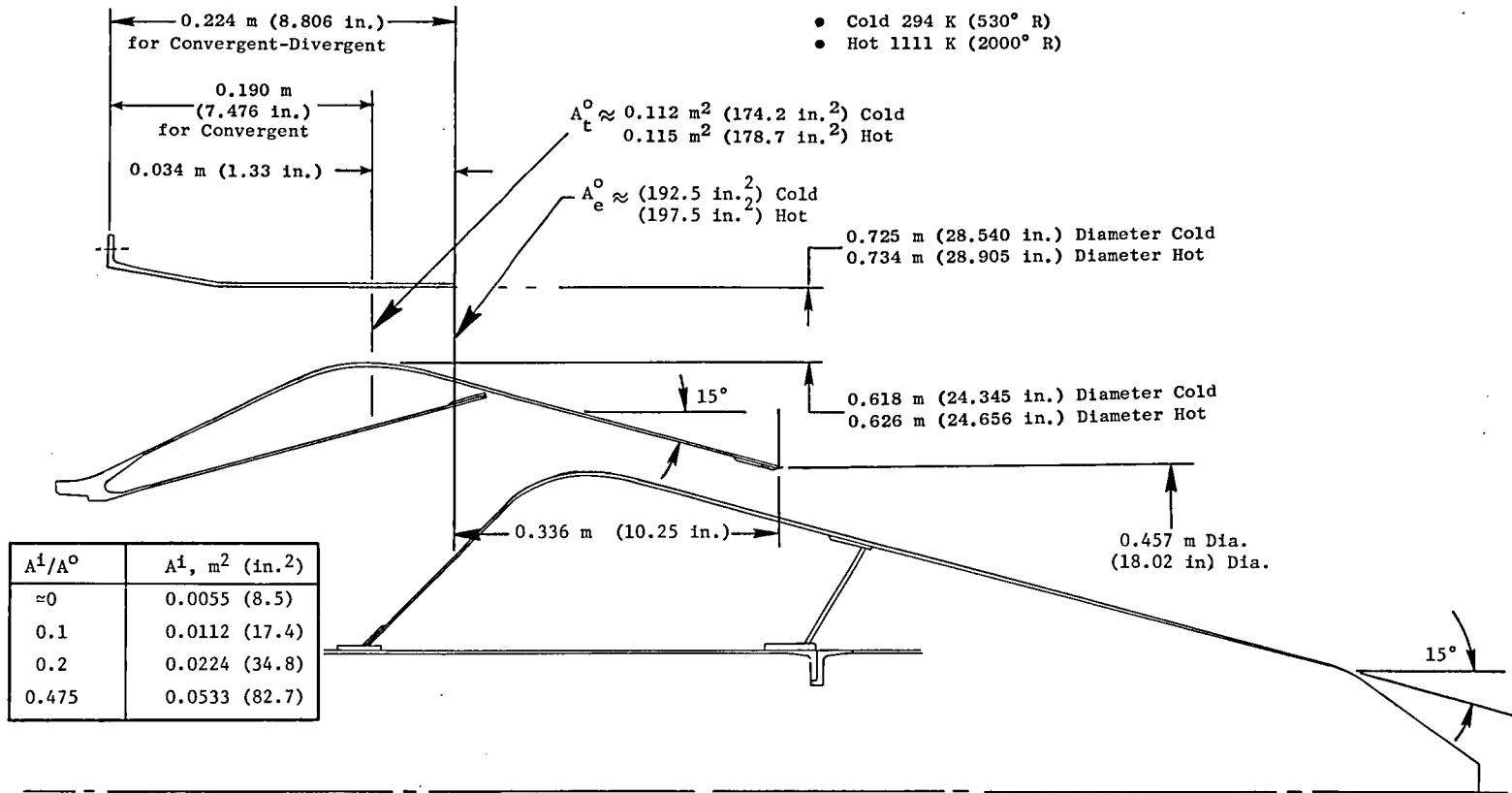


Figure 43. $R_r^0 = 0.853$ Convergent-Divergent and $R_r^0 = 0.853$ Convergent Outer Annular Nozzle System.

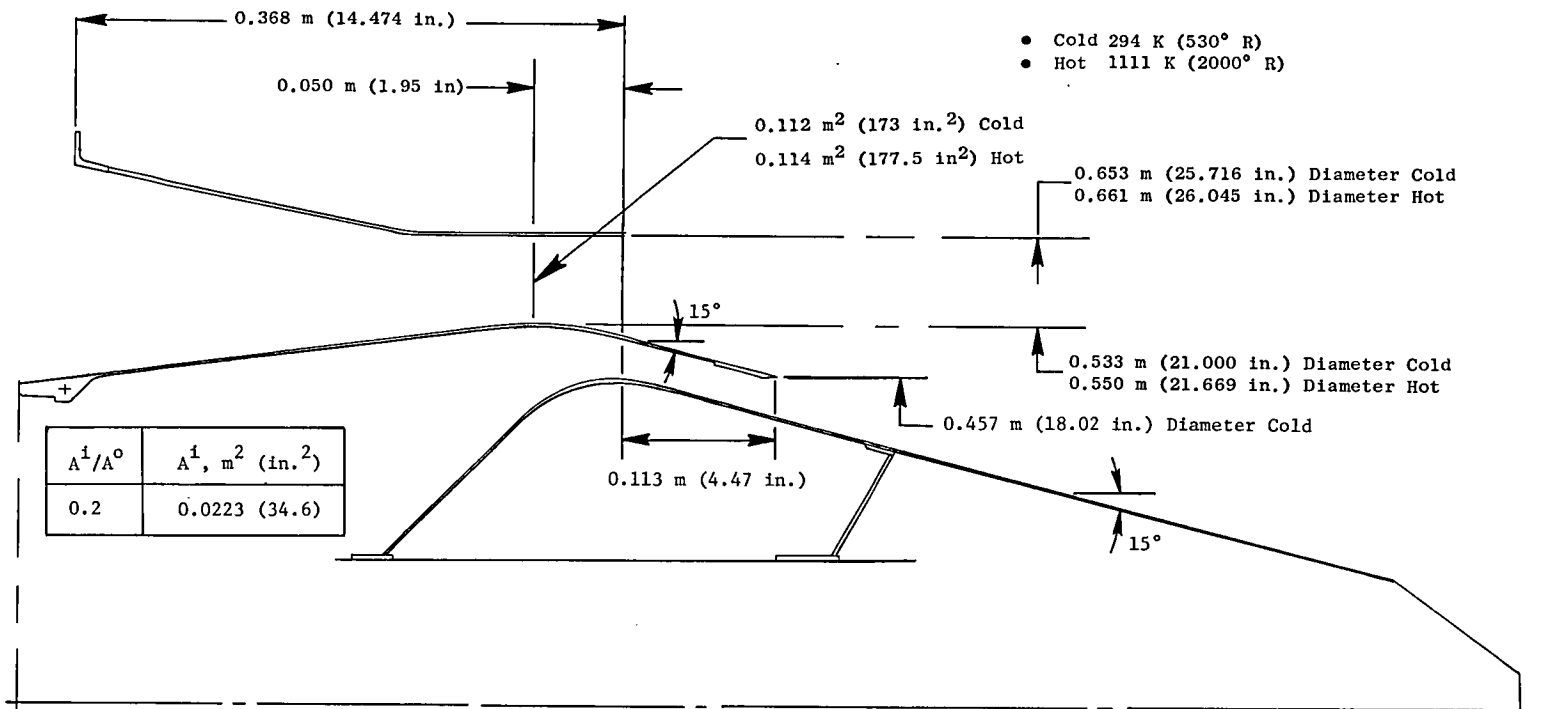


Figure 44. $R_r^0 = 0.816$ Convergent-Divergent Outer Annular Nozzle System.

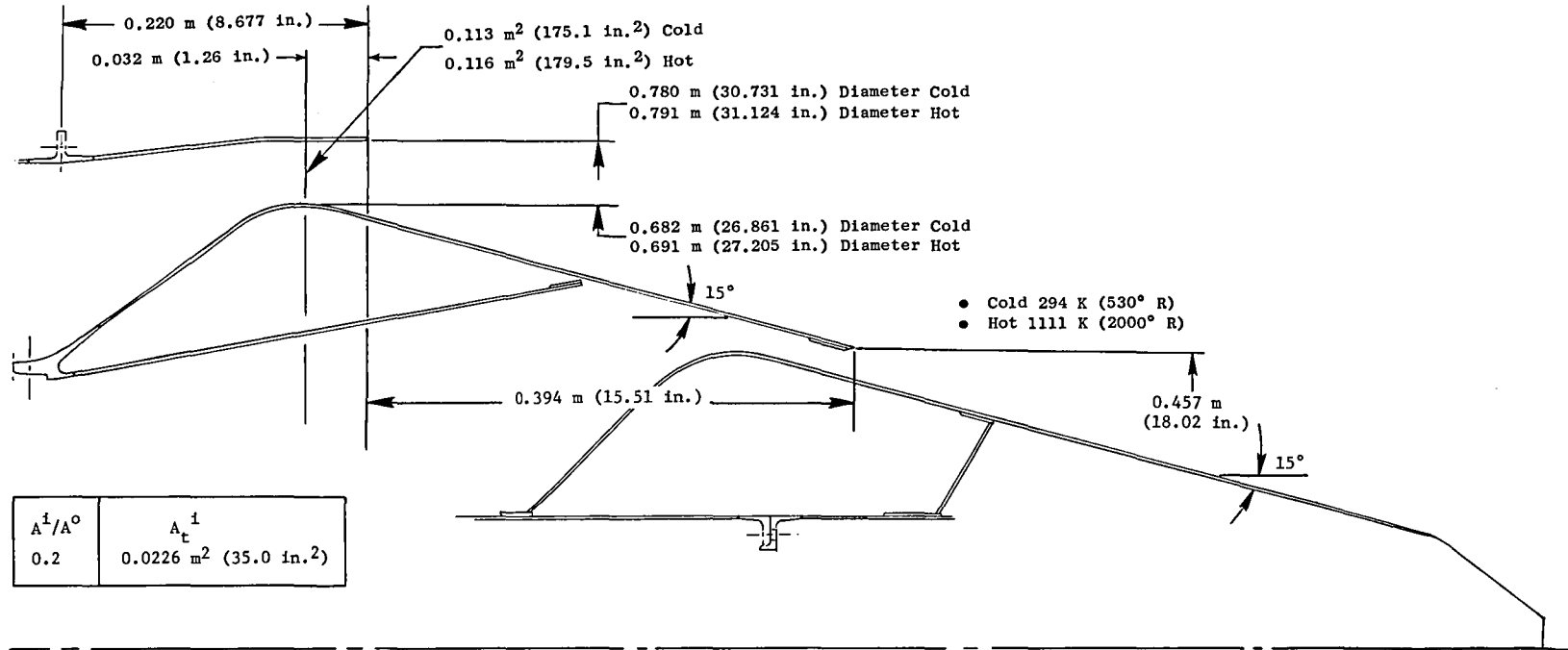


Figure 45. $R_r^0 = 0.875$ Convergent-Divergent Outer Annular Nozzle System.

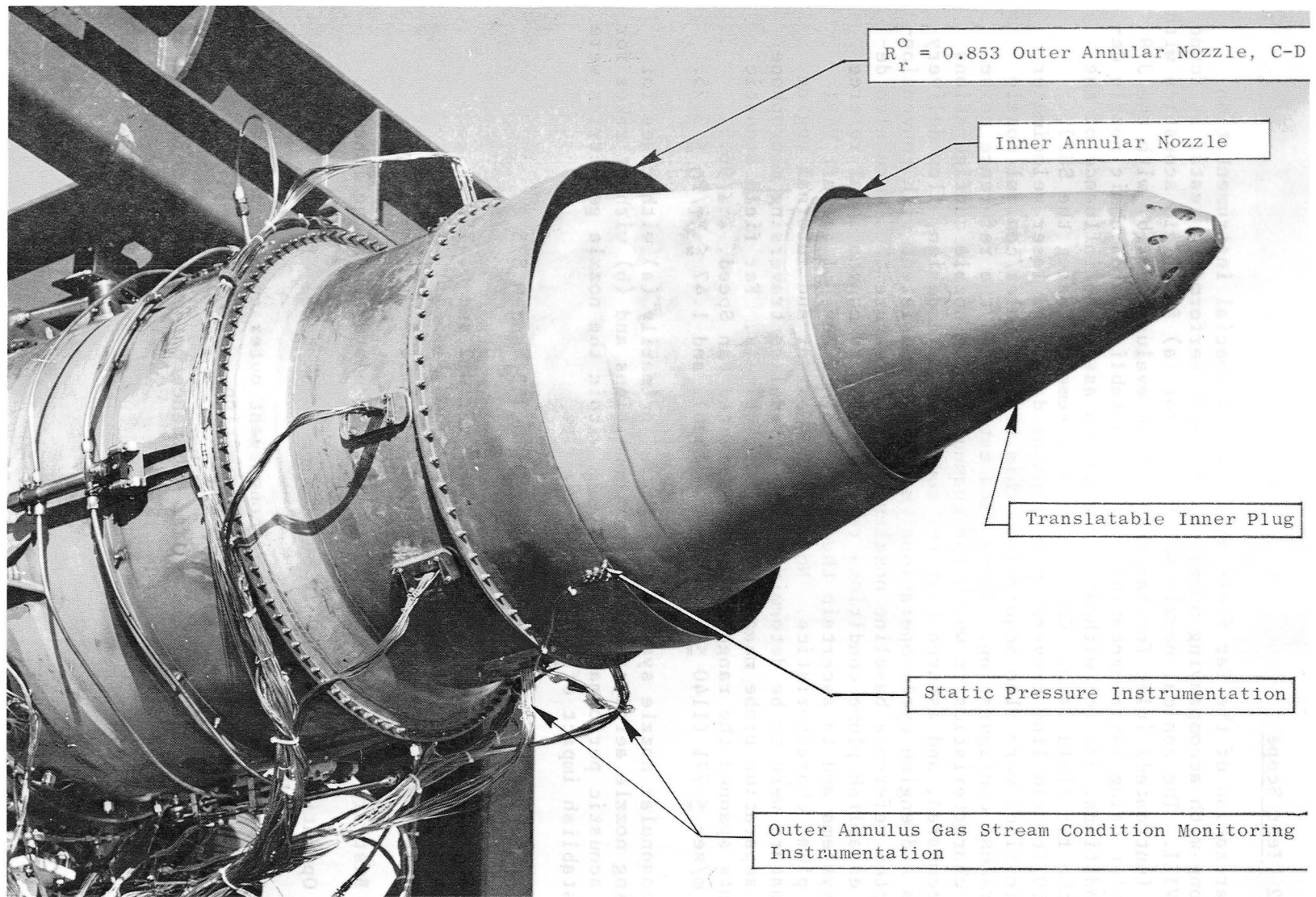


Figure 46. $R_r^O = 0.853$ Convergent-Divergent Outer Annular Nozzle System
 with $A^i/A^O = 0.2$ Setting of the Inner Annular Nozzle.

5.4.2 Test Scope

Summarization of the far field acoustic and special instrumentation tests, along with accompanying nozzle aerodynamic performance tests, is found in Table VIII. The conical nozzle was tested for (a) far field acoustics with the YJ101 (untreated) inlet for fan inlet noise evaluation, (b) with the J79 treated inlet using instrumentation rakes to establish aerodynamic nozzle delivery conditions, and (c) without the rakes to assure no influence of the rakes on the far field data. Core noise measurements (using the SSP), 3.048 m (10 ft) sideline traversing microphone data, and laser velocimeter plume definitions were also acquired on this treated inlet/conical nozzle (without rakes) configuration. These data established the reference noise and plume characteristics to which the coannular plug nozzle configurations would be compared, and assured that the conical nozzle design, flow delivery conditions and engine cycle operational mode were consistent with conventionally accepted reference baseline nozzles. The LV measurements were also designed to establish plume conditions referenceable to conventional referee baseline systems and to ascertain the influence, if any, of the aft VABI chutes on plume characteristics. Noise source extent and internal engine noise signature were to be determined by the sideline traversing microphone and sound separation probe measurements, respectively. Far field acoustic measurements spanned the ranges of $65 \leq \text{Corrected Fan Speed, \%} \leq 96.5$, $347 \leq V_j, \text{ m/sec} \leq 771$ ($1140 \leq V_j, \text{ ft/sec} \leq 2530$), and $1.47 \leq P_T/P_0 \leq 3.25$.

The coannular nozzle systems were tested primarily (a) with rakes for establishing nozzle aerodynamic delivery conditions and (b) without rakes for far field acoustic performance. Variations within the nozzle geometries were made to establish impact of:

- R_r° variation with values at 0.816, 0.853, and 0.875
- A_i/A° variation with values at ≈ 0 , 0.1, 0.2 and 0.475
- Single bypass versus double bypass operation
- Best sfc operating line relative to standard operating line
- Operation at design $P_T/P_0 = 2.9$ for shock noise effect
- Convergent-divergent versus convergent outer annular nozzle flow-path designs for shock noise mitigation
- Removal of aft VABI sideplates influence on jet mixing noise and/or internal obstruction noise

Table VIII. Summary of Far Field Acoustics and Special Instrumentation Tests,

TABLE 5.4.2-1 YJ101 AST/VCE TEST SCOPE

TEST CONFIGURATION		CONICAL NOZZLE		COANNULAR NOZZLES (ALL WITH J79 TREATED INLET)			
		YJ101(Untreated) Inlet	J79 Treated Inlet	$R_r^0 = 0.853$, Convergent-Divergent	$R_r^0 = 0.853$, Convergent $A^1/A^0 = 0.2$	$R_r^0 = 0.816$, Convergent-Divergent $A^1/A^0 = 0.2$	$R_r^0 = 0.875$, Convergent-Divergent $A^1/A^0 = 0.2$
FAR FIELD ACOUSTICS	With Nozzle Rake(s)	20 #65-94% Speed (5) #Vj=381-742.2 m/sec (1250-2435 ft/sec) #P _T /P _O =1.45-3.07	(13) #65-96.5% Speed #Vj=372-771 m/sec (1220-2530 ft/sec) #P _T /P _O =1.48-3.25	(60) #A ¹ /A ⁰ = 0, .1, .2 & .475 #Single Bypass & Double Bypass #Rear VABI Open & Closed #Best SFC Operating Line #Operation at P _T ⁰ /P _O =2.9 Design Pt. #Influence of Rakes	(6) #Influence of Rakes #Influence of Aft VABI Sideplates #65-98% Speed Nom. #V ^{mix} =295.6-707 m/sec (970-2320 ft/sec) Nom.	14 #69 #94.3% Speed #V ^{mix} =314-696.5 m/sec (1030-2285 ft/sec) Nom.	12 #69 #96.7% Speed #V ^{mix} =308-722 m/sec (1010-2370 ft/sec) Nom.
	Without Nozzle Rake(s)	—	17 #65-96.5% Speed #Vj=347-771 m/sec (1140-2530 ft/sec) #P _T /P _O =1.47	79	21	—	—
CORE NOISE	#Sound Separation Probe(SSP) #Wall Kulites (Coannular Only)	—	4 #65,70,75 & 80% Speed	#A ¹ /A ⁰ =0.475 #65,70,75 & 80% Speed	—	—	—
SIDELINE TRAVERSING MICROPHONE	#3.048 m (10 ft)	—	7 #65-89% Speed	7 #A ¹ /A ⁰ = 0.2 #65-90% Speed	—	—	—
LASER VELOCIMETER		—	#2 Plumes Defined, Vj=451 & 626 m/sec (1480 & 2055 ft/sec) -Influence of Flow Struts -Exit Plane Flow Uniformity	#3 Plumes Defined -Influence of Aft VABI Chutes -A ¹ /A ⁰ =0.2 & 0.475 -Annular Flow Symmetry	—	—	—

NOTE: Unbracketed numbers are total of prime acoustic or LV data points, bracketed numbers are total of non-prime acoustic data points taken during prime aerodynamic performance tests. Only prime data was reduced for this report.

- Influence of nozzle rakes on far field acoustics*

For special instrumentation measurements, emphasis was placed on the $R_T^* = 0.853$ convergent-divergent system; the SSP and wall Kulites being used to establish internal noise signature, the 3.048 m (10 ft) sideline traversing microphones to validate noise source extent and some near field noise characteristics and the LV to (a) define plume decay characteristics relative to the conical nozzle and (b) ascertain influence of struts and rear VABI chutes on plume structure. Typical test condition ranges are included within Table VIII. Aerodynamic nozzle delivery conditions for specific test points can be found in the companion Comprehensive Data Report (Reference 4).

5.5 ACOUSTIC TEST RESULTS

The analysis of the jet and shock noise, fan noise, core noise, and exhaust plume laser velocimeter velocity profile measurements for several engine size, high-radius-ratio, coannular plug nozzle configurations and a conic nozzle configuration are discussed in this section. The description of nozzle configurations and scope of testing was discussed in Section 5.4.

This section consists of seven major subsections. Subsection 5.5.1 discusses the verification of jet and shock exhaust noise reduction for the high radius-ratio coannular plug nozzle configurations tested. Illustrated in this subsection are the effects of nozzle geometry and engine cycle variations on the coannular plug nozzle acoustic trends. Subsection 5.5.2 presents acoustic scaling results for the engine conic nozzle and the coannular plug nozzle. Discussed in Subsection 5.5.3 are preliminary observations concerning the fan inlet noise source characteristics. Presented in Subsection 5.5.4 are core engine noise measurements and a series of 3.048 m (10 ft) sideline traversing microphone acoustic measurements. These measurements are used to identify the extent of combustor/core noise present in the performed measurements, and the jet acoustic source extent for the conic and coannular plug nozzles. Subsection 5.5.5 describes mean velocity and turbulent velocity profile measurements taken to evaluate the exhaust plane turbulence level, the extent of core/fan mixing, and the possible influences of variable cycle engine geometry on the exhaust plumes. Contained in Subsection 5.5.6 are comparisons of engine data with acoustic theory prediction for a set of selected conditions. The quality of the prediction comparison and reference of fan exhaust generated data are highlights of this subsection. From the results of Subsection 5.5.6 and selected acoustic measurements, product size AST/VCE flight projections are

Preliminary analysis of several test series on the conical nozzle and dual flow coannular nozzle at $A_i/A^ = 0.2$, with and without exhaust nozzle instrumentation rakes, has indicated no influence on far field acoustics due to the presence of rakes, particularly on parameters of OASPL and PNL. A more detailed analysis, comparing predicted tone and broadband levels to 1/3 octave band and narrowband spectra, will be done prior to the NAS3-20582 Mod. No. 8 Exhibit C YJ101 CDFS test program planning.

performed at the three FAR 36 (1969) acoustic monitoring points in Subsection 5.5.7. Additionally, a sensitivity study regarding possible forward quadrant and aft quadrant shaping on typical coannular plug nozzle noise reduction are presented.

5.5.1 Verification of Coannular Plug Nozzle Jet Exhaust Noise Reduction

The primary purpose for VCE early acoustic nozzle test program was to verify in a YJ101 engine size the acoustic benefit of General Electric's un-suppressed high-radius-ratio coannular plug nozzle. Additionally, from an engine design point-of-view, it was desirable to obtain sufficient parametric data on geometry and cycle variations to establish an acoustic design data bank for possible product engine application. Contained in this subsection are illustrations of the coannular plug nozzle jet and shock exhaust noise reductions and observed acoustic data trends due to variation in nozzle geometry and engine cycle variations.

5.5.1.1 General Results

Under two NASA-Lewis sponsored small-scale model nozzle test programs (References 9 and 10) a substantial noise reduction was observed for high-radius-ratio coannular plug nozzles. Shown here is a verification of these model scale test results, but now on a modified YJ101 engine with a unique coannular plug nozzle exhaust system designed for a high-radius-ratio with an inverted velocity profile.

Figures 47 and 48 illustrate the coannular plug nozzle jet and shock noise reduction observed from an extensive series of engine far field acoustic tests. The results presented here, as well as throughout most of this text, are for a typical product engine size represented by a total nozzle throat area of 0.9032 m², (1400 in.²) at an acoustic range 731.5 m (2400 ft) typical of the sideline monitoring station for FAR 36 (1969).

Figure 47 illustrates the peak aft quadrant PNL coannular plug nozzle jet noise reduction relative to a conic nozzle for all of the coannular plug nozzles tested for this program. Shown on the ordinate is a normalized peak PNL (normalized for constant ideal thrust and fully-expanded jet density), while on the abscissa is the ideal total specific thrust (i.e., the ideal total thrust divided by the total weight flow). The total thrust velocity is defined here as:

$$v_j^{mix} = \frac{v_j^o \dot{W}_j^o + v_j^i \dot{W}_j^i}{\dot{W}_T}$$

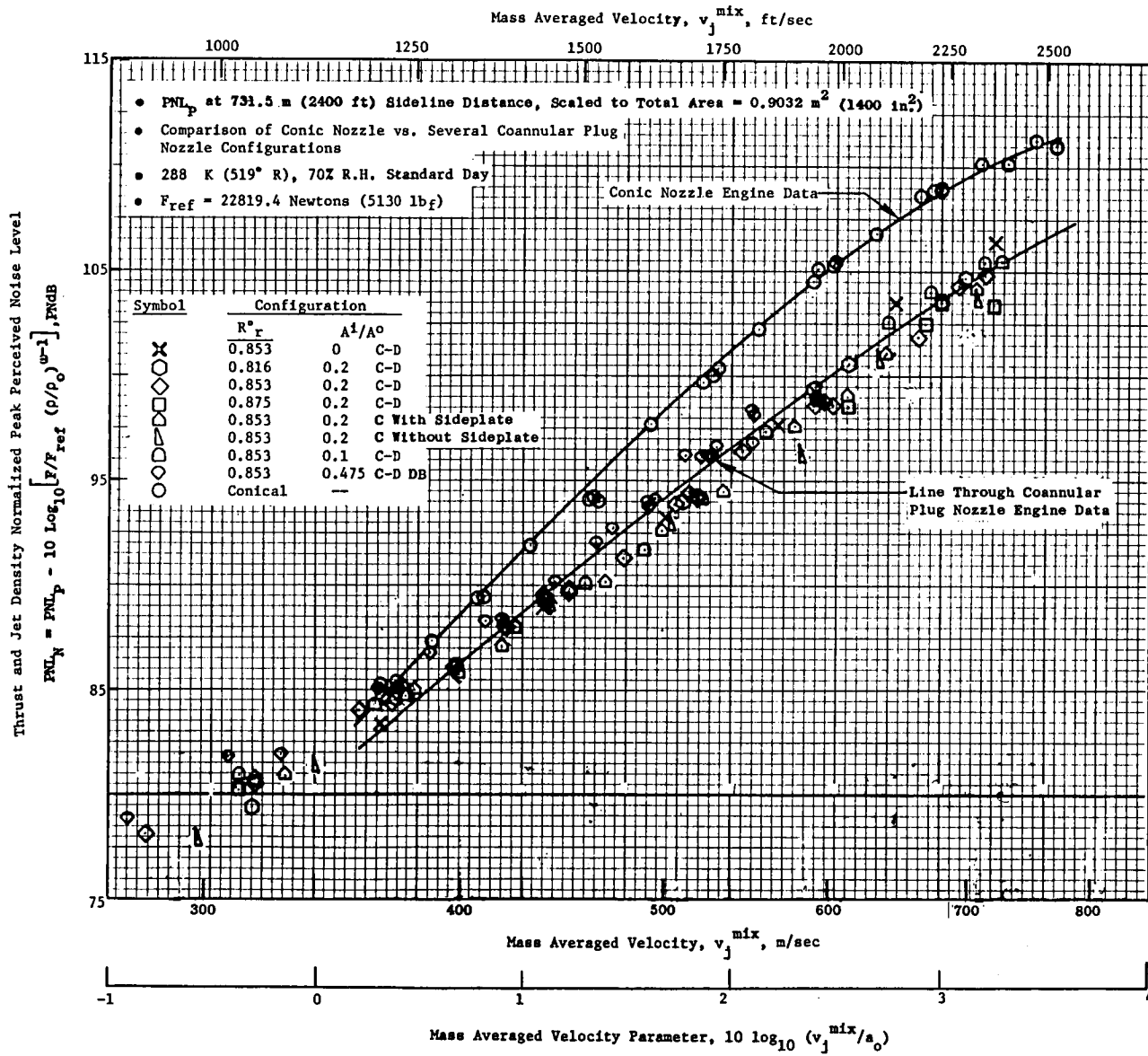


Figure 47. Verification of Coannular Plug Nozzle Engine Jet Noise Reduction for a Typical FAR 36 (1969) Sideline Acoustic Range at Peak Aft Angle.

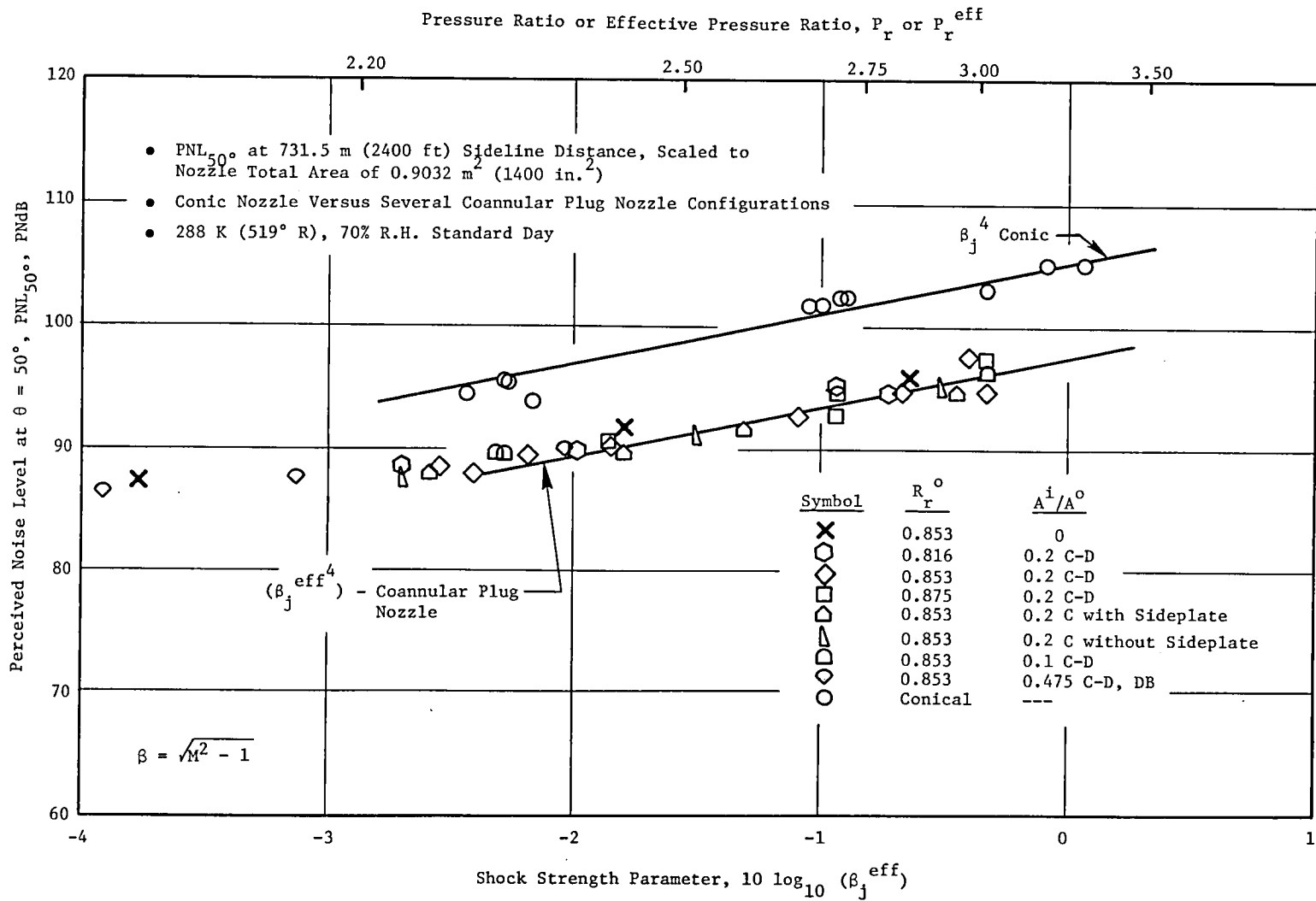


Figure 48. Verification of Coannular Plug Nozzle Engine Shock Noise Reduction.

where:

v_j^o = Ideal outer stream velocity

\dot{W}_j^o = Ideal outer stream weight flow

v_j^i = Ideal inner stream velocity

\dot{W}_j^i = Ideal inner stream weight flow

$$\dot{W}_T = \dot{W}_j^o + \dot{W}_j^i$$

The results show that in the velocity range of 488 m/sec (1600 fps) to 701 m/sec (2300 fps) an average of 4 to 6 PNdB coannular jet noise benefit is realized. In the lower velocity regions [~ 381 m/sec (~ 1250 fps)] the coannular benefit is observed to diminish. It will be shown later that the reduced coannular plug nozzle jet noise reduction can be attributed to inner-to-outer-stream velocity ratio (V_r^i) effects, and also to the possibility of fan exhaust noise radiation (see Section 5.5.6).

Figure 48 is an illustration of coannular plug nozzle shock noise reduction for several coannular plug nozzle configurations. Shown on Figure 48 is the PNL at $\theta_i = 50^\circ$ versus the shock strength parameter β_j^{eff} . The shock strength parameter β_j^{eff} is defined as:

$$\beta_j^{\text{eff}} = \sqrt{M^2 - 1}$$

where

$$M^2 = \left[\begin{array}{c} \frac{\gamma-1}{\gamma} \\ (P_r^{\text{eff}})^{\frac{2}{\gamma-1}} \end{array} \right]^{\frac{2}{\gamma-1}}$$

$$P_r^{\text{eff}} = \frac{P_r^o + P_r^i A_r^i}{1 + A_r^i}$$

A_r^i = Inner to outer stream area ratio (A^i/A^o)

P_r^o = Outer nozzle pressure ratio

P_r^i = Inner nozzle pressure ratio

As a guide, for conic nozzles, theory (Reference 11) indicates the forward quadrant noise varies as β^4 . For the coannular plug nozzle it was found that PNL_{50° varies as $(\beta_j^{eff})^4$.

The results indicate a rather uniform 7 PNdB reduction over the range of interest, and the data trends typically follow a $(\beta_j^{eff})^4$ power law.

Typical values of $10 \log \beta_j^{eff}$ or P_r^{eff} for AST/VCE operation are:

Sideline: $10 \log \beta_j^{eff} \sim -1+0$ or $P_r^{eff} \sim 2.8+3.20$

T/O Flyover: $10 \log \beta_j^{eff} \sim -3$ or $P_r^{eff} \sim 2.2$

Below $10 \log \beta_j^{eff}$ of -3 , jet mixing noise generally overrides the shock noise. Approach conditions are usually at subcritical pressure ratios where shock noise is not present.

The results presented above were for a typical product size engine at an acoustic range typical of the FAR 36 (1969) sideline monitoring point. For the FAR 36 (1978) sideline monitoring point the acoustic range is somewhat less than that used for FAR 36 (1969). Figures 49 and 50 illustrate the coannular jet and shock noise reduction relative to the conic nozzle at a 511.5 meter (1678 ft) sideline [more typical of FAR 36 (1978)]. The same levels of coannular plug nozzle jet and shock noise reduction are observed here as in Figures 47 and 48. These results indicate that the suppression levels quoted for jet and shock noise reduction should be valid for either the FAR 36 (1969) or FAR 36 (1978) type sideline monitoring stations.

As an illustration of the typical noise reduction capability of the coannular plug nozzle on PNL directivity and spectral bases, Figures 51 and 52 are shown. Figure 51 compares PNL directivity measurements for engine conic nozzle test results with an engine coannular plug nozzle configuration - outer stream radius ratio (R_r^o) of 0.853 and inner to outer stream area ratio (A_r^i) of 0.2. The results are for a $V_j^{mix} = 595$ m/sec (1950 fps) and $P_r^{mix} = 2.261$. These measurements show that coannular plug nozzle suppression is realized at all observation angles. At the peak aft quadrant noise observation angles, up to 6 PNdB coannular plug nozzle suppression is realized. At and near $\theta_i \sim 90^\circ$ the noise reduction is a minimum, whereas up to 7 PNdB noise reduction is observed in the forward quadrant. These results suggest that in the aft quadrant the coannular plug nozzle suppression benefit is realized through advantageous jet mixing and propagative influences associated with the high-radius-ratio inverted coannular plug nozzle flow. At $\theta_i \sim 90^\circ$, where propagative effects and convection effects are absent, the basic source noise reduction is observed. In the forward quadrant, where shock wave noise dominates both the conic and coannular nozzle acoustic signatures, the coannular nozzle shock noise reduction is observed to be substantial. Such a shock noise reduction may be due to an effective reduction in the number of noise contributing shock cells as well as presence of the plug nozzle itself.

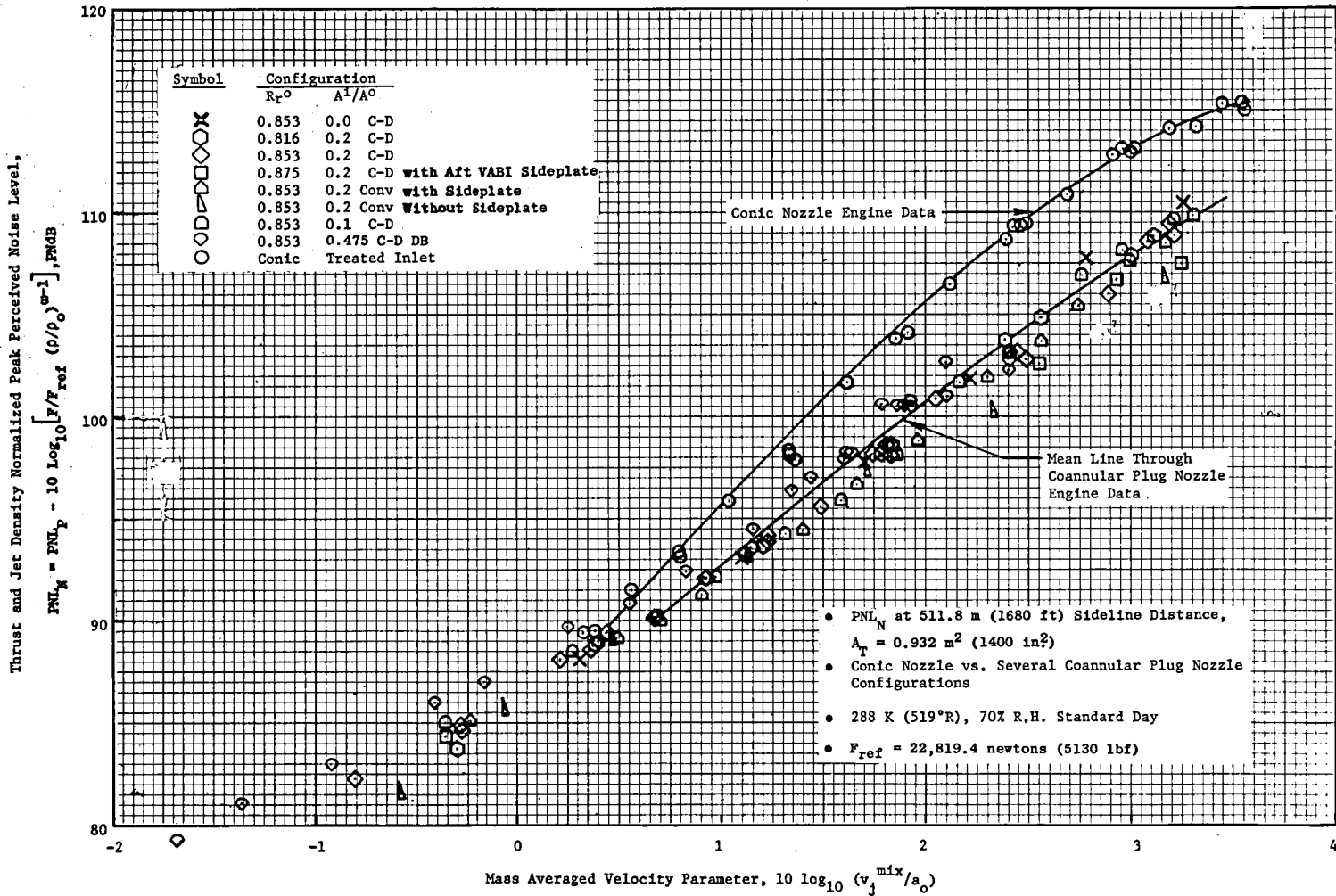


Figure 49. Verification of Coannular Plug Nozzle Engine Jet Noise Reduction for a Typical FAR 36 (1978) Sideline Acoustic Range.

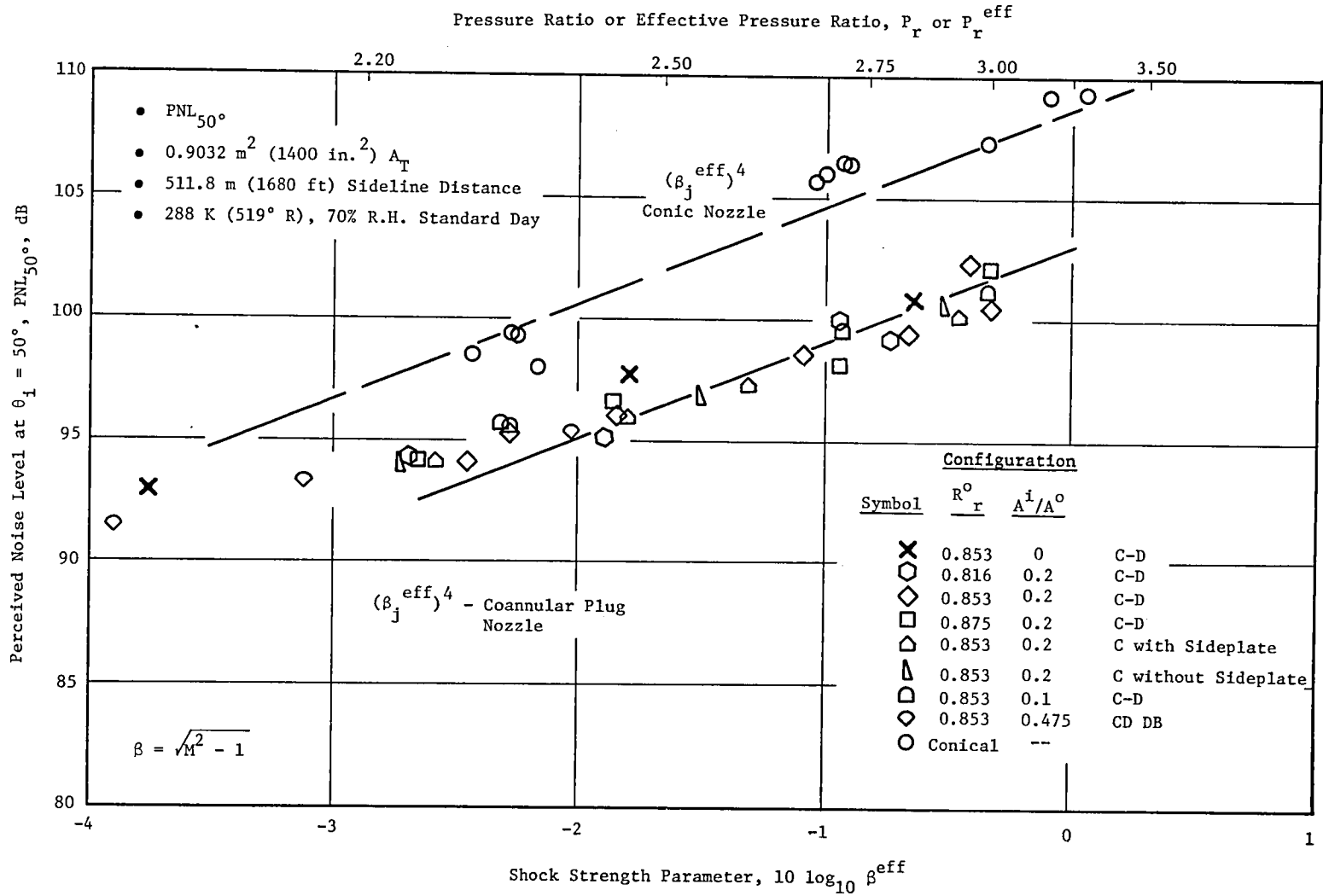


Figure 50. Verification of Coannular Plug Nozzle Engine Shock Noise Reduction for a Typical FAR 36 (1978) Sideline Acoustic Range.

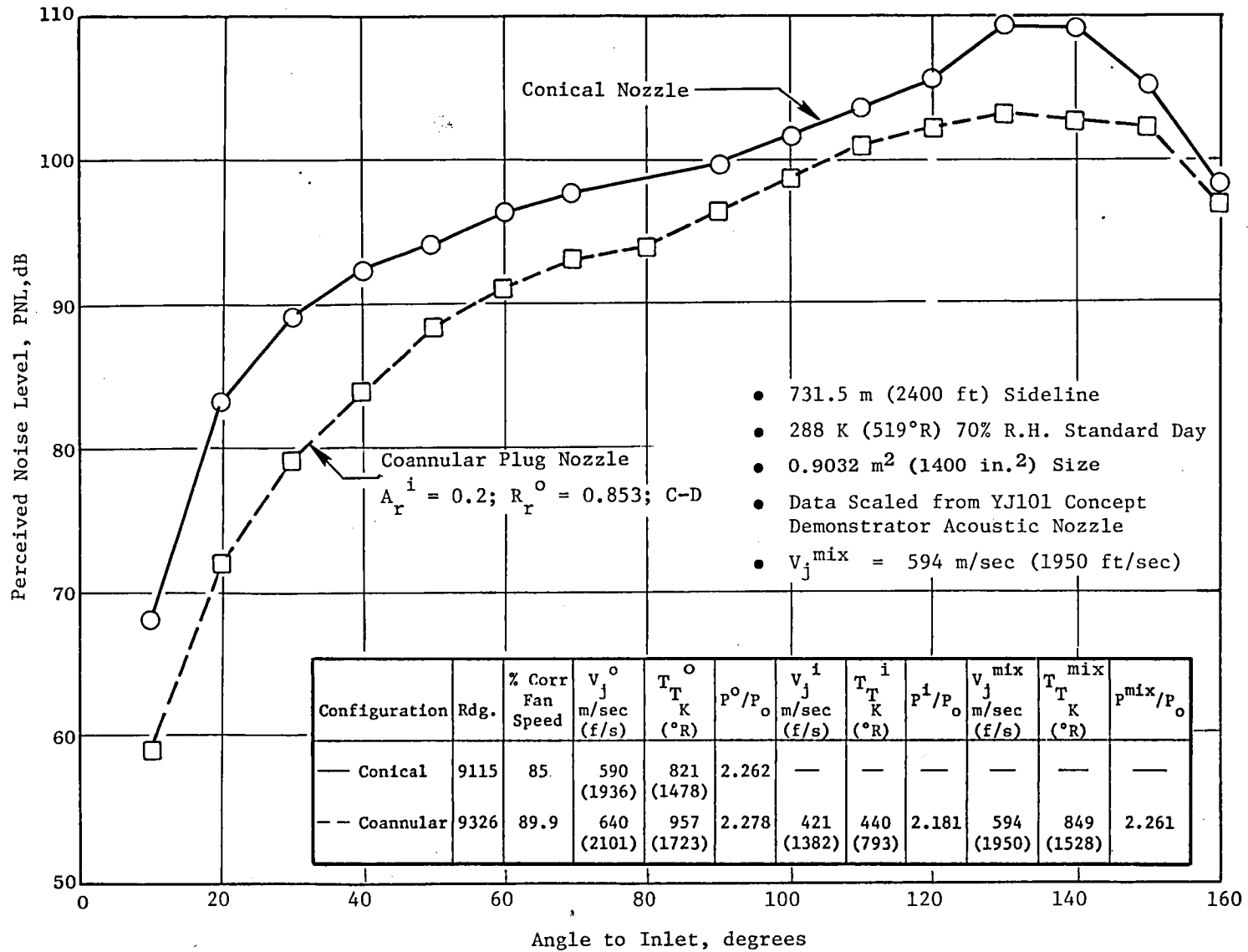


Figure 51. Typical Engine PNL Directivity Characteristics - Conical and Coannular Plug Nozzle.

Preliminary Data

Configuration	Rdg.	% Corr Fan Speed	v_j^o m/sec (f/s)	T_T^o K (°R)	P^o/P_o	v_j^i m/sec (f/s)	T_T^i K (°R)	P^i/P_o	v_j^{mix} m/sec (f/s)	T_T^{mix} K (°R)	P^{mix}/P_o
— Conical	9115	85	590 (1936)	821 (1478)	2.262	—	—	—	—	—	—
- - Coannular	9326	89.9	640 (2101)	957 (1723)	2.278	421 (1382)	440 (793)	2.181	594 (1950)	849 (1528)	2.261

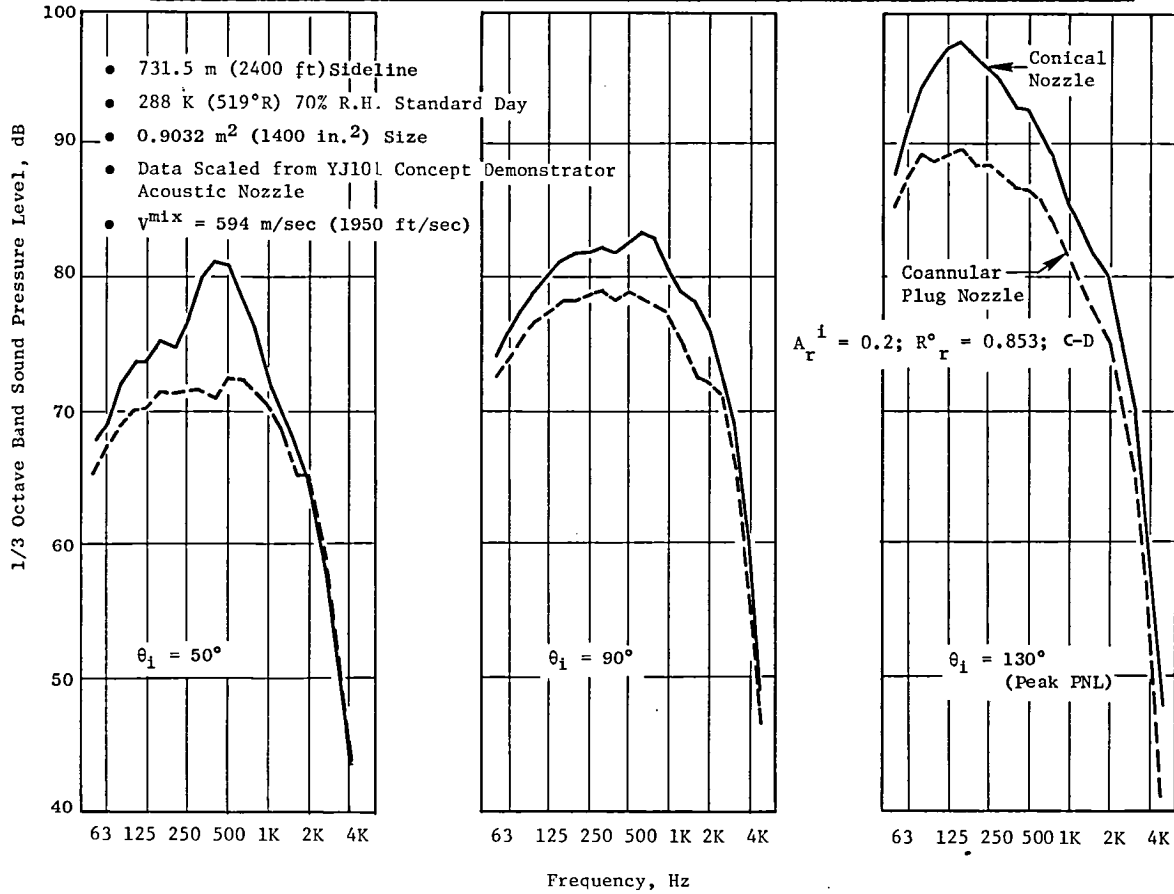


Figure 52. Typical Engine Spectra Characteristics - Conical and Coannular Plug Nozzle.

On a spectral basis these beneficial coannular properties are illustrated in Figure 52. Shown in this figure are the one-third octave-band spectra at $\theta_i = 50^\circ, 90^\circ$ and 130° . The rather dramatic reduction in SPL for the coannular plug nozzle configuration relative to the conic nozzle is well illustrated.

5.5.1.2 Influence of Radius Ratio on Coannular Plug Nozzle Jet Noise Reduction

Model scale testing (Reference 10) has shown that radius ratio is a key coannular suppression parameter. Verification of these results with engine test data is shown in Figure 53. Shown in Figure 53 is normalized peak aft quadrant PNL at $A_{8_{mix}} = 0.9032 \text{ m}^2$ (1400 in.²) at a 731.5 m (2400 ft) sideline. The results represent engine measurements where the A_r^i was fixed at 0.2 (for a fixed outer throat area) and the outer stream radius ratio was parametrically varied as $R_r^o = 0.816, 0.853, \text{ and } 0.875$. The engine measurements show that at high specific thrusts [(533 m/sec (1749 fps) to 762 m/sec (2500 fps)], PNL_p is reduced, as a result of increasing R_r^o . As an example, at v_j^{mix} of approximately 587 m/sec (1926 fps), increasing radius ratio (R_r^o) from 0.816 to 0.875 reduces the normalized peak PNL by 1.9 PNdB. This would indicate that coannular plug nozzle jet noise reduction, at high specific thrusts, is close to a 6.26 power law on radius ratio.

The spectral characteristics for the three radius ratio configurations tested are shown in Figure 54. Shown in Figure 54 are the one-third octave band SPL spectra for $\theta_i = 50^\circ, 90^\circ$ and 140° for v_j^{mix} approximately 587 m/sec (1926 fps). Increase in radius ratio is seen to reduce, and somewhat reshape, the spectral content of the coannular plug nozzle.

The PNL directivity pattern for the above tests are shown in Figure 55. The general feature observed is that the noise levels are reduced at all observation angles, but the more favorable reduction occurs in the aft quadrant with increasing R_r^o .

5.5.1.3 Influence of Area Ratio on Coannular Plug Nozzle Jet Noise Reduction

Another nozzle design parameter for coannular jet noise reduction is the inner stream to outer stream nozzle area ratio (A_r^i). At high specific thrusts (~700 mps), model scale tests (Reference 10) have shown that as A_r^i increases the coannular suppression increases. In relation to R_r^o , A_r^i has a smaller influence on noise reduction for the range of interest ($0.1 \leq A_r^i \leq 0.6$). Previous testing had been limited to $0.33 \leq A_r^i \leq 1.42$. An objective for the engine tests was to obtain measurements to fill our information gap in the lower A_r^i range. Tests were conducted where radius ratio was fixed at $R_r^o = 0.853$, and A_r^i was varied as: 0.475, 0.2, 0.1, 0.*

*Note should be taken that even when the inner plug nozzle was placed in the most aft position, to close off the inner stream flow, there was a flow leakage. The $A_r^i = 0$ test results should be viewed as a "leaky" plug nozzle.

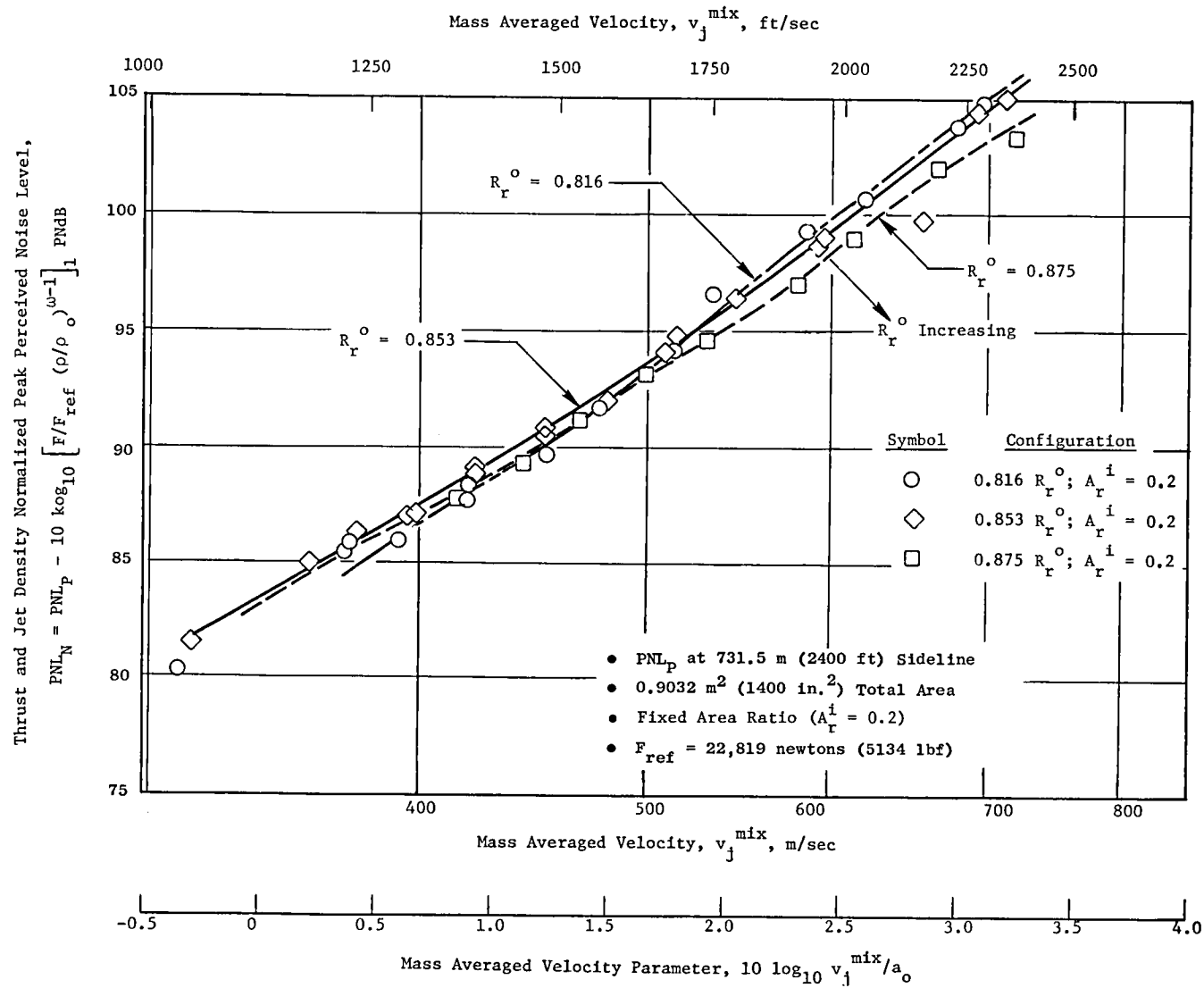


Figure 53. Influence of Radius Ratio on Jet Noise.

Symbol	R_r^o	V_j^o m/sec (ft/sec)	T_T^o K (°R)	P_r^o	V_j^i m/sec (ft/sec)	T_T^i	P_r^i	V_j^{mix} m/sec (ft/sec)	T_T^{mix} K (°R)	P_r^{mix}	$10 \text{ Log } (F/F_{ref}) (\rho_j^{mix}/\rho_o)^{-1}$	Bdg.
----	0.816	639 (2095)	973 (1752)	2.23	420 (1380)	443 (798)	2.163	586 (1921)	845 (1521)	2.219	-4.4	446
—	0.853	640 (2101)	957 (1723)	2.278	421 (1382)	440 (793)	2.181	594 (1950)	849 (1528)	2.261	-4.7	326
---	0.875	625 (2051)	929 (1672)	2.242	410 (1347)	428 (771)	2.141	579 (1901)	822 (1480)	2.226	-4.7	460

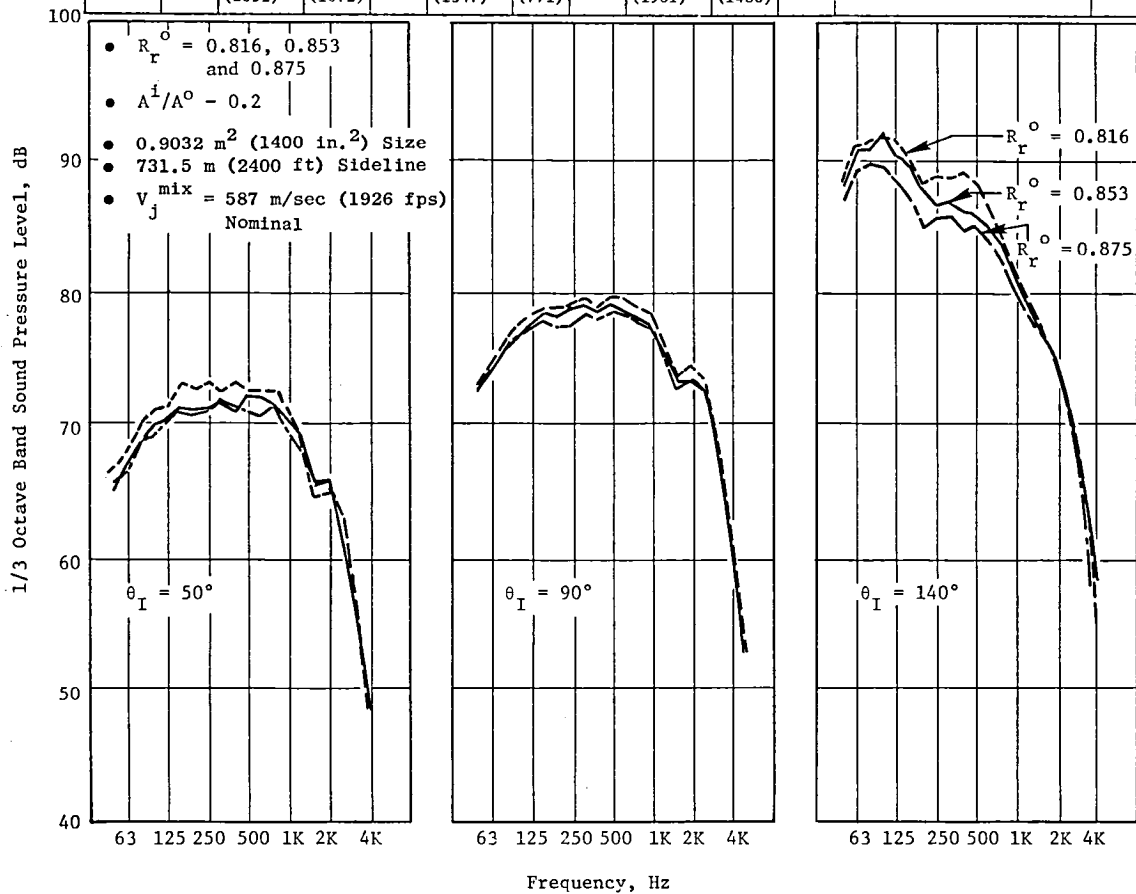


Figure 54. Influence of Outer Nozzle Radius Ratio on Coannular Nozzle Noise Spectra Characteristics.

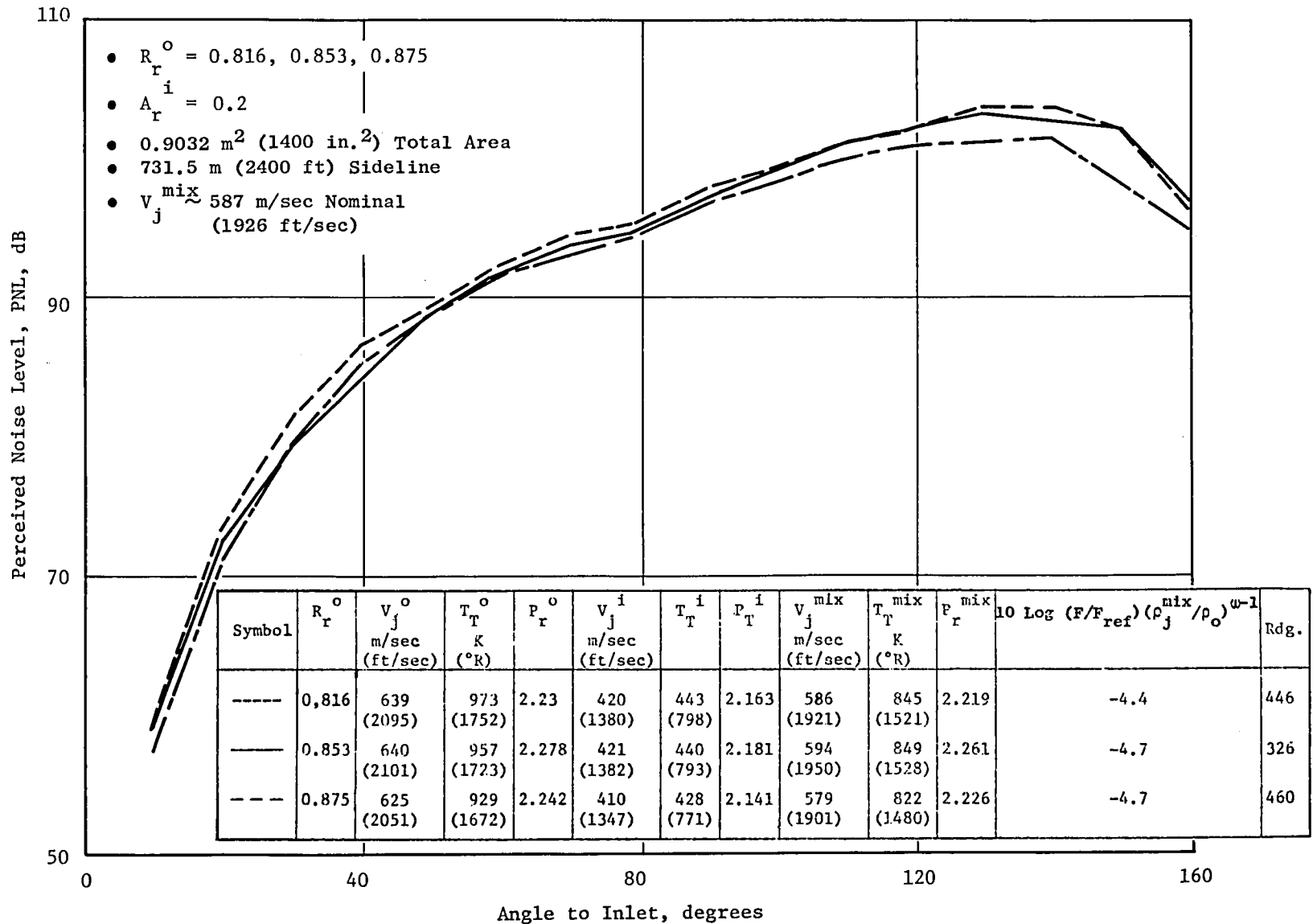


Figure 55. Influence of Outer Nozzle Radius Ratio on Coannular Plug Nozzle PNL Directivity.

Figure 56 presents a summary of the engine test results illustrating area ratio effects on coannular plug nozzle peak aft angle jet noise. All results are presented at product size [0.9032 m² (1400 in.²)] on a 731.5m (2400 ft) sideline. In the V_j^{mix} range of 381 m/sec (1250 fps) to 610 m/sec (2000 fps) (typical approach conditions and up to the lower end of typical sideline cycle operation), the trend is to decrease jet noise with decrease in A_r^i ; this includes the $A_r^i \sim 0$ case. As an example, at $V_j^{mix} \approx 427$ m/sec (1400 fps) $\Delta PNLp \approx 1.7$ between the highest and lowest area ratios shown.

This indicates the coannular plug nozzle PNLp would follow a $10 \log(1 + A_r^i)$ dependency in this region. For the higher velocities [$V_j^{mix} \sim 610$ m/sec (2000 fps) to 700 m/sec (2296 fps)] a reversal in trend is observed (note should be taken that data for $A_r^i = 0.475$ is not available). In this region the $A_r^i = 0.2$ data is lowest with the $A_r^i = 0.1$ about 0.5 PNdB higher, and with the $A_r^i \approx 0$ data being about 1.5 PNdB higher than the $A_r^i = 0.2$ data.* This would correspond to a $-1.89 \times [\log(1 + A_r^i)]$ dependency for peak angle coannular plug nozzle jet noise. As a gauge on the levels of static peak PNL reduction observed relative to the conic nozzle:

$$\begin{array}{l}
 \text{at } V_j^{mix} \sim 700 \text{ m/sec} \\
 \quad (2296 \text{ fps}) \\
 \quad \Delta PNLp \approx \left\{ \begin{array}{l} -4, A_r^i \sim 0 \\ -4.5, A_r^i = 0.1 \\ -5.2, A_r^i = 0.2 \end{array} \right. \\
 \\
 \text{at } V_j^{mix} \sim 487 \text{ m/sec} \\
 \quad (1598 \text{ fps}) \\
 \quad \Delta PNLp \approx \left\{ \begin{array}{l} -4.7, A_r^i \sim 0 \\ -4.5, A_r^i = 0.1 \\ -3.5, A_r^i = 0.2 \\ -2.5, A_r^i = 0.475 \end{array} \right.
 \end{array}$$

*Subsequent review of model scale test data for plug nozzles and plug nozzles with small amounts of inner stream leakage have verified the trends observed from these engine tests: namely, that for $V_j^{mix} \geq 2000$ fps coannular suppression increases with increase in A_r^i ; at $V_j^{mix} < 2000$ fps this trend reverses, although over the entire velocity range substantial suppression exists relative to the conic baseline nozzle. The engine results for the $A_r^i \sim 0$ (or leaky flow plug nozzle) also fall within what past test results have illustrated. At $V_j^{mix} < 2000$ fps, a high radius ratio single stream plug nozzle and a low area ratio coannular plug nozzle should have about the same amount of suppression. However, for selection of a nozzle system which would have the lowest noise for all monitoring points on other criterion such as ability to high flow (operate at lower specific thrust for the same actual thrust) has to be included. The coannular plug nozzle designs to date indicate more flexibility in this regard than single stream designs.

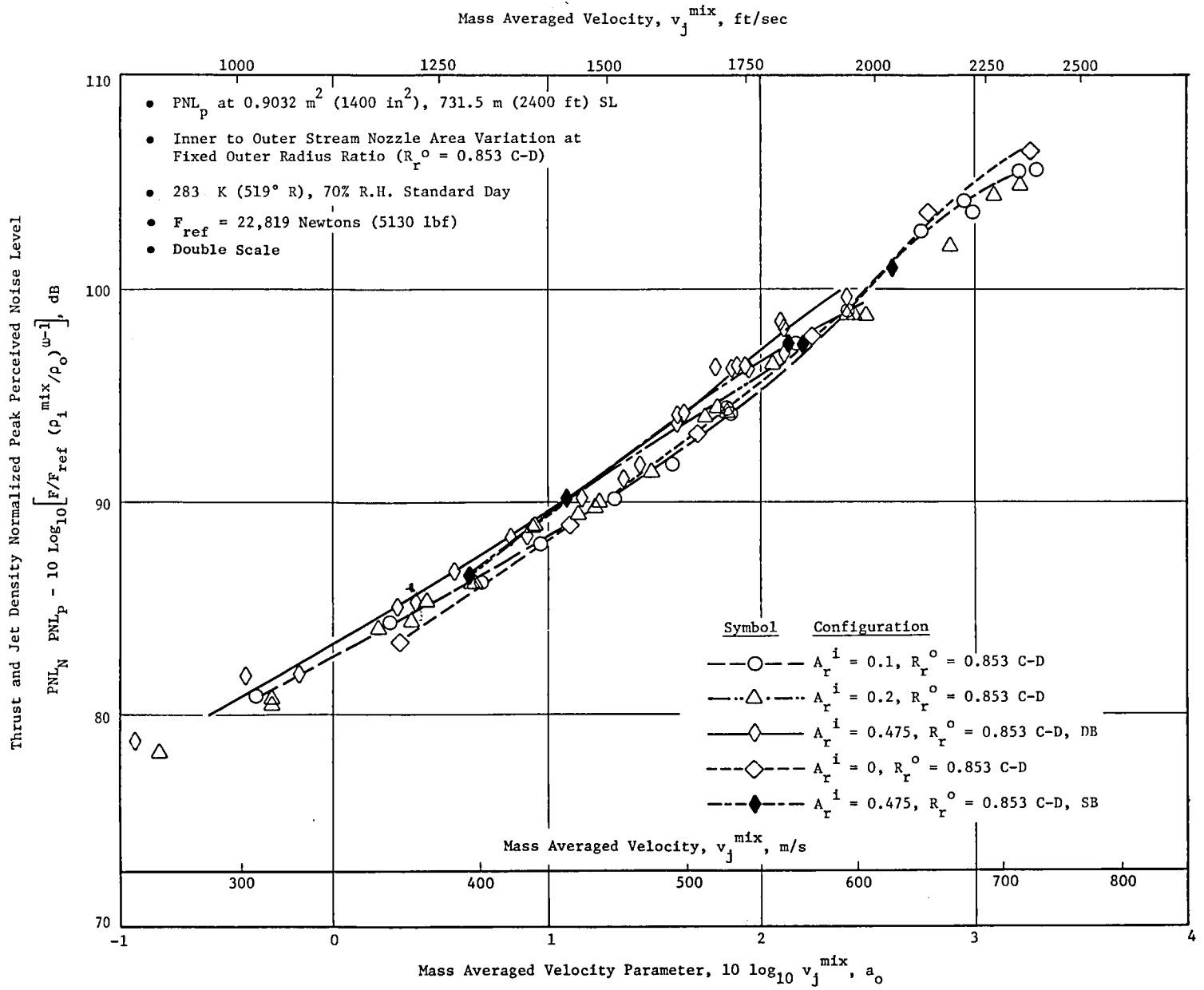


Figure 56. Influence of Area Ratio on Peak Noise for Coannular Plug Nozzles.

At $\theta_i = 90^\circ$ the normalized PNL is shown in Figure 57. The results shown here indicate that, over the entire velocity range shown, PNL₉₀ for a given V_j^{mix} decreases with decrease in A_r^i -- no reversal effect as noted at θ_p is observed here.

Example comparisons of the spectral characteristics for the tested area ratio variations are shown in Figures 58, 59, and 60.

5.5.1.4 Influence of Outer Stream Nozzle Exit Termination

Subsection 5.5.1.1 summarized the basic shock noise reduction features for the coannular plug nozzle. The key observation was that, at an equivalent shock strength (β_j^{eff}), the forward quadrant shock noise was substantially reduced (~ 7 PNdB at $\theta_i = 50^\circ$) and the data trend observed a $(\beta_j^{eff})^4$ power law (see Figure 48). In order to examine the shock noise features more closely, engine tests were performed on the $R_r^O = 0.853$, $A_r^i = 0.2$ nozzle such that in addition to the C-D nozzle, the outer stream nozzle was terminated at the throat station* (conic nozzle termination). One of the prime objectives was to compare the noise levels between these two configurations, particularly when the C-D configuration was at design operation, and the shock noise was expected to be mitigated further than previously observed.

A comparison of normalized peak PNL between the C-D terminated coannular plug nozzle configuration and the conic terminated coannular plug nozzle configuration is shown on Figure 61. It is observed that over the entire operating range ($V_j^{mix} \sim 321$ m/sec (1053 fps) to 720 m/sec (2362 fps), the conic-terminated coannular plug nozzle is observed to be uniformly lower (~ 0.5 PNdB) than the C-D terminated coannular configuration. The same data trend is observed at $\theta_i = 90^\circ$ (see Figure 62), but the level of reduction is even less.

In the forward quadrant ($\theta_i = 50^\circ$), where shock noise dominates at the high power settings, a comparison between the outer stream C-D and conic-terminated coannular plug nozzles is shown in Figure 63. The design pressure

*Recall that all the basic coannular plug nozzle tests were run with the outer stream nozzle having a convergent-divergent (C-D) termination. The exit to throat area ratio was selected for a $P_r^O = 2.9$ design point pressure ratio. Thus most of the tests were run for the outer nozzle operating in the overexpanded mode. The conic outer stream termination tests described here were only done for the $R_r^O = 0.853$, $A_r^i = 0.2$ nozzle configuration. Note further that the inner stream, for all A_r^i configurations, had a conic termination.

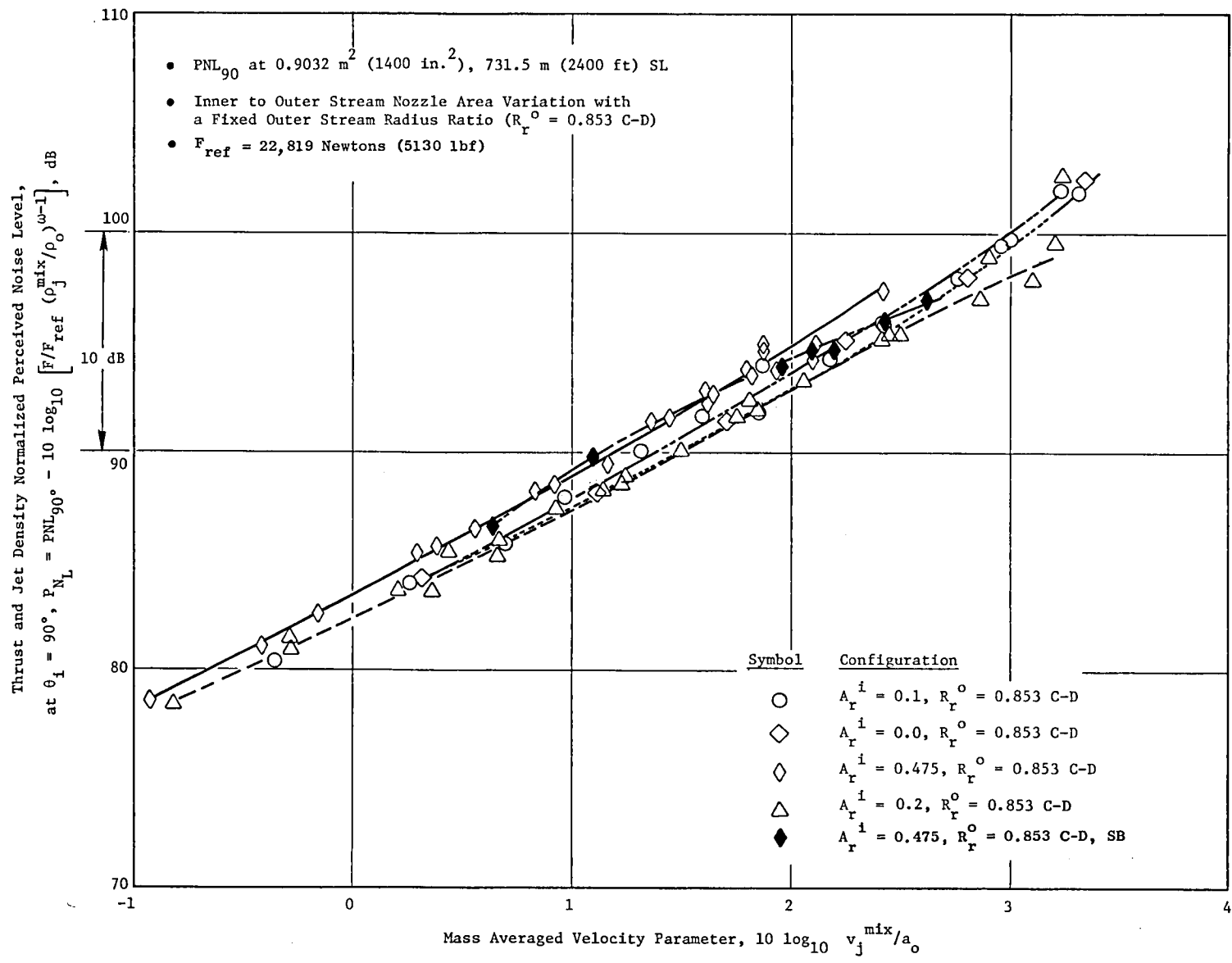


Figure 57. Area Ratio Effects on Coannular Plug Nozzle Jet Noise Reduction, $\theta_i = 90^\circ$.

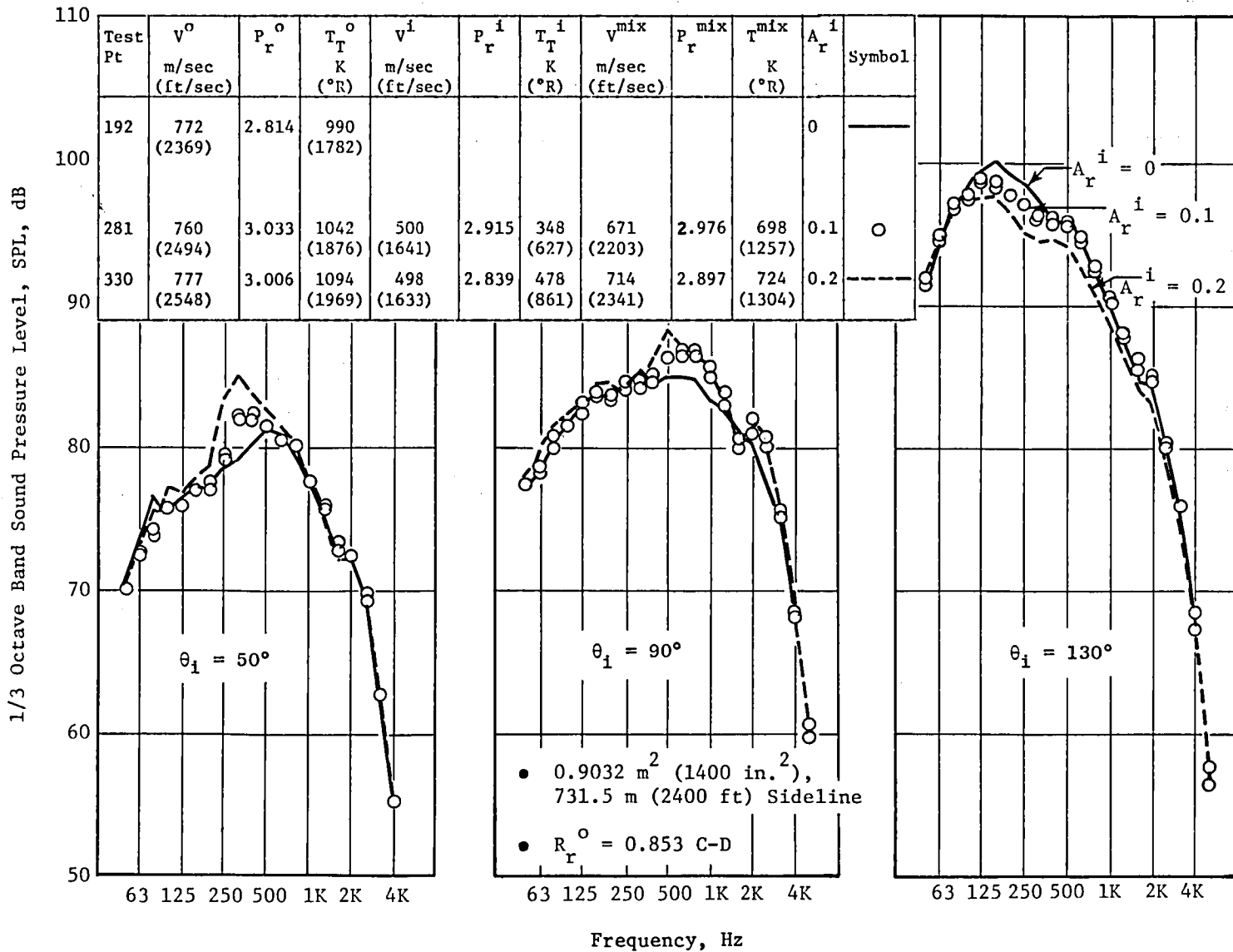


Figure 58. Influence of Area Ratio Variation on Coannular Plug Nozzle Spectra,
 $V_j^{mix} \sim 701 \text{ m/sec}$ (2300 ft/sec).

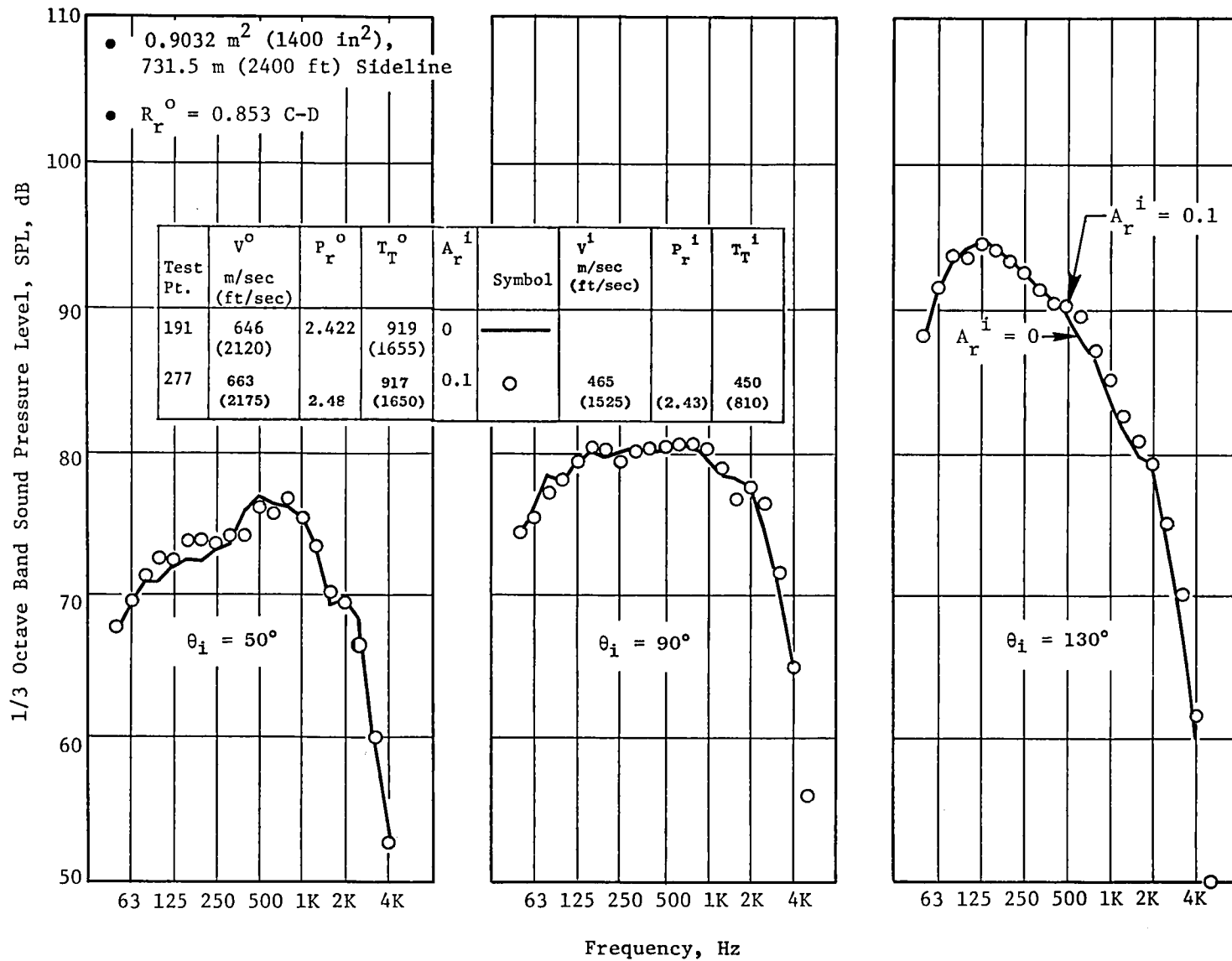


Figure 59. Influence of Area Ratio Variation on Coannular Plug Nozzle Spectra,
 $V_j^{\text{mix}} \sim 646 \text{ m/sec} (2120 \text{ ft/sec})$.

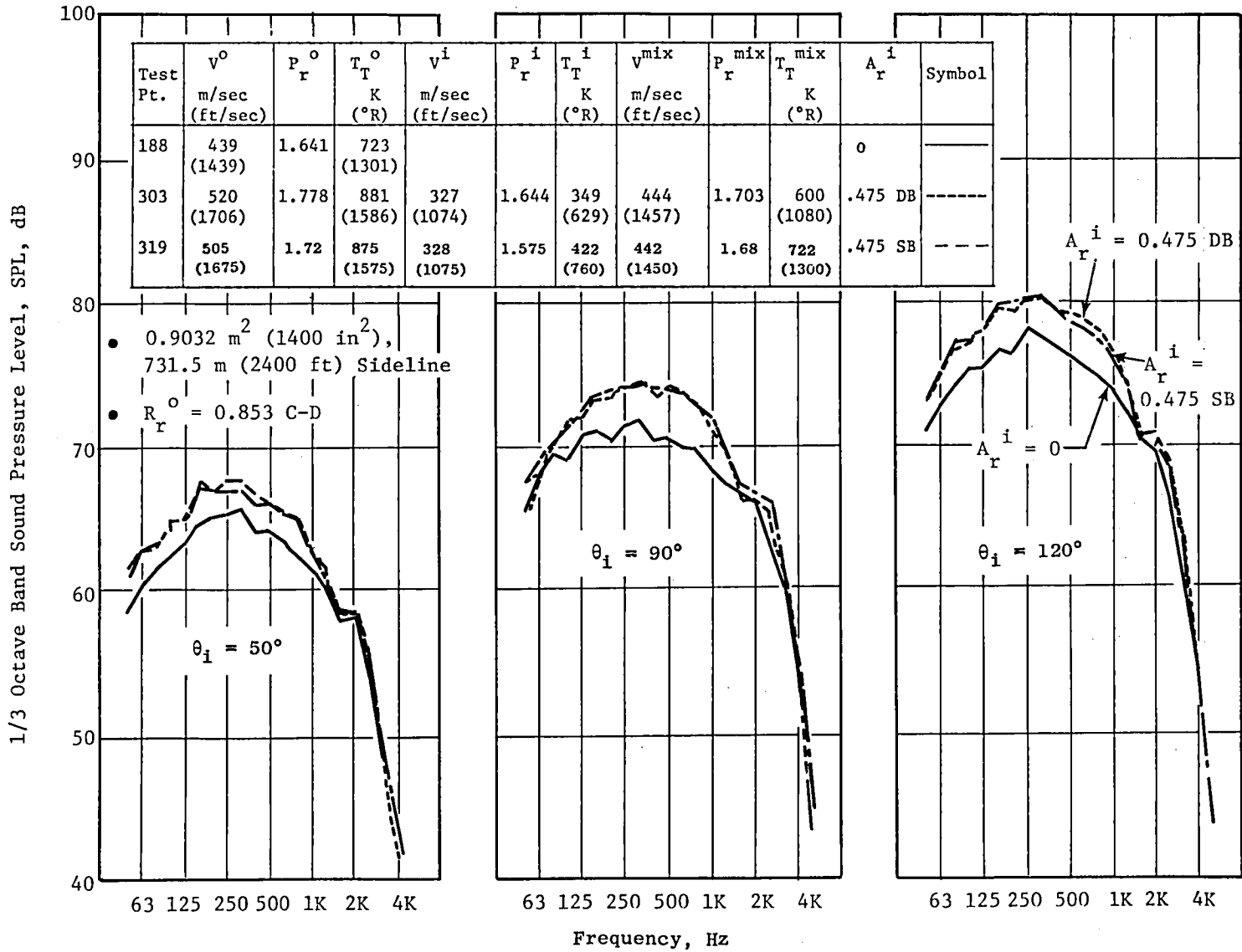


Figure 60. Influence of Area Ratio Variation on Coannular Plug Nozzle Spectra,
 $v_j^{mix} \sim 441 \text{ m/sec}$ (1447 ft/sec).

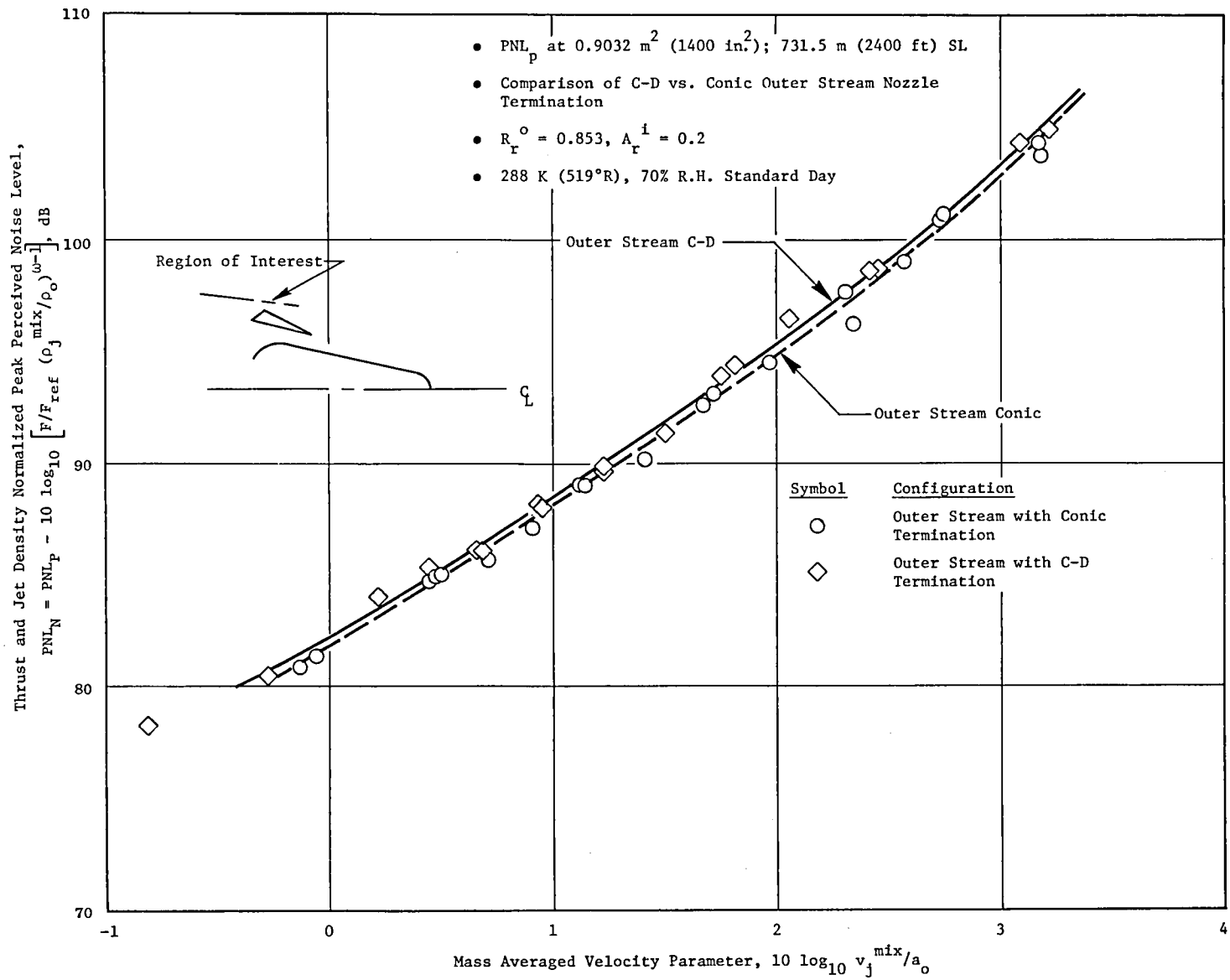


Figure 61. Influence of Outer Nozzle Termination on Coannular Plug Nozzle Jet Peak Perceived Noise.

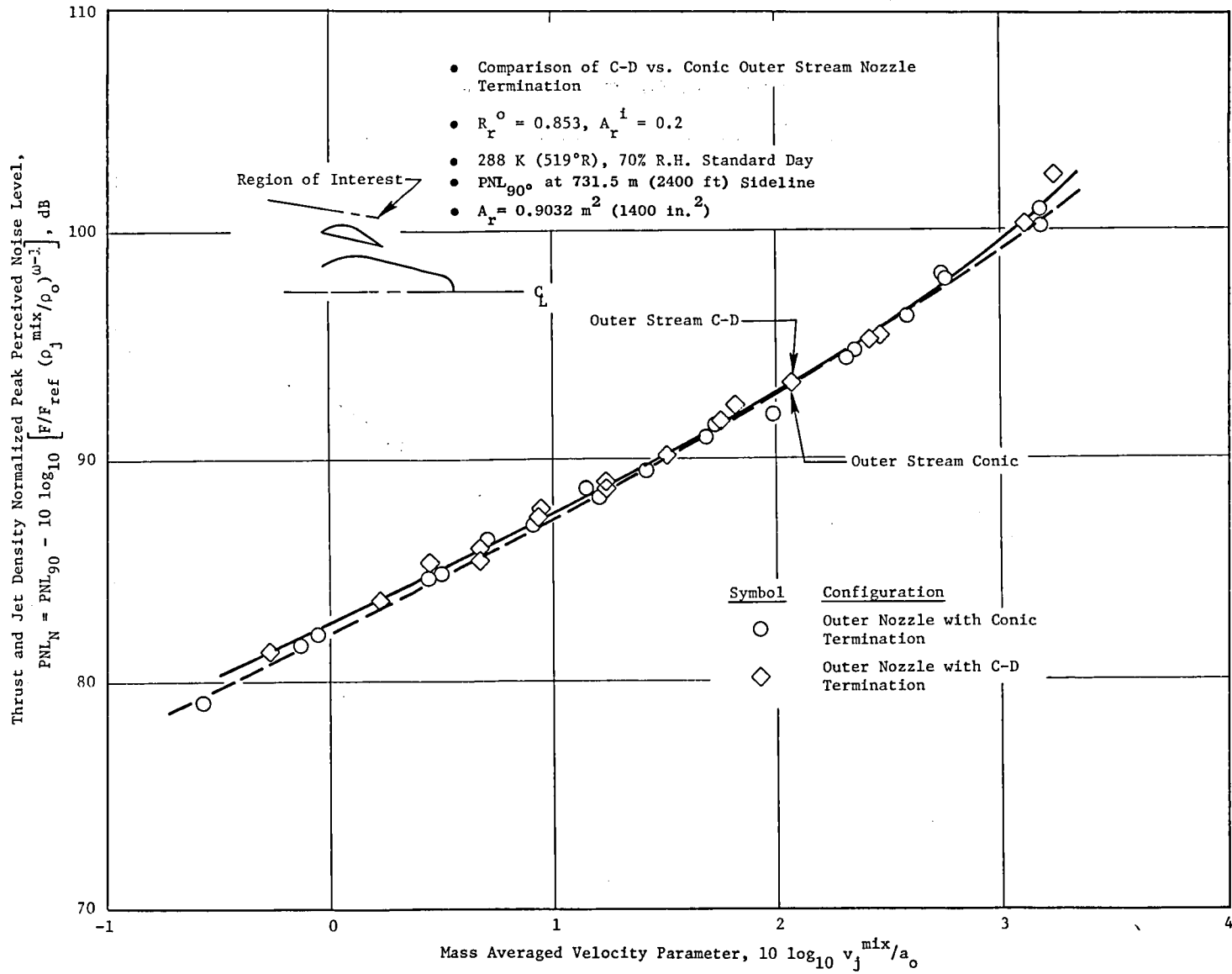


Figure 62. Influence of Outer Stream Nozzle Termination on Coannular Plug Nozzle Jet Perceived Noise at $\theta_i = 90^\circ$.

- PNL₅₀ at 731.5 m (2400 ft) Sideline
- A_r^o = 0.9032 m² (1400 in.²)
- Comparison of C-D vs. Conic Outer Stream Nozzle Termination
- R_r^o = 0.853, A_rⁱ = 0.2
- 288 K (519°R), 70% R.H. Standard Day

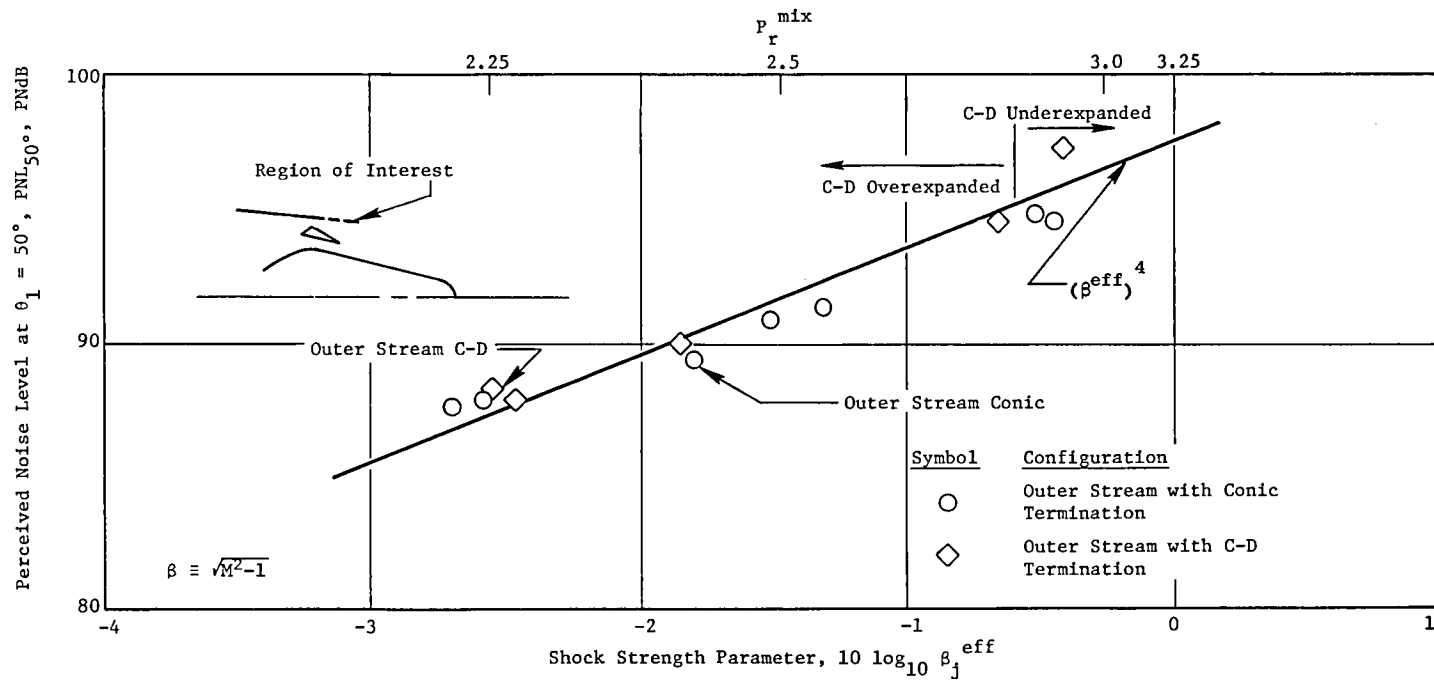


Figure 63. Influence of Outer Stream Nozzle Termination on Coannular Plug Nozzle Shock Noise at $\theta_i = 50^\circ$.

ratio points correspond to $10 \log \beta_j^{\text{eff}} \approx -0.55^*$. Two observations can be made from Figure 63. The first is that for most of the data presented there was no clear advantage obtained for either the C-D or conic outer stream nozzle termination. The shock noise data trends for both nozzles appear to correlate well with β_j^{eff} . The second observation to note is that in the region of perfect expansion for the C-D termination, there appears to be an abrupt increase in shock noise as it passes from overexpanded operation to underexpanded operation. (The conic coannular nozzle, which is always highly underexpanded, does not appear to exhibit this trend.)

The spectral characteristics for the test points near the design P_r^0 are shown in Figure 64. Figure 65 shows a spectral comparison at $P_r^0 \sim 1.7$ for illustration purposes. Shown in Figure 64 are the spectra at $\theta_1 = 50^\circ, 90^\circ,$ and 130° for the C-D-overexpanded (but near the design P_r^0), the C-D underexpanded (also near the design P_r^0), and the conic terminated nozzle near the outer stream C-D nozzle design pressure ratio. Similar spectral data are shown in Figure 65 for C-D data which is considerably overexpanded, again in comparison to overexpanded conic data at the same P_r^0 .

Of particular note are the spectra at $\theta_1 = 50^\circ$ and 90° ** shown in Figure 64. There the shock noise for the underexpanded C-D nozzle is observed to be substantially above the overexpanded C-D nozzle and the (underexpanded) conic coannular nozzle. The difference in level is certainly not due to the difference in computed shock strength (based on a $40 \log \beta_j^{\text{eff}}$, a $\Delta \text{PNdB} \approx 1$ would exist between the overexpanded and underexpanded coannular plug nozzles). Similarly, based on the high data quality experienced for these tests, the measured increased shock noise is not expected to be due to data scatter.

One conclusion which can be drawn is that a strong sensitivity exists in obtaining shock-free coannular flow through C-D nozzle designs. Since shock noise will be amplified in flight, the risk of trying to completely eliminate coannular shock wave noise and instead cause much higher shock noise due to this sensitivity may not be worth it. Perhaps the use of a conic termination would be more rewarding in the long run.

A clear rationale for why peak angle jet noise was reduced for the conically terminated coannular plug nozzle as compared with the C-D nozzle cannot be made at this time. The only observation which can be offered is that overexpanded and underexpanded flows will have different shock patterns. These

*Engine operation of $P_r^0 \sim 2.9$ for the $R_r^0 = 0.853, A_i^1 = 0.2$ nozzle represented an upper limit region for safe operation. Although it would have been desirable to obtain a series of closely spaced points below, at and above $P_r^0 = 2.9$, it was impractical to do for this test series. Engine operation was set at or around the condition desired, aero and acoustic data were taken, and then the engine throttle setting was reduced to a safer operation range. We do not know with any certainty whether perfect expansion was achieved for the outer stream nozzle during this test series.

**The level of difference at 130° is due more to the differences in V_j^{mix} and T_S^{mix} , than due to the underexpansion of the outer stream nozzle.

Rdg.	v_j^o m/sec (ft/sec)	T_T^o K (°R)	P_r^o	v_j^i m/sec (ft/sec)	T_T^i K (°R)	P_r^i	v_j^{mix} m/sec (ft/sec)	T_T^{mix} K (°R)	P_r^{mix}	Outer Stream	Symbol
329	752 (2467)	1066 (1918)	2.84	485 (1590)	474 (853)	2.68	699 (2292)	947 (1705)	2.814	C-D	—
330	777 (2548)	1094 (1969)	2.97	488 (1633)	478 (861)	2.833	718 (2355)	964 (1736)	2.946	C-D	---
414	769 (2523)	1080 (1944)	2.942	489 (1604)	468 (842)	2.782	707 (2318)	942 (1697)	2.914	Conic	- - -

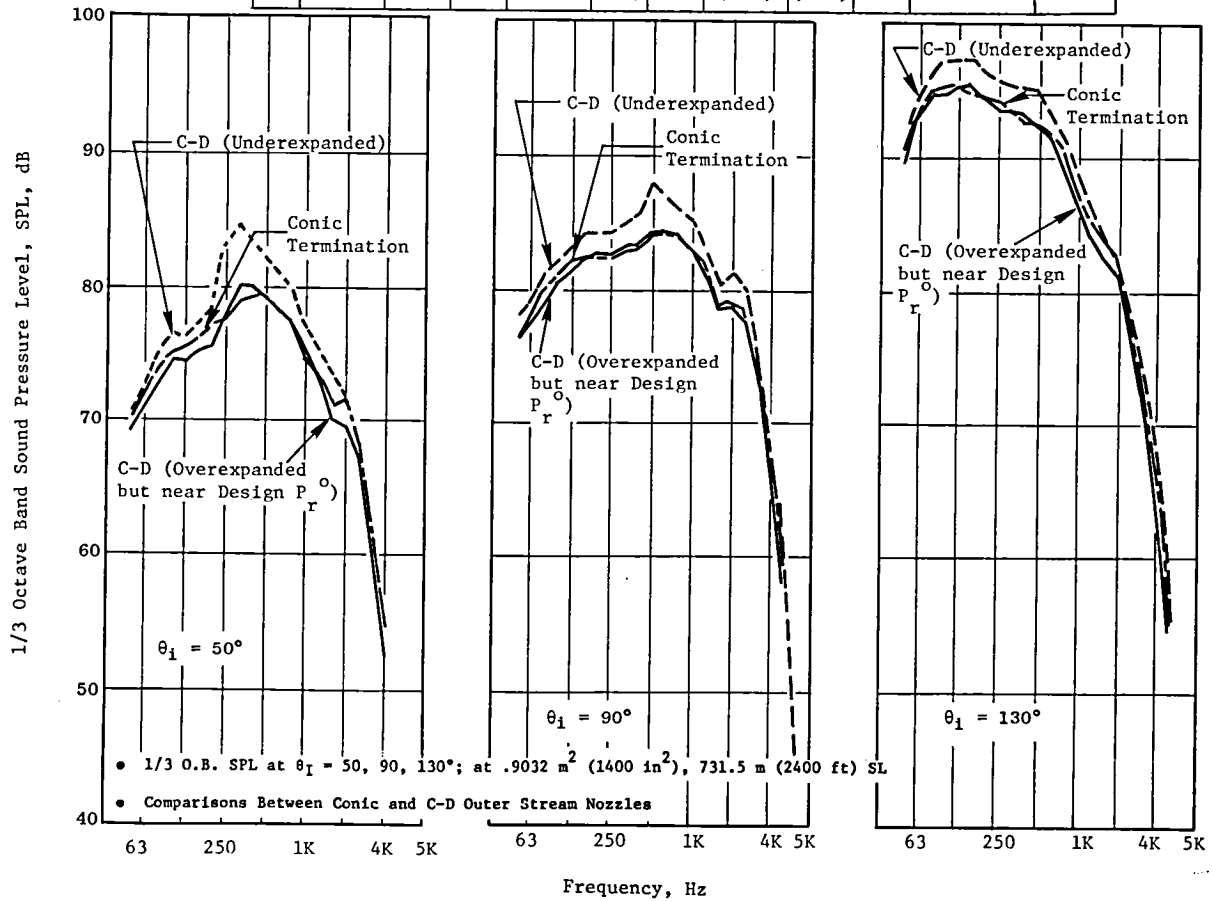


Figure 64. Influence of Outer Stream Nozzle Termination on Coannular Plug Nozzle Spectral Characteristics Near Design P_r^o .

Rdg.	V_j^o m/sec (ft/sec)	T_T^o K (°R)	P_r^o	V_j^i m/sec (ft/sec)	T_T^i K (°R)	P_r^i	$V_{j\text{ mix}}$ m/sec (ft/sec)	$T_{T\text{ mix}}$ K (°R)	$P_{r\text{ mix}}$	Symbol
322	484 (1588)	807 (1452)	1.716	335 (1099)	399 (719)	1.69	453 (1487)	722 (1300)	1.722	—
407	471 (1548)	776 (1396)	1.704	328 (1076)	385 (696)	1.68	442 (1451)	696 (1253)	1.70	- - -

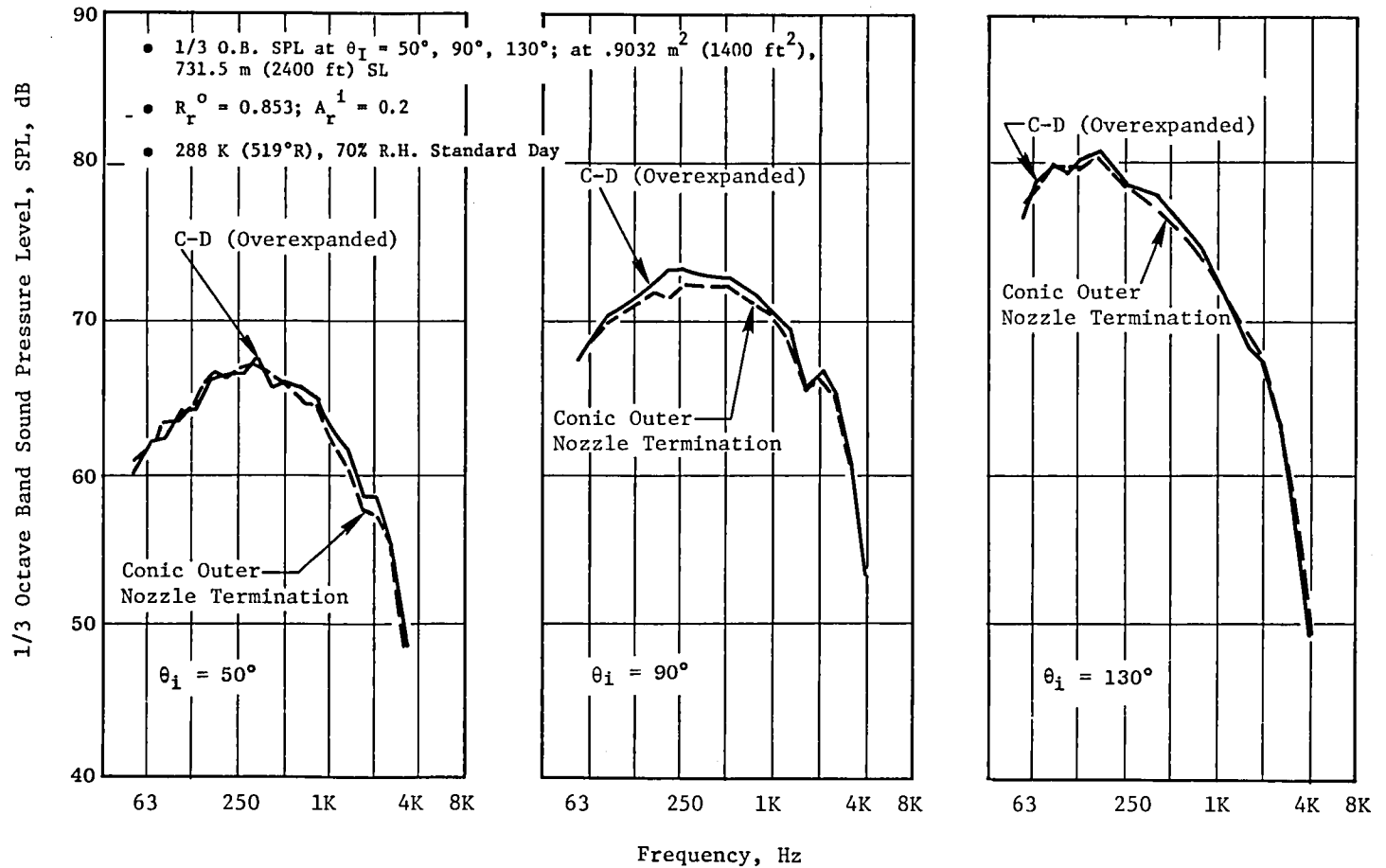


Figure 65. Influence of Outer Stream Nozzle Termination on Coannular Plug Nozzle Spectral Characteristics at Subsonic Conditions in Both Streams.

different flow patterns may result in different jet mixing patterns, which in turn may be responsible for the results shown in Figure 61. Further analysis and aero and acoustic test information is required to resolve this issue.

Another observation which has been made regarding coannular plug nozzle shock noise relief (Reference 10) was that the coupling role between inner and outer streams at high pressure ratios must be better defined, especially when the inner stream pressure ratio approaches that of the outer stream. Model scale results suggested that as these pressure ratios come closer together the coannular plug nozzle shock noise relief could be considerably reduced. These observations as well as the possibility of further "softening" the shock wave development with the plug itself should be pursued with model scale testing (see Reference 12).

5.5.1.5 Influence of Aft VABI Sideplates on the Coannular Plug Nozzle Jet Noise

In order to ensure proper mixing of the fan flow with the core, the aft VABI's were designed with fixed sideplates. In total there were forty-eight sideplates. One of the acoustic objectives was to determine if these sideplates contributed to the exhaust noise - particularly at the lower power settings. Except for the sideplates-off test series, the sideplates were in place for all tests. The test configuration for the aft sideplates-off was the $RQ = 0.853$, conic outer stream nozzle, $A_R^i = 0.2$.

Figure 66 shows the normalized PNL at the peak aft quadrant and at $\theta_i = 90^\circ$ over a V_j^{mix} range of 330 m/sec (1083 fps) to 720 m/sec (2362 fps) --- all at typical product engine size. The results show that the sideplates do not influence the perceived noise levels at these angles.

Figures 67 and 68 illustrate spectral comparisons between tests with and without aft VABI sideplates. Shown on these figures are spectra at $\theta_i = 50^\circ$, 90° , 130° for $V_j^{mix} = 443$ m/sec (1453 fps) and $V_j^{mix} \sim 333$ m/sec (1096 fps) respectively. For the first case, where $V_j^{mix} \sim 443$ m/sec, (1453 fps) no discernable difference can be observed between the results with or without aft VABI sideplates. For the second case (Figure 68), where $V_j^{mix} \sim 333$ m/sec (1096 fps), (conditions typical of an aircraft approach condition), the appearance of aft VABI sideplate noise at $\theta_i = 50^\circ$ is observed. This observation may be deduced from the fact that obstruction noise (of which category the aft VABI sideplates could be classified is expected to have a directivity of $\sin^2\theta_I$, whereas subsonic jet noise is expected to make a directivity of $1/(1+M_c \cos\theta_I)^5$ where M_c (convective Mach No.) = $0.7 \times V_j^{mix}/a_0$. Of these two expressions, the jet noise is predicted to drop off faster with decrease in θ_i than will the obstruction noise*. In flight, such an internally generated noise should be amplified, whereas the jet noise (subsonic) would be

*For this case the jet noise drop from 90° to 50° would be 7.56 dB. For obstruction noise it would be 2.31 dB. The difference is 5.25 dB.

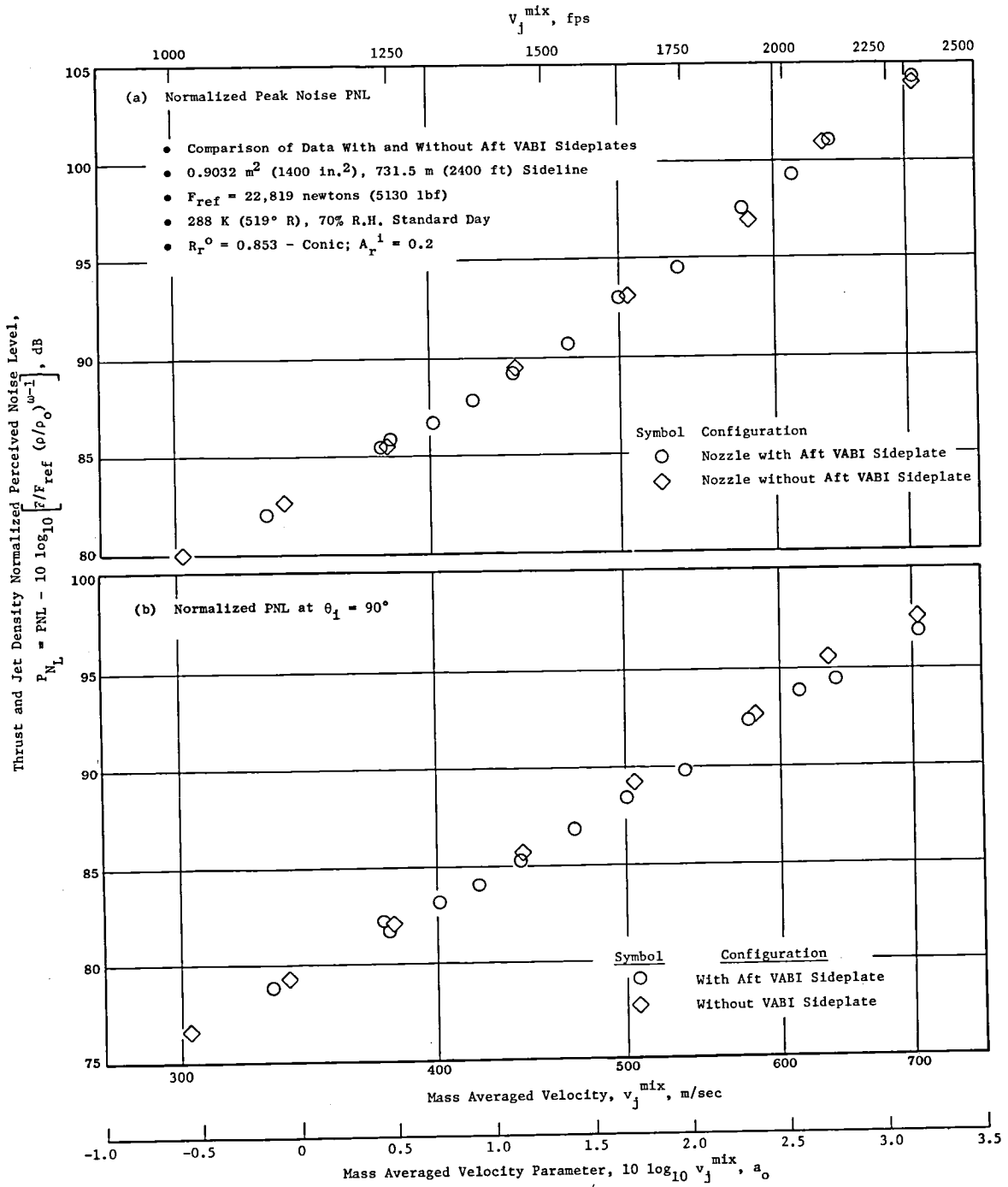


Figure 66. Influence of Aft VABI Sideplates on Coannular Plug Nozzle Jet Noise.

Rdg	V_j^o m/sec (ft/sec)	T_T^o K (°R)	P_r^o	V_j^i m/sec (ft/sec)	T_T^i K (°R)	P_r^i	V_j^{mix} m/sec (ft/sec)	T_T^{mix} K (°R)	P_r^{mix}	Configuration
407	471 (1548)	776 (1396)	1.704	328 (1076)	387 (696)	1.680	442 (1451)	696 (1253)	1.700	With Sideplates
431	474 (1557)	801 (1441)	1.685	324 (1063)	389 (701)	1.654	443 (1453)	713 (1284)	1.680	Without Sideplates

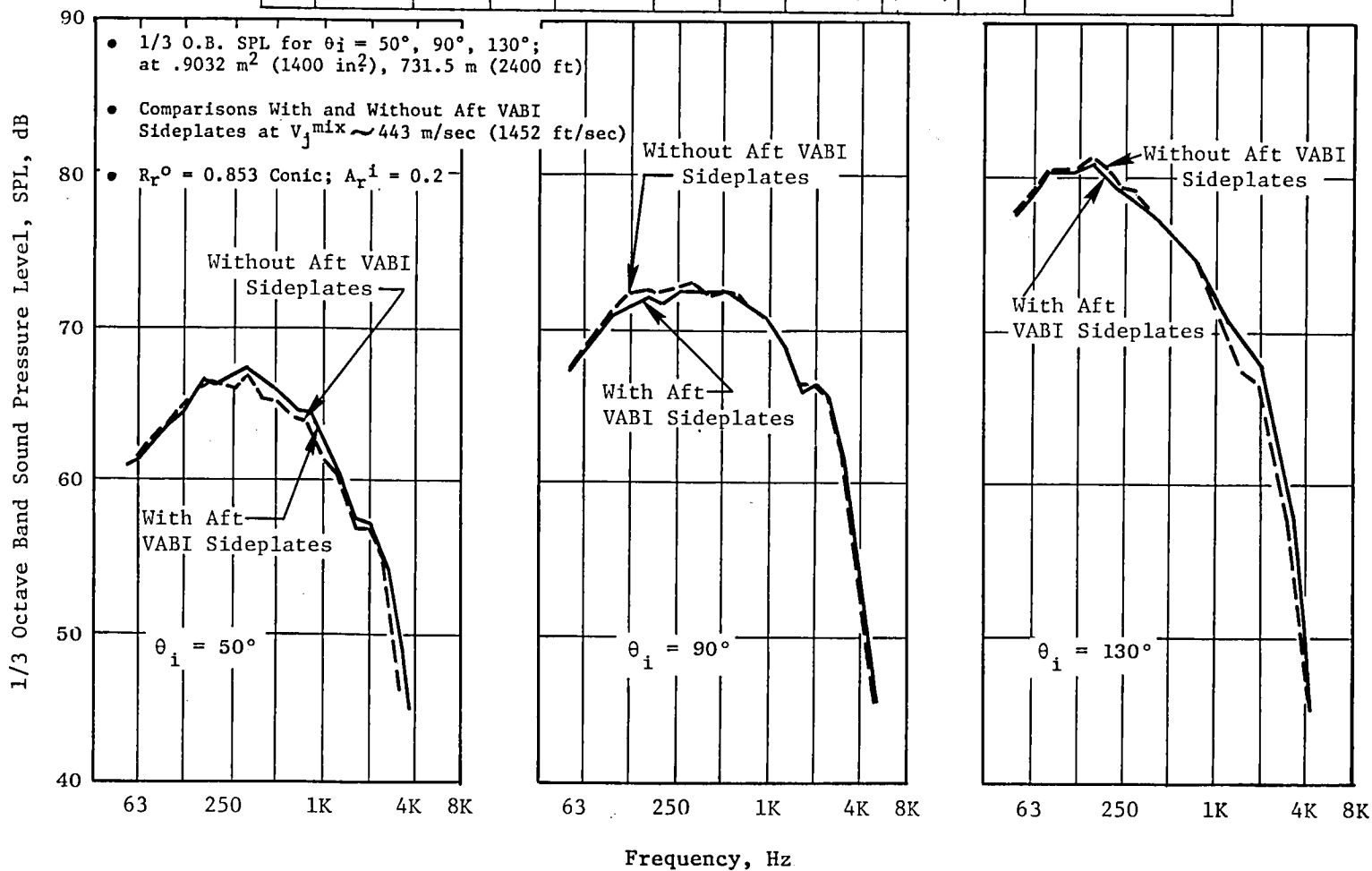


Figure 67. Influence of Aft VABI Sideplates on Coannular Plug Nozzle Spectral Characteristics at $V_j^{Mix} = 443 \text{ m/sec}$ (1452 ft/sec).

Rdg	V_j^o m/sec (ft/sec)	T_T^o K (°R)	P_r^o	V_j^i m/sec (ft/sec)	T_T^i K (°R)	P_r^i	V_j^{mix} m/sec (ft/sec)	T_T^{mix} K (°R)	P_r^{mix}	Configuration
401	349 (1145)	673 (1212)	1.388	259 (851)	361 (649)	1.405	332 (1088)	561 (1010)	1.390	With Aft VABI Sideplates
429	357 (1172)	704 (1267)	1.389	259 (851)	366 (659)	1.397	337 (1105)	633 (1139)	1.390	Without Aft VABI Sideplates

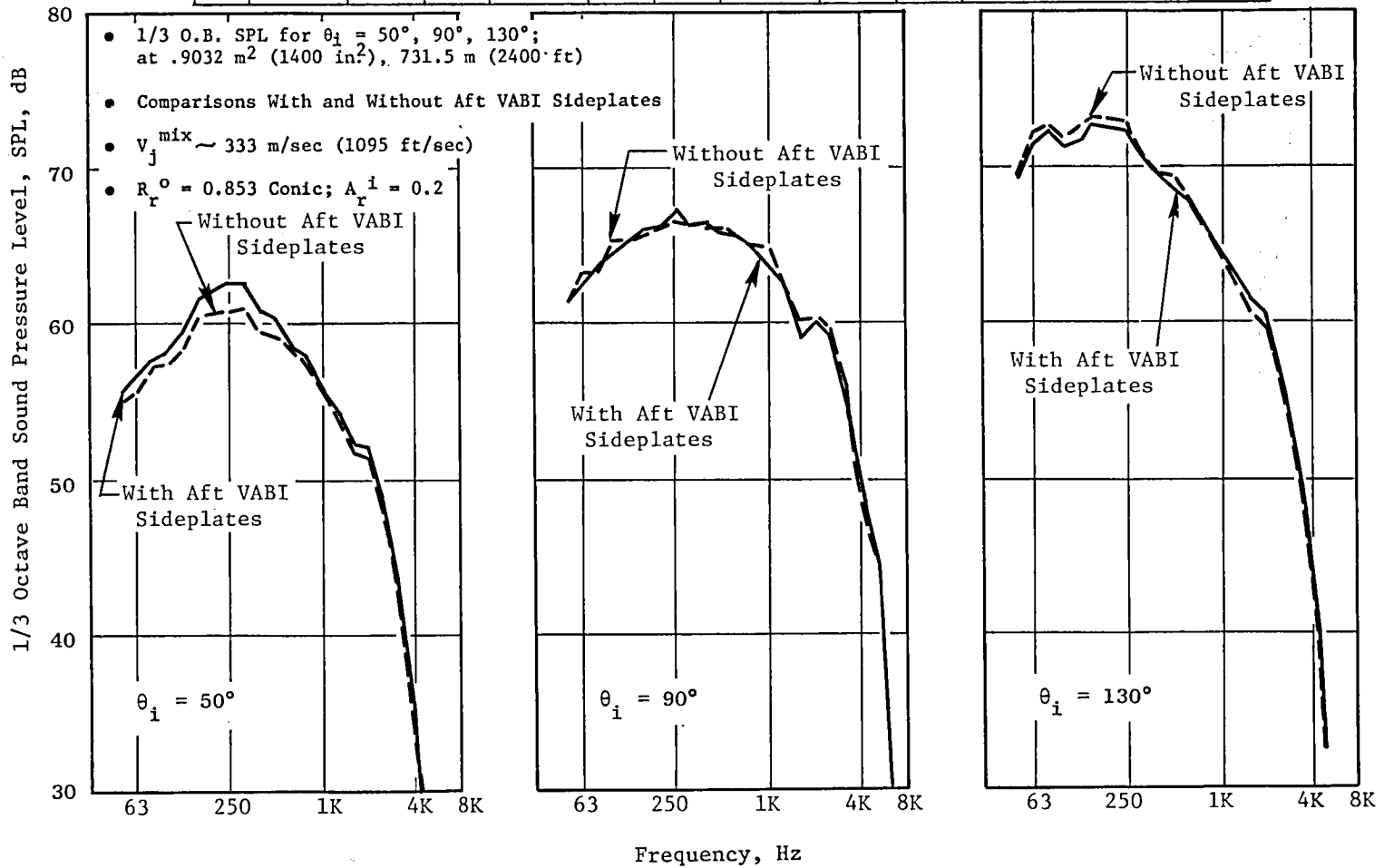


Figure 68. Influence of Aft VABI Sideplates on Coannular Plug Nozzle Spectral Characteristics at $V_j^{mix} = 333 \text{ m/sec}$ (1095 fps).

somewhat reduced beyond the static levels. From an acoustic point of view, it would be desirable not to have the sideplates.

5.5.1.6 Influence of Engine Cycle Parameters on Coannular Plug Nozzle Exhaust Noise Reduction

Of interest for the coannular plug acoustic nozzle for VCE/AST application is the effect of high flowing the engine, and the selection of inner to outer stream velocity ratio (V_r^i) for "best" coannular plug nozzle noise reduction.

In terms of engine high flowing, the idea is as follows. For a given thrust, operation of the engine at its lowest specific thrust is desirable. The lower specific thrust brings the noise level down because jet noise is directly and strongly dependent on V_j^{mix} . As an example, a typical product 10% oversize front block fan VCE would have a $V_j^{mix} \sim 500$ m/sec (1640 fps). This reduction in specific thrust could mean up to 3 EPNdB reduction in the basic jet noise levels. To operate at "optimum" high flow conditions, the double bypass has been found to be most efficient. For this program, tests were performed to compare single bypass operation versus double bypass operation over similar cycle operating ranges in terms of specific thrust. These results (single bypass versus double bypass) will be compared below. The configuration for which these tests were performed was the $A_r^i = 0.475$, $R_r^i = 0.8953$ -C-D.

Model test results (Reference 10) have shown that the velocity ratio (V_r^i) at which the optimum coannular plug nozzle jet noise reduction occurs is at $V_r^i \sim 0.6$. For the YJ101 testbed engine, as well as the expected product engine cycles, operation at this optimum (V_r^i) was not always possible. Figure 69 shows the variation of V_r^i versus V_j^{mix} for the current engine test series. As can be observed from Figure 69, as V_j^{mix} is decreased, V_r^i increases - the rate of increase is greater the lower the area ratio. For instance, for the $A_r^i = 0.475$, the V_r^i range is $0.6 \lesssim V_r^i \lesssim 0.7$, whereas for the $A_r^i = 0.1$ configuration the range is $0.66 \lesssim V_r^i \lesssim 0.84$. Thus the data presented in Figure 47, should be adjusted for V_r^i effects at the lower V_j^{mix} range for the $A_r^i \sim 0.1$ configurations. The effect of V_r^i variation on PNL_p will be illustrated below.

Single Bypass Versus Double Bypass

Figure 70 presents the engine test results of normalized PNL_p and PNL_{90° for measurements in which the $A_r^i = 0.475$ nozzle was operated in the single bypass and double bypass mode. The results are presented versus V_j^{mix} for the

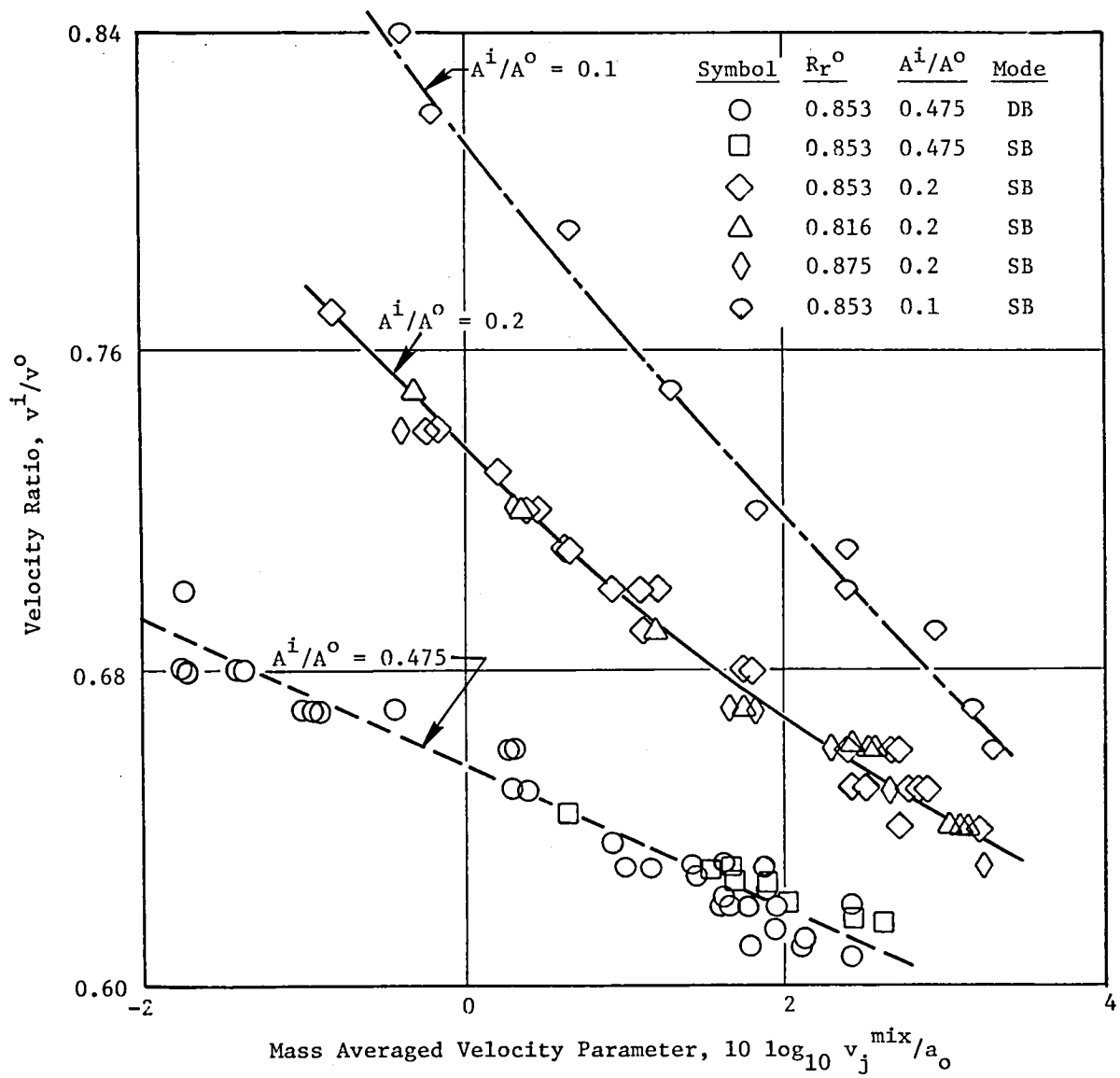


Figure 69. Inner to Outer Stream Velocity Ratio Variation with Specific Thrust for the Coannular Plug Nozzles Tested.

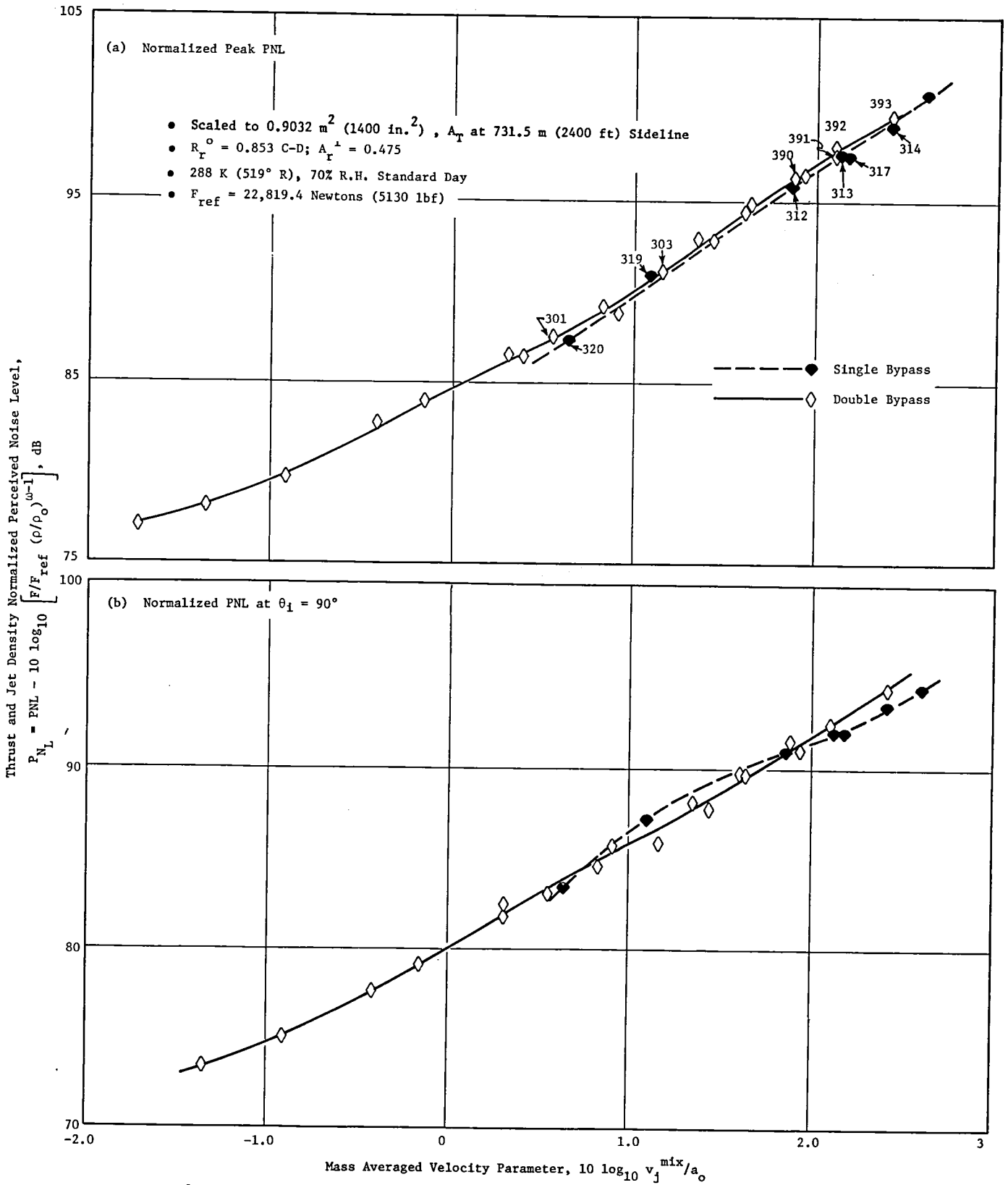


Figure 70. Comparisons of Normalized PNL for Single Bypass and Double Bypass Engine Operation, (a) Normalized Peak PNL, (b) Normalized PNL at $\theta_i = 90^\circ$.

two illustrations. The observation to be made is that very little change in PNL can be observed between single bypass and double bypass operation at a given specific thrust*. This result implies that the engine internal geometry changes basically had little influence on the measured acoustic radiation. As long as the specific thrust and mixed temperatures match between the two systems, the noise will be the same.

Figures 71 and 72 show a typical comparison of the single bypass versus the double bypass for PNL directivity and one-third-octave band SPL at 50, 90 and 120°, respectively. These results illustrate the close similarity in acoustic signatures between the two engine cycle operations.

Velocity Ratio Effects

To illustrate the influence of velocity ratio (V_r^i) on the coannular plug nozzle jet noise, Figure 73 is shown. Plotted on the ordinate is a V_j^{mix} normalized PNLp**, and on the abscissa is velocity ratio. The results indicate that as V_r^i leads toward higher values the coannular suppression is considerably reduced. These test results show that coannular nozzle operation at off-design V_r^i (but at the same specific thrust) could result in a complete loss in suppression capability, and that V_r^i is an important acoustic design parameter. This is, to a large extent, the reason why the coannular results shown on Figure 47 migrate to the noise levels of the conic nozzle at the lower velocity (V_j^{mix}) range. Figure 74 shows what the expected coannular nozzle data, compared with a conic nozzle, would be like if the velocity ratio were kept at $V_r^i \sim 0.64$. This implies that, as long as R_r^o is high and V_r^i is maintained at its optimum value, (~ 0.6), coannular suppression relative to the conic nozzle is expected to be maintained, even at low velocity levels.

*Upon close evaluation, the single bypass data in the higher V_j^{mix} range may be 1/4 PNdB lower than the double bypass cycle operation. A consistent trend could not be determined.

**The results presented here are normalized to a constant V_j^{mix} . This was done by normalizing the thrust and density PNLp normalization [PNLp - 10 log $(F/F_{\text{ref}})\rho/\rho_o)^{\omega-1}$] by $[8.14* 10 \log V_j^{\text{mix}}/a_o + 78.83]$.

This last factor is a normalization factor based on several model scale configurations operated over a range of V_j^{mix} conditions. This normalization also happens to be in accord with the engine data trend at high V_j^{mix} where $V_r^i \sim 0.6$.

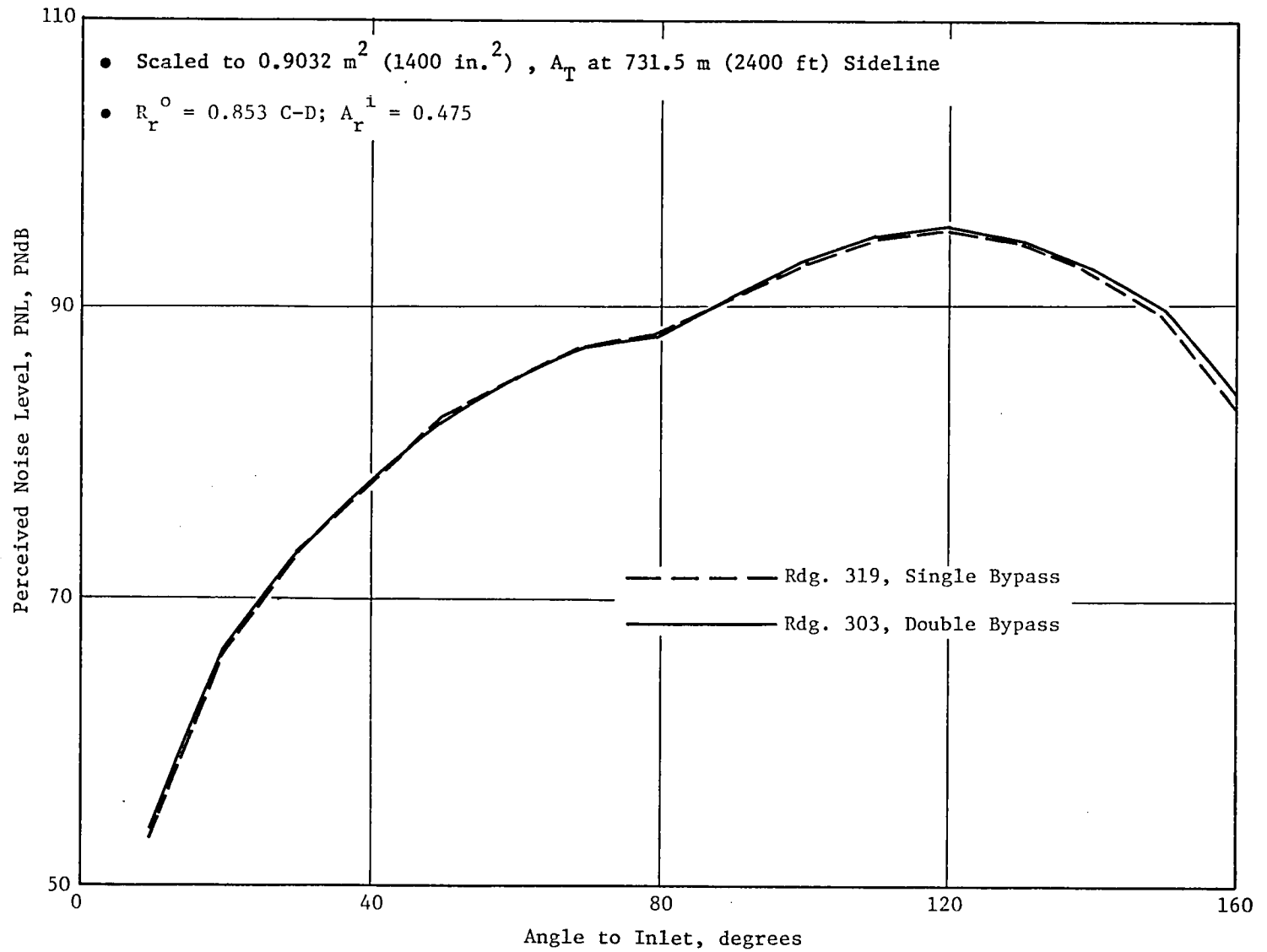


Figure 71. PNL Directivity Comparison Between Single and Double Bypass Engine Operation at the Same Specific Thrust.

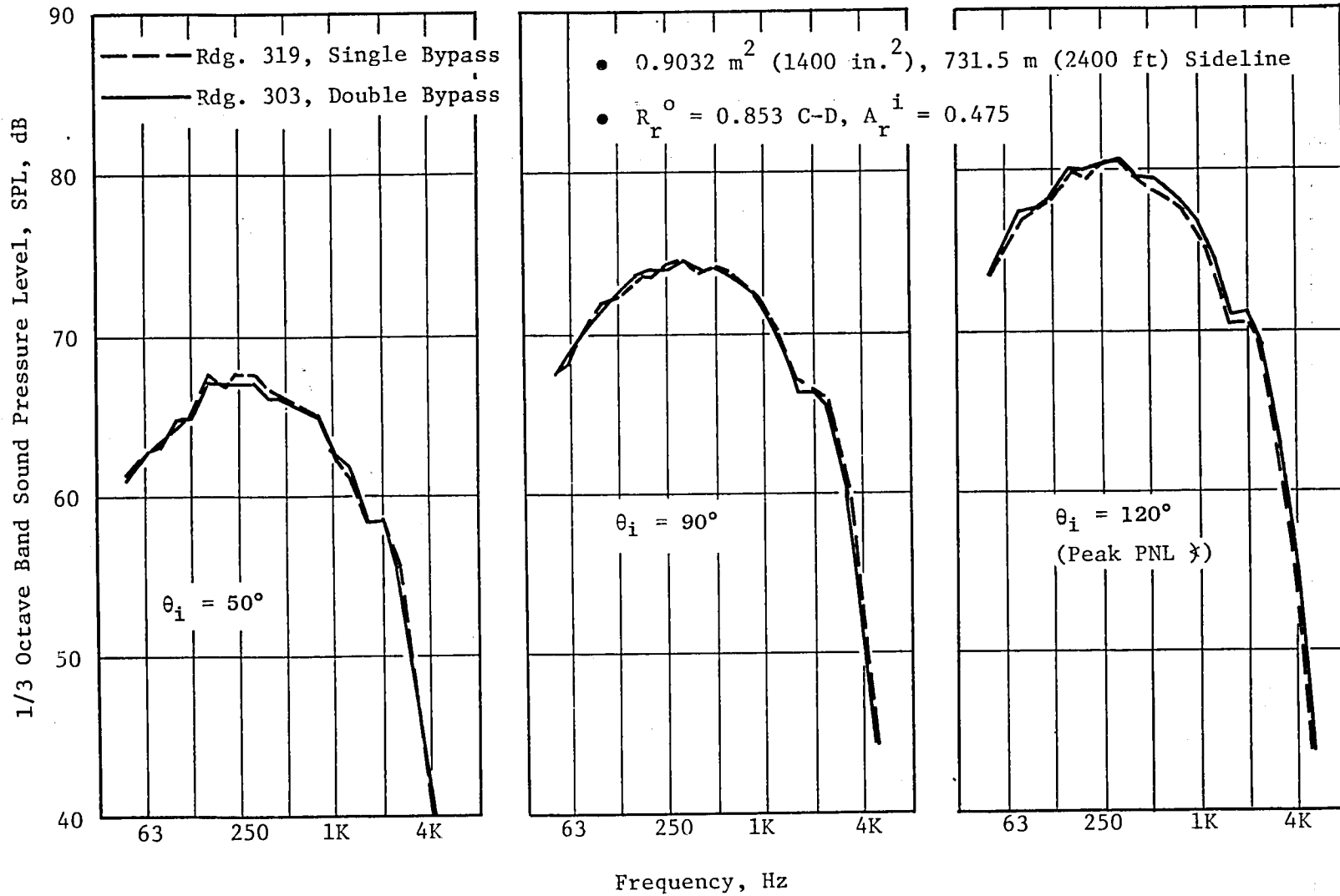


Figure 72. Spectra Comparisons Between Single and Double Bypass Engine Operation at the Same Specific Thrust.

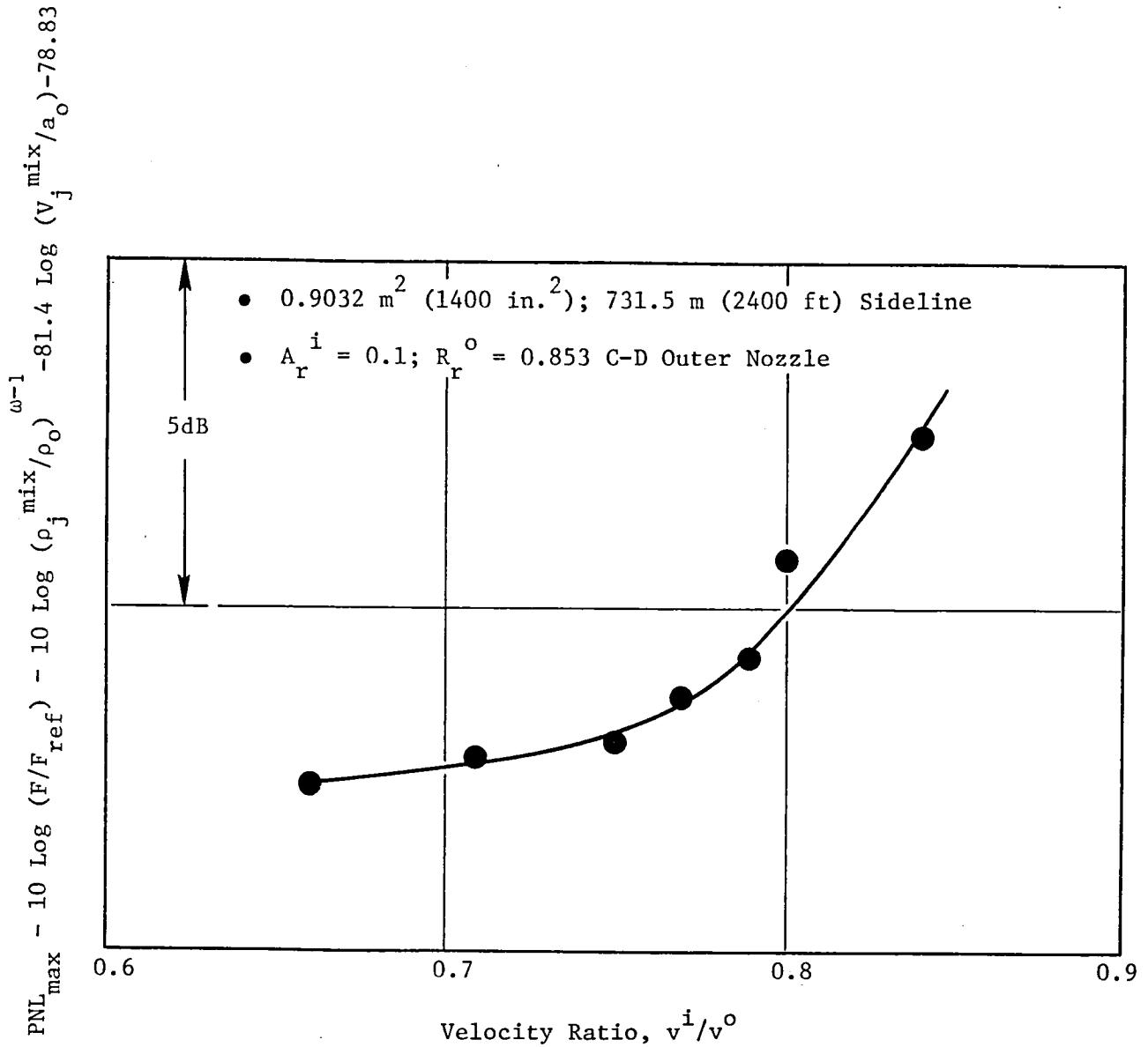


Figure 73. Effect of Velocity Ratio Variation on the Normalized Peak PNL.

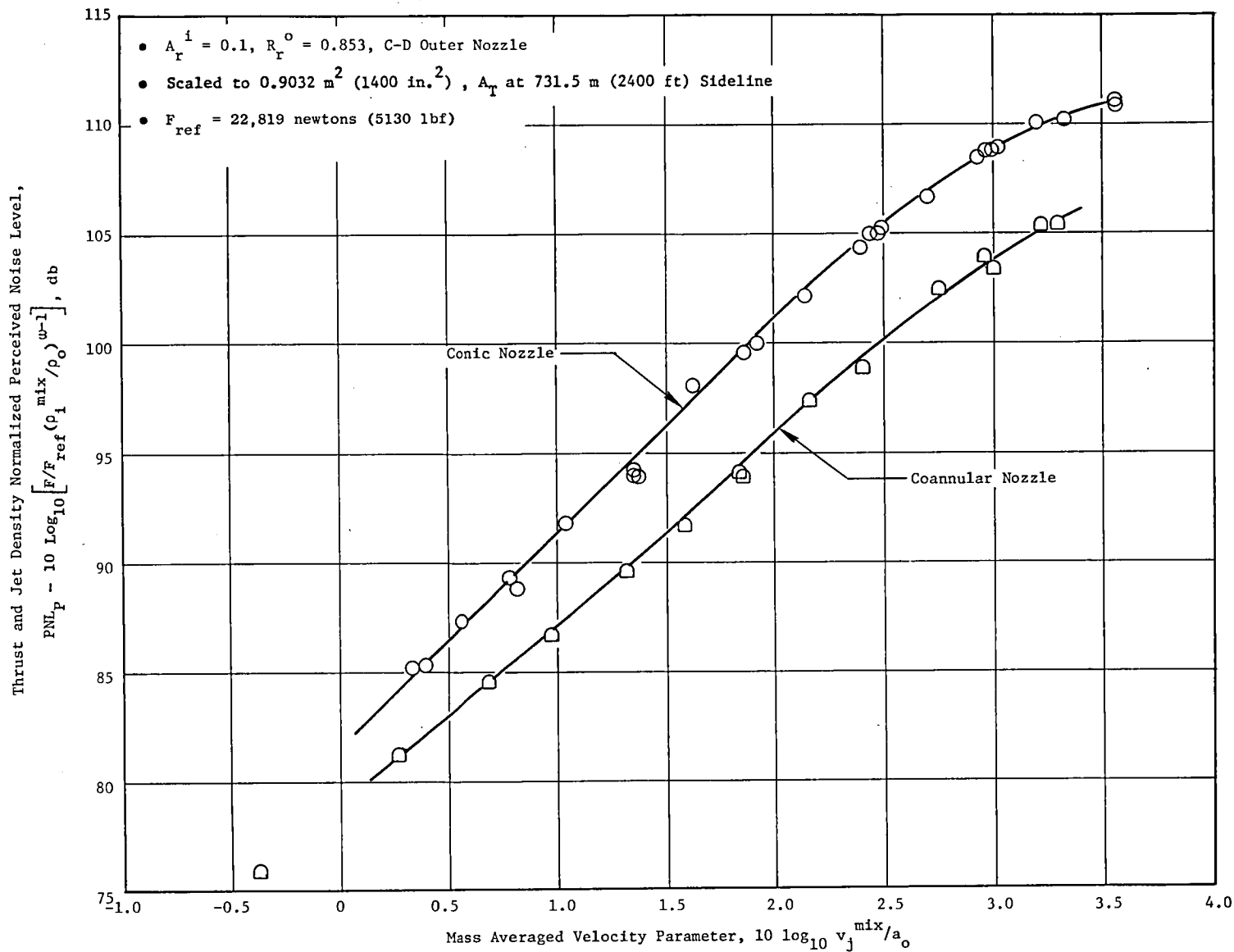


Figure 74. Comparison of the Measured and Predicted Variation of Normalized Peak PNL Versus $10 \text{ Log} (V_j^{mix}/a_0)$.

5.5.2 Acoustic Scaling

One question which is important to answer for this investigation is whether model-scale acoustic measurements can be used to project the results expected from full-size engines. Although this type of jet acoustic scaling has been verified for turbojet types of exhaust nozzle configurations, no such jet nozzle scaling has ever been performed for coannular plug nozzles of the type used in AST/VCE applications. If reasonable acoustic scaling confidence can be obtained from the static measurements of the type taken on this program, then a greater credibility will be established for future screening-type static and simulated-flight-type model scale tests in support of acoustic technology development programs for advanced propulsion systems such as the AST/VCE.

Discussed below are results of acoustic scaling for the conic nozzle and one coannular plug nozzle configuration for which some model scale test results existed (References 10 and 13). For the comparisons used here, the model scale test results, and the YJ101 engine measurements were diametrically scaled to a typical product engine size - $A_{g_{mix}} = 0.9032 \text{ m}^2$ (1400 in.²) at a 731.5 meter (2400 ft) sideline. All comparisons are one engine free-field results.

5.5.2.1 Conic Nozzle Results

Figure 75 compares normalized peak PNL between model-scale conic nozzle data taken in General Electric's anechoic test facility and the YJ101 engine conic nozzle measurements. The engine measurements are designated by open symbols whereas the model scale data are designated by solid symbols. All data have been scaled to a common size and distance. The results show that on a PNL_p basis, good acoustic scaling was obtained.

Typical PNL directivity and spectral comparisons are shown in Figures 76 through 78. The PNL directivity for velocities at 663 m/sec (2177 fps) and 732 m/sec (2403 fps) are shown in Figure 76. The one-third octave band SPL at 50°, 90°, 130° for the corresponding velocities are given in Figures 77 and 78, respectively. As was observed earlier, the scaling comparisons are good. One observation which can be made from the spectral comparisons of Figures 77 and 78 is that the engine conic nozzle data has a screech tone which appears in all angles. This screech, which could easily be eliminated in any product type configuration, may contribute up to 0.75 PNdB of increased noise at the peak angles for the high velocity test points. This shock screech was not observed for the mid-range velocity cases.

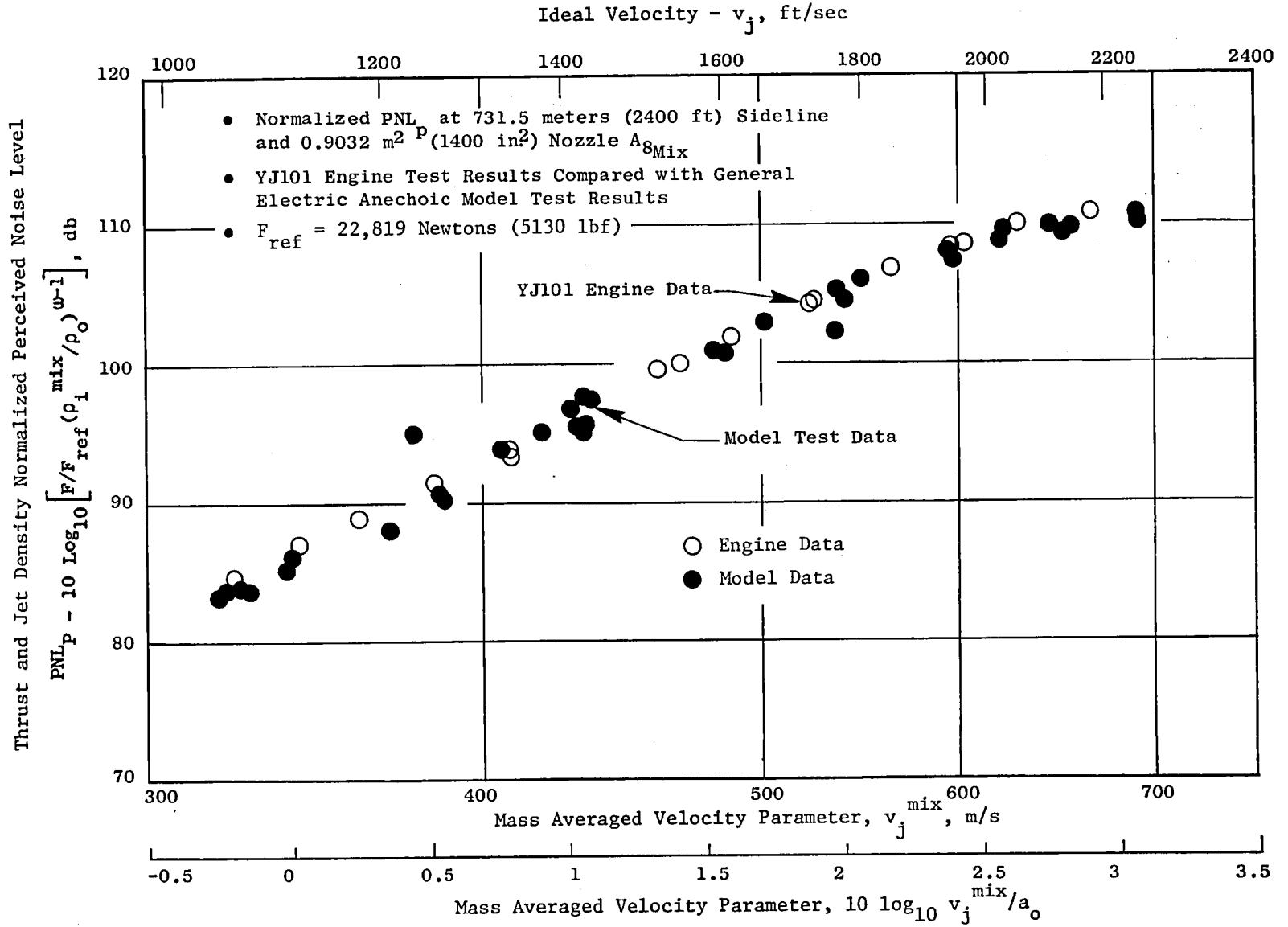


Figure 75. Conic Nozzle Peak PNL Acoustic Scaling Comparison.

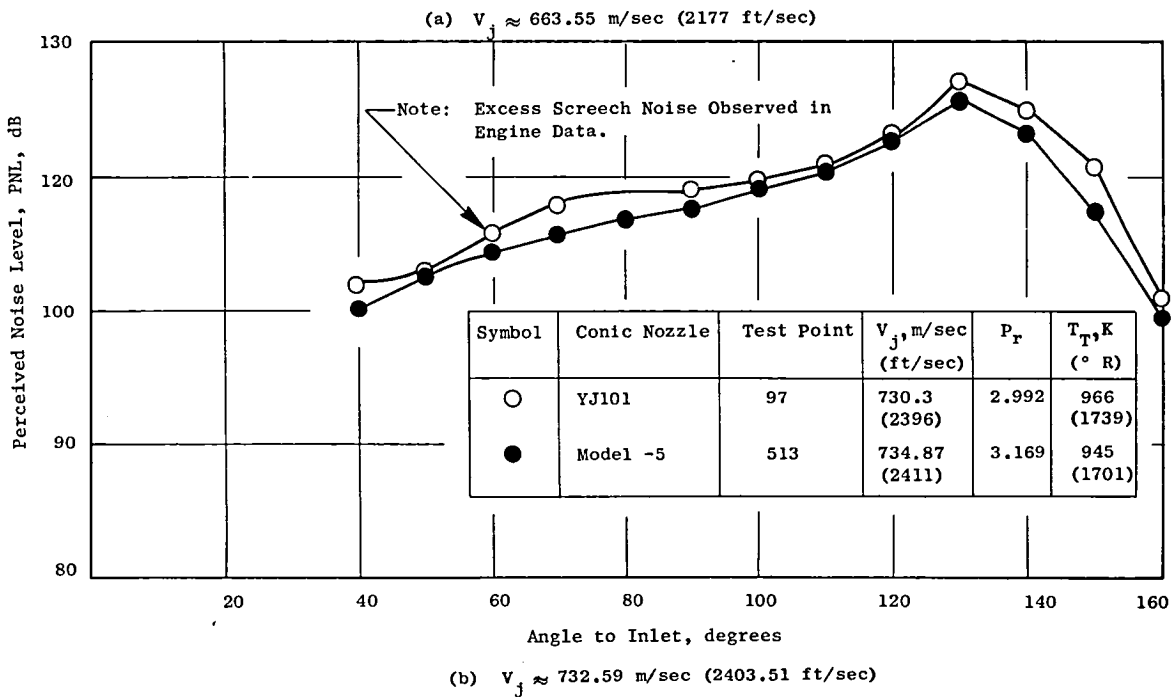
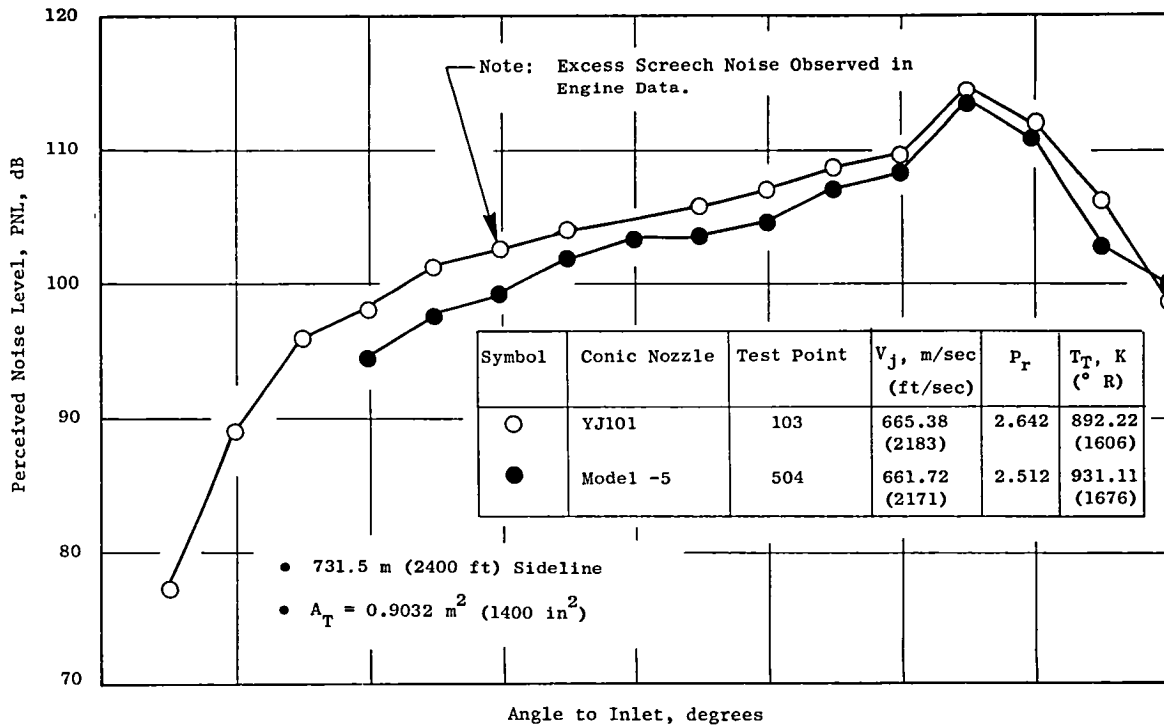


Figure 76. Conic Nozzle YJ101 Engine/Model Scale PNL Directivity Comparison.

Symbol	Conic Nozzle	Test Point	V_j , m/sec (ft/sec)	P_r	T_T , K (° R)
○	YJ101	103	665 (2183)	2.642	892 (1606)
●	Model -5	504	662 (2171)	2.512	931 (1676)

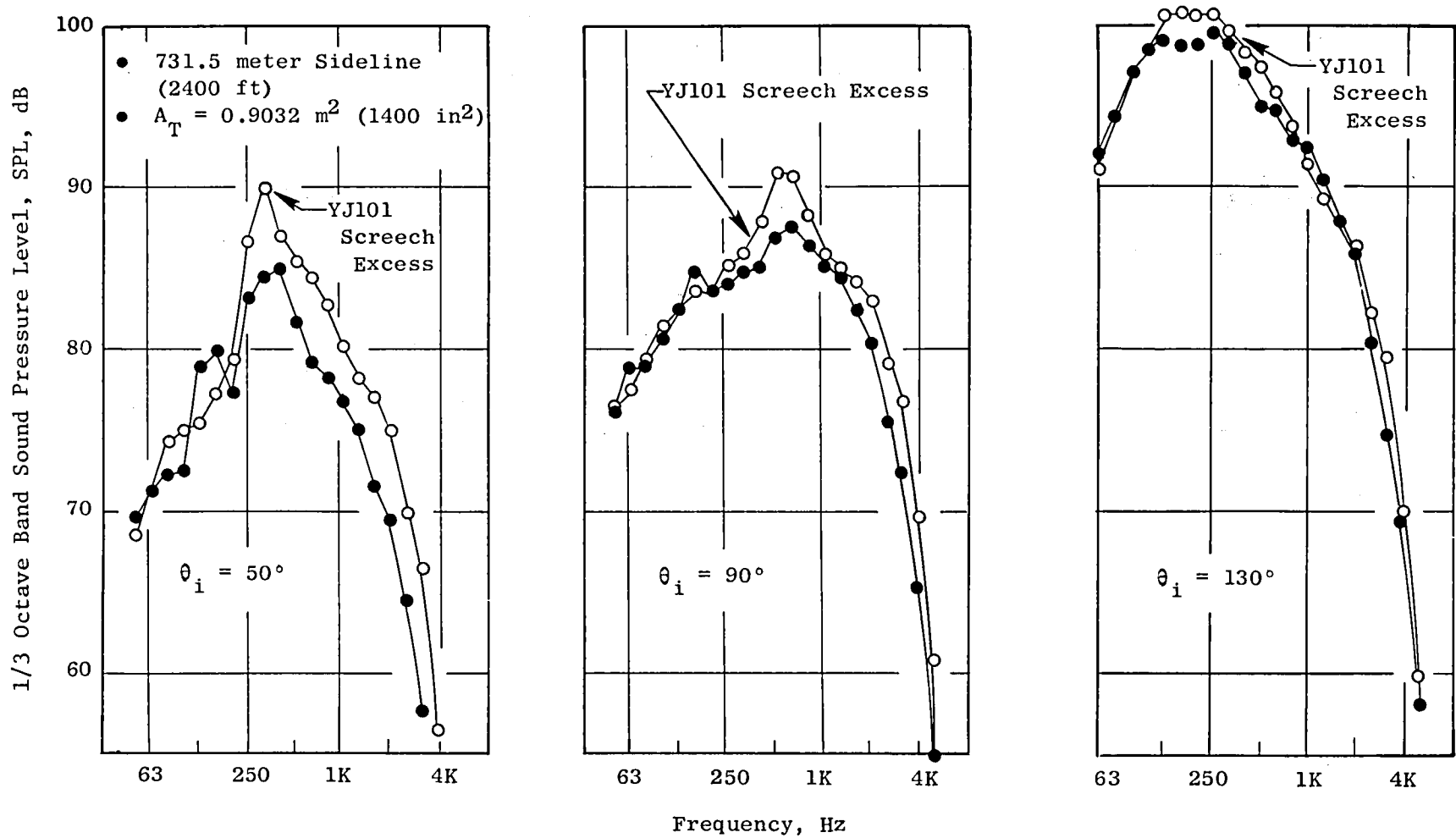


Figure 77. Conic Nozzle YJ101 Engine/Model Scale Spectral Comparisons;
 $V_j = 663.55 \text{ m/sec}$ (2177 ft/sec).

Symbol	Conic Nozzle	Test Point	V_j , m/sec (ft/sec)	P_r	T_T , K (° R)
○	YJ101	97	731 (2396)	2.992	966 (1739)
●	Model -5	513	735 (2411)	3.169	945 (1701)

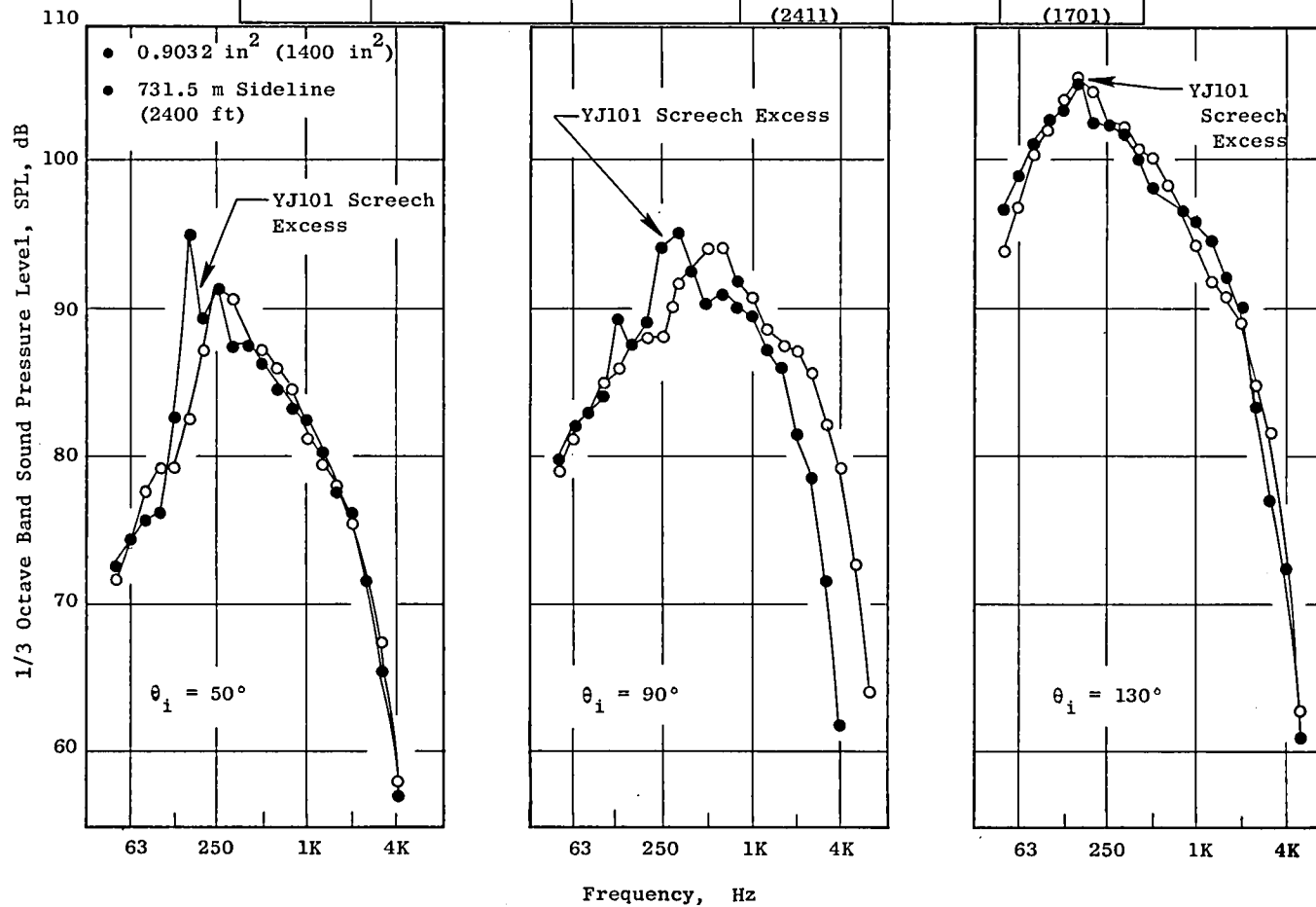


Figure 78. Conic Nozzle YJ101 Engine/Model Scale Spectral Comparisons;
 $V_j = 732.59$ m/sec (2403 ft/sec).

5.5.2.2 Coannular Plug Nozzle Scaling

Figure 79 shows normalized PNL_p versus V_j^{mix} for engine test results and model scale data*. The agreement between the two sets of data, even on the expanded scale used, is observed to be very good. At the lower velocities, where some divergence between model and engine data is observed, the engine was operating at higher velocity ratio (see Figure 69) than the model. The typical velocity ratio for model scale tests is 0.6.

Figure 80 illustrates a PNL directivity for a closely matched cycle point at $V_j^{\text{mix}} \sim 591$ m/sec (1939 fps) between the engine and model coannular data. The model configuration was built to be geometrically similar to the engine test configuration under NASA Contract NAS3-206189. For this same test point one-third octave band SPL comparisons at $\theta_i = 50, 90, 130^\circ$ are shown in Figure 81. In general, these results are found to be good, although the model-scale results appear to be slightly higher than the engine data.

5.5.2.3 Summary of Observations

The results shown above indicate that diametrical scaling of model test results for the conic nozzle and coannular plug nozzle appear to be verified. The conic nozzle engine data appears to have some screech noise at high power settings. The shock screech may increase the PNL_p values up to 0.75 PNdB. At the mid velocity settings this does not occur.

Favorable coannular plug nozzle scaling results were also found. However, it would be desirable to obtain additional scaling data on the configuration constructed under Contract NAS3-20619 at several matched cycle operating conditions. Additional tests would allow better evaluation of the spectral characteristics between model and engine results.

5.5.3 Fan Inlet Noise and Treated Inlet Effectiveness

The YJ101 three stage fan was system-tested in the VCE testbed with an untreated YJ101 inlet so that fan noise characteristics could be identified and absolute noise level could be evaluated relative to other systems. The

*The model scale data for this presentation was taken from static measurements in General Electric's Anechoic Facility for Configuration 7 of Reference 10 (under Contract NAS3-19777). This configuration had $R_r^o = 0.853$, $A_r^i = 0.33$. Although this configuration was not identical to the engine configuration, the main parameters governing coannular jet noise were sufficiently close to be a valid comparison.

Thrust and Jet Density Normalized Peak Perceived Noise Level,

$$PNL_N = PNL_p - 10 \log_{10} \left[\frac{F}{F_{ref}} \left(\frac{\rho_j^{mix}}{\rho_0} \right)^{\omega-1} \right], \text{ dB}$$

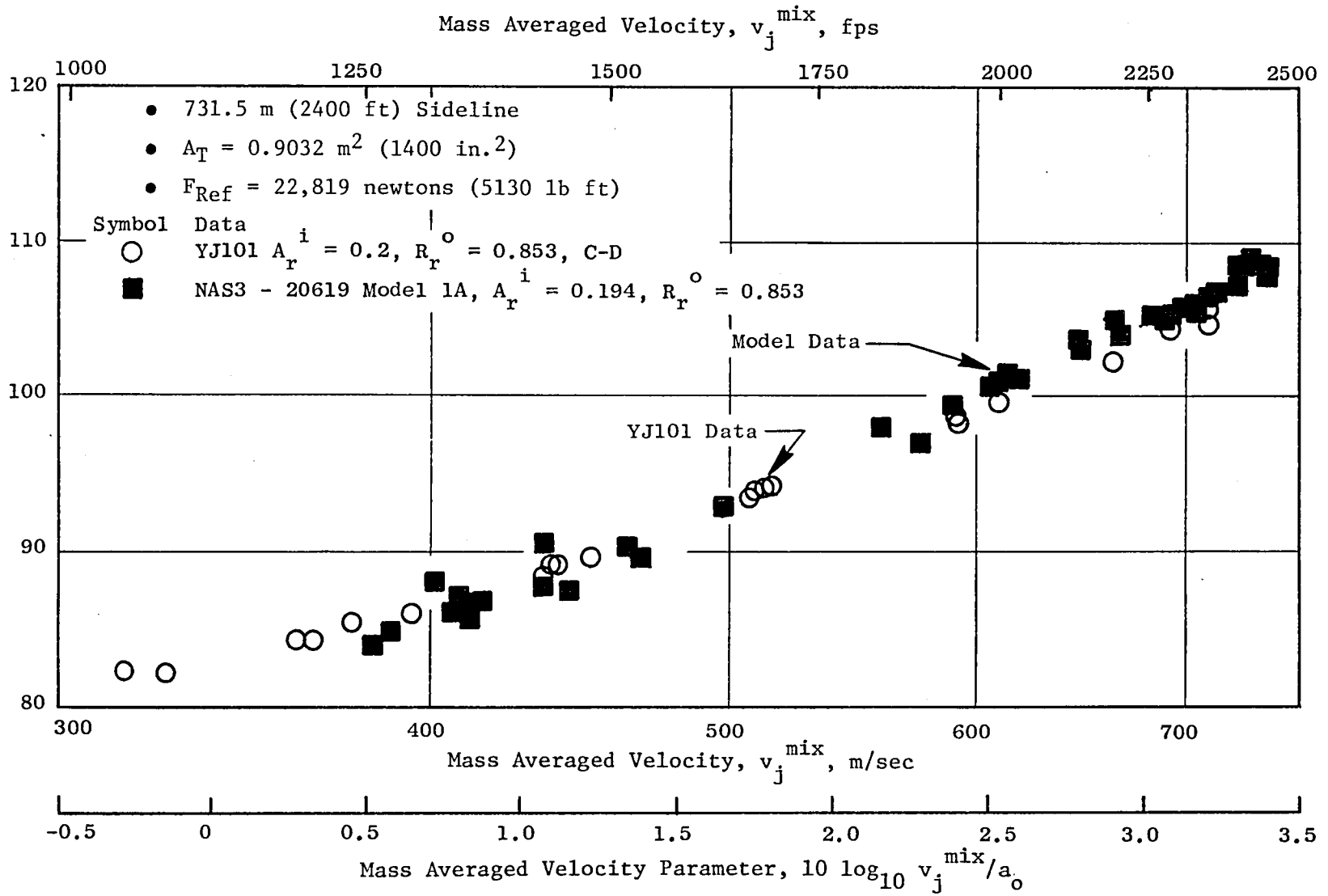


Figure 79. Coannular Plug Nozzle Peak PNL Acoustic Scaling Comparison.

	Rdg.	$N/\sqrt{\theta}, \%$	$V_j^o, \text{ m/sec}$ (ft/sec)	$T_T^{\text{mix}} \text{ K}$ ($^{\circ} \text{ R}$)	P_r^o	$V^i, \text{ m/sec}$ (ft/sec)	$T_T^o, \text{ K}$ ($^{\circ} \text{ R}$)	P_r^i	$V_j^{\text{mix}} \text{ m/sec}$ (ft/sec)	$T_t^{\text{mix}} \text{ K}$ ($^{\circ} \text{ R}$)	P_r^{mix}
○—J101	9326	89.9	640.38 (2101)	957 (1723)	2.278	421 (1382)	440 (793)	2.181	594 (1950)	849 (1528)	2.261
●---Model	113	-	643 (2110)	958 (1724)	2.307	389 (1276)	398 (716)	2.084	588 (1930)	678 (1220)	2.223

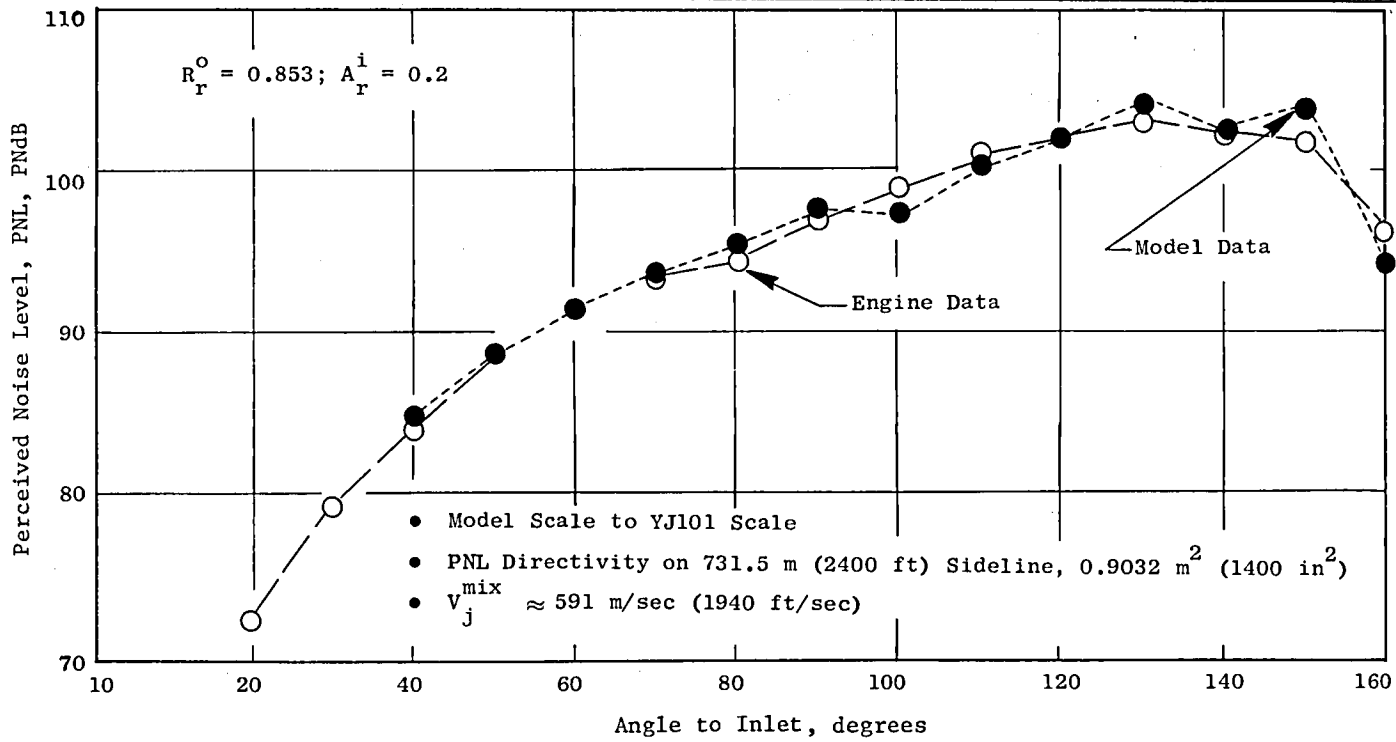


Figure 80. Coannular Plug Nozzle Directivity Acoustic Scaling Comparison.

- 1/3 O.B. SPL Spectra
- Scaled to 0.9032 m^2 (1400 in.²), A_T at 731.5 m (2400 ft) Sideline
- $v_j^{\text{mix}} \approx 591 \text{ m/sec}$ (1940 ft/sec)

	Rd.	$N/\sqrt{\theta}$, %	V_j^o , m/sec (ft/sec)	T_T^o , K (° R)	P_r^o	V^i m/sec (ft/sec)	T_T^i , K (° R)	P_r^i	V_t^{mix} , m/sec (ft/sec)	T_T^{mix} , K (° R)	P_r^{mix}
--□--YJ101	9326	89.9	640 (2101)	957 (1723)	2.278	421 (1382)	440 (793)	2.181	594 (1950)	849 (1528)	2.261
○-Model	113	-	643 (2110)	958 (1724)	2.307	389 (1276)	398 (716)	2.084	588 (1930)	678 (1220)	2.223

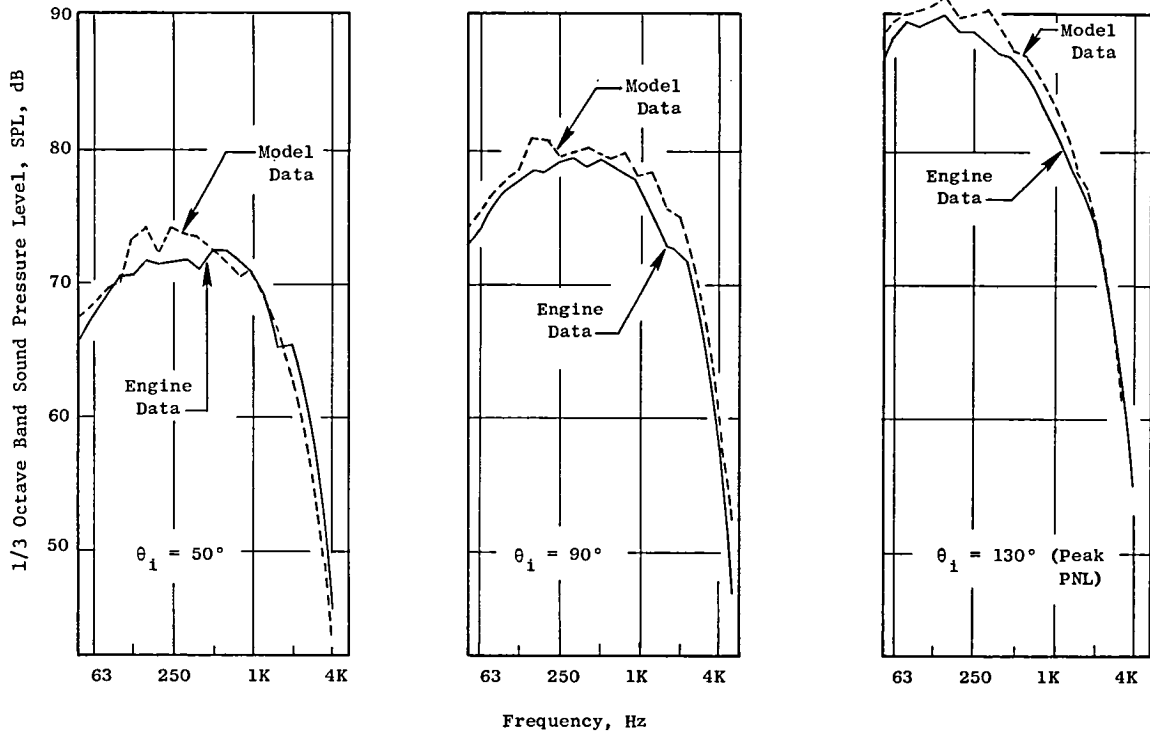


Figure 81. Coannular Plug Nozzle Scaling.

baseline mixed-flow conic nozzle was used in this test with the untreated inlet. An acoustically-treated inlet system was then applied to suppress all forward-radiated fan noise so that exhaust nozzle noise characteristics and suppression effectiveness could be independently evaluated. The following sections discuss the fan inlet noise characteristics and treated inlet effectiveness.

5.5.3.1 Fan Inlet Noise

To establish the level and characteristics of fan inlet noise from the YJ101 VCE testbed engine, test data from the engine configuration using the conical exhaust nozzle (Figure 42) and the YJ101 untreated inlet (Figure 39) were reviewed. Data points were selected, as shown in Table IX to span the normal engine speed, jet velocity and nozzle pressure ratio range of operation. Exhaust nozzle parameters as well as calculated shock screech frequencies for the underexpanded flow cases are also tabulated.

Fan Stages 1 through 3 have 32, 42 and 52 blades, respectively, and are all low pressure turbine driven. Therefore, blade passing frequencies (f_1 , f_2 , f_3) and difference tones ($f_2 - f_1$, etc.) are all associated with fan physical speed. High-pressure and low-pressure turbine stages have 82 and 58 blades, respectively, high pressure driving the core compressor and low pressure driving the fan.

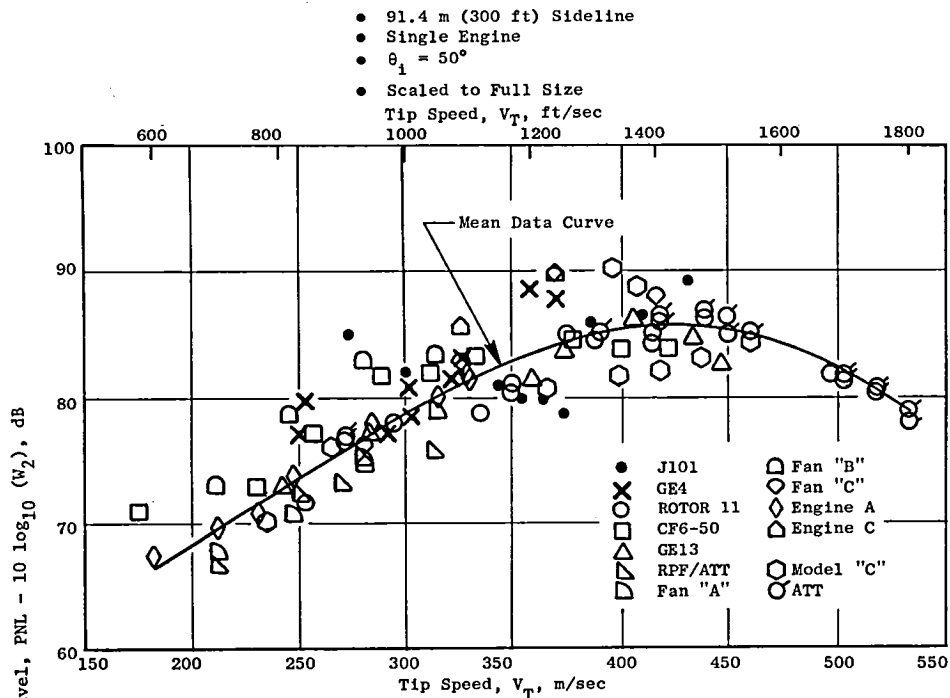
As an initial approximation to which forward quadrant noise levels can be compared, Figure 82(a) shows a correlation of fan inlet noise with fan tip speed at a 91.44 m (300 ft) sideline and 50° to the inlet. Various data sources are presented, including a J101 scale model fan vehicle of similar geometry to that of the YJ101 engine fan. The J101 fan vehicle was previously tested on the GE-Peebles Test Operation's component rig, results being reported in Reference 8.

For this correlation all noise sources other than fan were removed and, where possible, fan exhaust noise contributions were also removed. The data are unsuppressed and have no corrections for number of fan stages. A mean curve is presented through the data and transferred to Figure 82(b). The YJ101 $\theta_i = 50^\circ$ measurements, scaled to 0.9032 m^2 (1400 in.^2) exhaust nozzle size and extrapolated to the 91.44 m (300 ft) sideline, are plotted on this graph. These normalized PNL levels are 2 to 12.5 PNdB above the mean data curve for the 70 to 93.9% speed range and indicate that forward quadrant noise levels are influenced by other than pure fan noise. To identify that portion of the spectrum attributable to the fan, $\theta_i = 50^\circ$ spectra for the selected five points are plotted in Figure 83. On this figure, the spectral locations where blade passing frequency tones, difference tones and shock tones may occur, are indicated.

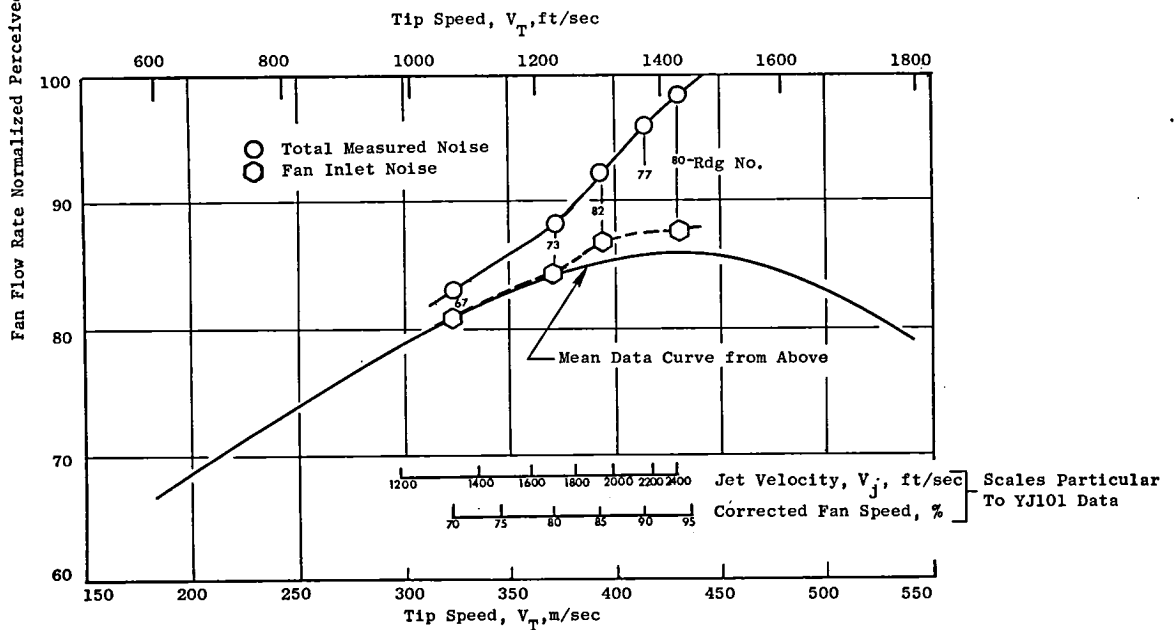
Several methods were used to identify the jet mixing and shock noise spectra such that their contribution to the total measured noise could be removed and the remaining fan noise spectrum deduced. The most fruitful method was through the use of treated versus untreated inlet results of which are

Table IX. Fan Inlet Noise Data Points.

Rdg. No.	Corr. Fan Speed, %	Fan Phys. Speed, rpm	Core Phys. Speed, rpm	Fan				Exhaust Nozzle			
				Stage 1 Tip Spd. m/sec (ft/sec)	f1, Hz	f2, Hz	f2-f1, Hz	Vel, m/sec (ft/sec)	T _T , K (° R)	P _T /P _O	f ^s screech, Hz
67	70.1	9523	12931	326.1 (1070)	4934	6477	1543	404.2 (1326)	669 (1204)	1.569	
73	80.4	10602	13700	373.6 (1226)	5654	7421	1767	519.7 (1705)	759 (1367)	1.963	
82	86.0	11276	14280	397.5 (1304)	6013	7893	1880	604.4 (1983)	832 (1497)	2.340	818
77	90.5	11915	14853	420.0 (1378)	6354	8340	1986	675.6 (2210)	904 (1628)	2.680	665
80	93.9	12356	15286	435.6 (1429)	6589	8649	2060	742.5 (2436)	978 (1762)	3.070	586



(a) Standardized Fan Inlet Turbomachinery Noise Prediction Curve.



(b) YJ101 Data Comparison to Standardized Prediction Curve.

Figure 82. Fan Inlet Turbomachinery Noise, YJ101 Data Relative to Previous Sources.

- 60.9 m (200 ft) Sideline
- Single Engine
- Scaled to Full Size; 0.9032 m² (1400 in.²) Exhaust Nozzle

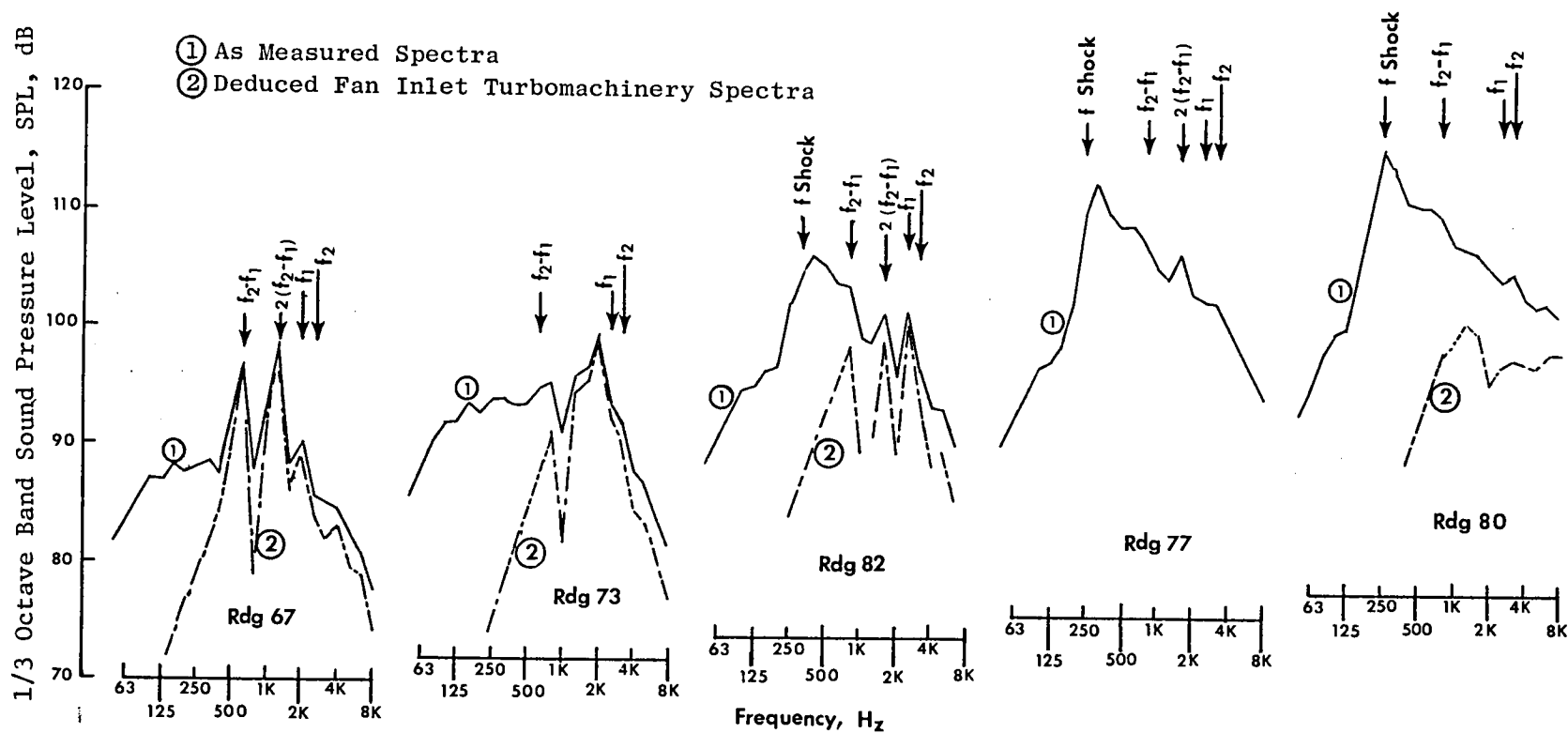


Figure 83. Spectra at $\theta_1 = 50^\circ$ for Fan Inlet Turbomachinery Noise Identification.

shown in the following section (i.e., Section 5.5.3-2). It was assumed that the treated inlet was effective in eliminating essentially all inlet radiated noise at $\theta_i = 50^\circ$ and that only jet mixing and shock noise remained. Spectral comparisons were made for the untreated YJ101 versus the treated J79 inlet/conical exhaust nozzle configurations (Figure 92 in Section 5.5.3-2) for the five data points above. In all cases, the low frequency jet noise spectra are near duplicate traces, indicating a high confidence factor in this data-to-data comparison method. For mid-to-high frequencies, the treated inlet data are normally under the YJ101 untreated inlet data. However, as increasing the exhaust nozzle pressure ratio and jet velocity raises the shock and jet mixing noise contribution to the total noise to values equal to or higher than the fan noise, the impact of fan inlet noise is lowered and the two spectra sets are nearly identical. For Reading 77, the spectra for the treated and untreated inlet cases are so similar that the fan spectrum cannot be deduced. For Reading 80, the levels are sufficiently dissimilar that a fan spectrum can be deduced but confidence in accuracy of the level is marginal. Nonetheless, these comparisons were used and the fan inlet turbomachinery spectra are included on Figure 83. Normalized PNL values for these spectra, adjusted to a 91.44 m (300 ft) sideline, are included on Figure 82(b). They now are in very good agreement with the correlated fan inlet turbomachinery noise prediction curve and fall well within the scatter band of Figure 82(a).

For a more in-depth look at the YJ101 fan noise characteristics, Figure 84 through 87 present 40Hz narrow band traces from the engine centerline height microphone at $\theta_i = 30^\circ, 50^\circ, 90^\circ$ and 140° for Reading 67 at 70.1% speed. The figures are labeled as to the apparent sources of distinct tones. The following are observed:

- Inlet angles, 30° and 50° , are highly contaminated with fan associated tones; 90° and 140° have a very slight hint of tones but with no major influence on 1/3 octave band levels.
- At 30° and 50° , fundamental tones for all three stages, up through the third harmonic ($4f_1$) of Stage 1 are seen and the first harmonic ($2f_2$) of Stage 2 is slightly noticeable. However, of greatest influence perhaps, is the Stage 2 to 1 difference tone ($f_2 - f_1$) and its harmonics. Its level is significant relative to the fundamental tones and their harmonics, up through the 3rd harmonic, $[4(f_2 - f_1)]$ at 30° , and up through the 5th harmonic, $[6(f_2 - f_1)]$ at 50° . The difference tone could also be associated with Stages 3 to 2 as the blading number difference is 10 between Stages 1 to 2 as well as 2 to 3.

5.5.3.2 Treated Inlet Effectiveness

The J79 treated inlet system, described in Section 5.4 and shown in Figures 39, 40 and 41, was used to suppress, as well as possible, the fan inlet forward-radiated turbomachinery noise. Without inlet noise, acoustic evaluation of the effectiveness of the exhaust nozzle configurations could be made,

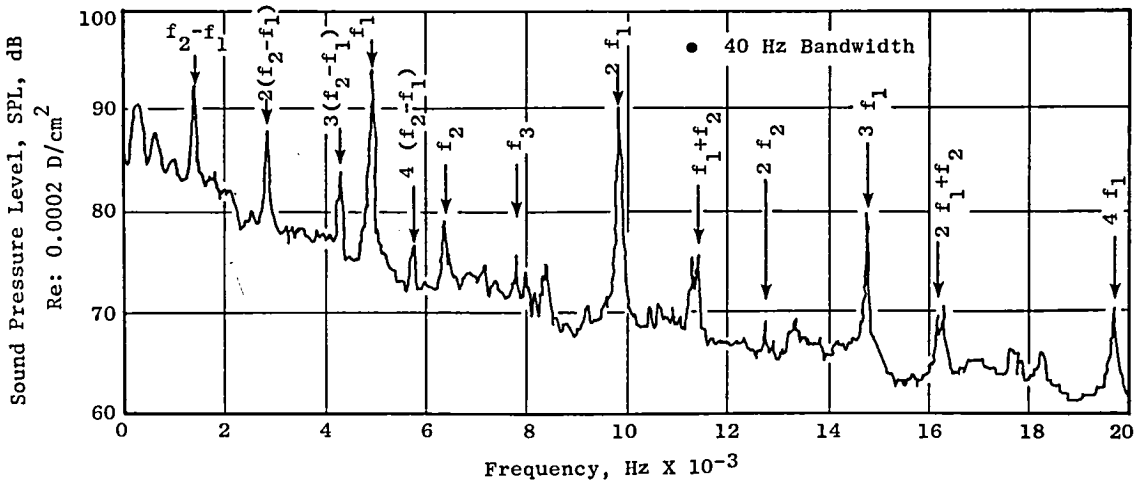


Figure 84. YJ101 Narrowband Spectrum for Rdg 67 at $\theta_i = 30^\circ$.

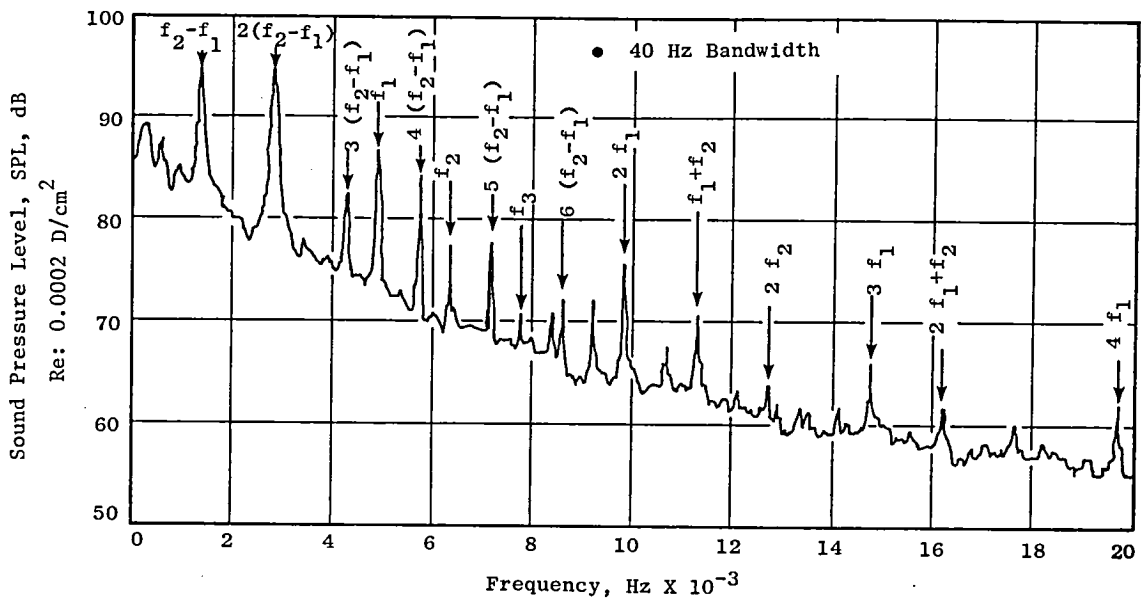


Figure 85. YJ101 Narrowband Spectrum for Rdg 67 at $\theta_i = 50^\circ$.

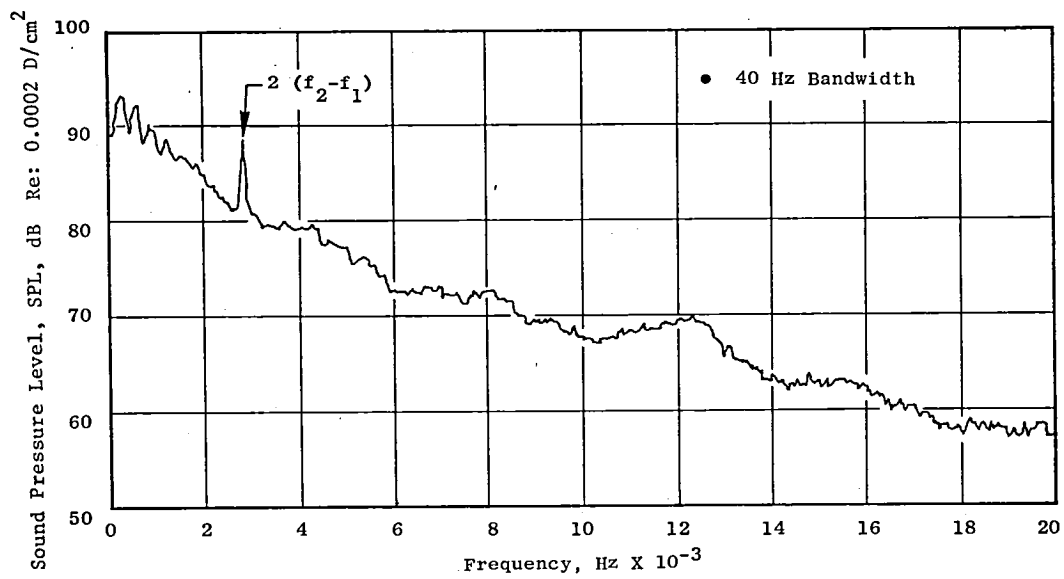


Figure 86. YJ101 Narrowband Spectrum for Rdg 67 at $\theta_i = 90^\circ$.

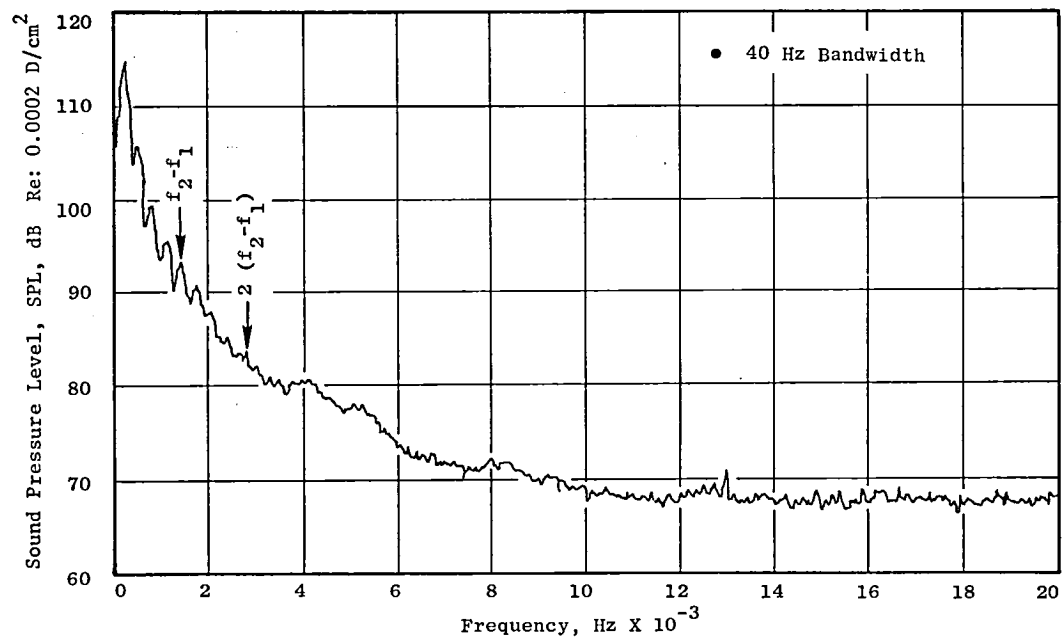


Figure 87. YJ101 Narrowband Spectrum for Rdg 67 at $\theta_i = 140^\circ$.

based solely on jet mixing and shock noise mitigation. The effectiveness of the inlet can be gauged through comparisons of the J79 treated versus YJ101 untreated inlet configurations, each using the conical exhaust nozzle and tested over the same engine speed range. For all other exhaust nozzle configurations, the J79 treated inlet was used.

On a PNL basis, for the 30.48 m (100 ft) measuring arc and 0.122m² (190 in.²) engine size, Figure 88 shows that the treated inlet was very effective in inlet noise reduction. Data are presented at $\theta_i = 20^\circ, 30^\circ, 40^\circ$ and 50° for the full velocity range of test and indicate:

- At $\theta_i = 20^\circ$, total noise levels (untreated) are 13 PNdB higher than jet alone noise levels (treated) at low velocity, and at high velocity the fan noise still raised the total noise by ≈ 3 PNdB.
- Contribution of untreated inlet fan noise to overall PNL normally decreased as inlet angle increased and as jet velocity/engine speed increased. In particular, at 40° and 50° , the total noise PNL levels above ≈ 609.6 m/sec (2000 fps) were uninfluenced by fan noise. However, it should be considered that at high jet velocity the jet shock noise may predominate the spectra and control PNL influence. Higher frequency portions of the spectra may still be influenced by fan inlet noise and can still be altered by the inlet suppressor but now show appreciable influence on PNL reduction.

For a broader look at treated inlet influence on directivity, Figures 89 and 90 present OASPL and PNL as a function of θ_i from 20° through 160° . Specific case comparisons of treated/untreated inlets are made at nominal fan speeds of 65, 70, 75, 80, 85 and 90%. The following are observed:

- PNL and OASPL changes occur similarly in the same speed ranges and angular locations. PNL changes between inlets in the forward quadrant, however, are normally somewhat greater than OASPL. This indicates the inlet is affecting mid-to-high frequency portions of the spectra, thus more heavily influencing PNL.
- On an OASPL basis, the treated inlet impacts 60° and further forward angles for 65 through 80% speeds. For angles more toward the exhaust and for higher speeds, the jet mixing and shock noise seem to control the OASPL.
- On a PNL basis, results are similar to OASPL, except that small changes at 70° and forward are also seen for PNL at higher speeds up through 90%.
- In all of these conical nozzle cases, the variance in the aft quadrant peak noise level is sufficiently small with inlet treatment to preclude any influence from forward radiated fan noise.

Further plots of 1/3 OBSPL spectra at $\theta_i = 30^\circ, 50^\circ, 90^\circ$ and 140° for the five speed points tabulated in Table IX are included as Figures 91

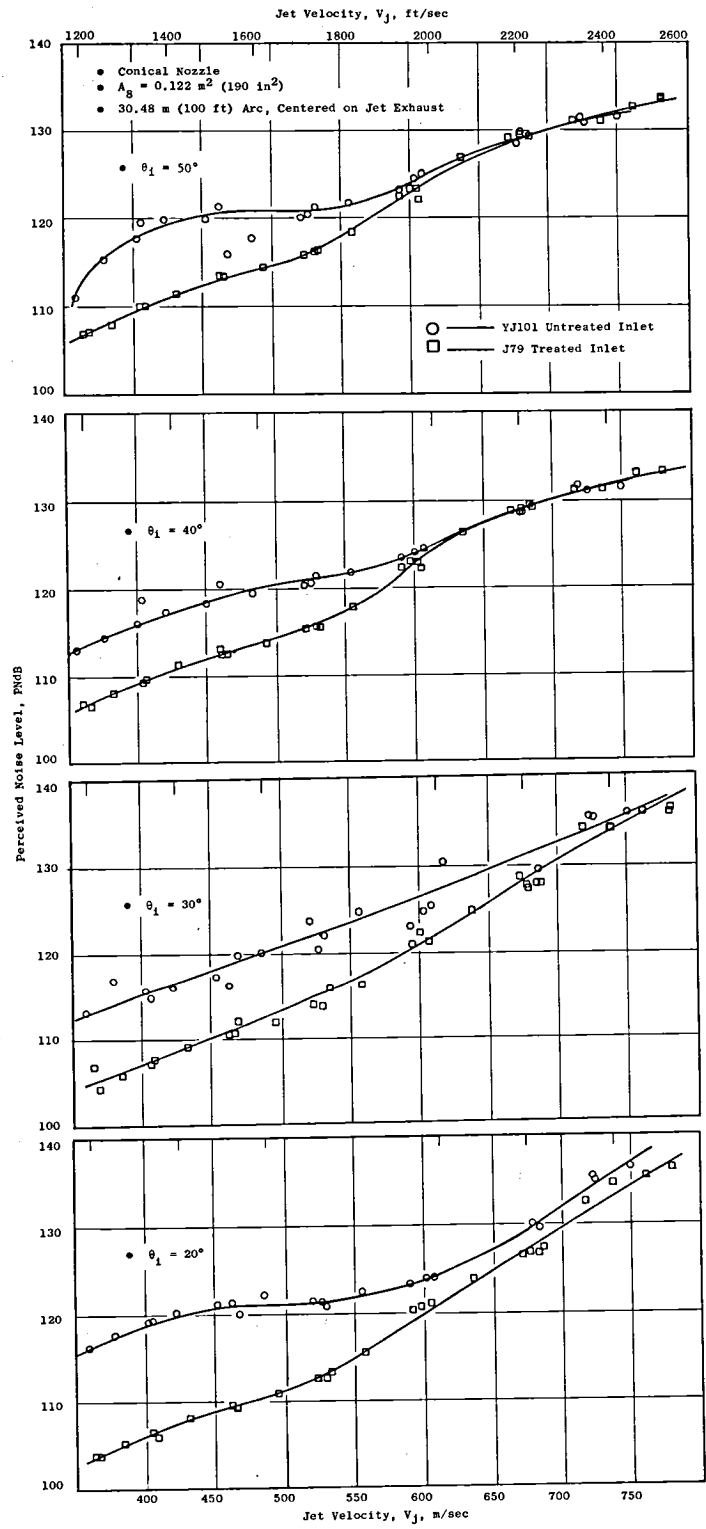


Figure 88. Effectiveness of Treated Inlet on Perceived Noise Level Reduction.

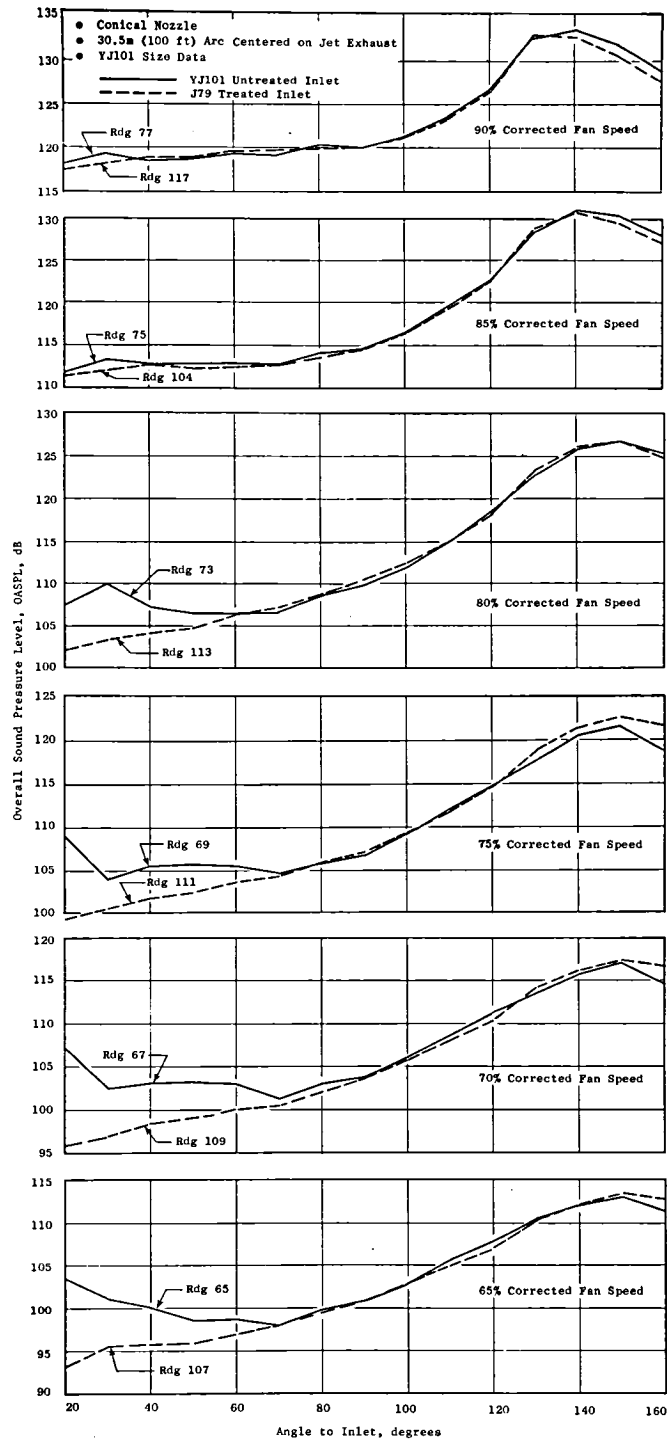


Figure 89. Comparison of Treated to Untreated Inlet, OASPL Directivity, 65-90 Percent Corrected Fan Speed.

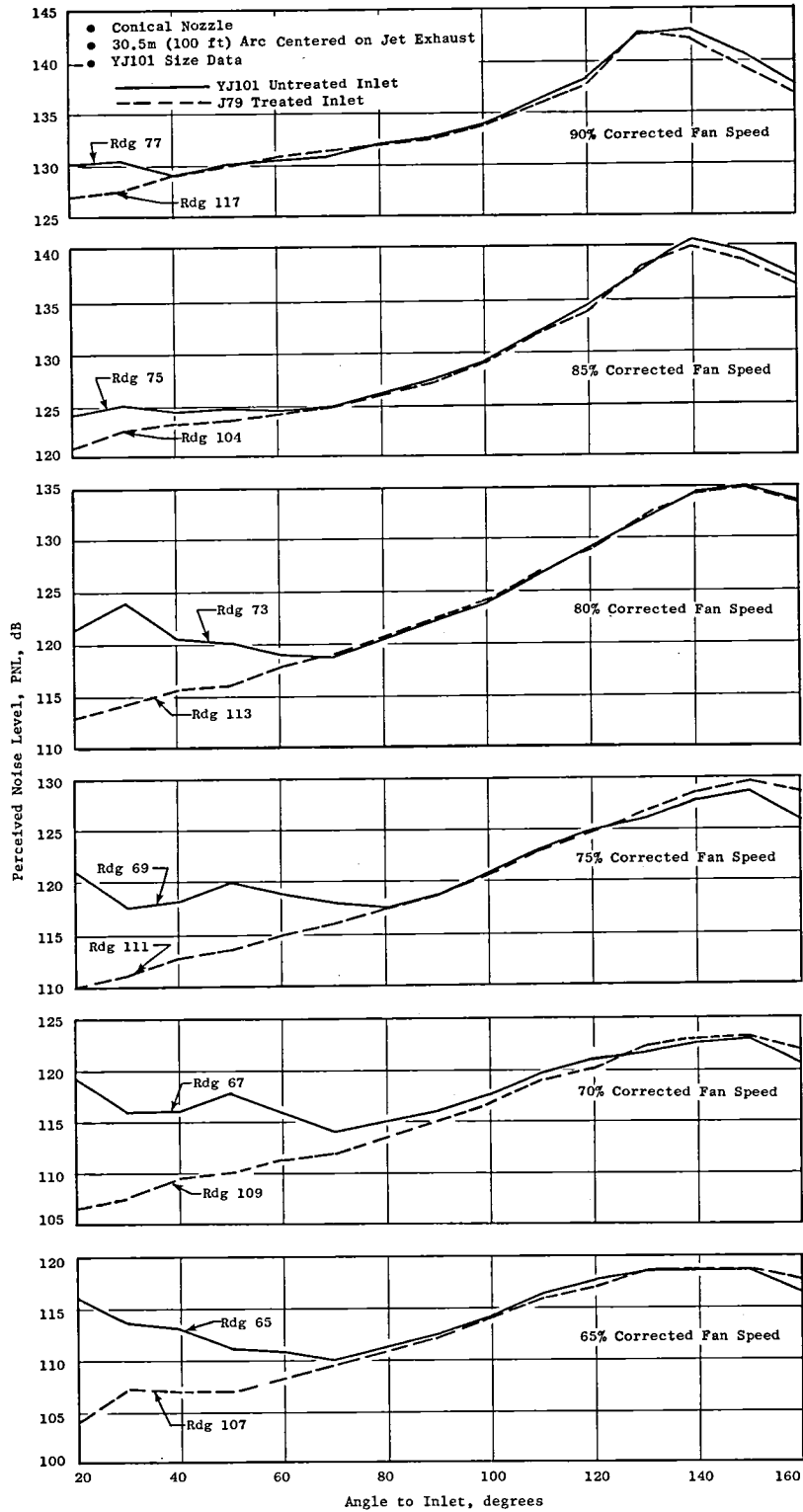


Figure 90. Comparison of Treated to Untreated Inlet, PNL Directivity, 65-90 Percent Corrected Fan Speed.

through 94. Treated versus untreated inlet spectra are included for these 30.48 m (100 ft) arc J101 size comparisons. The following observations are made:

- At $\theta_i = 30^\circ$, the mid-to-high frequency parts of the spectra at all speed points are heavily influenced by fan inlet turbomachinery noise for the untreated inlet cases. The fan noise controls OASPL and PNL for the 70 and 80% speed cases: contributes only mildly to OASPL and moderately to PNL at the 86 to 90% speed points as shock noise is contributing heavily and even overrides jet mixing noise; and then contributes nothing to either PNL or OASPL at the 93.9% speed as shock noise strongly controls the spectra while operating at this highly underexpanded nozzle condition. The treated inlet is very effective in mitigating the 30° fan inlet noise including the blade passing frequency and difference tones which predominate at lower speeds.
- At $\theta_i = 50^\circ$, fan noise contributes to the total untreated inlet spectra in the same frequencies as at $\theta_i = 30^\circ$, but not as strongly. The inlet still effectively reduces all fan inlet radiated noise. At 90.5% speed, the first harmonic of the difference tone (4 kHz band) was still noticeable above the jet mixing and shock noise and is effectively controlled by the treated inlet. At 93.9% speed, high frequency broadband noise is slightly lower for the treated inlet case, although differences may be due to jet noise variance. For both treated and untreated inlet cases, a slight increase in the 8 kHz band, in which the second stage blade passing frequency occurs, is observed.
- At $\theta_i = 90^\circ$ and 140° , little variance is seen between treated/untreated inlet spectral sets at any speed. The small differences that are seen, particularly at the two lower speed settings, could be inlet radiated turbomachinery noise propagated to the aft quadrant and effectively reduced by the treated inlet. The higher speed spectral variances between treated and untreated inlets are probably data scatter. Of significance, perhaps, at the higher speeds are the spectral shapes and the small data peaks in the 4 to 8 kHz bands. The levels do not drop off as fast as should be expected from conventional jet mixing noise sources and the spikes in the data are of similar level for both treated and untreated inlets. This suggests that the source is other than fan inlet aft radiated noise, as the treated inlet would have controlled the levels, reducing the high-frequency hump to a jet spectrum roll-off characteristic. The source could, therefore, be aft propagated, through the engine, or casing-radiated turbomachinery noise. This will be discussed further in Section 5.5.6.

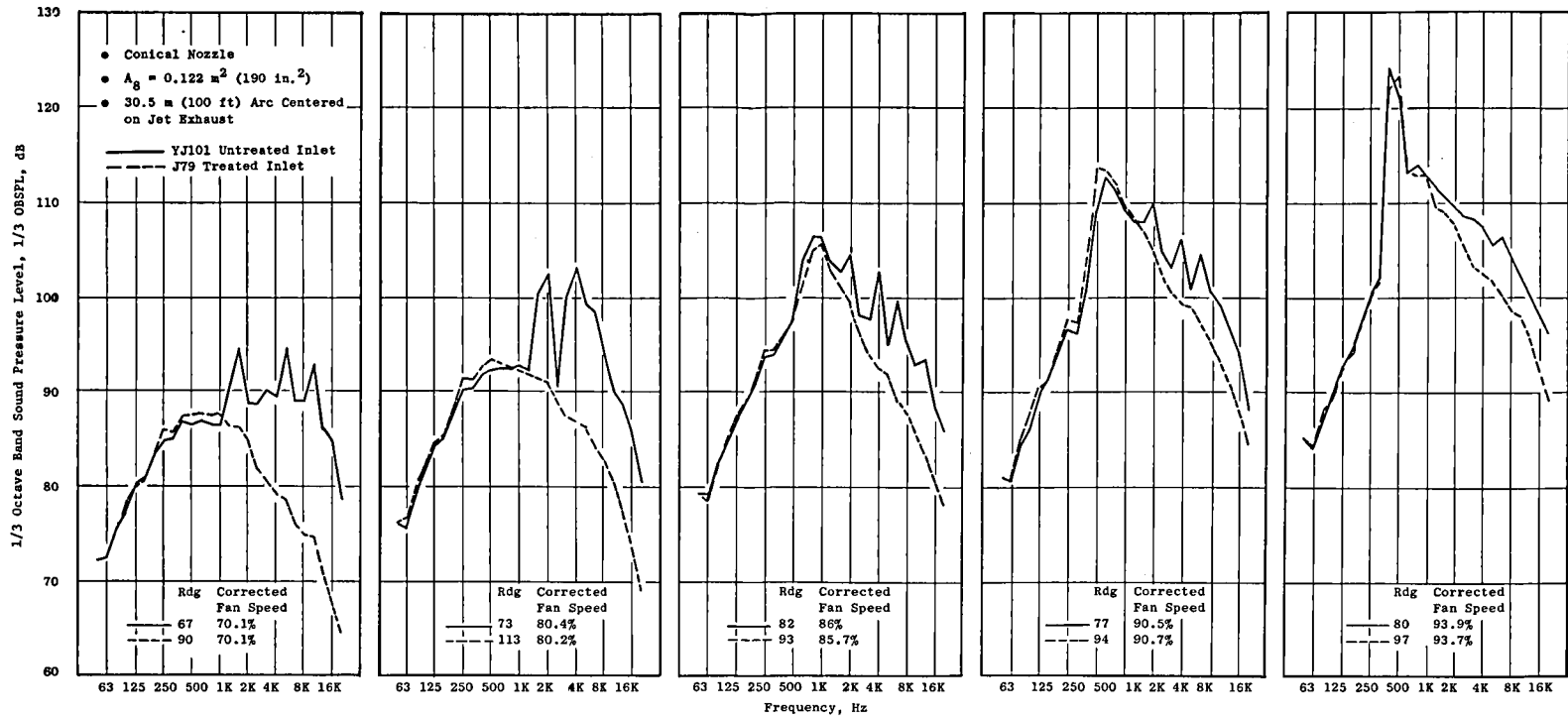


Figure 91. Spectral Comparison of Treated Versus Untreated Inlet at $\theta_i = 30^\circ$.

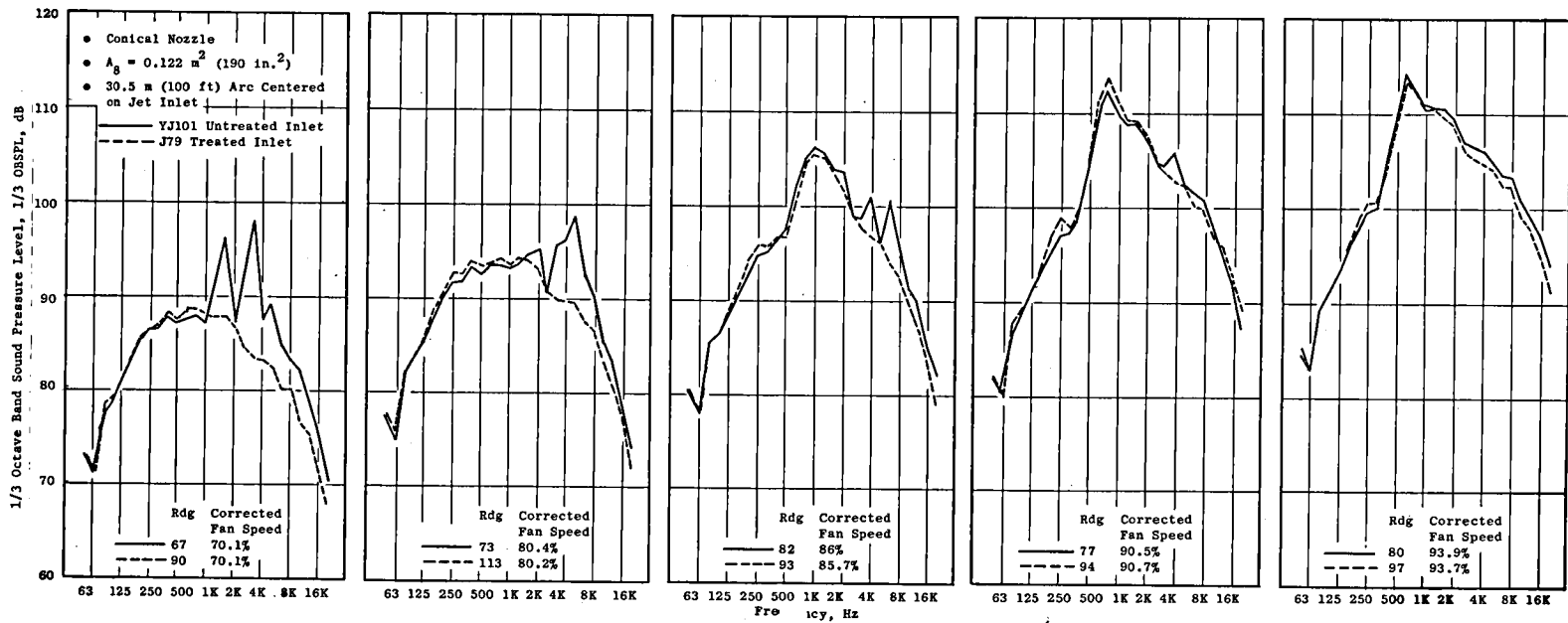


Figure 92. Spectral Comparison of Treated Versus Untreated Inlet at $\theta_i = 50^\circ$.

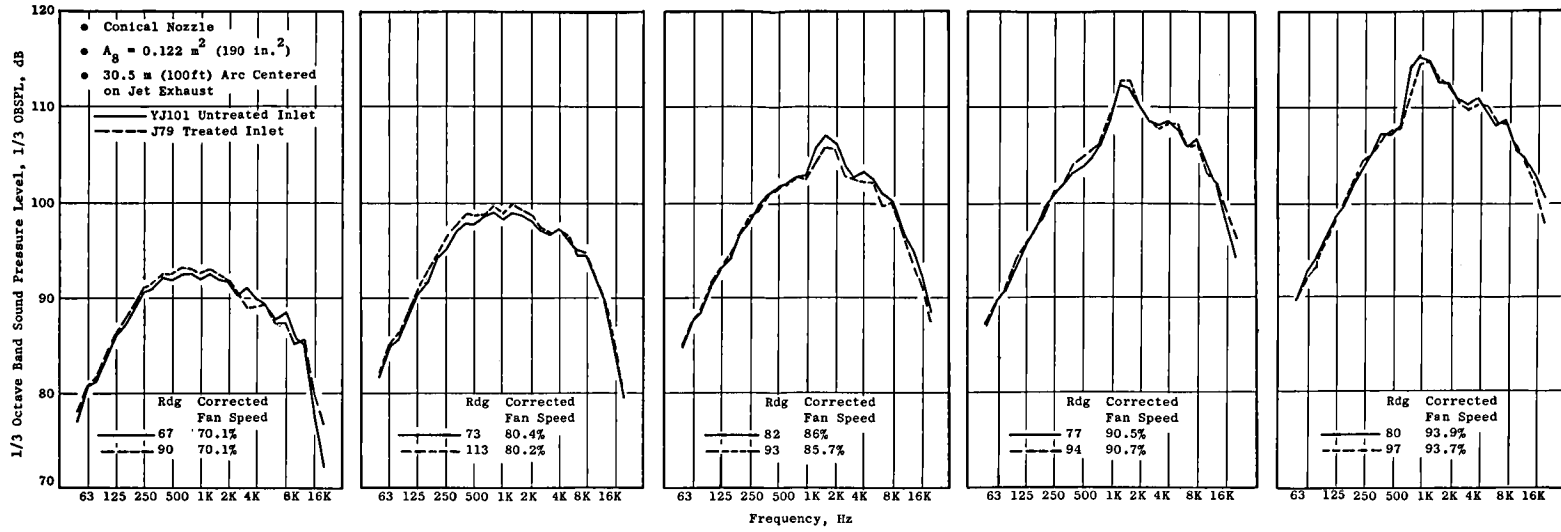


Figure 93. Spectral Comparison of Treated Versus Untreated Inlet at $\theta_i = 90^\circ$.

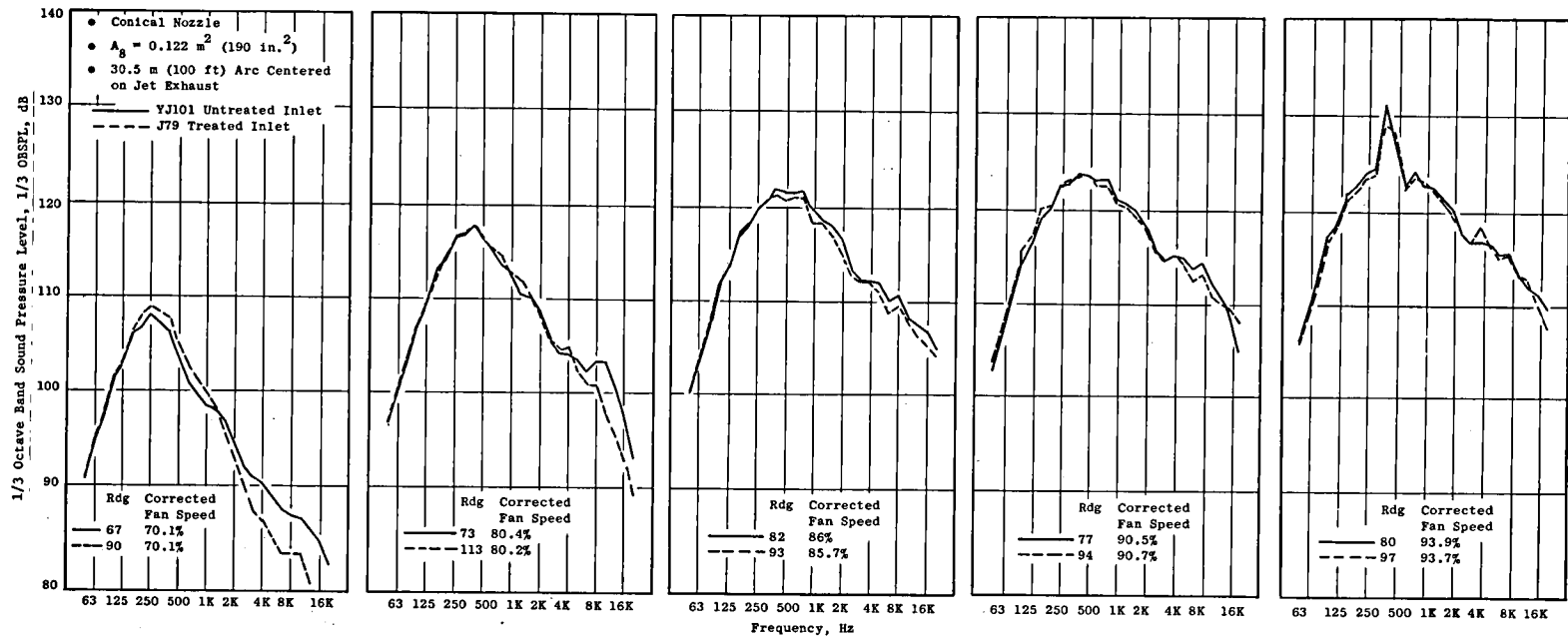


Figure 94. Spectral Comparison of Treated Versus Untreated Inlet at $\theta_i = 140^\circ$.

5.5.3.3 Summary of Observations

Initial analysis of the YJ101 data for fan inlet component noise identification is not as conclusive as hoped for, particularly on an absolute level basis, due primarily to the strong influence of the conic nozzle shock noise in the forward quadrant overriding the fan noise. Through removal of jet mixing and shock noise in order to identify fan noise spectra, indications are, however, that the YJ101 fan noise follows closely the standard PNL prediction curve and is certainly well within the band of data from which the curve was established.

Fan noise tone characteristics are well identified and indicate that at low fan speeds the difference tone generated from Stage 1 to 2, or from Stage 2 to 3, strongly influences noise levels in the forward quadrant. The amplitude of the difference tone is well above that of the fundamental blade passing frequency tone. Its harmonics are also observed and influence PNL. The fact that difference tones exist is not unique in itself. The YJ101 fan is a closely spaced, multistage fan. The controlling noise source mechanisms are believed to be strong wake-interaction and potential field interaction tone noise from the close coupling of IGV-rotor and rotor-OGV. An important part of the spectra of a multistage fan would be the appearance of sum and difference tones as shown in Figures 84 and 85. These spectral components arise when the blade passing tones of the two stages interact with the IGV's and the OGV's. This usually results in either a tone frequency which is the sum of the two blade passing frequency tones or the differences between the two tones. These "combination" tones are the natural result of multistage fans and therefore will be important to the eventual evaluation of an AST fan and inlet attenuation process. For the results of Reference 8 (where the axial spacing between the 2nd and 3rd stage fan was not as great as the current configuration and where emphasis of analysis was at high tip speeds), multiple pure tones and blade passing frequency dominated the fan inlet source characteristics. The area of trade between where blade passing frequency and/or combination tones dominate the fan spectrum will be a function of mode order and directivity for each mode. Further test and analysis of the YJ101 fan, when the jet noise is suppressed, to better isolate the influences of blade passing frequency, combination tones, and multiple pure tones in the spectral characteristics, is needed.

The J79 treated inlet was observed to be very effective in reducing forward-radiated fan noise. It essentially reduced the forward-radiated turbomachinery noise to a point where exhaust nozzle noise spectra are readily identifiable and the influence of exhaust nozzle configuration effectiveness with regard to jet mixing and shock noise suppression can be identified. Indications are, however, that aft-propagated or casing-radiated fan noise may be influencing the high-frequency spectrum for the coannular plug nozzle measurements.

5.5.4 Core Noise and Sideline Traverse Measurements

5.5.4.1 Core Noise Results

The purpose of the core noise survey was to ascertain the influence of combustor noise and flow turbulence noise on the far field measurements of the YJ101/VCE testbed engine with untreated inlet/conic nozzle configuration and the treated inlet $A_r^i = 0.475$, $R_r^o = 0.853$ conannular plug nozzle configuration.

Kulite instrumentation was used to measure the engine internal pressure fluctuations. The engine far field signature was measured simultaneously on an array of ground plane microphones around a 30.48 meter (100 ft) arc. Coherence analysis between internal to far field signals was conducted to determine the level of coherent signals in the far field.

Conic Nozzle Core Noise Results

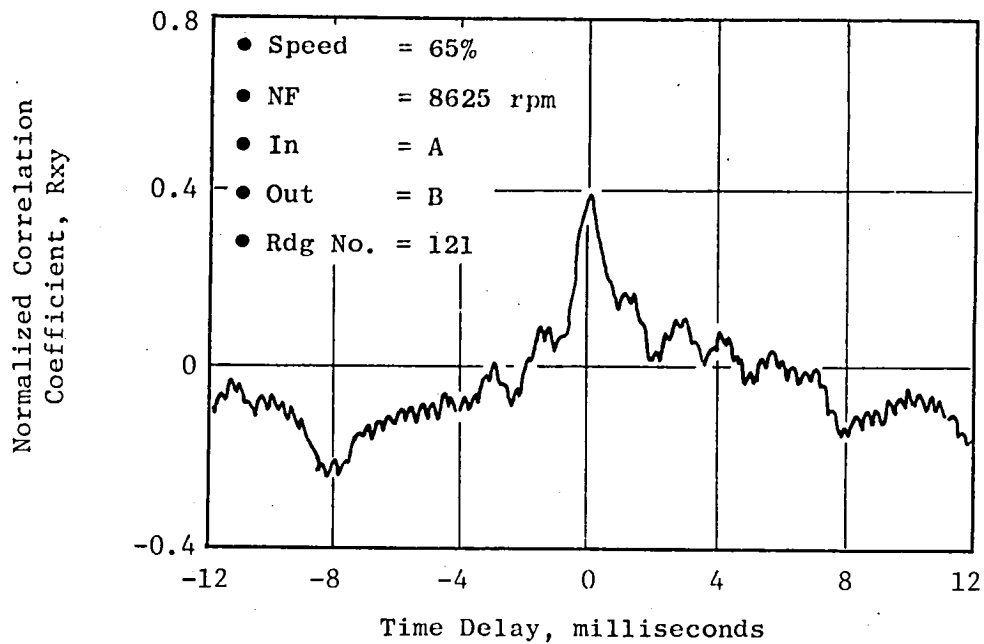
Internal measurements taken with the sound separation probe in the conic nozzle were obtained at four radial immersions centered on equal areas at the nozzle exit plane at four (4) speed points corresponding to 65, 70, 75 and 80% fan speeds. Far field measurements were recorded simultaneously with the probe data.

Figure 95(a) shows typical cross-correlation results between the probe A and B Kulites (see Figure 36(b) for probe and Kulite description) at 65% fan speed for probe immersion three, while Figure 95(b) shows the 1/3 octave band results of the coherence analysis from 0 to 2000 Hz. The upper curve of Figure 95(b) is the raw fluctuating pressure spectrum at Kulite B while the lower curve is that part of the Kulite A signal that is coherent with Kulite B. The results indicate that the most coherent regions are at frequencies below 630 Hz and the amount of coherence suggests that this region is mostly sound and not turbulence. Similar results were obtained for the 80% fan speed condition.

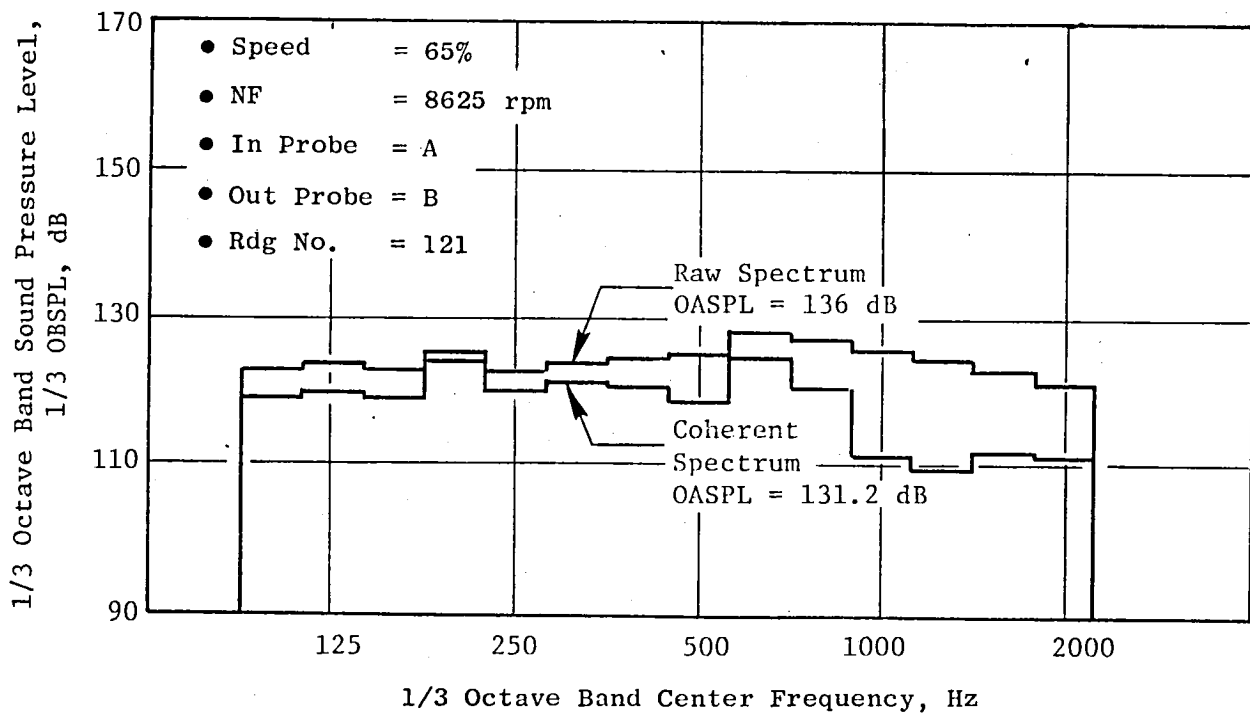
Correlations were obtained with the Probe B Kulite to far field microphones at 60°, 90°, 120° and 150°. Time delays corresponding to the ambient acoustic velocity over the 30.48 meter (100 ft) distance were identified from the cross-correlation analysis. These results are shown in Figure 96.

Typical results of the coherence analysis in Figure 97 showed no significant core noise influence on the far field measurements since the coherent spectra in the core noise region (315 to 630 Hz) were at least 10 to 15 dB below the raw spectra levels at 65% fan speed*. Similar results were noted at 80% speed, except at 150°, where the coherent spectrum was about 8.5 dB below the raw spectrum at 400 Hz. This may suggest a small core noise influence on the far field measurement at this angle. The 200 Hz band shows

*The 65% fan speed point represents a low power setting for the conic nozzle. If any strong core noise influences are to be noticed, they would be expected at the lower power settings where jet noise is low.



(a) Cross-Correlation of A (Delayed) with B



(b) Coherent Spectrum of Element B

Figure 95. VCE Core Probe for Conic Nozzle, Immersion 3; Fan Speed of 65%.

- J101/AST
- Conic Nozzle to Far Field

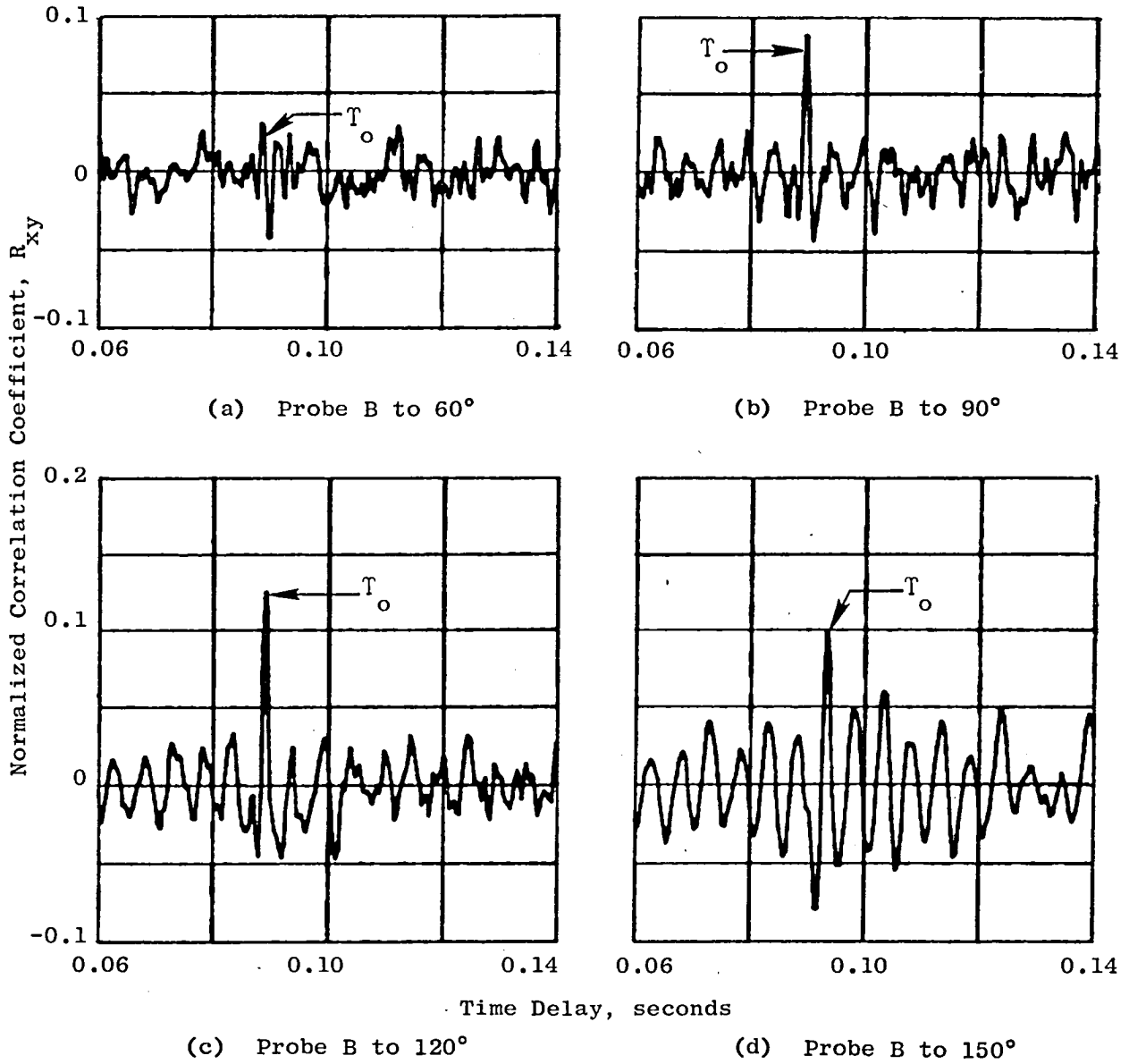


Figure 96. Internal-to-Far Field Cross-Correlation Results for the Conic Nozzle at 65 percent Fan Speed.

the highest amount of coherence from results of both the internal measurements and internal-to-far field comparisons.

Coannular Plug Nozzle Core Noise Results

The core noise survey on the YJ101 VCE testbed with a 0.853 radius ratio coannular plug nozzle at an area ratio of 0.475 was conducted at four points corresponding to fan speeds of 65, 70, 75 and 80 percent along the engine sea level static operating line. The exhaust nozzle instrumentation consisted of two Kulites in both the fan and core streams (see Figure 36 for description).

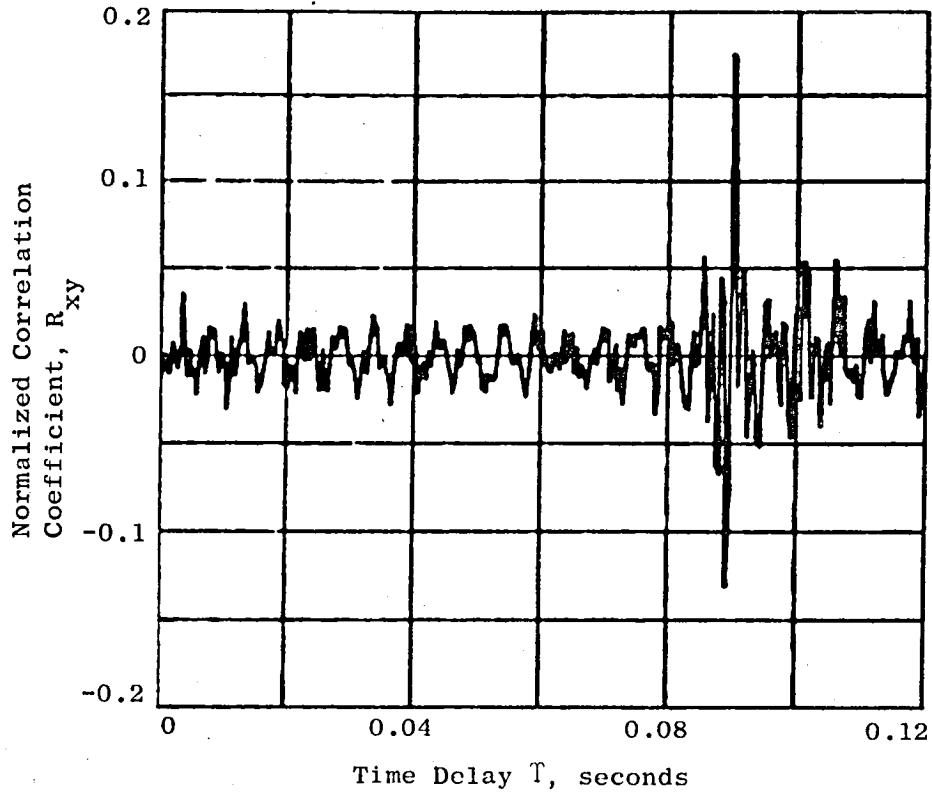
The amount of internally generated sound that is transmitted to the far field from the YJ101/VCE test bed engine with the coannular plug nozzle is illustrated by typical cross-correlograms and coherent 1/3 octave band spectra (0 to 2000 Hz) for an internal sensor and the 120° mic (typical peak angle for core noise). Figure 98 shows the results at 65% speed from the aft Kulite (B) in the core wall (outer stream) to the far field microphone. The 0.09 sec time delay of the large positive peak from the cross-correlation (Figure 98(a)) corresponds to the acoustic propagation time over the 30.48 meter (100 ft) distance to the far field microphones at ambient conditions. The relative strength of the correlation coefficient ($R_{xy} = 0.175$) in the time domain is reflected by the degree of coherence in the frequency domain as shown by the difference in 1/3 OBSPL spectra for the raw and coherent signals in Figure 98(b). The upper curve is the spectrum of the raw signal at the 120° microphone position while the lower curve is that portion of the far field signal that is coherent with the internal signal once the acoustic propagation time delay is removed.

The predicted General Electric core noise spectrum for the 65 percent speed point shown in Figure 98(b) is about 5 dB higher than the coherent spectrum level at the generally recognized combustor noise peak frequency of 400 Hz. However, the predicted level is still 5 to 8 dB below the raw signal. A worst case assumption would suggest that the core noise from the predicted level might influence this peak frequency region by about 1.5 dB.

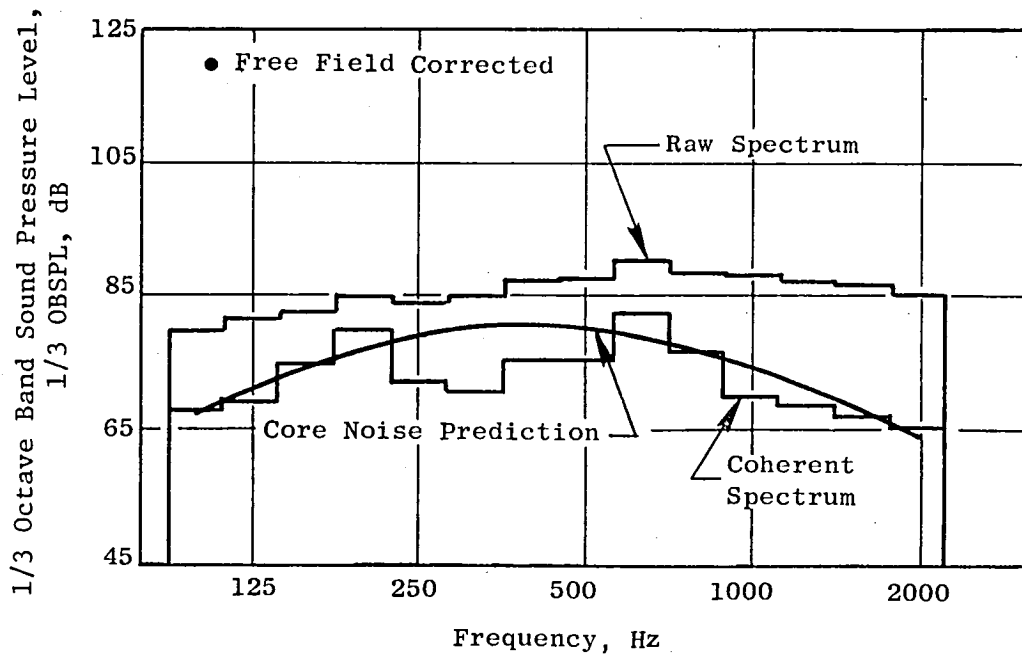
Figure 99 is a similar internal-to-far field display for the forward Kulite A in the fan probe (inner stream) to the 120° microphone. The time delays of the peaks in the cross-correlation are again associated with the acoustic propagation time to the far field but are of considerably lower magnitude ($R_{xy} = 0.05$) than for the core (outer) stream. Figure 99(b) shows a similar coherent region around 200 Hz, but the rest of the coherent spectrum (with time delay removed) is greater than 10 dB down from the raw level and, consequently, has little or no influence on the static measurements.

The 200 Hz 1/3 octave band was a region of relatively high coherence around the arc for both nozzle configurations at each of the conditions tested. High resolution narrow band (2 Hz bandwidth) spectral analysis of the far field microphones from 0 to 2000 Hz revealed a notable tone at about 180-200 Hz which also occurred in similar analysis of the internal sensors.

- J101/VCE Test, 10-78
- Rdg 264, Core Wall Kulite B to Far Field
- Coannular Nozzle, $0.853 R_r^0$
- 30.48 m (100 ft) Arc



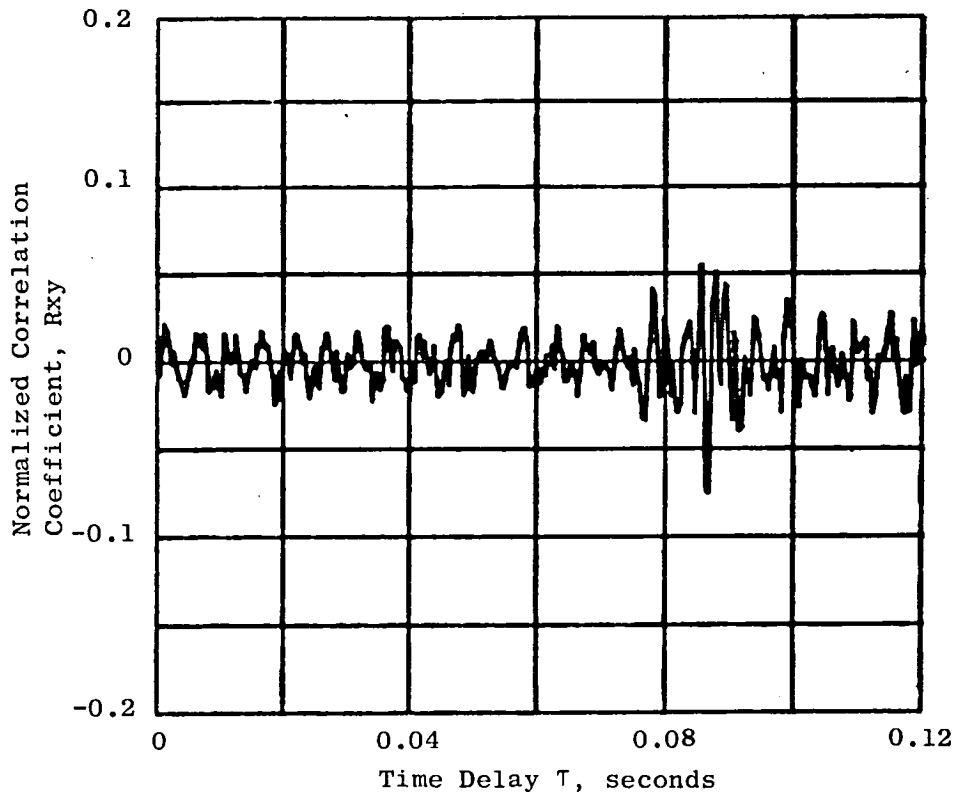
(a) Cross-Correlation



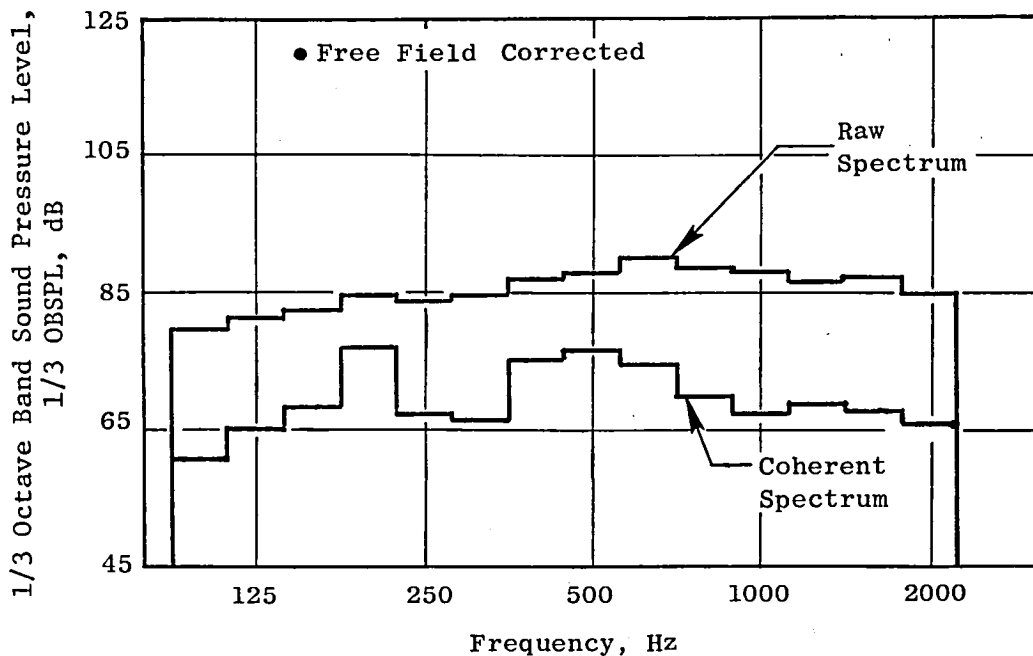
(b) Coherent Spectrum

Figure 98. Internal to Far Field Noise Survey at 65 percent Speed from Core Exhaust to 120° Microphone.

- J101/VCE Test, 10-78
- Rdg 264, Fan Probe Kulite A to Far Field
- Coannular Nozzle, $0.853 R_r^o$
- 30.48 m (100 ft) Arc



(a) Cross-Correlation



(b) Coherent Spectrum

Figure 99. Internal to Far Field Noise Survey at 65 percent Speed from Fan Exhaust to 120° Microphone.

This was true even for the high-pass filtered data above 80 Hz, as seen in Figures 100 and 101, which show typical narrow band results from an internal sensor and far field microphone, respectively. This tone is suspected to be the third harmonic of electronic noise and is not related to the broadband combustion noise process.

Figure 102 illustrates the directivity of the magnitude of the peak correlation coefficient (R_{xy}) corresponding to the time delay associated with the propagation of the acoustic signal to the far field. These cross-correlation analysis results were obtained for the range of frequencies from 0 to 2000 Hz. The core (gas generator) stream results indicate the largest correlation coefficients ($R_{xy} \sim 0.18-0.25$) occur at 120° , which is also peak angle for core noise. The fan stream results show approximately a constant average level ($R_{xy} \sim 0.08$) at all angles over the speed range. These low level correlations ($R_{xy} \sim 0.08$) indicate that there is very little signal correlation between the internal sensors and the far field microphone measurements and should be considered as inaccurate for noise amplitude assessment.

Conclusions

The results of the core noise survey on the YJ101 AST/VCE acoustic engine nozzle configurations show that core noise for the static data does not to any significant degree influence the levels of the far field measurements taken with the conic and 0.853 radius ratio coannular nozzles. Because of the low level of correlations observed in the fan (or inner) stream, an absolute internal noise level assessment is inappropriate, but indicative of not influencing the jet noise measurements. For the core (or outer) stream, at $\theta_i \sim 120^\circ$, a representative comparison between measured core noise and predicted was obtained. However, additional theory/data comparisons should be made with the test results obtained in the future in order to make any definitive evaluation of absolute levels of core noise, or regarding refinements/improvements of prediction methods.

5.5.4.2 Sideline Traverse Results

The traverse microphone data acquired during the testing of the YJ101 AST/VCE acoustic demonstrator engine at Edwards Air Force Base was analyzed to obtain an estimate of the axial source location for the conic and coannular exhaust nozzle configurations. Traversing (centerline height) microphone measurements were taken along a 3.048 meter (10 ft) sideline simultaneously with far field (ground plane) microphone arrays which were located along a 30.48 meter (100 ft) arc and 21.34 meter (70 ft) sideline. Angular coverage was from 35° in the forward quadrant to an aft quadrant angle of 165° . The test conditions covered the range from 65 to approximately 90% fan speed.

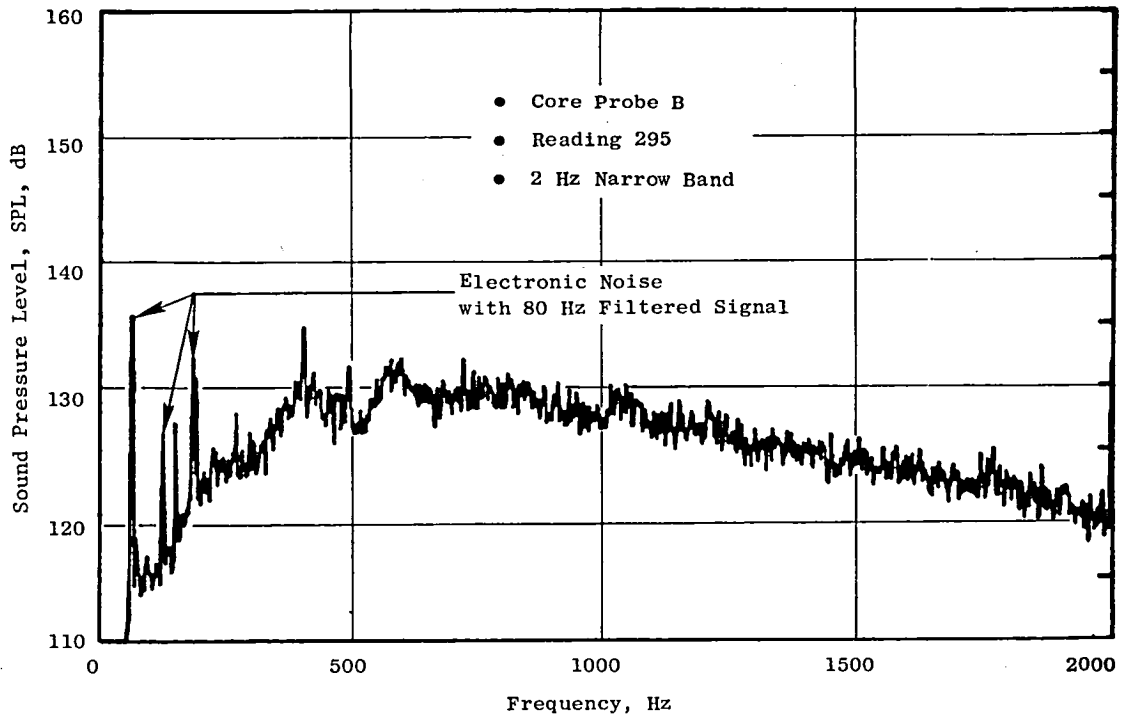


Figure 100. Narrow Band Spectrum from YJ101/VCE Internal Acoustic Sensor.

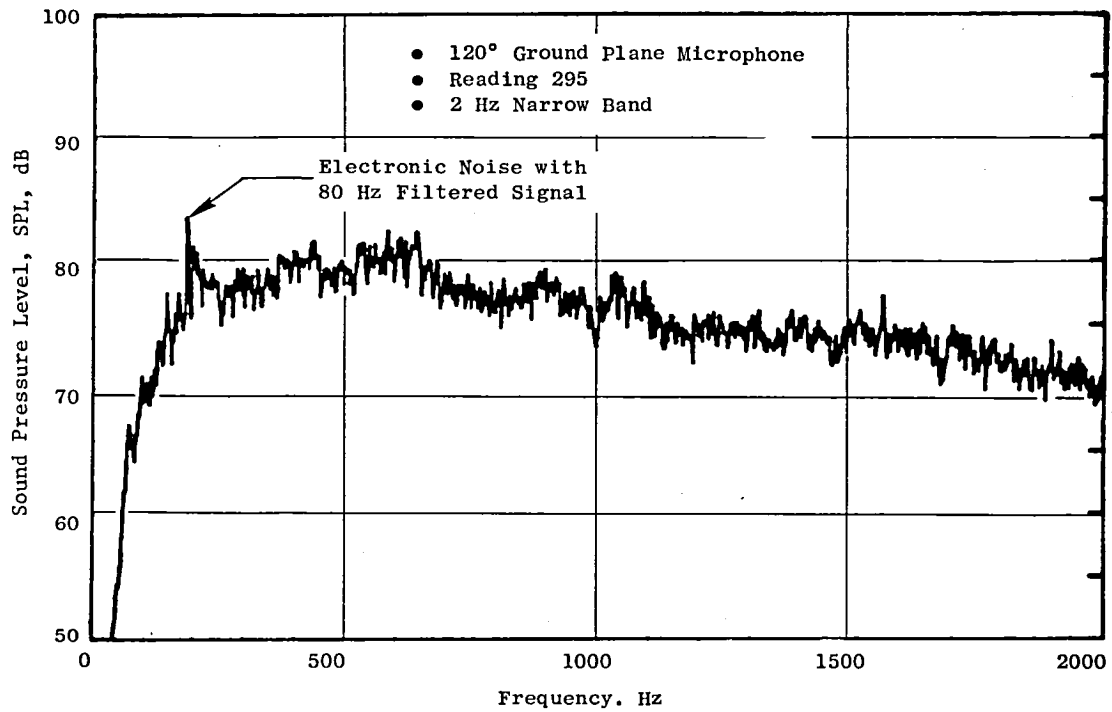


Figure 101. Narrow Band Spectrum from YJ101 VCE Acoustic Far Field Microphone.

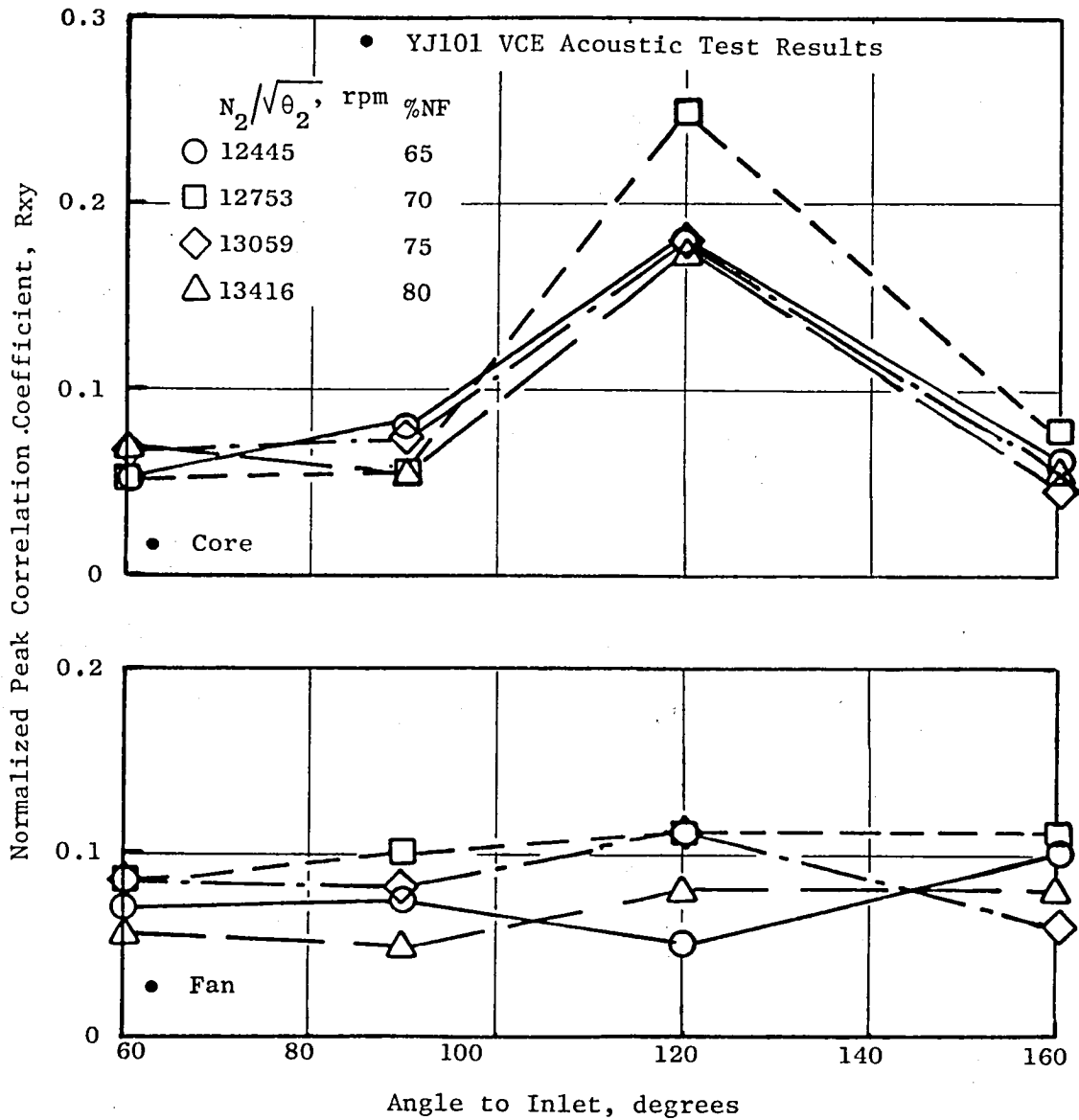


Figure 102. Magnitude of Correlation Coefficient Versus Acoustic Angle for Coannular Nozzle.

Sideline Traverse Results for Conic and Coannular Nozzles

The traverse microphone results at the 3.048 m (10 ft) sideline were paired with the fixed far field measurements taken on the 30.48 m (100 ft) arc and 21.34 m (70 ft) sideline and extrapolated back to the near field sideline. A common intermediate exhaust velocity condition $V_j = 518$ m/sec (1700 fps) was selected for comparison.

SPL directivity for each 1/3 octave band frequency (50 to 10,000 Hz) were plotted for the near field traverse and far field data on the common 3.048 m (10 ft) sideline. The angle of peak noise at each frequency was tabulated for both sets of data and plotted versus frequency. These peak angle distributions were smoothed and values at each 1/3 octave band center frequency (1/3 OBCF) obtained. Figure 103(a) and (b) show these angle distributions for the conic and coannular nozzles, respectively.

The peak noise source extent along the nozzle axis was estimated utilizing the multiple sideline technique which is described in detail in the NASA-Ames J79/32 Chute Program Final Report (Reference 14). This procedure is schematically illustrated in Figure 104.

The axial location of each 1/3 OBCF peak noise source was determined and is shown for the conic nozzle in Figure 105 and for the coannular nozzle in Figure 106. The conic nozzle exit diameter D and equivalent conical diameter D_{eq} of the 0.853-radius-ratio, 0.2-area-ratio, coannular nozzle were used as distance-normalizing parameters. The low frequencies (63 Hz) extend to an XS/D of about 7, while the high frequency end (>4000 Hz) is less than one nozzle diameter downstream of the nozzle exit plane for the coannular nozzle. In between these extremes, the other 1/3 OBCF's are uniformly spaced.

A comparison of the Strouhal distribution of peak noise source locations and far field radiation angles is shown in Figure 107 for the J79 (Reference 14) and YJ101/VCE conic nozzles. The comparison shows that the source extent estimation for the YJ101/VCE conic nozzle is quite similar to the J79 conic nozzle results.

Figure 108 shows the comparison of the Strouhal distributions for the peak noise locations of both nozzle configurations at a velocity of 518 m/sec (1700 fps). The figure indicates the shift of the higher frequencies towards the exit plane of the coannular nozzle.

Conclusions

The conic nozzle results agree with previous test results. The coannular nozzle displays a source location pattern that is similar to the conic nozzle at the 518 m/sec (1700 fps) condition, except that the higher frequencies (>1000 Hz) are drawn closer to the nozzle exit (see Figure 106). This is in keeping with the suppressive nature of the inverted flow concept on the coannular nozzle.

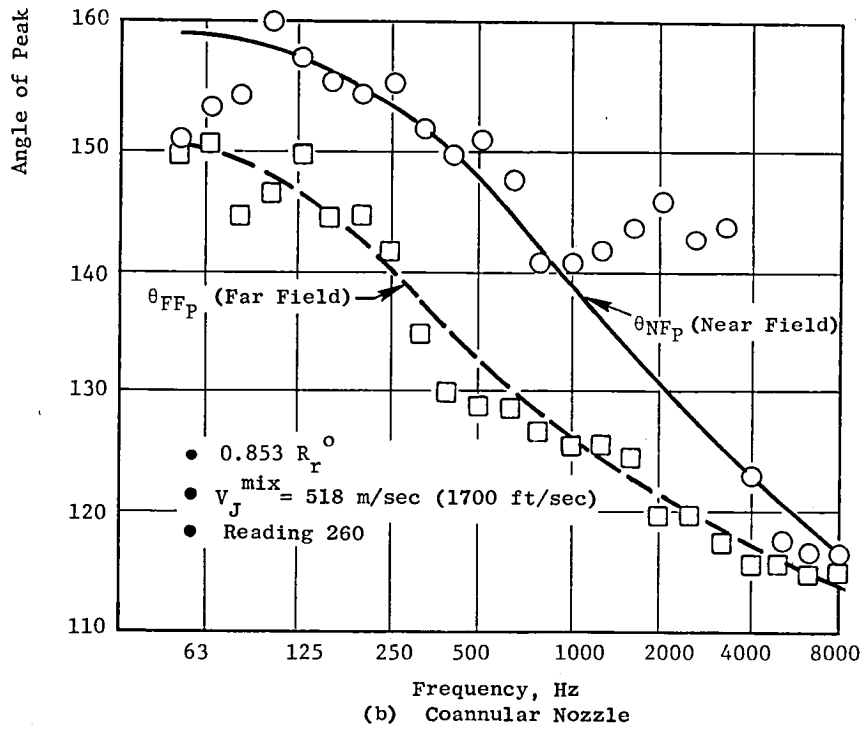
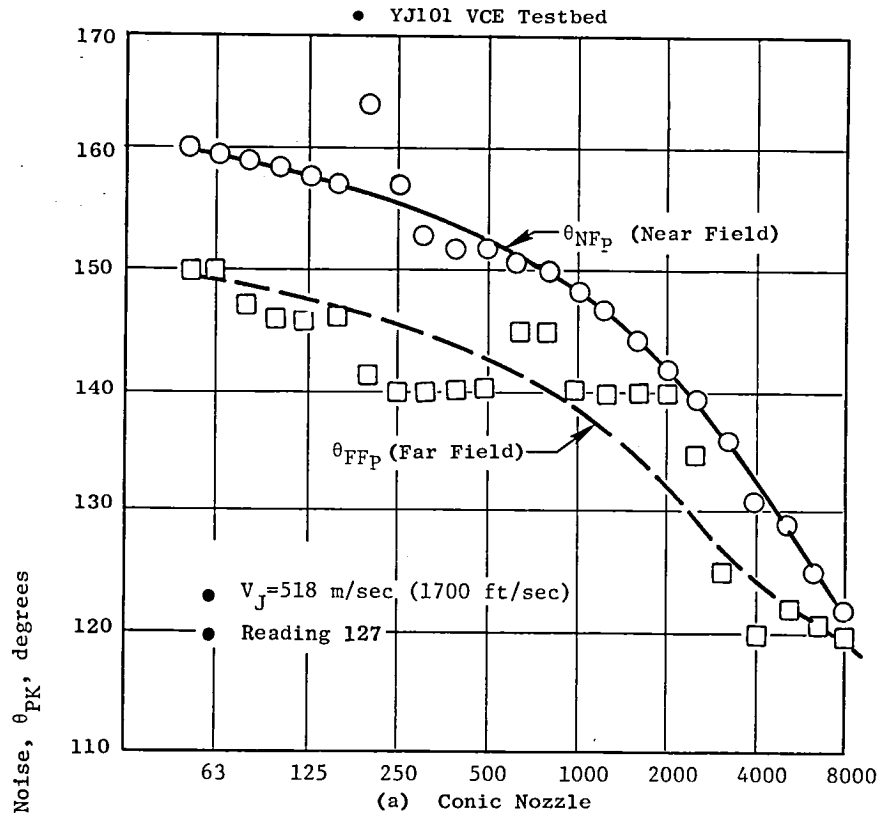


Figure 103. Peak Angle Distributions for Far Field and Traverse Microphones.

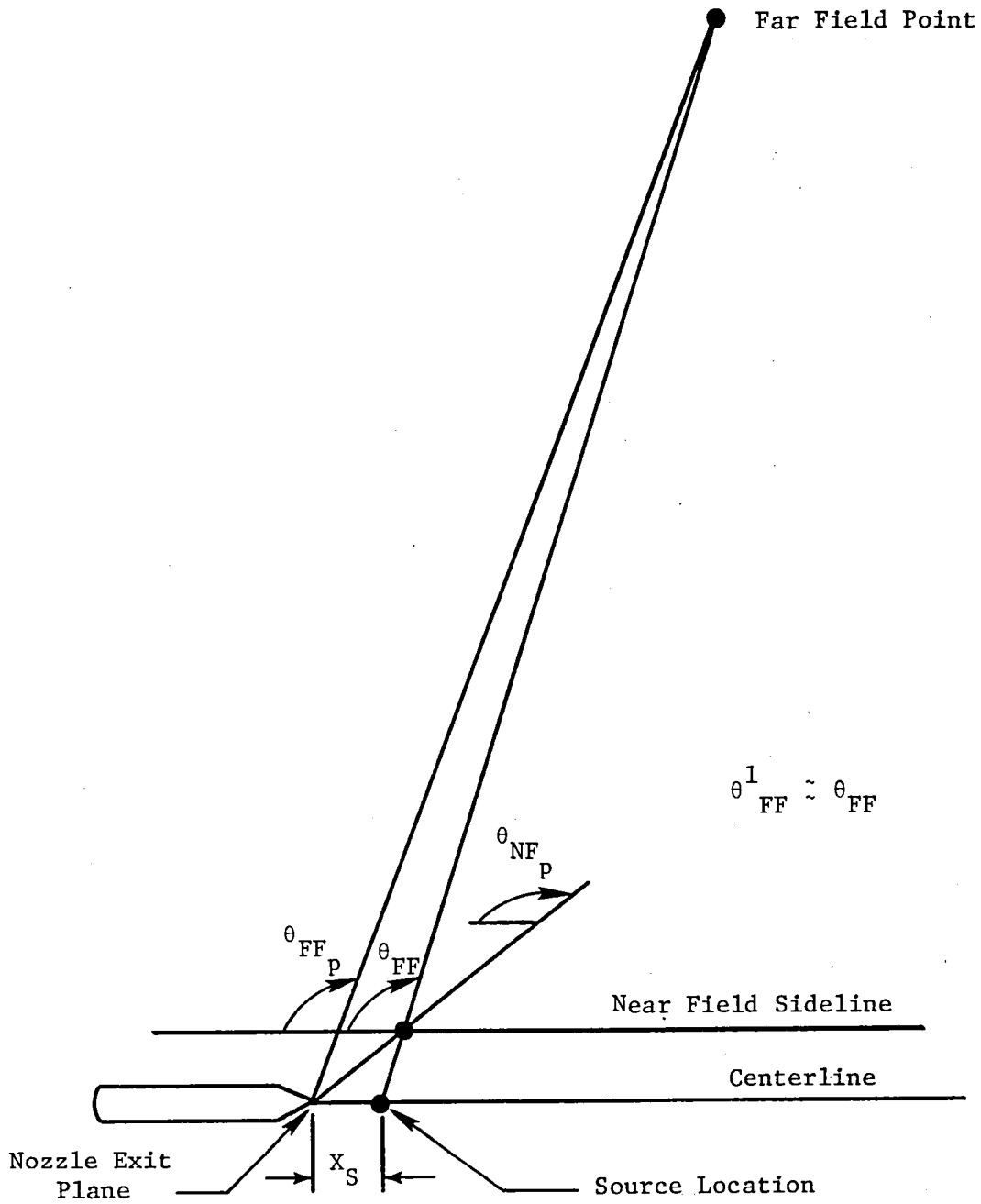


Figure 104. Source Location Effect on Noise Radiation Angles.

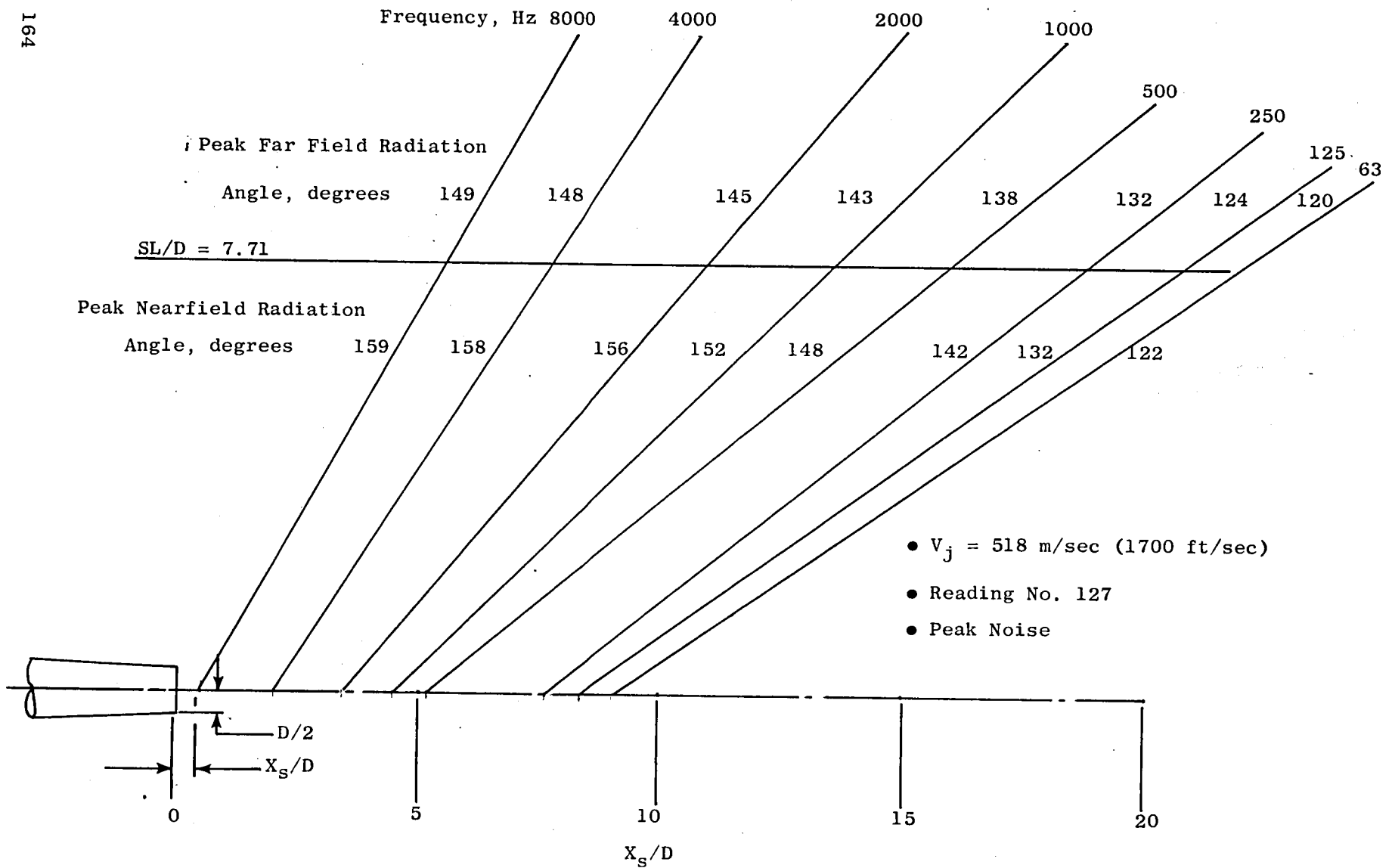


Figure 105. Source Location for the YJ101 VCE Unsuppressed Conic Nozzle.

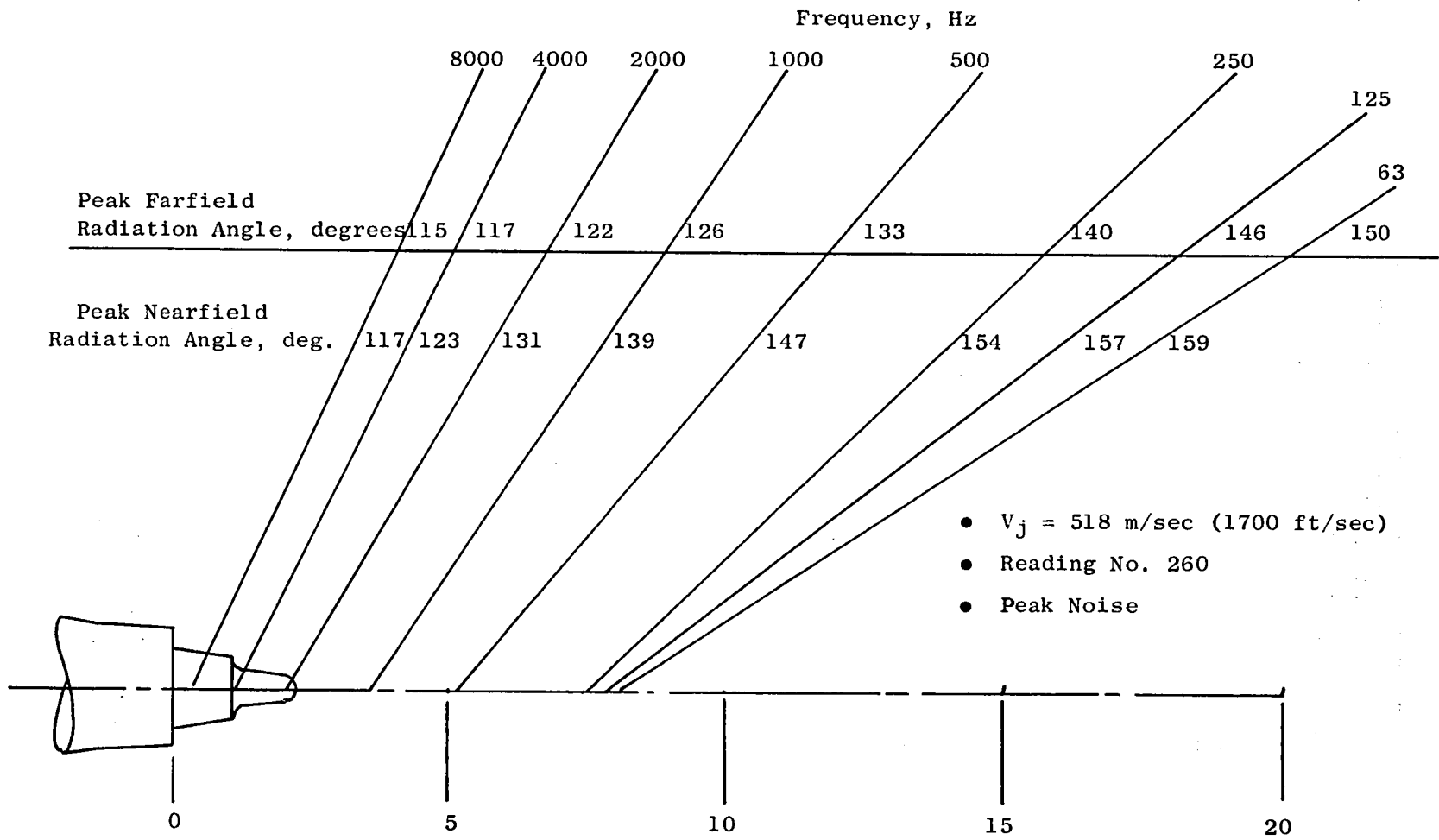


Figure 106. Source Location for YJ101/VCE - $0.853 R_r^0$ Coannular Nozzle.

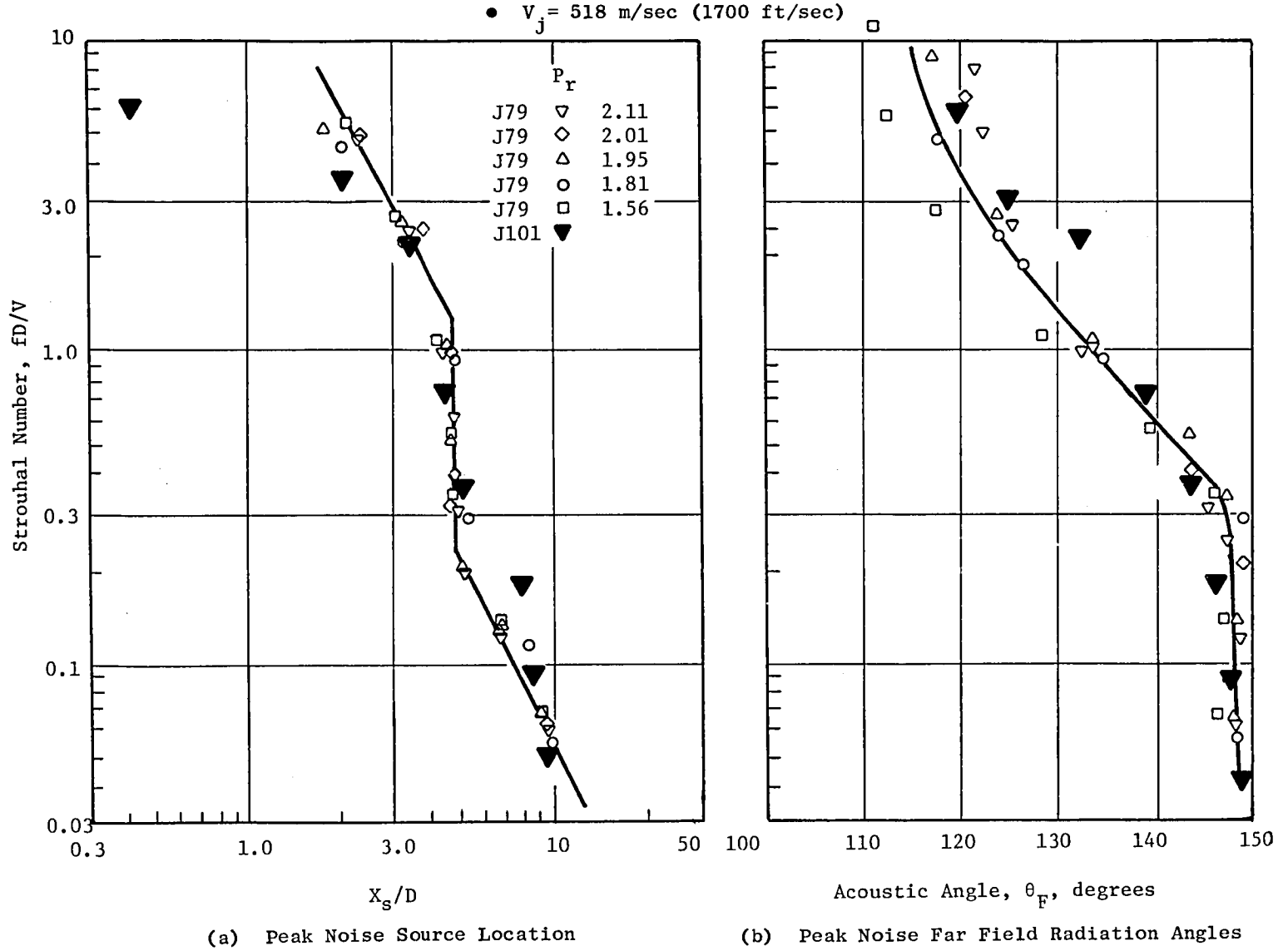


Figure 107. Strouhal Distribution of Peak Noise Source Locations and Far Field Radiation Angles for J79 and YJ101/VCE Conic Nozzles.

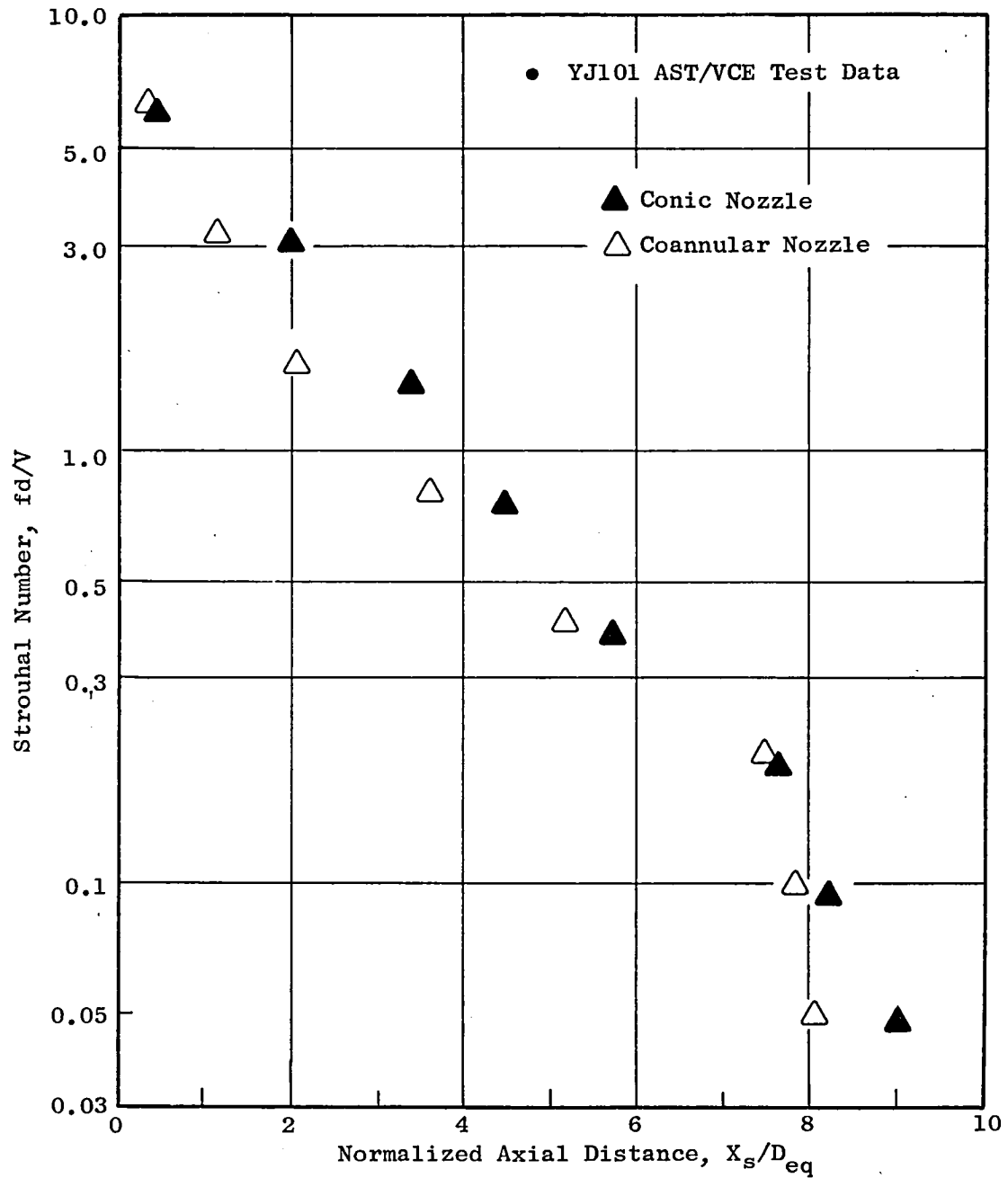


Figure 108. Strouhal Number Distribution as a Function of Peak Noise Source Locations at $V_j^{mix} = 518$ m/sec (1700 ft/sec) for Conic and Coannular Plug Nozzles.

5.5.5 Laser Velocimeter Measurements

A laser velocimeter (LV) has been employed as a non-invasive diagnostic tool to measure jet plume characteristics of conic and coannular nozzles of the YJ101/VCE acoustic testbed. A knowledge of the turbulent mixing characteristics of the jets gives an insight into the noise radiation from the jets. Extensive surveys of the mean and turbulent (rms) velocity characteristics were performed on supersonic and subsonic jet exhaust plumes of conic and coannular plug nozzles.

5.5.5.1 Conic Nozzle Test Results

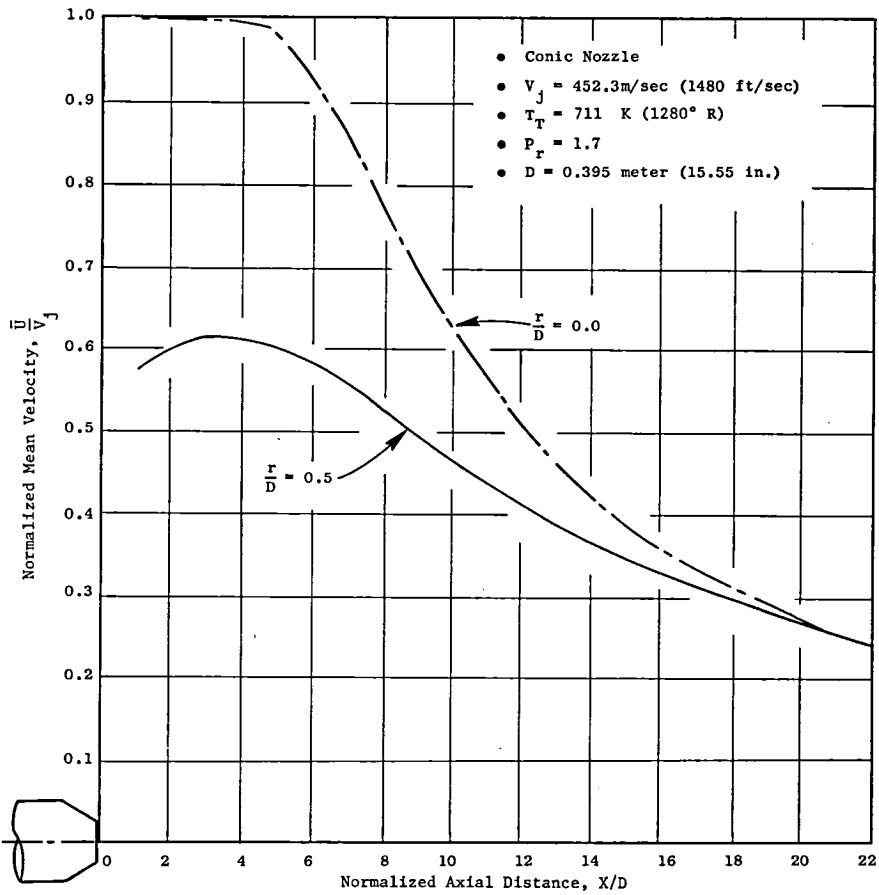
The baseline conic nozzle had an exit diameter of 0.395 m (15.6 in.) and was tested for two engine power settings. One power setting corresponded to a near-sonic case ($V_j \cong 452.4$ m/sec (1484 fps), $Pr = 1.7$, $T_T = 711$ K (1280° R), and the other corresponded to a shocked supersonic case $V_j \cong 626.36$ m/sec (2055 fps), $Pr = 2.37$, $T_T \cong 877.78$ K (1580° R). The measured profiles of mean and rms turbulent velocities are presented herein, along with comparisons with the available model scale test data.

5.5.5.1.1 Near Sonic Conic Jet

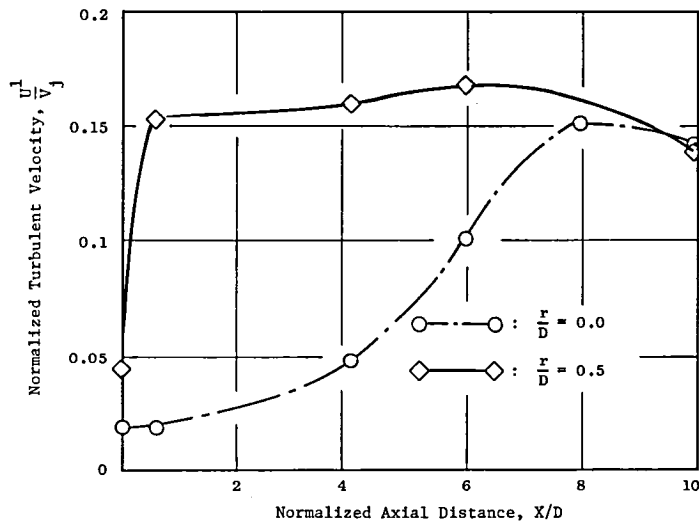
Figure 109 shows the mean and turbulent velocity variation at two radial locations. Within the potential core ($x/D \leq 4$) the centerline mean velocity is uniformly constant and the turbulent velocity remains within 5% of V_j . The mean velocity at $r/D = 0.5$ increases initially due to entrainment of the static ambient air by the jet and the turbulent velocity increases rapidly from the exit plane value of 4% to 15% of V_j and remains fairly constant downstream. A histogram measurement of the exit plane mean and turbulence velocity indicates that the mean velocity is constant within the potential core ($r/D < 0.5$) and the turbulent velocity remains within 5% of V_j , as seen in Figure 110. A typical LV chordwise traverse is shown in Figure 111. Figure 112 shows the mean and turbulent velocities measured by histograms on either side of an aft VABI chute. Note that the VABI chutes do not noticeably influence either the mean or the turbulent velocities. These results illustrate that the conic nozzle flow obtained from the two-flow mixed engine system is quite normal and similar to that expected from a single flow conic nozzle.

5.5.5.1.2 Supersonic Conic Jet

The mean velocity variation shown in Figure 113(a) indicates the presence of a shock structure consisting of eleven cells at the centerline of the conic nozzle. An average spacing of $0.64D$ between shocks yields a shock spacing constant of 0.96 instead of 1.1 in the Harper-Bourne Fisher model (Reference 11). The axial traverse at $r/D = 0.25$ shows only eight shock cells because of the impressed slow moving shear layer. The axial traverse at $r/D = 0.5$ does not show any shock structure due to the deceleration of the jet by the ambient air. The axial variation of the turbulent velocity at $r/D = 0.0$ and 0.5 shown in Figure 113(b) is similar

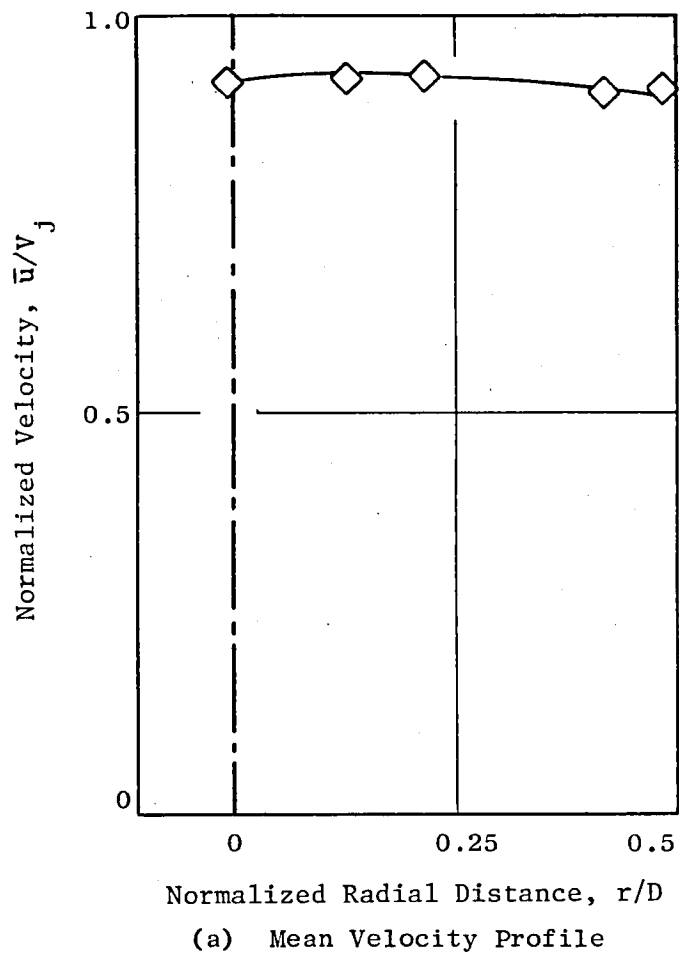


(a) Normalized Mean Velocity Axial Variation.



(b) Normalized Turbulent Velocity Axial Variation.

Figure 109. Laser Velocimeter Measured Mean and Turbulent Velocities at Two Radial Locations for a Near Sonic YJ101 Engine Conic Nozzle.



- LV Measurements on a Conic Nozzle
- $X/D = 0$
- $V_j = 452.3$ m/sec (1484 ft/sec): $P_r = 1.7$; $T_T = 711$ K (1280° R)
- Engine Measurements on YJ101 AST/VCE Concept Demo
- Existence of Potential Core for $r/D \cong 0.5$

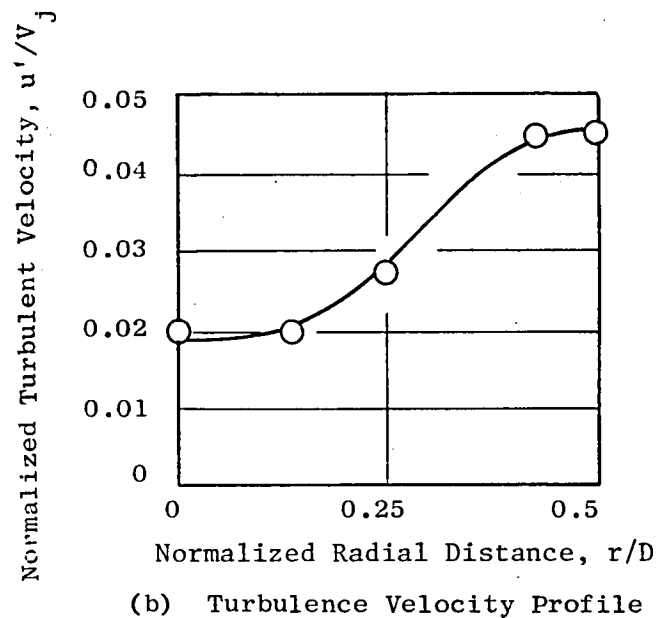


Figure 110. Conic Nozzle Exit Plane Mean and Turbulence Velocity Profiles.

LV Traverse

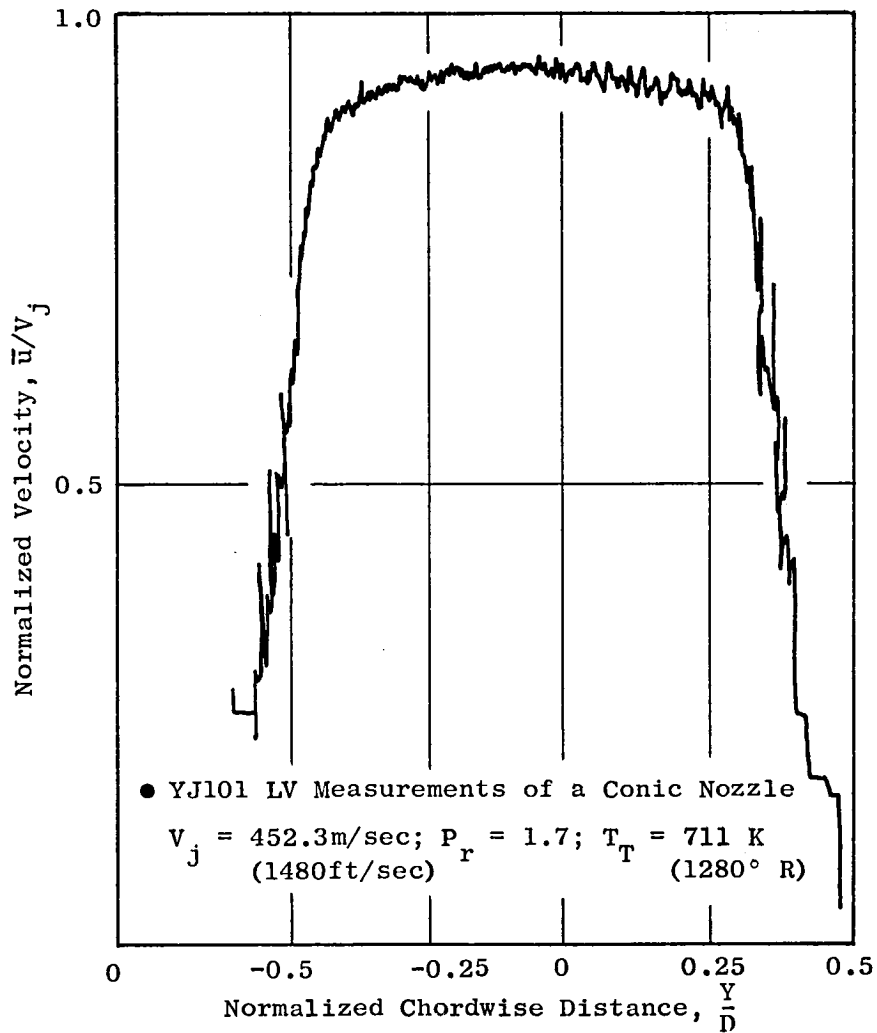
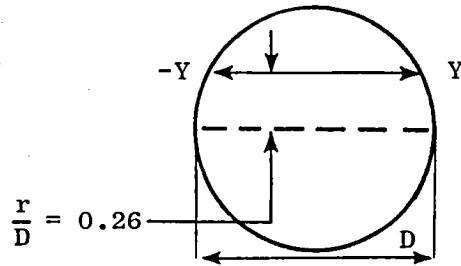
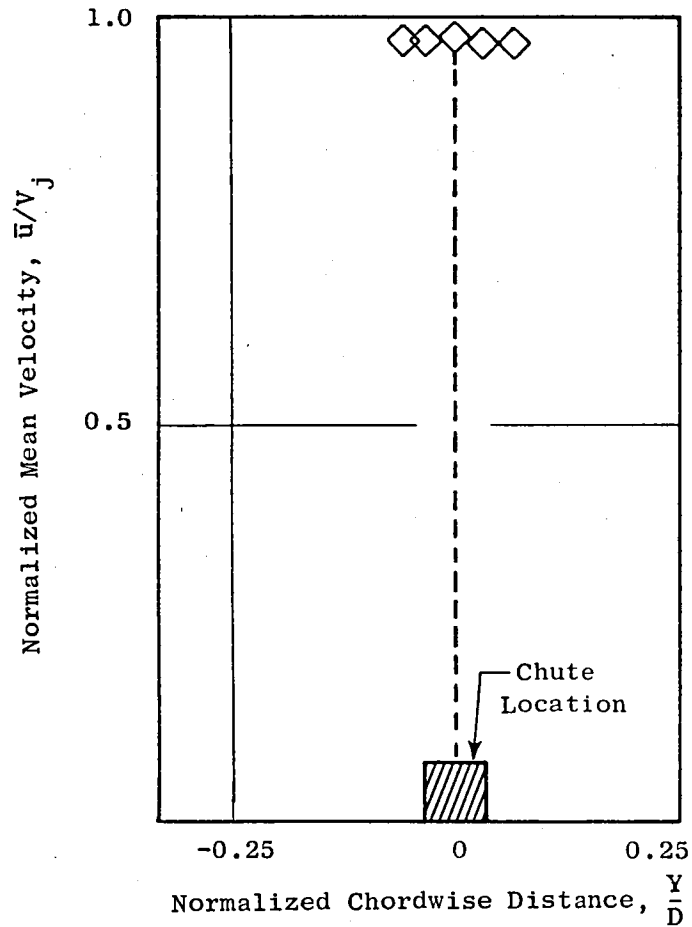
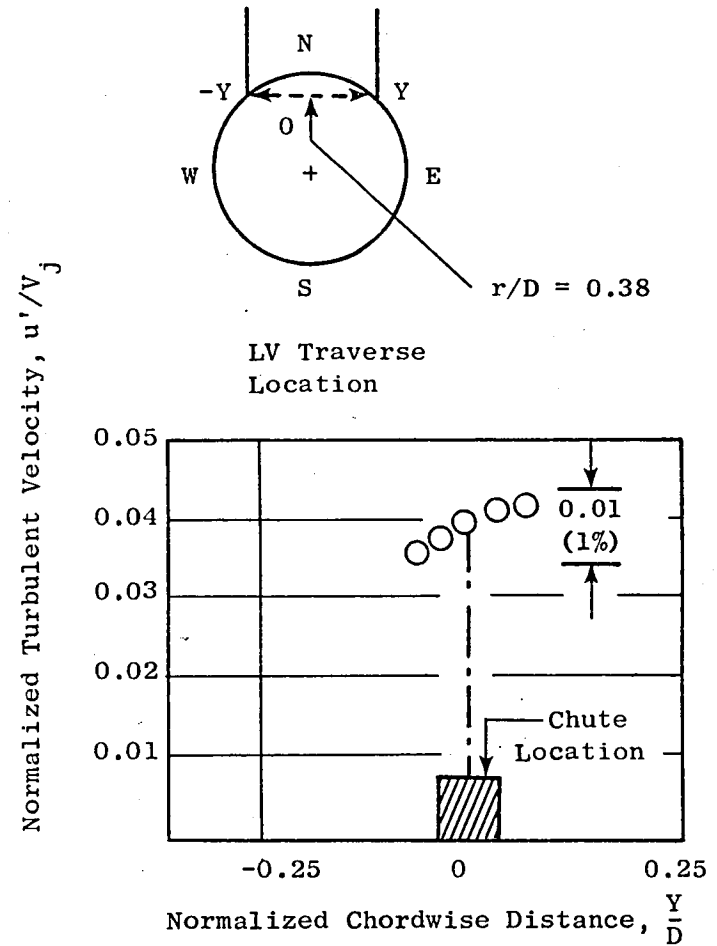


Figure 111. Chordwise Traverse at $X/D = 0.6$

- $V_j = 453 \text{ m/sec (1484 fps)}$; $P_r = 1.7$; $T_T = 711 \text{ K (1280}^\circ \text{ R)}$
- $X/D = 0.6$; $r/D = 0.38$
- Engine Measurements on YJ101 AST/VCE Concept Demo

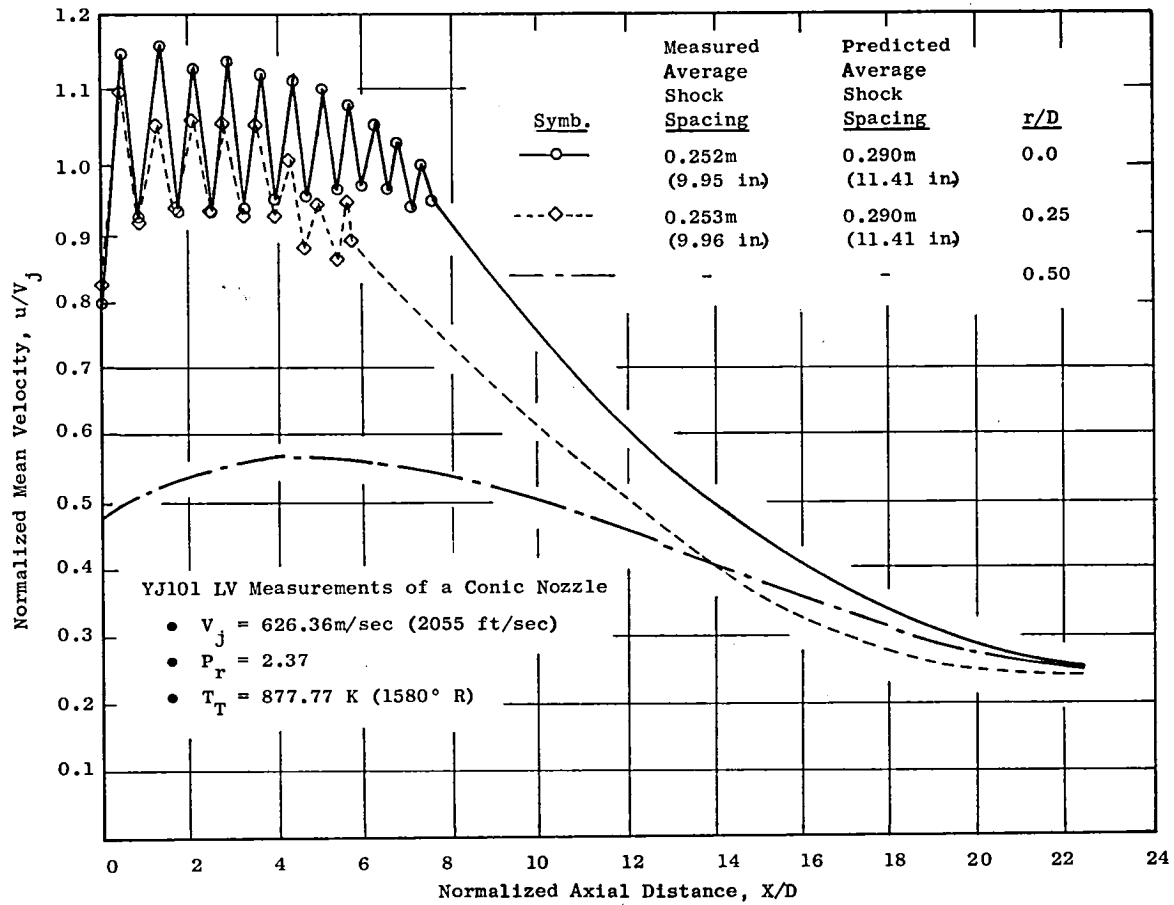


(a) Mean Velocity Profile

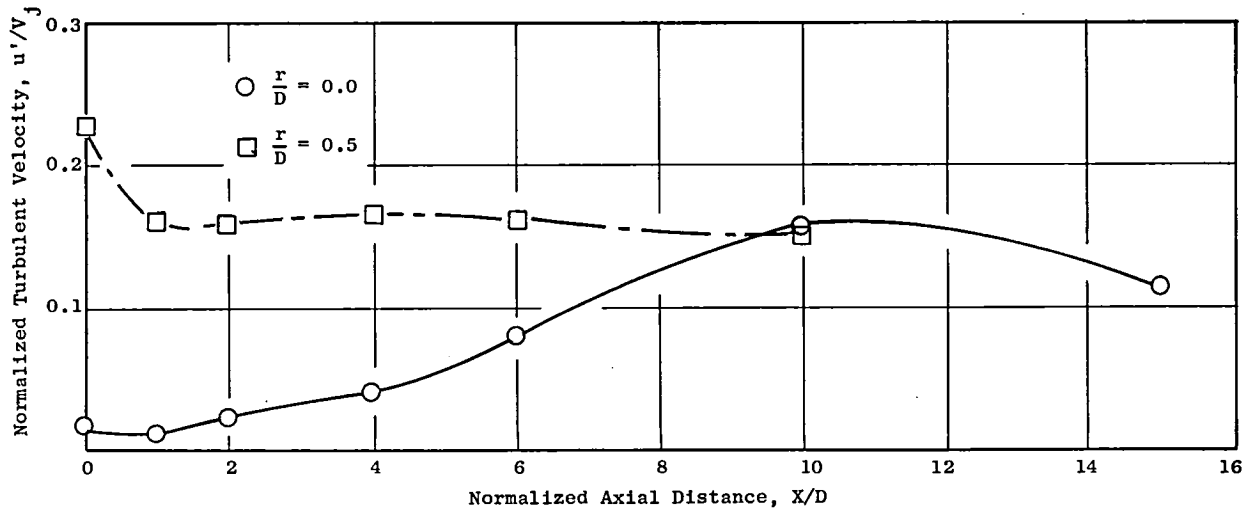


(b) Turbulent Velocity Profile

Figure 112. Influence of Rear VABI Chutes on Mean and Turbulent Velocity Profiles with Conic Nozzle, as Determined by LV Measurements.



(a) Mean Velocity Profile



(b) Turbulent Velocity Profile

Figure 113. Laser Velocimeter Measured Mean and Turbulent Velocities at Two Radial Locations for a Supersonic Conic Nozzle.

to the subsonic case except that the centerline turbulent velocity now reaches a peak value at $x/D = 10$ as compared to $x/D = 8$ in the subsonic case. This is due to the lengthening of the potential core for the supersonic case and, hence the downstream shift of the turbulent mixing region.

5.5.5.1.3 Comparison of Engine and Model-Scale Test Results

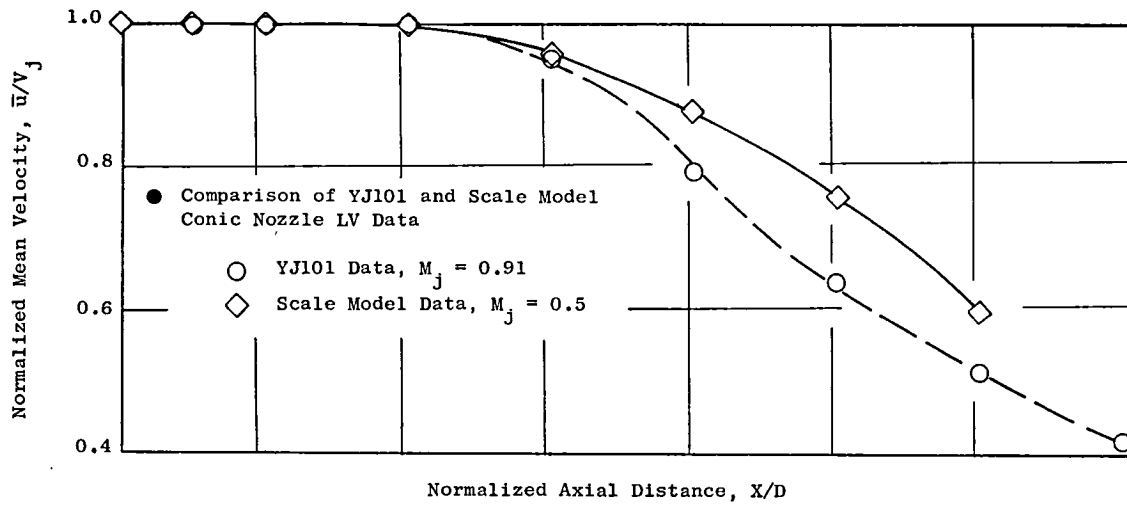
Mean and turbulent velocity profiles of the YJ101 and available model scale test results for a conic nozzle are compared in Figure 114 for subsonic conditions. The normalized turbulent velocity levels are higher for the YJ101 as compared to the scale model. The higher levels of turbulence result in a faster decay of the normalized centerline mean velocity for the YJ101. Figure 115 shows the radial profiles of the normalized mean and turbulent velocities at two axial stations namely $x/D = 4$ and 6. The mean velocity profiles are similar and the turbulent velocities are higher for the YJ101 as compared to those of the model. Next, the normalized mean and turbulent velocity profiles of the YJ101 and model scale test results for a shocked supersonic conic nozzle are compared in Figure 116. As the model is operating under higher pressure ratio, the shock strength parameter, $\beta (\sqrt{M_j^2 - 1})$ is higher and hence the average spacing of the shocks is higher for the model as compared to the YJ101. The turbulent velocities for the engine are seen to be slightly higher than those of the model. These comparisons indicate that YJ101 and model scale conic nozzle operating under similar operating conditions depict similar flow characteristics.

5.5.5.2 Coannular Plug Nozzle Test Results

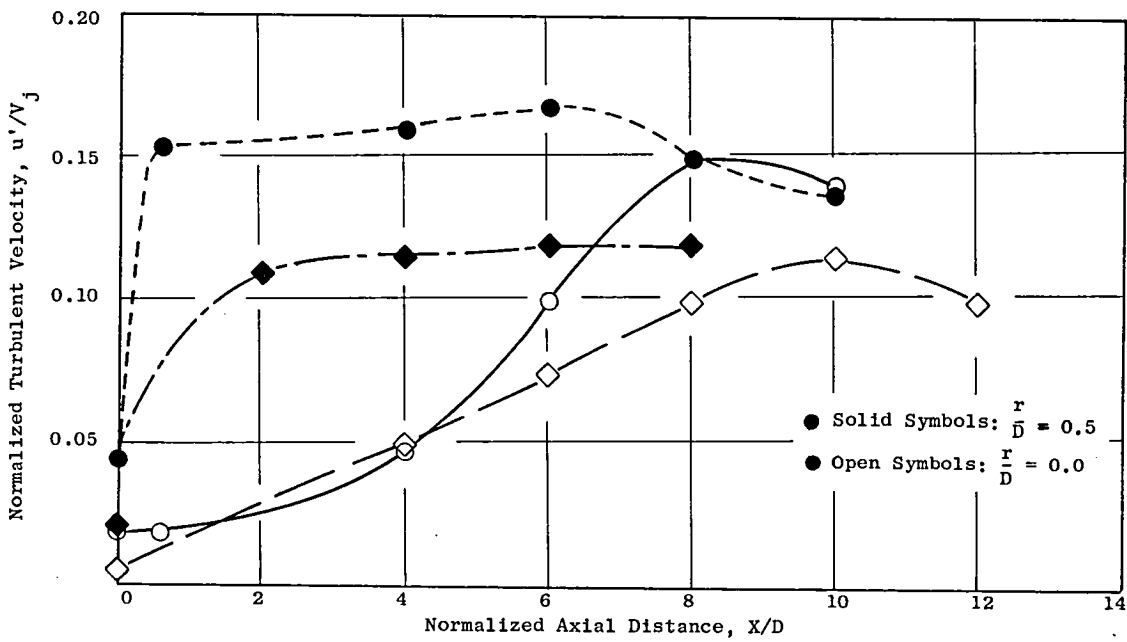
Jet plume LV surveys of an inverted velocity profile coannular plug nozzle having an equivalent diameter of 0.4196 meters (16.52 in.) with an outer radius ratio of 0.853 and inner to outer area ratio of 0.2 were conducted. The coannular nozzle was tested for a mass averaged jet velocity of 606.55 m/sec (1990 fps); the outer and inner stream velocities being 655.3 m/sec (2150 fps) and 426.72 (1400 fps), respectively.

5.5.5.2.1 Coannular Nozzle with $A_r^i = 0.2$, $R_r^o = 0.853$

Figure 117 shows the axial variation of normalized mean velocity at four radial locations. The axial traverse at $r/D^o = 0.25$ alone shows the presence of a shock structure, although not nearly so evident as for the conical nozzle, indicating the effective suppression of the associated shock noise by an inverted velocity profile coannular plug nozzle. A radial LV traverse of the jet at $x/D_{eq} = 1.1$, shown in Figure 118, shows the inner and outer streams distinctly. The outer stream is mixing rapidly and the inner stream is still maintaining a step profile at this axial station. The radial profiles of the jet taken in two mutually perpendicular directions at $x/D_{eq} = 5$ are shown in Figure 119 for the case with the aft VABI chutes open. One observes a slight profile asymmetry for the east-west traverse and a large profile asymmetry for the north-south traverse which can be attributed to geometric asymmetry

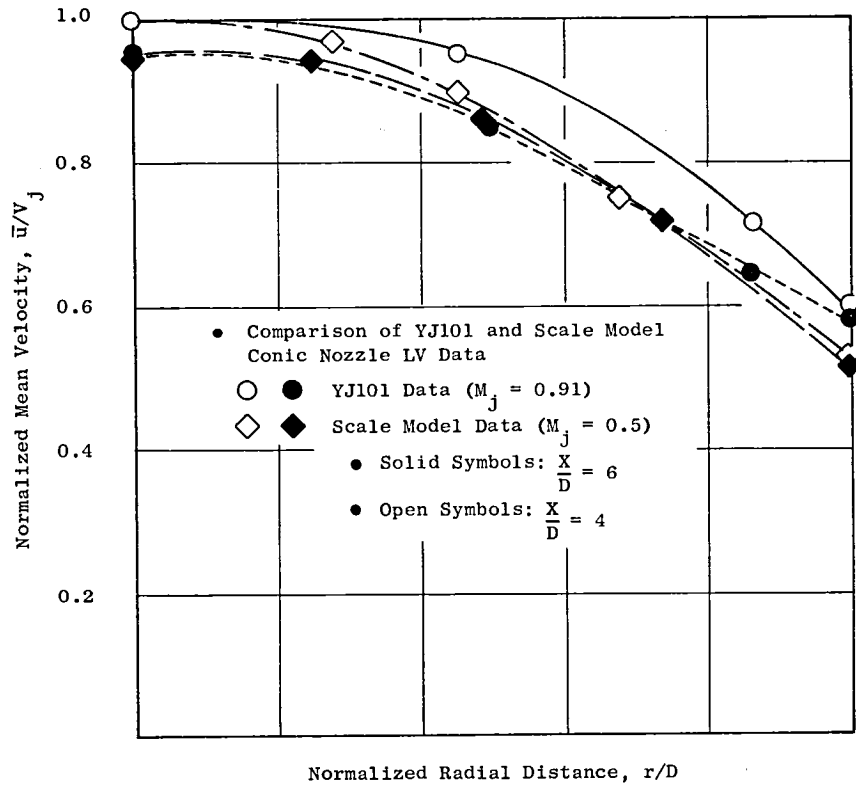


(a) Normalized Mean Velocity Axial Variation

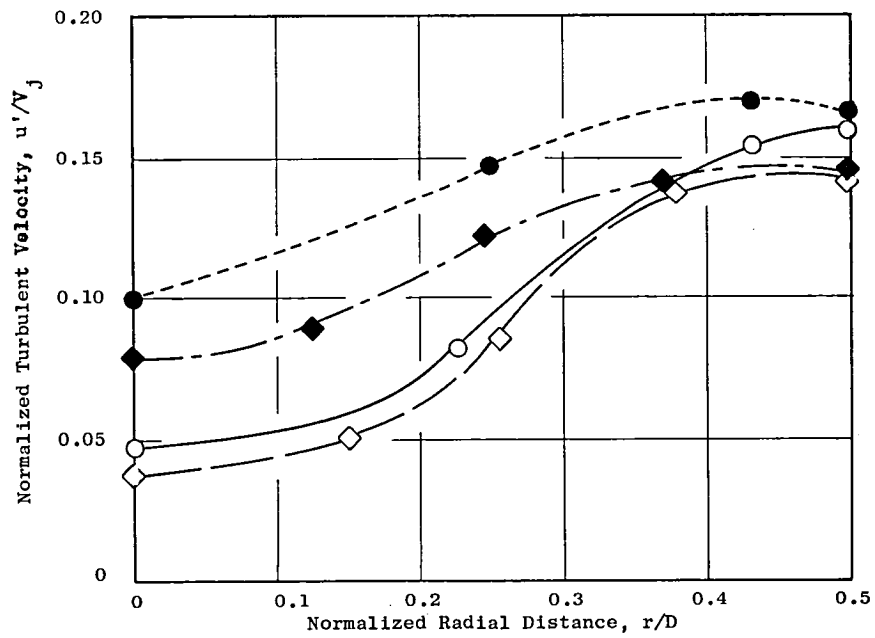


(b) Normalized Turbulent Velocity Axial Variation

Figure 114. Comparison of Measured Mean and Turbulent Velocities for YJ101 Engine and Scale Model Conic Nozzles.

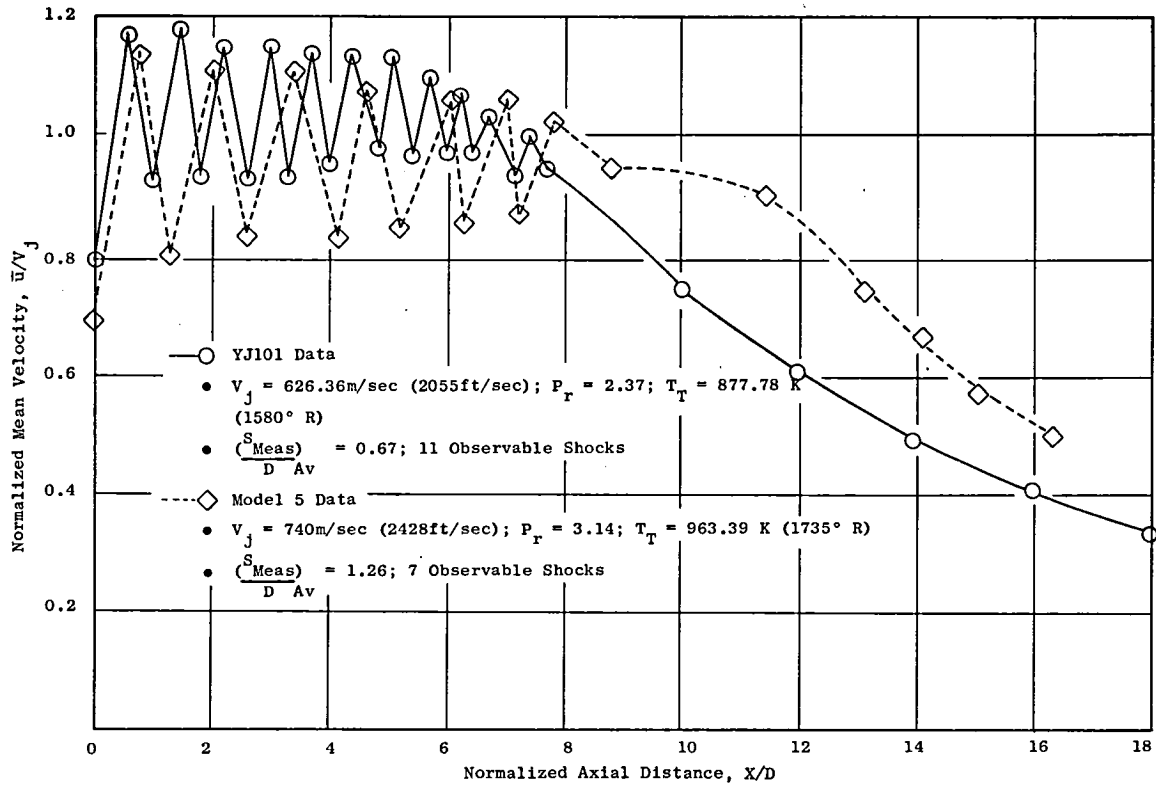


(a) Normalized Mean Velocity Radial Variation

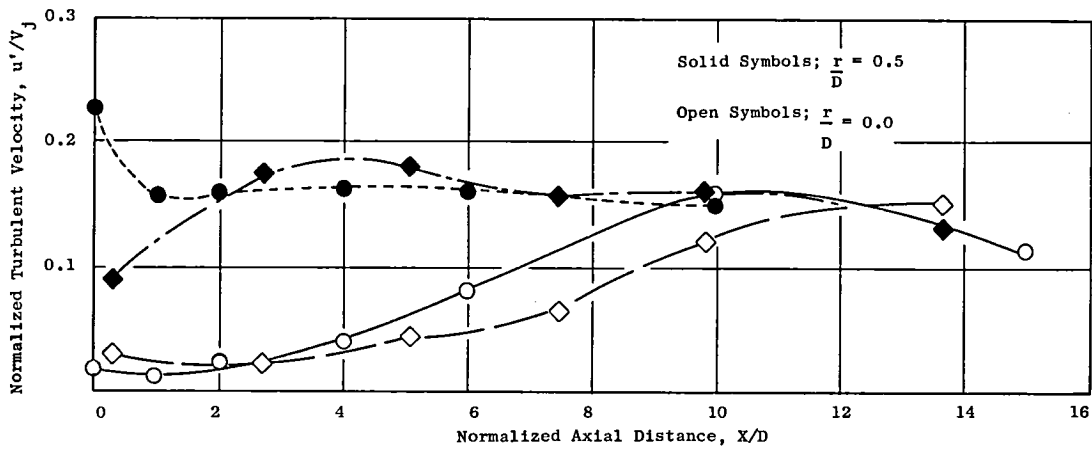


(b) Normalized Turbulent Velocity Radial Variation

Figure 115. Comparison of Measured Mean and Turbulent Velocities for YJ101 and Scale Model Conic Nozzles.



(a) Normalized Mean Velocity Axial Variation



(b) Normalized Turbulent Velocity Axial Variation

Figure 116. Comparison of Measured Mean and Turbulent Velocities for YJ101 Engine and Model Scale Conic Nozzles.

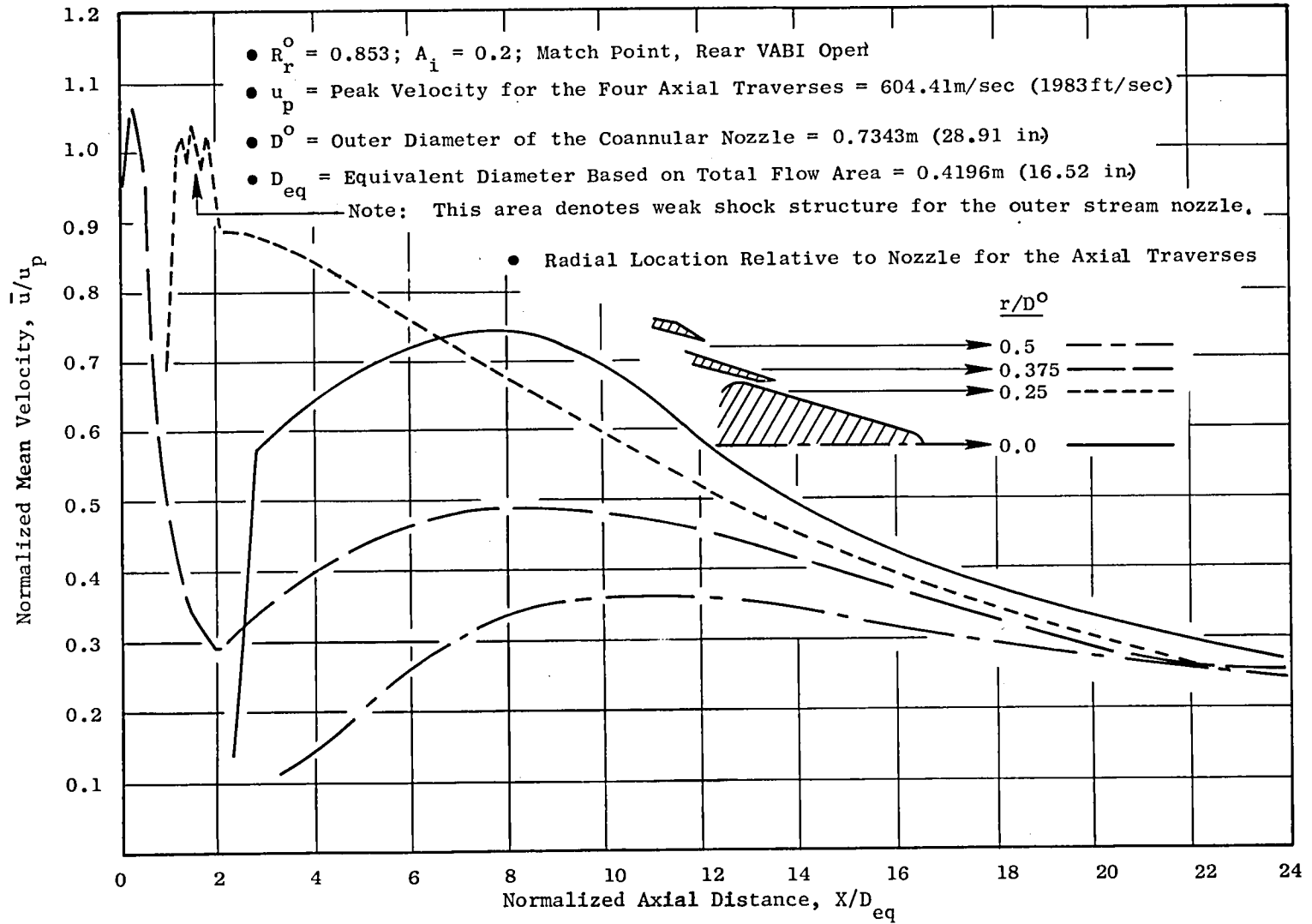


Figure 117. Normalized Mean Velocity Variation at Four Radial Locations.

- $R_r^O = 0.853$; $A_i = 0.2$; Match Point; Aft VABI Open
- u_p = Peak Velocity at this Traverse = 623.93m/sec (2047ft/sec)
- D_{eq} = Equivalent Diameter Based on Total Flow Area = 0.4196m (16.52 in)

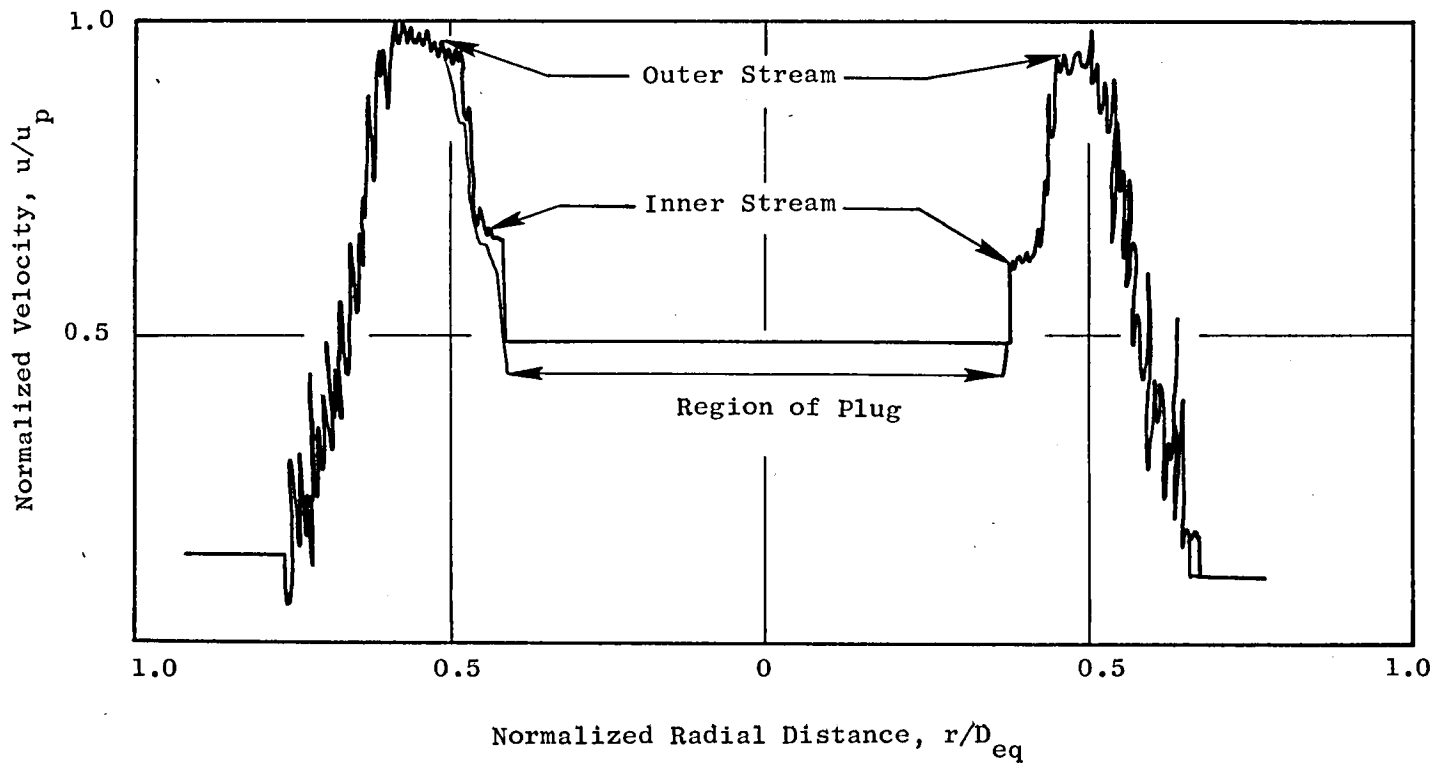
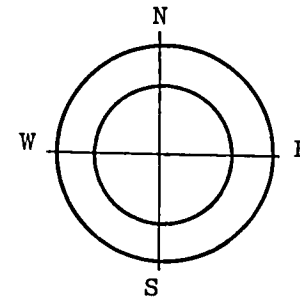
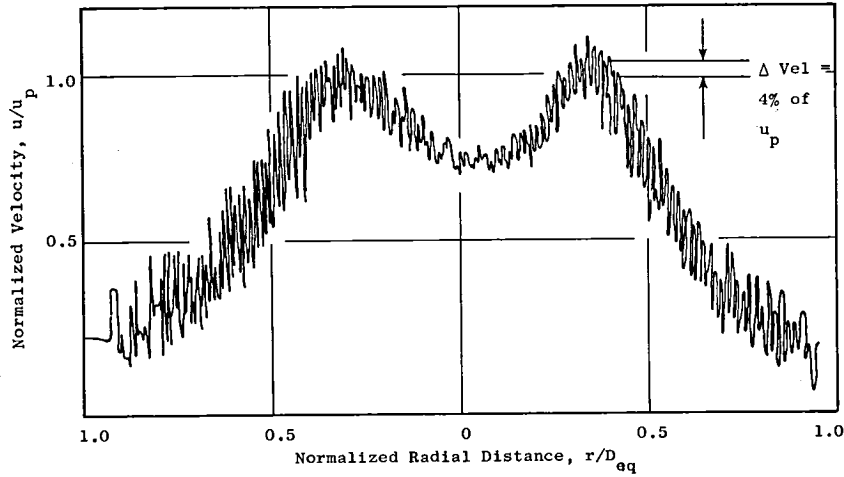
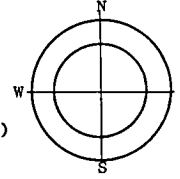


Figure 118. N-S Traverse of the Jet at $X/D_{eq} = 1.1$.

YJ101 LV Measurements of a Coannular Nozzle

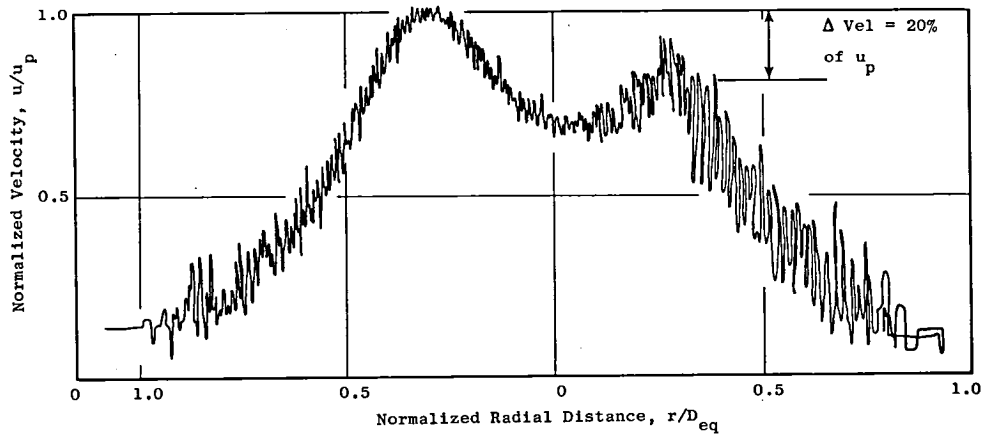
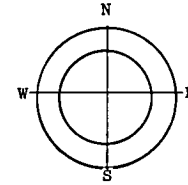
- $R_r^o = 0.853$; $A_1 = 0.2$; Match Point; Aft VABI Open
- u_p = Peak Velocity at this Traverse = 545.89 m/sec (1791 ft/sec)
- D_{eq} = Equivalent Diameter Based on Total Area = 0.4199m (16.52 in.)



(a) E-W Traverse of the Jet Indicating Slight Velocity Profile Assymetry

YJ101 LV Measurements of a Coannular Nozzle

- $R_r^o = 0.853$; $A_1 = 0.2$; Match Point; Aft VABI Open
- u_p = Peak Velocity at this Traverse = 584.91 m/sec (1919 ft/sec)
- D_{eq} = Equivalent Diameter Based on Total Flow Area = 0.4199 m (16.52 in.)



(b) N-S Traverse of the Jet Indicating Velocity Profile Assymetry

Figure 119. Laser Velocimeter Measured Radial Velocity Profiles at $X/D_{eq} = 5$ in Two Mutually Perpendicular Directions (VABI Open).

of the coannular nozzle in the north-south direction. An almost identical observation is made in Figure 120 where the aft VABI chutes are kept closed.*

To further investigate the influence of chutes and struts on jet exit plane mean and turbulent velocities, LV histogram readings are taken behind (along a streamline external to the nozzle) the chutes and the struts. Figures 121 and 122, respectively, show the influence of struts and chutes on the mean and turbulent velocities with the aft VABI chutes kept open and closed. The drop in the mean velocity in Figure 121(a) is due mainly to the proximity of the outer wall of the nozzle. The turbulence levels behind the strut and the chute are not significantly different from the centerline value, indicating that their influence is minor.

5.5.5.2.2 Comparison of Engine and Model Scale Test Results

Next, YJ101 data are compared with scale model coannular data for similar operating conditions. Figure 123 indicates the axial variation of normalized mean velocity variation at $r/D^{\circ} = 0.0$ and 0.5 for both sets of data. One notes the reasonable agreement between the two. The faster decay of the mean velocity for the model data can be attributed to the higher mixed jet velocity which in turn leads to a greater shear in the flow field and, hence, a faster decay in terms of normalized coordinates.

5.5.5.3 Summary of Observations

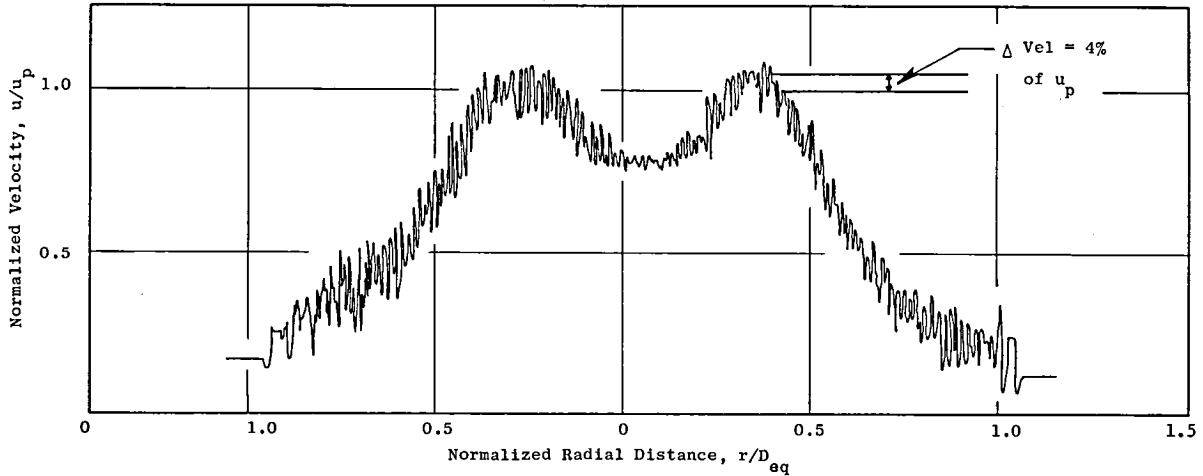
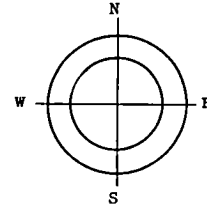
The laser velocimeter measurements of the YJ101 engine conic nozzle showed that the fan flow and core flow mixed satisfactorily so that the conic nozzle exit flow was typical of any conic nozzle flow. Thus, the acoustic results for the conic nozzle are expected (as verified in Section 5.5.2) to be representative of any simple conic nozzle. Additionally, it was found that the exhaust turbulence levels were relatively low and indicative of a rather "clean" engine flow. Reasonable agreement between the engine conic test results and model scale test results were also found.

*Note is taken here to indicate that similar flow assymetry was observed in model tests conducted on Contract NAS3-20619. The flow assymetry is directly proportional to the nozzle build up or manufacturing assymetry; i.e., \bar{u} north/ \bar{u} south $\sim h^{\circ}$ north/ h° south, where h° is the outer nozzle annulus height.⁺ The answer to the question of how does the flow assymetry influence the acoustic suppression (for better or worse) has not been addressed in either the model tests or the engine tests.

⁺For supercritical condition at the nozzle exit plane, the velocity on the side of larger annular height (/area) is expected to be higher from continuity considerations. (An exactly opposite trend will be expected for subcritical exit conditions.)

YJ101 LV Measurements of a Coannular Nozzle

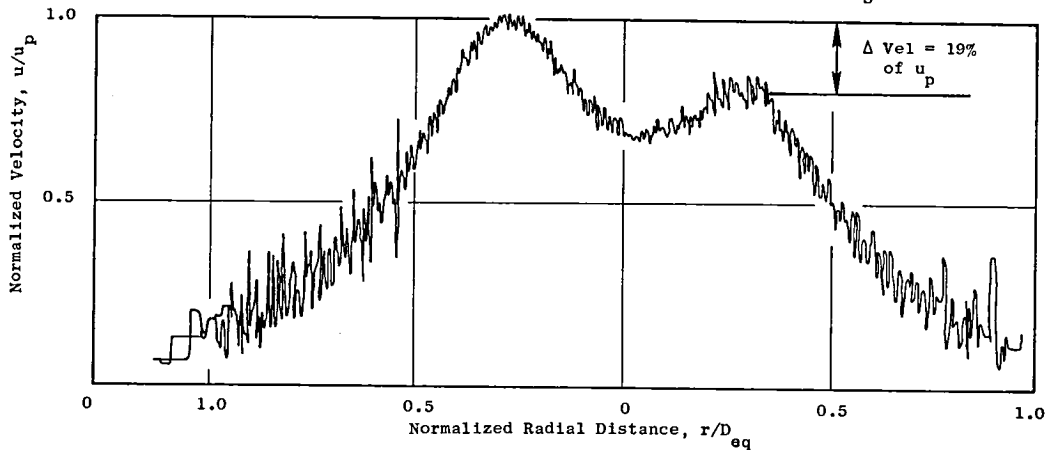
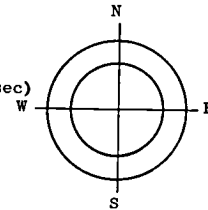
- $R_r^o = 0.853$, $A_i = 0.2$; Match Point; Aft VABI Closed
- u_p = Peak Velocity at this Traverse = 559 m/sec (1834 ft/sec)
- D_{eq} = Equivalent Diameter Based on Total Flow Area = 0.4199 m (16.52 in.)



(a) E-W Traverse of the Jet Indicating Slight Velocity Profile Assymetry

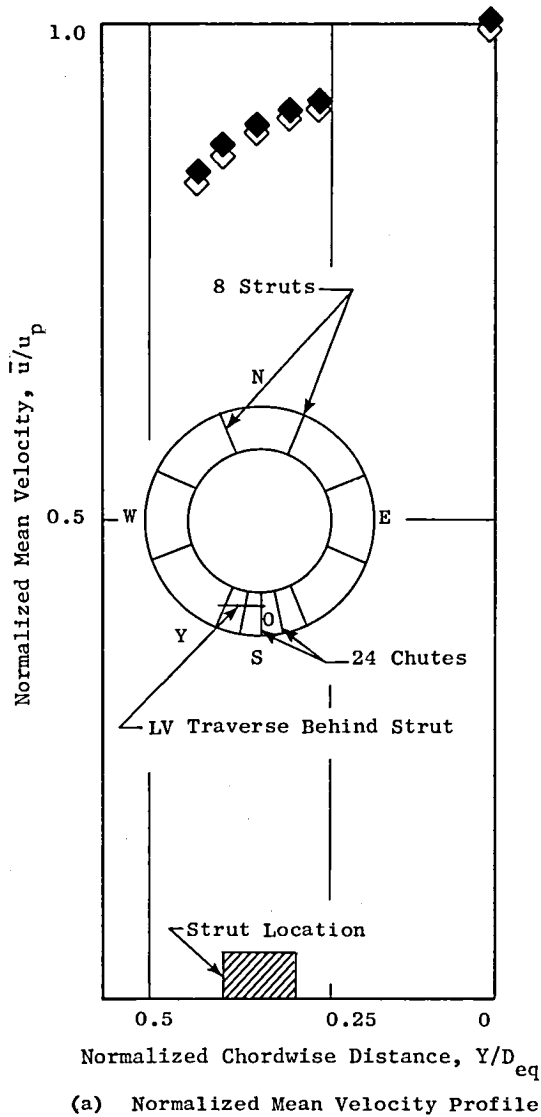
YJ101 LV Measurements of a Coannular Nozzle

- $R_r^o = 0.853$; $A_i = 0.2$; Match Point; Aft VABI Closed
- u_p = Peak Velocity at this Traverse = 584.91 m/sec (1919 ft/sec)
- D_{eq} = Equivalent Diameter Based on Total Flow Area = 0.4199 m (16.52 in.)



(b) N-S Traverse of the Jet Indicating Velocity Profile Assymetry

Figure 120. Laser Velocimeter Measured Radial Velocity Profiles at $X/D_{eq} = 5$ in Two Mutually Perpendicular Directions (VABI Closed).



- LV Measurements on Coannular Plug
Nozzle ($R_r^o = 0.853$ C-D; $A_r^i = 0.2$)
- $X/D_{eq} = 0$, $r/D_{eq} = 0.43$, $\bar{u}_p = 731.5\text{m/sec}$
(2400ft/sec)
- Engine Measurements on YJ101 VCE
 $D_{eq} = 0.4199\text{m}$ (16.51 in.)
 $D^o = 0.7343\text{m}$ (28.91 in.)
- Solid Symbols Denote Aft VABI Closed
- Open Symbols Denote Aft VABI Open

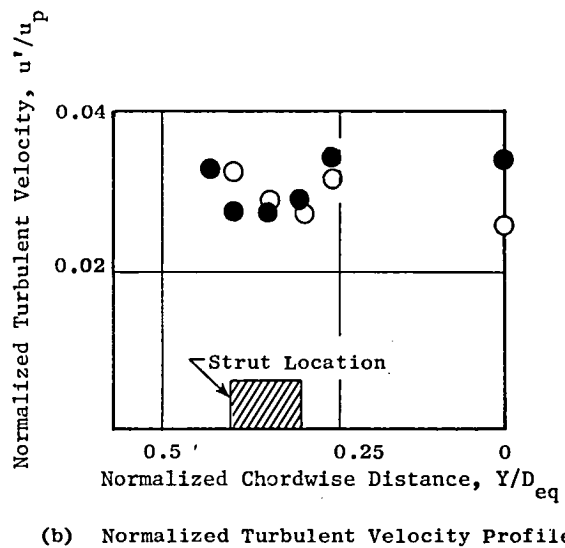
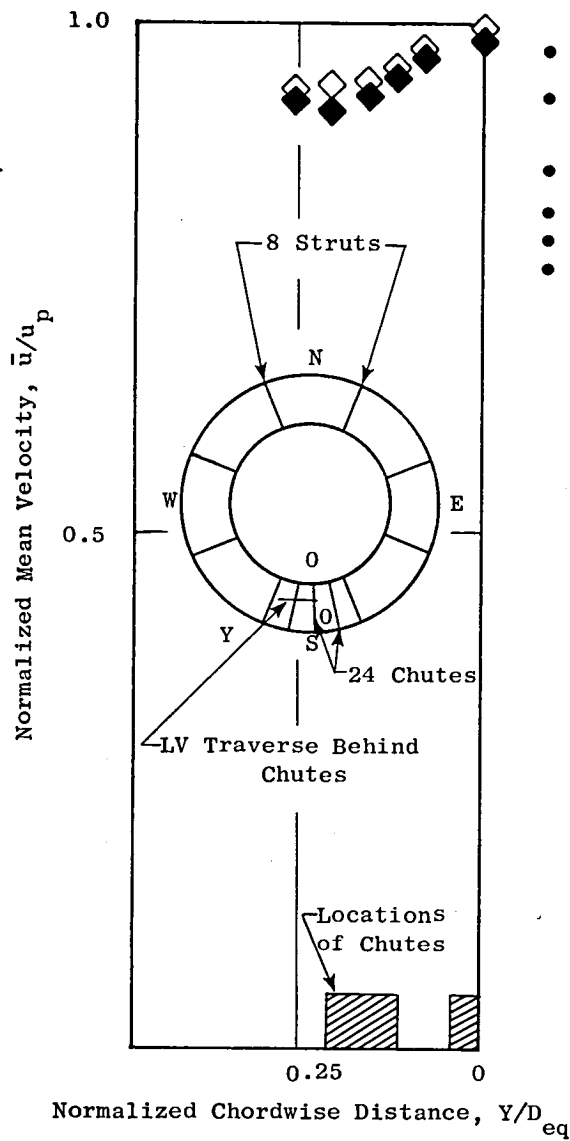
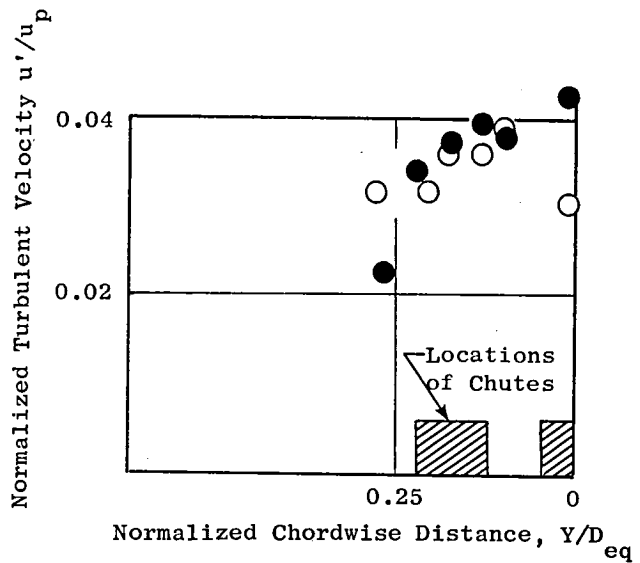


Figure 121. Influence of Flow Struts on Mean and Turbulent Velocity Profiles.



(a) Normalized Mean Velocity Profile

- $R_r^o = 0.853$ C-D, $A_r^i = 0.2$
- $X/D_{eq} = 0$; $r/D^o = 0.45$; $\bar{u}_p = 694.94$ m/sec (2280 ft/sec)
- $D_{eq} = 0.4199$ m (16.52 in.)
- $D^o = 0.7343$ m (28.91 in.)
- Solid Symbols Denote Aft VABI Closed
- Open Symbols Denote Aft VABI Open

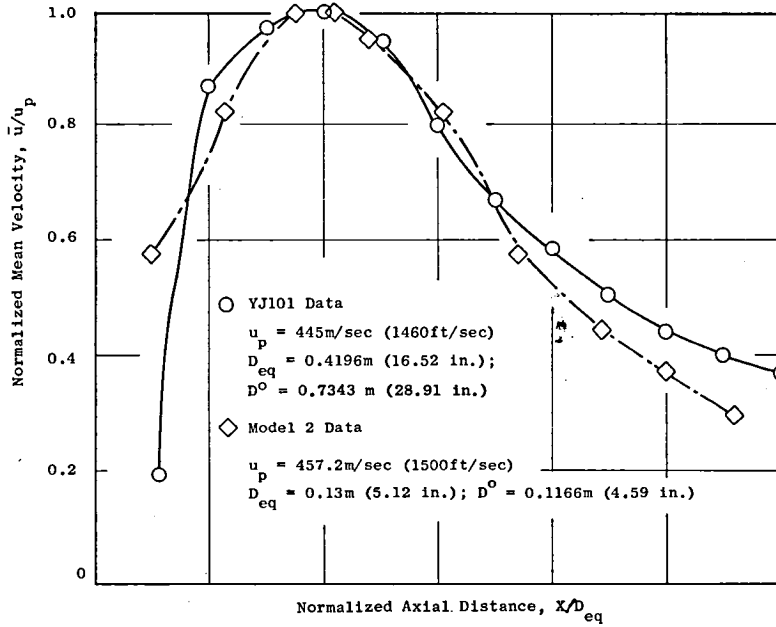


(b) Normalized Turbulent Velocity Profile

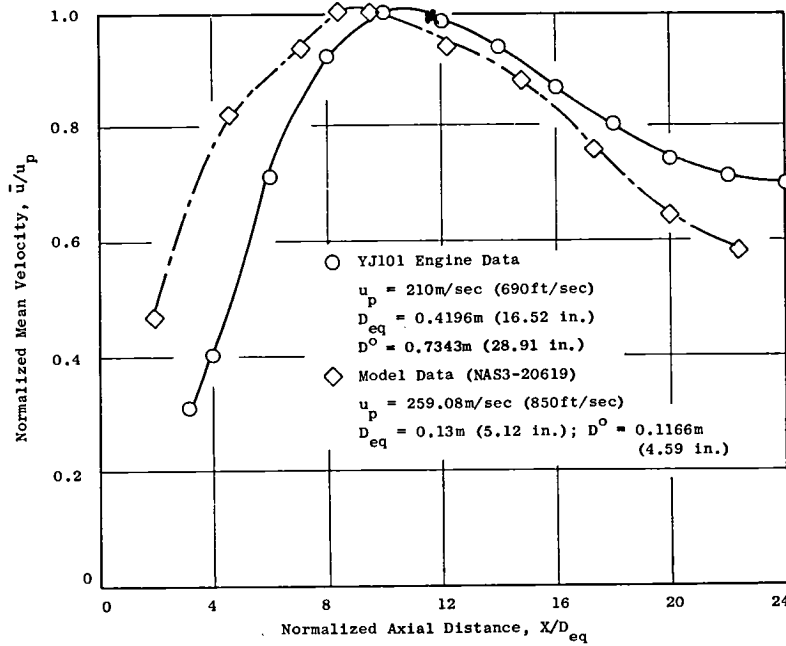
Figure 122. Influence of Chutes on Mean Velocity and Turbulent Velocity Profiles.

Comparison of YJ101 and Model 2 Coannular Nozzle LV Data

$R_r^0 = 0.853$; $A_1 = 0.2$ for Both Cases D^0 = Outer Diameter of the Coannular Nozzle
 u_p = Peak Velocity of the Axial Traverse D_{eq} = Equivalent Diameter Based on Total Flow Area



(a) Normalized Mean Velocity Axial Variation at $\frac{r}{D_0} = 0.0$



(b) Normalized Mean Velocity Axial Variation at $\frac{r}{D_0} = 0.5$

Figure 123. Comparison of Measured Mean Velocity of Two Radial Locations for YJ101 Engine and Model Coannular Plug Nozzles.

The key observation made from the LV measurements on the coannular plug nozzle is that the inverted velocity profile of a coannular nozzle suppresses the shock noise by weakening the shock cell structure as compared to an equivalent conic nozzle. It was also found that the influence of struts and chutes on the mean and turbulent velocity characteristics of the YJ101 nozzle is minimal. Comparison of YJ101 engine and scale model data for similar operating conditions yield comparable mean and turbulent velocity profiles.

These measurements suggest that the internal flow obstructions, etc., will not cause any significant influence in the exhaust plume mixing to cause excess jet noise.

5.5.6 Engine Data Noise/Prediction Comparisons

In order to more closely examine the engine acoustic measurements, a series of engine data versus acoustic prediction comparisons were performed. The point-of-view taken here is to evaluate the extent to which nozzle jet mixing and shock noise and other engine component noise sources (fan, turbine, core, internal obstructions, etc.) were influencing the measured data, and to assess the validity of the prediction schemes selected. Described below is the methodology of the prediction methods used in this study and the engine data/prediction comparisons for three sample cases.

5.5.6.1 Methodology of Predictions

The various methods used to predict the engine component noise sources are briefly outlined below.

a. Coannular Plug Nozzle Jet Mixing Noise Prediction

The coannular plug nozzle jet mixing noise prediction method was developed under NASA Contract NAS3-20619 (Reference 13). It is based on analytical principles and is supported by the data base obtained under NAS3-19777 (Reference 10) and NAS3-20619. The prediction procedure as briefly summarized below has four main steps:

- (i) Predict the spectrum at $\theta = 90^\circ$, also called the source spectrum. Two regions are identified in this spectrum, namely
 - Outer flow region producing the high frequency spectrum
 - Fully mixed or merged region producing the low frequency spectrum

Characteristic velocity and length scales are identified for each of the two regions. Normalized spectra for the two regions were empirically determined based on coannular and conic nozzle data. The

normalized curves were within $\pm 1/2$ dB for the low frequency spectrum, and $\pm 1 1/2$ dB for the high frequency spectrum. The data base consisted of 7 coannular plug nozzles operated over a wide temperature/velocity range.

- (ii) Apply convective amplification and doppler shift to the low and high frequency source spectra. The theoretical expressions for convective amplification and doppler shift are functions of convection Mach number, M_c and θ respectively.
- (iii) Apply fluid shielding for appropriate angles. A normalized universal fluid shielding curve was devised from modern theoretical jet acoustic concepts and calibrated from coannular plug nozzle data. The shielding expression used is a function of angle and frequency for both the low and high frequency components of the convection amplified source spectrum.
- (iv) Having individually applied convective amplification and fluid shielding to the low and high frequency components of the source spectrum, they are merged to obtain the combined spectrum at each angle. Thus, the spectrum at each angle is predicted. Details of this method are found in Reference 13.

b. Coannular Shock Noise Prediction

This method, also developed under NASA Contract NAS3-20619 (Reference 13), is based on the Fisher-Harper Bourne theory for conic nozzles with a few modifications. The parameters that were modified were

- The shock cell spacing.
- The number of shock cells.
- The effective pressure ratio which is determined based on the total thrust and flow area.

Details of this method are found in Reference 13.

c. Fan Noise Prediction

The method of Heidman (Reference 15) adopted in the NASA ANOPP aircraft noise prediction computer program, was used to predict the fan noise from each of the three fan stages. This method separates the noise into six components—namely, broadband fan exhaust noise, rotor-stator tone exhaust noise, inlet broadband noise, inlet combination tone noise, inlet rotor-stator tone noise and inlet flow distortion tone noise. It must be noted that this method does not account for treatment on the inlet or any attenuation/amplification of the fan exhaust noise.

d. Turbine Noise Prediction

The method due to Kresja et. al., (Reference 16), also adopted in ANOPP, was used to predict the noise from both the low and high pressure turbines. This method predicts both the broadband and discrete tone components of the turbine noise.

e. Core Noise Prediction

The GE core noise prediction (Reference 17) procedure, also adopted in ANOPP, was used to predict the combustion noise. This method predicts the low frequency core noise spectrum at every angle.

f. Strut/Obstruction Noise

The strut/obstruction noise program was developed based on Hayden's (Reference 18) method and some earlier work at GE (Reference 19). Two basic components are predicted -

- Broadband noise due to fluctuating lift/drag
- Narrow band noise due to vortex shedding off the trailing edge of the strut/obstruction.

It must be noted that this procedure also assumes no amplification/attenuation of the noise as it passes through the flowpath.

5.5.6.2 Illustration of Engine Component Noise Breakdown and Comparison With Predictions

a. Coannular Jet Mixing and Shock Noise Comparisons

As jet mixing and shock noise are expected to be the dominant noise sources for the engine over most of the range of operating conditions, comparisons between the data and prediction of these components are discussed first. Three operating conditions for the 0.853 radius-ratio, 0.2 area-ratio, coannular nozzle with CD outer nozzle were selected to represent typical take-off, cutback and approach conditions. The mass-averaged velocities at these three conditions were 713.8 m/sec (2342 ft/sec), 507.8 m/sec (1666 ft/sec) and 368.2 m/sec (1208 ft/sec), respectively. Figures 124(a) through 124(c) show comparisons between the measured and predicted total jet mixing and shock noise OASPL directivities for the engine on a 100 ft arc for these three conditions. The comparisons show very good agreement at the highest mass averaged velocity condition [Figure 124(a)] at all angles. At the two lower mass averaged velocity conditions, the agreement is still good except at a few angles ($\theta_i = 110, 120^\circ$). The discrepancies at these angles could be due to the shielding model used in the predictions. To further assess the accuracy of the prediction procedure, the predicted spectra at $\theta_i = 50^\circ, 90^\circ$ and 140° were compared with

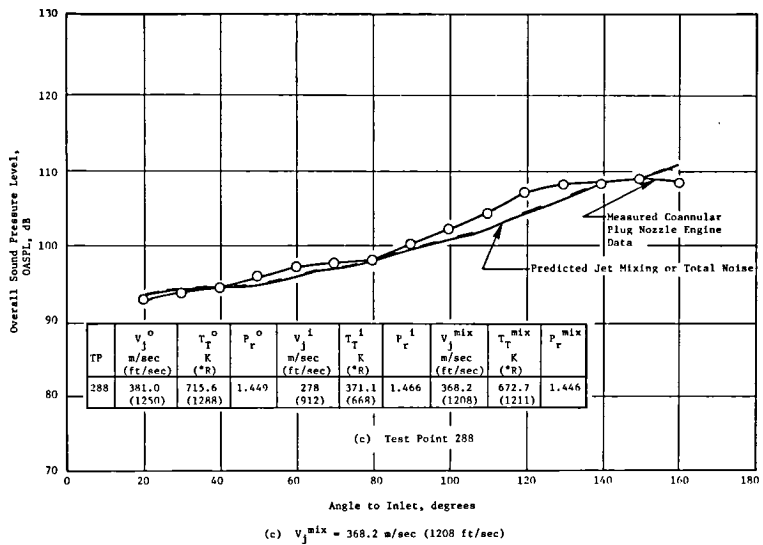
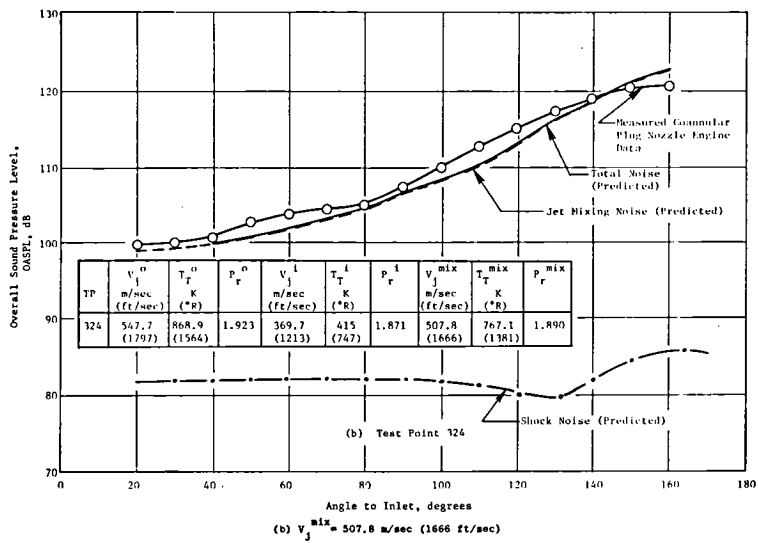
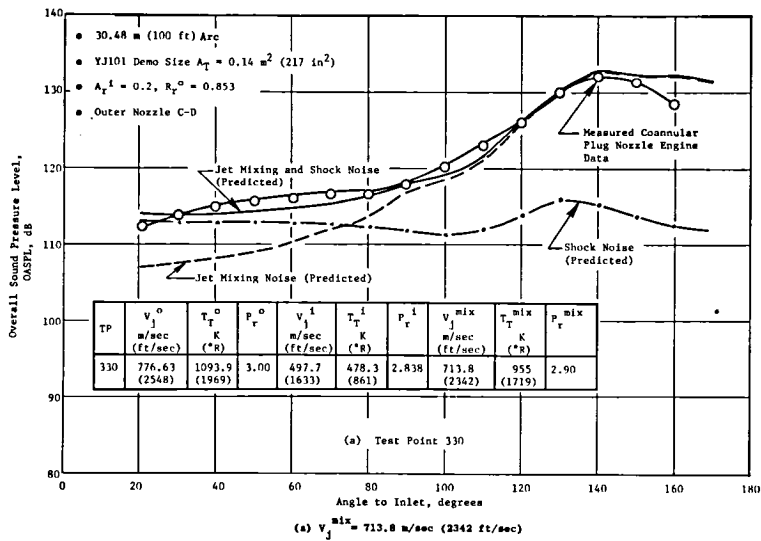


Figure 124. Comparison of the Measured YJ101 Coannular Plug Nozzle Engine OASPL Directivity with That Predicted for Jet Mixing and Shock Noise.

data (Figure 125 through 127). The predicted and measured spectra at all three angles and test conditions show good agreement for all frequencies except in the aft quadrant in the 5-20 KHz, 1/3 octave bands, where the engine data appears to have additional noise related to the aft-fan-radiated noise, as discussed later in this section. It is evident that this high frequency hump contributes more to the OASPL at the lower power settings than at the higher power settings, thus resulting in an increase in engine OASPL's. Additional comparisons on the 30.48 m (100 ft) arc for other coannular nozzle configurations are presented in Reference 4.

- Additional Jet Noise Predictions

As the jet mixing noise prediction procedure does account for the influence of outer nozzle radius ratio and inner to outer nozzle area ratio effects, in order to demonstrate these influences, additional predictions were made for a full-scale engine [i.e., $A_T = 0.9032 \text{ m}^2$ (1400 in.²)] at a 731.5 m (2400 ft) sideline distance. Figures 128 through 130 show comparisons of the predicted peak PNL's normalized for thrust and density vs $10 \log_{10} (V_j^{\text{mix}}/a_o)$ for three area ratios ($A_T^i = 0.1, 0.2$ and 0.475) at the same outer nozzle radius ratio ($R_r^o = 0.853$). The predicted levels are observed to agree with the measured engine data for large values of $10 \log_{10} V_j^{\text{mix}}/a_o$.

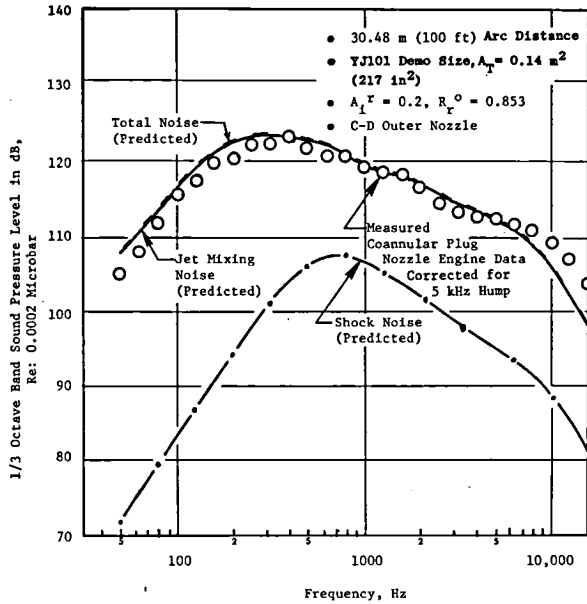
At lower power settings, the predicted levels are observed to be lower than those measured. The high frequency hump identified above was removed from the engine data and the PNL's recalculated. Removal of the high frequency hump resulted in the lowering of PNL's at the lower power setting by as much as 1.5 dB at the 731.5 m (2400 ft) sideline, thus bringing the predictions much closer to the measured data (solid symbols on the Figures 128 through 130 represent the data corrected for the high frequency hump).

To demonstrate the outer nozzle radius ratio effects, the PNL_{max} normalized for thrust and density were predicted over a range of mass averaged velocities for three outer nozzle radius ratios ($R_r^o = 0.816, 0.853, 0.875$) at the same area ratio ($A_T^i = 0.2$), as shown in Figures 131 through 133. The predicted trends agree with measured data (corrected for the aft-radiated turbomachinery noise). Thus the coannular plug nozzle jet and shock noise predictions developed by GE under Contract NAS3-20619 show excellent agreement with the measured YJ101 engine data over a wide range of cycle conditions and coannular plug nozzle geometries.

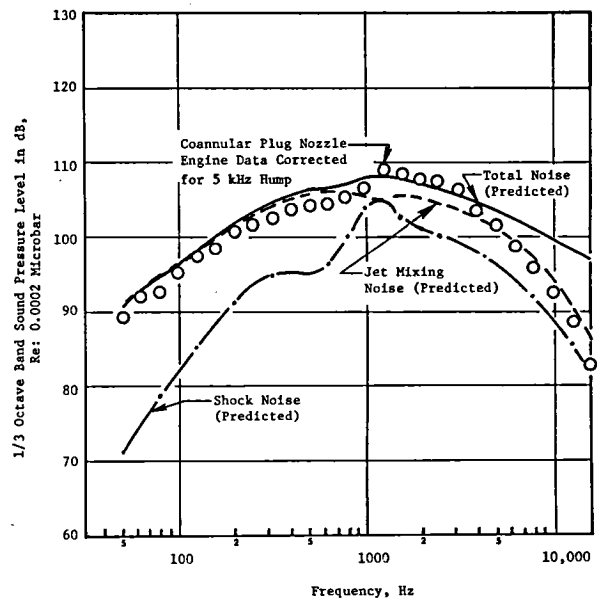
- b. Fan Noise Comparisons

As the Heidman method (Reference 15) predicts the noise from each stage of the fan separately and then adds the noise levels from each stage assuming them to be uncorrelated noise sources, the ANOPP run was set up in such a way

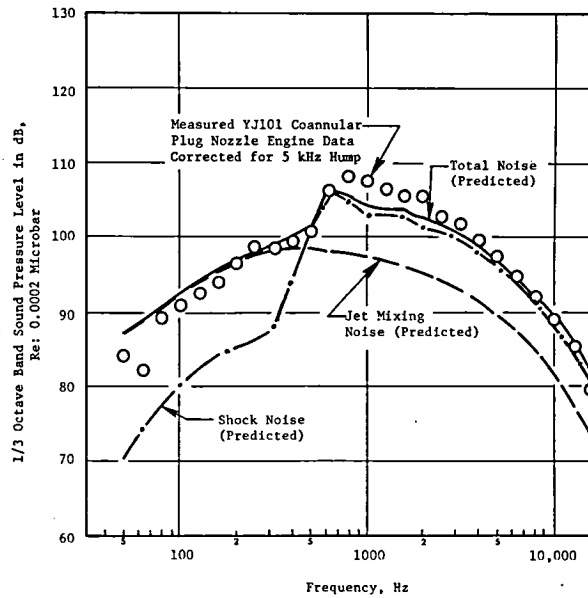
Test Point	V_j^o m/sec (ft/sec)	T_{T^o} K (*R)	P_{T^o}	V_j^i m/sec (ft/sec)	T_{T^i} K (*R)	P_{T^i}	V_j^{mix} m/sec (ft/sec)	$T_{T^{mix}}$ K (*R)	$P_{T^{mix}}$
330	776.63 (2548)	1093.9 (1969)	3.0	497.7 (1633)	478.3 (861)	2.838	713.8 (2342)	955 (1719)	2.90



(a) $\theta_1 = 140^\circ$



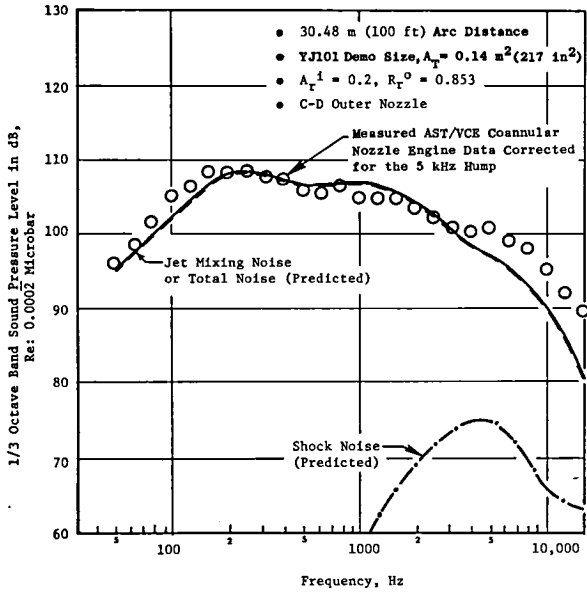
(b) $\theta_1 = 90^\circ$



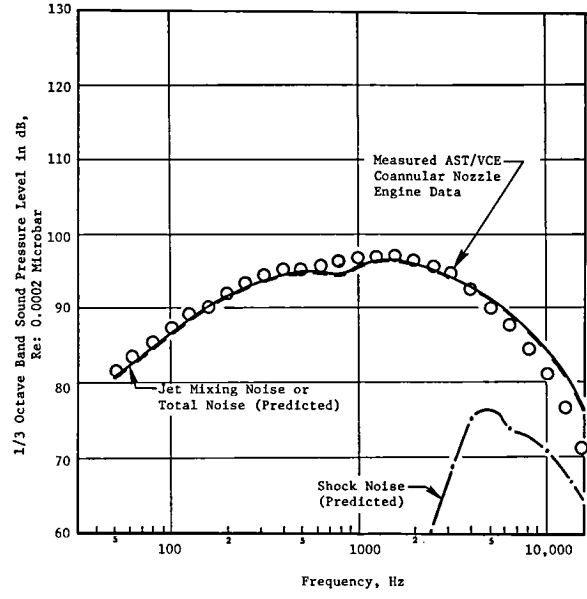
(c) $\theta_1 = 50^\circ$

Figure 125. Comparison of the Predicted Jet Mixing and Shock Sound Pressure Spectra with the Measured Coannular Plug Nozzle Engine Data at $V_j^{mix} = 713.8$ m/sec (2342 ft/sec), a Typical Takeoff Condition.

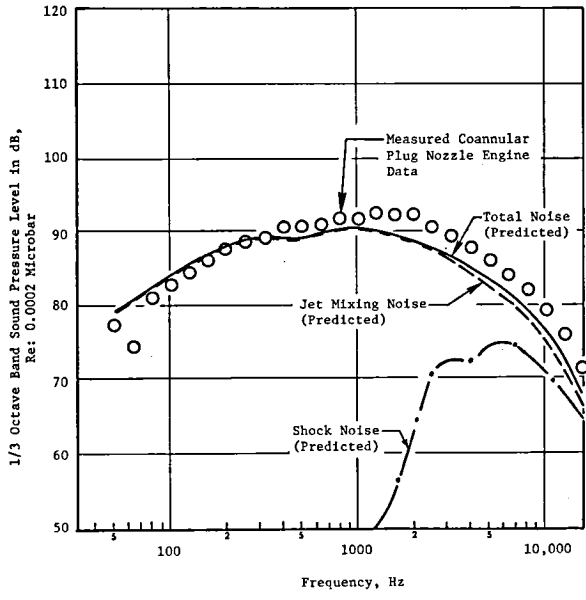
Test Point	V_j^o m/sec (ft/sec)	T_T^o K (*R)	P_r^o	V_j^i m/sec (ft/sec)	T_T^i K (*R)	P_r^i	V_j^{mix} m/sec (ft/sec)	T_T^{mix} K (*R)	P_r^{mix}
324	547.7 (1797)	868.9 (1564)	1.923	369.7 (1213)	415 (747)	1.871	507.8 (1666)	767.1 (1381)	1.890



(a) $\theta_1 = 140^\circ$



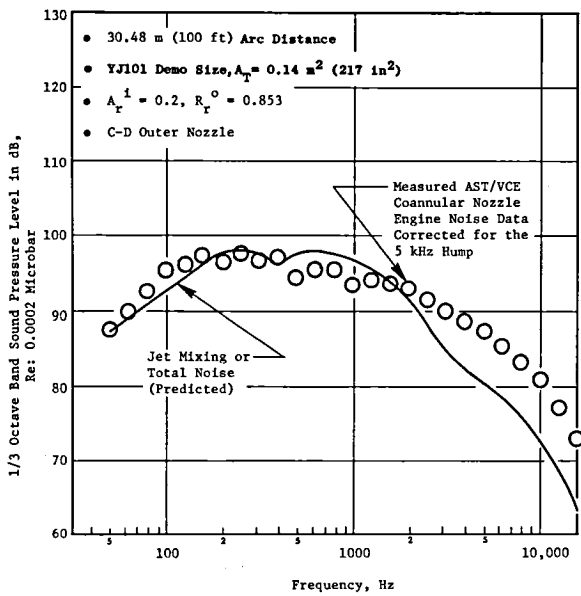
(b) $\theta_1 = 90^\circ$



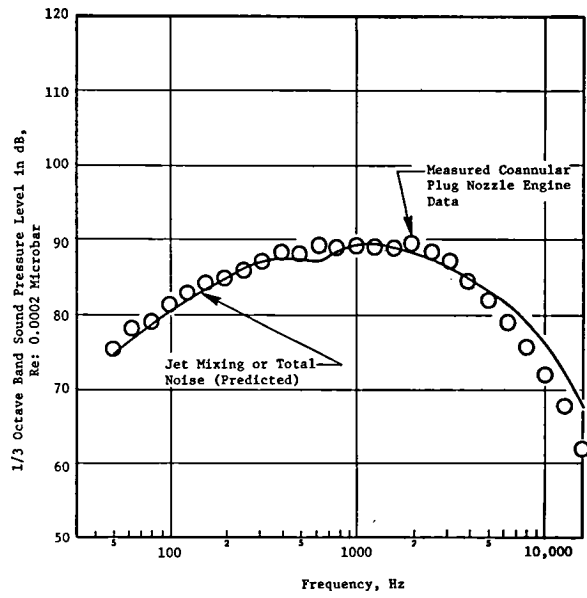
(c) $\theta_1 = 50^\circ$

Figure 126. Comparison of the Predicted Jet Mixing and Shock Sound Pressure Spectra with the Measured Coannular Plug Nozzle Engine Data at $V_j^{mix} = 507.8$ m/sec (1666 ft/sec), a Typical Takeoff Cutback Condition.

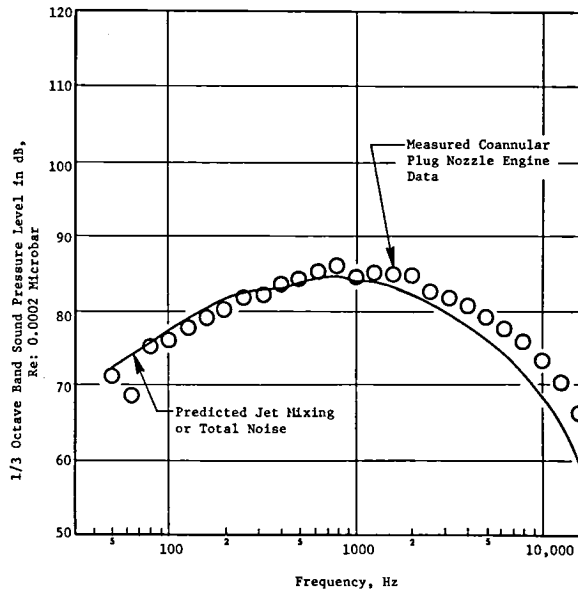
Test Point	V_j^o m/sec (ft/sec)	T_T^o K (*R)	P_r^o	V_j^i m/sec (ft/sec)	T_T^i K (*R)	P_r^i	V_j^{mix} m/sec (ft/sec)	T_T^{mix} K (*R)	P_r^{mix}
288	381.0 (1250)	715.6 (1288)	1.449	278 (912)	371.1 (668)	1.466	368.2 (1208)	672.7 (1211)	1.446



(a) $\theta_1 = 140^\circ$



(b) $\theta_1 = 90^\circ$



(c) $\theta_1 = 50^\circ$

Figure 127. Comparison of the Predicted Jet Mixing Sound Pressure Spectra with the Measured Coannular Plug Nozzle Engine Data at $V_j^{mix} = 368.2$ m/sec (1208 ft/sec), a Typical Approach Condition.

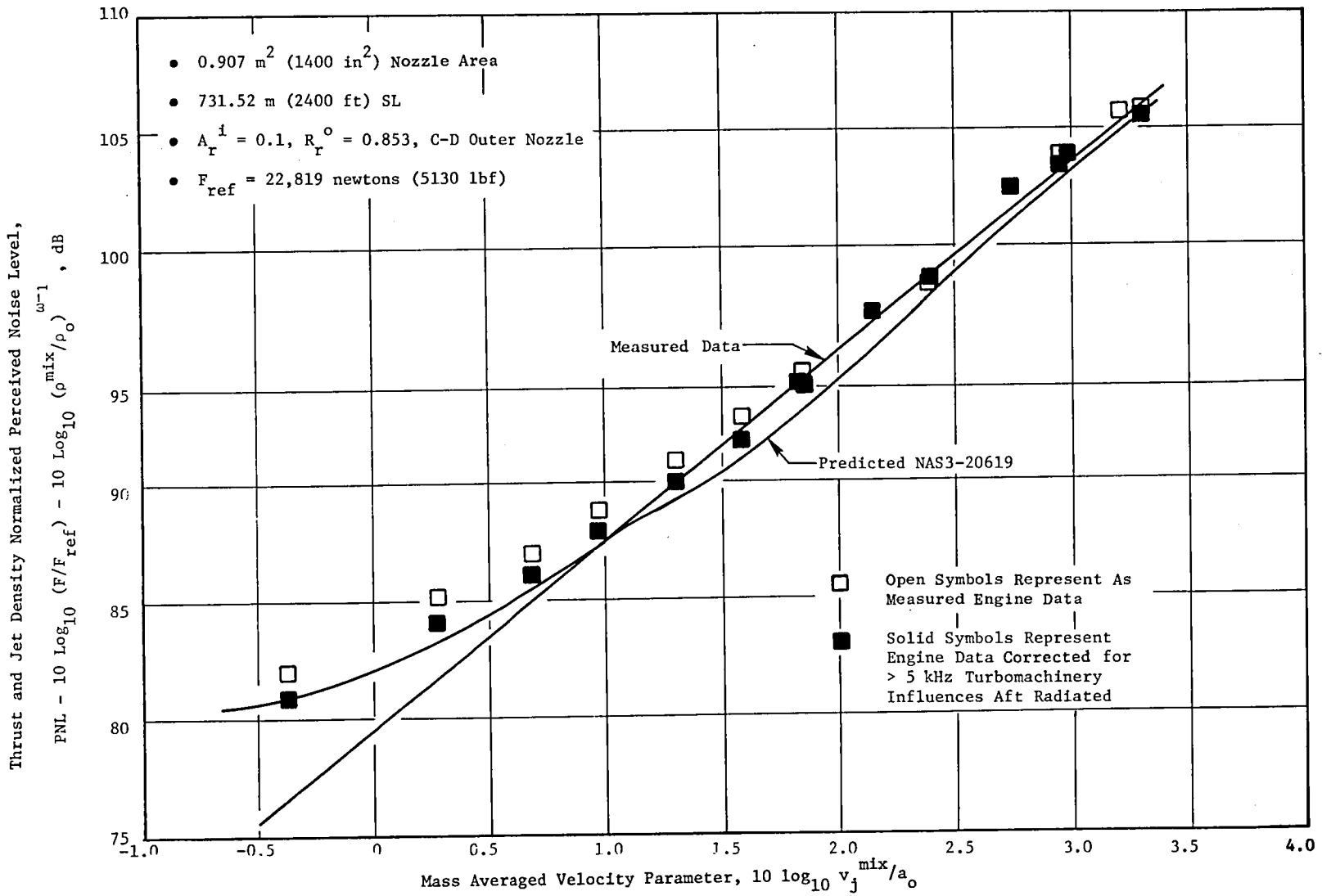


Figure 128. Comparison of the Measured and Predicted Variation of Normalized PNL at $A_r^i = 0.1$.

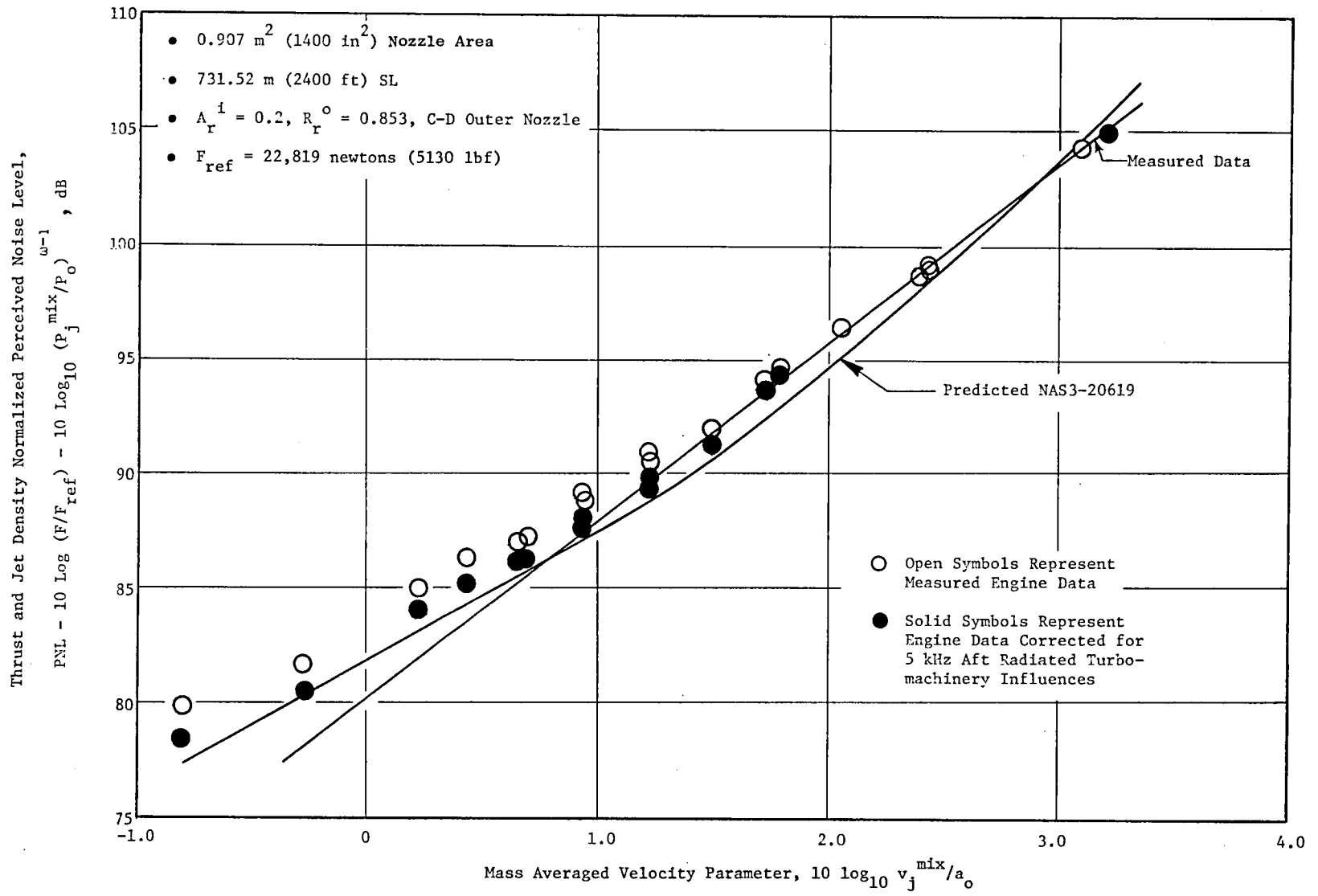


Figure 129. Comparison of the Measured and Predicted Variation of Normalized PNL at $A_r^i = 0.2$

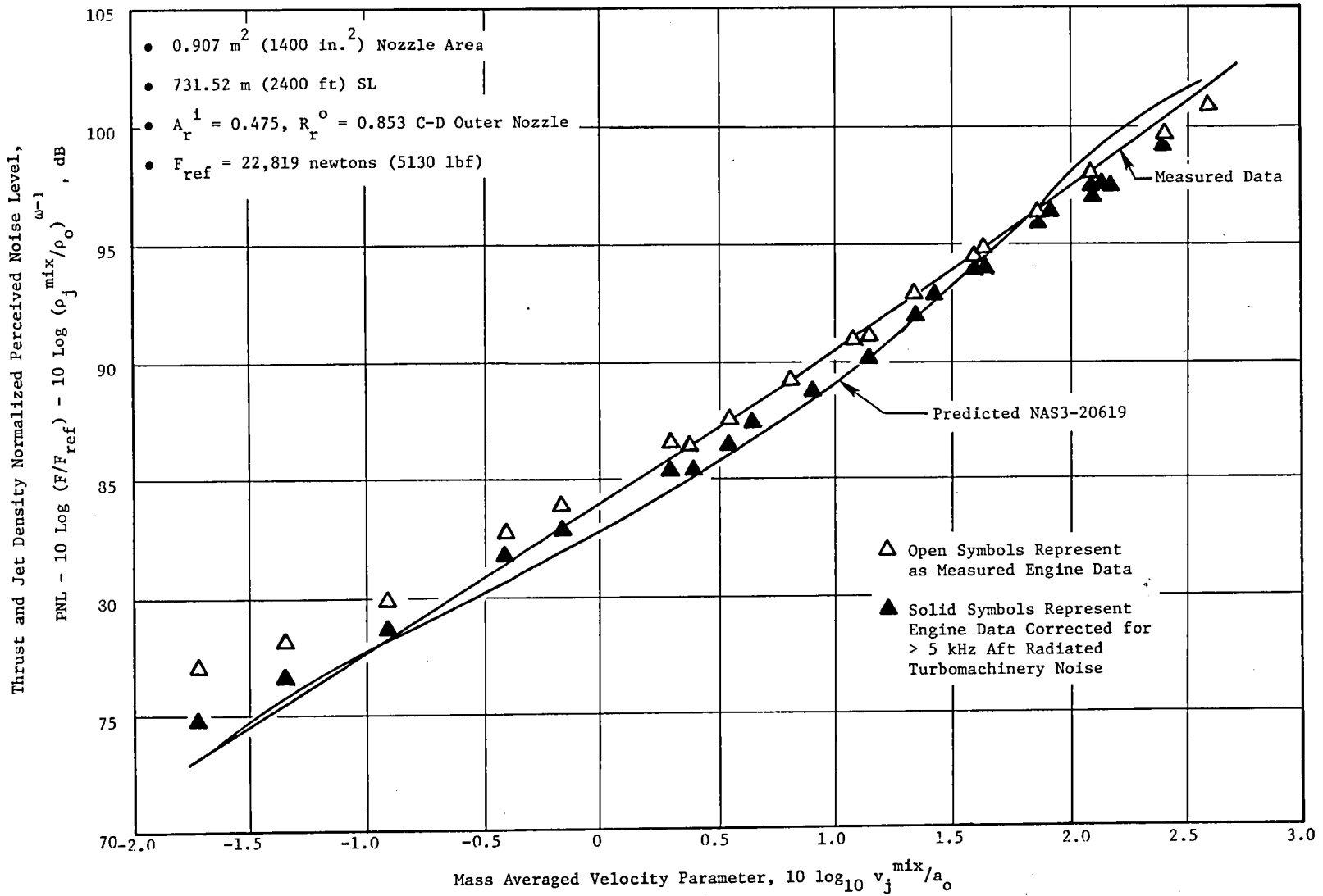


Figure 130. Comparison of the Measured and Predicted Variation of Normalized PNL at $A_r^i = 0.475$.

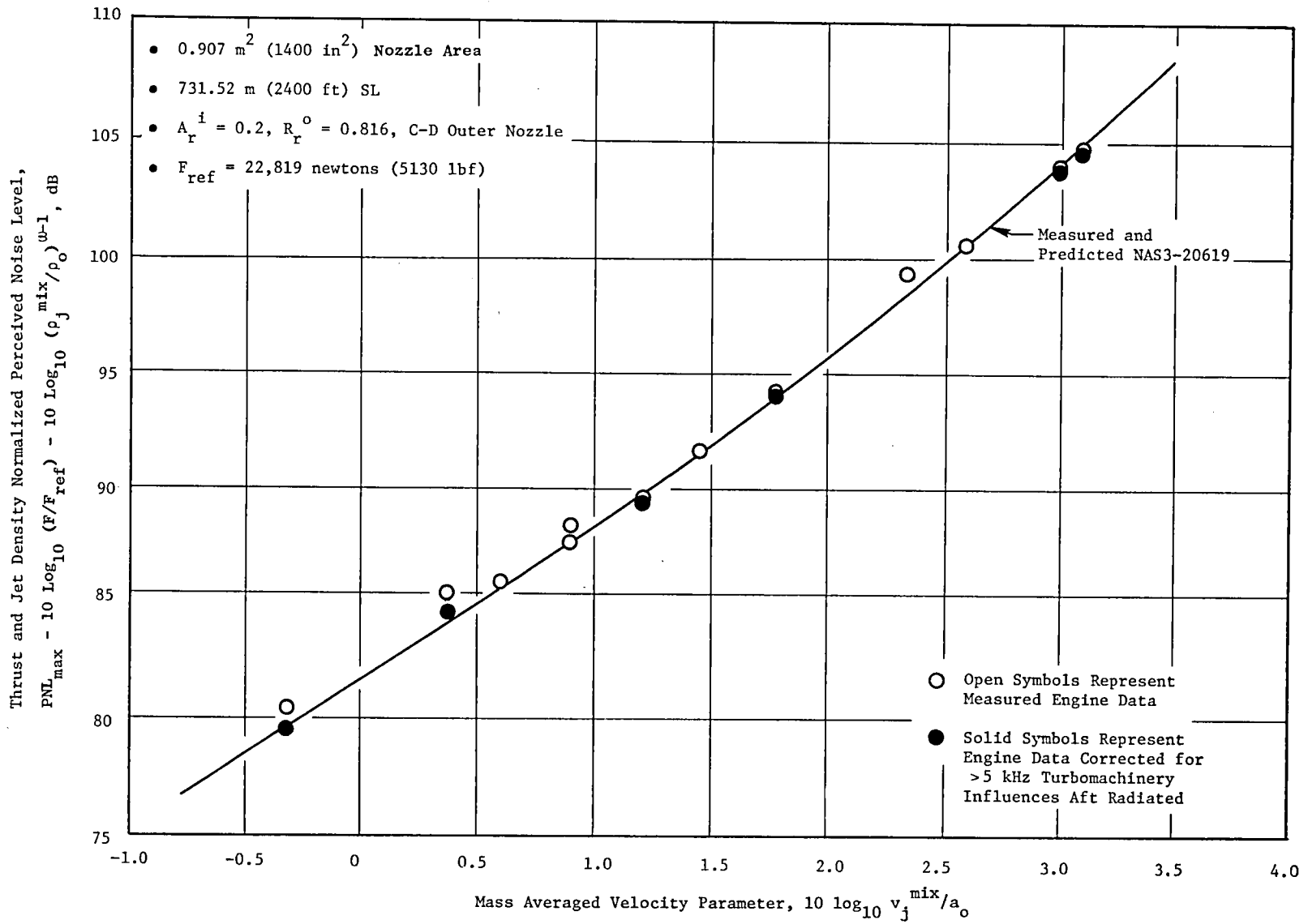


Figure 131. Comparison of the Measured and Predicted Variation of Normalized PNL at $R_r^o = 0.816$.

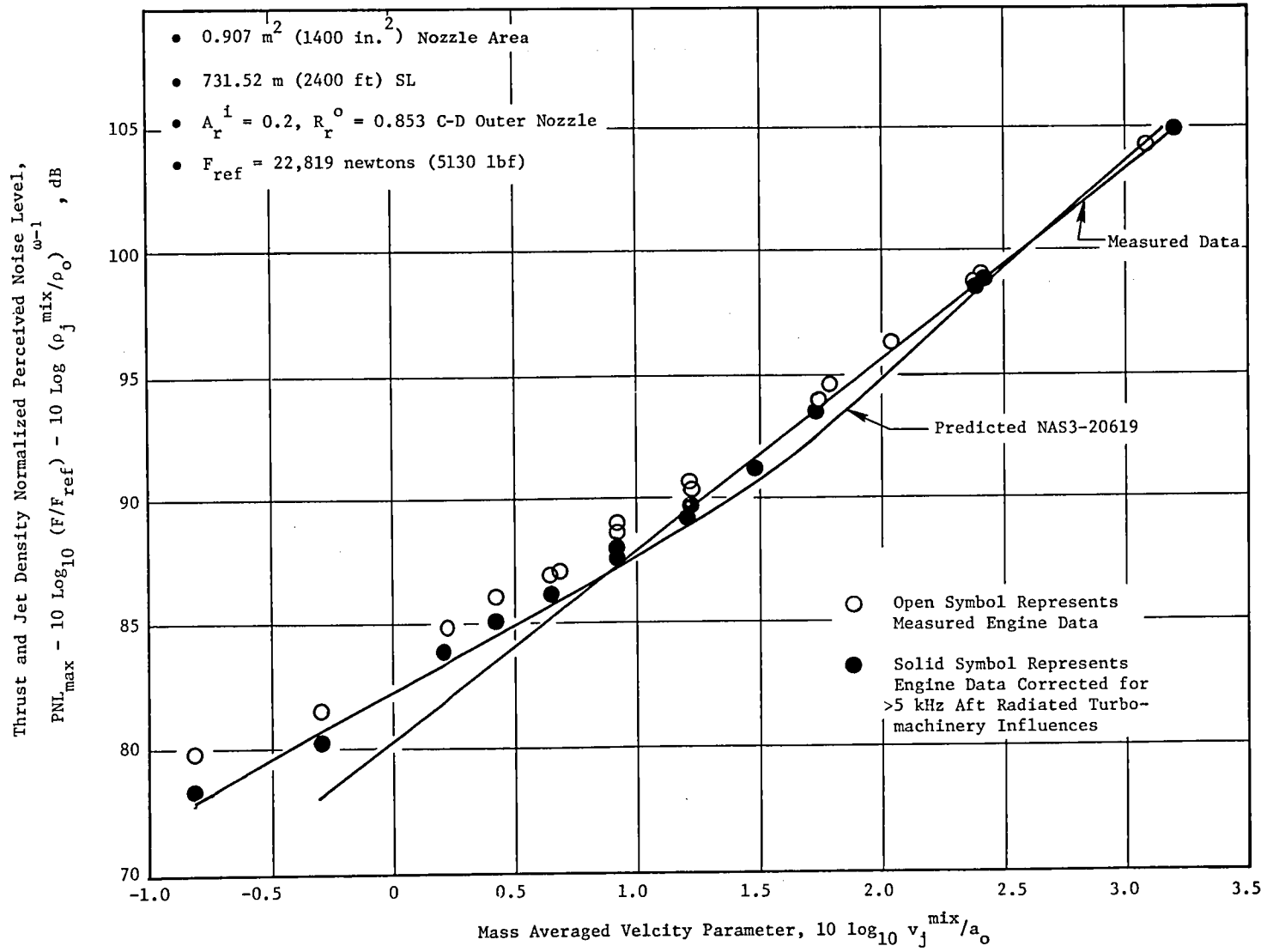


Figure 132. Comparison of the Measured and Predicted Variation at Normalized PNL at $R_r^o = 0.853$.

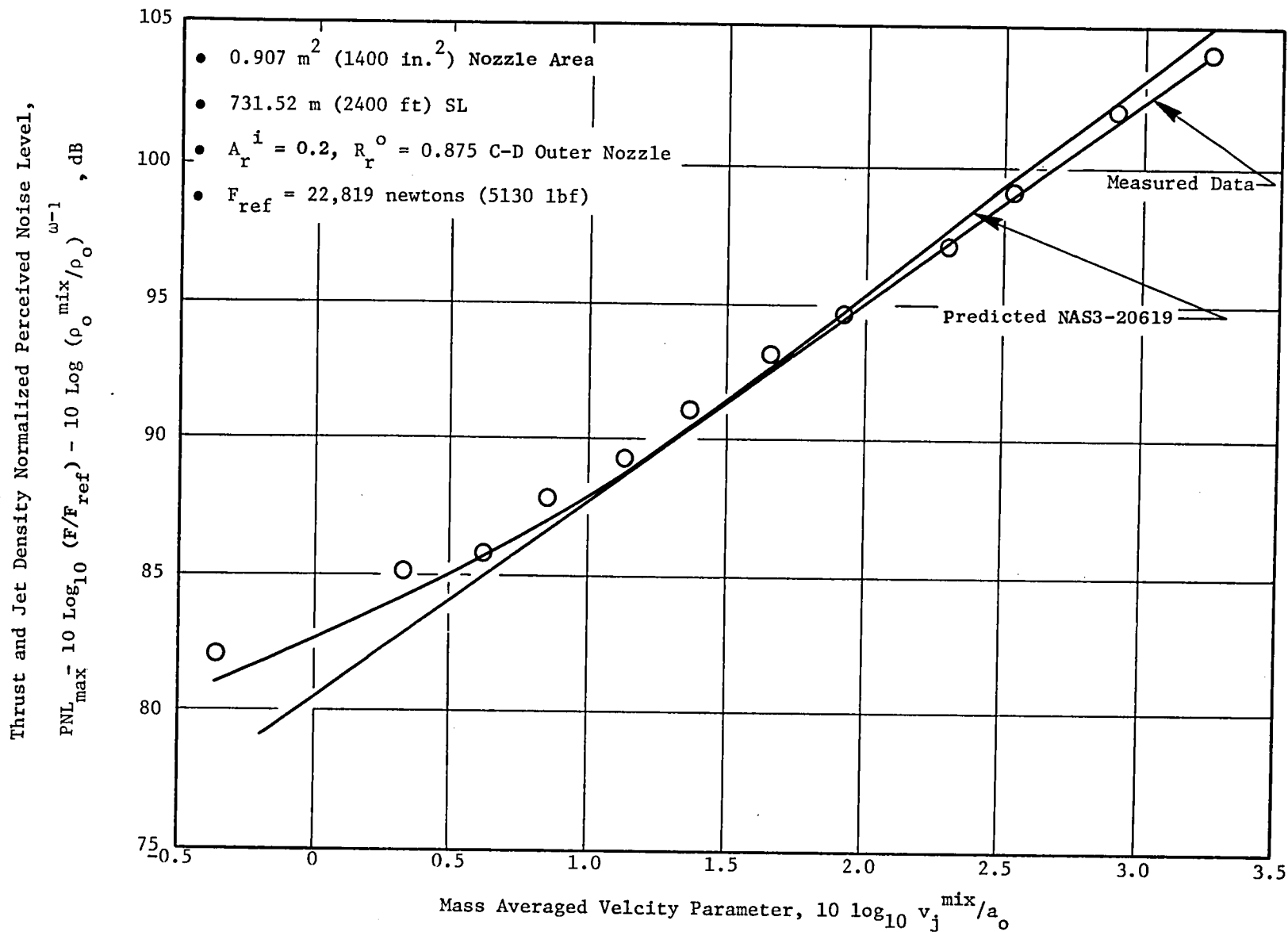


Figure 133. Comparison of the Measured and Predicted Variation of Normalized PNL at $R_r^o = 0.875$.

that the noise from each fan stage was printed separately. Engine tests with the coannular nozzle were run with a treated inlet, whereas the ANOPP prediction was for untreated forward quadrant noise. Also, the fan exhaust noise prediction is assumed to propagate through the engine into the far field without undergoing any attenuation/amplification. Hence, the predicted versus measured fan exhaust noise, will have to be viewed qualitatively rather than quantitatively.

With these points in mind, the fan noise predictions at three power settings (same conditions as used for jet noise cases) were made. Figures 134(a) to (c) show a comparison of the predicted OASPL directivities of the fan inlet and exhaust noise from each of the three fan stages with the total measured engine noise. At the highest power setting ($V_j^{mix} = 713.8$ m/sec (2342 ft/sec)), it is clear that on an OASPL basis, fan noise does not contribute any to the total engine noise even with the assumptions of an untreated inlet (Figure 134(a) used in the ANOPP prediction. Hence, with the engine as it was run (with a treated inlet), fan inlet or exhaust noise does not appear to be a problem.

At the intermediate power setting [$V_j^{mix} = 507.8$ m/sec (1666 ft/sec)], the fan inlet noise levels (without a treated inlet) are predicted to be substantially influencing the measurements in the forward quadrant (Figure 134(b)), but the measurements do not reflect this influence. This implies that having a treated inlet has indeed lowered the influence of forward radiated fan noise.

Finally, at the lowest power setting [$V_j^{mix} = 368.2$ m/sec, (1208 ft/sec)], the fan inlet noise is predicted to be significantly higher (Figures 134(c) than the measured test results in the forward quadrant. On an OASPL basis, the measured noise in the aft quadrant is expected to be influenced by the fan exhaust noise, assuming no attenuation of this component of noise.

To confirm the deductions made on the influence of fan noise on the total engine noise signature, the predicted spectra at $\theta_i = 50^\circ, 90^\circ, 120^\circ$ and 140° were compared with the measured engine noise spectra at the same angles for each of the three power settings, as shown in Figures 135 through 137. At all three power settings, the measured data has a hump in the 5K-20 kHz 1/3 octave bands which is suspected to be fan exhaust noise, based on comparisons with the predicted spectra. The contributions of this hump to the OASPL at any given angle increases at the lower power settings as well as in the forward quadrant. To confirm whether the hump was indeed comprised of the tones predicted by the fan noise program, narrow band analyses were performed for some of these cases. The narrow band spectra for one of these power settings (Figure 138) did not show any tones, though the hump did peak at the predicted frequencies. As this hump was observed in all the data, another configuration ($A_i^* = 0.475$, $R_r^0 = 0.853$) was selected and narrow band spectra obtained at a given power setting. This did indeed show tones at the BPF of the fan stages as seen in Figure 139. As the tones showed up stronger for a larger area ratio configuration, it can be conjectured that the tones could get modified by the shear layers through which they pass and show up as tones or narrow band noise depending on the configuration. Also, as this noise could not be attributed to

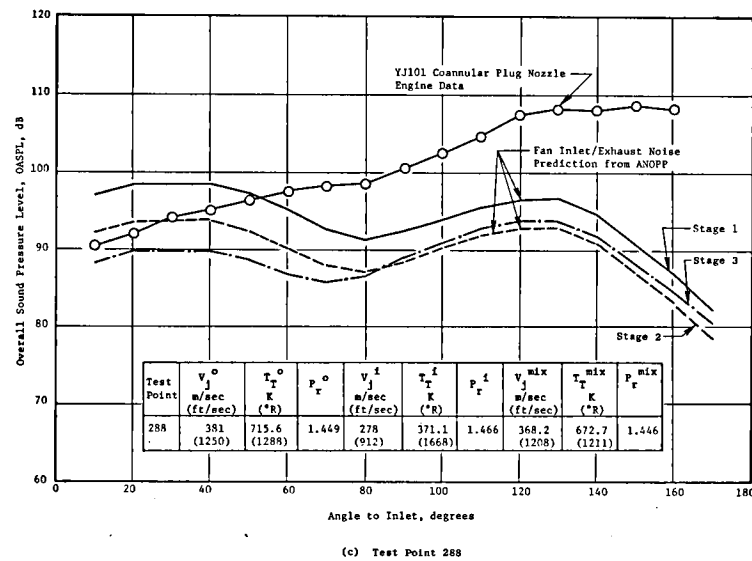
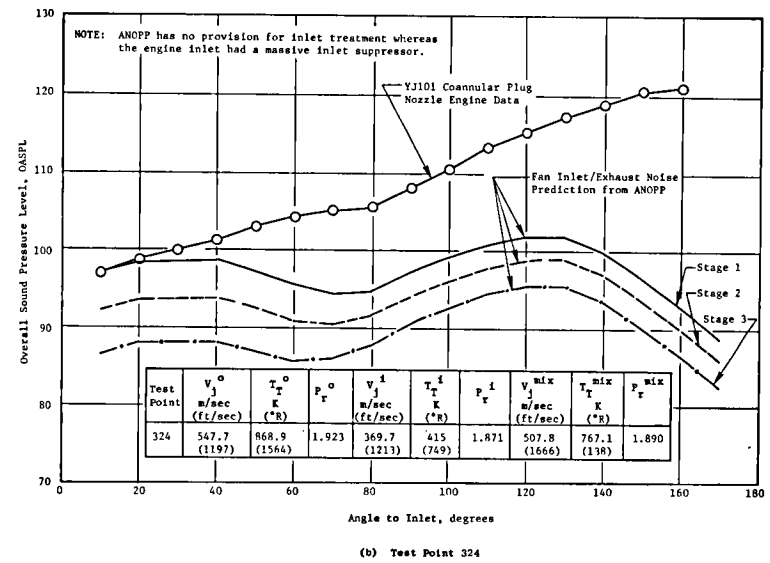
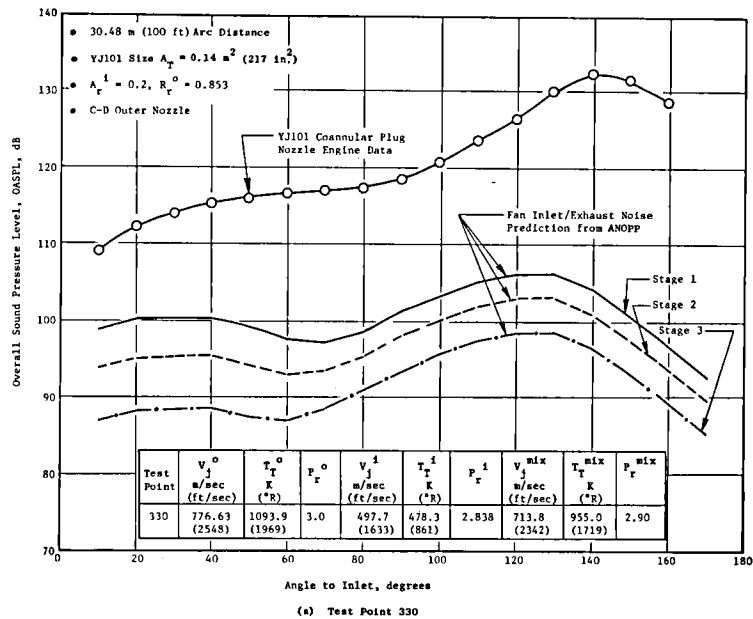


Figure 134. Comparison of the Measured Engine OASPL Directivity with the Predicted Fan Inlet and Exhaust Noise.

Test Point	V_j^o m/sec (ft/sec)	T_T^o K (°R)	P_r^o	V_j^i m/sec (ft/sec)	T_T^i K (°R)	P_r^i	V_j^{mix} m/sec (ft/sec)	T_T^{mix} K (°R)	P_r^{mix}
330	776.63 (2548)	1093.9 (1969)	3.00	497.7 (1633)	478.3 (861)	2.838	713.8 (2342)	955.0 (1719)	2.90

- 30.48 m (100 ft) Arc Distance
- YJ101 Size $A_T = 0.14 \text{ m}^2$ (217 in²)
- $A_x^i = 0.2, R_r^o = 0.853$
- C-D Outer Nozzle

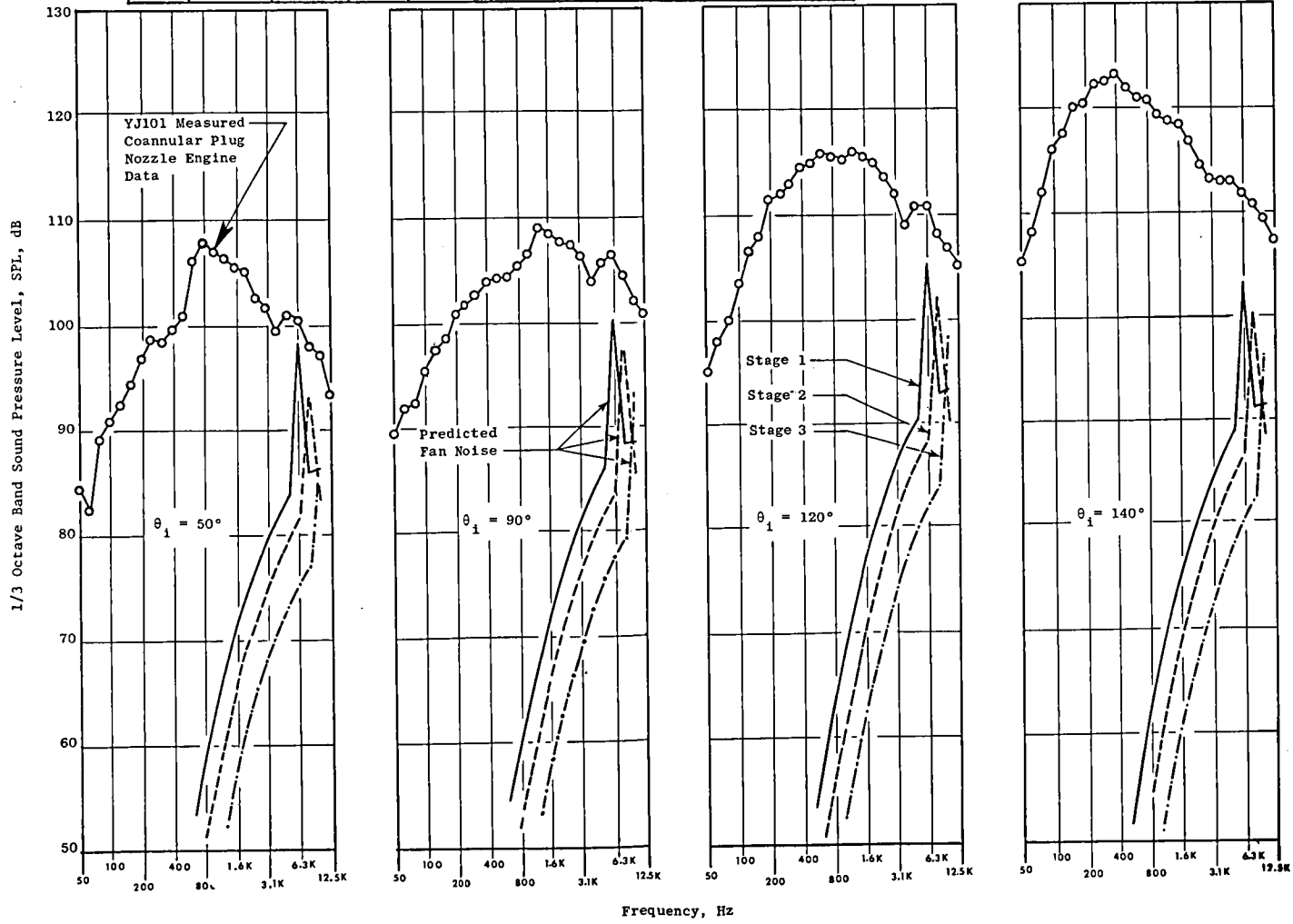


Figure 135. Comparison of the Measured Engine Spectra with the Predicted Fan Noise Spectra at $V_j^{mix} = 713.8 \text{ m/sec}$ (2342 ft/sec).

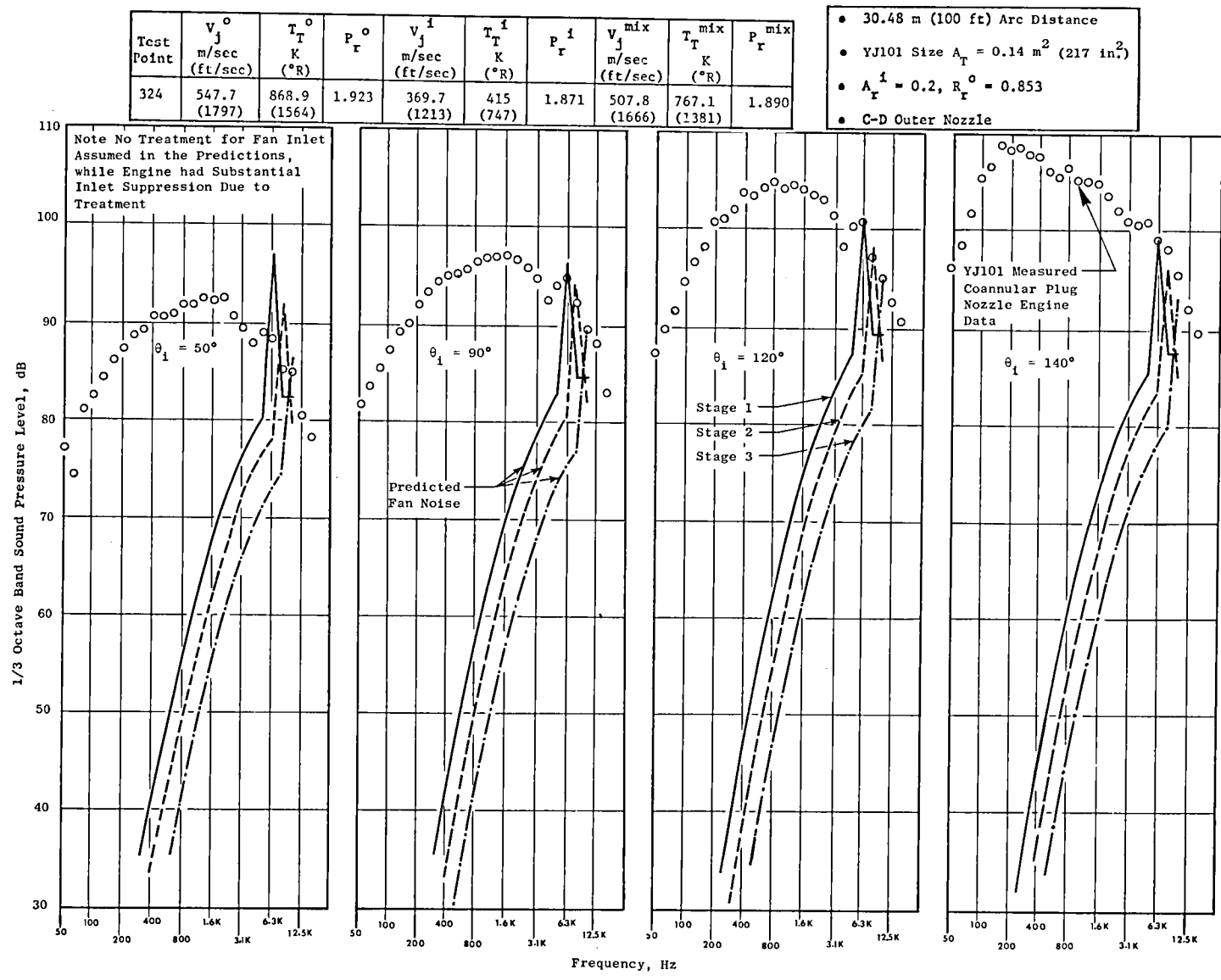


Figure 136. Comparison of the Measured Engine Spectra with the Predicted Fan Noise Spectra at $V_j^{mix} = 507.8 \text{ m/sec}$ (1666 ft/sec).

Test Point	V_j^o m/sec (ft/sec)	T_T^o K (°R)	P_r^o	V_j^i m/sec (ft/sec)	T_T^i K (°R)	P_r^i	V_j^{mix} m/sec (ft/sec)	T_T^{mix} K (°R)	P_r^{mix}
228	381.0 (1250)	715.6 (1288)	1.449	278 (912)	371.1 (668)	1.466	368.2 (1208)	672.7 (1211)	1.446

- 30.48 m (100 ft) Arc Distance
- YJ101 Size $A_T = 0.14 \text{ m}^2$ (217 in.²)
- $A_r^i = 0.2$, $R_r^o = 0.853$
- C-D Outer Nozzle

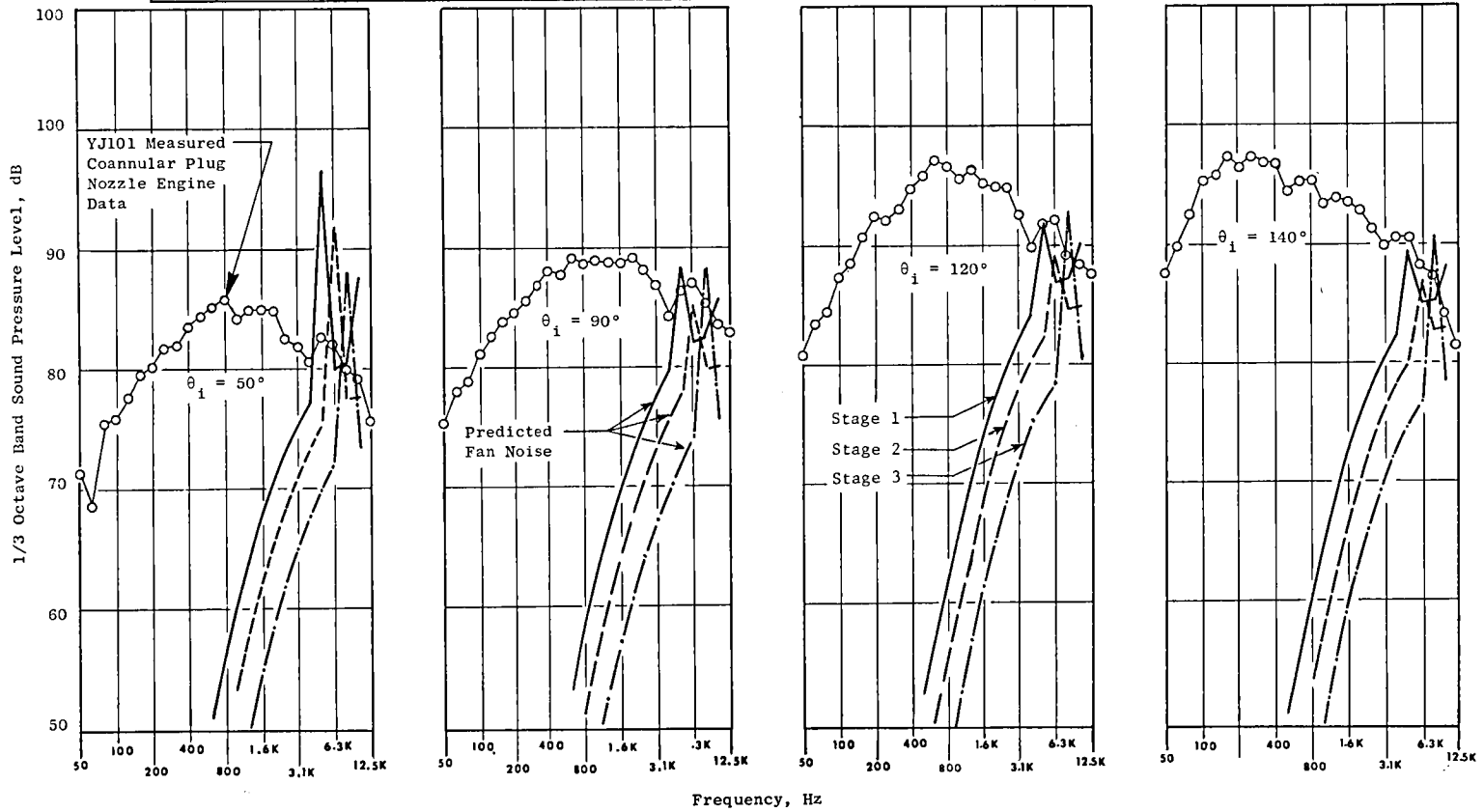


Figure 137. Comparison of the Measured Engine Spectra with the Predicted Fan Noise Spectra at $V_j^{mix} = 368.2 \text{ m/sec}$ (1208 ft/sec).

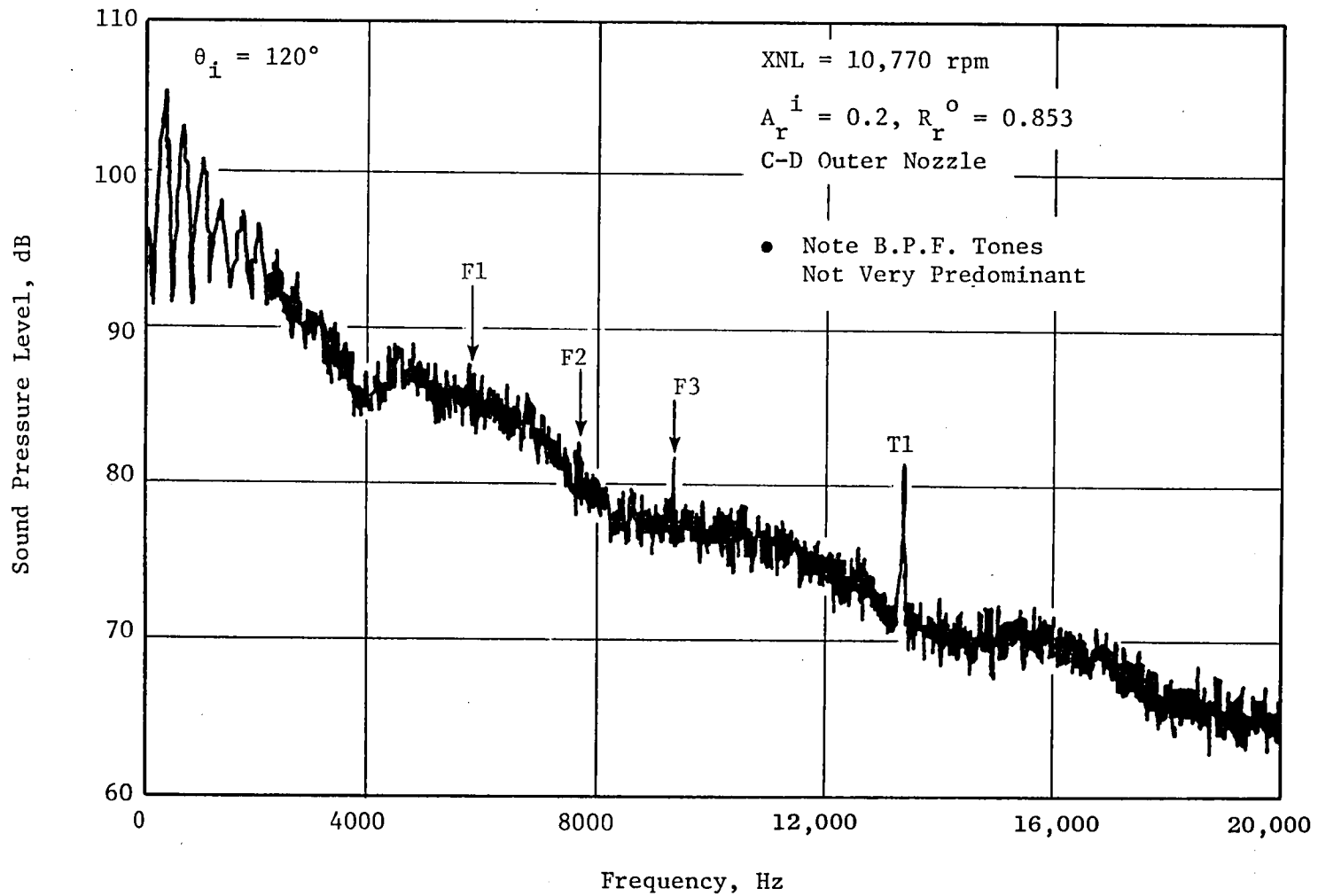


Figure 138. Narrow Band Analysis of the Measured YJ101 Coannular Plug Engine Data Showing Humps in the 5 kHz - 20 kHz 1/3 Octave Bands.

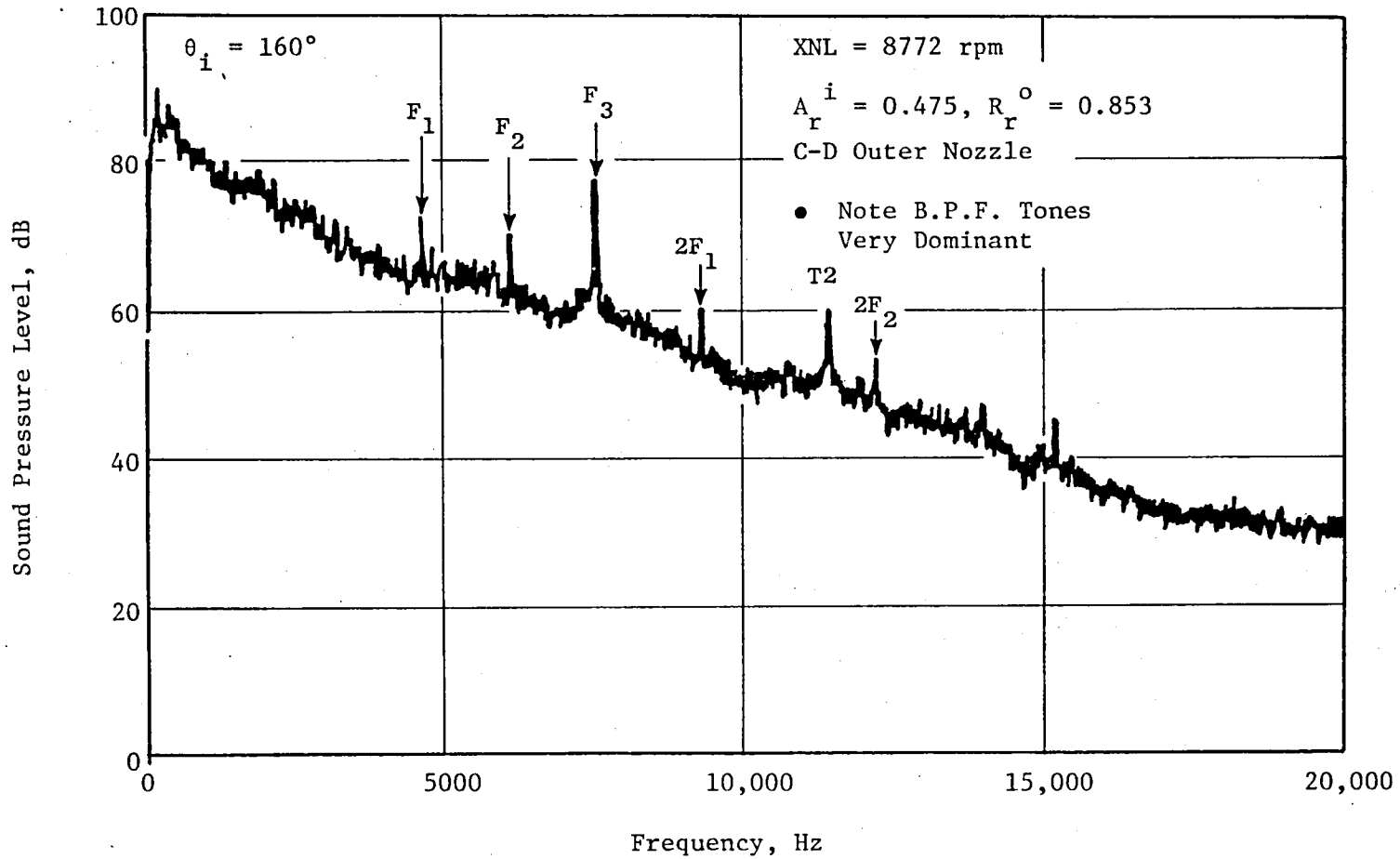


Figure 139. Narrow Band Analysis of the Measured YJ101 Coannular Plug Engine Data Showing Humps in the 5 kHz - 20 kHz 1/3 Octave Bands.

any other noise source except the fan, it appears that the above deduction may not be totally fortuitous. Means of measuring or suppressing this aft-fan-radiated noise may have to be considered for the next series of engine tests.

c. Turbine Noise Comparisons

For the prediction procedure of Krejsa et. al., (Reference 16), the noise from each turbine stage was separately predicted. Hence, the high pressure (HP) and low pressure (LP) turbine noise spectra were predicted for the same power settings at which the jet and fan noise predictions were made. Figures 140(a) through 140(c) compare the predicted LP and HP turbine OASPL directivities with the measured engine noise at the three power settings. It is evident from the figures that turbine noise does not contribute to the total engine noise at any of these power settings. To further confirm this observation, predicted turbine noise sound pressure spectra at 50°, 90°, 120°, and 140° were compared with the measured engine data as shown in Figure 141 to 143. The figures confirm the above deduction that turbine noise is not a contributing engine noise source. It should be noted here that the ANOPP turbine prediction method predicts only up to 10 kHz. For these tests the turbine tones fall in the 12.5 kHz - 16 kHz 1/3 octave bands. Further review of data and predictions in these higher frequencies are probably worthwhile.

d. Core Noise Comparisons

Core noise predictions at the three power settings (discussed earlier) were made using the GE core noise prediction program as adopted in ANOPP. Figure 144(a) through 144(c) show comparisons of the predicted core noise OASPL directivities with the measured engine data. It is evident from these figures that core noise does not influence the engine noise even at the low power settings. To confirm this on a Spectral basis, predicted spectra at $\theta_i = 50^\circ, 90^\circ, 120^\circ$ and 140° were compared with the data as shown in Figures 145 through 147 for the three power settings. Once again, these figures demonstrate that the engine data are not contaminated by core noise.

e. Strut/Obstruction Noise Comparisons

Strut noise predictions were made for the three power settings (discussed earlier) using the prediction program developed at General Electric. Figure 148(a) through 148(c) show comparisons of the measured and predicted OASPL directivities. At the highest power setting, the predicted strut noise does not contribute to the total noise. However, at the lower power settings, the predictions indicate that there may be some influence of strut noise on the total noise. To confirm/verify these observations, spectral comparisons at $\theta_i = 50^\circ, 90^\circ, 120^\circ$ and 140° were made between the engine data and predictions as shown in Figures 149 through 151. The strut noise levels predicted at the higher power setting are much lower than the engine data, and, hence confirm the earlier observations. However, at the lower power settings, the

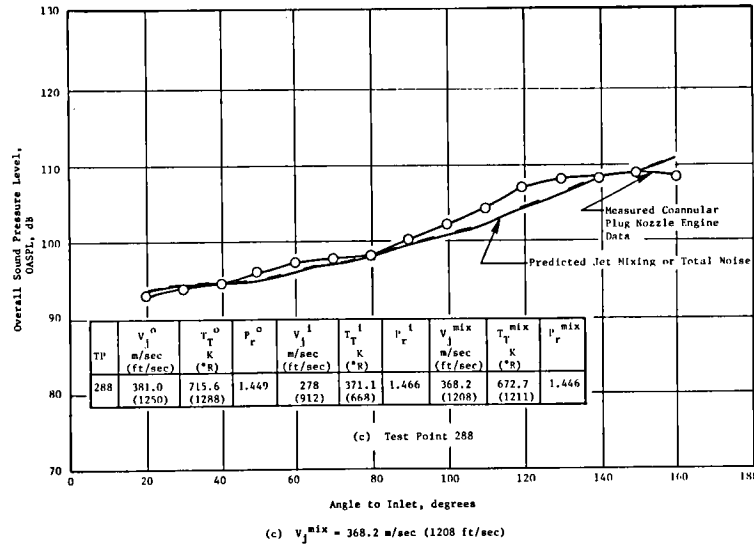
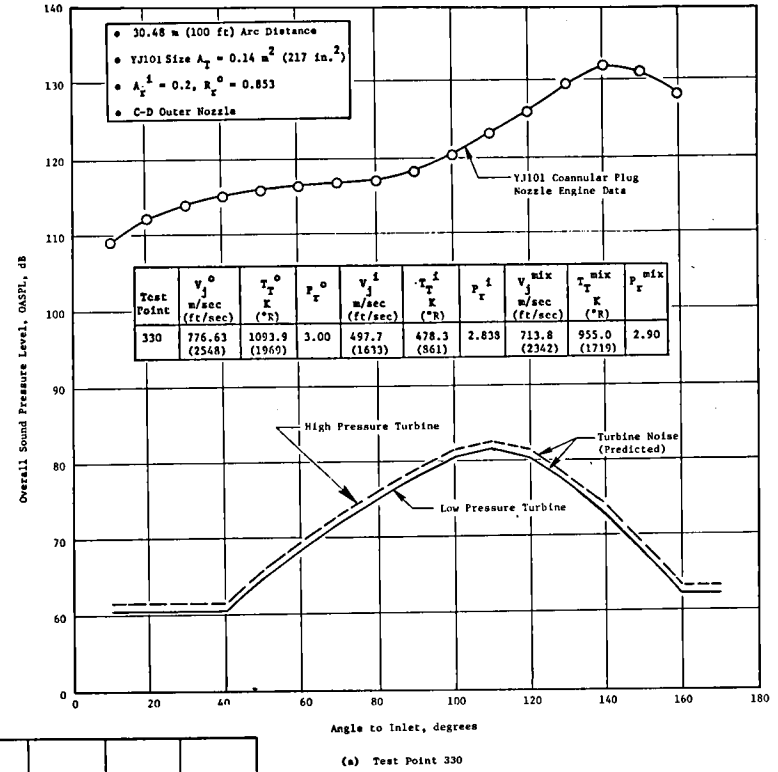
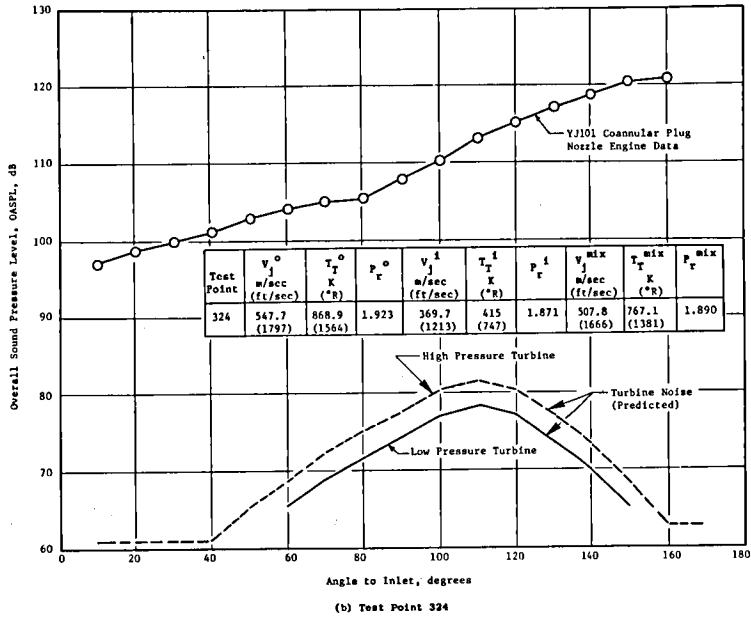


Figure 140. Comparison of the Measured Engine OASPL Directivity with the Predicted Turbine Noise.

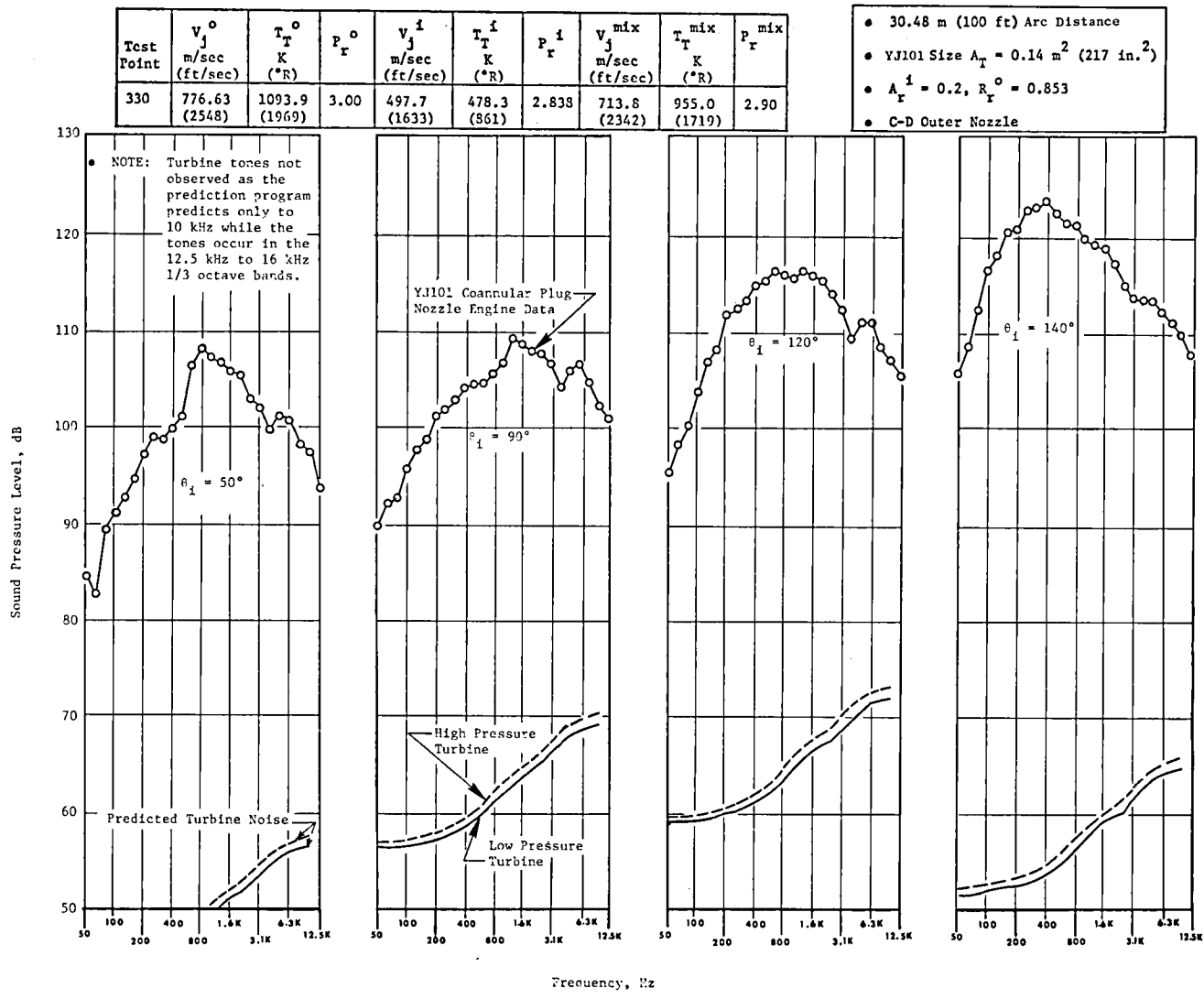


Figure 141. Comparison of the Measured Engine SPL Spectra with the Predicted Turbine Noise Spectra at Test Point 330.

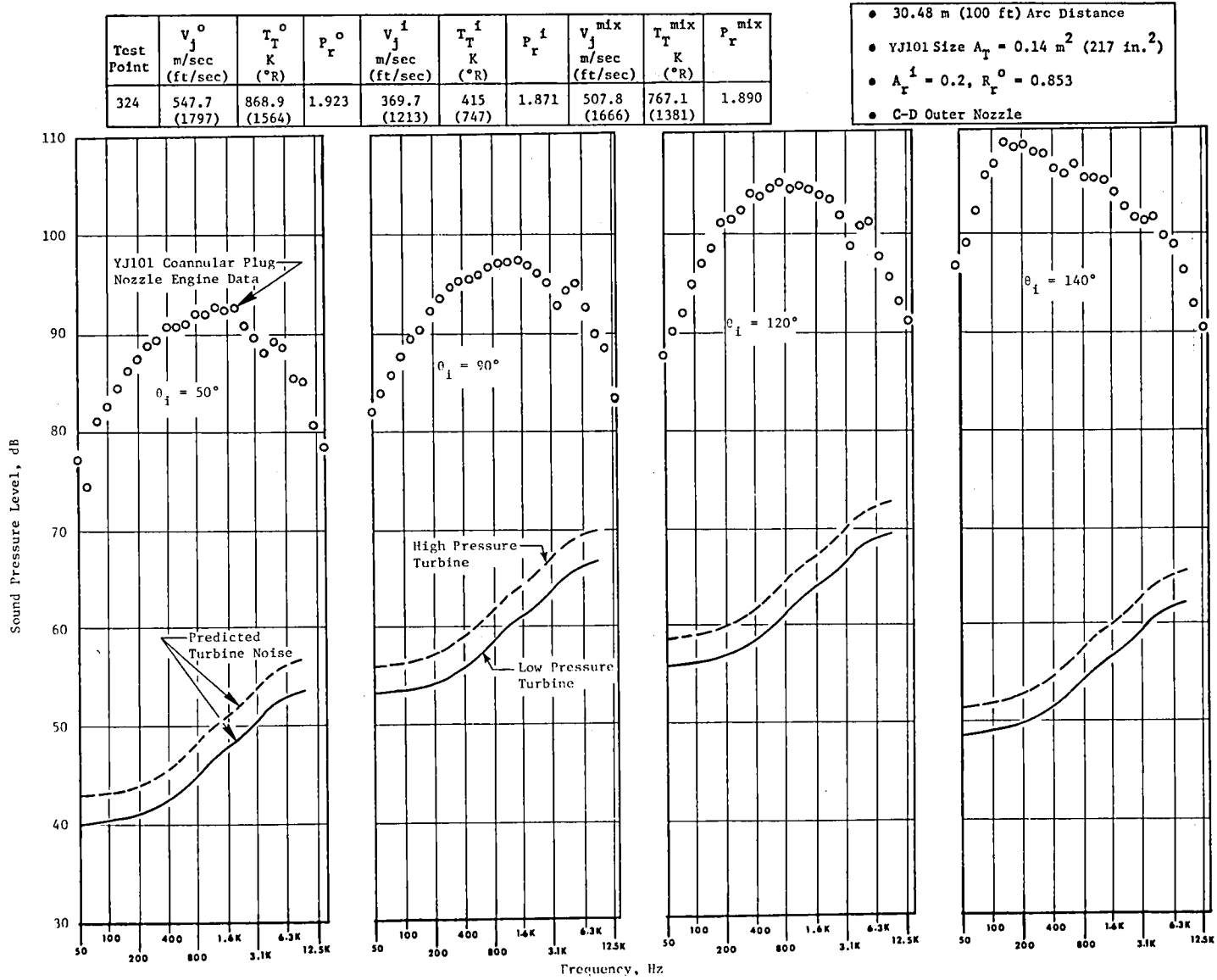


Figure 142. Comparison of the Measured Engine SPL Spectra with the Predicted Turbine Noise Spectra at Test Point 324.

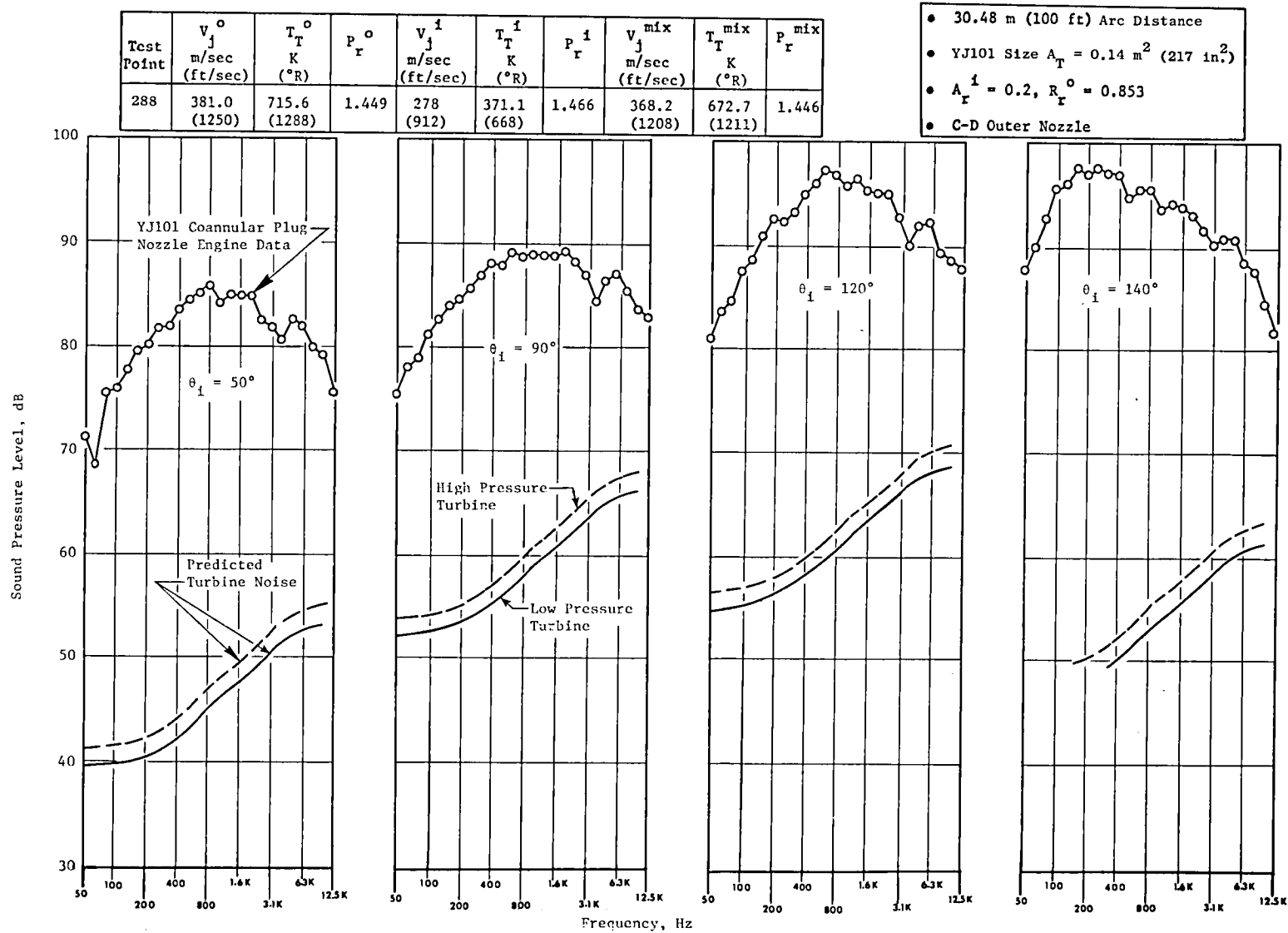


Figure 143. Comparison of the Measured Engine SPL Spectra with the Predicted Turbine Noise Spectra at Test Point 288.

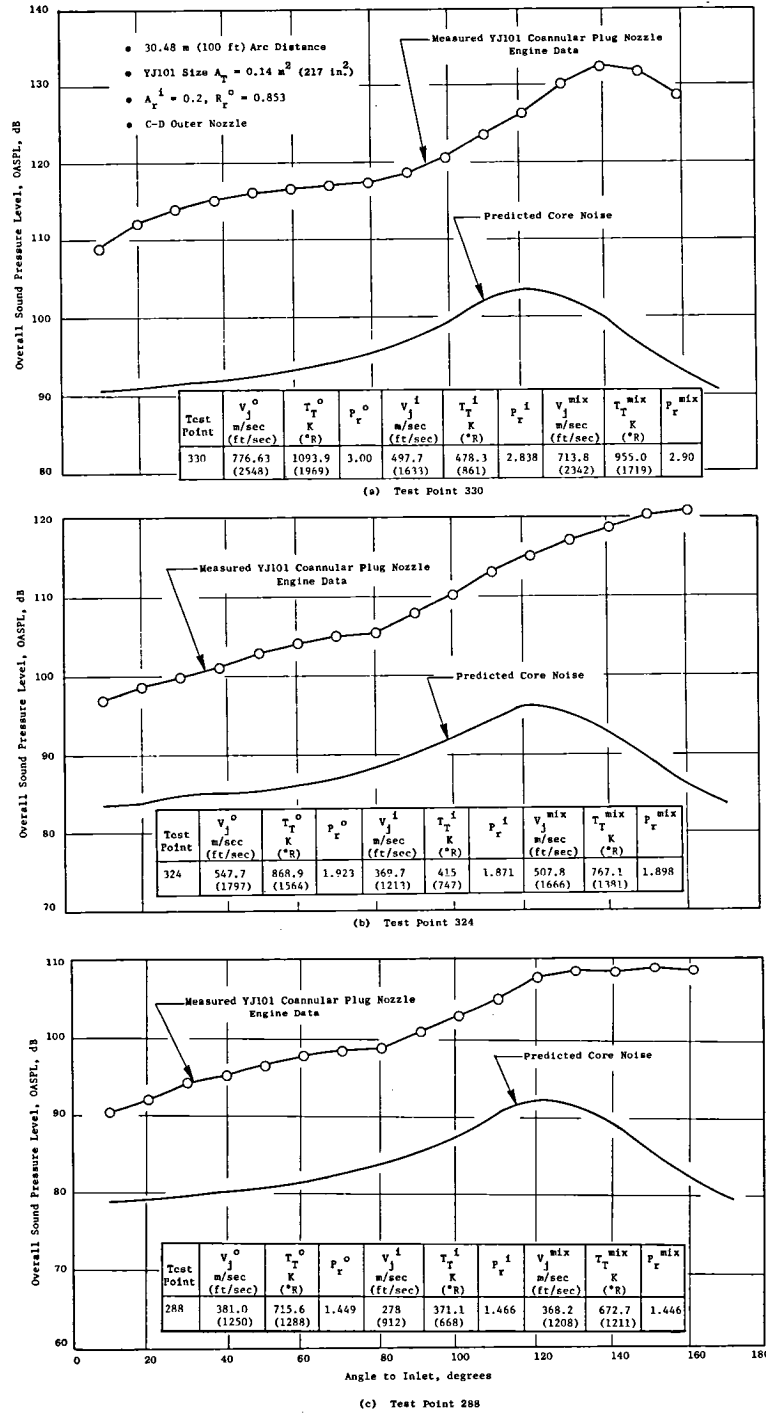


Figure 144. Comparison of the Measured Coannular Plug Nozzle Engine OASPL Directivity with the Predicted Core Noise.

Test Point	V_j^o m/sec (ft/sec)	T_T^o K (°R)	P_r^o	V_j^i m/sec (ft/sec)	T_T^i K (°R)	P_r^i	V_j^{mix} m/sec (ft/sec)	T_T^{mix} K (°R)	P_r^{mix}
330	776.63 (2548)	1093.9° (1969)	3.00	497.7 (1633)	478.3 (861)	2.838	713.8 (2342)	955.0 (1719)	2.90

- 30.48 m (100 ft) Arc Distance
- YJ101 Size $A_T = 0.14 \text{ m}^2$ (217 in.²)
- $A_r^i = 0.2$, $R_r^o = 0.853$
- C-D Outer Nozzle

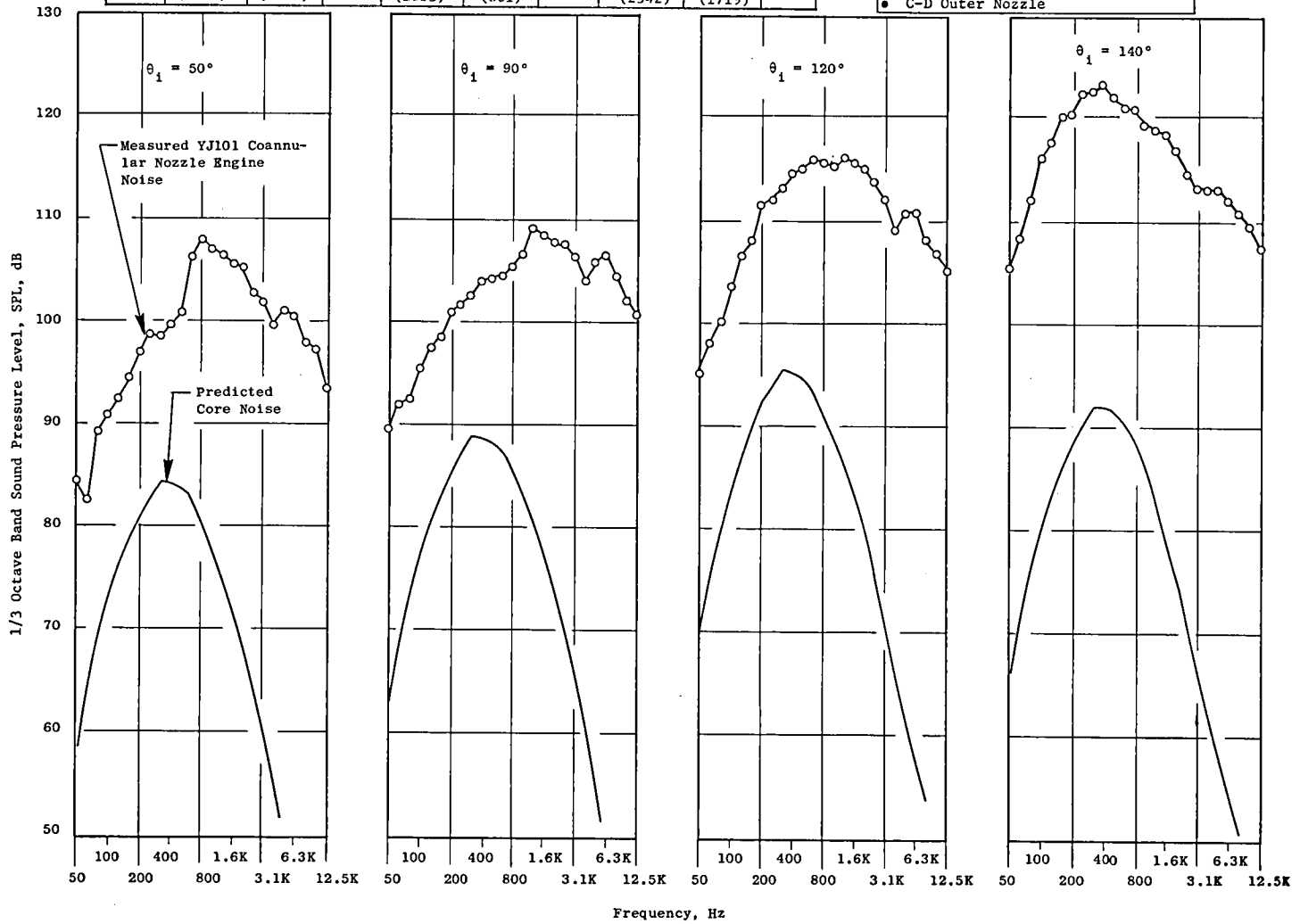


Figure 145. Comparison of the Measured Coannular Nozzle Engine Spectra with the Predicted Core Noise Spectra for Test Point 330.

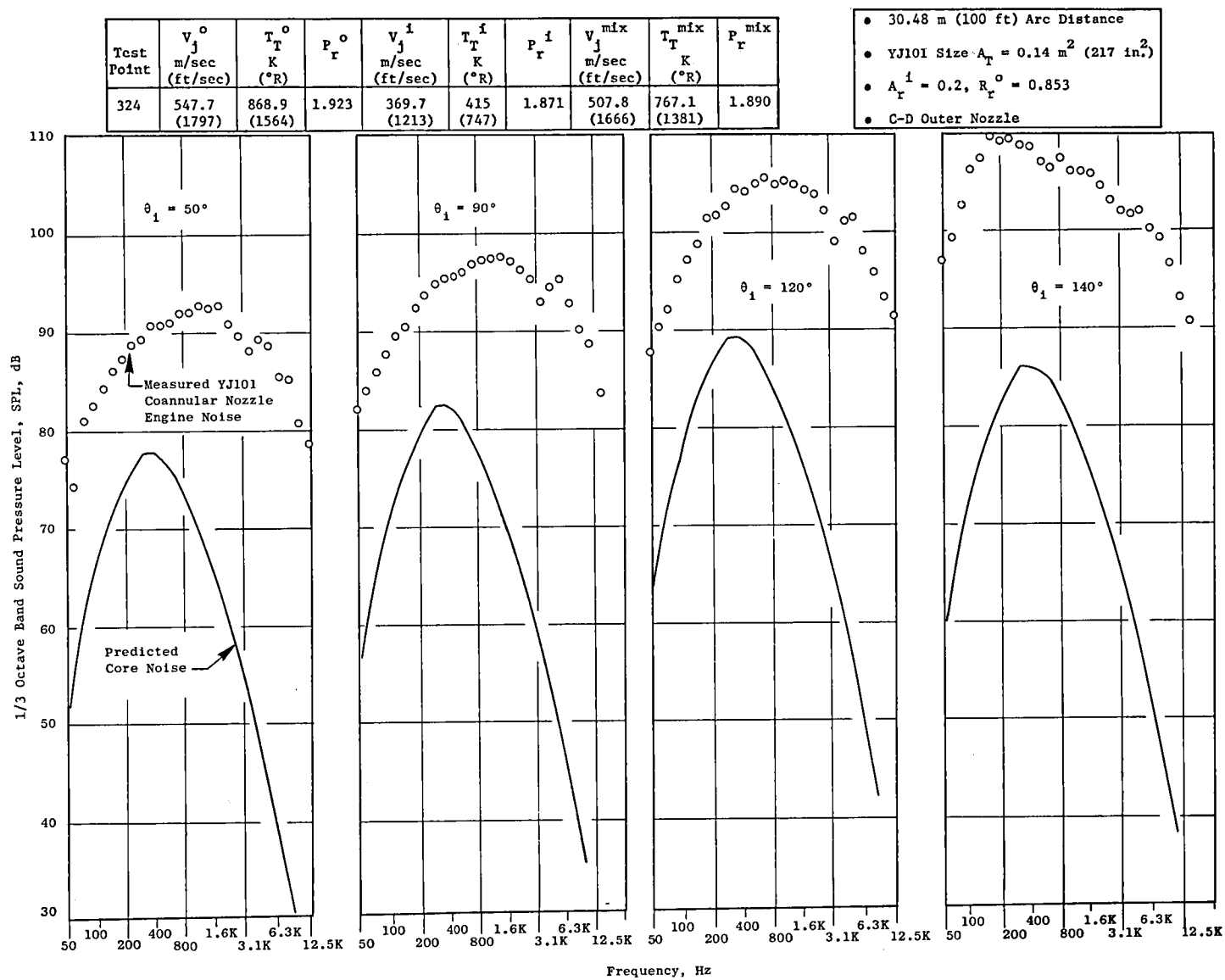


Figure 146. Comparison of the Measured Coannular Nozzle Engine Spectra with the Predicted Core Noise Spectra for Test Point 324.

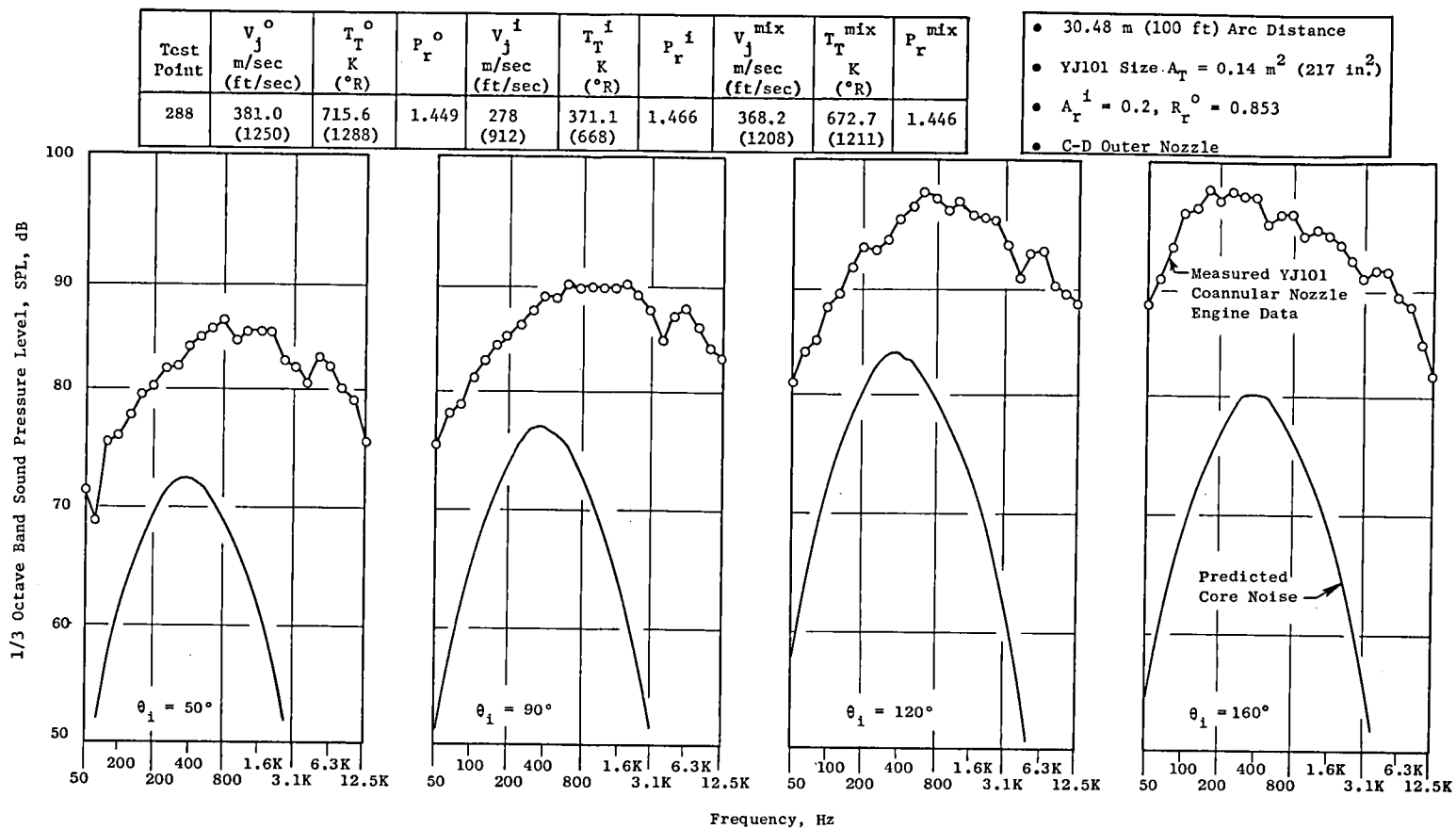
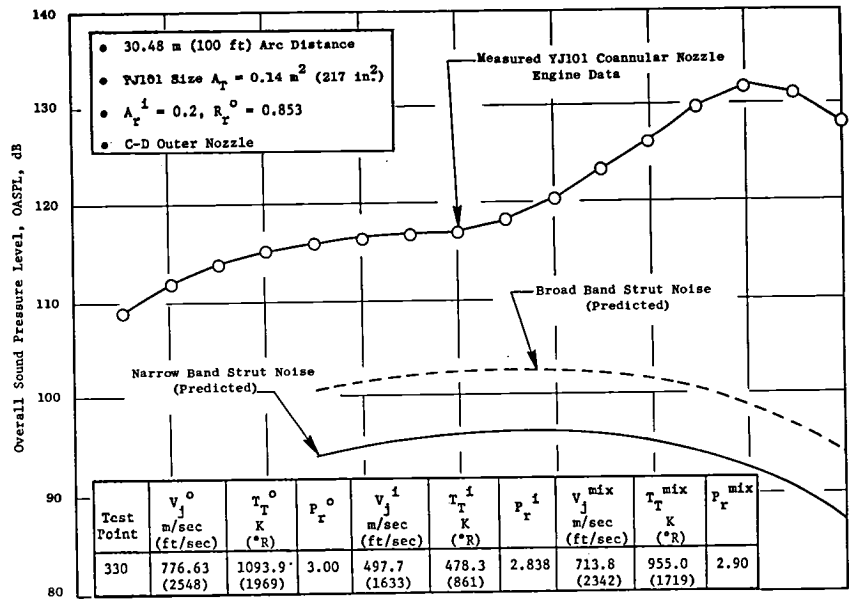
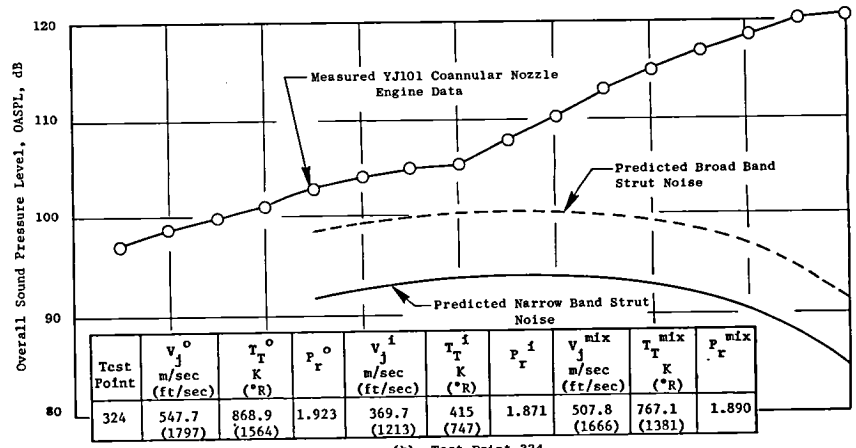


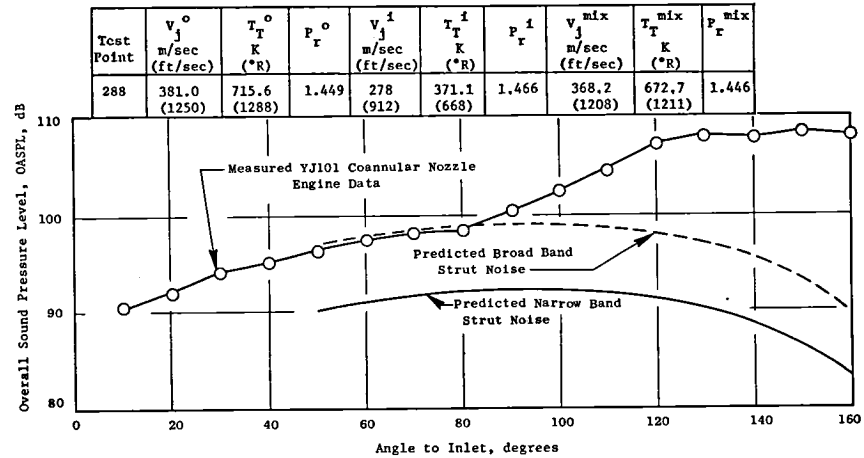
Figure 147. Comparison of the Measured Coannular Nozzle Engine Spectra with the Predicted Core Noise Spectra for Test Point 288.



(a) Test Point 330



(b) Test Point 324



(c) Test Point 288

Figure 148. Comparison of the Measured Coannular Nozzle Engine OASPL Directivity with That Predicted for Strut Noise.

Test Point	V_j^o m/sec (ft/sec)	T_T^o K (°R)	P_r^o	V_j^i m/sec (ft/sec)	T_T^i K (°R)	P_r^i	V_j^{mix} m/sec (ft/sec)	T_T^{mix} K (°R)	P_r^{mix}
330	776.63 (2548)	1093.9 (1969)	3.00	497.7 (1633)	478.3 (861)	2.838	713.8 (2342)	955.0 (1719)	2.90

- 30.48 m (100 ft) Arc Distance
- YJ101 Size $A_T = 0.14 \text{ m}^2$ (217 in.²)
- $A_r^i = 0.2$, $R_r^o = 0.853$
- C-D Outer Nozzle

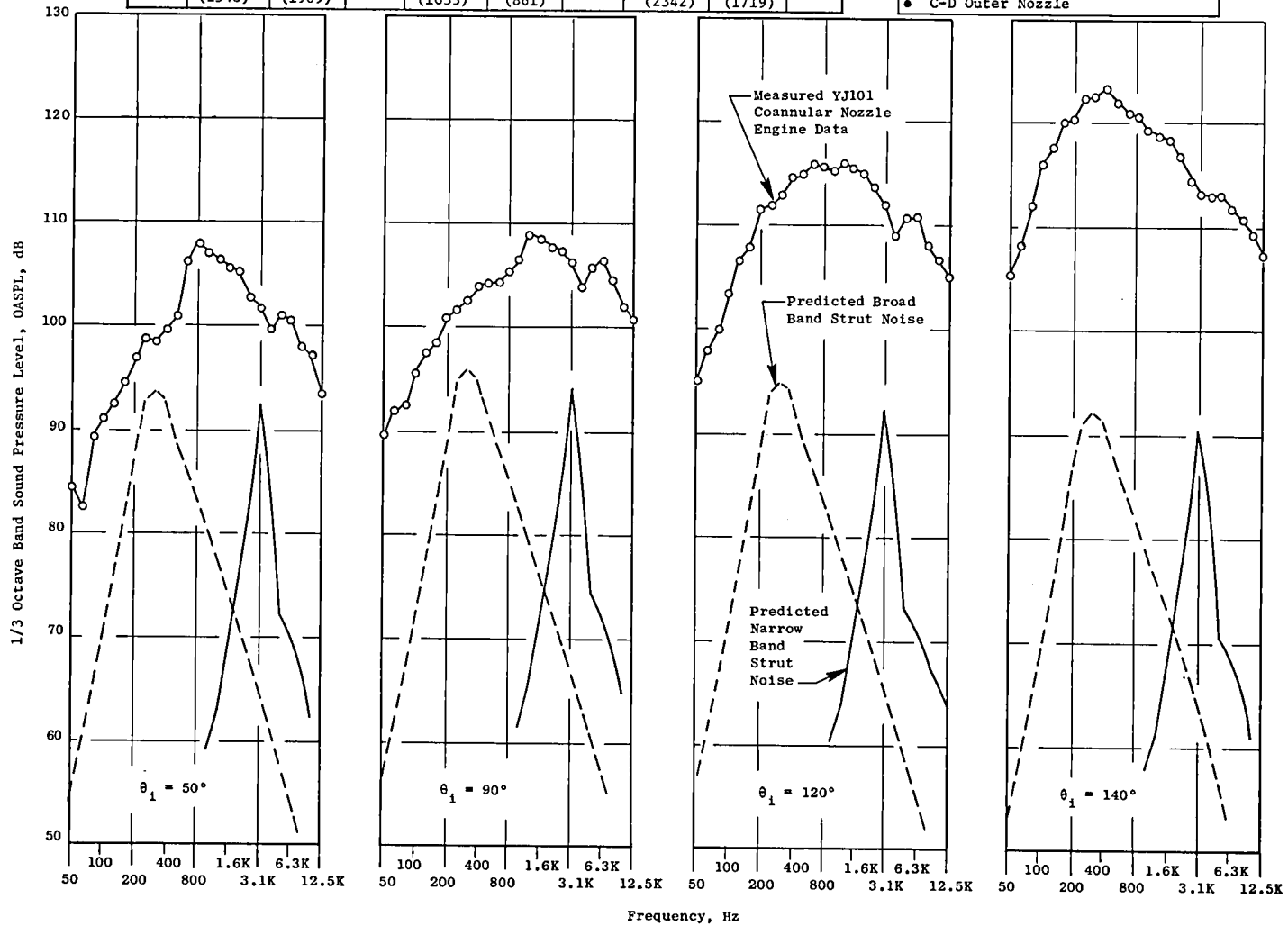


Figure 149. Comparison of the Measured Coannular Nozzle Engine Spectra with Predicted Strut Noise Spectra at Test Point 330.

Test Point	V_j^o m/sec (ft/sec)	T_T^o K (°R)	P_r^o	V_j^i m/sec (ft/sec)	T_T^i K (°R)	P_r^i	V_j^{mix} m/sec (ft/sec)	T_T^{mix} K (°R)	P_r^{mix}
324	547.7 (1797)	868.9 (1564)	1.923	369.7 (1213)	415 (747)	1.871	507.8 (1666)	767.1 (1381)	1.890

- 30.48 m (100 ft) Arc Distance
- YJ101 Size $A_T = 0.14 \text{ m}^2$ (217 in²)
- $A_r^i = 0.2$, $R_r^o = 0.853$
- C-D Outer Nozzle

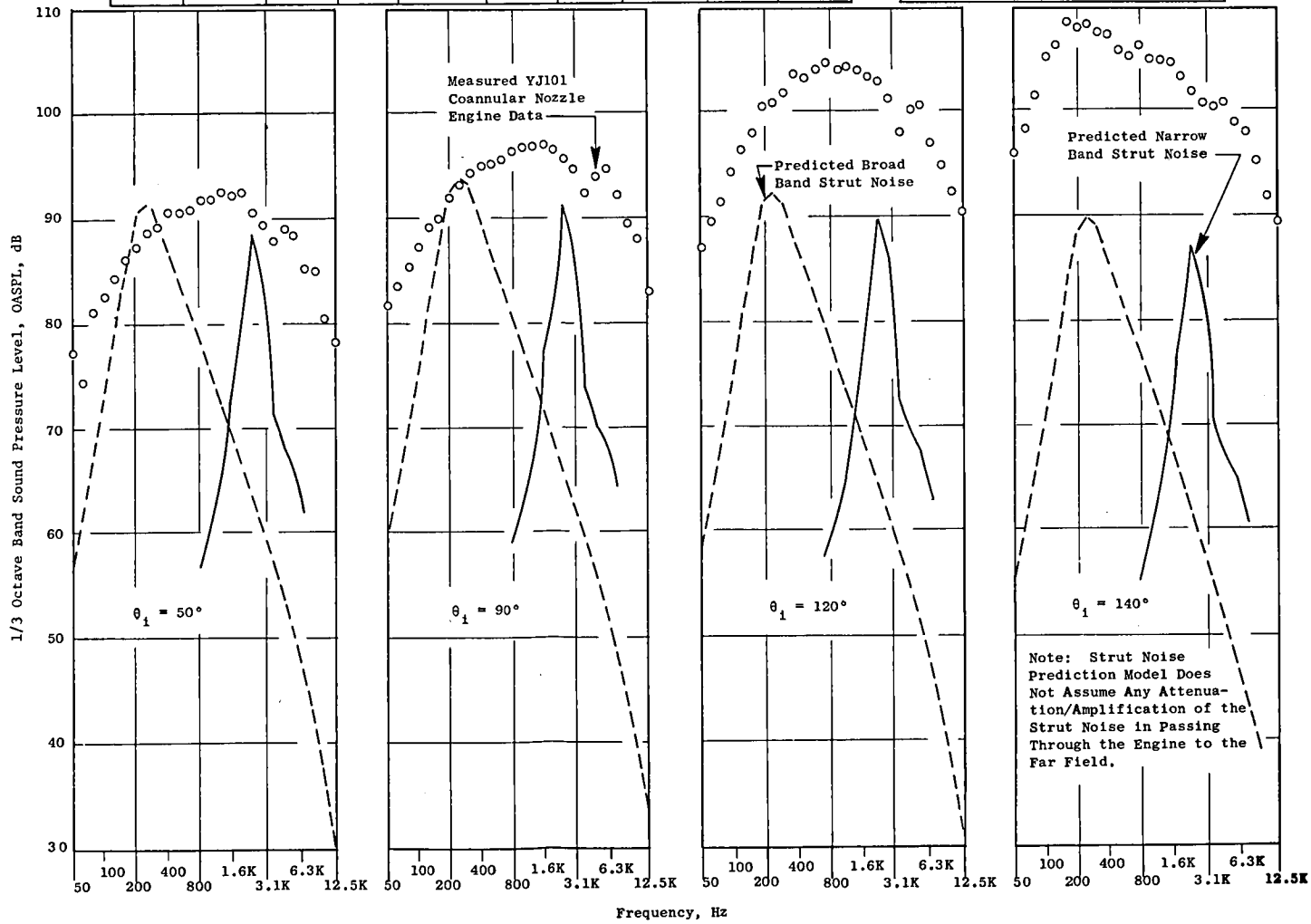


Figure 150. Comparison of the Measured Coannular Nozzle Engine OASPL Directivity with That Predicted for Strut Noise at Test Point 324.

Test Point	V_j^o m/sec (ft/sec)	T_T^o K (°R)	P_r^o	V_j^i m/sec (ft/sec)	T_T^i K (°R)	P_r^i	V_j^{mix} m/sec (ft/sec)	T_T^{mix} K (°R)	P_r^{mix}
288	381.0 (1250)	715.6 (1288)	1.449	278 (912)	371.1 (668)	1.466	368.2 (1208)	672.7 (1211)	1.446

- 30.48 m (100 ft) Arc Distance
- YJ101 Size $A_T = 0.14 \text{ m}^2$ (217 in.²)
- $A_r^i = 0.2$, $R_r^o = 0.853$
- C-D Outer Nozzle

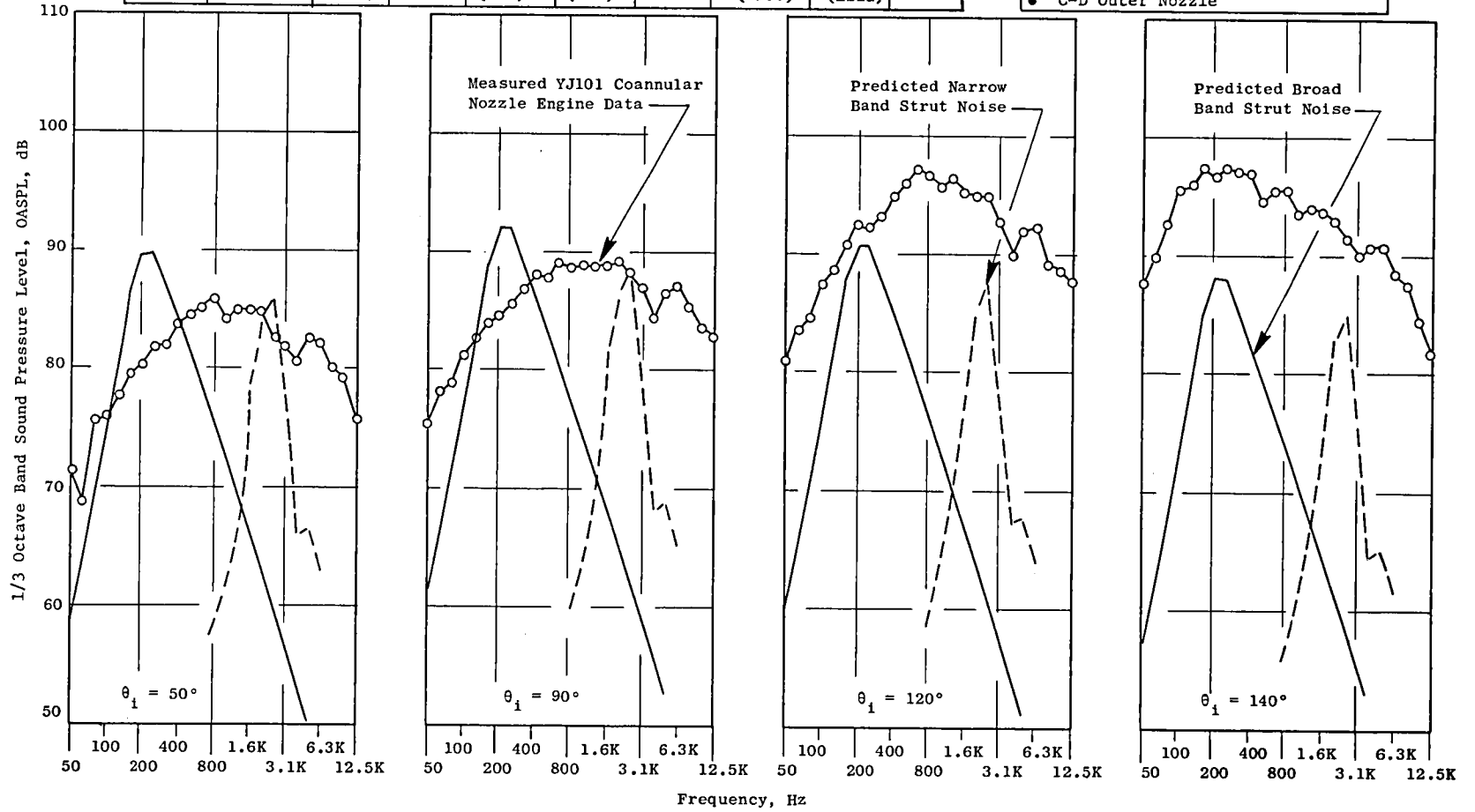


Figure 151. Comparison of the Measured Coannular Nozzle Engine Spectra with Predicted Strut Noise Spectra at Test Point 288.

predicted values of broadband strut noise in the forward quadrant are higher than the measured data. This would suggest that the assumption made in the prediction model that the noise is not amplified/attenuated as it passes through the flowpath is not very good and that both the broadband as well as narrow band noise levels could be attenuated. As the data do not show any contamination at the frequencies where strut noise is expected to peak (and the jet noise predictions are very good here), it can be concluded that strut noise is indeed not a problem at the above power settings.

5.5.7 Projection of Static Full-Scale Engine Data to Flight

In the previous section, engine static acoustic measurements were compared with engine component noise predictions. The general finding was that the data obtained for this program were indeed jet noise dominated with exceptions noted for particular power settings or 1/3 octave bands. The one key exception was a hump of noise in the 5kHz frequency region, which was associated with aft-radiated turbomachinery noise. For a GE VCE product-type SST engine, any such aft-radiated noise source would be taken care of through treatment designs of fan duct streams. The engine data used for these product engine projections had this 5kHz hump removed from the data.

In a similar vein, the product engine study to be discussed does not consider fan inlet noise (appropriate inlet acceleration suppression is assumed, and the actual engine data had a massive inlet suppressor so that no fan inlet noise is contained in the engine measurements). The other engine noise sources (core, turbine, obstruction, etc.) are also considered insignificant relative to the jet noise (as was verified in Section 5.5.6). Thus, this study is basically an estimate of a product VCE coannular plug exhaust nozzle configuration based on engine jet noise measurements and available relative velocity jet noise flight effect models.

Discussed below is the methodology of approach used in these projected product jet engine noise estimates for typical noise monitoring locations as specified for FAR 36 (1969).

5.5.7.1 Methodology Used for Product Engine Jet Noise Flight Projections

To assess the inflight signature of the coannular plug nozzle jet mixing and shock noise components, flight effects were applied to the measured engine noise data scaled to a total nozzle area of 0.9032 m² (1400 in.²). Several methods were evaluated in this sensitivity study. These included:

1. Method due to Bushell (Reference 20)
2. Method due to M.J.T. Smith (Reference 21)

3. Hoch's method as proposed for the SAE committee (Reference 22)
4. Method suggested by results from Task 6 of the D.O.T. program at GE (Reference 21)
5. M*G*B method approximated to the form used by the above methods (Ref. 20).

Each of the above methods used the basic relationship

$$\text{for level flight} \quad \begin{array}{c} \Delta\text{OASPL}(\theta_i) \\ \text{or} \\ \Delta\text{PNL}(\theta_i) \end{array} = 10 \log_{10} \left[\left(\frac{v_j}{v_j - v_a} \right)^{m(\theta_i)} \times \left(1 - \frac{v_a}{A_o} \cos \theta_i \right) \right]$$

where

$$\Delta\text{OASPL} = \text{OASPL}_{\text{static}} - \text{OASPL}_{\text{flight}}$$

or

$$\text{OASPL}_{\text{flight}} = \text{OASPL}_{\text{static}} - \Delta\text{OASPL}$$

$$\text{PNL}_{\text{flight}} = \text{PNL}_{\text{static}} - \Delta\text{PNL}$$

The variation of $m(\theta_i)$ with θ_i is quite different for each of the above methods. Using these values of $m(\theta_i)$, the flight effects were calculated for each of the above methods and applied to the static PNL's obtained from scaling the engine data (corrected for the 5kHz hump) to 0.9032 m² (1400 in.²) and an appropriate acoustic range. The engine data points chosen are typical of take-off, cutback and approach conditions considered for AST/VCE applications.* The points taken here are for reasonably matched mixed conditions for conic and coannular plug nozzle data. The flight effects were determined for each of the above methods, thus resulting in the flight PNL directivities for each of these methods. These flight path directivities were then used to determine the EPNL's. The EPNL's thus obtained were free field single-engine EPNL's. To account for 4 engines, 10 log₁₀ (4) (i.e., 6 dB) is added; to account for soft ground reflections, 1.5 dB is added; and to account for extra ground attenuation (EGA) and some aircraft shielding for the takeoff case, a curve of shielding vs. look angle** was used. These factors were added algebraically to the single engine EPNL's and resulted in four-engine EPNL estimates.

In addition to comparisons made using the above methods, the flight predictions using a spectral jet mixing and shock noise prediction program developed by GE under NASA Contract NAS3-20619 were made. This procedure does not use the jet velocity index formulation used by the other methods. That

*It is emphasized here that 'typical' is not meant to imply these noise calculations resulted from engine/aircraft cycle matching and trajectory analysis. It means only that estimated noise levels were made for the engine at cycle and flight conditions found to be typical in previous studies with advanced supersonic cruise airplanes.

**Hay, J A., Lateral Noise Propagation, Memorandum, Acoustics Department, British Aircraft Corporation Ltd, Weybridge, Surrey, England, 21 April 1977, Unpublished.

is, it does not add a Δ OASPL/ Δ PNL to the static OASPL's/PNL's, but rather predicts the spectra incorporating the changes in the flow due to the aircraft velocity and change in convection Mach number, convective amplification as well as fluid shielding. This method is not in its final form but predictions were made using the prediction method as it exists to date.

Finally, to assess the effects of flight on the engine component noise characteristics, the components (YJ101 test bed engine size) were scaled to incorporate a 0.9032 m^2 (1400 in.^2) nozzle exit area. The component geometric dimensions were scaled as the ratio of the square root of 0.9032 m^2 (1400 in.^2) to the test bed engine size 0.1394 m^2 (216 in.^2) coannular [or 0.1226 m^2 (190 in.^2) conic]. The fan tip speed was maintained the same, thus resulting in a reduced rpm for the same exit flow conditions. With these changes, the component noise predictions were made using ANOPP.

Thus, the flight noise signature of the scaled version of the AST/VCE Engine with a coannular and conic nozzle were predicted.

5.5.7.2 Discussion of the Results

The measured static free-field sound pressure spectra were scaled up for an engine size of 0.9032 m^2 (1400 in.^2) and extrapolated to 112.7 m (370 ft), 304.8 m (1000 ft) and 731.5 m (2400 ft) acoustic ranges for level fly-over, depending on whether the point corresponded to approach, cutback or takeoff sideline conditions, respectively. Thus, the static PNL directivities for each of the three operating conditions were determined. A computer program was written to determine the flight PNL directivity for each of the methods described in Section 5.5.7.1. In addition, the GE spectral prediction method was used separately to predict the jet noise flight PNL directivity. Figure 152 shows the variation of $m(\theta_i)$ with θ_i for the methods considered. From this figure, a large variation in $m(\theta_i)$ is evident for the various methods (m varies from -2 to $+1$ at $\theta_i = 20^\circ$ and from 1 to 10 at $\theta_i = 160^\circ$). As will be shown, these variations translate into variations in PNL field shape. To illustrate these effects, the cases considered are found in Table X.

EPNL Jet Noise Projection for Typical Sideline Conditions

Figures 153 and 154 illustrate the projected EPNL's for "typical" sideline noise conditions selected from the YJ101 coannular plug nozzle ($R_r^0 = 0.853$, $A_r^i = 0.2$) data base. Depending on the method used, the peak flight PNL variation is seen to be as much as 3PNdB. Additionally, the angle at which peak noise occurs is observed to vary from 130° to 140° . In spite of these rather large variations in flight PNL amplitude and field shape, the computed EPNL variations are relatively small (about 1EPNdB for all but the GE/NAS3-20619 method). These results suggest that EPNL projections using any of the methods considered would predict about the same levels.

The results of Figures 153 and 154 indicate that for "typical" sideline noise engine cycle conditions, the projected EPNL seems to range from 106 to

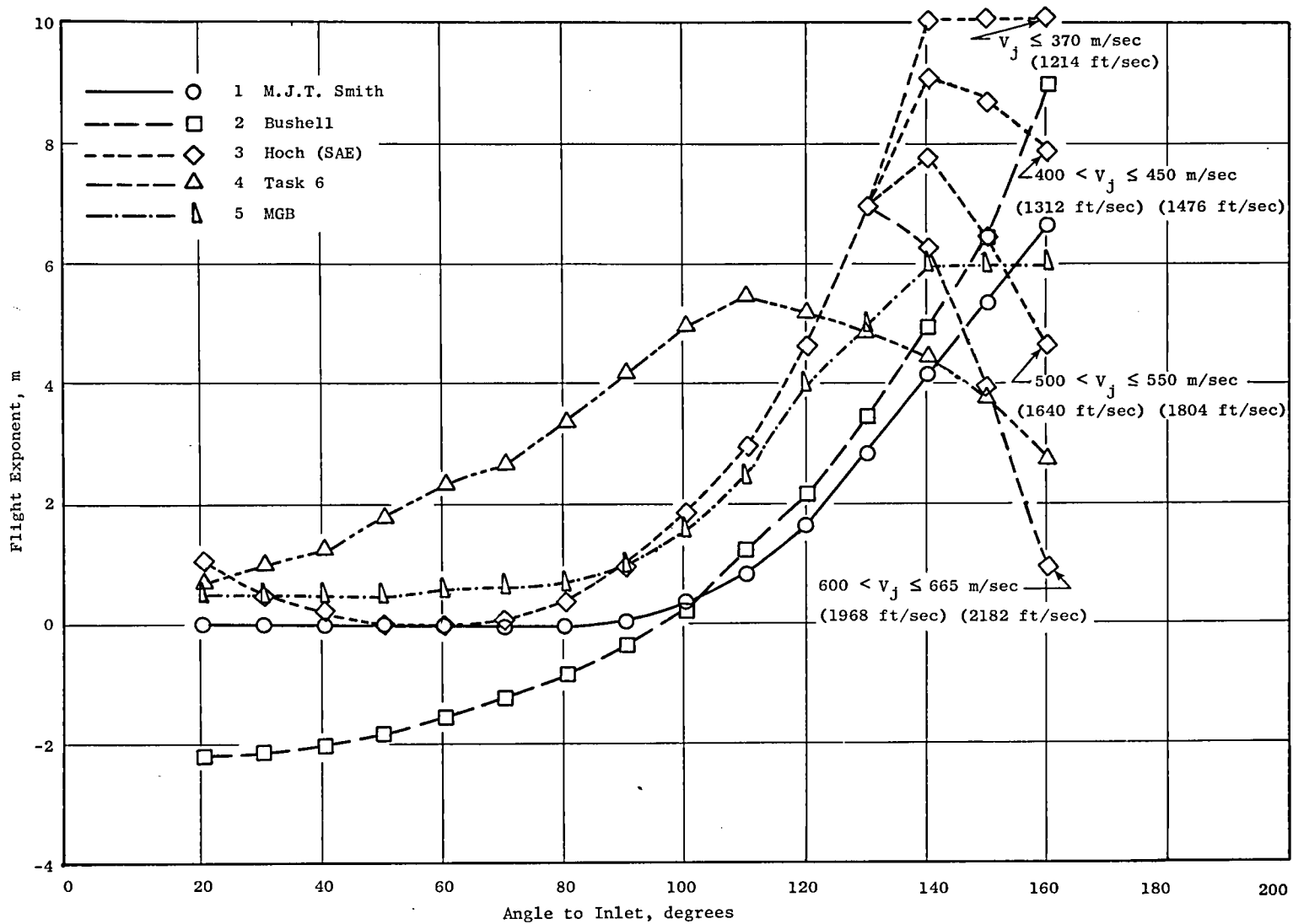


Figure 152. Variation of the Flight Effects Index, $m(\theta_i)$, for Several Proposed Flight Simulation Models.

Table X. Test Cases Considered in Comparative Flight Acoustic Projection.

Test Case	Test Point	V_j^o m/sec (ft/sec)	T_t^o K (° R)	P_r^o	V_j^i m/sec (ft/sec)	T_t^i K (° R)	P_r^i	V_j^{mix} m/sec (ft/sec)	Acoustic Range m. (ft)
Sideline	329	751.94 (2467)	1065.55 (1918)	2.87	484.63 (1590)	473.88 (853)	2.695	692.38 (2272)	731.52 (2400)
	413	693.72 (2276)	992.22 (1786)	2.591	450.19 (1499)	446.67 (804)	2.45	639.56 (2098)	731.52 (2400)
Cut-Back	324	547.72 (1797)	868.88 (1564)	1.92	369.72 (1213)	415.00 (747)	1.87	508.10 (1667)	304.8 (1000)
Approach	288	381.00 (1250)	715.55 (1288)	1.49	277.97 (912)	371.11 (688)	1.47	368.19 (1208)	112.77 (370)

Type Case	Test Point	V_j^o m/sec (ft/sec)	T_T^o K (°R)	P_r^o	V_j^i m/sec (ft/sec)	T_T^i K (°R)	P_r^i	V_j^{mix} m/sec (ft/sec)
Sideline	329	751.94 (2467)	1065.55 (1918)	2.87	484.63 (1590)	473.88 (853)	2.70	692.38 (2272)

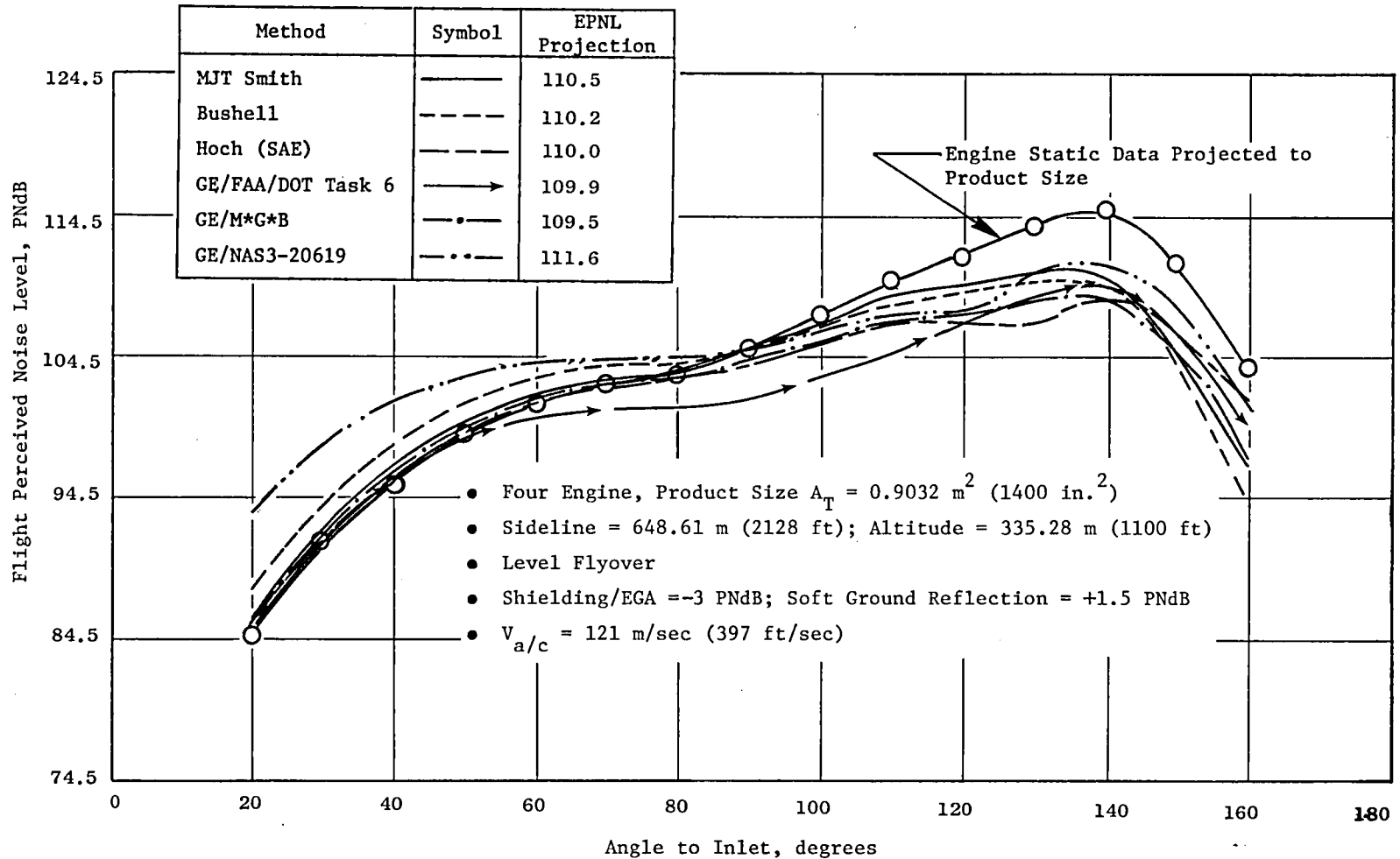


Figure 153. Variation of Projected Flight PNL for Several Flight Effects Methods for a Typical Sideline Noise Condition at $V_j^{mix} = 692 \text{ m/sec}$ (2272 ft/sec).

Type Case	Test Point	V_j^o m/sec (ft/sec)	T_T^o K (°R)	P_r^o	V_j^i m/sec (ft/sec)	T_T^i K (°R)	P_r^i	V_j^{mix} m/sec (ft/sec)
Sideline	413	693.72 (2276)	992.22 (1786)	2.59	450.19 (1477)	446.67 (804)	2.45	639.56 (2098)

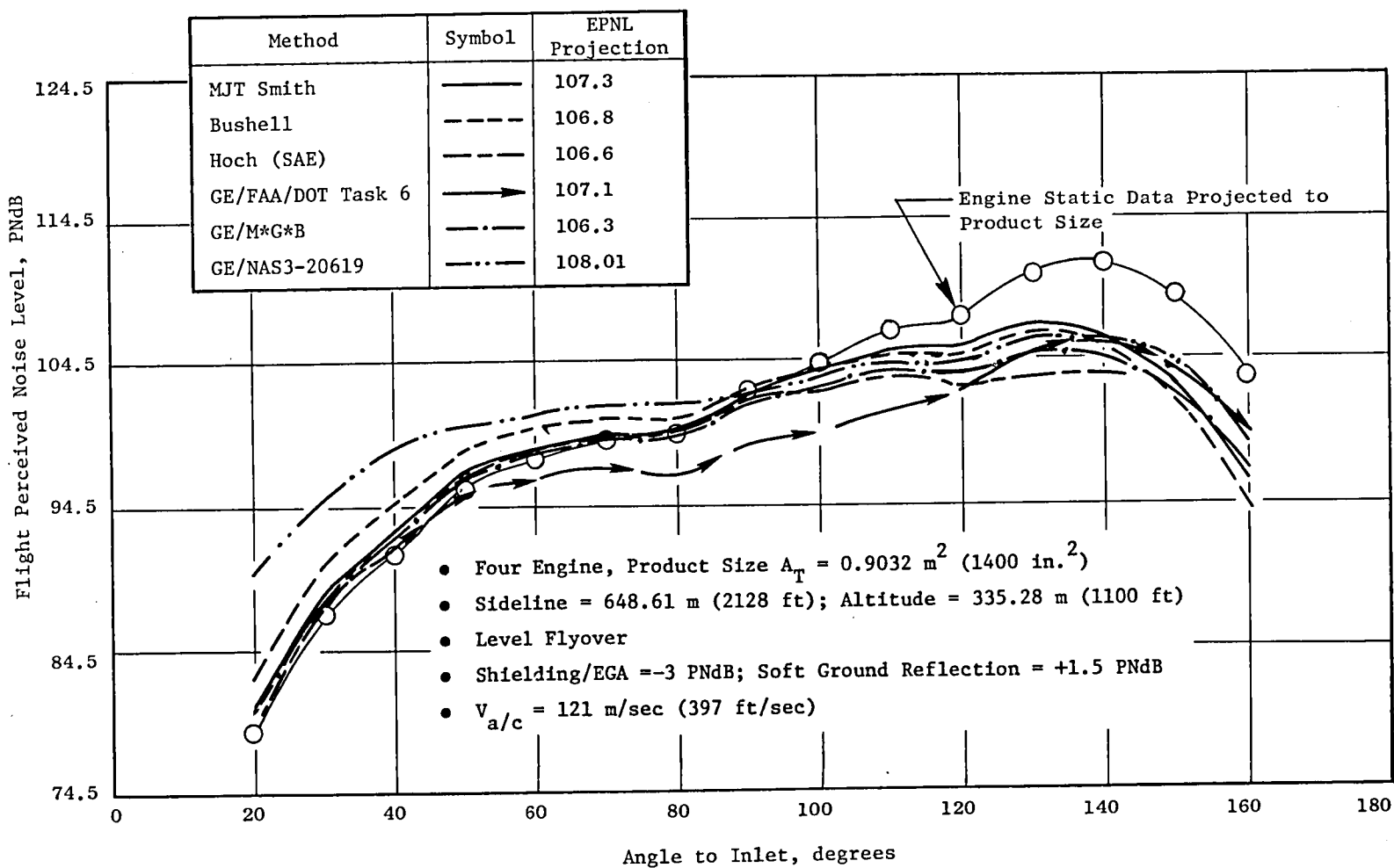


Figure 154. Variation of Projected Flight PNL for Several Flight Effects Methods for a Typical Sideline Noise Condition at $V_j^{mix} = 639.5 \text{ m/sec}$ (2098 ft/sec).

111 EPNdB for the models used. It is cautioned here that these estimates are based on level fly-over projections from static test results that are in the range of velocities, pressures, and temperatures typical of sideline takeoff conditions. Since aircraft engine cycle and matching flight conditions are very important in establishment of absolute values, the projections shown are only representative in nature.

With regard to the scatter obtained from the use of the different flight EPNL projection methodologies, the results show that the GE/NAS3-20619 method is generally higher by 1 EPNdB than any of the other methods used. The reason for the higher EPNL prediction is that the GE/NAS3-20619 method accounts fully for the flight shock noise forward quadrant lift, whereas none of the other methods have this capability.

EPNL Jet Noise Projections for Typical Cut-Back Conditions

At the typical cut-back flight condition [$v_j^{\text{mix}} = 508 \text{ m/sec (1667 ft/sec)}$], similar variations in flight PNL peak amplitude and field shape are observed. Figure 155 illustrates these projections. Once again, however, the projected EPNL variation is only about 1 EPNdB. The typical level found for this condition is about 107 EPNdB. The GE/NAS3-20619 method is now observed to be within 0.5 EPNdB of the average of the other models. This closer agreement is due to the cycle condition being less influenced by shock noise.

In terms of absolute levels, considerable reductions in the EPNL levels shown here can be expected for GE AST/VCE product designs. The improvement from the levels here would come through the high flow capability of the GE product design. This means that at the same thrust the total weight flow is increased to reduce the v_j^{mix} . Such improvements would result in EPNL levels typical of FAR 36 (1978) requirements.

EPNL Jet Noise Projections for Typical Approach Conditions

For the "typical" approach EPNL projections, Figure 156 is given. As was observed for the sideline and cut-back cases, rather large variations in peak flight PNL and PNL field shape are observed for the different methods of flight projection assumed; but again the EPNL variation is small (all methods are within ± 1.2 EPNdB of the average value obtained from all methods), ranging from 104.1 to 106.7 EPNdB.

• Conic Nozzle Projections

For comparison purposes, a series of conic nozzle test points were used to make product size noise projections in the same fashion as for the coannular plug nozzle. Table XI summarizes the conic nozzle EPNL flight projections using the models discussed in Section 5.5.7.1. Table XII shows the difference between the conic nozzle EPNL projection and the coannular plug nozzle projection when the conic nozzle is compared with the coannular plug nozzle results at the same mixed stream velocity, (v_j^{mix}) , density, (ρ_j^{mix}) , and total area.

Type Case	Test Point	V_j^o m/sec (ft/sec)	T_T^o K (°R)	P_r^o	V_j^i m/sec (ft/sec)	T_T^i K (°R)	P_r^i	V_j^{mix} m/sec (ft/sec)
Cut-Back	324	547.72 (1797)	868.88 (1564)	1.92	369.72 (1213)	415 (747)	1.87	508.1 (1667)

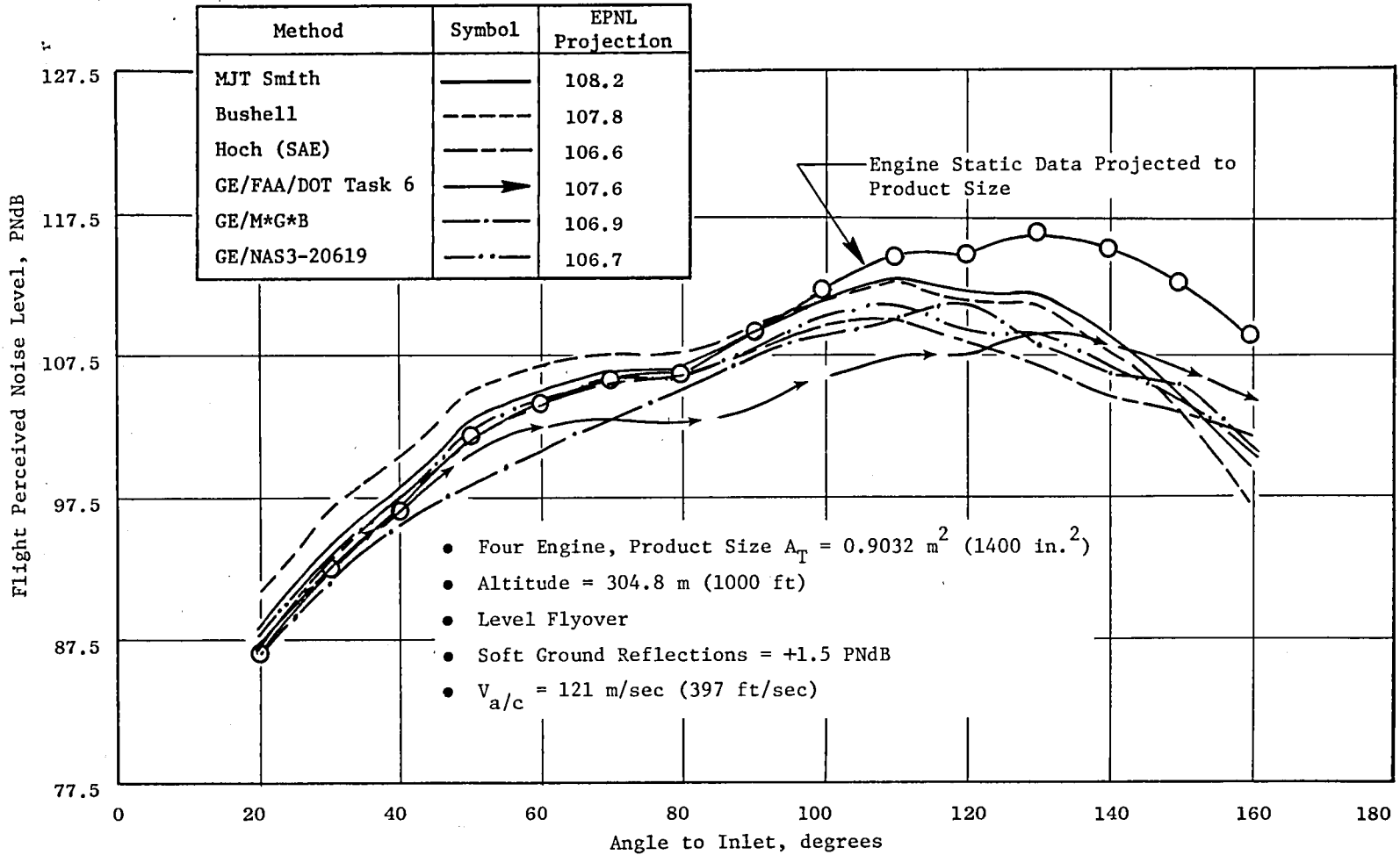


Figure 155. Variation in Projected Flight PNL for Several Flight Effects Methods for a Typical Cutback Noise Condition.

Type Case	Test Point	V_j^o m/sec (ft/sec)	T_T^o K (°R)	P_r^o	V_j^i m/sec (ft/sec)	T_T^i K (°R)	P_r^i	V_j^{mix} m/sec (ft/sec)
Approach	288	381.00 (1250)	715.55 (1288)	1.45	277.97 (912)	371.11 (668)	1.45	368.19 (1208)

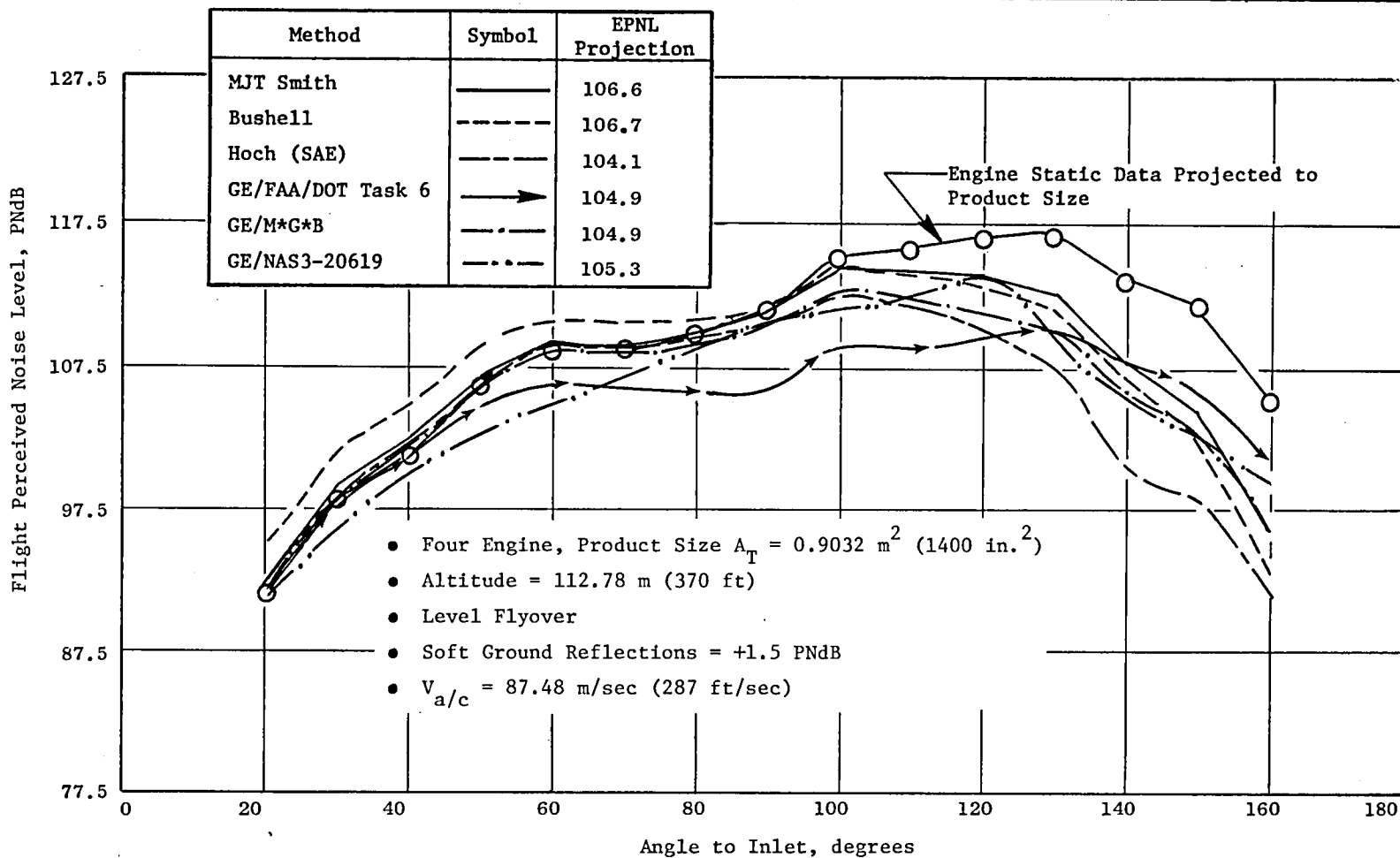


Figure 156. Variation in Projected Flight PNL for Several Flight Effects Methods for a Typical Approach Noise Condition.

Table XI. Conic Nozzle EPNL Projections Using Several Jet Noise Flight Projection Methods for Typical Sideline, Cutback and Approach Conditions. ,

Method	EPNL (4 Engines)		
	S/L TP97	C/B TP112	A/P TP107
MJT Smith	116.9	111.5	107.9
Bushell	117.0	111.0	108.1
Hock (SAE)	116.0	109.3	105.5
Task 6	115.8	110.6	106.0
MGB	115.9	109.9	106.5

Test Pt	V, (m/sec) (ft/sec)	T _T K (°R)	P _r	Sideline, meters (ft)	Alt., meters (ft)	Va/c, m/sec (ft/sec)
97	730.3 (2396)	966.11 (1739)	3.024	648.61 (2128)	335.28 (1100)	121 (397)
112	494.39 (1622)	734.44 (1322)	1.877	0	304.8 (1000)	121 (397)
107	366.67 (1203)	633.89 (1139)	1.476	0	112.78 (370)	87.48 (287)

Table XII. Projected Difference in EPNL Between the Conic Nozzle and Coannular Plug Nozzle* at Typical Sideline, Cutback and Approach Conditions.

Method	EPNL - EPNL			
	Sideline	Conic Sideline	Coannular Cut-Back	Approach
M J T Smith (IKO)	5.1	6.05	4.53	1.72
Bushell	5.6	6.65	4.43	2.42
Hock (SAE)	4.8	5.85	3.93	1.82
Task 6	4.7	5.15	4.23	1.52
MGB	5.1	6.05	4.23	2.02

*Conic nozzle conditions corrected to match coannular plug nozzle V_j^{mix} , ρ_j^{mix} and A_T . See Figures 153 through 156 for cycle conditions at which comparisons were made.

The results of Table XII show that on an EPNdB basis the coannular plug nozzle is about 5-6 EPNdB lower than the conic nozzle at typical sideline engine cycle conditions; about 4 EPNdB at cutback conditions; and about 2 EPNdB at approach conditions. The reason for the projected reduction of coannular plug nozzle suppression at the lower velocities is that the engine coannular plug nozzle data used were at non-optimum velocity ratios (See Section 5.5.1.6). Actual product engines would be able to operate at a more favorable $V\frac{1}{2}$ and thus a better noise reduction relative to the conic nozzle would be obtained.

5.6 ENGINE AND ACOUSTIC NOZZLE PERFORMANCE

5.6.1 Engine and Nozzle Performance Summary

During the Edwards Acoustic Nozzle Test the test bed engine operated essentially the same as was observed in the prior Lynn Forward VABI test. Engine component performance was stable throughout the test and was essentially the same as measured in the Forward VABI test. Transitioning and double bypass operation presented no problem with the flow inverting, two stream coannular nozzle.

Nozzle performance was repeatable and consistent throughout the test. Essentially, all nozzle performance objectives were obtained. Maximum nozzle velocities over 762 m/sec (2500 ft/sec) and 610 m/sec (2000 ft/sec) were obtained for the conic and coannular 0.475 area ratio nozzles, respectively. Both inner and outer nozzle maximum pressure ratio at 0.2 area ratio exceeded 2.9. These were key objectives for the acoustic evaluation.

5.6.2 Engine and Nozzle Performance Results

5.6.2.1 Engine Performance

A comparison of the Lynn 2x1 Forward VABI engine performance with the Edwards acoustic nozzle engine performance is shown in Figures 157 through 167. Generally, the Edwards acoustic test data is in very good agreement with the Lynn Forward VABI test data. This comparison has been made, where possible, using the Forward VABI test final calibration data at a nozzle area of 0.122 m² (190 in.²) which is similar to the conic nozzle areas used in the acoustic nozzle test. The selected figures contain data from the beginning, middle and end of the test, showing consistency and absence of deterioration throughout the test.

Figure 157 shows that there was no front block speed flow change (flow calculated upstream of treated inlet) with the treated inlet, indicating the treated inlet had no significant pressure loss. This is reasonable since the treated inlet was sized for an engine with higher airflow. All coannular nozzle testing was accomplished with the treated inlet. Figure 157

ACOUSTIC NOZZLE PERFORMANCE

Single Bypass

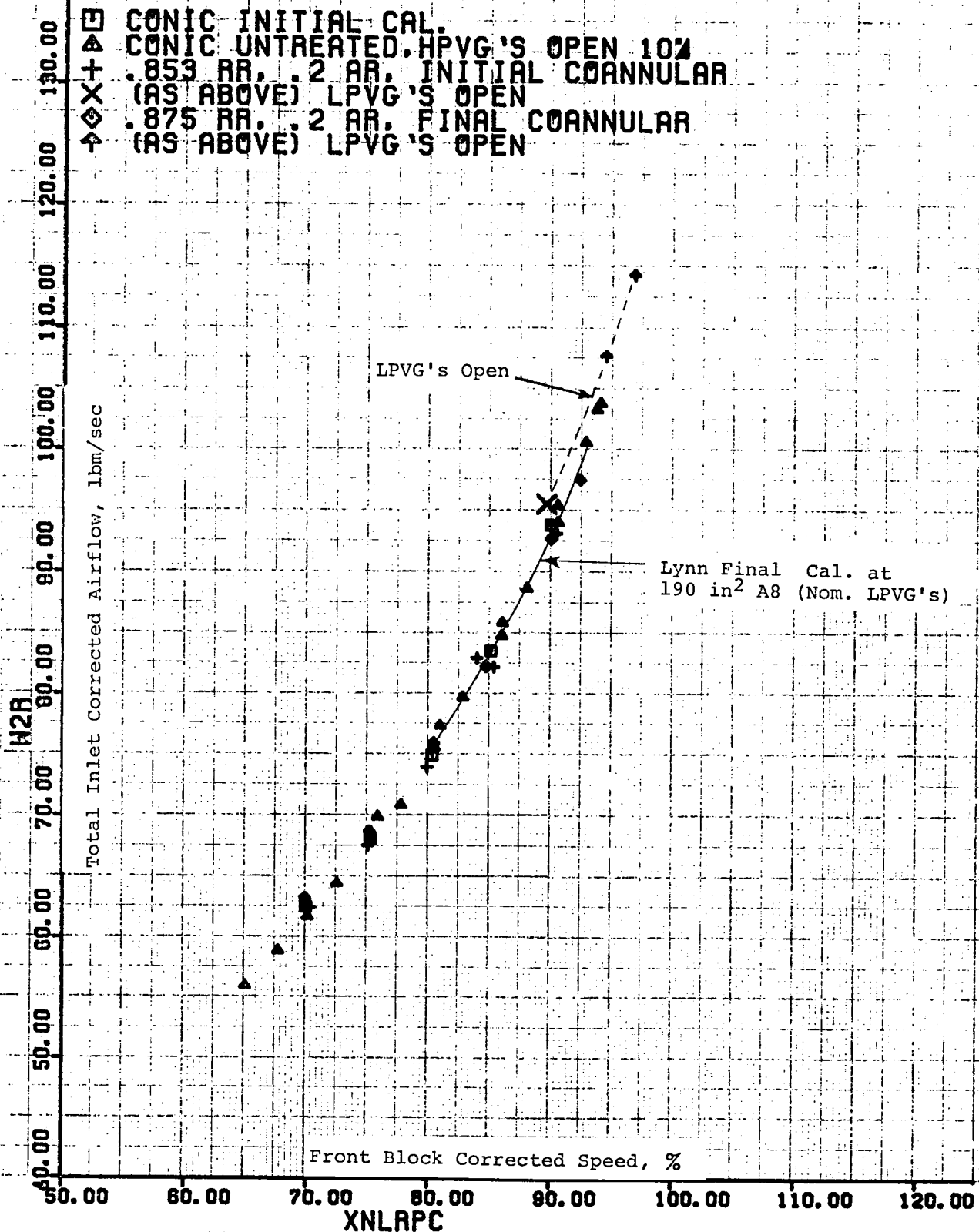


Figure 157 (a). Total Inlet Corrected Airflow Versus Front Block Corrected Speed.

ACOUSTIC NOZZLE PERFORMANCE

Single Bypass

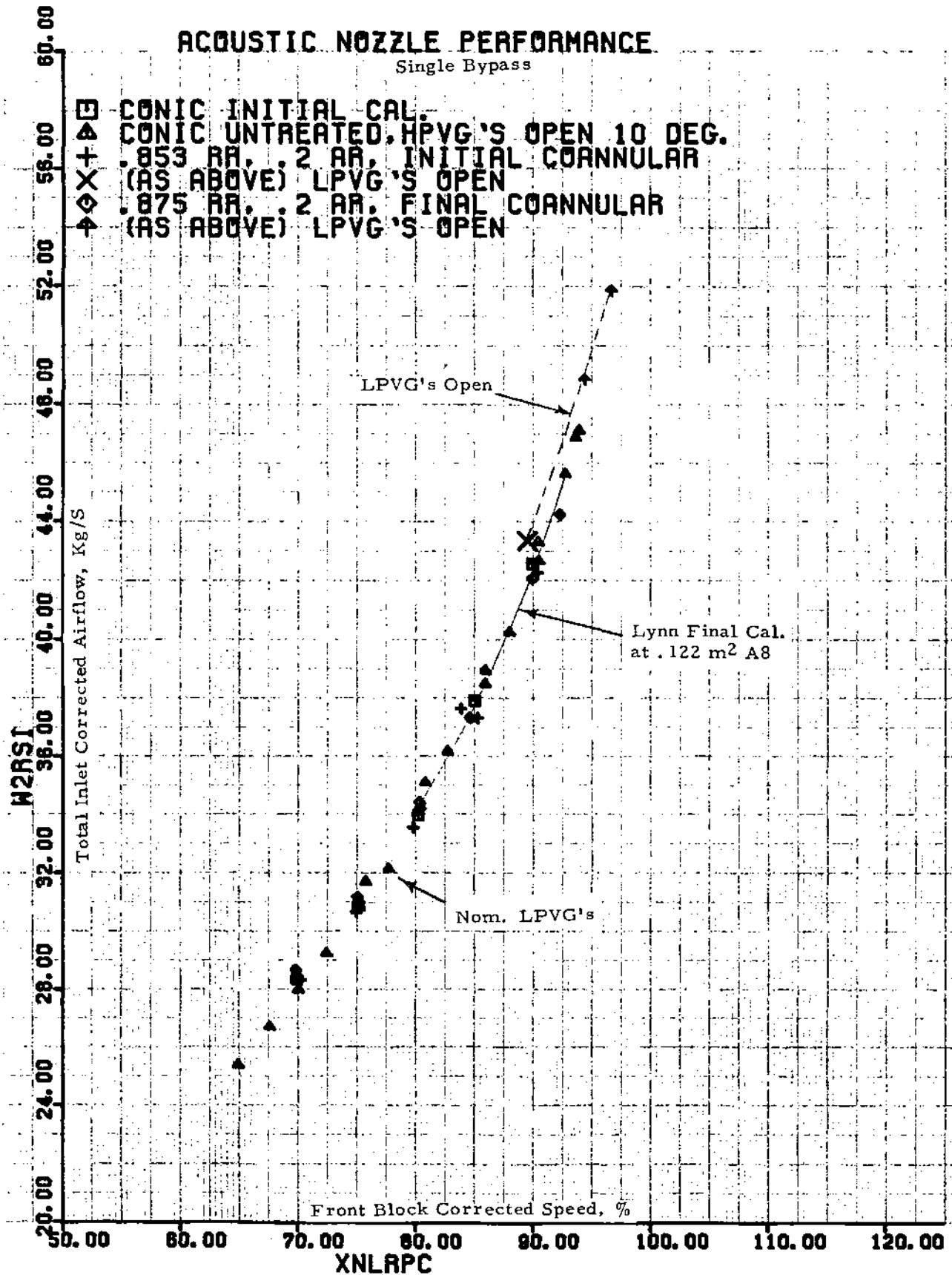


Figure 157 (b). Total Inlet Corrected Airflow Versus Front Block Corrected Speed.

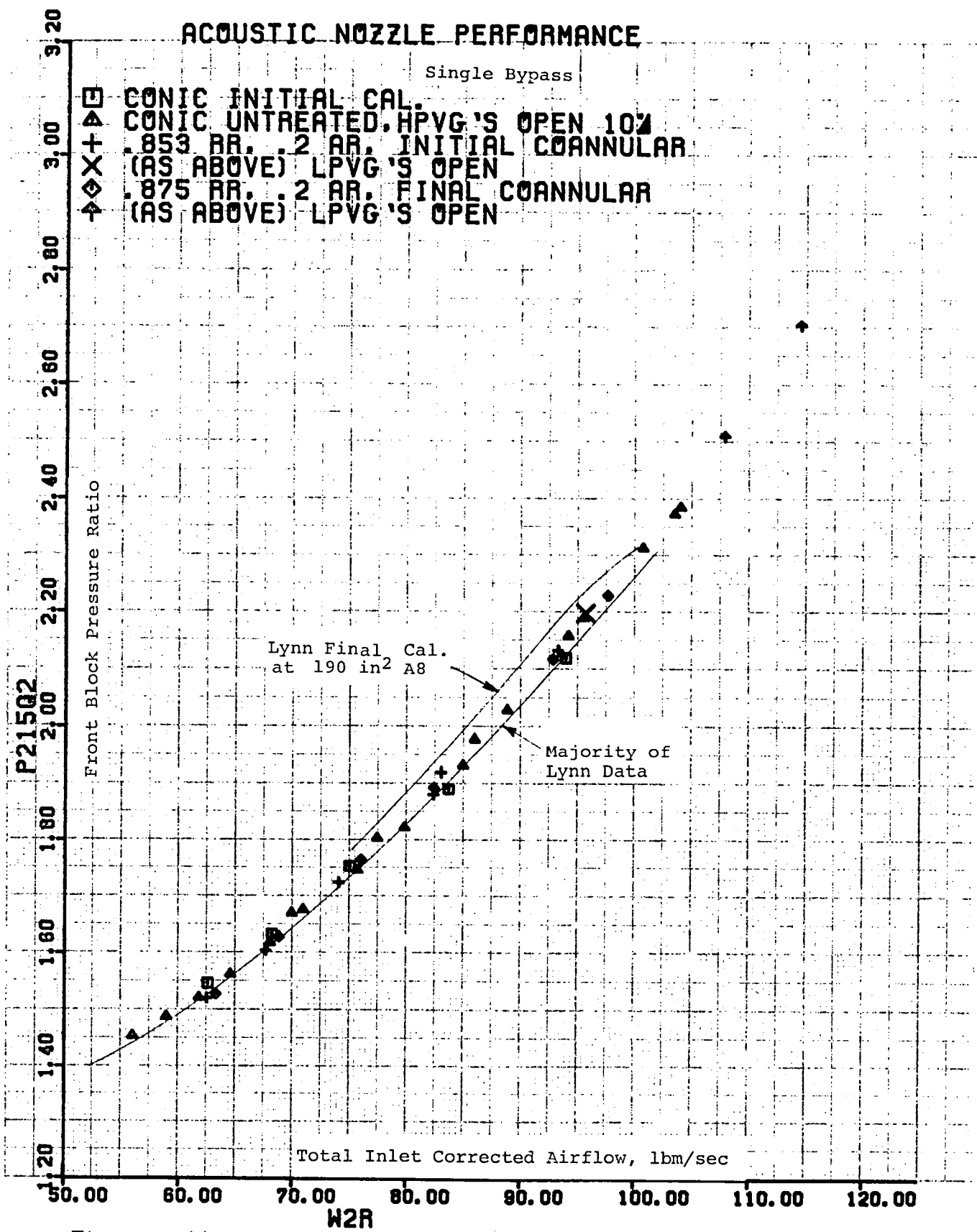


Figure 158 (a). Front Block Pressure Ratio Versus Total Inlet Corrected Airflow.

ACOUSTIC NOZZLE PERFORMANCE

Single Bypass

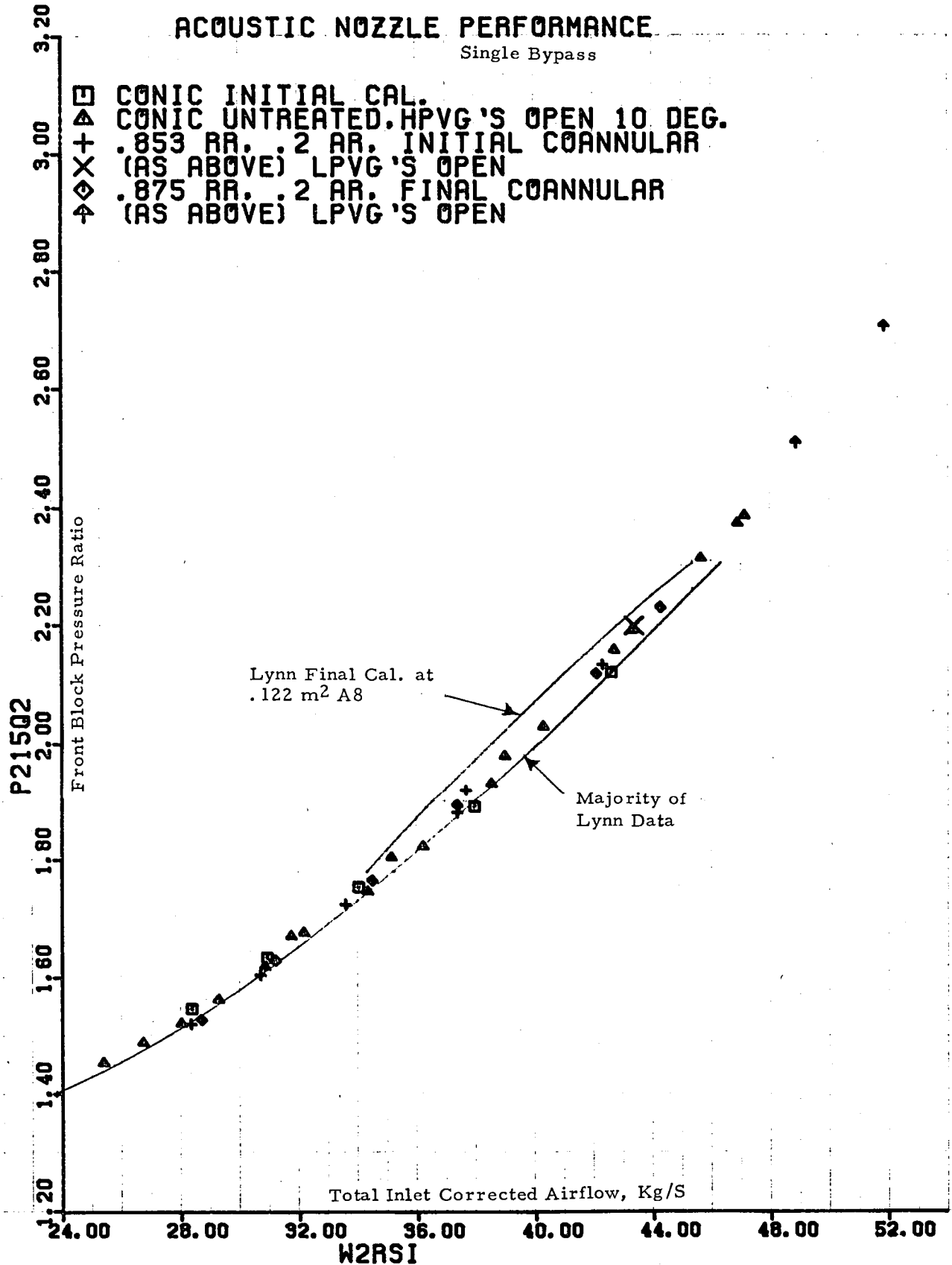


Figure 158 (b). Front Block Pressure Ratio Versus Total Inlet Corrected Airflow.

ACOUSTIC NOZZLE PERFORMANCE

Single Bypass

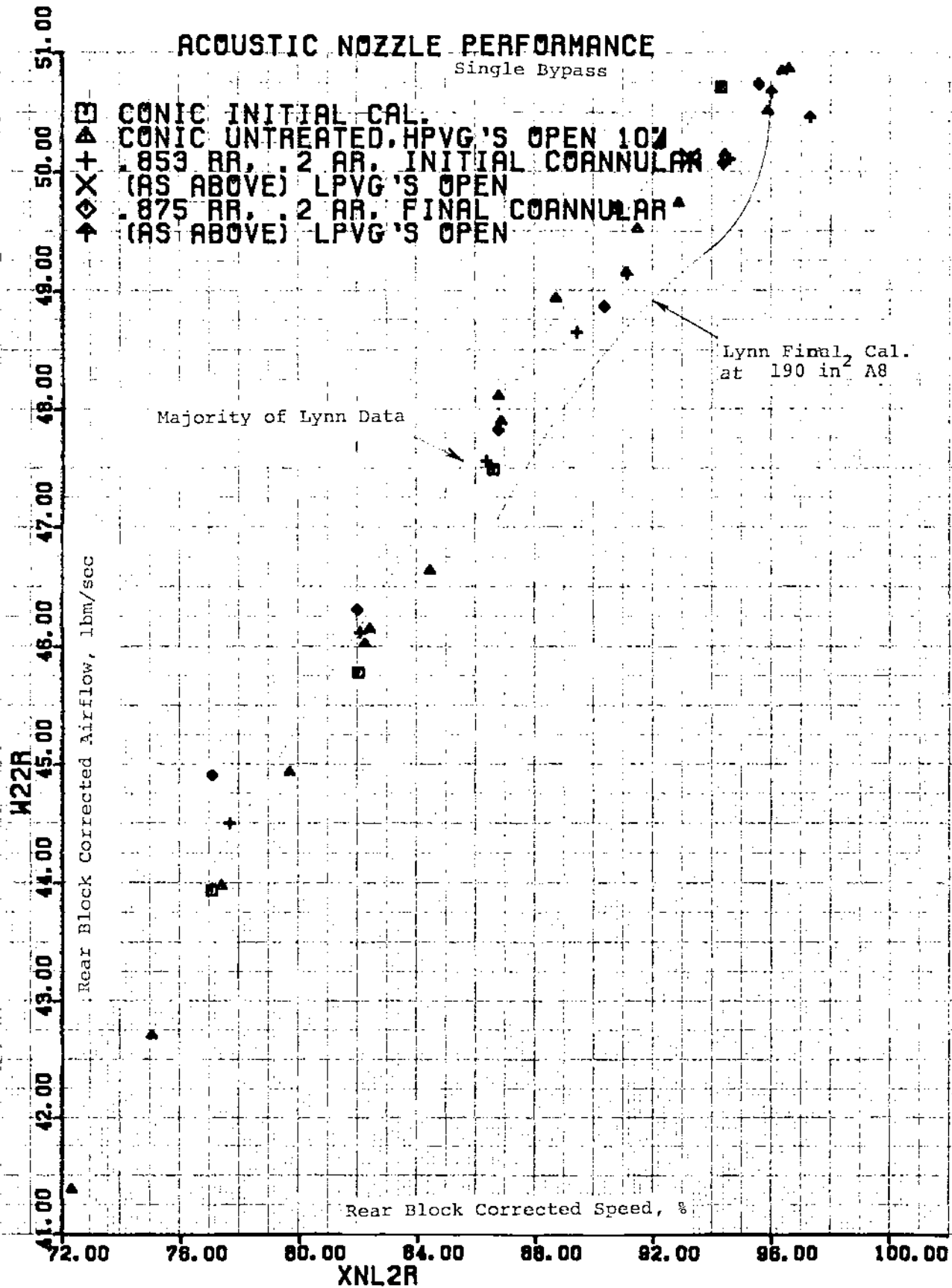


Figure 159 (a). Rear Block Corrected Airflow Versus Rear Block Corrected Speed.

ACOUSTIC NOZZLE PERFORMANCE

Single Bypass

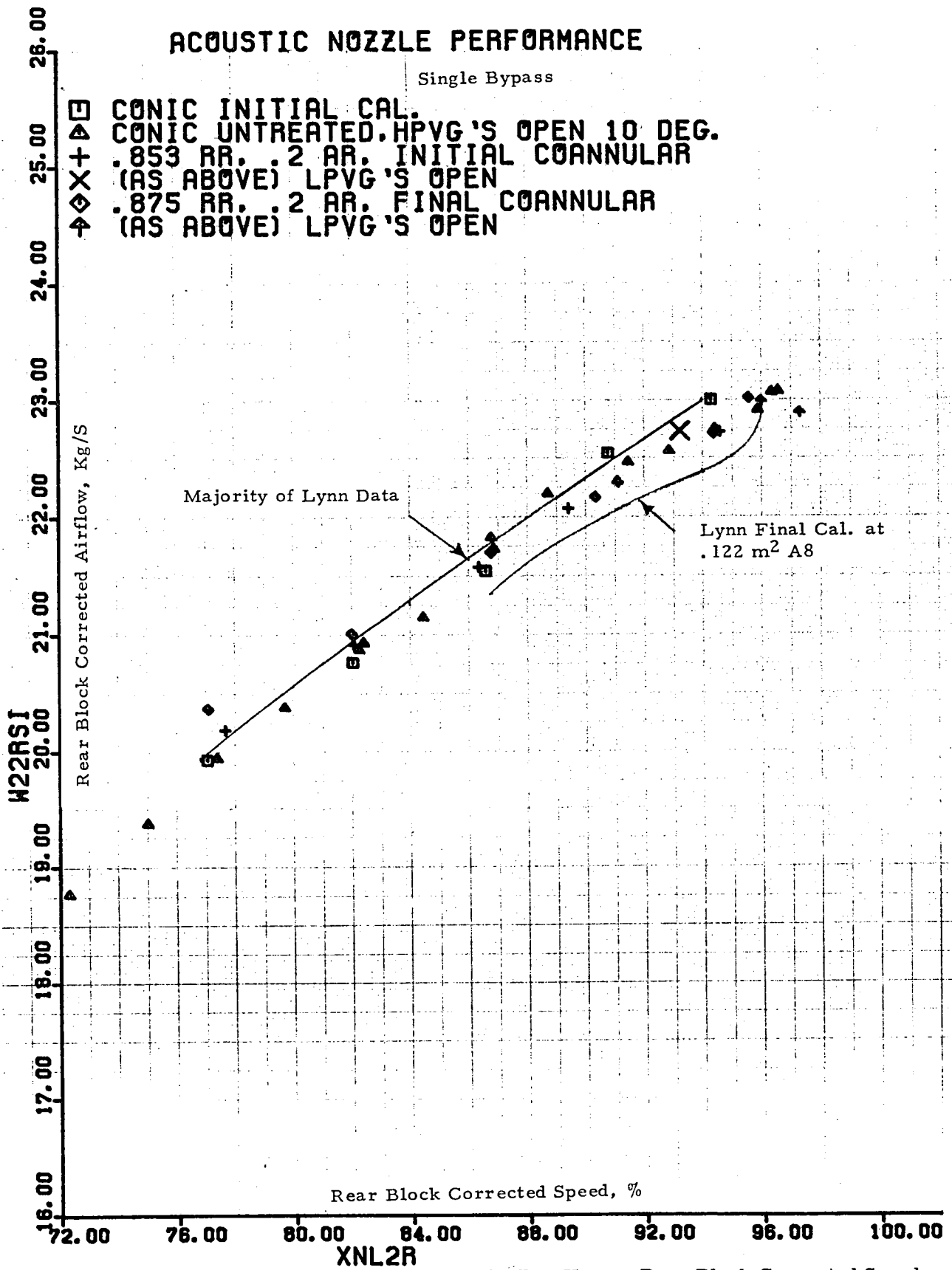


Figure 159 (b). Rear Block Corrected Airflow Versus Rear Block Corrected Speed.

ACOUSTIC NOZZLE PERFORMANCE

Single Bypass

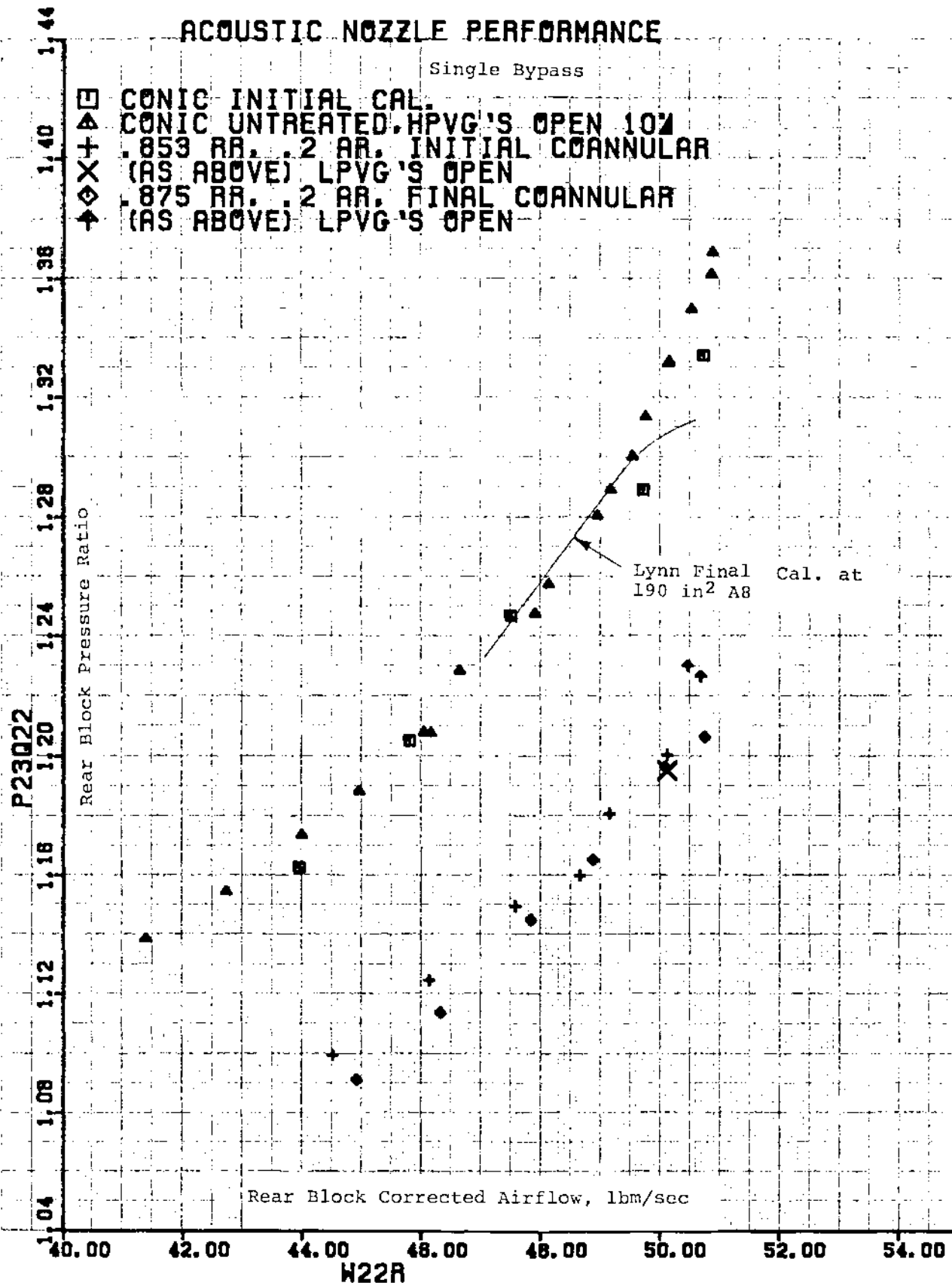


Figure 160 (a). Rear Block Pressure Ratio Versus Rear Block Corrected Airflow.

ACOUSTIC NOZZLE PERFORMANCE

Single Bypass

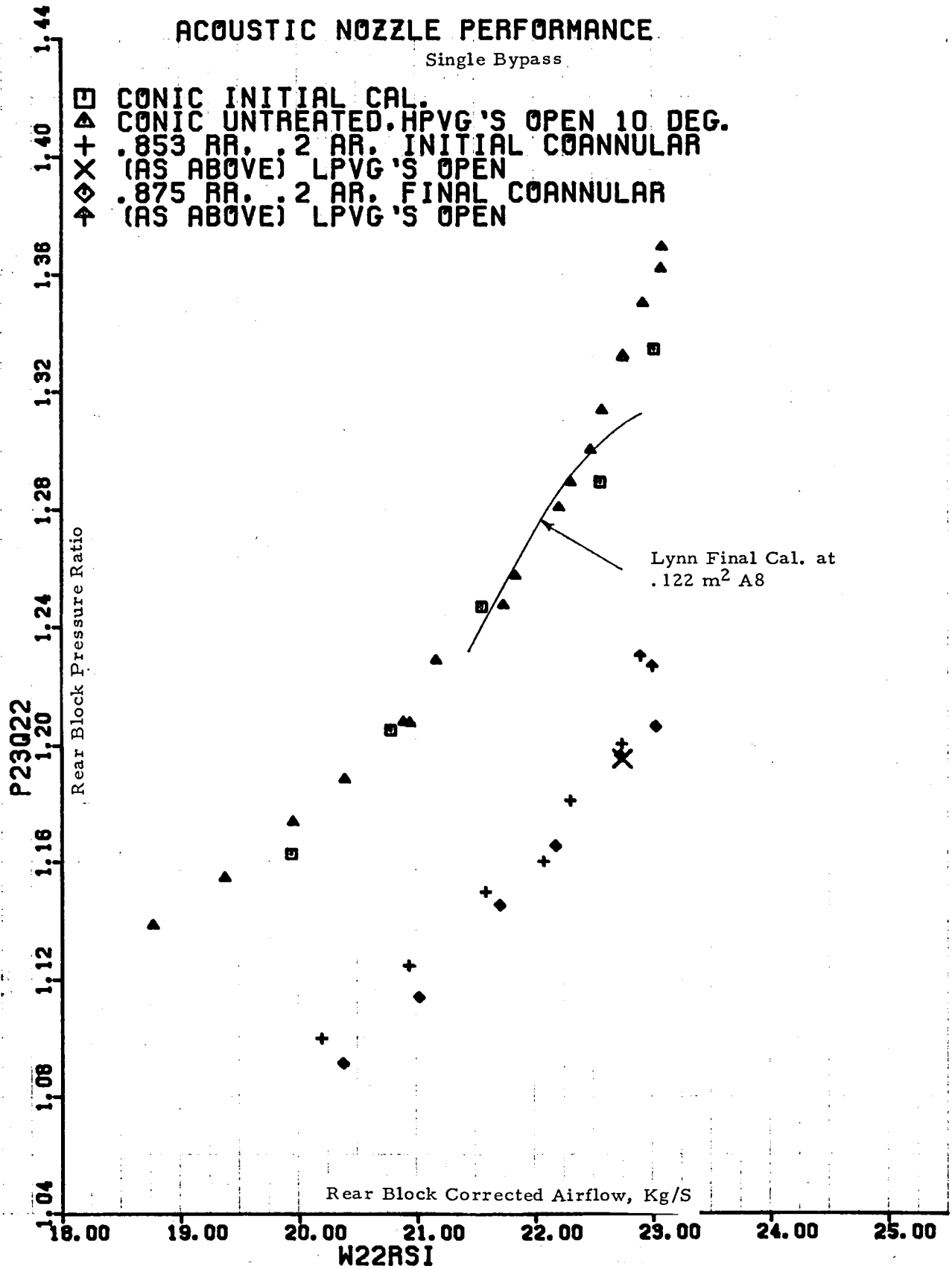


Figure 160 (b). Rear Block Pressure Ratio Versus Rear Block Corrected Airflow.

ACOUSTIC NOZZLE PERFORMANCE

Single Bypass

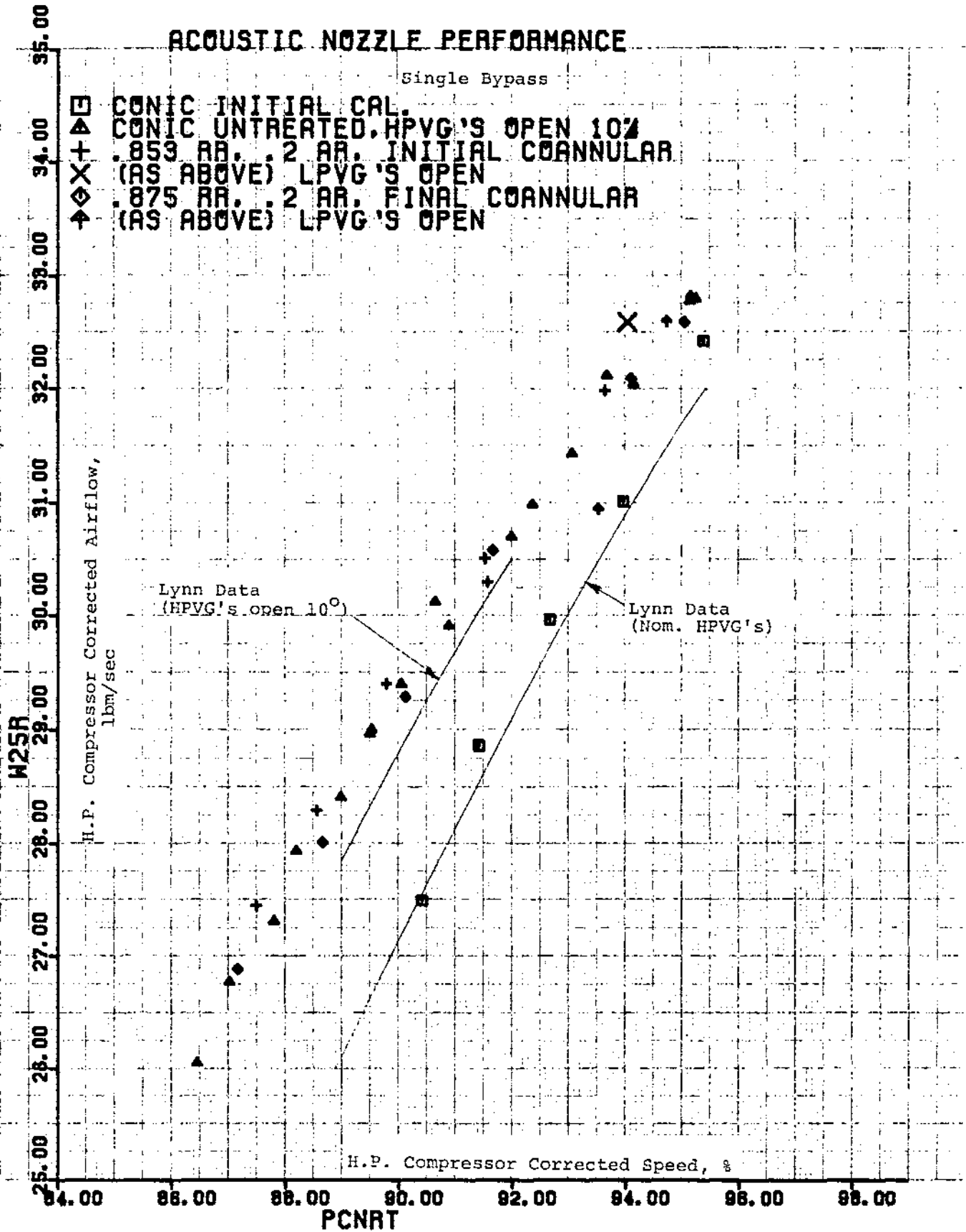


Figure 161 (a). H. P. Compressor Corrected Airflow Versus H. P. Compressor Corrected Speed.

ACOUSTIC NOZZLE PERFORMANCE

Single Bypass

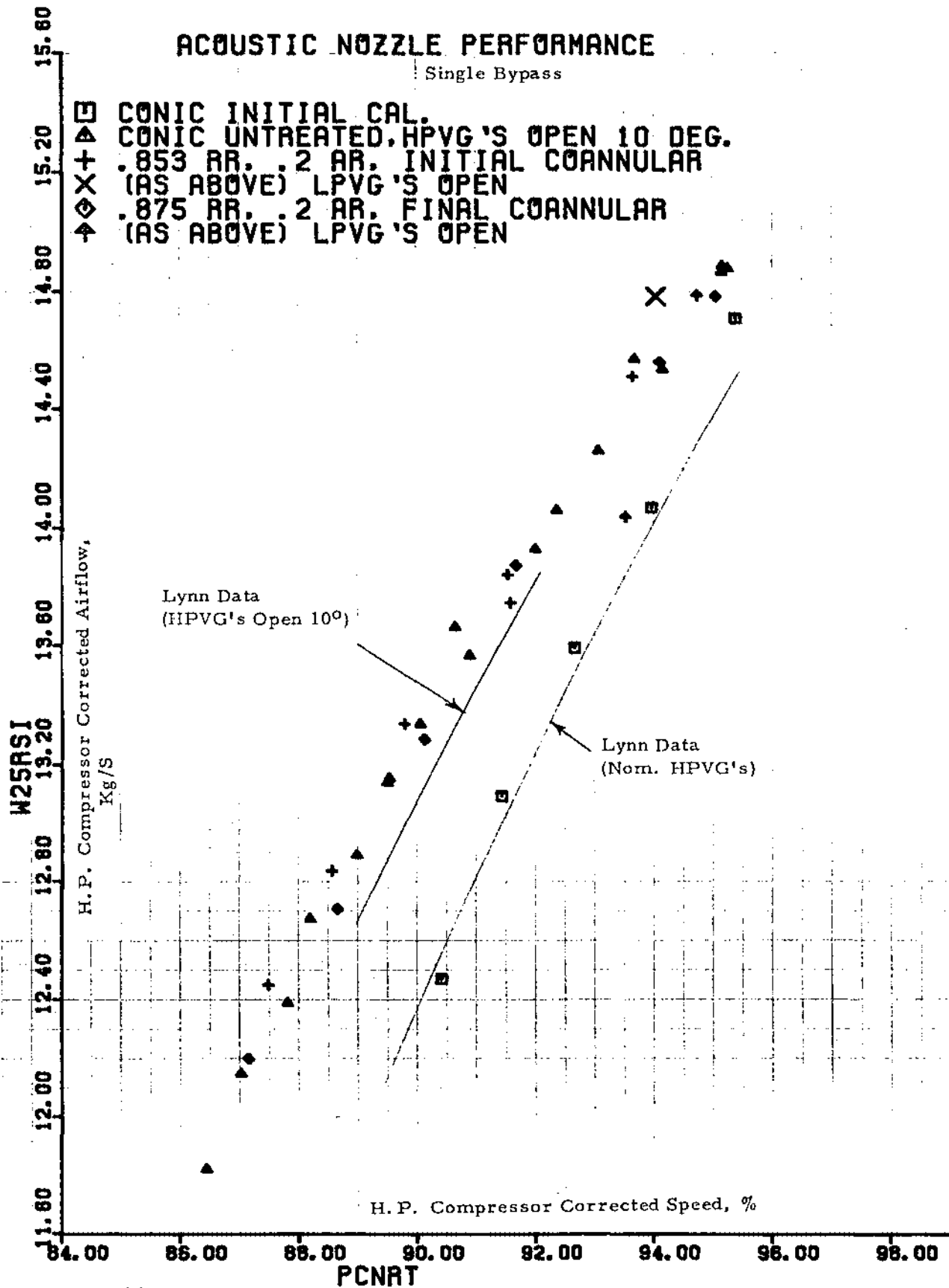


Figure 161 (b). H.P. Compressor Corrected Airflow Versus H.P. Compressor Corrected Speed.

ACOUSTIC NOZZLE PERFORMANCE

Single Bypass

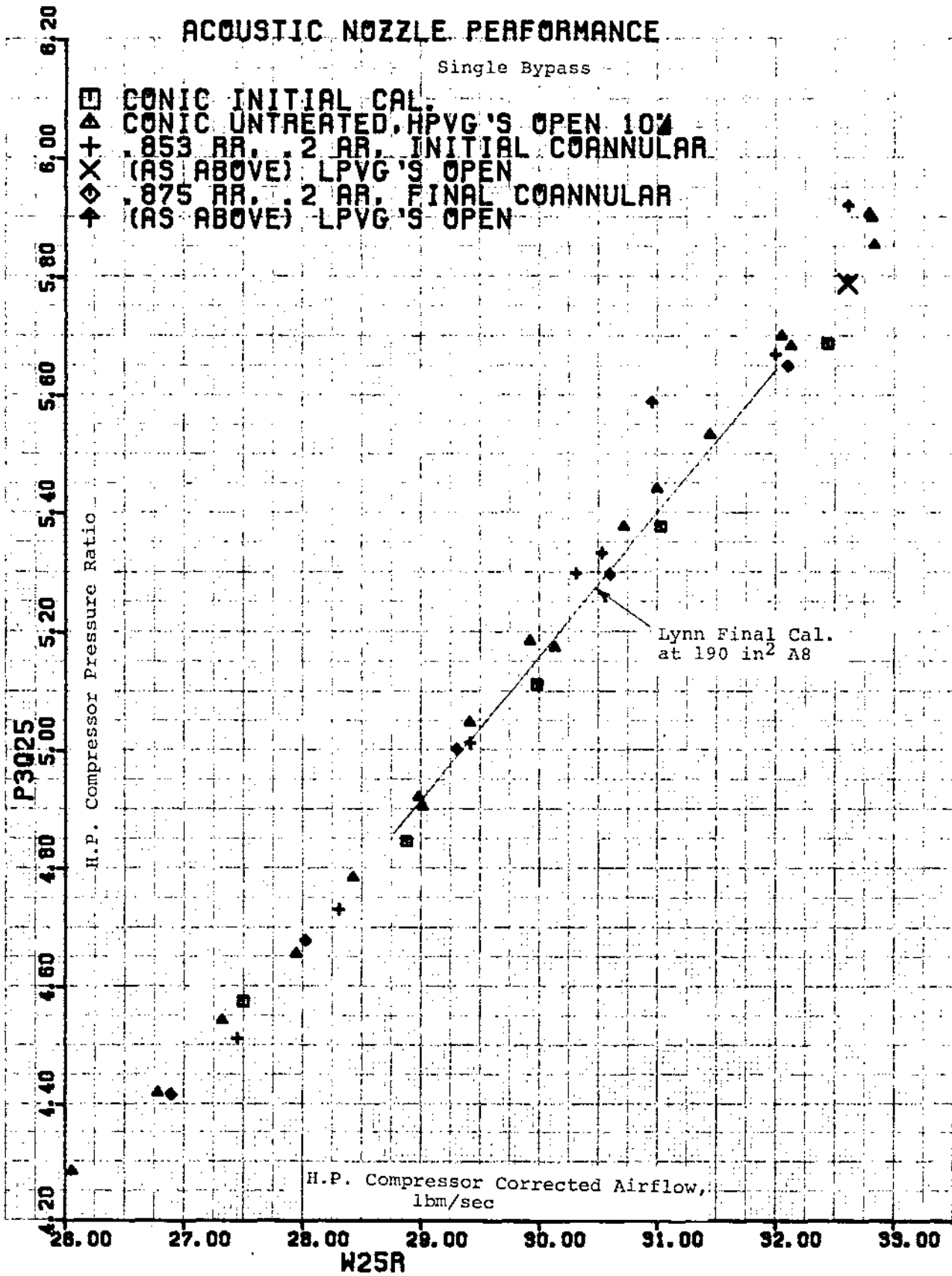


Figure 162 (a). H.P. Compressor Pressure Ratio Versus H.P. Compressor Corrected Airflow.

ACOUSTIC NOZZLE PERFORMANCE

Single Bypass

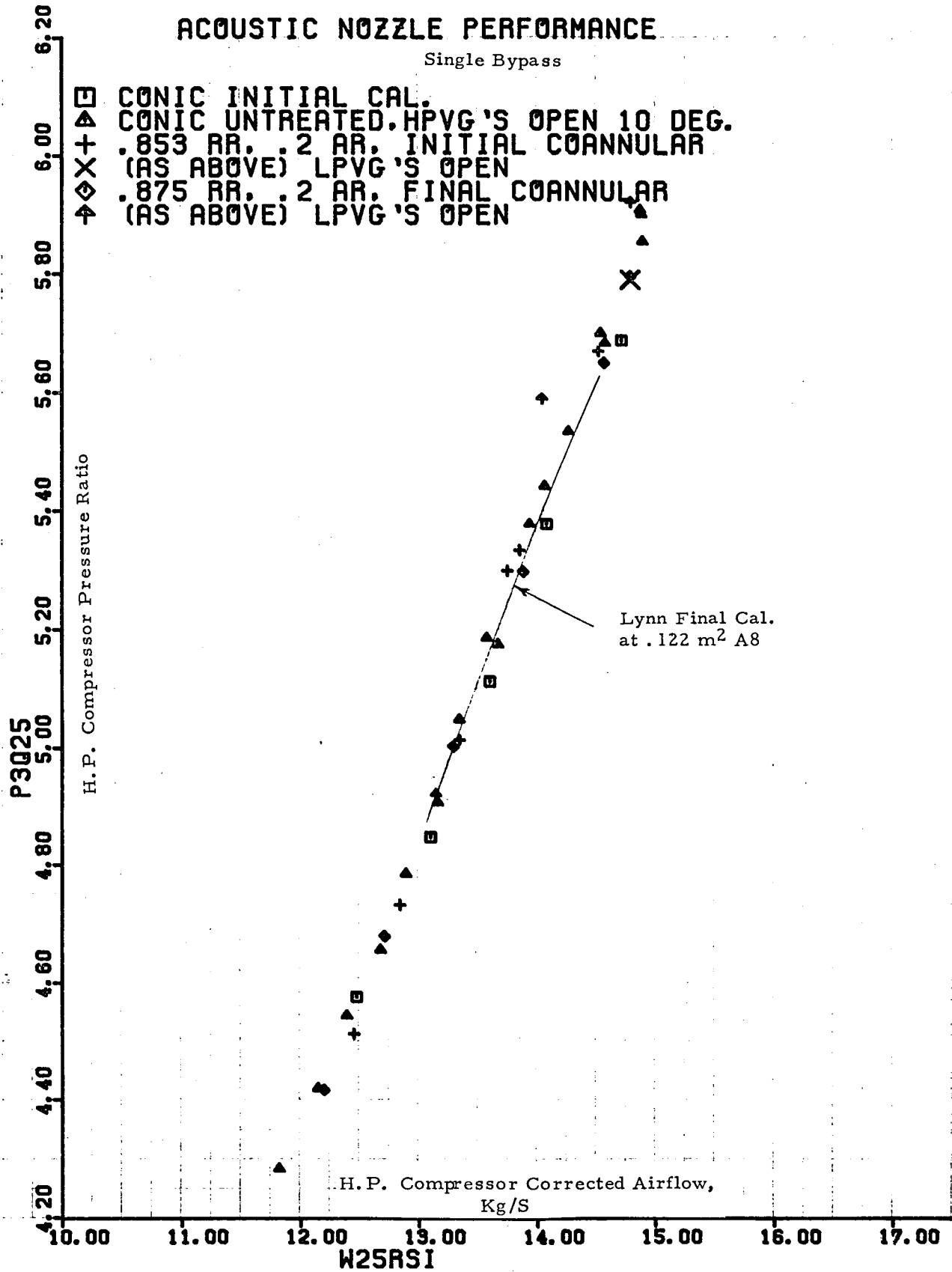


Figure 162 (b). H. P. Compressor Pressure Ratio Versus H. P. Compressor Corrected Airflow.

ACOUSTIC NOZZLE PERFORMANCE

Single Bypass

- CONIC INITIAL CAL.
- ▲ CONIC UNTREATED, HPVG'S OPEN 10%
- + .853 RR, .2 RR, INITIAL COANNULAR
- X (AS ABOVE) LPVG'S OPEN
- ◇ .875 RR, .2 RR, FINAL COANNULAR
- ▲ (AS ABOVE) LPVG'S OPEN

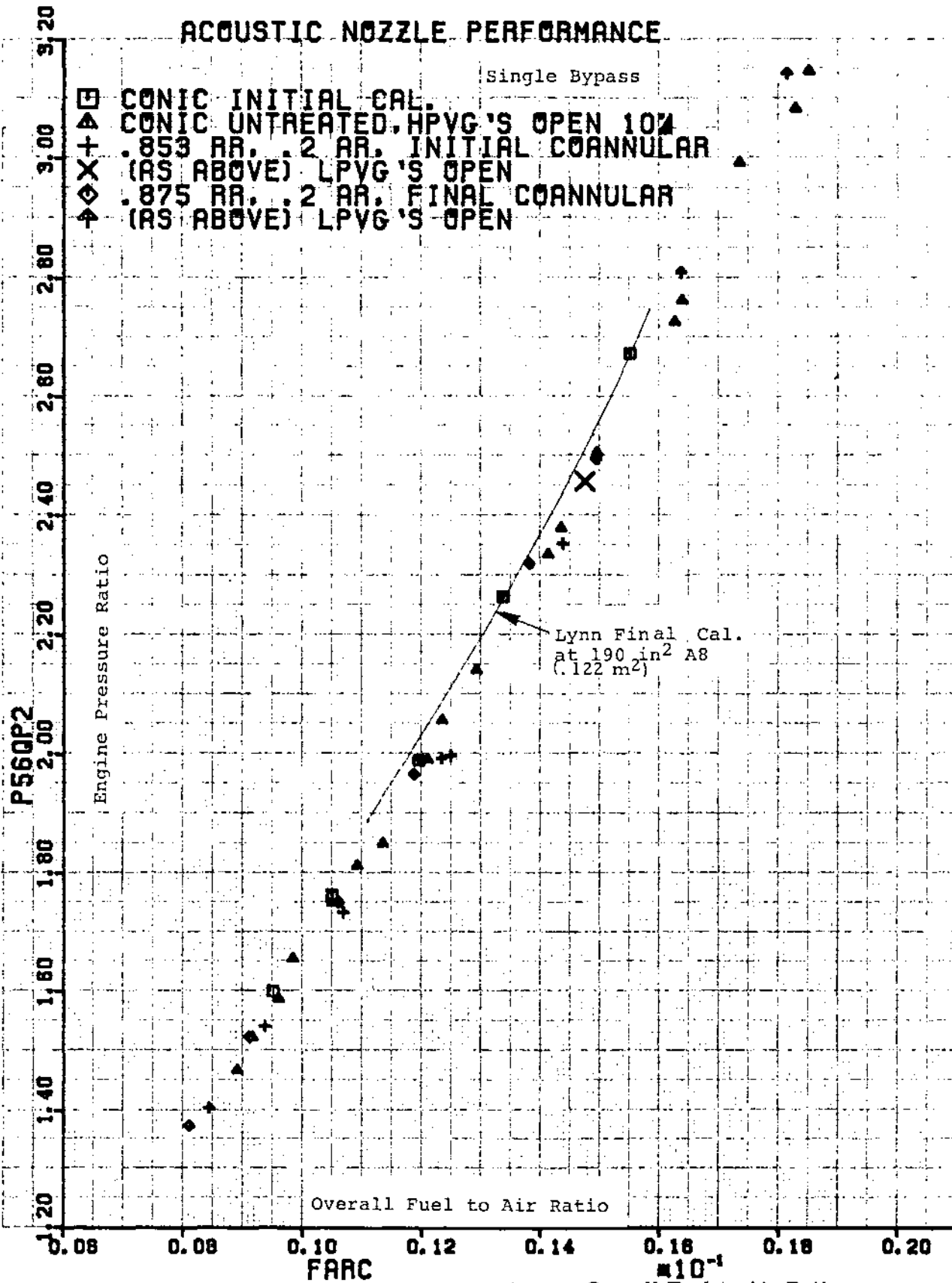


Figure 163. Engine Pressure Ratio Versus Overall Fuel to Air Ratio.

ACOUSTIC NOZZLE PERFORMANCE

Single Bypass

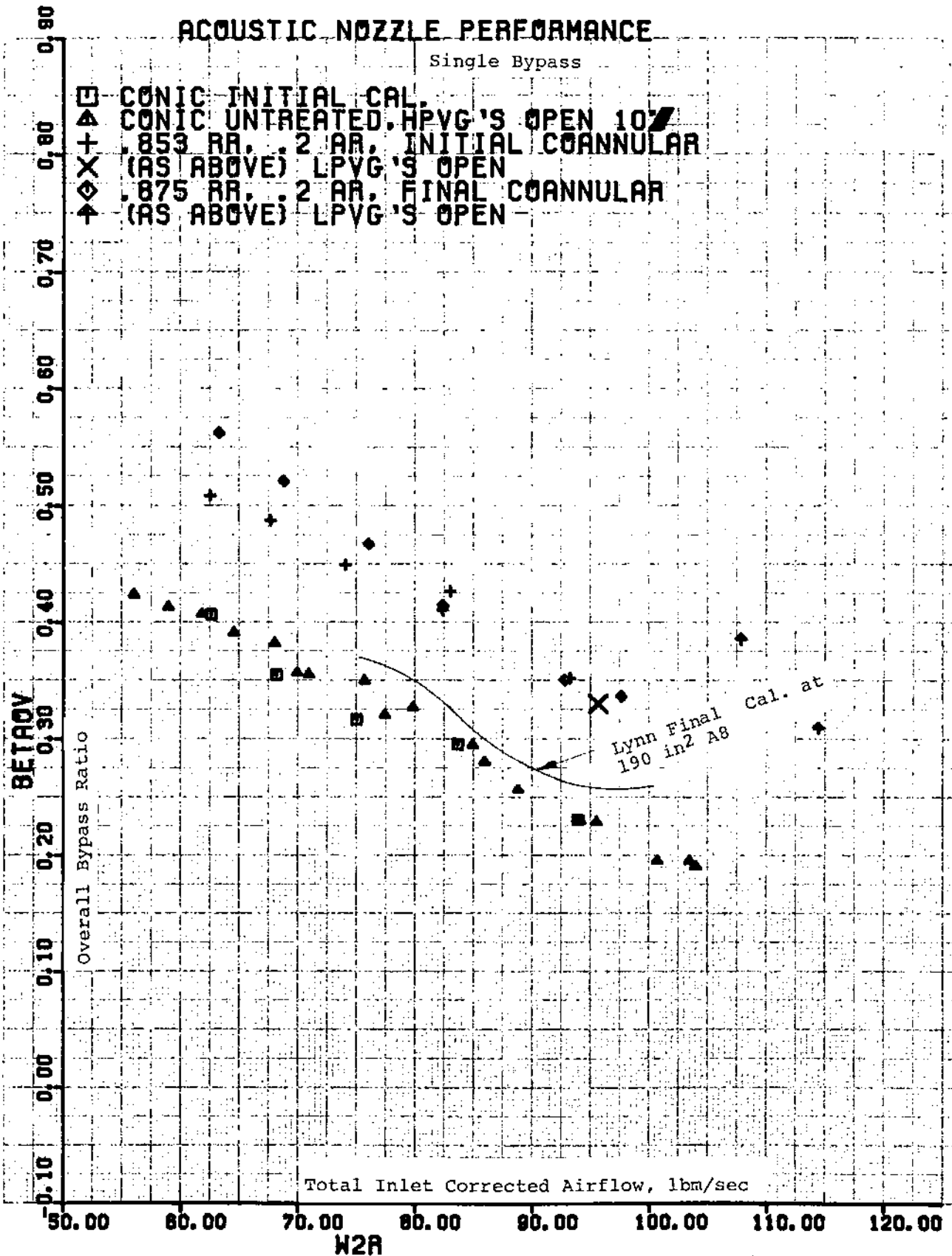


Figure 164 (a). Overall Bypass Ratio Versus Total Inlet Corrected Airflow.

ACOUSTIC NOZZLE PERFORMANCE

Single Bypass

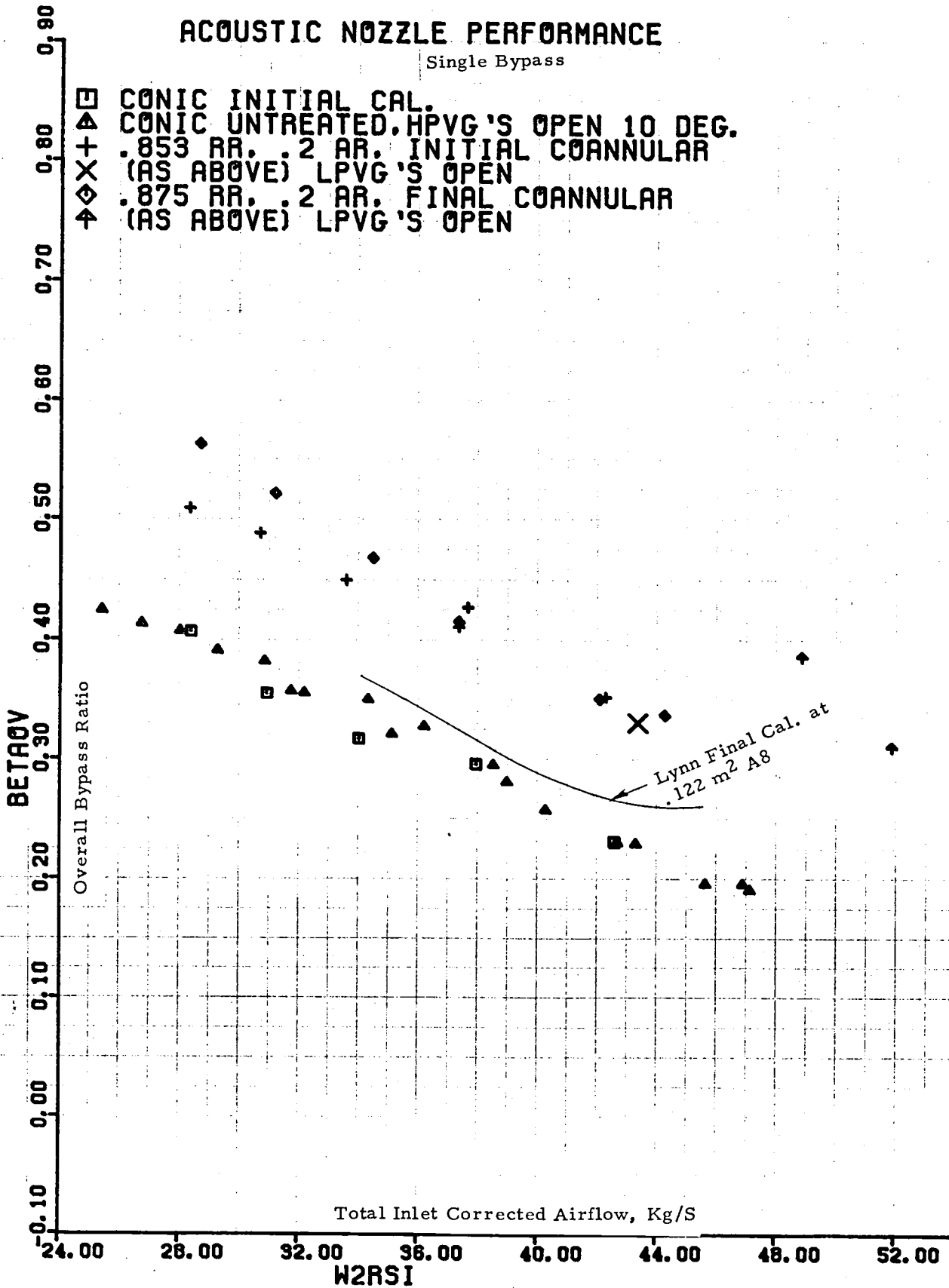


Figure 164 (b). Overall Bypass Ratio Versus Total Inlet Corrected Airflow.

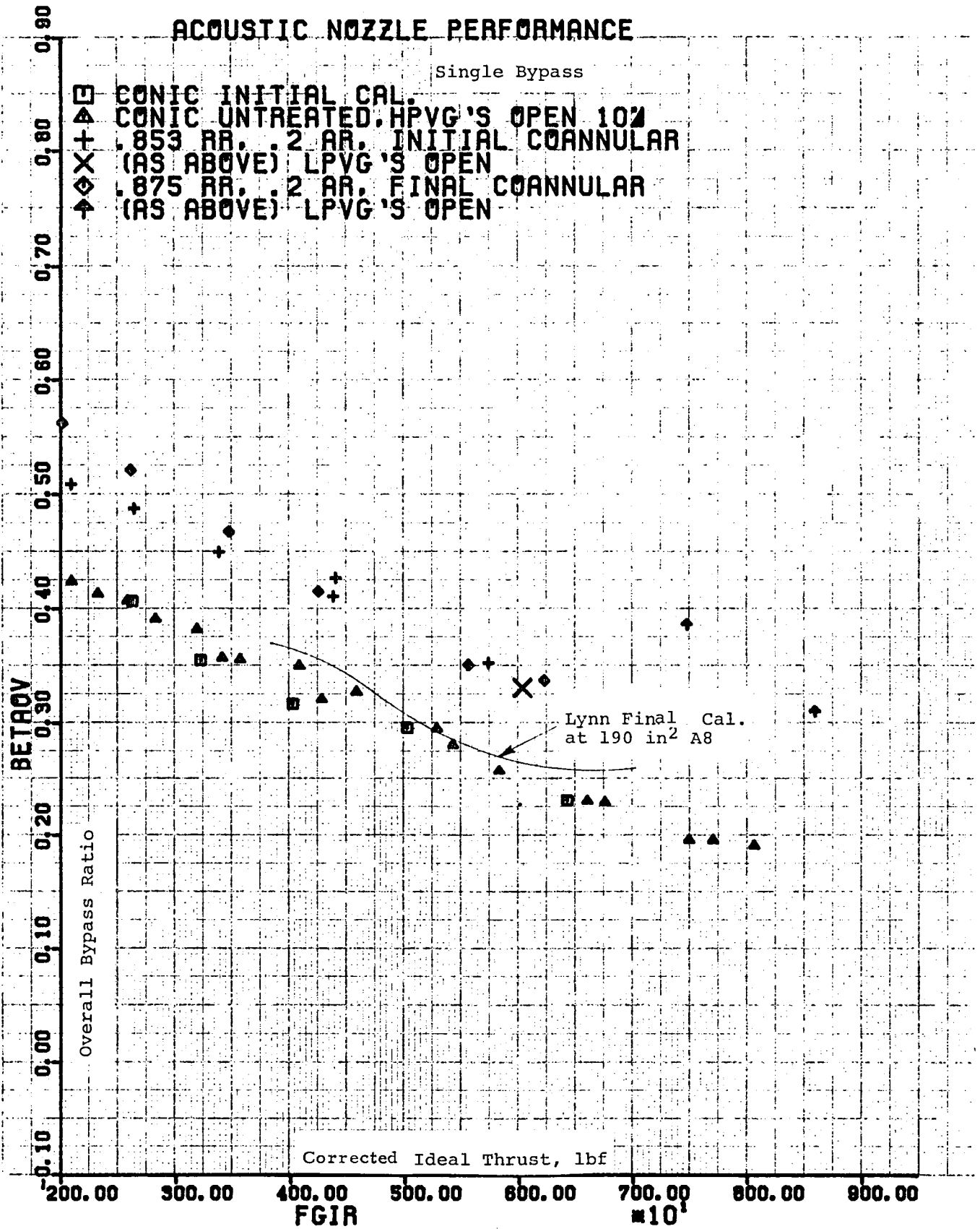


Figure 165 (a). Overall Bypass Ratio Versus Corrected Ideal Thrust.

ACOUSTIC NOZZLE PERFORMANCE

Single Bypass

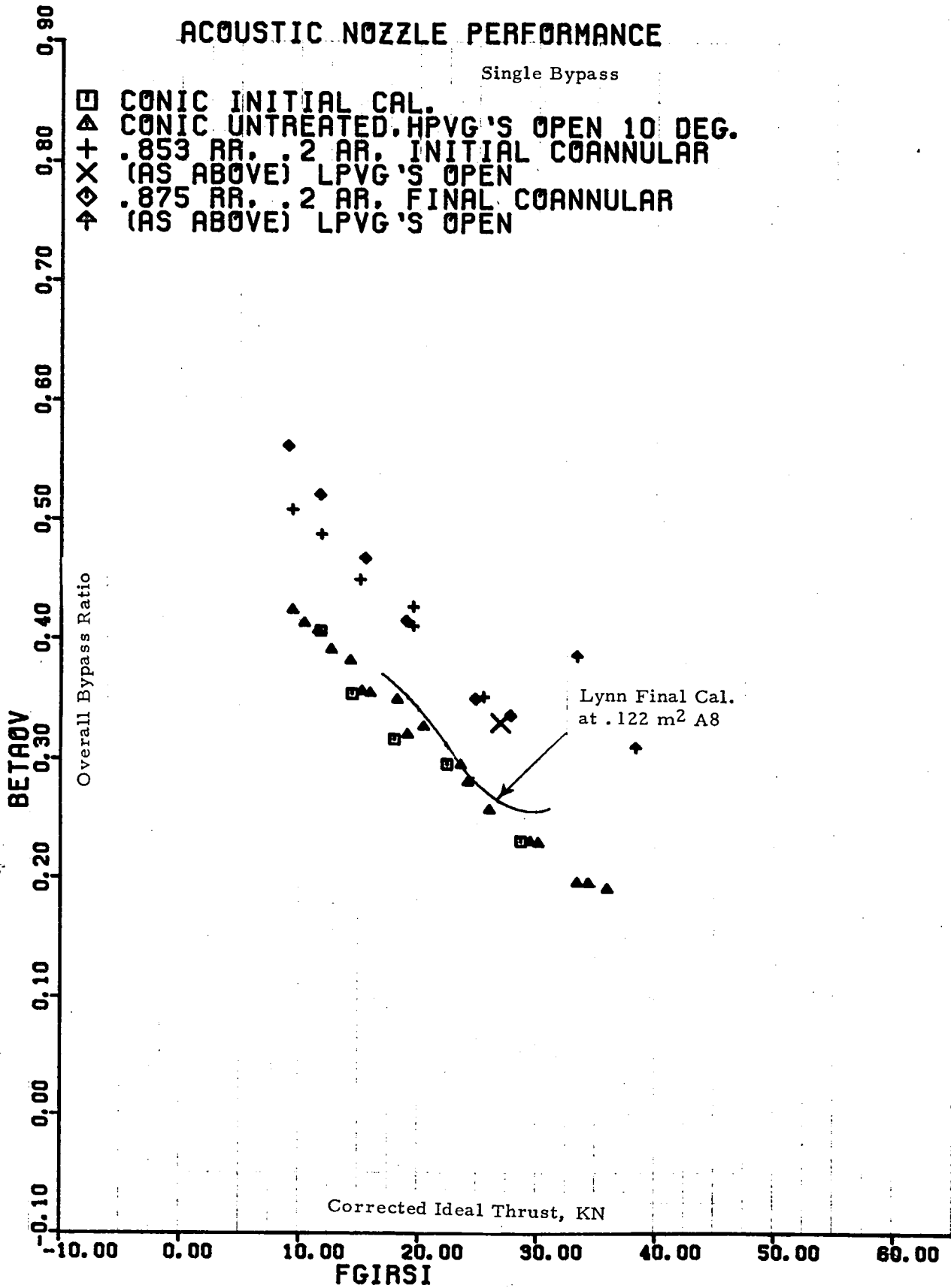


Figure 165 (b). Overall Bypass Ratio Versus Corrected Ideal Thrust.

ACOUSTIC NOZZLE PERFORMANCE

Single Bypass

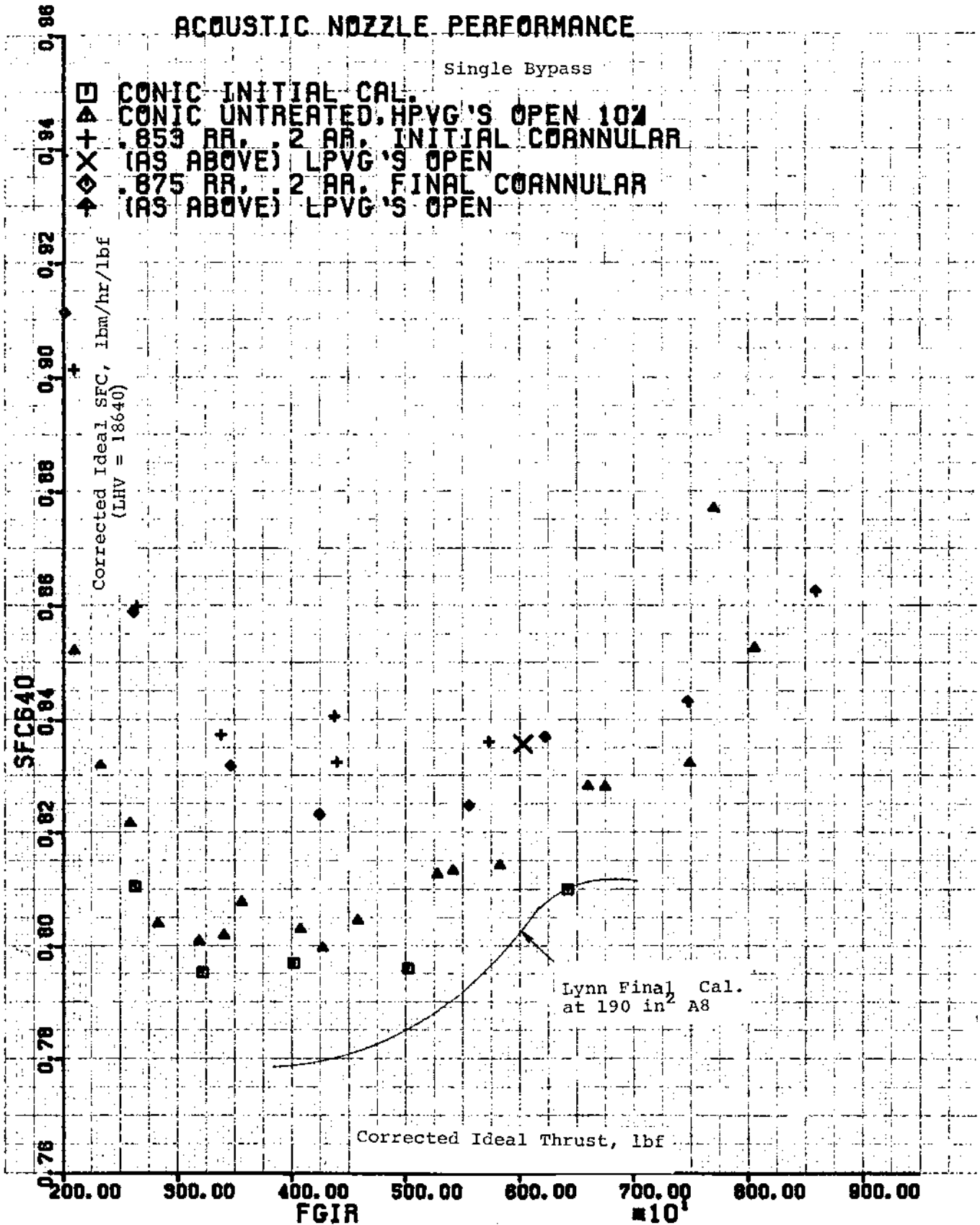


Figure 166 (a). Corrected Ideal SFC Versus Corrected Ideal Thrust.

ACOUSTIC NOZZLE PERFORMANCE

Single Bypass

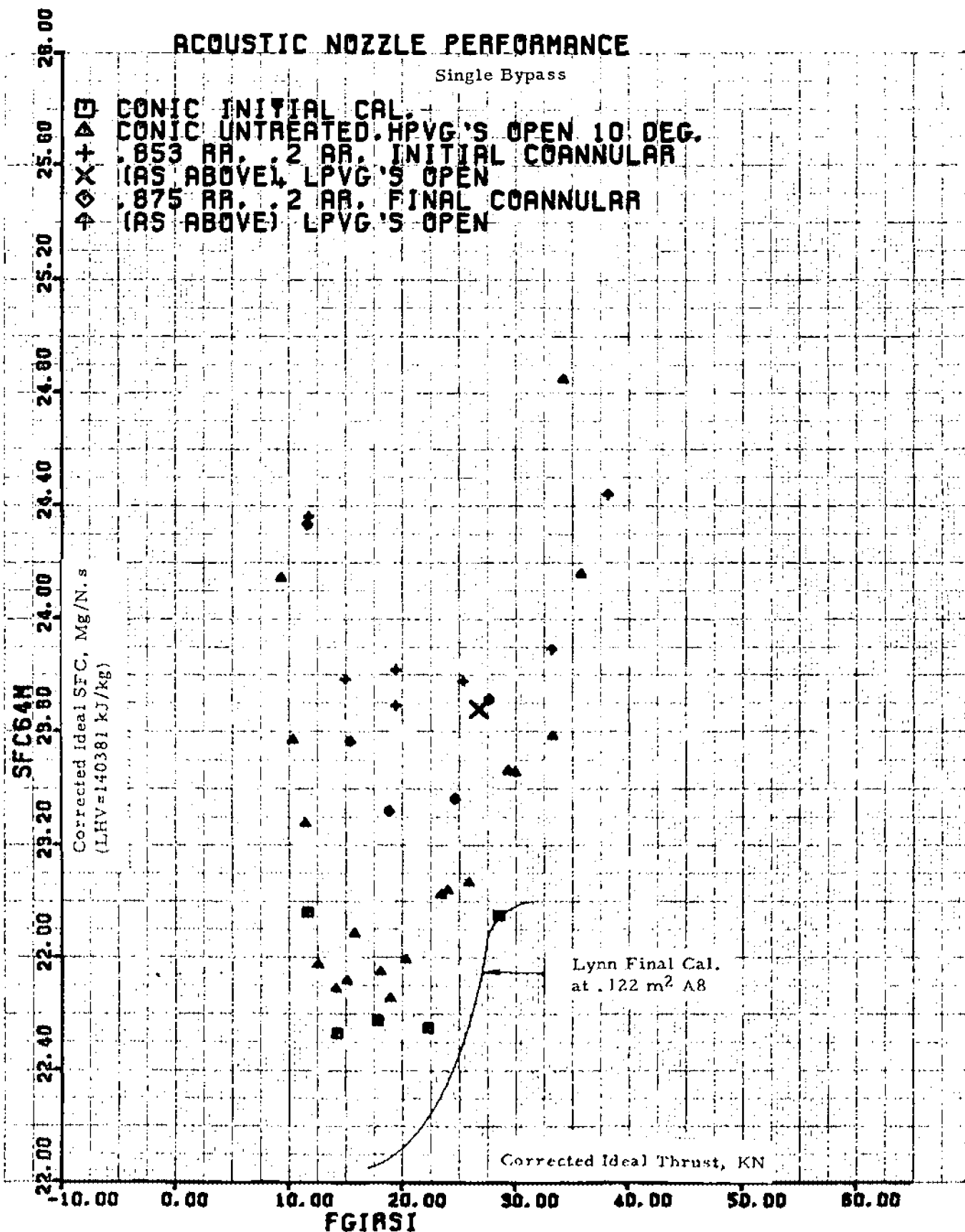


Figure 166 (b). Corrected Ideal SFC Versus Corrected Ideal Thrust.

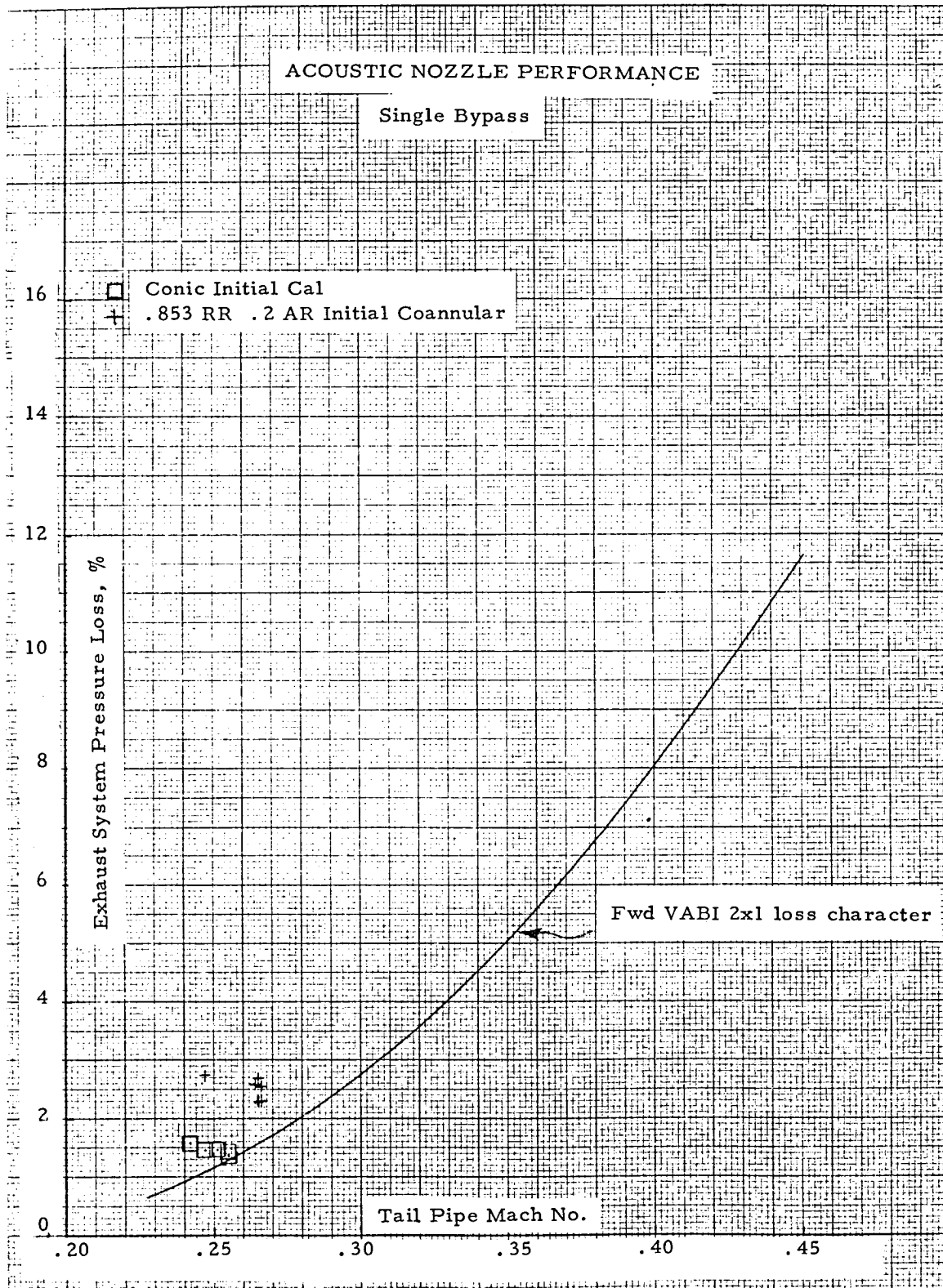


Figure 167. Exhaust System Pressure Loss Versus Tail Pipe Mach Number.

also shows a slight increase in flow with open low pressure variable geometry (LPVG). The nominal LPVG data falls directly in line with the Forward VABI test data previously measured.

Figures 158 and 159 indicate that the fan rear block IGV may have been slightly closed during the Lynn final calibration. This would cause the front block fan operating line to be raised slightly as shown in Figure 158 and the rear block fan flow to be reduced slightly as indicated in Figure 159. In both cases, the Edwards acoustic nozzle data agrees very well with the rest of the Lynn Forward VABI test data. Although the fan rear block IGV position indicator did not show it being open for the Lynn final calibration, there was some difficulty early in the test with the indicator slipping on its shaft.

Figure 160 shows the fan rear block operating line shift with nozzle area for the conic and coannular nozzles. The smaller area conic nozzle has the higher operating line.

Figure 161 shows that the high pressure variable geometries (HPVG's) were set slightly more open for the Edwards acoustic test than for the Lynn Forward VABI test. It was desirable to err on the open side to keep the speed low and have the best opportunity of satisfying the desired nozzle delivery conditions within the physical speed limit. The nominal HPVG data is in very good agreement for both tests.

The high pressure compressor operating lines were the same for both tests as shown in Figure 162.

The final check on the engine operation is shown in Figure 163. It shows the overall engine pressure ratio versus fuel/air ratio to be very similar between the two tests.

Differences in bypass ratio and sfc shown in Figures 164, 165, and 166 for both tests are the result of different rear VABI's and tailpipes. The two different levels of bypass ratio and sfc for the acoustic test is the result of the different nozzle areas and losses for the conic and coannular nozzles. It should be noted that this test was directed toward achieving nozzle delivery conditions for acoustic test purposes and that no effort was made to optimize sfc.

Figure 167 shows the difference in exhaust system pressure loss for the conic and coannular nozzles used in the Edwards Acoustic Nozzle Test, and also compares them to the exhaust system loss for the Lynn Forward VABI test. The greater conic nozzle loss as compared to the Forward VABI engine loss caused a cycle rematch to lower bypass ratio resulting in the poorer sfc shown in Figure 166. The same trend can be seen for the higher exhaust system loss of the coannular nozzle.

5.6.2.2 Nozzle Delivery Conditions and Overall Performance Effects

Figures 168 through 170 present a comparison of nozzle performance parameters for all the different nozzle configurations tested. This data shows consistent trends with little scatter. Figures 168 through 170 show nozzle pressure ratio and velocity varying inversely with total nozzle area at any given total airflow or thrust. There is no significant difference in nozzle performance for the three nozzle radius ratios tested at 0.2 area ratio. The 0.475 area ratio data shows a slightly lower level of pressure ratio and velocity for double bypass than single bypass operation at the same airflow. In double bypass the bypass flow does not experience as many stages of compression as it does in single bypass and the bypass ratio is higher resulting in lower average exhaust gas temperature. This allows nozzle continuity to be satisfied at lower pressure ratio and velocity.

Figure 171 also shows a consistent trend where the smallest area nozzle (zero area ratio) has the smallest bypass ratio and successively larger area nozzles have successively larger bypass ratios. There is, of course, a much higher bypass ratio in double bypass than in single bypass.

Figure 172 shows sfc for the different nozzle configurations. The single bypass data shows a trend with nozzle area where the conic and 0.1 area ratio nozzles, both with approximately the same exhaust area 0.122 m^2 (190 in.^2), have the best sfc. Both larger (0.2 area ratio and 0.475 area ratio) and smaller (zero area ratio) nozzle areas produce poorer sfc. The slightly different characteristics of the conic and 0.1 area ratio coannular nozzles represents the difference between a conic and a coannular nozzle with the same total area, the conic nozzle having a slightly flatter sfc bucket. All the 0.2 area ratio configurations are grouped together with the predicted best sfc configurations (based on forward VABI test results) exhibiting the best sfc.

Figure 172 also shows a significant improvement in sfc for double bypass, similar to that seen in the Lynn Forward VABI test.

5.6.3 Rear VABI Aero Performance

Rear VABI aerodynamic performance data was obtained with the conic exhaust system test configuration. Performance data for the conic test configuration consisted of total pressure and total temperature data at the entrance to the rear VABI and just ahead of the conic nozzle exit. For this test configuration, neither the rear VABI sideplates nor the flow inverting struts were installed in order to obtain an uninhibited acoustic demonstration of the reference conic exhaust nozzle.

A summary of typical aerodynamic results is presented in Figure 173. In the figure, the pressure loss data is illustrated as a function of the Mach number at the turbine frame exit. The data presented in the figure

ACOUSTIC NOZZLE - NOZZLE PERFORMANCE

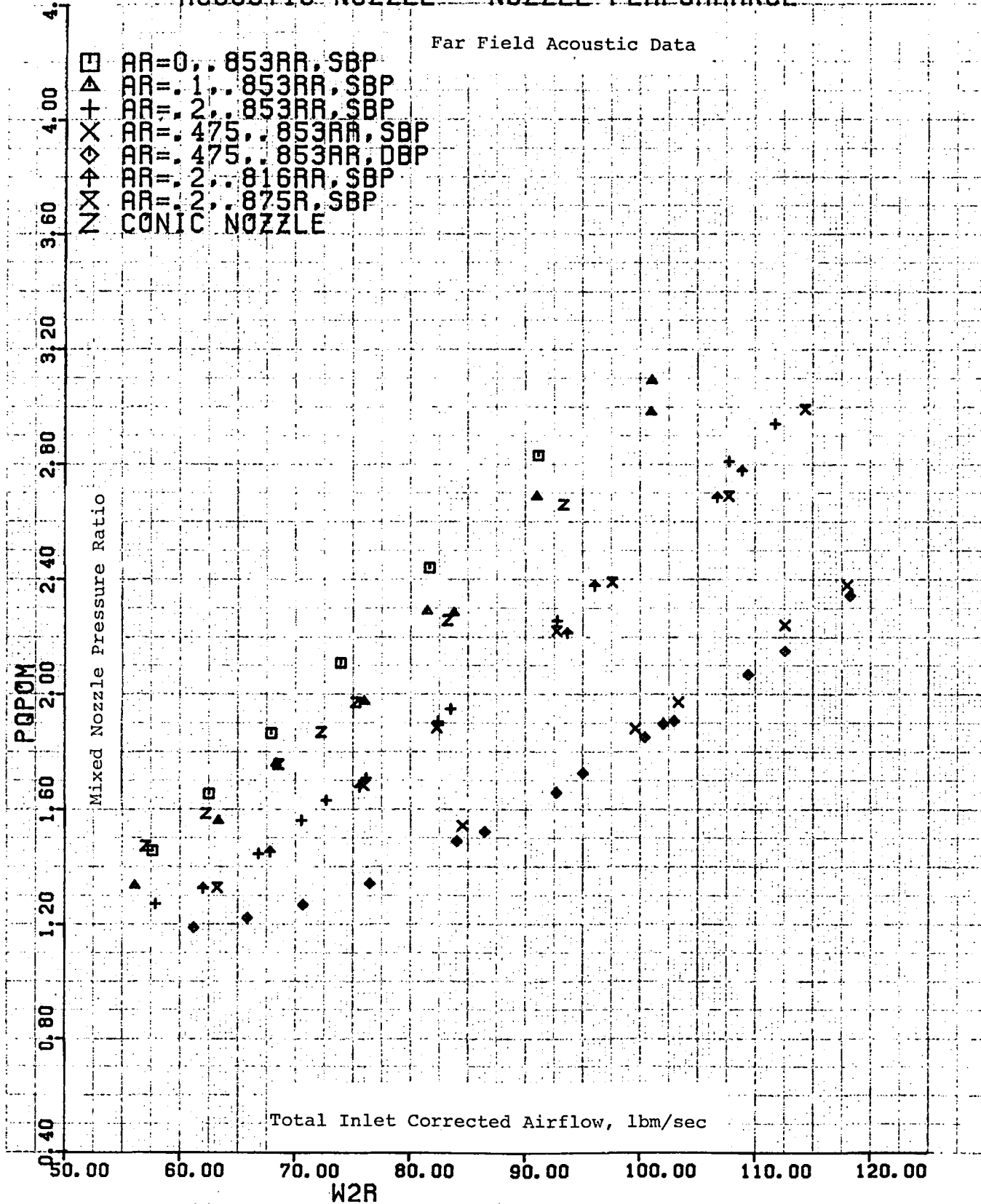


Figure 168 (a). Mixed Nozzle Pressure Ratio Versus Total Inlet Corrected Airflow.

ACOUSTIC NOZZLE - NOZZLE PERFORMANCE

Far Field Acoustic Data

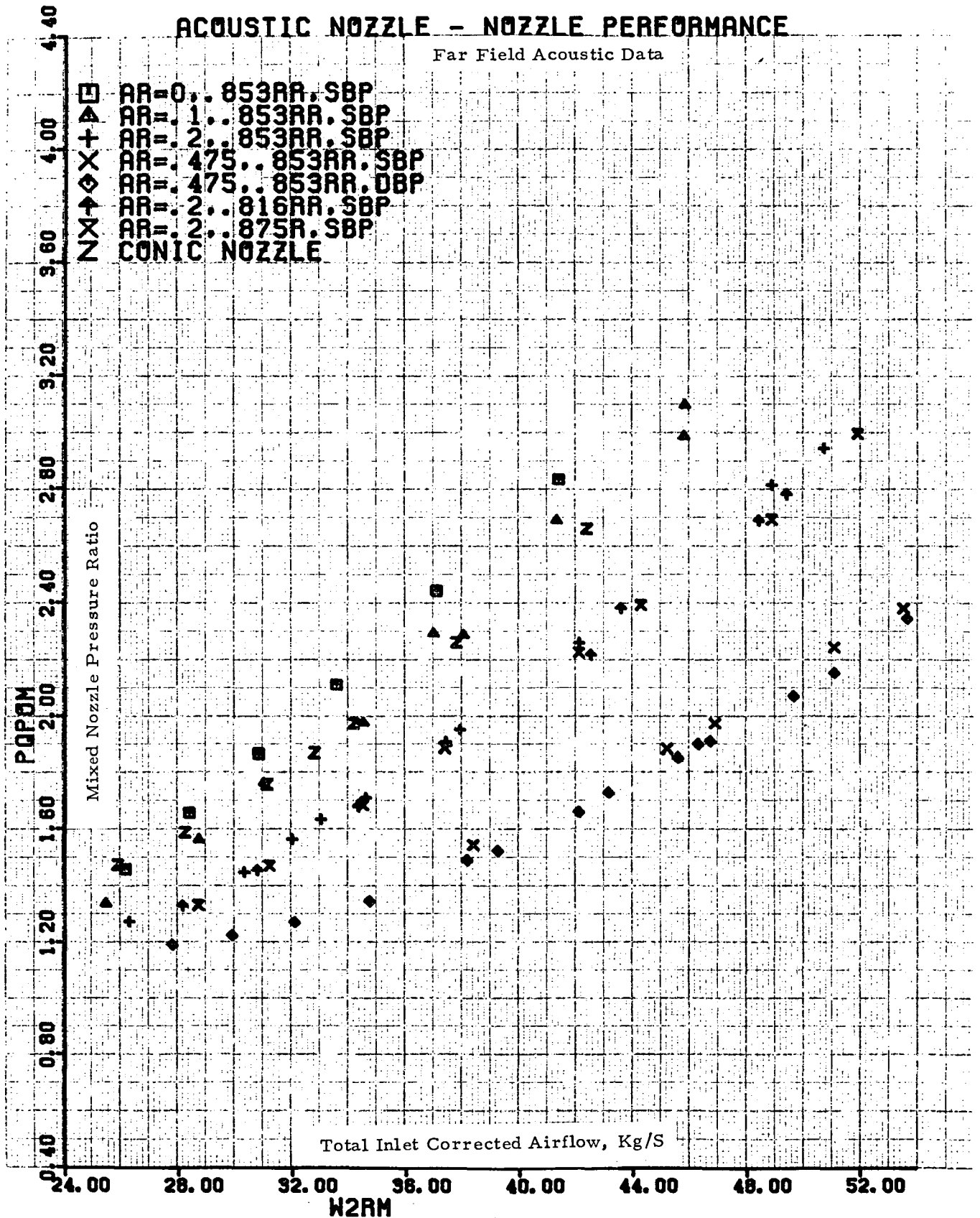


Figure 168 (b). Mixed Nozzle Pressure Ratio Versus Total Inlet Corrected Airflow.

ACOUSTIC NOZZLE - NOZZLE PERFORMANCE

Far Field Acoustic Data

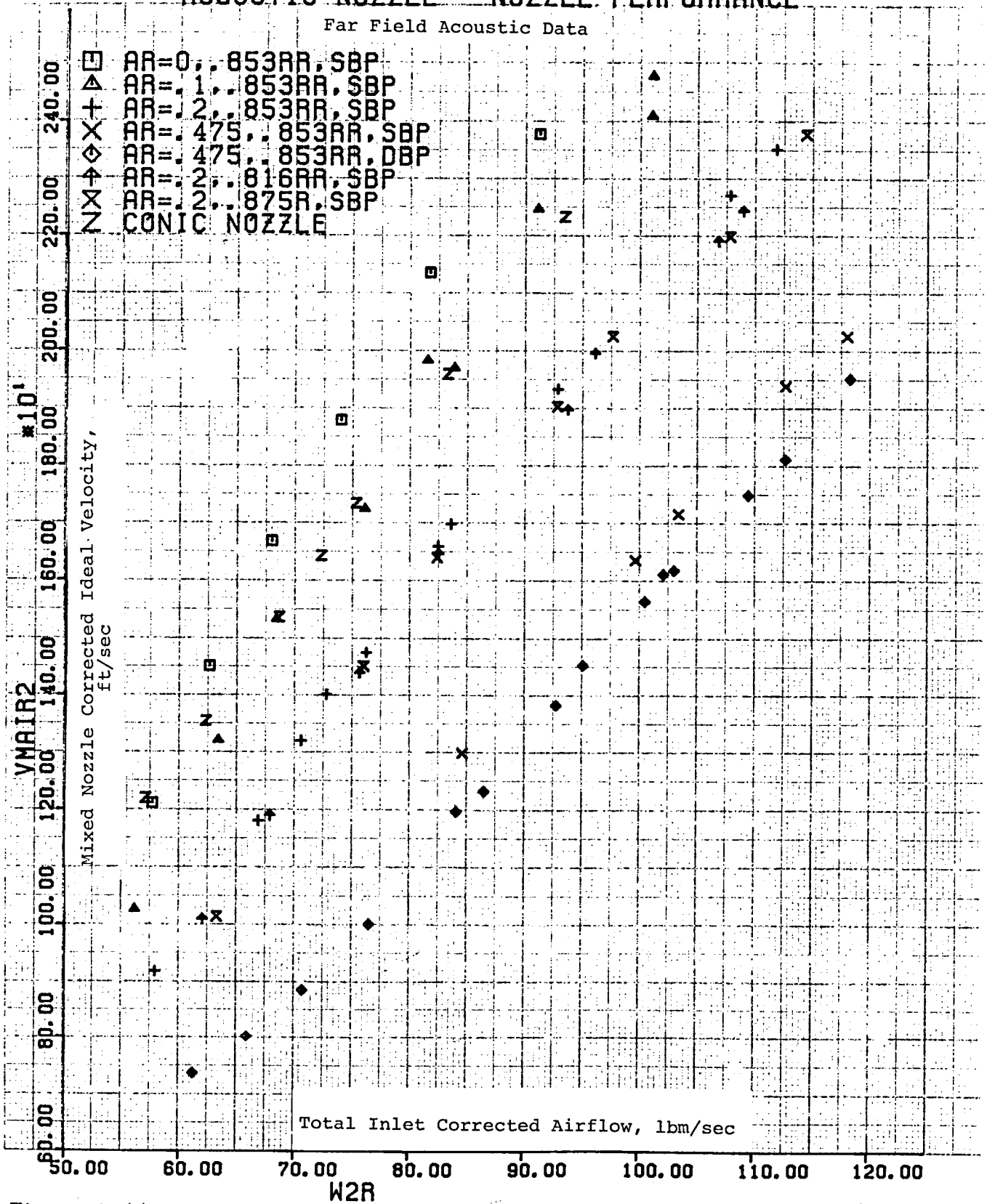


Figure 169 (a). Mixed Nozzle Corrected Ideal Velocity Versus Total Inlet Corrected Airflow.

ACOUSTIC NOZZLE - NOZZLE PERFORMANCE

Far Field Acoustic Data

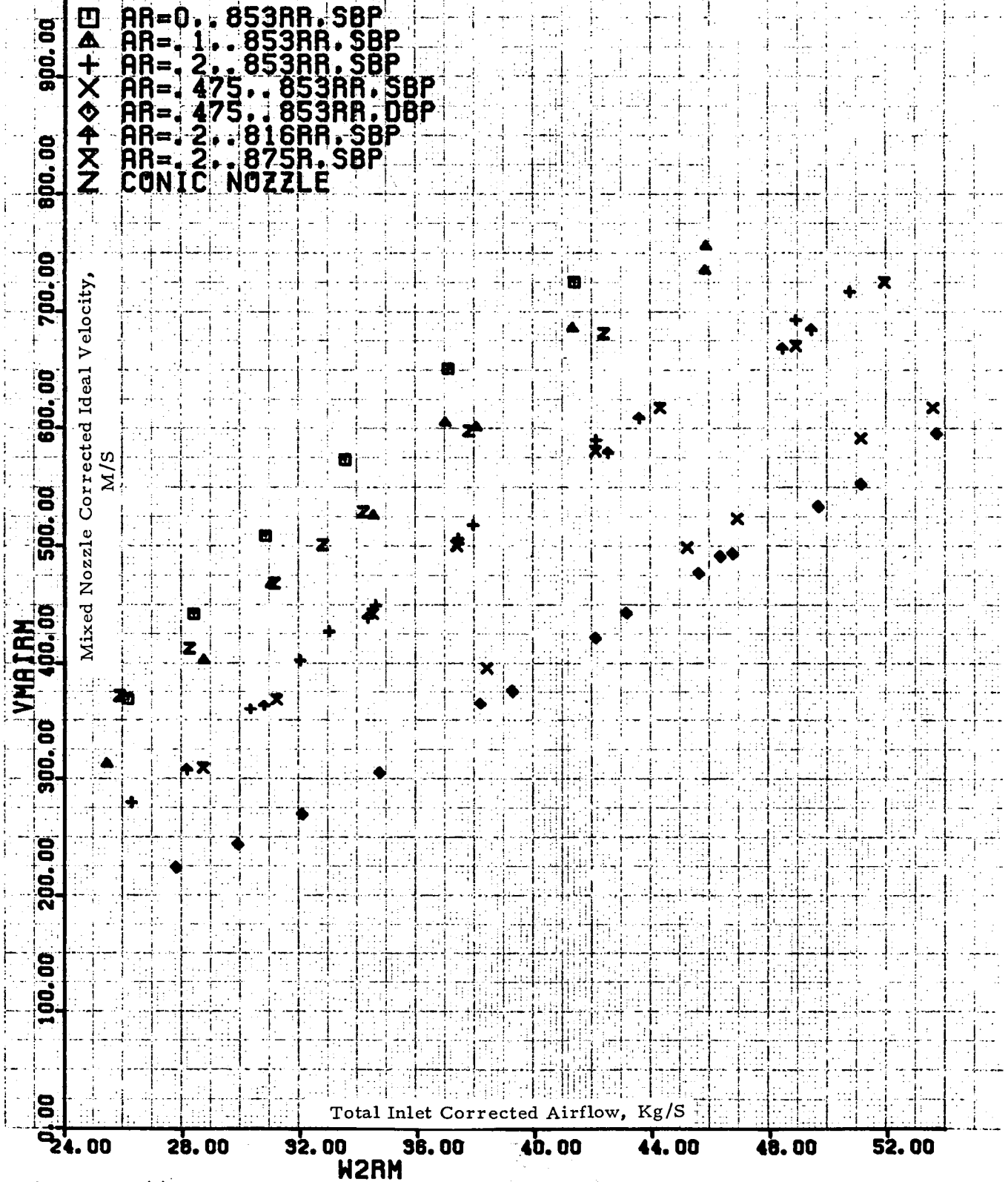


Figure 169 (b). Mixed Nozzle Corrected Ideal Velocity Versus Total Inlet Corrected Airflow.

ACOUSTIC NOZZLE PERFORMANCE

Far Field Acoustic Data

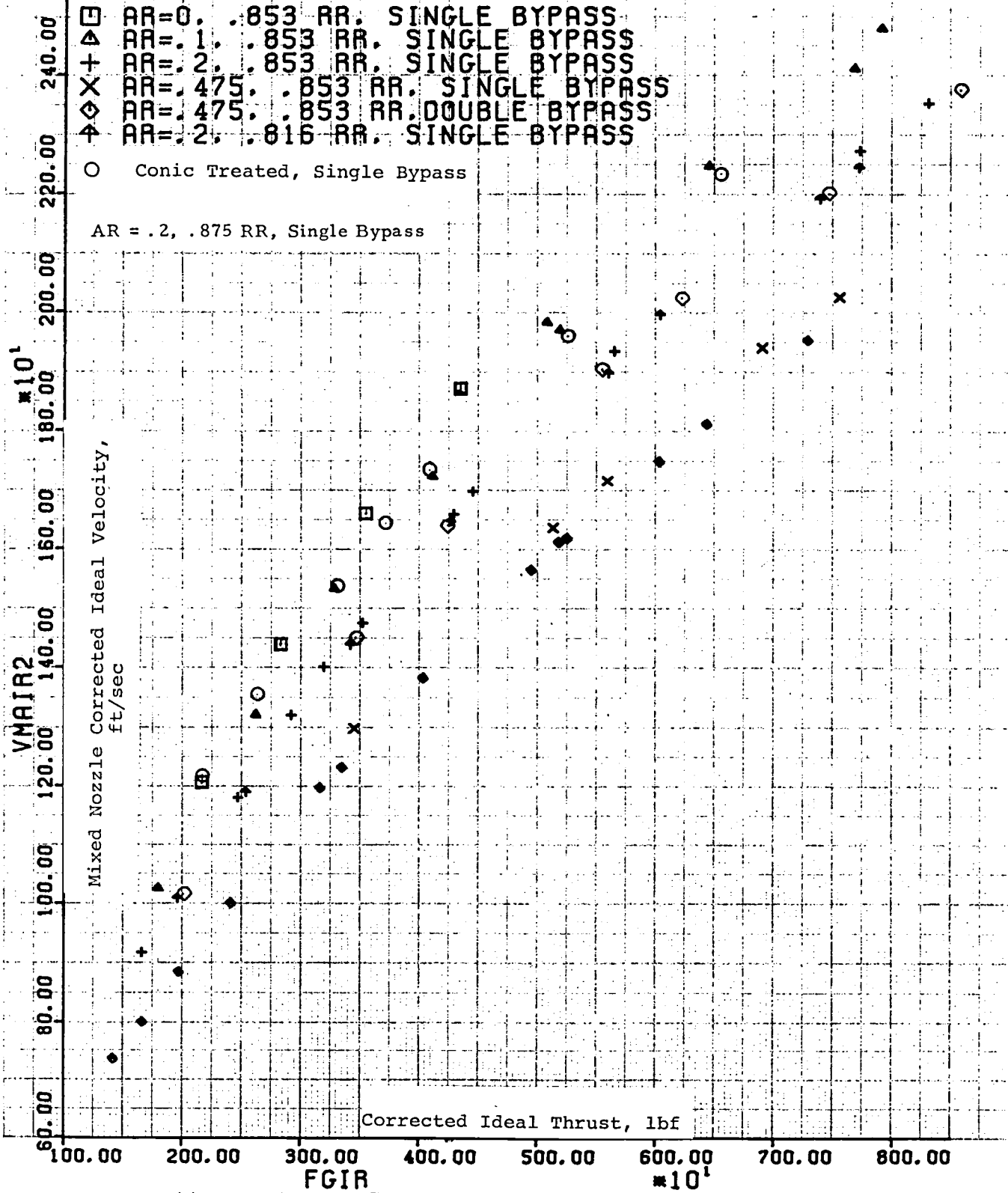


Figure 170 (a). Mixed Nozzle Corrected Ideal Velocity Versus Corrected Ideal Thrust.

ACOUSTIC NOZZLE - NOZZLE PERFORMANCE

Far Field Acoustic Data

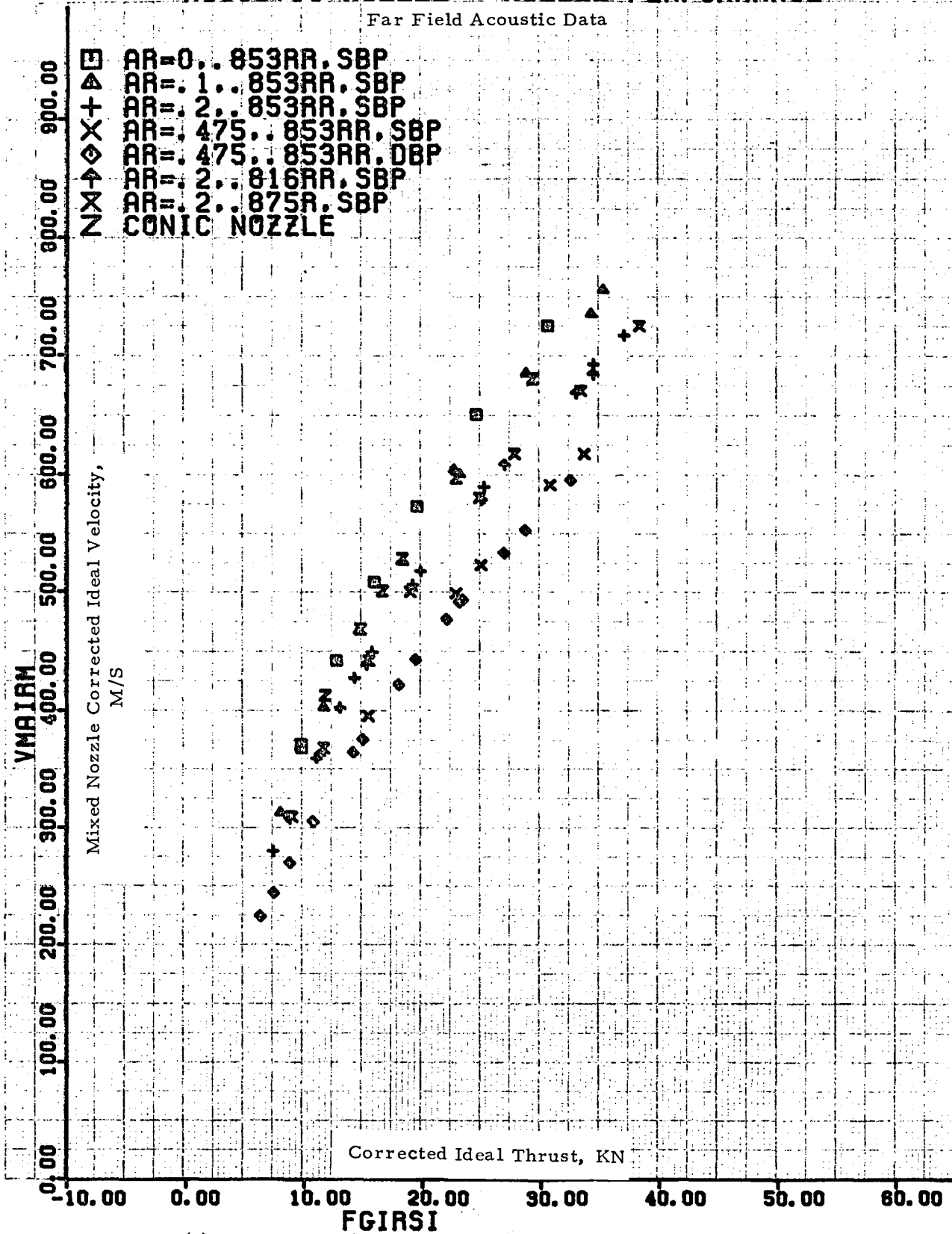


Figure 170 (b). Mixed Nozzle Corrected Ideal Velocity Versus Corrected Ideal Thrust.

ACOUSTIC NOZZLE - NOZZLE PERFORMANCE

Far Field Acoustic Data

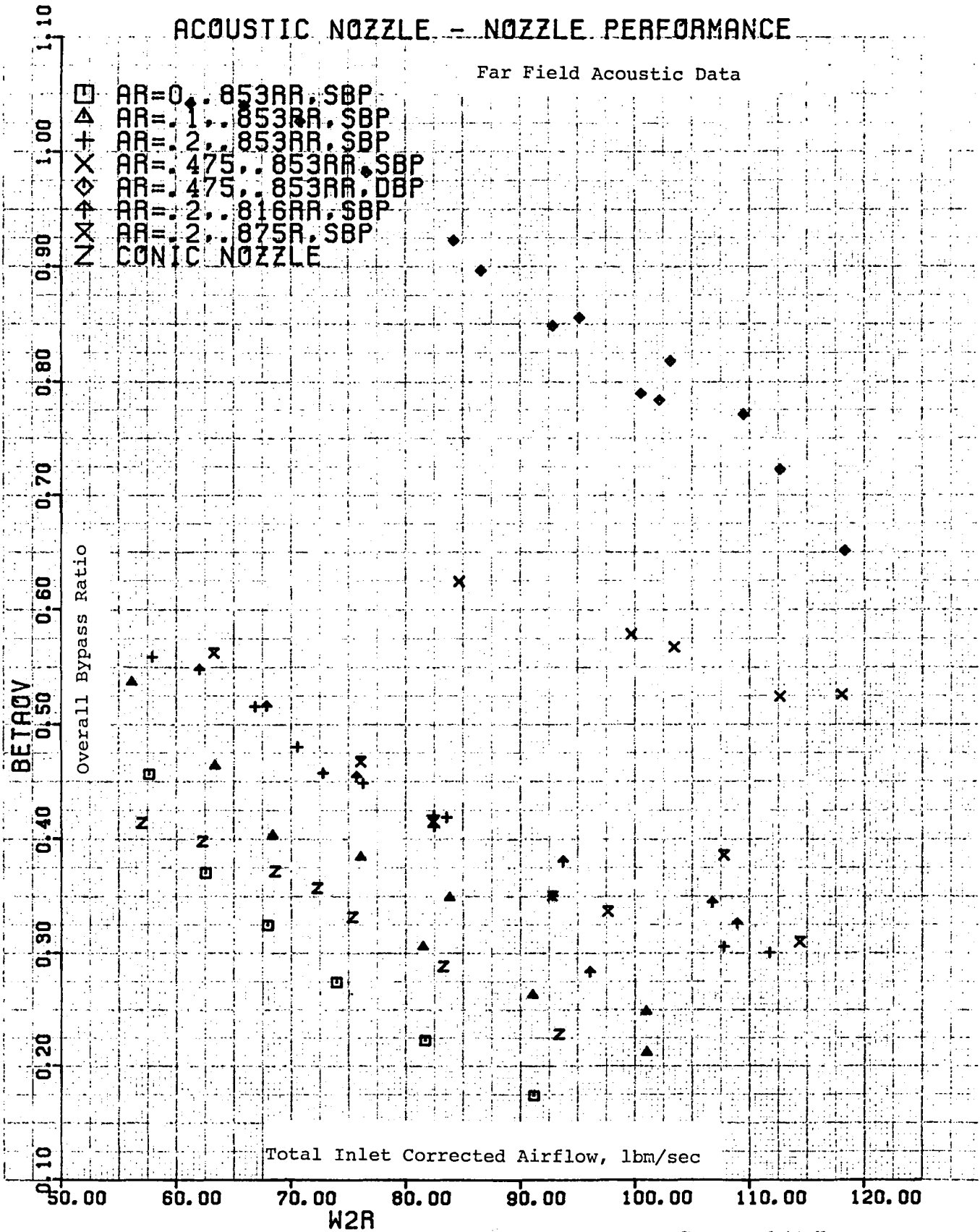


Figure 171 (a). Overall Bypass Ratio Versus Total Inlet Corrected Airflow.

ACOUSTIC NOZZLE - NOZZLE PERFORMANCE

Far Field Acoustic Data

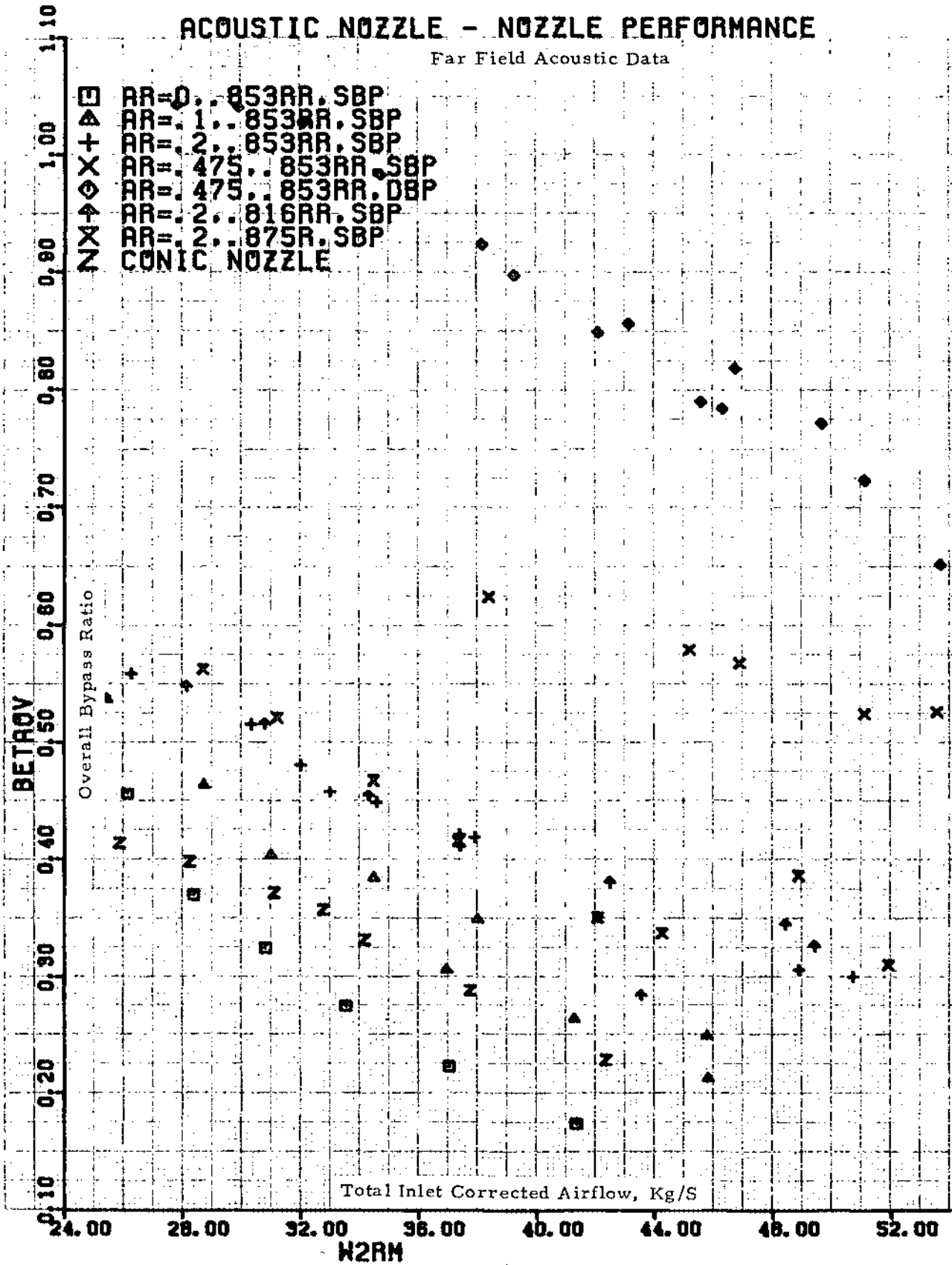


Figure 171 (b). Overall Bypass Ratio Versus Total Inlet Corrected Airflow.

ACOUSTIC NOZZLE PERFORMANCE

Far Field Acoustic Data

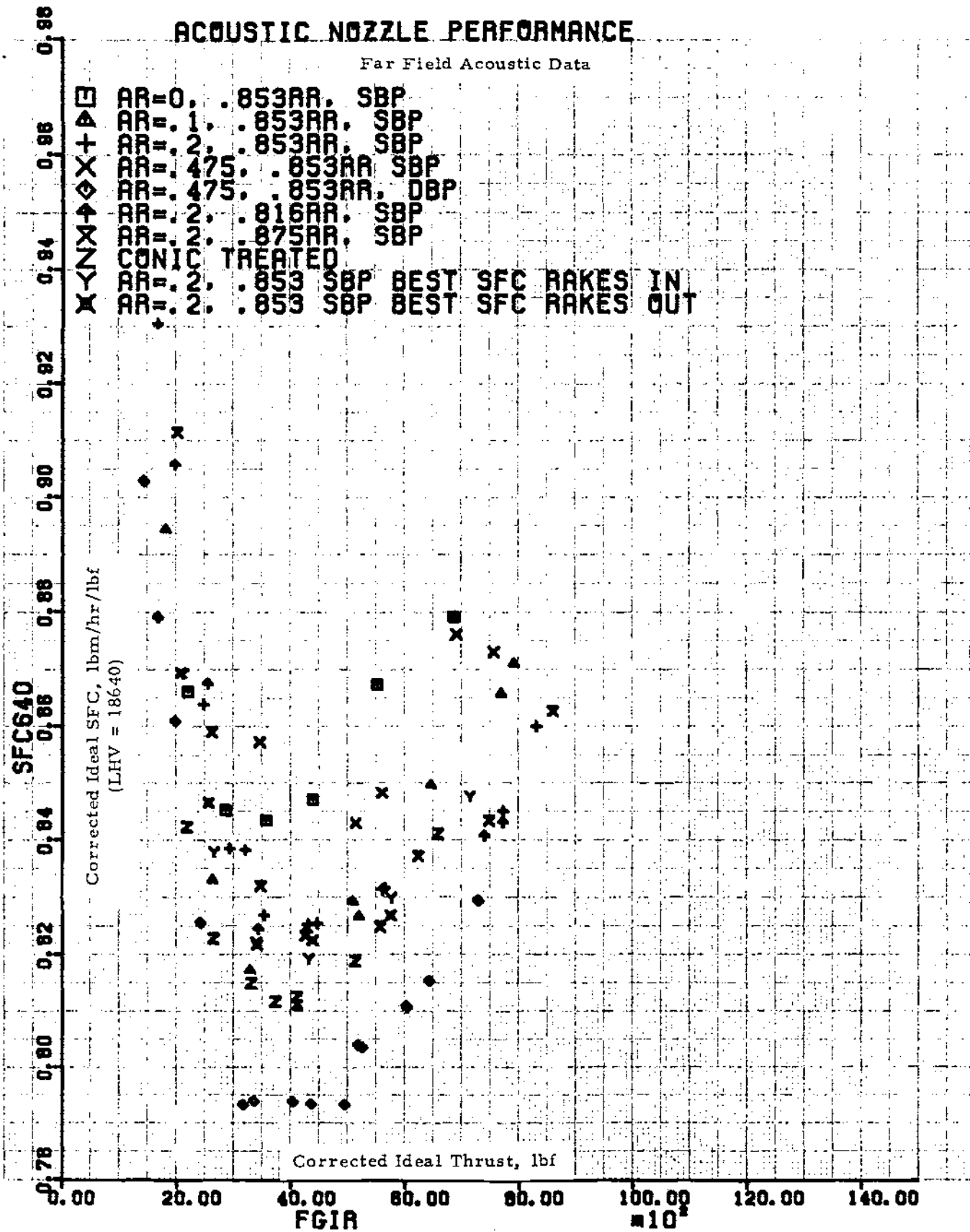


Figure 172 (a). Corrected Ideal SFC Versus Corrected Ideal Thrust.

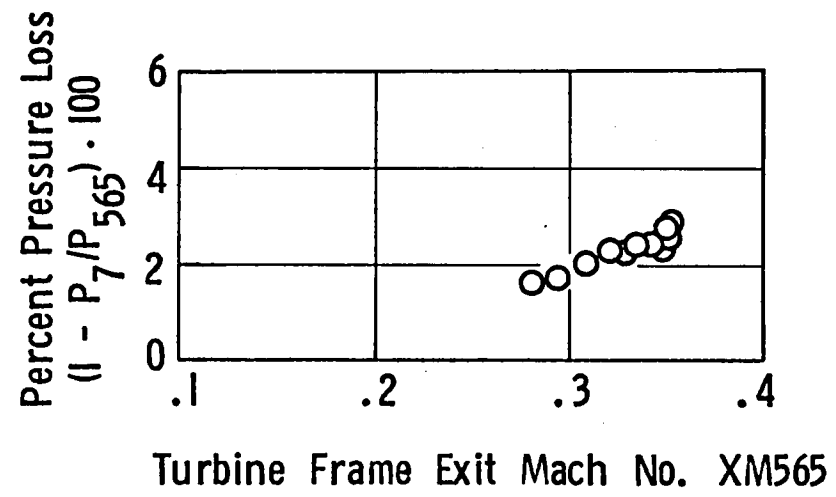
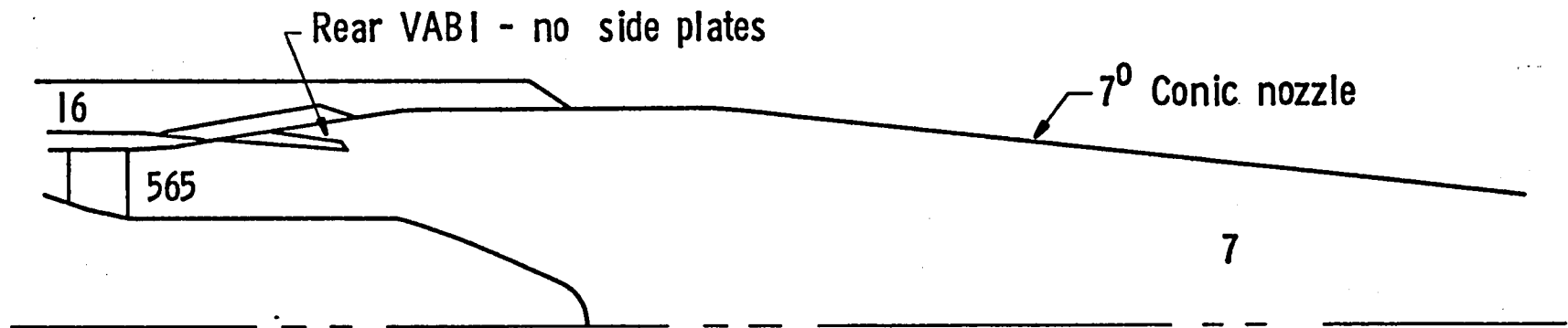


Figure 173. NASA Acoustic Nozzle Performance Results, Conic Nozzle Configuration.

indicates that a low loss configuration was achieved, and that no major detrimental performance penalties occurred due to the rear VABI and tail-pipe configuration.

Aerodynamic performance data was also obtained for the coannular exhaust system incorporating the rear VABI and flow inverting struts. Performance data for the coannular exhaust system consisted of total pressure and total temperature data at the entrance to the rear VABI and just ahead of each of the exhaust nozzle exits. In addition, diagnostic total pressure and static pressure data were obtained at intermediate locations within the exhaust system.

A summary of typical aerodynamic results is presented in Figure 174 for the coannular configuration with the rear VABI sideplates installed. In the figure, the pressure loss data is illustrated as a function of the Mach number at the turbine frame exit for the hot nozzle or as a function of strut entrance Mach number for the cold flow inverting strut system. The data presented in the figure indicates that a low core loss configuration was achieved and that no major detrimental performance penalties occurred due to the rear VABI, sideplates, or strut configuration. This data also compares favorably with the previously illustrated conic nozzle configuration. The pressure loss data for the flow inverting struts was low relative to expected results. The diagnostic data provided insight into further understanding of the loss mechanisms and verified the overall levels of the observed performance data.

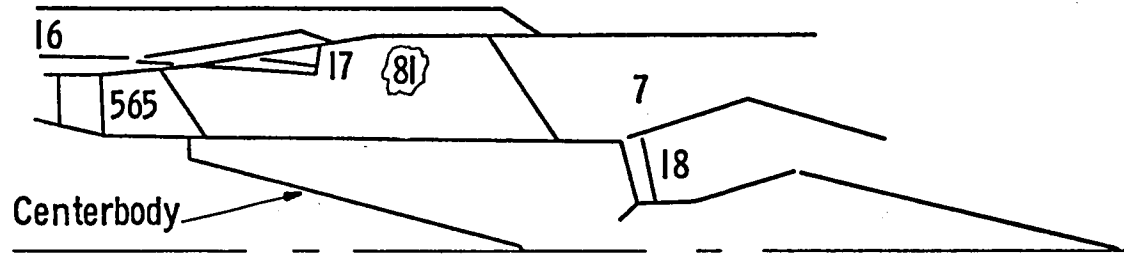
Additional aerodynamic performance data was obtained for the coannular exhaust nozzle with the rear VABI sideplates removed. This data is presented in Figure 175 as loss data with and without the rear VABI sideplates and approximates the predicted performance difference attributed to the sideplates.

The level of mixing effectiveness, K_4 , illustrated for the data in Figure 175 shows that the ideal thermodynamic thrust gain due to complete mixing of two confluent gas streams is approached. ($K_4 = 0$ implies a step temperature profile and no mixing layer between the streams.)

5.6.4 Nozzle Aerodynamic Performance

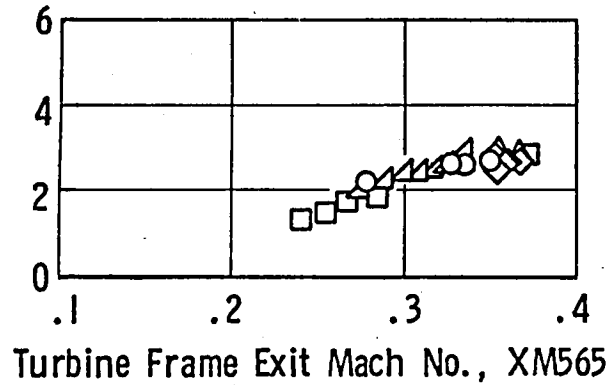
The performance of the demonstrator nozzle was estimated based on the scale model wind tunnel test results reported in Reference 23. The radius ratio of the models tested ranged from 0.853 to 0.926. Data for three typical models from Reference 23 are shown in Figures 176, 177 and 178. The key here is that the nozzle performance is relatively insensitive to the pressure ratio of either stream over the primary range of interest.

Based on these scale model data, the performance of the demonstrator nozzle was predicted to be as shown in Figure 179 between inner and outer nozzle pressure ratios of 1.5 to 3.5. It was expected that performance would



Sym	A17		A18	
	m ²	in ²	m ²	in ²
○	.0261	40	.0130	20
□	.0391	60	.0547	84
◇	.0078	12	.0228	35
△	.0261	40	.0228	35
◁	.0391	60	.0228	35

Percent Core/Tailpipe Pressure Loss
(1 - P7/P565) · 100



Percent Strut Pressure Loss
(1 - P18/P16) · 100

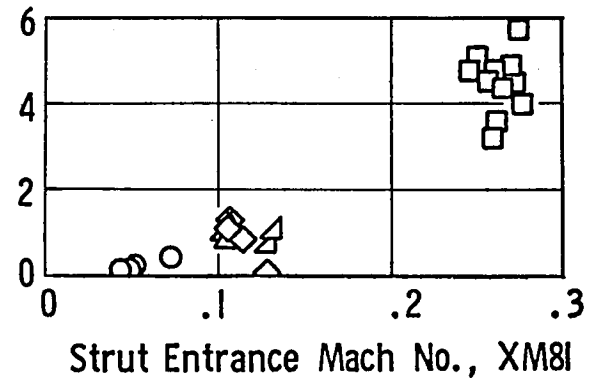


Figure 174. NASA Acoustic Nozzle Performance Results, Coannular Nozzle Configuration.

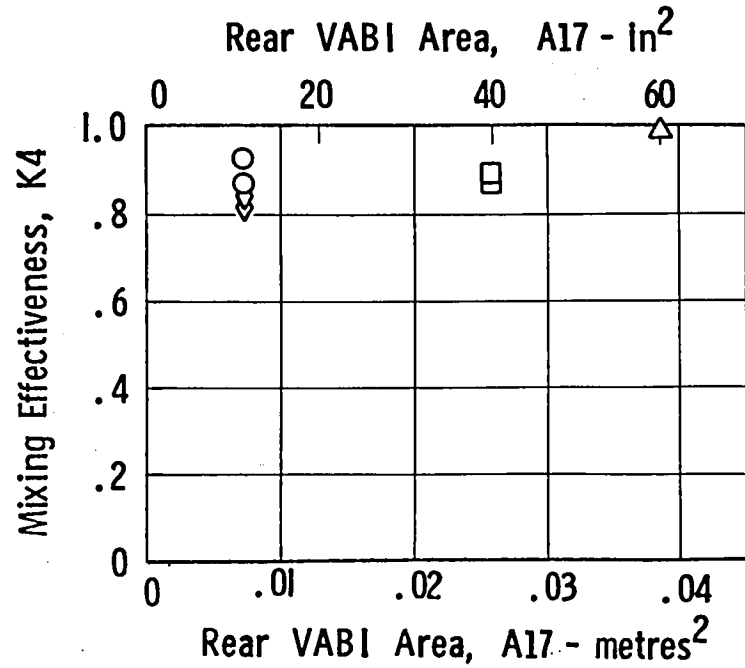
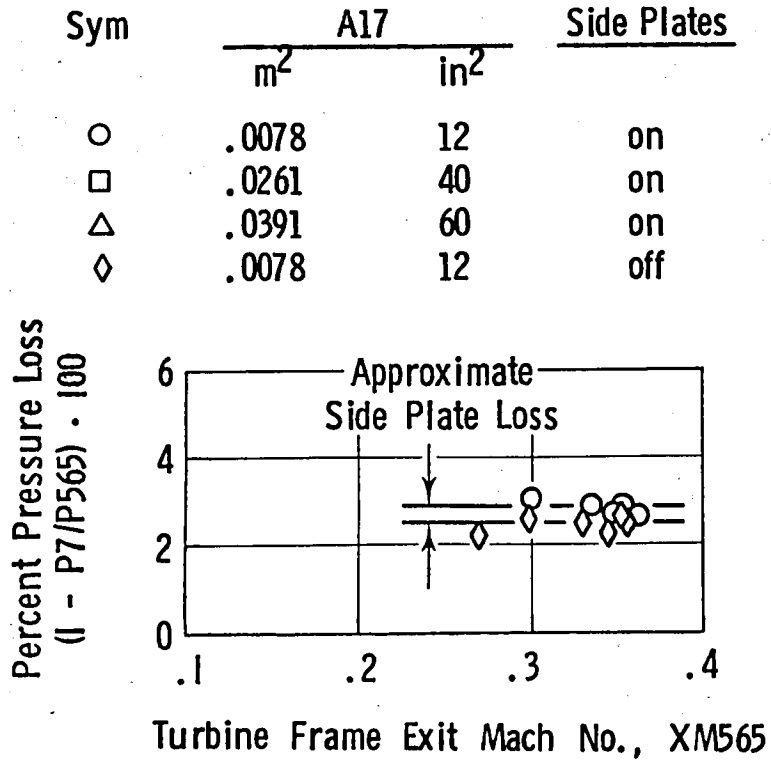
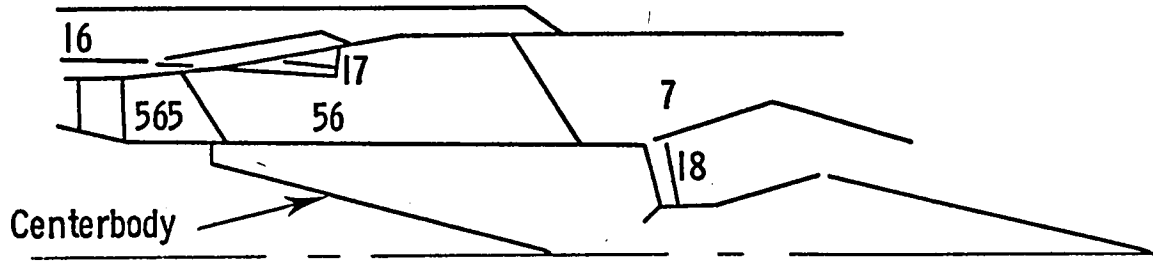


Figure 175. NASA Acoustic Nozzle Performance Comparisons.

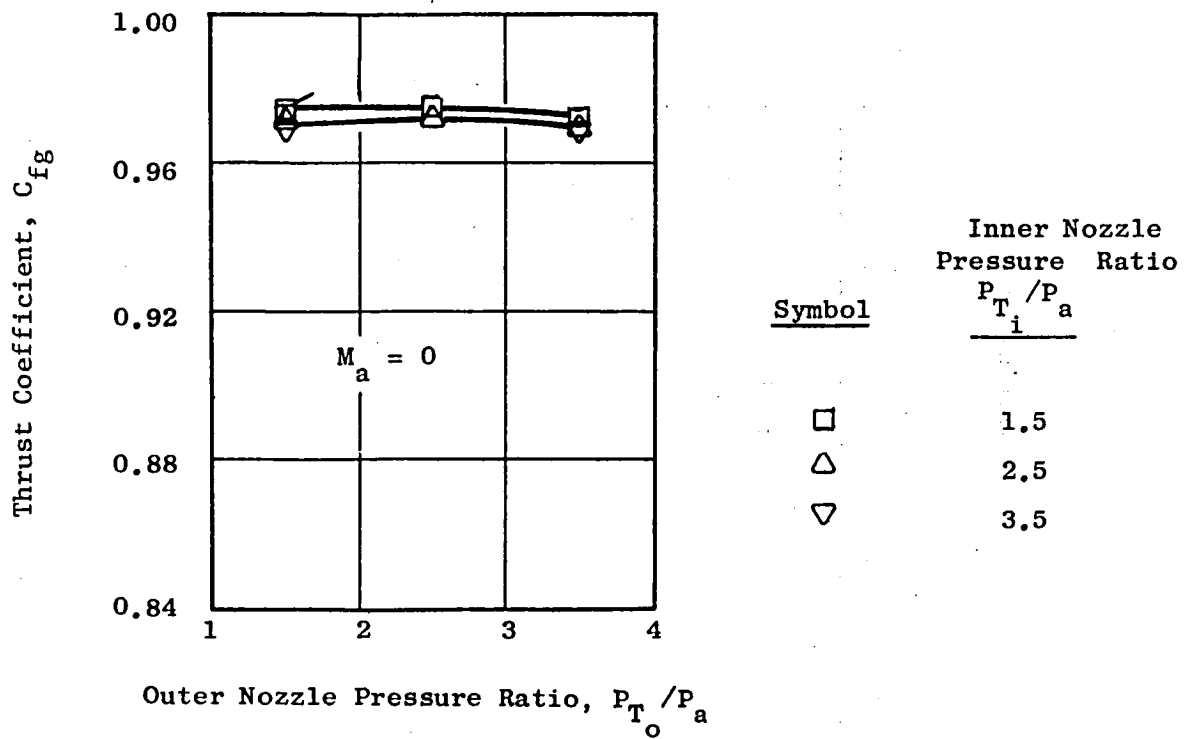
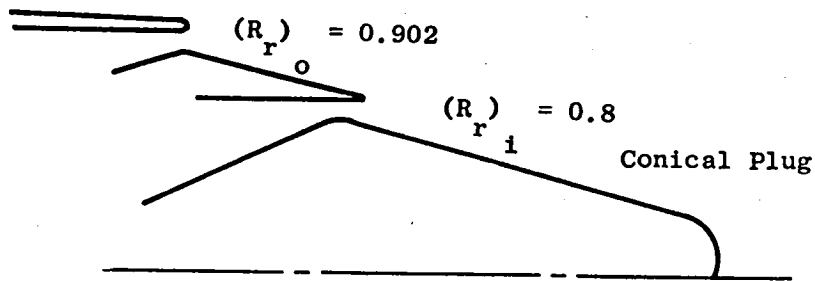


Figure 176. Thrust Coefficients for Configuration 2 [$(R_r)_o = 0.902$, $(R_r)_i = 0.8$, Conical Inner Plug] with High Inner Flow Rates.

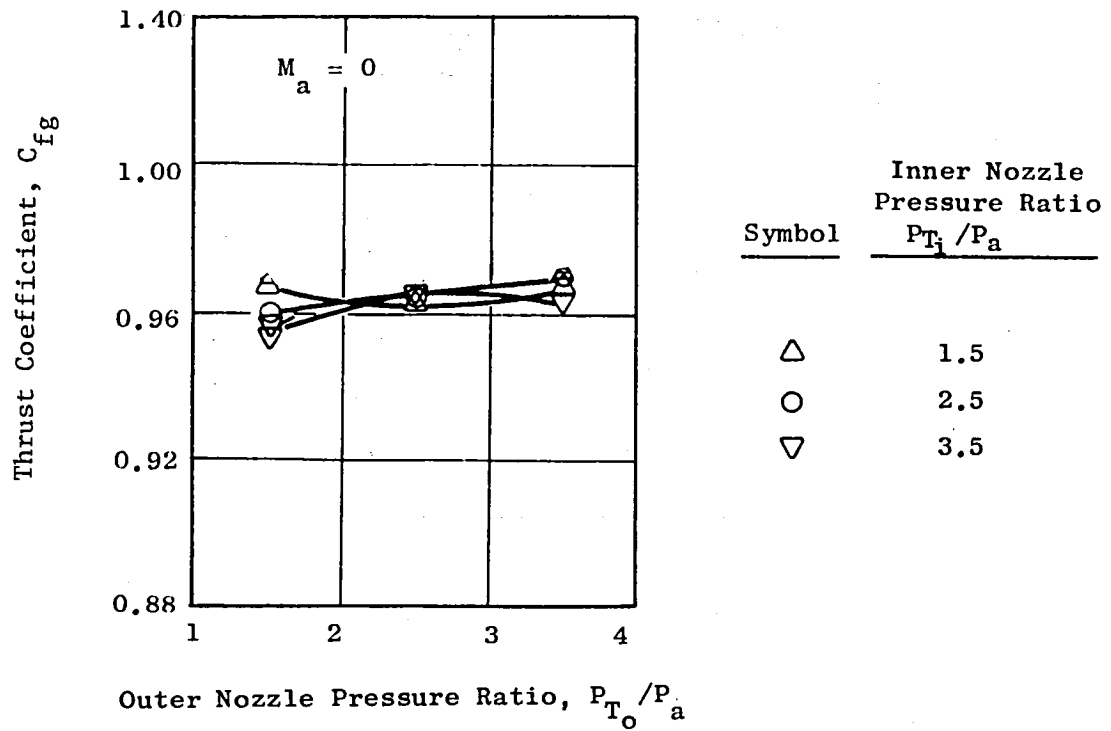
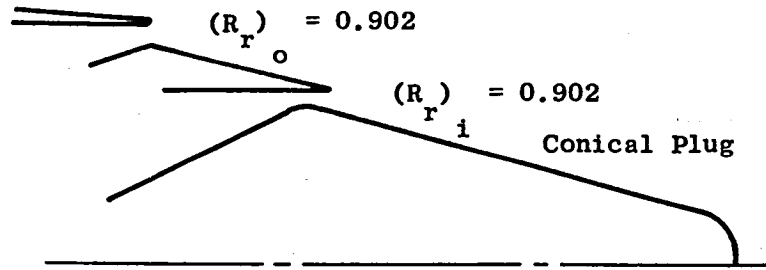


Figure 177. Thrust Coefficients for Configuration 3 [$(R_r)_o = 0.902$, $(R_r)_i = 0.902$, Conical Inner Plug] with High Inner Flow Rates.

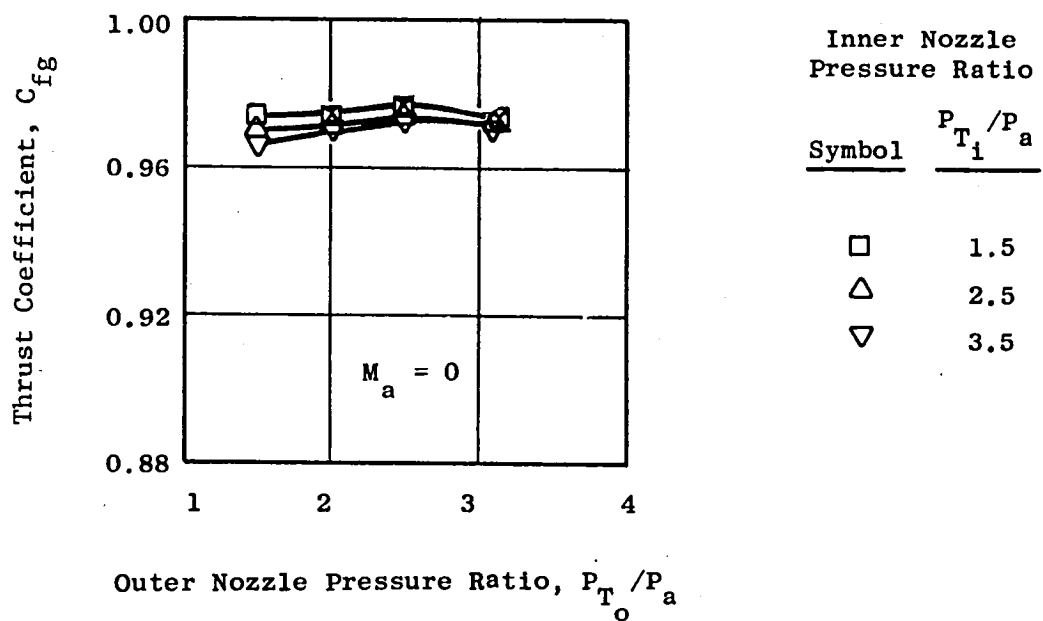
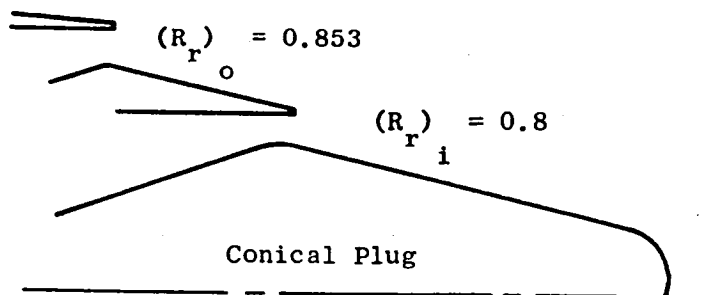


Figure 178. Thrust Coefficients for Configuration 5 [$(R_r)_o = 0.853$, $(R_r)_i = 0.8$, Conical Inner Plug] with High Inner Flow Rates.

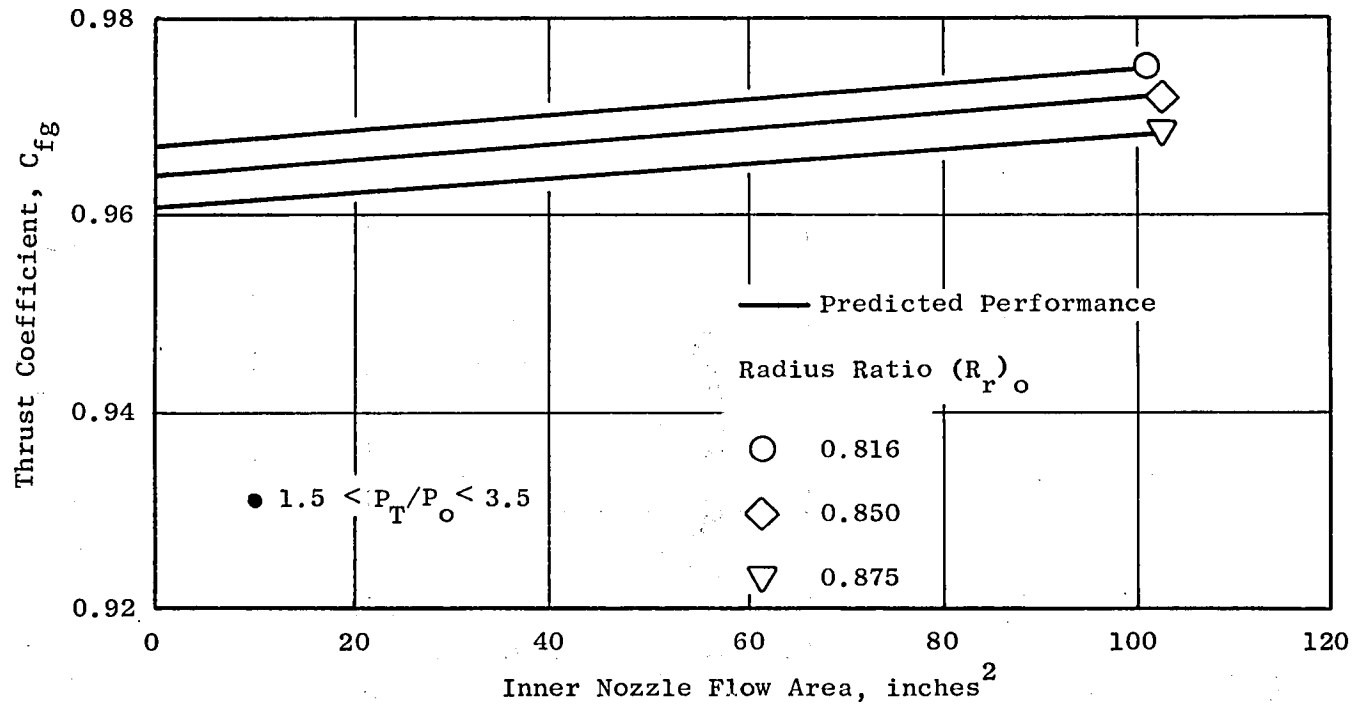


Figure 179. Nozzle Thrust Coefficient.

be somewhat dependent on both radius ratio and the relative areas of the outer and inner nozzles, with the 0.816 (R_r^0) nozzle providing the highest performance when the inner nozzle is open to its highest area. Between inner and outer nozzle pressure ratios of 1.5 to 3.5, the total range of performance for the three nozzles was expected to be between $C_{fg} = 0.961$ and $C_{fg} = 0.975$.

Thrust data was taken for both the conic nozzle and the coannular acoustic nozzles. Conic nozzle data, for pressure ratios above choked and runs with rakes and the treated inlet (same inlet used for coannular tests) are presented in Figure 180. These data agree relatively well with the prediction.

Data for the 0.853 radius ratio nozzle is shown in Figure 181. Here, the data is grouped according to the area ratio between the inner and outer nozzles, A_i/A_o . The dashed lines on Figure 181 represent the predicted levels (from Figure 179) for these area ratios. In general, the trend seems consistent with the prediction, i.e., as A_i/A_o increases, the relative level of the test data increases. However, the general level of the data is higher than could reasonably be expected. Ignoring the two low points for the $A_i/A_o = 0.2$ data, the scatter is about 3%. Considering the accuracy of the prediction, the level is biased 1 1/2% to 3% high.

Valid thrust data were not obtained for the radius ratio 0.816 and 0.875 nozzles.

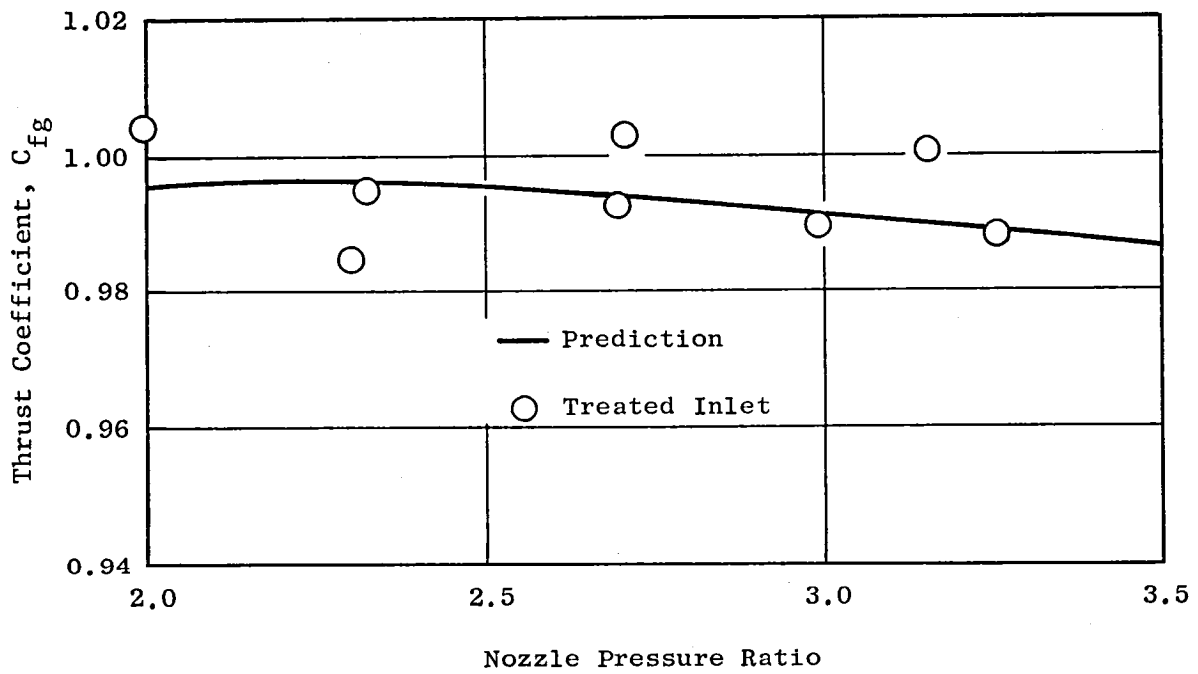


Figure 180. Conic Nozzle Performance.

6.0 SUMMARY OF RESULTS, CONCLUSIONS AND RECOMMENDATIONS

6.1 SUMMARY OF RESULTS

The NASA YJ101/VCE Forward Variable Area Bypass Injector (VABI) test represented the fourth in a series of major YJ101/VCE Concept Tests and the first of several under NASA program auspices. All technical objectives were successfully attained. These objectives were principally aimed at the demonstration of the overall feasibility of the forward VABI concept for simplification of advanced double bypass engine configurations, the satisfactory aerodynamic and mechanical performance of the forward VABI component, the demonstration of transitioning between single and double bypass operating modes using the dual valve VABI features, and the evaluation of engine sfc and airflow extension capabilities. Additional test objectives satisfactorily accomplished were the first evaluation of a VCE variable cycle engine with inlet distortion, the evaluation of aft fan block aerodynamic design improvements and the baseline testing of this engine for conditions pertinent to the ensuing NASA Acoustic Nozzle VCE Test.

The forward VABI as an aerodynamic component, performed as expected from a pressure loss/flow characteristic standpoint, for all the flow circuits. Transitions using the integrated modulating/selector valve arrangement (forward VABI) were successfully accomplished between single and double bypass operation (and in reverse) over a range of engine speeds with no observed aerodynamic or aeromechanical difficulties/problems. From the engine performance standpoint the part power sfc was lower (better) than predicted in both single and double bypass operating modes. The airflow extensions with double bypass operation were notably broad and in good agreement with the previously tested Navy 2x1 Split Fan Double Bypass results. Mechanical operation of the special forward VABI hardware was satisfactory, and the breadboard control positioning of desired VCE geometries was completely successful.

This forward VABI engine was then configured for the NASA VCE Acoustic Nozzle Test, which was an extensive acoustic evaluation at a specially prepared test site at Edwards Air Force Base. The latter test was principally aimed at demonstrating (in engine size) the low noise characteristics of the coannular acoustic exhaust nozzle which had previously been tested in scale models under other related NASA contracts. This testing also involved running a mixed flow conic (baseline) nozzle with both standard and treated bellmouth inlet systems. The standard bellmouth was used to establish engine air flow/performance characteristics, which were correlated with the results of the previous forward VABI test. Subsequent tests were made with the treated inlet system to nullify the fan noise and allow jet noise to be measured directly.

The conic nozzle testing was followed by testing of the coannular nozzle over a broad range of geometric and aerodynamic variables using a variety of special acoustic measuring techniques including - near field, far field, internal sound probe, and laser velocimeter. The test results showed that the expected

noise reduction attributable to the coannular nozzle was attained. All major test objectives including acoustic and performance evaluation using the coannular nozzle and associated deep chute rear VABI were satisfactorily accomplished. The coannular exhaust system and the flow inverting strut system exhibited flow/pressure loss characteristics better than predicted. Aerodynamic variations of the rear VABI (i.e., sideplate removal) were also accomplished. Three outer stream radius-ratio variations of the acoustic nozzle were evaluated with emphasis on the mean (0.853) radius ratio configuration. The laser-velocimeter was used to measure the exhaust velocity profiles at the nozzle discharge and at several planes aft of the discharge, for comparison with counterpart scale model results.

In general, agreement of acoustic and aerodynamic characteristics between scale model and engine results was very favorable. The acoustic nozzle demonstrated 5-6 PNdB lower noise (relative to the conic baseline) in the aft quadrant, in agreement with expectations. A shock noise reduction of 7 PNdB in the front quadrant was also attained. Very encouraging agreement between test results and the most recently developed prediction methods on noise level, directivity and spectrum was also obtained. Mechanical operation of the hydraulically actuated inner plug was very satisfactory with no indication of aerodynamic instability/vibration. Positive positioning responses to the slave control were noted. Metal temperatures and vibration levels were well within design limits and the condition of the rear VABI/coannular nozzle hardware following this extensive test was excellent.

The YJ101 engine proved to be a flexible and dependable test vehicle and engine performance showed no significant deterioration or variation over the course of both test phases. The known mechanical YJ101/VCE problems (i.e., No. 4 bearing vibration) were held within acceptable limits by utilizing open variable stator schedules on the fan and the compressor to attain airflow at reduced speed. An effective unique oil cooling method was also devised and implemented. The overall engine mechanical condition was satisfactory following the tests and the engine was then prepared for the Navy VCE/FADEC Test Program.

6.2 CONCLUSIONS AND RECOMMENDATIONS

The NASA YJ101/VCE Forward VABI Test effectively accomplished all major technical objectives and established the overall forward VABI concept feasibility as applicable to advanced double bypass engine configurations. The forward VABI feature allows a typical VCE to operate in either single or double bypass modes with a single bypass duct which in conjunction with a rear VABI can use a single exit exhaust nozzle, or a dual-exit coannular acoustic nozzle.

The NASA VCE Acoustic Nozzle Test effectively demonstrated the noise suppression capabilities of the coannular (dual-exit) plug nozzle and verified

test results obtained from corresponding scale model tests. The extensive coannular acoustic test data also allows further refinement of the acoustic prediction methodology applicable to jet noise.

Both the forward VABI and the acoustic nozzle are integral elements of the follow-on NASA Core-Driven Fan Stage VCE testbed, which is scheduled for test in 1980. The forward VABI results also apply to the next in the series of YJ101/VCE tests - the Navy Full Authority Digital Electronic Control (FADEC) test scheduled earlier in 1980. In this test an advanced FADEC control system will be implemented to operate the various variable cycle features of the same basic engine configuration used for the NASA Forward VABI Test. The follow-on NASA testbed engine with the core driven aft fan block requires some different approaches to the forward VABI selector valve due to the relocation of the engine mid-frame for a better aero/mechanical simulation of projected product study engine features. Otherwise, it is conceptually similar to the earlier Acoustic Nozzle Test Configuration. The testbed engine configuration will use additional interchangeable coannular acoustic nozzle hardware including a larger outer stream area for improved part-throttle aero/acoustic performance and a mechanical (outer stream) suppressor for greater noise reduction. The planned acoustic testing is being expanded in the testbed phase to pursue the evaluation of a treated nozzle ejector shroud and fan noise propagation in conjunction with a boilerplate hybrid supersonic inlet.

Beyond the planned sea level testbed engine test phase, recommended options for continued testing which have been discussed include simulation of forward flight speed effects in the NASA Ames 40 x 80 foot wind tunnel.

The NASA Acoustic Nozzle Engine Tests have verified and further substantiated the results obtained in scale model acoustic tests. A follow-on scale model acoustic program aimed at the definition of the mechanical suppressor to be used in the testbed engine is one element of an extended scale model program which has recently been initiated. This scale model program should be further extended/broadened beyond this scope to include such alternatives as ejector shroud effects, as described earlier, and further advances of the basic coannular nozzle for improved (lower) noise levels, applicable to the projected requirements of an AST product engine. The YJ101/VCE testbed has proven to be a flexible, effective low cost vehicle for advancing/verifying variable cycle concepts. Over 300 hours of testing in five sequential programs has been successfully accomplished to further VCE technology for both Military and Commercial application. The NASA testbed engine program should be extended as described and eventually integrated with a possible F404 based follow-on technology program now in the planning stage.

SYMBOLS AND ABBREVIATIONS

A	Area
A_{Liner}	Surface Area of the Liner
A_0	Ambient Speed of Sound
AR	Area Ratio
A_r	Inner to Outer Stream Flow Area Ratio
AST	Advanced Supersonic Technology
A_T	Total Exhaust Flow Area
A_g^{Mix}	Total Exhaust Area of the Nozzle
BETAOV	Overall Bypass Ratio
BP	Bypass
BPF	Blade Passing Frequency
BPFRI	Inner Bypass Pressure Ratio
BPROV	Overall Bypass Pressure Ratio
CFF	H.P. Compressor Corrected Airflow
C_{f_g}	Thrust Coefficient
D	Conic Nozzle Diameter
DDP14	Inner Duct Inlet (Test Pressure Loss - Predicted Pressure Loss)
DDP15	Bypass Duct Inlet (Test Pressure Loss - Predicted Pressure Loss)
DDP156	Aft Bypass Duct (Test Pressure Loss - Predicted Pressure Loss)
DDP59	Tailpipe (Test Pressure Loss - Predicted Pressure Loss)
DDP94Q	Outer Duct Inlet (Test Pressure Loss - Predicted Pressure Loss)
DDP95Q	Outer Duct (Test Pressure Loss - Predicted Pressure Loss)

SYMBOLS AND ABBREVIATIONS (Continued)

D_{eq}	Equivalent Conic Nozzle Diameter Based On Total Nozzle Flow Area ($D_{eq} = \sqrt{4A_T/\pi}$), ft
DETA22	Rear Block Fan (Test Eff. - Predicted Eff.)
DLETAC	H.P. Compressor (Test Eff. - Predicted Eff.)
DLETAF	Front Block Fan (Test Eff. - Predicted Eff.)
DPB	Double Bypass
DP14	Inner Duct Inlet Pressure Loss
DP15	Bypass Duct Inlet Pressure Loss
DP156	Aft Bypass Duct Pressure Loss
DP59	Tailpipe Pressure Loss
DP61Q7	Total Exhaust Loss
DP94Q	Outer Duct Inlet Pressure Loss
DP95Q	Outer Duct Pressure Loss
EPNL	Effective Perceived Noise Level
ETAC	H.P. Compressor Efficiency
ETAF	Front Block Fan Efficiency
ETAFOV	Overall Fan Efficiency
ETAT	High-Pressure Turbine Efficiency
ETA2T	Low-Pressure Turbine Efficiency
ETA22	Rear Block Fan Efficiency
F	Total Ideal Thrust
FARC	Overall Fuel to Air Ratio
FFF	Total Inlet Corrected Airflow
FF15	Bypass Mixed Stream Flow Function

SYMBOLS AND ABBREVIATIONS (Continued)

FF156	Bypass Mixed Stream Flow Function
Fg or FG	Gross Thrust
FGIR	Corrected Ideal Thrust, Lbf
F _i	1/3 Octave Band Free Field SPL, dB
FN	Net Thrust
F _{ref}	Reference Nozzle Ideal Thrust
f ₁	Blade Passing Frequency (BPF) for the Fan
f ₂	First Harmonic of the BPF for the Fan
f ₃	Second Harmonic of the BPF for the Fan
G _i	SPL Measured by the Ground Plane Microphone for its 1/3 Octave Band
HP	High Pressure
HPC	High-Pressure Compressor
i	Index for 1/3 Octave Band
IDC	Index of Distorted Circumferential
IDR	Index of Distortion Radial
IGV	Inlet Guide Vane
LP	Low Pressure
LPT	Low-Pressure Turbine
M	Mach Number
m	Flight Exponent
MFC	Main Fuel Control
NL	Fan Speed, rpm
OASPL	Overall Sound Pressure Level, dB

SYMBOLS AND ABBREVIATIONS (Continued)

OBSPL	Octave Band Sound Pressure Level, dB
PCNFRT	Front Fan Corrected Speed, %
PCNQRT/PCNRT	H.P. Compressor Corrected Speed, %
PCN1R	Rear Block Corrected Speed, %
p_i	SPL Measured by the Engine Centerline Microphone for the IR 1/3 Octave Band
P_i	Total Pressure of Inner Stream, lb/ft ²
PNL	Perceived Noise Level, PNdB
PNL _N	Thrust and Jet Density Normalized PNL
PNL _p	Peak PNL, PNdB
PNL ₅₀	PNL at $\theta_i = 50^\circ$
PNL ₉₀	PNL at $\theta_i = 90^\circ$
p^o	Total Pressure of Outer Stream
P_o	Ambient Pressure
$\frac{p_i}{r}$	Inner Stream Pressure Ratio
$\frac{p^o}{r}$	Outer Stream Pressure Ratio
p_{r}^{eff}	Defined as $[\frac{P^o}{r} + A \frac{p_i}{r} / 1 + A \frac{p_i}{r}]$
p_{r}^{mix}	Pressure Ratio of the Mass Averaged Stream
PQPOM	Mixed Nozzle Pressure Ratio
PWL	Acoustic Power Level
P3QP25/P3Q25	H.P. Compressor Pressure Ratio
P21521	Front Block Fan Pressure Ratio

SYMBOLS AND ABBREVIATIONS (Continued)

P23Q21	Overall Fan Pressure Ratio
P23Q22	Rear Block Fan Pressure Ratio
P56QP2	Engine Pressure Ratio
R_i	Weighting Factor for the Ground Plane Microphone
RR/RV	Radius Ratio
R_r^i	Inner Stream Radius Ratio
R_r^o	Outer Stream Radius Ratio
R_{xy}	Normalized Correlation Coefficient for Fan Noise
SBP	Single Bypass
SCAR	Supersonic Cruise Aircraft
SFC	Specific Fuel Consumption
SFC640/SF64M	Corrected Ideal Specific Fuel Consumption
SFCIR	Corrected Ideal Specific Fuel Consumption
SI (Suffix)	System Internationale Units
S_i	Weighting Factor for the Engine Centerline Microphone
SPL	Sound Pressure Level
SSP	Sound Separation Probe
T^i	Static Temperature of Inner Stream
T^{mix}	Static Temperature of the Mass Averaged Conditions
T^o	Static Temperature of Outer Stream
T_T^i	Total Temperature of Inner Stream
T_T^{mix}	Mass Averaged Total Temperature

SYMBOLS AND ABBREVIATIONS (Continued)

T_T^O	Total Temperature of Outer Stream
T_1	BPF for the Turbine
T_2	First Harmonic of the BPF for the Turbine
\bar{U}	Time Averaged Mean Turbulent Velocity
u'	Turbulent Velocity
V_a	Aircraft Velocity
VABI	Variable Area Bypass Injector
VATN	Variable Area Turbine Nozzle
VCE	Variable Cycle Engine
VG	Variable Geometry
V_j	Ideal Jet Velocity of Inner Stream
v_j^{mix}	Mass Averaged Jet Velocity
V_j^O	Ideal Jet Velocity of Outer Stream
V_j^i	Ideal Jet Velocity of Inner Stream
VMAIR2/VMAIRM	Mixed Nozzle Corrected Ideal Velocity
V_{iR}	Inner to Outer Stream Velocity Ratio
V_T	Tip Speed of the Fan
\dot{W}_j^i	Inner Stream Ideal Weight Flow Rate
\dot{W}_j^O	Outer Stream Ideal Weight Flow Rate
\dot{W}_T	Total Ideal Weight Flow Rate
$W2/\theta/W2R/W2RM$	Total Inlet Corrected Airflow
W22R	Rear Block Corrected Airflow, lbm/sec

SYMBOLS AND ABBREVIATIONS (Concluded)

W25R	H.P. Compressor Corrected Airflow, lbm/sec
X	Distance Downstream Measured from Nozzle Exit Plane
XETA2T	Low-Pressure Turbine Efficiency
XM	Reference Mach Number
XM14	Inner Duct Inlet Mach Number
XM81	Strut Entrance Mach Number
XM565	Turbine Frame Exit Mach Number
XM59	Mixed Tailpipe Mach Number
XM94	Outer Duct Inlet Mach Number
XM95	Outer Duct Mach Number
XN	Physical Core Speed
XNLRPC	Front Block Corrected Speed
XNF	Physical Fan Speed
β_j	Shock Noise Parameter for Conic Jet, $\beta_j = \sqrt{M_j^2 - 1}$
	where:
	$M = \sqrt{2/\gamma - 1} \times \left[\left(\frac{p_r^{eff}}{r} \right)^{\gamma - 1/\gamma} - 1 \right]$
β_j^{eff}	Shock Noise Parameter for Coannular Jet, $\beta_j^{eff} = \sqrt{M^2 - 1}$
γ	Specific Heat Ratio
ω	Jet Density Exponent
ρ, ρ^{mix}	Jet Density Based on Mass Averaged Conditions
ρ_o	Ambient Air Density
θ_i	Angle Measured with Respect to the Inlet

<u>STATION</u>	<u>DESCRIPTION</u>
2, 2.1	- Front Fan Block Entrance
3	- Compressor Exit
3c	- Control Static Location
8	- Outer Nozzle Throat
14	- Inner Bypass Duct Inlet
14.5	- Inner Bypass Duct Exit
14.6	- Inner Bypass Duct Cooling Flow Scoop
14.8 (or 148)	- Inner Bypass Duct Forward VABI Match Plane
15	- Bypass Duct Inlet
15.5	- Bypass Duct Exit
15.6 (or 156)	- Bypass Duct Rear Frame Entrance
16	- Rear VABI Entrance
18	- Inner Nozzle Throat
21.5 (or 215)	- Front Fan Block Exit
22	- Rear Fan Block Entrance
23	- Rear Fan Block Exit
25	- Compressor Inlet
27 (16.5)	- Rear VABI Exit
47	- Variable Area Turbine Nozzle
56	- Rake Location at LP Turbine Discharge
59	- Mixed Conditions at Matched Plane
94	- Outer Bypass Duct Throat
95	- Compressor Mid-Frame Strut

REFERENCES

1. Allan, R.D.; Advanced Supersonic Propulsion System Technology Study - Phase II, Final Report NASA CR-134913, December 1975.
2. Allan, R.D., and Joy, W. (General Electric Company); Advanced Supersonic Propulsion System Technology Study - Phase III and Phase IV, Final Report, NASA CR-135236, November 1977.
3. Knott, P.R., Stringas, E.J., Brausch, J.F. Staid, P.S., Heck, P.H., and Latham, D.; Acoustic Tests of Duct-Burning Turbofan Jet Noise Simulation - NASA CR-2966, July 1978, (GE NAS3-18008).
4. VCE Early Acoustic Test - Forward Variable Area Bypass Injector and Coannular Acoustic Nozzle Test, CDR-1, NASA (NAS3-20582).
5. FAA RD-76-79-III-IV High Velocity Jet Noise Source Location and Reduction Program. Task III Experimental Investigation of Suppression Principles Volume IV - Laser Velocimeter Time Dependent Cross Correlation Measurements.
6. NASA CR 2760 June 1977, Atmospheric Absorption of High Frequency Noise and Application to Fractional Octave Bands, F.D. Shields and H.E. Bass.
7. Crow, E.L., Davis, F.A., and Maxfield, M.W.; Statistics Manual, Dover Publications, New York, N.Y. 1960, Pages 37 and 226.
8. FAA SS-73-29-1 Supersonic Transport Noise Reduction Technology Program Phase II Volume II, September 1975.
9. Knott, P.R., Stringas, E.J., Brausch, J.F., et al; "Acoustic Tests of Duct-Burning Turbofan Jet Noise Simulation, "NASA CR 2966, July 1978.
10. Knott, P.R., Blozy, J.T., Staid, P.S.; "Acoustic and Performance Investigation of Coannular Plug Nozzles," (NAS3-19777 Contract), NASA CR-3149, June, 1979.
11. Harper-Borne, M., Fisher, M.J.; "The Noise from Shock Waves in Supersonic Jets, AGARD CPF-131, 1973.
12. Maestrello, L.; "An Experimental Study on Porous Plug Jet Noise Suppressor," AIAA Paper No. 79-0673, March 1979.
13. Bhutiani, P.K.; A Unique Coannular Plug Nozzle Jet Noise Prediction Procedure. AIAA Paper 80-1007, June 1980.
14. Moore, M.T., NASA CR-152175 Flight Effects on the Jet Noise Signature of a 32-Chute Suppressor Nozzle as measured in the NASA-Ames 40 by 80 foot wind tunnel, January 1979.

15. Heidman, M.F.; Interim Prediction Methods for Fan and Compressor Source Noise, NASA TMX-71763.
16. Krejsa, E.A., Valerino, M.F.; Interim Prediction Method for Turbine Noise, NASA TMX-73566.
17. Matta, Ram K.; Proposed Appendix to ARP876 - Combustion Noise Prediction. Submitted to SAE21, Jet Noise Subcommittee, July 1977.
18. Hayden, R.E., "Noise from Interaction of Flow with Rigid Surfaces, a Review of the Current Status of Prediction Techniques," Bolt, Bernack and Newman, Report No. 2276.
19. Kazin, S.B. et al; Core Engine Noise Control Program, Volume II - Identification of Noise Generation and Suppression Mechanisms. Section 6.0, Obstruction Noise. (K.R.Bilwakesh) FAA-RD-74-125, II.
20. FAA-RD-76-79, II High Velocity Jet Noise Source Location and Reduction - Task 2, "Theoretical Developments and Basic Experiments," October 1977.
21. FAA-RD-76-79, VI High Velocity Jet Noise Source Location and Reduction - Task 6, "Noise Abatement Nozzle Design Guide," April 1979.
22. Proposed Appendix A of ARP 866 (Static to Flight Jet Noise Estimates) - Letter to SAE A-21 Committee Dated August 5, 1978. (Unpublished)
23. Staid, P.S., "Wind Tunnel Performance Tests of Coannular Plug Nozzles," NASA Report 2990, April 1978.

DISTRIBUTION LIST

NASA CR-159869

NASA-Lewis Research Center
21000 Brookpark Road
Cleveland, OH 44135

Attention:	Report Control Office	M.S. 5-5	1
	Library	M.S. 60-3	2
	J.F. McCarthy	M.S. 3-2	1
	W.L. Stewart	M.S. 3-5	1
	A. Long	M.S. 500-305	1
	M.A. Beheim	M.S. 86-1	1
	D.N. Bowditch	M.S. 86-7	1
	D.C. Mikkelson	M.S. 86-7	1
	R.E. Coltrin	M.S. 86-1	1
	J.F. Wasserbauer	M.S. 86-1	1
	R.J. Weber	M.S. 501-10	1
	L.H. Fishbach	M.S. 501-10	1
	L.C. Franciscus	M.S. 501-10	1
	C.L. Zola	M.S. 501-10	1
	R.A. Rudey	M.S. 60-4	1
	R.G. Willloh	M.S. 60-5	1
	L.M. Hibben	M.S. 500-211	1
	D.A. Petrash	M.S. 60-6	1
	M.J. Hartmann	M.S. 5-3	1
	L.J. Herrig	M.S. 5-9	1
	R. Signorelli	M.S. 106-1	1
	R.W. Schroeder	M.S. 500-207	1
	U.H. von Glahn	M.S. 500-208	1
	J.R. Stone	M.S. 500-208	1
	C.E. Feiler	M.S. 500-208	1
	O.A. Guttierrez	M.S. 500-208	1
	A.G. Powers	M.S. 500-127	12
	Maj. Alan Willoughby	M.S. 501-3	1
	N.T. Musial	M.S. 500-318	1
	J.A. Biaglow	M.S. 60-6	1

NASA Scientific and Technical Information Facility
P.O. Box 8757
Baltimore, Washington International Airport, MD 21240
Attention: Accessioning Department

20

NASA Headquarters
Washington, D.C. 20546

Attention:	W.S. Aiken, Jr.	Code RD-5	1
	J.A. Suddreth	Code RJH-2	1
	J. Levine	Code RJH-2	1
	P. Renas	Code RJP-2	1
	D. Poferl	Code RJP-2	1
	G. Banerian	Code RTP-6	1

NASA-Langley Research Center
Hampton, VA 23665

Attention:	D. Maglieri	M.S. 249B	1
	C. Driver	M.S. 249A	1
	A.J. Morris	M.S. 249B	1
	E. Boxer	M.S. 249B	1
	S. Hoffman	M.S. 249B	1

NASA-Dryden Flight Research Center
P.O. Box 273
Edwards, CA 93523

Attention:	F.W. Burcham	Room 2005	1
------------	--------------	-----------	---

NASA-Ames Research Center
Moffett Field, CA 94035

Attention:	L. Roberts	M.S. 200-3	1
------------	------------	------------	---

Naval Air Propulsion Test Center
Trenton, NJ 08268

Attention:	A.A. Martino	Code PE4	1
	J.J. Curry	Code PE43	1

Air Force Aero Propulsion Lab
Wright Patterson AFB, OH 45433

Attention:	E.E. Bailey	AFAPL/TBD	1
	E.C. Simpson	AFAPL/TB	1
	R. Leo	AFAPL/TBP	1

Pratt & Whitney Aircraft Group
Commercial Products Division
East Hartford, CT 06108

Attention: J.S. Westmoreland	Eng. 3NJ	1
R.B. Hunt	Eng. 3NJ	1
R.W. Hines	Eng. 2NJ	1

The Boeing Commercial Airplane Group
P.O. Box 3999
Seattle, WA 98124

Attention: P. Johnson	Development Center	1
	M.S. 41-52	
G. Evelyn	Development Center	1
	M.S. 41-52	
W. C. Swan	Development Center	1
	M.S. 41-52	
A.D. Welliver	Development Center	1
	M.S. 41-52	

Lockheed-California Company
P.O. Box 551
Burbank, CA 91503

Attention: J. Clauss	Dept. 75-21, Bldg. 63-3	1
	Plant A-1	
L. Bangert	Dept. 75-21, Bldg. 63-3	1
	Plant A-1	

Rockwell International Corporation
Aircraft Products Operations
International Airport
Los Angeles, CA 90009

Attention: R. Tyson	Advanced Transports	1
J. Ford	Advanced Transports	1

Douglas Aircraft Company
3855 Lakewood Boulevard
Long Beach, CA 90801

Attention: R.D. FitzSimmons	Code 35-74	1
W. Rowe	Code 35-74	1

Mr. A.K. Forney
DOT Federal Aviation Administration
Washington, D.C. 20591

1

Mr. Richard Munt
Environmental Protection Agency
2565 Plymouth Road
Ann Arbor, MI 48105

1

DO NOT REMOVE SLIP FROM MATERIAL

Delete your name from this slip when returning material to the library.

NAME	MS
F. Brinkley	149
A. Carty	5/96 168